UNIVERSITÀ DEGLI STUDI DI CATANIA

DIPARTIMENTO DI INGEGNERIA ELETTRICA ELETTRONICA E INFORMATICA

XXXIV ciclo di Dottorato di Ricerca in Ingegneria dei Sistemi Energetici Informatici e delle Telecomunicazioni

---

Thesis of Doctor of Philosophy in Electrical Engineering

Investigation of Approaches for Improving the Performance of Sensorless and Sensor-based AC Motor Drives

by

Luigi Danilo Tornello

PhD Advisor:
Prof. Giacomo Scelba
PhD Coordinator:
Prof. Paolo Pietro Arena

Referees:
Prof. Gianmario Pellegrino
Prof. Roberto Petrella

A. A. 2018-2021

SUMMARY

Acknowledgment

Ringrazio la mia famiglia che mi ha supportato nell'intraprendere il percorso del dottorato di ricerca e che si è sempre resa disponibile ad ogni problema.

Un ringraziamento speciale va alla mia ragazza, Angela, che in questi anni trascorsi insieme abbiamo sempre passato dei bellissimi momenti indimenticabili che hanno sempre più consolidato il nostro amore. Sperando di andare avanti così per altri cento anni, ti ringrazio per avermi sempre sostenuto, supportato e sopportato e dato forza per superare ogni difficoltà.

Ringrazio il mio tutor didattico prof. Giacomo Scelba per avermi supportato durante gli studi di dottorato e per avermi fatto crescere professionalmente.

Ringrazio il gruppo di ricerca di cui faccio parte: Macchine Elettriche, Azionamenti Elettrici ed Elettronica di Potenza, quindi i professori: prof. Giuseppe Scarcella, prof. Mario Cacciato e prof. Giacomo Scelba; i vari collaboratori di ricerca, "i ragazzi del CePTIT", che si sono succeduti negli anni e quelli con cui tutt'ora conviviamo quotidianamente le varie attività di ricerca e non solo.

Infine, ma non per ultimi, ringrazio i miei amici con i quali ho sempre passato delle belle esperienze di vita e di divertimento.

List of Symbols

v_{abcs}	*Three phase stator voltages*
i_{abcs}	*Three phase stator currents*
λ_{abcs}	*Three phase stator fluxes*
p	*Derivative operator*
R_s	*Stator resistance*
L_{ls}	*Leakage inductance*
L_A	*Synchronous inductance*
L_B	*Saliency inductance*
L_{mq}	*q-axis Magnetizing inductance*
L_{md}	*d-axis Magnetizing inductance*
L_q	*q-axis Inductance*
L_d	*d-axis Inductance*
λ_{pm}	*Permanent magnet flux linkage*
T_e	*Electromagnetic torque*
T_L	*Load torque*
θ_{re}	*Electrical angular rotor position*
θ_{rm}	*Mechanical angular rotor position*
ω_{re}	*Electrical rotor speed*
ω_{rm}	*Mechanical rotor speed*
pp	*Pole pairs*
J	*Mechanical inertia*
F	*Viscous Friction Coefficient*
qd	*Synchronous reference frame axes*
$\alpha\beta$	*Stationary reference frame axes*
v_{xyz}	*Search coils voltages*
i_{xyz}	*Search coils currents*
λ_{xyz}	*Search coils linkage fluxes*
M_A	*Synchronous mutual inductance*
M_B	*Saliency mutual inductance*
M_{mq}	*q-axis Magnetizing mutual inductance*
M_{md}	*d-axis Magnetizing mutual inductance*
N_s	*Main winding number of coils*
N_{sSC}	*Search coils number of coils*
λ_{pmSC}	*Search coils linkage permanent magnet flux*
v_{qd1}	*Main stator winding qd-axes voltages*
i_{qd1}	*Main stator winding qd-axes currents*
λ_{qd1}	*Main stator winding qd-axes fluxes*
v_{qd2}	*Search coils winding qd-axes voltages*
i_{qd2}	*Search coils winding qd-axes currents*
λ_{qd2}	*Search coil winding qd-axes fluxes*
$v_{\alpha\beta}$	*Stator winding $\alpha\beta$ - axes voltages*
$i_{\alpha\beta}$	*Stator winding $\alpha\beta$ - axes currents*

$\lambda_{\alpha\beta}$	*Stator winding $\alpha\beta$ - axes fluxes*
^	*Estimated quantities*
ε_θ	*Rotor position error*
ε_ω	*Rotor speed error*
γ	*Vector current angle*
I_s	*Vector current magnitude*
$\Theta_{\alpha\beta}^{(q)}(\theta_{re})$	*Quasi-rotating space vector*
$\theta_{re}^{(q)}$	*Quantized electrical angular rotor position*
$\omega_{re}^{(q)}$	*Instantaneous quantized electrical rotor speed*
N_{DS}	*Rotor position resolution*
f_{BWi}	*Current loop frequency bandwidth*
$f_{BW\omega}$	*Speed loop frequency bandwidth*
f_{BWvto}	*VTO frequency bandwidth*

Acronyms

MOSFET	Metal Oxide Silicon Field Effect Transistor
IGBT	Insulated Gate Bipolar Transistor
SiC	Silicon Carbide
GaN	Gallium Nitride
FOC	Field Oriented Control
VSD	Variable Speed Drives
VFD	Variable Frequency Drives
PM	Permanent Magnet
PMSM	Permanent Magnet Synchronous Machine
IM	Induction Machine
SynchRel	Synchronous Reluctance
PMSynchRel	Permanent Magnet Assisted Synchronous Reluctance Motor
SPMSM	Surface Permanent Magnet Synchronous Motor
IPMSM	Interior Permanent Magnet Synchronous Motor
DTC	Direct Torque Control
PC	Predictive Control
MPDTC	Model Based Predictive Direct Torque Control
MPCC	Model Based Predictive Control
EMF	Electromotive Force
PWM	Pulse Width Modulation
FPE	Fundamental PWM Excitation Based Method
PI	Proportional-Integral Controller
PLL	Phase Locked Loop
VTO	Vector Tracking Observer
SC	Search Coil
CLK	Clock
MVPT	Maximum Voltage Point Tracking
LPF	Low Pass Filter
BLDC	Brushless DC Motor
LPP	Line per Period
FTM	Fixed Time Method
FPM	Fixed Position Method
TSE	Taylor Series Expansion
BDE	Backward Difference Expansion
ZOH	Zero Order Hold
VTSF	Vector Tracking State Filter

List of Figure

List of Tables

Scientific Publications

Articles in International SCI Journals

1) L. D. Tornello et al., "Combined Rotor-Position Estimation and Temperature Monitoring in Sensorless, Synchronous Reluctance Motor Drives," in IEEE Transactions on Industry Applications, vol. 55, no. 4, pp. 3851-3862, July-Aug. 2019.
2) S. Foti, A. Testa, G. Scelba, S. De Caro and L. D. Tornello, "A V2G Integrated Battery Charger Based on an Open End Winding Multilevel Configuration," in IEEE Open Journal of Industry Applications, vol. 1, pp. 216-226, 2020.
3) Tornello, L.D.; Foti, S.; Cacciato, M.; Testa, A.; Scelba, G.; De Caro, S.; Scarcella, G.; Rizzo, S.A. "Performance Improvement of Grid-Connected Induction Motors through an Auxiliary Winding Set", Energies 2021, 14, 2178.
4) G. Scelba, G. De Donato, A. A. M. Elsman, L. D. Tornello, G. Scarcella and F. G. Capponi, "Resolution of Rotor Position Measurement: Modelling and Impact on Speed Estimation," in IEEE Journal of Emerging and Selected Topics in Power Electronics.

Articles in International Conference Proceedings

5) M. Pulvirenti, G. Scelba, G. Scarcella, M. Cacciato and L. Tornello, "On-line stator winding resistance and rotor permanent magnet flux estimation for dual-three phase PMSM drives," IECON 2017 - 43rd Annual Conference of the IEEE Industrial Electronics Society, 2017, pp. 2104-2109.
6) L. D. Tornello, G. Scelba, M. Cacciato, G. Scarcella, A. Palmieri, E. Vanelli, C. Pernaci, R. Di Dio, "FPGA - Based Real-Time Models of IGBT Power Converters," 2018 International Symposium on Power Electronics, Electrical Drives, Automation and Motion (SPEEDAM), 2018, pp. 519-526.
7) G. Aiello, G. Scelba, G. Scarcella, M. Cacciato, L. D. Tornello, A. Palmieri, E. Vanelli, C. Pernaci, R. Di Dio, "Real-Time Emulation of Induction Machines for Hardware in the Loop Applications," 2018 International Symposium on Power Electronics, Electrical Drives, Automation and Motion (SPEEDAM), 2018, pp. 1340-1345.
8) G. Scelba, L. D. Tornello, G. Scarcella, M. Cacciato, A. Testa, S. Foti, M. Pulvirenti, "Combined Rotor Position Estimation and Temperature Monitoring in Sensorless Synchronous Motor Drives," 2018 IEEE 9th International Symposium on Sensorless Control for Electrical Drives (SLED), 2018, pp. 30-35.
9) G. Aiello L. D. Tornello, G. Scelba, G. Scarcella, M. Cacciato, A. Palmieri, E. Vanelli, C. Pernaci, R. Di Dio, "FPGA-Based Design and Implementation of a Real Time Simulator of Switched Reluctance Motor Drives," 2019 21st European Conference on Power Electronics and Applications (EPE '19 ECCE Europe), 2019, pp. P.1-P.8.
10) S. Foti, A. Testa, S. de Caro, T. Scimone, G. Scelba and L. D. Tornello, "A Fault Tolerant AC/DC Converter for Electrical Gen-Set Applications," 2019 21st European Conference on Power Electronics and Applications (EPE '19 ECCE Europe), 2019, pp. P.1-P.10.
11) S. Foti, A. Testa, T. Scimone, S. de Caro, G. Scelba and L. D. Tornello, "An Integrated Battery Charger for EV applications based on an Open End Winding

Multilevel Converter configuration," 2019 21st European Conference on Power Electronics and Applications (EPE '19 ECCE Europe), 2019, pp. P.1-P.8.

12) G. Nobile et al., "A novel model-based approach for the energy management of distributed storage systems in utility-scale PV fields," 2019 21st European Conference on Power Electronics and Applications (EPE '19 ECCE Europe), 2019, pp. P.1-P.10.
13) L. D. Tornello, G. Scelba, G. Scarcella, M. Cacciato, S. Foti and A. Testa, "Sensorless Control of PMSM Drives through Modified Thermistors Wirings," 2019 IEEE 10th International Symposium on Sensorless Control for Electrical Drives (SLED), 2019, pp. 1-6.
14) S. De Caro, S. Foti, T. Scimone, A. Testa, L. D. Tornello and G. Scelba, "A New Self-Commissioning Technique for Sensorless Synchronous Reluctance Motor Drives," 2019 IEEE 10th International Symposium on Sensorless Control for Electrical Drives (SLED), 2019, pp. 1-6.
15) S. Foti, A. Testa, S. De Caro, T. Scimone, L. D. Tornello, G. Scarcella, G. Scelba, "A Novel Three-Phase Multilevel Inverter Topology with Reduced Device Count for Open-end Winding Motor Drives," 2019 IEEE Energy Conversion Congress and Exposition (ECCE), 2019, pp. 3624-3630.
16) S. Foti, A. Testa, S. De Caro, T. Scimone, L. D. Tornello, G. Scarcella, G. Scelba, "A novel Hybrid N-Level T-Type Inverter Topology," 2019 IEEE Energy Conversion Congress and Exposition (ECCE), 2019, pp. 5507-5513.
17) S. Foti, S. De Caro, A. Testa, L. D. Tornello, G. Scelba and G. Scarcella, "Grid-Connected Open-end Winding Induction Motor Drives," 2020 International Symposium on Power Electronics, Electrical Drives, Automation and Motion (SPEEDAM), 2020, pp. 30-35.
18) S. Foti, S. D. Caro, A. Testa, L. D. Tornello, G. Scelba and M. Cacciato, "An Open-End Winding Hybrid Transformer," 2020 International Symposium on Power Electronics, Electrical Drives, Automation and Motion (SPEEDAM), 2020, pp. 173-177.
19) A. Testa, S. Foti, S. De Caro, L. D. Tornello, G. Scelba and G. Scarcella, "Optimal Selection of the Voltage Modulation Strategy for an Open Winding Multilevel Inverter," 2020 IEEE Energy Conversion Congress and Exposition (ECCE), 2020, pp. 2231-223.
20) L. D. Tornello, G. Scelba, G. De Donato, F. Giulii Capponi, G. Scarcella and Mark Harbaugh, "Selection of Rotor Position Sensor Resolution for Variable Frequency Drives Utilizing Fixed-Position-Based Speed Estimation", Accepted and under publication in 2021 IEEE Energy Conversion Congress and Exposition (ECCE 2021).
21) L. D. Tornello, G. Scelba, A. Spampinato, G. Forte, "Performance Analysis of a Fault Isolation System for Fault-Tolerant Voltage-Fed PWM Motor Drives", Accepted and under publication in 2021 IEEE Energy Conversion Congress and Exposition (ECCE 2021).

Some of the work presented in the journal and conference papers above has been implemented in this thesis. The link between the chapters of this thesis and the papers listed above is given in Table I.

Table I *Link between the chapters and the published papers.*

Chapter	1	2	3	4	5
Paper	-	1,8,13	4	4, 20	10,15,19, 21

Introduction

The reduction of greenhouse gases is still a serious problem that is faced by all industrialized countries and partly by emerging ones. In this regard, the transport sector is one of the main responsible for CO_2 emissions, which must be subjected to substantial improvements regarding environmental efficiency.

The electrification of vehicles is considered as the main choice for achieving this objective; in fact, the most promising technology, from the point of view of competitiveness, is that of hybrid/electric vehicles. In recent years, some changes in the automotive industry are increasingly pushing scientific research into finding innovative technical solutions to improve existing hybrid vehicle technology.

Even the European Commission, in addressing the problem of the use of energy and greenhouse gas emissions, has acknowledged that to improve efficiency and energy savings it is necessary to adopt appropriate strategies in the transport sector. To this end, the European Commission has recently published two packages related to road transport: "Europe on the move" (proposal for clean, competitive and connected mobility, May 2017 [1]) and "Guide to clean mobility" (proposal to strengthen global EU leadership in clean vehicles, November 2017 [2]). In both proposals, the European Commission indicates CO_2 emission reductions, in particular, both for cars and vans, average CO_2 emissions must be 30% lower in 2030, compared to 2021. Targets set for 2030 they are not only meant to provide less polluting vehicles, but also to provide long-term stability to producers' investments, as the new CO_2 standards will have a significant impact on the research and development expenditure of European vehicle manufacturers. In the US, such an effort is driven by Vehicle Technologies Office of the Department of Energy.

The latest regulation issued by the European Parliament "COM (2017) 676" [3], examines the types of light commercial vehicles (Light Duty Vehicles - LDV) to accelerate the production of low-emission vehicles, since these are responsible for approximately 15% of total EU CO_2 emissions. To reach these emission levels it is necessary to increase the level of electrification within the propulsion unit, i.e., by developing increasingly electric hybrid engines. The specifications required for electrical units are demanding in terms of power density, temperature, efficiency, fault tolerance, material recycling and related cost. The electrification of the vehicle requires an integrated approach, including the advanced design of electronic power converters, coupled with the development of appropriate control algorithms to overcome the current technological barriers.

Limited space, efficiency and thermal requirements also influence the electric drive design. In this regard, Wide Band Gap (WBG) devices are a very promising technology [4]. The use of gallium nitride (GaN) or silicon carbide (SiC) devices, thanks to higher switching frequencies (>> 100 kHz) and junction temperature (> 150 ° C), compared to silicon technology (Si), they allow the use of reduced cooling systems and increasingly smaller filters, maintaining the highest possible levels of efficiency even for medium power drives.

In Figures 1 and 2, market trends and invested capital related to Wide Band Gap technologies (SiC and GaN) are presented; while, in Figure 3, the market segments that the WBG semiconductor devices will occupy compared to the existing silicon (Si) technology are presented:

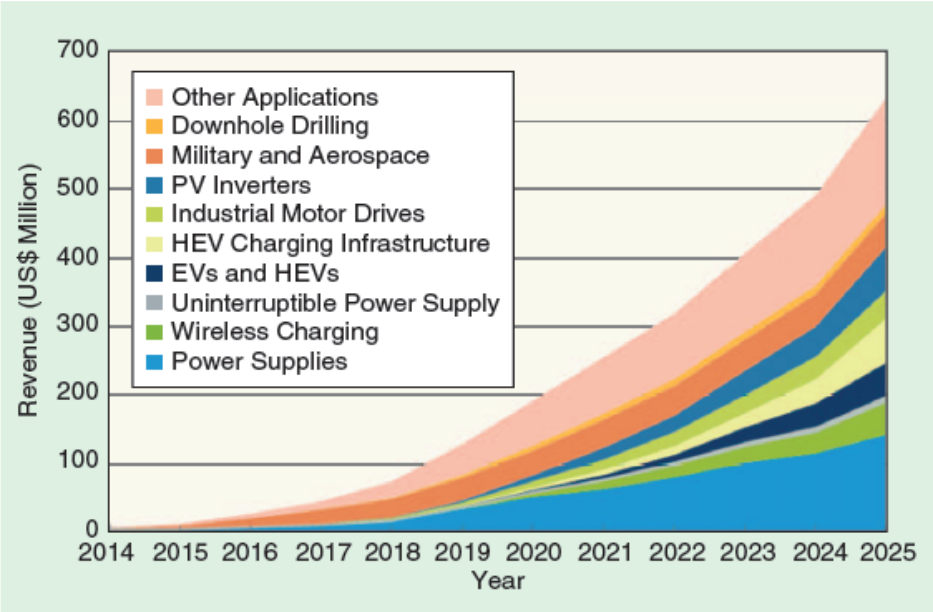

Figure 1 *Market analysis conducted by research firm IHS Markit Technology which shows earnings estimates from sales of GaN devices in the coming years [5].*

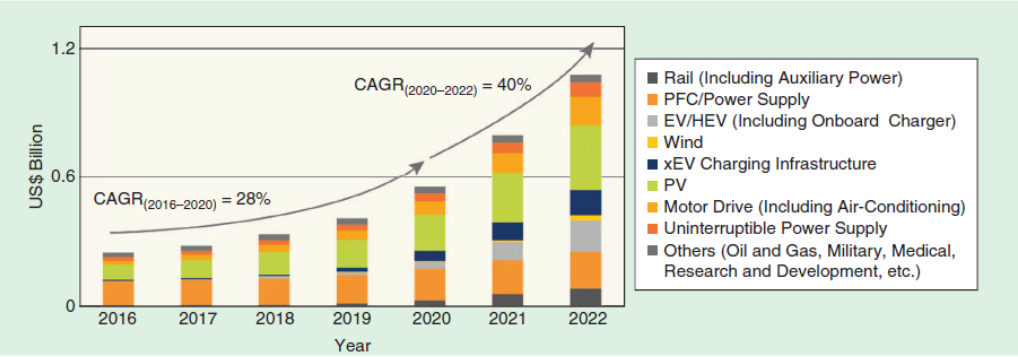

Figure 2 *Market forecast on SiC (Yole Developpement) devices [5].*

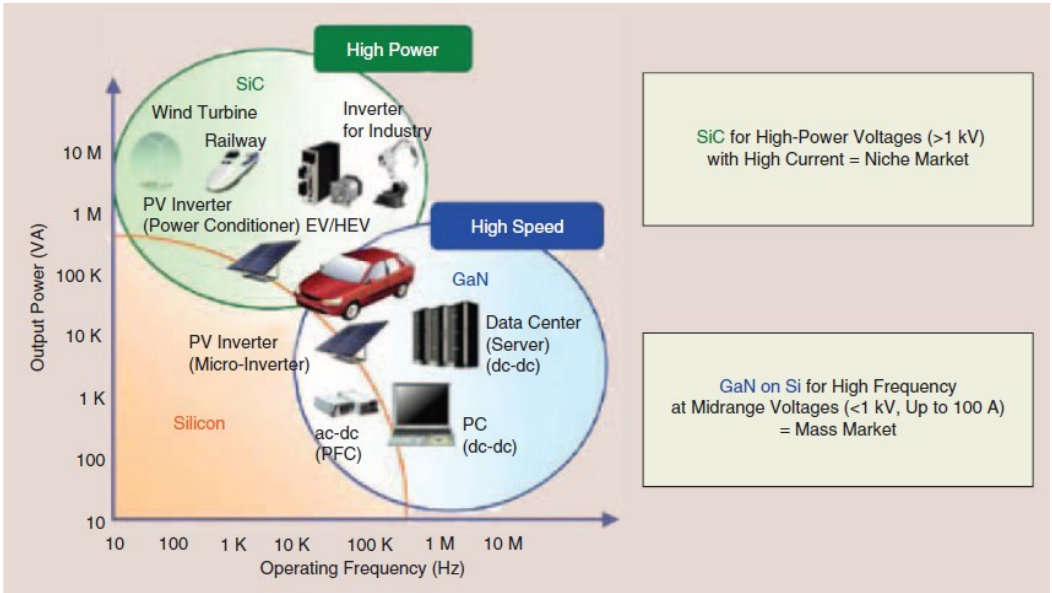

Figure 3 *Market slices occupied by WBG and Si technologies in terms of frequency and power (Rensselaer Polytechnic Institute) [6].*

Currently, both the Department of Energy (U.S.) and the European Commission are providing significant funding for the development of WBG technology in automotive applications [7]-[8].

Another important aspect concerning the electrification of the vehicle is related to the energy saving and the reduction of greenhouse gases is obtained by using also high-performance electric machines.

Electric machines in electric vehicles (EVs) are expected to be high efficiency, have high rated torque, high starting torque, wide speed range, high overload capacity, high power at cruising speeds, high constant power speed range, high specific power and power density, fast dynamic response, good flux weakening capability at high speeds, high reliability, and good fault tolerance characteristics. These important requirements are essential regardless of machine type. However, the topology and principle of operation of the machine dictates the design and control measures that are needed to meet these requirements. The machine that meets all these requirements must be at a cost that is acceptable. Table 1 shows the specification parameters of recent vehicles, gleaned from various sources. Even if some insight can be obtained, putting these data side by side, it is difficult to compare these values without putting the vehicle traction drive system architecture and/or hybridization strategy in perspective. Even then, the machines are different in several respects including the fact that some vehicles use two machines while others use one. It is therefore difficult to compare these machines in any meaningful way, however, it is informative to see some trends including moving away from induction machines (IMs) toward the use of permanent magnet (PM) machines for most of the traction applications. However, there are a lot more machine types that can be potentially applied in electric vehicles [10].

Table 1 *Traction machine specifications [10].*

Model	***Year***	***Motor Type***	***Peak Power kWp***	***Peak Torque Nm***	***Max Speed rpm***	***Poles***	***Peak Specific Power kW/kg***	***Peak Power Density kW/L***
Roadster	*2008*	*IM*	*215*	*370*	*14000*	*4*	*4.05*	*-*
Tesla S60	*2013*	*IM*	*225*	*430*	*14800*	*4*	*-*	*-*
Model 3	*2017*	*PM*	*192*	*410*	*18000*	*6*	*-*	*-*
Prius	*2004*	*PM*	*50*	*400*	*6000*	*8*	*1.1*	*3*
Prius	*2010*	*PM*	*60*	*207*	*13500*	*8*	*1.6*	*4.8*
Prius	*2017*	*PM*	*53*	*163*	*17000*	*8*	*1.7*	*3.35*
Accord	*2006*	*PM*	*12*	*136*	*6000*	*16*	*0.53*	*2.83*
Accord	*2014*	*PM*	*124*	*-*	*14000*	*8*	*2.9*	*2.93*
Spark	*2014*	*PM*	*105*	*540*	*4500*	*12*	*-*	*-*
Volt	*2016*	*PM*	*111*	*370*	*12000*	*12*	*-*	*-*
Bolt	*2017*	*PM*	*150*	*360*	*8810*	*8*	*-*	*-*
Leaf	*2012*	*PM*	*80*	*280*	*10390*	*8*	*1.4*	*4.2*
Leaf	*2017*	*PM*	*80*	*280*	*10390*	*8*	*1.4*	*4.2*
Camry	*2007*	*PM*	*70*	*270*	*14000*	*8*	*1.7*	*5.9*
Camry	*2013*	*PM*	*70*	*270*	*14000*	*8*	*1.7*	*5.9*
Lexus	*2008*	*PM*	*110*	*300*	*10230*	*8*	*2.5*	*6.6*
Sonata	*2011*	*PM*	*30*	*205*	*6000*	*16*	*1.1*	*3.0*
BMW i3	*2016*	*PM*	*125*	*250*	*11400*	*12*	*3*	*9.1*

Figure 4 shows the potential motor types and possible choices for EV applications. The basic types of machines used in electric vehicles are: induction machines, permanent magnet synchronous machines, switched reluctance machines and synchronous reluctance machines. In most recent vehicles, three classes of machines have been applied including induction machines, synchronous machines, permanent magnet machines and reluctance machines. Various configurations of machines have been used or are potential motors to be used, including radial flux and axial flux permanent magnet synchronous machines, induction machines, switched reluctance machines and flux switching machines [10].

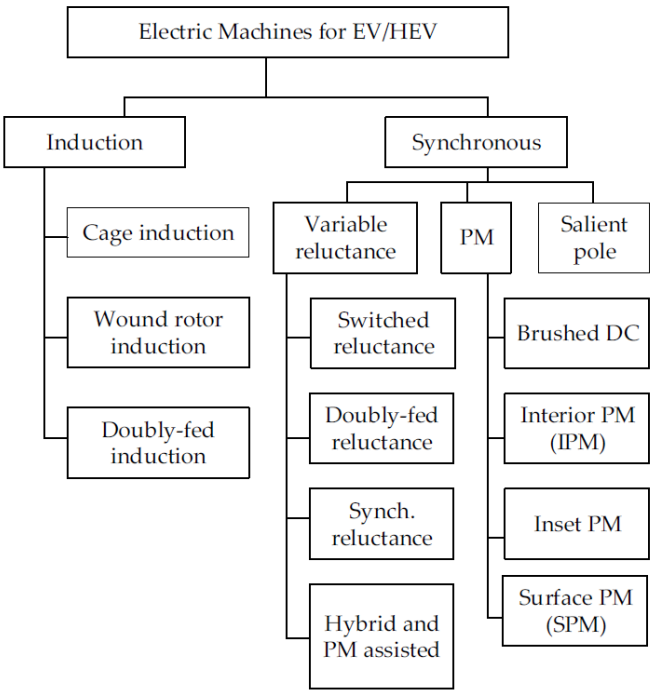

Figure 4 *Motor types aviable for electric vehicles/hybrid electric vehicles (EV/HEVs) [10].*

In this new general context, the vector controls in the electric drives are used to save electric energy and increase the productivity in variable-output work process of all new and well-established industries such as: digital information gadgets, digital home appliances, automotive and robotic electric actuators, pump compressors, hybrid and electric vehicles, industrial processes, and distributed and renewable energy system electric generators. With power levels that go from less then 1W to 100MW, VSDs have become in the last 20 years a very dynamic worldwide industry/market [9].

Vector controls represents a very robust way to control electrical machines in alternating current (AC), in fact it are generally used in all those systems that require high dynamics in terms of torque and speed and in particular in automotive systems. The basic idea that guarantees a decoupled control of the magnetic flux and electromagnetic torque.

Vector controls are used on AC electrical machines, both asynchronous and synchronous and in both cases, it is necessary to measure or estimate the rotor flux position, but in any case, it is necessary the rotor position measurement.

Then, when we talk about sensored control, we will indicate a vector control where it exploits the position sensors to measure the rotor position. This type of control has been widely used in electric drives for more than 20 years.

In recent decades, sensorless control techniques have been developed as well. The latter are used a wide application as they don't require mechanical sensors to measure the rotor position and therefore allow to realize electrical drives with high dynamic

performance but with reduced costs and sensors data transmission cables. Obviously, since vector control relies on knowing the rotor position is necessary, sensorless controls need an algorithm that allows to estimate the position of the rotor flux.

The advantages of a sensorless control allow to realize electric drives with good dynamic performance, comparable with the sensored ones, or lower costs and high reliability; on the contrary, the disadvantages are related to the type of the rotor position estimation algorithm; in fact, many rotor position estimation algorithms don't guarantee a good operating work in the whole operating range of the drive; moreover, many rotor position estimation algorithms are sensitive to parametric variation and other limits are related to the signal-to-noise ratio (SNR).

In most applications, where high dynamic performances are required, the measurement of the rotor position is essential. For example, in automotive applications, such as: electric vehicles, avionics or marine applications, or aerospace applications, etc., for safety reasons, the presence of the position sensor is necessary; while the sensorless algorithms are mostly used when the position sensor fails; in fact, in order to maintain the same performance of the drive, the control unit start the sensorless algorithm when a fault in the position sensor is detect. Obviously, the control unit recommends replacing the faulty position sensor, as it is necessary for safety reasons.

Also widespread are those applications in which it is necessary to vary the speed of the drive; in fact, variable speed drives (VSDs) are widespread in many sectors, from household appliances to large compressors, pumps and fans, wherever speed control is required for energy saving or process control. Speed control requires speed feedback; on the other hand, position feedback is mandatory for field orientation in frequency converters, for switching in BLDC drives and for any application that requires position control. Due to cost, reliability and space constraints, the only motion sensor used in VSDs is the position sensor: the speed must be estimated from the position measurement.

Recently a particular interest in low-cost sensors has been considered, for instance, high resolution linear and magnetoresistive Hall effect sensors [11] – [14]. The main concern with these technologies is their limited accuracy, in fact several methods have been proposed to improve it [13]. In other cases, it has focused on the effect of low-resolution binary Hall effect sensors.

The main concern is related to quantization noise present in the measurement and ways to reduce it have been investigated. Although it is known that when the resolution of the position sensor decreases the speed estimate deteriorates, however, a complete understanding of the effects of position sensor resolution in VSDs has yet to be achieved. A fundamental but open problem is: how does a specific resolution of the position sensor affect the performance of the drive in the event of periodic torque disturbances? Such knowledge would be of great help to a technician when selecting the resolution of the position sensor, in order to minimize costs while at the same time achieve the desired command tracking and the required disturbance rejection.

The main of this thesis are to contribute to the improvement of performances of electric drives, by reducing the costs, reducing the assessment volume, increasing energy efficiency and improving the dynamic performance both with low resolution position sensors and also sensorless algorithms and at the same time guaranteeing some key aspects related to the reliability of AC motor drives such as fault tolerant, overheating protection, rotor position sensor failure and unexpected shutdowns. These objectives are achieved by exploiting the presence of thermistors for thermal monitoring of the AC motor for the development of sensorless algorithms able of replacing the position sensor, but also by reducing costs on the position sensor by selecting its resolution based on the application and desired dynamic performance. Furthermore, the combination between the

multilevel converter topologies and open-end winding motors allows to achieve fault tolerant solutions, increasing the energy efficiency and improving the power quality.

The thesis is composed of five chapters:

1. The chapter 1 deals with a review on state of art existing sensorless algorithms, examining the history of sensorless algorithms and focusing on one kind of sensorless algorithm based on back-EMF which will be used in the chapter 2;
2. The chapter 2 deals an alternative way to estimate the rotor position in AC motors, exploiting the wiring of thermistor embedded in the stator winding for temperature monitoring purposes. Specifically, thermistor wirings embedded in the stator winding are suitably modified in order to turn them in a set of search coils. Since these coils can be connected to the drive control system exploiting existing Thermistor cablings, only a minimal departure from a standard machine design is required. A suitable rotor position estimation technique fully independent from motor parameters will be presented by using the obtained set of search coils. Such a technique can be used alone or to improve the performance of conventional Back-EMF based sensorless techniques. In the proposed approach as well as the compatibility between rotor position estimation and temperature monitoring have been assessed.
3. The chapter 3 introduces the different technologies of the position sensors and their properties; in particular, the chapter involves the development of mathematical models through spatial Fourier approach to descript the effects of a finite resolution in a position sensor. Since in most applications it is preferred to estimate the speed from the measurement of the rotor position, chapter 3 will continue with the introduction of the main speed estimation algorithms used both electric drives with position sensors and electric drives with sensorless algorithms.
4. In those applications where safety comes first, the use of the position sensor is essential. In this chapter 4, the main contribution was to provide guidelines for the best selection of the position sensor based on the specifications and dynamic performance required for the drive. These guidelines will be addressed for two different types of speed estimation algorithms.
5. Finally, the chapter 5 summarizes the other research activities developed to improve the energy efficiency, power quality and fault tolerant capability of electric drives. In particular, the research activities focused on the investigation of technical solutions for double three-phase winding motors and/or open-end winding motors solutions, by using multilevel power conversion topologies. These solutions allowed to increase the energy efficiency, the power quality improvement and the fault tolerant ability of the drive.

References

[1]“Energy union and climate Priority: Making energy more secure, affordable and sustainable”.
[2] “Europe on the Move: Commission takes action for clean, competitive and connected mobility”.
[3] https://eur-lex.europa.eu/legal-content/EN/TXT/?qid=1531729403464&uri=CELEX:52017PC0676R(01)

[4] C. Pavel et al., “Substitution of critical raw materials in low-carbon technologies: lighting, wind turbines and electric vehicles”, JRC Science for Policy Report, Publications Office of the European Union, 2016.
[5] Ashok Bindra, “Wide-Bandgap Poer Devices: Adoption Gathers Momentum”, IEEE Power Electronics Magazine, vol. 5, 2018.
[6] Juan Carlos Balda, Alan Mantooth, “Power-Semiconductor Devices and Components for New Power Converter Developments: A key enabler for ultrahigh efficiency power electronics”, IEEE Power Electronics Magazine, vol. 3, 2016.
[7] Ashok Bindra, “Wide-Bandgap-Based Power Devices: Reshaping the power electronics landscape”, IEEE Power Electronics Magazine, vol. 2, pages: 42-47, 2015.
[8] https://www.energy.gov/eere/vehicles/power-electronics-research-and-development
[9]I. Boldea, "Control issues in adjustable speed drives," in IEEE Industrial Electronics Magazine, vol. 2, no. 3, pp. 32-50, Sept. 2008.
[10] Agamloh, E.; von Jouanne, A.; Yokochi, A. An Overview of Electric Machine Trends in Modern Electric Vehicles. Machines 2020, 8, 20.
[11] C.W. Secrest, J.S. Pointer, M.R. Buehner, and R.D. Lorenz, “Improving position sensor accuracy through spatial harmonic decoupling, and sensor scaling, offset, and orthogonality correction using self-commissioning MRAS methods,” IEEE Trans. Ind. Appl., vol. 51, no. 6, pp. 4492 – 4504, Nov./Dec. 2015.
[12] L. Masisi, and P. Pillay, “High-resolution low-cost position sensor for traction applications,” in Proc. of IEEE IECON, Oct. 2017, pp. 1971-1976.
[13] D. Reigosa, D. Fernandez, C. Gonzalez, S.-B. Lee, and F. Briz, “Permanent magnet synchronous machine drive control using analog Hall-effect sensors,” IEEE Trans. Ind. Appl., vol. 54, no. 3, pp. 2358 – 2369, May/Jun. 2018.
[14] R. Raja, T. Sebastian, M. Wang, A. Gebregergis, and M.S. Islam, “Effect of position sensor error on the performance of permanent magnet machine drives,” IEEE Trans. Ind. Appl., vol. 53, no. 6, pp. 5518 – 5526, Nov./Dec. 2017.

Chapter 1. Sensorless Techniques for Synchronous Motor Drives

1.1 Introduction

Today, permanent magnet (PM) synchronous motors are the dominant technologies for many applications: industrial applications, household appliances, electric traction, marine propulsion, aerospace, elevators and wind power generation [1]. The high efficiency, high torque density, high overload capability, fast dynamic response and desirable wide speed range performance of these motors have made the technology popular with manufacturers [2] - [4]. PM materials are the most important elements of PMSMs. Two commonly applicable PM materials for PMSMs are neodymium iron-boron (Nd-Fe-B) and samarium-cobalt (Sm-Co), both of which contain rare earth elements [5] - [6].

Although the excellent performance and high efficiencies of PMSMs have already conquered much of the power application market, the dramatic rise and fall in the price of permanent magnets has directed research towards rare earth-free machines to [7] - [8]. Reliability issues in PMSM due to possible magnet failures are also considered.

The rotor design of the SynchRel sets it apart from IM and PMSM. Compared to those conventional motors, the SynchRel achieves higher reliability and easier maintenance (due to the very low temperature of the winding and bearing, and also missing the cage rotor structure or PM) [9] - [10], lower cost (due to lack of PM than PMSMs), faster dynamic response (due to smaller size in the same power range and lower moment of inertia), higher speed range (due to wide operation at constant power compared to IM) [11] and higher efficiency in the same power range with the same size (due to cold rotor operation compared to IM) [12] - [18], and higher power density and higher torque per ampere with respect to IM [19] - [23]. In this sense, SynchRel offers the high performance of a PMSM, while it can be as cheap, simple and easy to service as the IM. Therefore, the attention paid to these motors in high-speed applications has seen a continuous growth in the literature which has convinced electric vehicle (EV) and hybrid electric vehicle (HEV) manufacturers to apply SynchRel as an alternative to PMSM [24] - [25]. That said, the ability to drive with the same VSDs for IM and PMSM in various newly designed VSDs has provided a solid development base for SynchRel [26]. Mainly, the high efficiency of SynchRel versus IM has attracted attention for applications such as pumps and fans. Furthermore, the ability to operate at high performance and particularly wide speeds with consideration of the lack of rare earth PMs compared to PMSMs prompted researchers to study these motors for traction applications. It is worth mentioning that in some applications such as pumps, fans and conveyors, IMs are the dominant motors, which can be designed to be replaced by SynchRels.

Although SynchRel avoids PM in its structures, it sacrifices the efficiency, power factor and torque density of PM motors. The torque produced by the SynchRel is purely reluctance torque due to the salience and anisotropy of the rotor. This contributes to the high saturation of this engine, which limits the flux density The addiction of ferrite PM to the rotor of the SynchRel allow to define a new synchronous motor type the Permanent

Magnet Assisted Reluctance Synchronous Machine (PMSynchRel) that exploits simultaneously the unique rotor characteristics of the SynchRel and the high performance of the PMSM, as shown in [63]. These motors have desirable performance at above basic speeds while meeting the requirements of the constant power speed range [27] - [28]. The currents for the same pair are decreased in the PMSynchRel. As a result, losses also decrease, especially for the partial load. A significant variation of the power factor increases of about 10% for low currents and 6% for high currents is achieved. On the other hand, in terms of maintenance, production and assembly, SynchRel and IM are superior to PMSynchRel. Also, similar to SynchRels, PMSynchRels suffer from higher torque ripple [29].

Nowadays, VSDs have been applied in many industries for efficient, high performance, robust and precise control of electric motors. In particular, as discussed above, these performances can be guaranteed by different synchronous motor topologies (PMSM, SynchRel and PMSynchRel). Without taking into account the strengths and weaknesses of each synchronous motor technology, vector control is able to guarantee the high performance discussed above.

There are several algorithms that are recognized as vector control methods, addressed in the literature, and implemented in many industrial VSDs; among them we classify them as: field-oriented control (FOC), direct torque control (DTC) and predictive control (PC) methods, including model-based DTC (MPDTC) and model-based predictive control (MPCC). The use of electric drives for alternating current motors exploiting vector controls are widely used in various applications: industrial automation, transport sector, automotive, electric traction and in the household appliances sector. Many of these applications require a position or speed or torque control with high dynamic performance, sturdiness and reliability are, in fact, guaranteed by vector control. However, in various applications where cost reduction, space reduction and greater robustness are required with respect to position sensor failures, sensorless algorithms represent the most suitable solution more than 20 years.

Meanwhile, sensorless controls (also known as self-sensing) are becoming more and more popular in many industrial but also domestic applications, presenting some advantages in synchronous motors (PMSM, SynchRel or PMSynchRel) due to cost reduction, scaling system and reliability. As shown in Fig. 1.1.1, an enormous effort has been made in the last 20 years to develop sensorless control techniques for a wide range of speeds: from low speeds to high speeds.

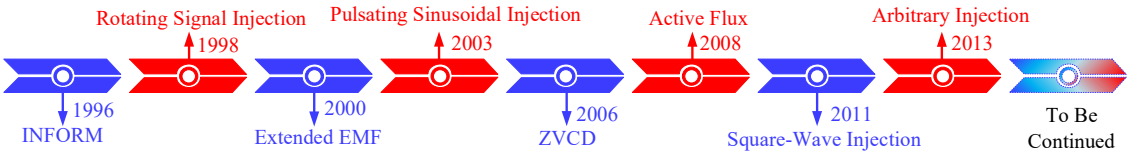

Figure 1.1.1 *Time Line of Sensorless Control on PMSM Motor Drives.*

Sensorless control schemes can be classified into two main categories:

- Model based sensorless (applied in medium-high-speed range)
- Saliency based sensorless (applied in the low-speed range)

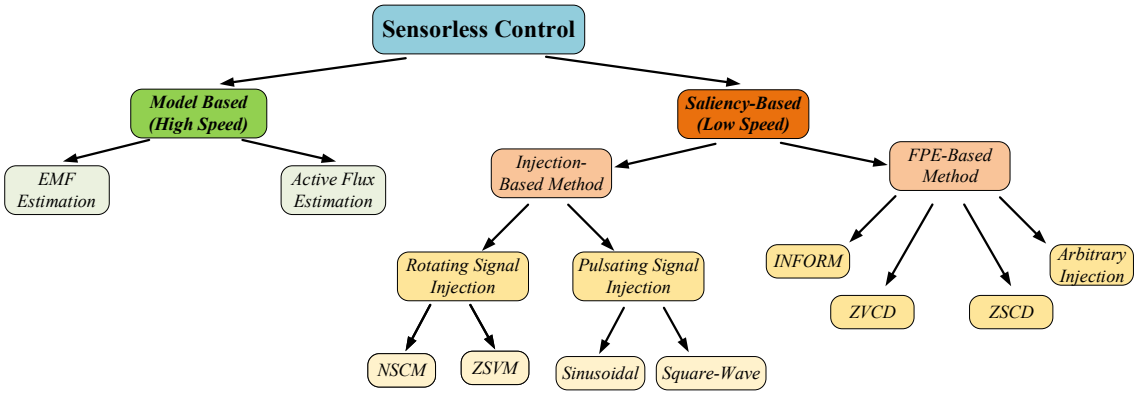

Figure 1.1.2 *Classification of Sensorless Control for Synchronous Motor Drives.*

The model-based method can be implemented using the electromotive force (EMF) or the flux associated with the fundamental excitation [30] - [50] and can be divided into open-loop and closed-loop methods. The first category are derived from the integration of the back-EMF of the machine without any correction term; while the latter makes use of the error between some estimated and measured quantities as feedback to increase their performance. Although model-based methods are first proposed and commercialized, they fail in the low-speed range due to low signal-to-noise ratio caused by model uncertainty, inverter non-linearities, etc. To expand control sensorless for low speed or zero speed, the method based on saliency monitoring has been developed, including methods based on additional high frequency magnetic field [51] - [67] and excitation-based methods by PWM (FPE) [68] - [77].

Due to the growing expansion of sensorless control applications in PMSM drives, this first chapter will describe some of the most known sensorless algorithms. In particular, the one based on the estimation of the back-EMF will be described in more details as a model-based sensorless algorithm; instead, the injection-based method will be described in more details as a sensorless algorithm based on saliency.

1.2 Model-Based Sensorless Control Methods

Model-based sensorless controls can be easily derived from the fundamental wave mathematical models of electrical machines they are used in various applications where the drives are operated at medium-high speeds.

In general, in model-based sensorless methods, the rotor flux position estimation procedure is conventionally divided into two parts, Fig.1.2.1, state filter or observer for EMF estimation and position/velocity observer for estimating the position of the rotor flux and mechanical speed:

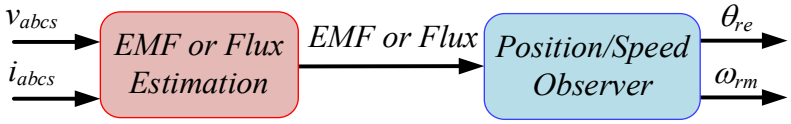

Figure 1.2.1 *General Structure of Model Bases Sensorless Algorithm.*

EMF or the flux associated can be implemented using open loop methods and closed loop methods. Generally closed-loop methods are the most used and are preferred for their strong robustness and high precision. The estimate of the EMF or the Active Flux can be achieved by exploiting the mathematical models of the synchronous machines expressed in the stationary reference $\alpha\beta$ or in a synchronous reference qd.

1.3 Synchronous Machine Model

The study of model-based sensorless controls it require the knowledge of the mathematical models of the various synchronous machines. In general, it is possible to consider the mathematical model of an interior permanent magnet synchronous machine as a reference model [78]. Therefore, the set of voltage and flux equations are given respectively in (1.3.1) and (1.3.2):

$$\begin{bmatrix} v_a \\ v_b \\ v_c \end{bmatrix} = \boldsymbol{R_s} \begin{bmatrix} i_a \\ i_b \\ i_c \end{bmatrix} + \frac{d}{dt} \begin{bmatrix} \lambda_a \\ \lambda_b \\ \lambda_c \end{bmatrix} \tag{1.3.1}$$

$$\begin{bmatrix} \lambda_a \\ \lambda_b \\ \lambda_c \end{bmatrix} = \boldsymbol{L_s}(\theta_{re}) \begin{bmatrix} i_a \\ i_b \\ i_c \end{bmatrix} + \boldsymbol{\Lambda_{pm}} \tag{1.3.2}$$

where $\boldsymbol{R_s}$, $\boldsymbol{\Lambda_{pm}}$ e $\boldsymbol{L_s}(\theta_{re})$ are the stator resistance matrix, the permanent magnet vector and the inductance coefficients matrix respectively:

$$\boldsymbol{R_s} = \begin{bmatrix} R_s & 0 & 0 \\ 0 & R_s & 0 \\ 0 & 0 & R_s \end{bmatrix} \qquad \boldsymbol{\Lambda_{pm}} = \lambda_{pm} \begin{bmatrix} sin(\theta_{re}) \\ sin(\theta_{re} - 2\pi/3) \\ sin(\theta_{re} + 2\pi/3) \end{bmatrix}$$

$$\boldsymbol{L_s}(\theta_{re}) = \begin{bmatrix} L_{ls}+L_A-L_B cos(2\theta_{re}) & -0.5L_A-L_B cos(2\theta_{re}-2\pi/3) & -0.5L_A-L_B cos(2\theta_{re}+2\pi/3) \\ -0.5L_A-L_B cos(2\theta_{re}-2\pi/3) & L_{ls}+L_A-L_B cos(2\theta_{re}-4\pi/3) & -0.5L_A-L_B cos(\theta_{re}+2\pi) \\ -0.5L_A-L_B cos(2\theta_{re}+2\pi/3) & -0.5L_A-L_B cos(2\theta_{re}+2\pi) & L_{ls}+L_A-L_B cos(2\theta_{re}+4\pi/3) \end{bmatrix}$$

where L_A is the magnetizing synchronous inductance and L_B is the saliency inductance:

$$L_A = \frac{L_{md} + L_{mq}}{3} \qquad L_B = \frac{L_{md} - L_{mq}}{3}$$

The electromagnetic torque expression and the mechanical system equation are defined in (1.3.3) and (1.3.4), respectively:

$$T_e = pp \left\{ [i_a\ i_b\ i_c] \frac{d\boldsymbol{\Lambda_{pm}}}{d\theta_{re}} + \frac{1}{2} [i_a\ i_b\ i_c] \frac{d\boldsymbol{L_s}(\theta_{re})}{d\theta_{re}} \begin{bmatrix} i_a \\ i_b \\ i_c \end{bmatrix} \right\} \tag{1.3.3}$$

$$\begin{cases} T_e = T_L + J\dfrac{d\omega_{rm}}{dt} + F\omega_{rm} \\ \omega_{rm} = \dfrac{d\theta_{rm}}{dt} \end{cases} \tag{1.3.4}$$

Equations (1.3.1) - (1.3.4) define the mathematical model of an IPMSM, neglecting the effects of magnetic saturation, magnetic hysteresis, and cross saturation. In general, in PMSM, the q-axis inductance is greater than the d-axis inductance, i.e., $L_q > L_d$ (or $L_B < 0$) this is due to the high reluctance of the magnetic material in the d-axis.

When a synchronous machine with surface mounted permanent magnets SPMSM is considered, i.e., an isotropic synchronous machine, the inductances of axis q and axis d

are identical, $L_d = L_q$ simplifying the matrix of inductances $\boldsymbol{L_s}$ and eliminating the dependence with the position of rotor:

$$L_{\mathrm{A}} = \frac{2}{3} L_{ms} \qquad L_{\mathrm{B}} = 0 \qquad \boldsymbol{L_s} = \begin{bmatrix} L_{ls}+L_A & -0.5L_A & -0.5L_A \\ -0.5L_A & L_{ls}+L_A & -0.5L_A \\ -0.5L_A & -0.5L_A & L_{ls}+L_A \end{bmatrix}$$

This simplification will have repercussions in (1.3.3) heading to an electromagnetic torque dependent only on the flux vector of the permanent magnet $\boldsymbol{\Lambda_{pm}}$.

Finally, if we consider a synchronous reluctance machine (SynchRel), there are not permanent magnets, i.e., $\lambda_{pm} = 0$, and d-axis inductance is greater than the q-axis inductance, $L_d > L_q$, and thus $L_B > 0$. This implies that the equation (1.3.3) of the electromagnetic torque is depending only on the magnetic saliency of the machine and therefore on $d\boldsymbol{L_s}(\theta_{re})/d\theta_{re}$, being $\boldsymbol{\Lambda_{pm}} = 0$.

1.4 Back-EMF State Filter

After having defined the mathematical models of the synchronous machines, now it is possible to refer these models in a synchronous reference frame with the rotor flux position (qd) to build the back-EMF estimator; suitable reference frame transformation matrices are required (1.4.1):

$$\boldsymbol{K_{qd}} = \frac{2}{3}\begin{bmatrix} \cos(\theta_{re}) & \cos(\theta_{re}-2\pi/3) & \cos(\theta_{re}+2\pi/3) \\ \sin(\theta_{re}) & \sin(\theta_{re}-2\pi/3) & \sin(\theta_{re}+2\pi/3) \end{bmatrix}$$

$$[\boldsymbol{K_{qd}}]^{-1} = \begin{bmatrix} \cos(\theta_{re}) & \sin(\theta_{re}) \\ \cos(\theta_{re}-2\pi/3) & \sin(\theta_{re}-2\pi/3) \\ \cos(\theta_{re}+2\pi/3) & \sin(\theta_{re}+2\pi/3) \end{bmatrix} \tag{1.4.1}$$

It is possible to define the mathematical model of an IPMSM in the synchronous reference frame with the rotor flux position:

$$\begin{bmatrix} v_q \\ v_d \end{bmatrix} = \begin{bmatrix} R_s & 0 \\ 0 & R_s \end{bmatrix}\begin{bmatrix} i_q \\ i_d \end{bmatrix} + \frac{d}{dt}\begin{bmatrix} \lambda_q \\ \lambda_d \end{bmatrix} + \begin{bmatrix} \omega_{re}\lambda_d & 0 \\ 0 & -\omega_{re}\lambda_q \end{bmatrix}$$

$$\begin{bmatrix} \lambda_q \\ \lambda_d \end{bmatrix} = \begin{bmatrix} L_q & 0 \\ 0 & L_d \end{bmatrix}\begin{bmatrix} i_q \\ i_d \end{bmatrix} + \begin{bmatrix} 0 \\ \lambda_{pm} \end{bmatrix} \tag{1.4.2}$$

By appropriate manipulations of (1.4.2) and writing the derivative operator with $p = d/dt$, obtain:

$$\begin{bmatrix} v_q \\ v_d \end{bmatrix} = \begin{bmatrix} R_s & 0 \\ 0 & R_s \end{bmatrix}\begin{bmatrix} i_q \\ i_d \end{bmatrix} + \begin{bmatrix} pL_q & \omega_{re}L_d \\ -\omega_{re}L_q & pL_d \end{bmatrix}\begin{bmatrix} i_q \\ i_d \end{bmatrix} + \begin{bmatrix} \omega_{re}\lambda_{pm} \\ 0 \end{bmatrix} \tag{1.4.3}$$

Note that in the mathematical model of PMSM the cross-saturation phenomena has been neglected and then the qd incremental inductances have been not considered in (1.4.3) and in the following analysis.

In order to compute the back-EMF, (1.4.3) is rewritten as:

$$\begin{bmatrix} pL_q & \omega_{re}L_d \\ -\omega_{re}L_q & pL_d \end{bmatrix}\begin{bmatrix} i_q \\ i_d \end{bmatrix} = \begin{bmatrix} pL_q + pL_d - pL_d & \omega_{re}L_d + \omega_{re}L_q - \omega_{re}L_q \\ -\omega_{re}L_q & pL_d \end{bmatrix}\begin{bmatrix} i_q \\ i_d \end{bmatrix} = \\ = \begin{bmatrix} pL_d & \omega_{re}L_q \\ -\omega_{re}L_q & pL_d \end{bmatrix}\begin{bmatrix} i_q \\ i_d \end{bmatrix} + \begin{bmatrix} pL_q - pL_d & \omega_{re}L_d - \omega_{re}L_q \\ 0 & 0 \end{bmatrix}\begin{bmatrix} i_q \\ i_d \end{bmatrix} \tag{1.4.4}$$

From the inductance matrix decomposition, the mathematical model of the electrical machine can be rewritten as:

$$\begin{bmatrix} v_q \\ v_d \end{bmatrix} = \begin{bmatrix} R_s & 0 \\ 0 & R_s \end{bmatrix}\begin{bmatrix} i_q \\ i_d \end{bmatrix} + \begin{bmatrix} pL_d & \omega_{re}L_q \\ -\omega_{re}L_q & pL_d \end{bmatrix}\begin{bmatrix} i_q \\ i_d \end{bmatrix} + \begin{bmatrix} \omega_{re}\lambda_{pm} + (L_q - L_d)(\omega_{re}i_d - pi_q) \\ 0 \end{bmatrix} \tag{1.4.5}$$

where E_{emf} is the extended back-EMF linked both permanent magnet flux and saliency:

$$E_{emf} = \omega_{re}\lambda_{pm} + (L_q - L_d)(\omega_{re}i_d - pi_q) \tag{1.4.6}$$

By applying the reference frame transform matrices $\boldsymbol{R_{qd\text{-}\alpha\beta}}$ (1.4.7) and (1.4.8), the previous model can be referred to an orthogonal stationary reference frame ($\alpha\beta$):

$$\boldsymbol{K_{\alpha\beta}} = \frac{2}{3}\begin{bmatrix} 1 & -\frac{1}{2} & -\frac{1}{2} \\ 0 & -\frac{\sqrt{3}}{2} & \frac{\sqrt{3}}{2} \end{bmatrix} \qquad [\boldsymbol{K_{\alpha\beta}}]^{-1} = \begin{bmatrix} 1 & 0 \\ -\frac{1}{2} & -\frac{\sqrt{3}}{2} \\ -\frac{1}{2} & \frac{\sqrt{3}}{2} \end{bmatrix} \tag{1.4.7}$$

$$\boldsymbol{R_{qd-\alpha\beta}} = \boldsymbol{K_{qd}}\,[\boldsymbol{K_{\alpha\beta}}]^{-1} = \begin{bmatrix} \cos(\theta_{re}) & -\sin(\theta_{re}) \\ \sin(\theta_{re}) & \cos(\theta_{re}) \end{bmatrix}$$

$$[\boldsymbol{R_{qd-\alpha\beta}}]^{-1} = \boldsymbol{K_{\alpha\beta}}\,[\boldsymbol{K_{qd}}]^{-1} = \begin{bmatrix} \cos(\theta_{re}) & \sin(\theta_{re}) \\ -\sin(\theta_{re}) & \cos(\theta_{re}) \end{bmatrix} \tag{1.4.8}$$

$$\begin{bmatrix} v_\alpha \\ v_\beta \end{bmatrix} = \boldsymbol{R_{qd\text{-}\alpha\beta}}\begin{bmatrix} v_q \\ v_d \end{bmatrix} = \boldsymbol{R_{qd\text{-}\alpha\beta}}\begin{bmatrix} R_s+pL_d & \omega_{re}L_q \\ -\omega_{re}L_q & R_s+pL_d \end{bmatrix}[\boldsymbol{R_{qd\text{-}\alpha\beta}}]^{-1}\begin{bmatrix} i_\alpha \\ i_\beta \end{bmatrix} + \boldsymbol{R_{qd\text{-}\alpha\beta}}\begin{bmatrix} E_{emf} \\ 0 \end{bmatrix}$$

Then, by rearranging the above set of equations, the mathematical model is rewritten as:

$$\begin{bmatrix} v_\alpha \\ v_\beta \end{bmatrix} = \begin{bmatrix} R_s+pL_d & -\omega_{re}(L_d-L_q) \\ \omega_{re}(L_d-L_q) & R_s+pL_d \end{bmatrix}\begin{bmatrix} i_\alpha \\ i_\beta \end{bmatrix} + \begin{bmatrix} E_\alpha \\ E_\beta \end{bmatrix} \qquad \begin{bmatrix} E_\alpha \\ E_\beta \end{bmatrix} = E_{emf}\begin{bmatrix} \cos(\theta_{re}) \\ -\sin(\theta_{re}) \end{bmatrix} \tag{1.4.9}$$

Starting from the IPMSM model in a stationary reference frame, it is possible to build the α-axis and β-axis block diagrams of the state filter in order to estimate the α-axis and β-axis back-EMF, as shown in Fig. 1.4.1(a) and 1.4.1(b), respectively:

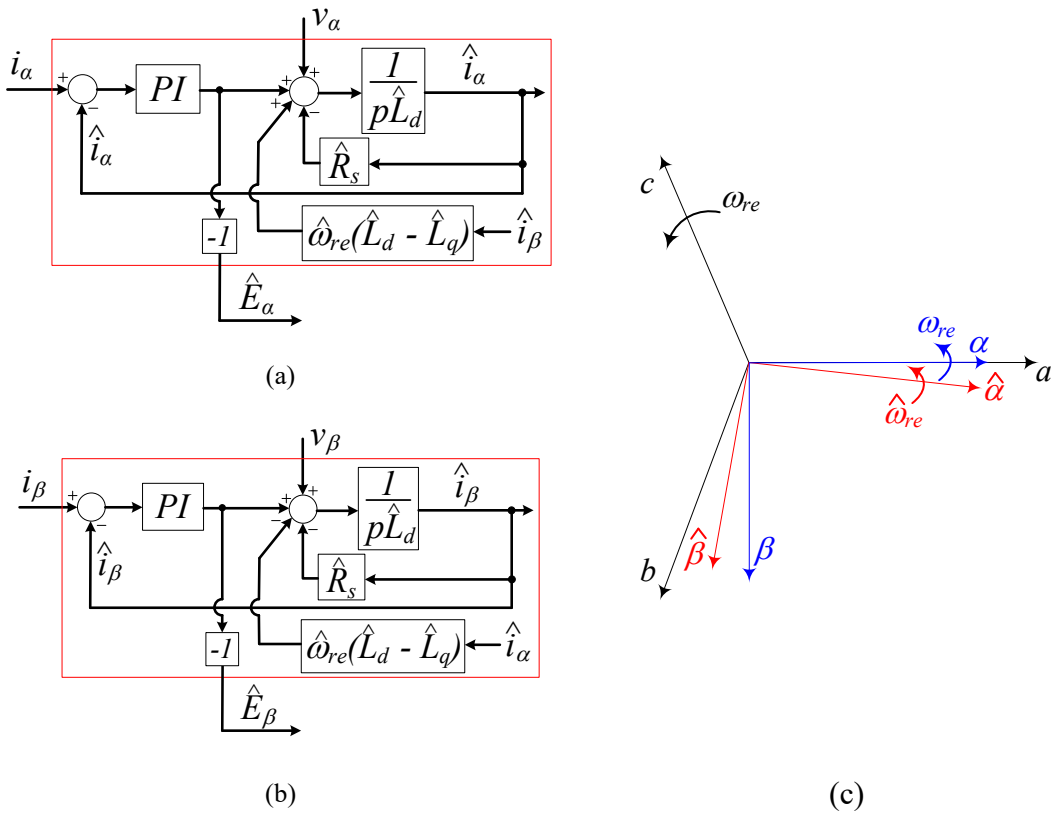

Figure 1.4.1 *Back-EMF State Filter: (a) α-axis and (b) β-axis and (c) stationary reference frame αβ.*

This state filter, allows to compute the back-EMF written in (1.4.5); the state filter defined in Fig. 1.4.1 is valid for IPMSM motor drive, but can be exploited for SPMSM or SynchRel motor drives; in those cases, the equivalent models are (1.4.10) and (1.4.11), respectively:

$$\begin{bmatrix} v_\alpha \\ v_\beta \end{bmatrix} = \begin{bmatrix} R_s+pL_s & 0 \\ 0 & R_s+pL_s \end{bmatrix} \begin{bmatrix} i_\alpha \\ i_\beta \end{bmatrix} + \omega_{re}\lambda_{pm} \begin{bmatrix} cos(\theta_{re}) \\ -sin(\theta_{re}) \end{bmatrix} \tag{1.4.10}$$

$$\begin{bmatrix} v_\alpha \\ v_\beta \end{bmatrix} = \begin{bmatrix} R_s+pL_d & -\omega_{re}(L_d-L_q) \\ \omega_{re}(L_d-L_q) & R_s+pL_d \end{bmatrix} \begin{bmatrix} i_\alpha \\ i_\beta \end{bmatrix} + (L_q - L_d)(\omega_{re} i_d - p i_q) \begin{bmatrix} cos(\theta_{re}) \\ -sin(\theta_{re}) \end{bmatrix} \tag{1.4.11}$$

In order to simplify the mathematical expressions, the reference frames models (1.4.5) and (1.4.9) can be rewritten in complex notation; in fact by placing $\boldsymbol{f_{xy}} = f_x - jf_y$ (with $xy = qd$ in synchronous reference frame cases; with $xy = \alpha\beta$ in stationary reference frame cases, then the models defined in (1.4.5) can be rewritten as:

$$\boldsymbol{v_{qd}} = R_s \boldsymbol{i_{qd}} + L_d p\boldsymbol{i_{qd}} + j\omega_{re} L_q \boldsymbol{i_{qd}} + E_{emf}\, e^{j0} \tag{1.4.12}$$

while the (1.4.9) can be rewritten as:

$$\boldsymbol{v_{\alpha\beta}} = R_s \boldsymbol{i_{\alpha\beta}} + L_d p\boldsymbol{i_{\alpha\beta}} + j\omega_{re} (L_d - L_q) \boldsymbol{i_{\alpha\beta}} + E_{emf}\, e^{-j\theta_{re}} \tag{1.4.13}$$

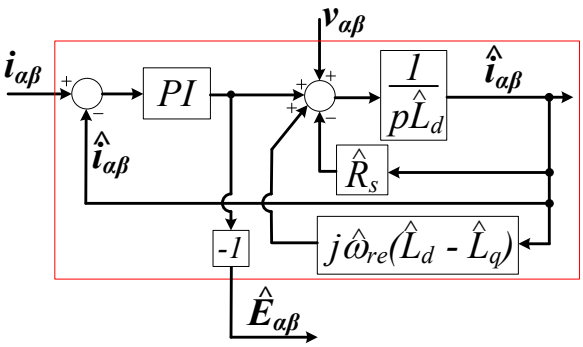

Figure 1.4.2 *Complex Vector Back-EMF State Filter*

In this way the complex vector equation system (1.4.13) allow to replicate the block diagrams shown in Fig. 1.4.1 in an only complex vector block diagram shown in Fig. 1.4.2, where $\boldsymbol{E}_{\alpha\beta} = E_{emf}\, e^{-j\theta_{re}}$ is the back-EMF complex vector.

Even the transform matrices defined in (1.4.8) can be rewritten in complex vector mode:

$$\boldsymbol{R}_{qd\text{-}\alpha\beta} = e^{j\theta_{re}} \qquad [\boldsymbol{R}_{qd\text{-}\alpha\beta}]^{-1} = e^{-j\theta_{re}} \tag{1.4.14}$$

1.5 Saliency-Based Sensorless Control Methods

Sensorless control schemes based on flux position estimation, known as model-based methods, generally compute the position of the rotor flux through an integration of the back EMF. Such an approach is very simple, but effective only at a sufficiently high speed. The back-EMF is, in fact, generally very small under 10% of the rated speed [51], [79], leading to incorrect estimations of the flux position, due to stator resistance variations, or simply measurement noises, and preventing continuous stable low, or zero speed, operations. Moreover, a generally accepted Safety Sensorless Operating Area (SSOA) has been defined to identify the speed and torque ranges where stable sensorless operations are guaranteed [51]. Signal injection-based sensorless control is widely adopted to obtain the position by tracking the saliency at low-speed region for PMSM drives [51]-[67]. According to the injection reference frame, the mainstream HF signal injection can be roughly categorized into rotating and pulsating signal injection methods. And pulsating injection can be further subdivided into pulsating sinusoidal injection and pulsating square-wave injection schemes. An intuitive comparison of different HF signal injection schemes is shown in Fig. 1.5.1.

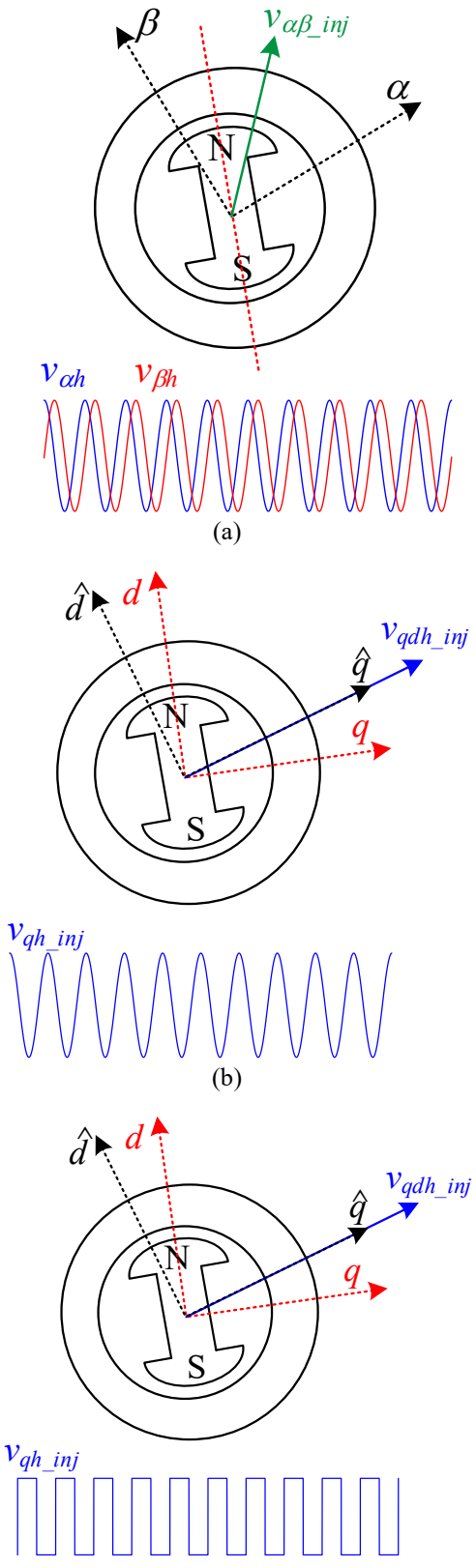

Figure 1.5.1 *Comparison of different HF signal injection behaviour principle: (a) rotating signal injection method, (b) pulsating sinusoidal injection method, (c) pulsating square-wave injection method.*

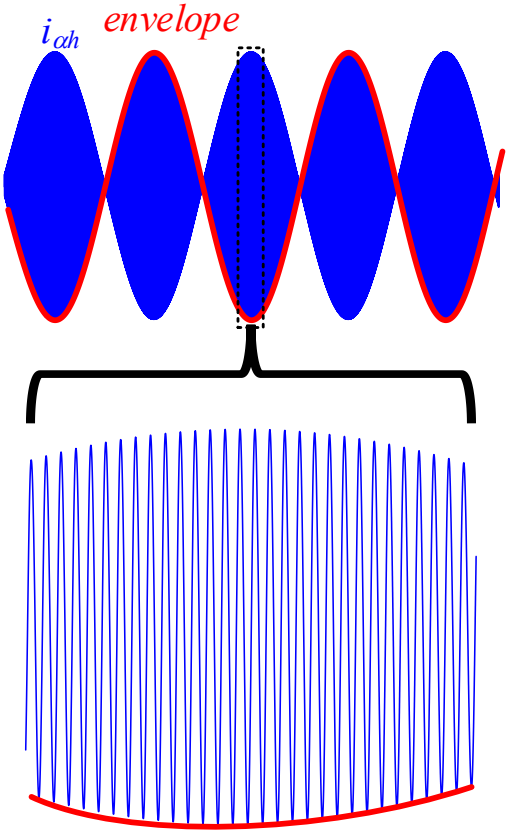

Figure 1.5.2 *High Frequency current response and its envelope.*

Although the high frequency signals injection methods are effective to estimate the rotor position of IPMSMs, a high frequency signal is injected and extra observers for signal processing are required to achieve accurate position tracking. Then, Fundamental PWM Excitation (FPE) based sensorless control methods was introduced to simplify the sensorless control structure [68] - [77].

The FPE-based sensorless control methods estimate the rotor flux position by measurement of the current or voltage response of a sequence of test voltage vectors applied in the PWM inverter and by calculating the leakage inductance which varies due to the main path and leakage saturation. The main concept is based on modified slightly the fundamental PWM signals switching by extending the duration of selected inherent switching vectors.

In this thesis the operating principle of the pulsating sinusoidal signal injection will be mentioned in the next paragraph.

1.6 High Frequency Pulsating Sinusoidal Signal Injection Method

Starting from the synchronous reference frame model of a IPMSM defined in (1.4.3) the analytical basis of the HF pulsating sinusoidal signal injection method can be developed in this paragraph.

Since the injection angular frequency ω_h is much higher than the operation speed, the voltage drops on the stator resistance and the term associated with the electrical rotor speed ω_{re} are assumed negligible. Then the HF-model IPMSM at low-speed region can be obtained in synchronous reference frame (1.6.1) with the rotor position θ_{re} and in stationary reference frame (1.6.2):

$$\begin{bmatrix} v_{qh} \\ v_{dh} \end{bmatrix} = \begin{bmatrix} L_q & 0 \\ 0 & L_d \end{bmatrix} \begin{bmatrix} pi_q \\ pi_d \end{bmatrix} \tag{1.6.1}$$

$$\begin{bmatrix} v_{\alpha h} \\ v_{\beta h} \end{bmatrix} = \begin{bmatrix} L_A - L_B \cos(2\theta_{re}) & L_B \sin(2\theta_{re}) \\ L_B \sin(2\theta_{re}) & L_A + L_B \cos(2\theta_{re}) \end{bmatrix} \begin{bmatrix} pi_{\alpha h} \\ pi_{\beta h} \end{bmatrix} \tag{1.6.2}$$

where the subscript *"h"* indicates HF component.

The HF pulsating sinusoidal injection voltage vector v_{qd_inj}, with angular frequency ω_h, is injected in qd-axis reference voltages:

$$v_{qd\_inj} = \begin{bmatrix} v_{qh\_inj} \\ v_{dh\_inj} \end{bmatrix} = V_h \cos(\omega_h t) \begin{bmatrix} 1 \\ 0 \end{bmatrix} \tag{1.6.3}$$

where V_h is the injected HF voltage amplitude. In order to ensure a good shape of the sinusoidal signal of injected voltages, the injection angular frequency cannot be set to high (usually lower than one-tenth of the PWM switching frequency).

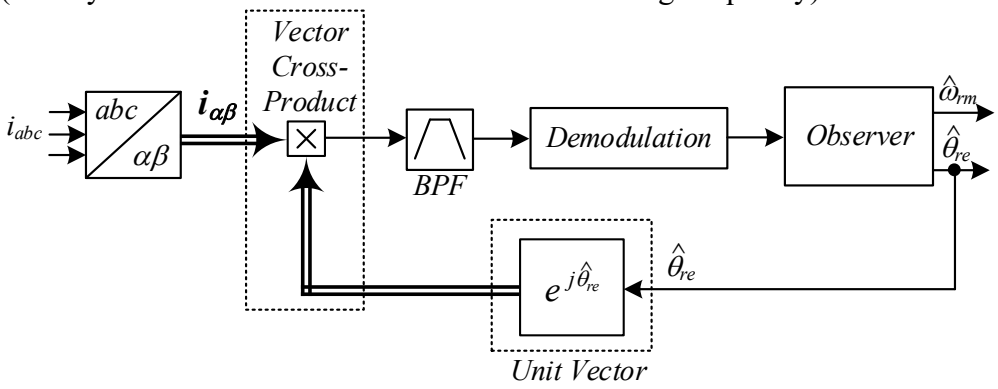

Figure 1.6.1 *Block Diagram of the demodulation algorithm.*

Transforming the injection voltage vector v_{qd_inj} to the stationary reference frame with the estimated rotor position $\hat{\theta}_{re}$, obtain:

$$v_{\alpha\beta\_inj} = \begin{bmatrix} v_{\alpha h} \\ v_{\beta h} \end{bmatrix} = V_h \cos(\omega_h t) \begin{bmatrix} \cos(\hat{\theta}_{re}) \\ -\sin(\hat{\theta}_{re}) \end{bmatrix} \tag{1.6.4}$$

By substituting (1.6.4) in (1.6.2), the HF measured currents, in stationary reference frame, under HF voltage injection can be obtained in (1.6.5):

$$\begin{bmatrix} i_{\alpha h} \\ i_{\beta h} \end{bmatrix} = \sin(\omega_h t) \begin{bmatrix} I_A \cos(\hat{\theta}_{re}) - I_B \cos(2\theta_{re} - \hat{\theta}_{re}) \\ -I_A \sin(\hat{\theta}_{re}) + I_B \sin(2\theta_{re} - \hat{\theta}_{re}) \end{bmatrix} \tag{1.6.5}$$

where the currents amplitudes I_A and I_B are defined as follow expressions:

$$I_A = \frac{V_h}{\omega_h} \frac{L_A}{L^2{}_A - L^2{}_B} \qquad\qquad I_A = \frac{V_h}{\omega_h} \frac{L_B}{L^2{}_A - L^2{}_B} \tag{1.6.6}$$

Finally, the d-axis component of the high frequency current in synchronous reference frame with the estimated rotor position is given by:

$$\hat{i}_{dh} = i_{\alpha h}\, sin\left(\hat{\theta}_{re}\right) + i_{\beta h}\, cos\left(\hat{\theta}_{re}\right) = I_B\, sin(\omega_h\, t)\, \sin\left[2\left(\theta_{re} - \hat{\theta}_{re}\right)\right] \qquad (1.6.7)$$

From (1.6.7) it is possible to extract the rotor position error between the actual rotor position and estimated rotor position. By using a band-pass digital filter and by demodulation process will be provided a signal proportional to the position error and then this error should be processed into an observer in order to estimate the rotor position by forcing the position error to zero.

Typically, in the HF signal injection methods a Vector Tracking Observer (VTO) is often used as an observer, in order to guarantee high rotor position estimation reliability and better dynamic performance.

1.7 Estimation of Rotor Position and Angular Speed

Once the back-EMF estimation has been obtained by means of the state filter of Fig. 1.4.2, it is possible to estimate the rotor position of a rotating vector by considering different methods [80]:

- By using the function arctangent.
- By using a PLL algorithm .
- By using state observers.

Rotor position estimation by arctangent, Fig.1.7.1, allows to obtain the angular position $\hat{\theta}_{re}$ in a very simple way; obviously, the speed estimation $\hat{\omega}_{re}$ will have to be done by an observer or directly by PLL. Therefore, the presence of noise on the measured signals results in noisy position estimates when using direct calculation methods such as the arctangent. To reduce the noise problem, filters have been applied to either the estimated position or the inputs signals, adding lag to the estimate [80].

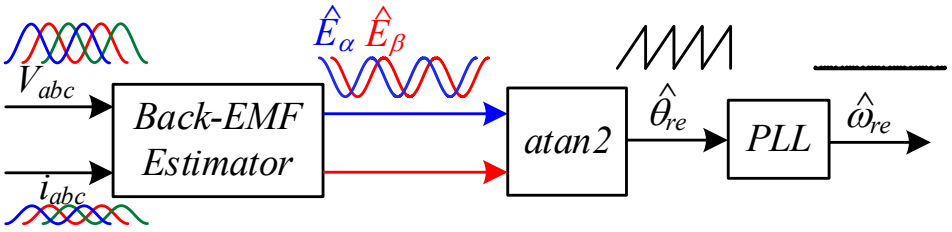

Figure 1.7.1 *Rotor Position Estimation through Arctangent method.*

The accuracy of the position/speed estimation can be improved by considering a state filter or observer. The position error signal is an input of the algorithm, which could be extracted through a vector cross product. Therefore, the PI type phase locking loop (PLL), Fig. 1.7.2, or the PID type Luenberger observer, Fig. 1.7.3, can be used to force the position error signal to zero and extract the position and speed information [80].

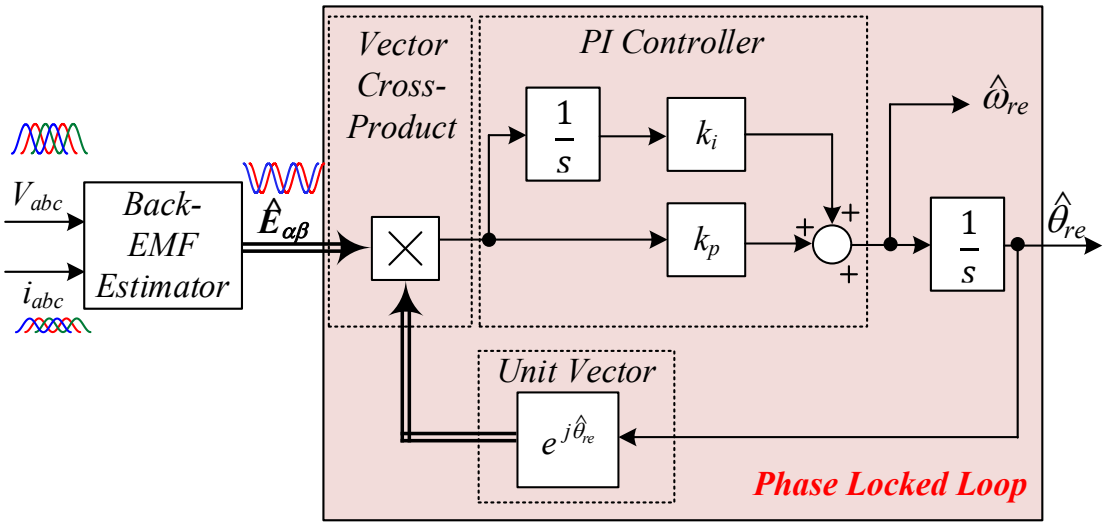

Figure 1.7.2 *Rotor Position Estimation through Phase Locked Loop (PLL)*

Compared to the PLL, the Luenberger observer although the moment of inertia is required, can provide better dynamic performance. One type of state observer used is the so-called Vector Tracking Observer (VTO), Fig. 1.7.3, which is obtained starting from a non-linear Luenberger observer structure.

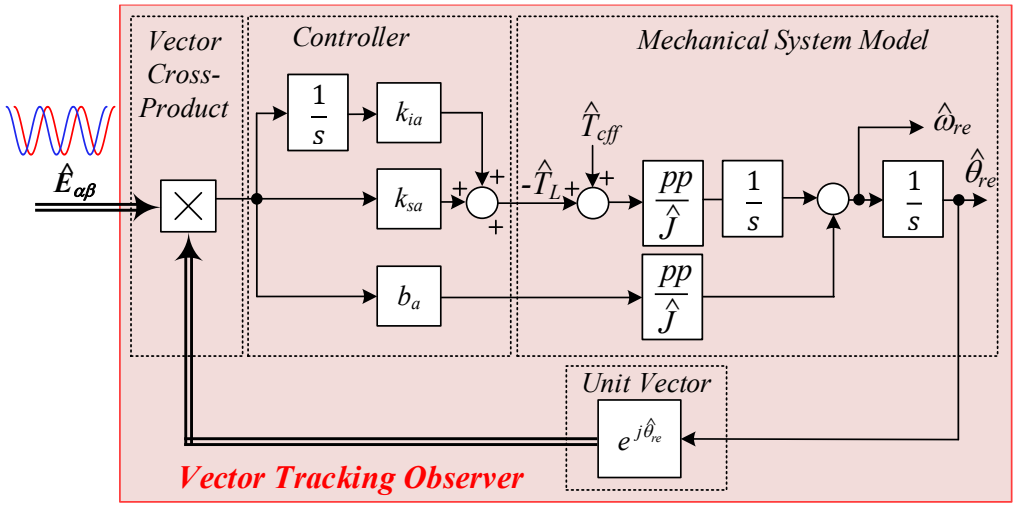

Figure 1.7.3 *Rotor Position Estimation through Vector Tracking Observer (VTO).*

1.8 References

[1] G. Wu, S. Huang, Q. Wu, F. Rong, C. Zhang and W. Liao, "Robust Predictive Torque Control of N*3-Phase PMSM for High-Power Traction Application," in IEEE Transactions on Power Electronics, vol. 35, no. 10, pp. 10799-10809, Oct. 2020.

[2]S. Fang, H. Liu, H. Wang, H. Yang and H. Lin, "High Power Density PMSM With Lightweight Structure and High-Performance Soft Magnetic Alloy Core," in IEEE Transactions on Applied Superconductivity, vol. 29, no. 2, pp. 1-5, March 2019.

[3]Xu, J.; Zhang, B.; Kuang, X.; Guo, H.; Guo, S. Influence analysis of slot parameters and high torque density optimisation for dual redundant permanent magnet motor in aerospace application. IET Electr. Power Appl. 2020, 14, 1263–1273.

[4]Y. Kong, M. Lin and L. Jia, "A Novel High Power Density Permanent-Magnet Synchronous Machine With Wide Speed Range," in IEEE Transactions on Magnetics, vol. 56, no. 2, pp. 1-6, Feb. 2020.
[5]Chau, K.T. Electric Vehicle Machines and Drives: Design, Analysis and Application; John Wiley and Sons: Chichester, UK, 2015.
[6]Korn, N.; Vaimann, T.; Kallaste, A.; Belahcen, A. Comparative study of slow speed slotless synchronous generator using SmCo and NdFeB permanent magnets. In Proceeding of the 2014 Electric Power Quality and Supply Reliability Conference (PQ), Rakvere, Estonia, 11–13 June 2014; pp. 247–250.
[7]Pellegrino, G.; Jahns, T.M.; Bianchi, N.; Soong,W.; Cupertino, F. The Rediscovery of Synchronous Reluctance and Ferrite Permanent Magnet Motors; Springer: Cham, Switzerland, 2016.
[8]I. Boldea, L. N. Tutelea, L. Parsa and D. Dorrell, "Automotive Electric Propulsion Systems With Reduced or No Permanent Magnets: An Overview," in IEEE Transactions on Industrial Electronics, vol. 61, no. 10, pp. 5696-5711, Oct. 2014.
[9]R. Moghaddam and F. Gyllensten, "Novel High-Performance SynRM Design Method: An Easy Approach for A Complicated Rotor Topology," in IEEE Transactions on Industrial Electronics, vol. 61, no. 9, pp. 5058-5065, Sept. 2014.
[10] N. Bianchi, E. Fornasiero and W. Soong, "Selection of PM Flux Linkage for Maximum Low-Speed Torque Rating in a PM-Assisted Synchronous Reluctance Machine," in IEEE Transactions on Industry Applications, vol. 51, no. 5, pp. 3600-3608, Sept.-Oct. 2015.
[11] M. D. Nardo, G. L. Calzo, M. Galea and C. Gerada, "Design Optimization of a High-Speed Synchronous Reluctance Machine," in IEEE Transactions on Industry Applications, vol. 54, no. 1, pp. 233-243, Jan.-Feb. 2018.
[12] A. T. de Almeida, F. J. T. E. Ferreira and G. Baoming, "Beyond Induction Motors—Technology Trends to Move Up Efficiency," in IEEE Transactions on Industry Applications, vol. 50, no. 3, pp. 2103-2114, May-June 2014.
[13] I. Boldea, "Control issues in adjustable speed drives," in IEEE Industrial Electronics Magazine, vol. 2, no. 3, pp. 32-50, Sept. 2008.
[14] F. Betin et al., "Trends in Electrical Machines Control: Samples for Classical, Sensorless, and Fault-Tolerant Techniques," in IEEE Industrial Electronics Magazine, vol. 8, no. 2, pp. 43-55, June 2014.
[15] M. Ojaghi, M. Sabouri and J. Faiz, "Performance Analysis of Squirrel-Cage Induction Motors Under Broken Rotor Bar and Stator Inter-Turn Fault Conditions Using Analytical Modeling," in IEEE Transactions on Magnetics, vol. 54, no. 11, pp. 1-5, Nov. 2018.
[16] L. A. Trujillo-Guajardo, J. Rodriguez-Maldonado, M. A. Moonem and M. A. Platas-Garza, "A Multiresolution Taylor–Kalman Approach for Broken Rotor Bar Detection in Cage Induction Motors," in IEEE Transactions on Instrumentation and Measurement, vol. 67, no. 6, pp. 1317-1328.
[17] M. Ojaghi, M. Sabouri and J. Faiz, "Performance Analysis of Squirrel-Cage Induction Motors Under Broken Rotor Bar and Stator Inter-Turn Fault Conditions Using Analytical Modeling," in IEEE Transactions on Magnetics, vol. 54, no. 11, pp. 1-5, Nov. 2018.
[18] S. Taghavi and P. Pillay, "A Sizing Methodology of the Synchronous Reluctance Motor for Traction Applications," in IEEE Journal of Emerging and Selected Topics in Power Electronics, vol. 2, no. 2, pp. 329-340, June 2014.
[19] S. S. R. Bonthu, A. Arafat and S. Choi, "Comparisons of Rare-Earth and Rare-Earth-Free External Rotor Permanent Magnet Assisted Synchronous Reluctance

Motors," in IEEE Transactions on Industrial Electronics, vol. 64, no. 12, pp. 9729-9738, Dec. 2017.
[20] J. Park, C. Kalev and H. F. Hofmann, "Control of High-Speed Solid-Rotor Synchronous Reluctance Motor/Generator for Flywheel-Based Uninterruptible Power Supplies," in IEEE Transactions on Industrial Electronics, vol. 55, no. 8, pp. 3038-3046, Aug. 2008.
[21] Subtitle, P. High Output Synchronous Reluctance Motor and Drive Package—Optimized Cost of Ownership for Pump and Fan Applications; ABB: Zurich, Switzerland, 2012.
[22] SIEMENS. Highest Efficiency Synchronous-Reluctance Drive System with IES2 Efficiency—Topics—Siemens.
[23] ABB. IE5 SynRM Motors Deliver Ultra-Premium Energy Efficiency. https://new.abb.com/news/detail/58874/abb-ie5-synrm-motors-deliver-ultra-premium-energy-efficiency
[24] T. A. Huynh and M. Hsieh, "Comparative Study of PM-Assisted SynRM and IPMSM on Constant Power Speed Range for EV Applications," in IEEE Transactions on Magnetics, vol. 53, no. 11, pp. 1-6, Nov. 2017.
[25] G. V. Kumar, C. Chuang, M. Lu and C. Liaw, "Development of an Electric Vehicle Synchronous Reluctance Motor Drive," in IEEE Transactions on Vehicular Technology, vol. 69, no. 5, pp. 5012-5024, May 2020.
[26] ABB. All-Compatible ACS880 Single Drives—Industrial Drives—Unlimited Possibilities for Your Business (Low Voltage AC). https://new.abb.com/drives/low-voltage-ac/industrial-drives/acs880-single-drives
[27] G. Pellegrino, E. Armando and P. Guglielmi, "Direct-Flux Vector Control of IPM Motor Drives in the Maximum Torque Per Voltage Speed Range," in IEEE Transactions on Industrial Electronics, vol. 59, no. 10, pp. 3780-3788, Oct. 2012.
[28] M. Barcaro, N. Bianchi and F. Magnussen, "Permanent-Magnet Optimization in Permanent-Magnet-Assisted Synchronous Reluctance Motor for a Wide Constant-Power Speed Range," in IEEE Transactions on Industrial Electronics, vol. 59, no. 6, pp. 2495-2502, June 2012.
[29] H. Liu, I. Kim, Y. J. Oh, J. Lee and S. Go, "Design of Permanent Magnet-Assisted Synchronous Reluctance Motor for Maximized Back-EMF and Torque Ripple Reduction," in IEEE Transactions on Magnetics, vol. 53, no. 6, pp. 1-4, June 2017.
[30] S. Bolognani, L. Ortombina, F. Tinazzi, and M. Zigliotto, “Model sensitivity of fundamental-frequency-based position estimators for sensorless PM and reluctance synchronous motor drives,” IEEE Trans. Ind. Electron., vol. 65, no. 1, pp. 77–85, Jan. 2018.
[31] R. Antonello, L. Ortombina, F. Tinazzi, and M. Zigliotto, “Enhanced low-speed operations for sensorless anisotropic PM synchronous motor drives by a modified back-EMF observer,” IEEE Trans. Ind. Electron., vol. 65, no. 4, pp. 3069–3076, Apr. 2018.
[32] Y. Lee, Y. Kwon and S. Sul, "Comparison of rotor position estimation performance in fundamental-model-based sensorless control of PMSM," 2015 IEEE Energy Conversion Congress and Exposition (ECCE), 2015, pp. 5624-5633.
[33] Y. Lee and S. Sul, "Model-Based Sensorless Control of an IPMSM With Enhanced Robustness Against Load Disturbances Based on Position and Speed Estimator Using a Speed Error," in IEEE Transactions on Industry Applications, vol. 54, no. 2, pp. 1448-1459, March-April 2018.

[34] Zhiqian Chen, M. Tomita, S. Doki and S. Okuma, "An extended electromotive force model for sensorless control of interior permanent-magnet synchronous motors," in IEEE Transactions on Industrial Electronics, vol. 50, no. 2, pp. 288-295, April 2003.
[35] G. Wang, T. Li, G. Zhang, X. Gui and D. Xu, "Position Estimation Error Reduction Using Recursive-Least-Square Adaptive Filter for Model-Based Sensorless Interior Permanent-Magnet Synchronous Motor Drives," in IEEE Transactions on Industrial Electronics, vol. 61, no. 9, pp. 5115-5125, Sept. 2014.
[36] I. Boldea, M. C. Paicu and G. Andreescu, "Active Flux Concept for Motion-Sensorless Unified AC Drives," in IEEE Transactions on Power Electronics, vol. 23, no. 5, pp. 2612-2618, Sept. 2008.
[37] T. Tuovinen and M. Hinkkanen, "Signal-injection assisted full-order observer with parameter adaptation for synchronous reluctance motor drives," 2013 IEEE Energy Conversion Congress and Exposition, 2013, pp. 3488-3495.
[38] T. Tuovinen and M. Hinkkanen, "Adaptive Full-Order Observer With High-Frequency Signal Injection for Synchronous Reluctance Motor Drives," in IEEE Journal of Emerging and Selected Topics in Power Electronics, vol. 2, no. 2, pp. 181-189, June 2014.
[39] T. Tuovinen, M. Hinkkanen, L. Harnefors and J. Luomi, "Comparison of a Reduced-Order Observer and a Full-Order Observer for Sensorless Synchronous Motor Drives," in IEEE Transactions on Industry Applications, vol. 48, no. 6, pp. 1959-1967, Nov.-Dec. 2012.
[40] C. Olivieri and M. Tursini, "A novel PLL scheme for a sensorless PMSM drive overcoming common speed reversal problems," International Symposium on Power Electronics Power Electronics, Electrical Drives, Automation and Motion, 2012, pp. 1051-1056.
[41] Shih-Chin Yang and R. D. Lorenz, "Surface permanent magnet machine self-sensing at zero and low speeds using improved observer for position, velocity, and disturbance torque estimation," 2011 IEEE International Electric Machines & Drives Conference (IEMDC), 2011, pp. 35-40.
[42] O. Wallmark and L. Harnefors, "Sensorless Control of Salient PMSM Drives in the Transition Region," in IEEE Transactions on Industrial Electronics, vol. 53, no. 4, pp. 1179-1187, June 2006.
[43] Z. Ma, J. Gao and R. Kennel, "FPGA Implementation of a Hybrid Sensorless Control of SMPMSM in the Whole Speed Range," in IEEE Transactions on Industrial Informatics, vol. 9, no. 3, pp. 1253-1261, Aug. 2013.
[44] O. Wallmark, L. Harnefors and O. Carlson, "An improved speed and position estimator for salient permanent-magnet synchronous motors," in IEEE Transactions on Industrial Electronics, vol. 52, no. 1, pp. 255-262, Feb. 2005.
[45] A. Piippo, M. Hinkkanen and J. Luomi, "Analysis of an Adaptive Observer for Sensorless Control of Interior Permanent Magnet Synchronous Motors," in IEEE Transactions on Industrial Electronics, vol. 55, no. 2, pp. 570-576, Feb. 2008.
[46] P. P. Acarnley and J. F. Watson, "Review of position-sensorless operation of brushless permanent-magnet machines," in IEEE Transactions on Industrial Electronics, vol. 53, no. 2, pp. 352-362, April 2006.
[47] L. Harnefors and H. -. Nee, "A general algorithm for speed and position estimation of AC motors," in IEEE Transactions on Industrial Electronics, vol. 47, no. 1, pp. 77-83, Feb. 2000.
[48] M. Tomita, T. Senjyu, S. Doki and S. Okuma, "New sensorless control for brushless DC motors using disturbance observers and adaptive velocity estimations," in IEEE Transactions on Industrial Electronics, vol. 45, no. 2, pp. 274-282, April 1998.

[49] C. Silva, G. M. Asher and M. Sumner, "Hybrid rotor position observer for wide speed-range sensorless PM motor drives including zero speed," in IEEE Transactions on Industrial Electronics, vol. 53, no. 2, pp. 373-378, April 2006.
[50] S. Ichikawa, M. Tomita, S. Doki and S. Okuma, "Sensorless control of permanent-magnet synchronous motors using online parameter identification based on system identification theory," in IEEE Transactions on Industrial Electronics, vol. 53, no. 2, pp. 363-372, April 2006.
[51] G. Scarcella, G. Scelba and A. Testa, "High performance sensorless controls based on HF excitation: A viable solution for future AC motor drives?," 2015 IEEE Workshop on Electrical Machines Design, Control and Diagnosis (WEMDCD), 2015, pp. 178-187.
[52] S. Kim, J. Im, E. Song and R. Kim, "A New Rotor Position Estimation Method of IPMSM Using All-Pass Filter on High-Frequency Rotating Voltage Signal Injection," in IEEE Transactions on Industrial Electronics, vol. 63, no. 10, pp. 6499-6509, Oct. 2016.
[53] D. Raca, P. Garcia, D. D. Reigosa, F. Briz and R. D. Lorenz, "Carrier-Signal Selection for Sensorless Control of PM Synchronous Machines at Zero and Very Low Speeds," in IEEE Transactions on Industry Applications, vol. 46, no. 1, pp. 167-178, Jan.-feb. 2010.
[54] D. Raca, M. C. Harke and R. D. Lorenz, "Robust Magnet Polarity Estimation for Initialization of PM Synchronous Machines With Near-Zero Saliency," in IEEE Transactions on Industry Applications, vol. 44, no. 4, pp. 1199-1209, July-aug. 2008.
[55] M. J. Corley and R. D. Lorenz, "Rotor position and velocity estimation for a salient-pole permanent magnet synchronous machine at standstill and high speeds," in IEEE Transactions on Industry Applications, vol. 34, no. 4, pp. 784-789, July-Aug. 1998.
[56] J. Holtz, "Acquisition of Position Error and Magnet Polarity for Sensorless Control of PM Synchronous Machines," in IEEE Transactions on Industry Applications, vol. 44, no. 4, pp. 1172-1180, July-aug. 2008.
[57] N. Bianchi, S. Bolognani, J. Jang and S. Sul, "Comparison of PM motor structures and sensorless control techniques for zero-speed rotor position detection," 2006 37th IEEE Power Electronics Specialists Conference, 2006, pp. 1-7.
[58] Ji-Hoon Jang, Jung-Ik Ha, M. Ohto, K. Ide and Seung-Ki Sul, "Analysis of permanent-magnet machine for sensorless control based on high-frequency signal injection," in IEEE Transactions on Industry Applications, vol. 40, no. 6, pp. 1595-1604, Nov.-Dec. 2004.
[59] Jung-Ik Ha, K. Ide, T. Sawa and Seung-Ki Sul, "Sensorless rotor position estimation of an interior permanent-magnet motor from initial states," in IEEE Transactions on Industry Applications, vol. 39, no. 3, pp. 761-767, May-June 2003.
[60] Ji-Hoon Jang, Seung-Ki Sul, Jung-Ik Ha, K. Ide and M. Sawamura, "Sensorless drive of surface-mounted permanent-magnet motor by high-frequency signal injection based on magnetic saliency," in IEEE Transactions on Industry Applications, vol. 39, no. 4, pp. 1031-1039, July-Aug. 2003.
[61] R. Ni, D. Xu, F. Blaabjerg, K. Lu, G. Wang and G. Zhang, "Square-Wave Voltage Injection Algorithm for PMSM Position Sensorless Control With High Robustness to Voltage Errors," in IEEE Transactions on Power Electronics, vol. 32, no. 7, pp. 5425-5437, July 2017.
[62] D. Kim, Y. Kwon, S. Sul, J. Kim and R. Yu, "Suppression of Injection Voltage Disturbance for High-Frequency Square-Wave Injection Sensorless Drive With

Regulation of Induced High-Frequency Current Ripple," in IEEE Transactions on Industry Applications, vol. 52, no. 1, pp. 302-312, Jan.-Feb. 2016.
[63] Y. Yoon and S. Sul, "Sensorless Control for Induction Machines Based on Square-Wave Voltage Injection," in IEEE Transactions on Power Electronics, vol. 29, no. 7, pp. 3637-3645, July 2014.
[64] C. Yu, J. Tamura, D. D. Reigosa and R. D. Lorenz, "Position Self-Sensing Evaluation of a FI-IPMSM Based on High-Frequency Signal Injection Methods," in IEEE Transactions on Industry Applications, vol. 49, no. 2, pp. 880-888, March-April 2013.
[65] S. Kim and S. Sul, "Sensorless control of AC motor — Where are we now?," 2011 International Conference on Electrical Machines and Systems, 2011, pp. 1-6.
[66] K. Ide, M. Takaki, S. Morimoto, Y. Kawazoe, A. Maemura and M. Ohto, "Saliency-based Sensorless Drive of Adequate Designed 1PM Motor for Robot Vehicle Application," 2007 Power Conversion Conference - Nagoya, 2007, pp. 1126-1133.
[67] Hyunbae Kim, Kum-Kang Huh, R. D. Lorenz and T. M. Jahns, "A novel method for initial rotor position estimation for IPM synchronous machine drives," in IEEE Transactions on Industry Applications, vol. 40, no. 5, pp. 1369-1378, Sept.-Oct. 2004.
[68] M. Schroedl, "Sensorless control of AC machines at low speed and standstill based on the "INFORM" method," IAS '96. Conference Record of the 1996 IEEE Industry Applications Conference Thirty-First IAS Annual Meeting, 1996, pp. 270-277 vol.1.
[69] F. Demmelmayr, M. Troyer and M. Schroedl, "Advantages of PM-machines compared to induction machines in terms of efficiency and sensorless control in traction applications," IECON 2011 - 37th Annual Conference of the IEEE Industrial Electronics Society, 2011, pp. 2762-2768.
[70] M. Hofer, M. Nikowitz and M. Schroedl, "Sensorless control of a reluctance synchronous machine in the whole speed range without voltage pulse injections," 2017 IEEE 3rd International Future Energy Electronics Conference and ECCE Asia (IFEEC 2017 - ECCE Asia), 2017, pp. 1194-1198.
[71] E. Robeischl and M. Schroedl, "Optimized INFORM measurement sequence for sensorless PM synchronous motor drives with respect to minimum current distortion," in IEEE Transactions on Industry Applications, vol. 40, no. 2, pp. 591-598, March-April 2004.
[72] M. Schrodl and M. Lambeck, "Statistic properties of the INFORM method for highly dynamic sensorless control of PM motors down to standstill," IECON'03. 29th Annual Conference of the IEEE Industrial Electronics Society (IEEE Cat. No.03CH37468), 2003, pp. 1479-1486 Vol.2.
[73] F. J. W. Barnard, W. T. Villet and M. J. Kamper, "Hybrid active-flux and arbitrary injection position sensorless control of reluctance synchronous machines," 2014 International Symposium on Power Electronics, Electrical Drives, Automation and Motion, 2014, pp. 1146-1151.
[74] D. Paulus, P. Landsmann, S. Kuehl and R. Kennel, "Arbitrary injection for permanent magnet synchronous machines with multiple saliencies," 2013 IEEE Energy Conversion Congress and Exposition, 2013, pp. 511-51.
[75] D. Paulus, P. Landsmann and R. Kennel, "Sensorless field- oriented control for permanent magnet synchronous machines with an arbitrary injection scheme and direct angle calculation," 2011 Symposium on Sensorless Control for Electrical Drives, 2011, pp. 41-46.

[76] J. Friedmann, R. Hoffmann and R. Kennel, "A new approach for a complete and ultrafast analysis of PMSMs using the arbitrary injection scheme," 2016 IEEE Symposium on Sensorless Control for Electrical Drives (SLED), 2016, pp. 1-6.
[77] D. Paulus, P. Landsmann and R. Kennel, "General arbitrary injection approach for synchronous machines," 2013 IEEE International Symposium on Sensorless Control for Electrical Drives and Predictive Control of Electrical Drives and Power Electronics (SLED/PRECEDE), 2013, pp. 1-6.
[78] Paul C. Krause, Oleg Wasynczuk, Scott D. Sudhoff, “Analysis of Eletric Machinery and Drive System”, Second Edition, 2002.
[79] R. W. Hejny and R. D. Lorenz, "Evaluating the Practical Low-Speed Limits for Back-EMF Tracking-Based Sensorless Speed Control Using Drive Stiffness as a Key Metric," in IEEE Transactions on Industry Applications, vol. 47, no. 3, pp. 1337-1343, May-June 2011.
[80] Hyunbae Kim, M. C. Harke and R. D. Lorenz, "Sensorless control of interior permanent-magnet machine drives with zero-phase lag position estimation," in IEEE Transactions on Industry Applications, vol. 39, no. 6, pp. 1726-1733, Nov.-Dec. 2003.

Chapter 2. Rotor Position Estimation Through Search Coils

2.1 Introduction

Today, the most common sensorless control techniques are those based on measurement of fundamental component of stator voltages and currents, estimating the rotor flux actual position through a mathematical model of the machine [1]-[4]. These techniques generally provide an effective estimation of the rotor position when correct values of motor electrical parameters are used in the model [5]-[8]. For instance, errors in estimating the winding resistance may strongly affect the performance of the sensorless control in the low speed region, especially at high load. Moreover, a similar effect may occur at high speeds due to errors in setting the inductance values. In order to improve the control performances in motor drives by reducing the effects of parameter and model uncertainties, different nonlinear control methods have been adopted, e.g., robust controls, sliding-mode controls (SMC), adaptive controls, predictive controls, intelligent controls, and so on [9]-[12]. However, the complexity of these approaches may remarkably increase the computational burden of control algorithms, making unpractical their implementation.

These techniques however must cope with the effects of magnetic saturation and cross-coupling, temperature variation and inverter nonlinearities. Indeed, this leads in many cases to a heavy computational burden, the need of self-commissioning procedures and/or accurate finite element analysis [1]-[4], [13]-[17].

For this reason, the basic concept, for the development of new sensorless algorithms is to be able to eliminate the effects related to saturation and non-linearity phenomena. Search Coils (SC) represent a viable solution to perform a direct measurement of stator flux amplitude and angular position. SC have been investigated since the ‘70s as a mean to improve the performance of direct field-oriented control techniques on sensorless or self-sensing induction motor drives [18]-[20]. Subsequently, they have been also successfully exploited on sensorless permanent synchronous motor drives (PMSMs) [21]. Search coils make possible the estimation of the rotor flux position through a direct evaluation of the stator flux amplitude and angular position, free from effects of stator resistance voltage drops and inverter non-linearities [22], [23]. However, SC are actually additional devices, normally not present on standard machines. Their introduction requires some departures from conventional AC motor designs, as well as changes in the coil winding process, thus increasing the drive complexity. Moreover, their introduction is in contrast with a basic goal of sensorless control techniques, which consists in removing from motor drives as many components as possible, in order to increase the reliability and reduce the cost [24]. SC became thus unpopular at the end of ‘80s, and large efforts were instead spent to develop sensorless control algorithms based on the mathematical model of the electrical machines, or on the injection of additional high frequency signals [25]-[34], which provide a satisfactory behavior in a wide operating range, while avoiding any modification of the conventional machine design.

A key aspect of AC motor drives reliability deals with overheating protection, to prevent failures and unexpected shutdowns, while extending the machine lifetime [35]-[43]. Temperature monitoring is thus accomplished through Thermistors, which are

semiconductor-based temperature transducers, normally installed in the end turns of the motor stator winding. On three phase AC motors a set of three Thermistors (T_a, T_b, T_c) is generally used, each one allocated in a phase winding and connected to the drive control system by external cables. Thermistors can be wired either in series, or according to a common lead circuit, as shown in Fig. 2.1.1.

(a) *(b)*

Figure 2.1.1 *Thermistors connection: (a) series and (b) common lead.*

In the first case, only an average stator winding temperature is obtained, while in the second case the temperature of each phase winding can be individually determined. The exploitation of Thermistor wirings to build up search coils for rotor position estimation and existing cables to connect them to the drive control system is investigated in this work. More precisely, search coils can be obtained by modifying the shape of Thermistor wirings. These search coils can be connected to the drive control system exploiting only existing cables if Thermistor are connected according to a common lead configuration. If Thermistors are instead series connected a single additional cable is required. According to such an approach, the realization of a set of SC should require a very small extra cost, therefore, a rotor position tracking technique has been developed exploiting the voltages induced in the obtained search coils. Such a technique is fully independent from motor parameters and overcomes some typical drawbacks of sensorless position estimation techniques based on the manipulation of fundamental components of stator voltages and currents, such as those related to inverter non-linearities and stator resistance voltage drops. Moreover, effects of magnetic saturation and cross-coupling effects are quite reduced, as verified by experimental testing.

Although of general use, the proposed technique is applied to a Surface Permanent Magnet Synchronous Motor (SPMSM) and Synchronous Reluctance Motor (SynchRel) drives. A theoretical analysis of the technique is first provided, followed by an exhaustive experimental validation.

2.2 Model of the Synchronous Machine with Search Coils (SCs)

A set of search coils can be obtained by modifying the wiring of three Thermistors featuring a common lead configuration placed on the stator winding of a three phase SynchRel, as shown in Fig. 2.2.1.

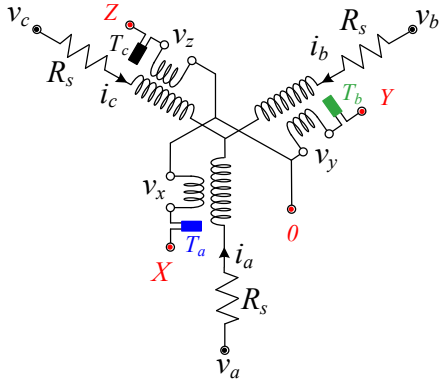

Figure 2.2.1 *Modified common lead thermistor installation.*

The Thermistors must be supplied with a DC current to monitor the temperature, by actual

resistance measurement. On the other hand, the voltage across at least two of the three search coils must be sampled to detect the rotor flux position. Thus, flux sensing can be easily made fully unaffected by temperature monitoring and vice-versa, by using in turn one of the three Thermistors for temperature monitoring, and the search coils connected to the other two Thermistors to estimate the rotor flux position. When the Thermistors are not supplied, the current flowing into the search coils is ideally null, due to the very high input impedance of the acquisition system used to sample the voltage at cabling terminals. Hence, the voltage drop caused by the Thermistors can be neglected for flux sensing purposes. On the other hand, AC voltages induced in the search coils can be eliminated through a low-pass filter for temperature monitoring purposes.

If the three Thermistors are series connected, or if only two Thermistors are used, two search coils can be obtained, according to Fig. 2.2.2.

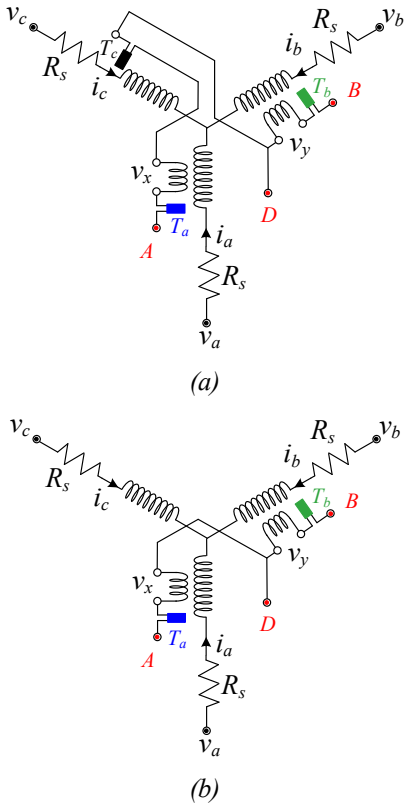

Figure 2.2.2 *(a) Modified series thermistors installation and (b) two thermistors arrangement.*

In this case, if not present, an additional cable is required to independently measure the voltages induced into the two search coils. Temperature measurement is accomplished at regular time intervals, whose length is suitably computed as function of the machine thermal time constant, in order to prevent dangerous overheating. When performing a temperature measurement, a straightforward procedure can be adopted to sample the voltage induced into the search coils. More precisely, alternatively the voltage of one of the search coils is turn sampled while the current flowing through the Thermistor, or the two Thermistors, connected in series to the other search coil is measured. This makes possible an independent measure of the temperature and the voltages induced in to the search coils, although the last is accomplished asynchronously. However, if the voltage sampling time is sufficiently high, the delay introduced does not affect the rotor position estimation, at least in the low and medium speed operational range. For the sake of clarity, Fig. 2.2.3 shows the results achieved by simulating the Thermistors configuration of Fig. 2.2.2a in which a 5V DC supply voltage is applied to the voltage loops including the Thermistors and the SCs. The voltages v_1 and v_2 measuring the connection between SCs and Thermistors are sampled and sequentially acquired at 20kHz, and then a high pass filter followed by a stationary reference frame

transformation $qd/\alpha\beta$ are used to extract only the AC components exploited to estimate the rotor position, as will be discussed in the next paragraphs. Low pass filters are instead used to isolate the DC voltage components allowing to estimate the Thermistor values.

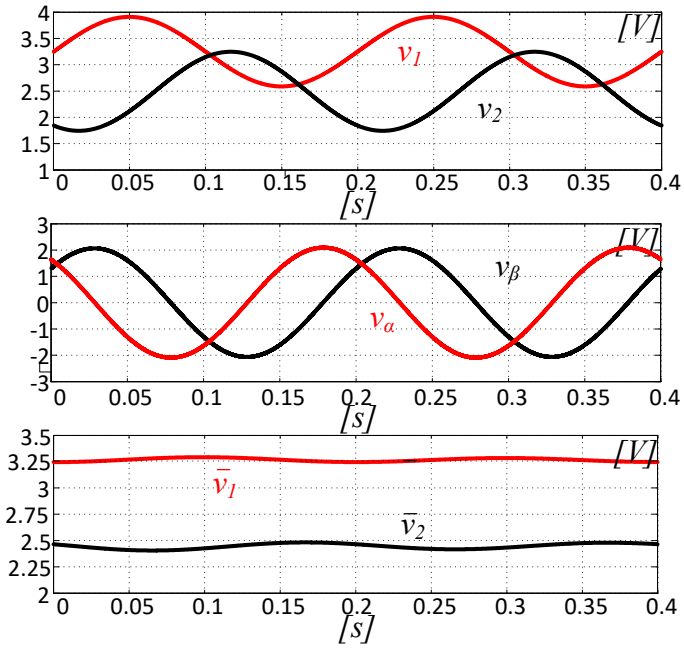

Figure 2.2.3 *Voltages at the terminal of the series connection of thermistors and SCs, AC and DC voltage components.*

A modified common lead installation is considered, where the Thermistors wirings are wound around the stator teeth. The spatial distribution of the main winding magnetomotive force is unmodified, as shown in Fig. 2.2.4.

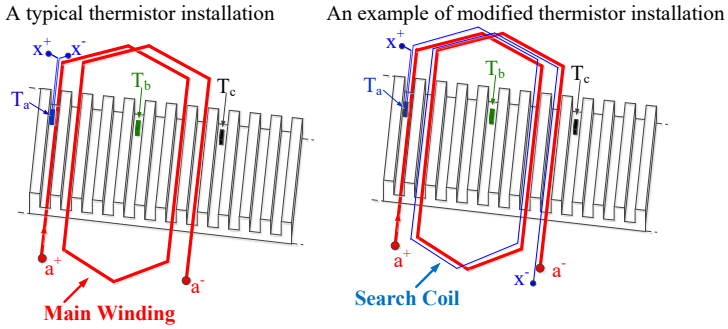

Figure 2.2.4 *Search coil installation utilized in this study.*

Thermistors feature very small size and mass and a medium impedance, hence the wires connecting the motor and the thermistor can be of inexpensive light gauge. Thermistors are physically placed inside the machine to sense the temperature of likely hot spots, whose location depends on the motor design. In some cases, the optimum location of these sensors may have to be determined from test experience.

In order to introduce the theoretical study on the proposed sensorless algorithms based on the SCs, it is useful to generalize the mathematical model with an IPMSM where the additional SC winding, characterized by a very low number of coils, has been included in the stator cave. In general, under the hypotheses that the SCs are operated at zero current ($\boldsymbol{i}_{xyz}$=0), the mathematical model of the machine including the set of search coils is given in the *a,b,c* stationary reference frame by the following equations, [44]:

$$\begin{bmatrix} v_a \\ v_b \\ v_c \end{bmatrix} = \boldsymbol{R_s} \begin{bmatrix} i_a \\ i_b \\ i_c \end{bmatrix} + \frac{d}{dt} \begin{bmatrix} \lambda_a \\ \lambda_b \\ \lambda_c \end{bmatrix} \qquad \begin{bmatrix} \lambda_a \\ \lambda_b \\ \lambda_c \end{bmatrix} = \boldsymbol{L_s}(\theta_{re}) \begin{bmatrix} i_a \\ i_b \\ i_c \end{bmatrix} + \boldsymbol{\Lambda_{pm}} \qquad \boldsymbol{\Lambda_{pmSC}} = \frac{N_{sSC}}{N_s} \boldsymbol{\Lambda_{pm}} \quad (2.2.1)$$

$$\begin{bmatrix} v_x \\ v_y \\ v_z \end{bmatrix} = \frac{d}{dt} \begin{bmatrix} \lambda_x \\ \lambda_y \\ \lambda_z \end{bmatrix} \qquad \begin{bmatrix} \lambda_x \\ \lambda_y \\ \lambda_z \end{bmatrix} = \boldsymbol{M_s}(\theta_{re}) \begin{bmatrix} i_a \\ i_b \\ i_c \end{bmatrix} + \boldsymbol{\Lambda_{pmSC}} \quad (2.2.2)$$

where v_a, v_b, v_c; i_a, i_b, i_c e λ_a, λ_b, λ_c are the phase voltages, phase currents and phase fluxes of the main winding, respectively; while v_x, v_y, v_z; i_x, i_y, i_z e λ_x, λ_y, λ_z are the phase voltages, phase currents and phase fluxes of the SCs winding, respectively. The stator resistance matrix $\boldsymbol{R_s}$, inductance matrix $\boldsymbol{L_s}(\theta_{re})$ and the permanent magnet flux vector $\boldsymbol{\Lambda_{pm}}$ are identical to those defined in paragraph 1.3, $\boldsymbol{M_s}(\theta_{re})$ is the inductance matrix of the SC set, which deals only with the magnetic coupling between the SCs and the main stator winding, as the current flowing through the search coils is supposed null and $\boldsymbol{\Lambda_{pmSC}}$ is the permanent magnet flux linkage vector induced in the Search Coils, depending by the product between $\boldsymbol{\Lambda_{pm}}$ and the ratio between the number of coils of the main windings N_s and the number of coils of the SCs N_{sSC}

For the same reason, the voltage drop across the Thermistors is neglected.

$$\boldsymbol{M_s}(\theta_{re}) = \begin{bmatrix} M_A\text{-}M_B\cos(2\theta_{re}) & -0.5M_A\text{-}M_B\cos(2\theta_{re}\text{-}2\pi/3) & -0.5M_A\text{-}M_B\cos(2\theta_{re}\text{+}2\pi/3) \\ -0.5M_A\text{-}M_B\cos(2\theta_{re}\text{-}2\pi/3) & M_A\text{-}M_B\cos(2\theta_{re}\text{-}4\pi/3) & -0.5M_A\text{-}M_B\cos(\theta_{re}\text{+}2\pi) \\ -0.5M_A\text{-}M_B\cos(2\theta_{re}\text{+}2\pi/3) & -0.5M_A\text{-}M_B\cos(2\theta_{re}\text{+}2\pi) & M_A\text{-}M_B\cos(2\theta_{re}\text{+}4\pi/3) \end{bmatrix}$$

where M_A is the synchronous mutual inductance coefficient and M_B is the saliency mutual inductance coefficient, between the main windings and the Search Coils:

$$M_A = \frac{M_{md} + M_{mq}}{3} \qquad M_B = \frac{M_{md} - M_{mq}}{3}$$

where M_{mq} and M_{md} are the qd-axis mutual inductance coefficients, respectively. In particular, the synchronous and saliency inductances, M_A and M_B respectively, have been evaluated by considering the measurement system setup presented in [55] (Fig. 1).

Voltages induced in the SCs, defined in (2.2.1) and (2.2.2), encompass a component which is function of the phase currents and a component related to the anisotropy of the machine, thus preventing a direct measurement of the rotor position from the last one.

The previous model can be also referred to an orthogonal reference frame qd synchronous with the electrical rotor position θ_{re} and at electrical speed ω_{re}, with d-axis aligned with the rotor flux vector. By exploiting the transformation matrix defined in (1.4.8), the equations of the mathematical model (2.2.1) - (2.2.2) can be rewritten:

$$\begin{bmatrix} v_{q1} \\ v_{d1} \end{bmatrix} = \boldsymbol{K_{qd}} \begin{bmatrix} v_a \\ v_b \\ v_c \end{bmatrix} = \boldsymbol{K_{qd}}\, \boldsymbol{R_s}\, [\boldsymbol{K_{qd}}]^{-1} \begin{bmatrix} i_{q1} \\ i_{d1} \end{bmatrix} + \boldsymbol{K_{qd}} \frac{d}{dt} \left([\boldsymbol{K_{qd}}]^{-1} \begin{bmatrix} \lambda_{q1} \\ \lambda_{d1} \end{bmatrix} \right) \quad (2.2.3)$$

$$\begin{bmatrix} \lambda_{q1} \\ \lambda_{d1} \end{bmatrix} = \boldsymbol{K_{qd}} \begin{bmatrix} \lambda_a \\ \lambda_b \\ \lambda_c \end{bmatrix} = \boldsymbol{K_{qd}}\, \boldsymbol{L_s}(\theta_{re})\, [\boldsymbol{K_{qd}}]^{-1} \begin{bmatrix} i_{q1} \\ i_{d1} \end{bmatrix}$$

$$\begin{bmatrix} v_{q2} \\ v_{d2} \end{bmatrix} = \boldsymbol{K_{qd}} \begin{bmatrix} v_x \\ v_y \\ v_z \end{bmatrix} = \boldsymbol{K_{qd}} \frac{d}{dt} \left([\boldsymbol{K_{qd}}]^{-1} \begin{bmatrix} \lambda_{q2} \\ \lambda_{d2} \end{bmatrix} \right)$$

$$\begin{bmatrix} \lambda_{q2} \\ \lambda_{d2} \end{bmatrix} = \boldsymbol{K_{qd}} \begin{bmatrix} \lambda_x \\ \lambda_y \\ \lambda_z \end{bmatrix} = \boldsymbol{K_{qd}}\, \boldsymbol{M_s}(\theta_{re})\, [\boldsymbol{K_{qd}}]^{-1} \begin{bmatrix} i_{q1} \\ i_{d1} \end{bmatrix} \tag{2.2.4}$$

where:

$$\begin{bmatrix} i_{q1} \\ i_{d1} \end{bmatrix} = \boldsymbol{K_{qd}} \begin{bmatrix} i_a \\ i_b \\ i_c \end{bmatrix} \tag{2.2.5}$$

By developing the computation of the above relationships, the model of synchronous machine with Search Coils is considered in *qd*-axis:

$$\begin{bmatrix} v_{q1} \\ v_{d1} \end{bmatrix} = \begin{bmatrix} R_s & 0 \\ 0 & R_s \end{bmatrix} \begin{bmatrix} i_{q1} \\ i_{d1} \end{bmatrix} + \begin{bmatrix} pL_q & \omega_{re} L_d \\ -\omega_{re} L_q & pL_d \end{bmatrix} \begin{bmatrix} i_{q1} \\ i_{d1} \end{bmatrix} + \begin{bmatrix} \omega_{re} \lambda_{pm} \\ 0 \end{bmatrix} \tag{2.2.6}$$

$$\begin{bmatrix} v_{q2} \\ v_{d2} \end{bmatrix} = \begin{bmatrix} pM_{mq} & \omega_{re} M_{md} \\ -\omega_{re} M_{mq} & pM_{md} \end{bmatrix} \begin{bmatrix} i_{q1} \\ i_{d1} \end{bmatrix} + \begin{bmatrix} \omega_{re} \lambda_{pmSC} \\ 0 \end{bmatrix} \tag{2.2.7}$$

where λ_{pmSC} is the permanent magnet flux linkage amplitude in the SCs:

$$\lambda_{pmSC} = \frac{N_{sSC}}{N_s} \lambda_{pm}$$

As already described above, the SCs phase currents are in steady state conditions null; therefore, the electromagnetic torque will depend by the main winding currents only; by using the generic expression of the electromagnetic torque defined in paragraph 1.3 and by applying the synchronous reference frame transformation, the electromagnetic torque in qd-axis for a generic IPMSM is given by:

$$T_e = \frac{3}{2} pp\, [\lambda_{pm}\, i_{q1} + (L_d - L_q)\, i_{q1}\, i_{d1}] \tag{2.2.8}$$

The equivalent circuit of the IPMSM including SCs in the synchronous reference frame is shown in Fig. 2.2.5:

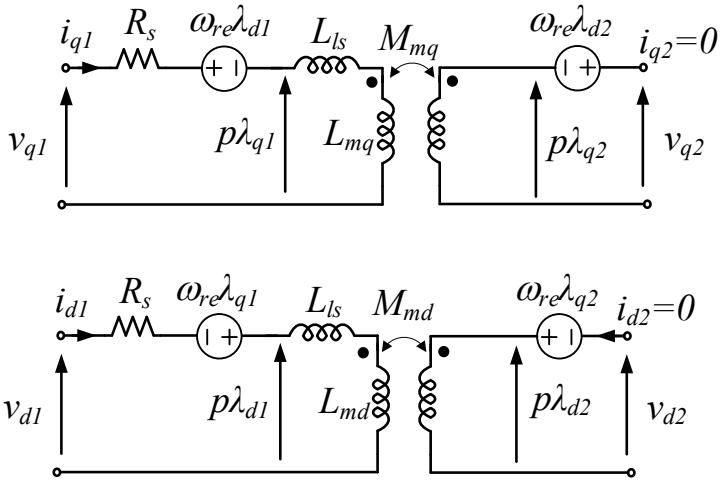

Figure 2.2.5 *Equivalent circuit of the IPMSM in the synchronous reference frame.*

2.3 Rotor Flux Position Estimation

After having described the mathematical model of the IPMSM including the SCs, both in a stationary reference frame (*abc*), and in orthogonal reference frame synchronous to the rotor flux position (*qd*), it is now necessary to find a way to estimate the rotor flux position through the direct measurement of the induced voltages on the SCs.

Referring to Fig. 2.3.1, it is possible to define several synchronous reference frame systems:

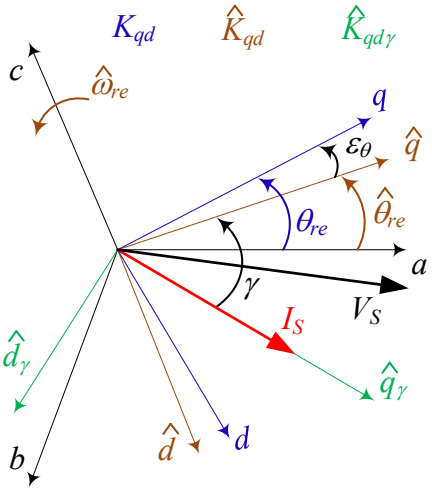

Figure 2.3.1 *Considered Synchronous reference frames*

- Synchronous reference frame aligned to rotor flux position θ_{re}, i.e., *qd-axes* reference frame.
- Synchronous reference frame aligned to the estimated rotor flux position $\hat{\theta}_{re}$, i. e., $\hat{qd}$*-axes* reference frame.
- Synchronous reference frame aligned to the angular position $\hat{\theta}_{re}$ - γ, i.e., $\hat{qd\gamma}$*-axes* reference frame.

Where γ is the angular phase shift between the stator current vector I_s and the estimated q-axis, i.e. $\hat{q}$. By defining with ε_θ, the rotor position estimation error, it can be written:

$$\theta_{re} = \hat{\theta}_{re} + \varepsilon_\theta \tag{2.3.1}$$

Henceforth the mathematical model of the IPMSM machine, defined in (2.2.6) – (2.2.7), will be analyzed step by step in order to find the most suitable reference frame system to estimate the rotor flux position. In any case, the following hypotheses will be considered:

- First hypothesis: the currents flowing in the stator winding are considered in steady state condition.
- Second hypothesis: ($\gamma = constant$).

Furthermore, by supposing that the estimation error ε_θ is constant or slowly variable, we can approximate the estimate electrical rotor speed $\hat{\omega}_{re}$ with the real electrical rotor speed ω_{re}:

$$\hat{\omega}_{re} \approx \omega_{re} \tag{2.3.2}$$

2.3.1 IPMSM Mathematical Model in qd-axes Reference Frame

When a synchronous reference frame with the real rotor flux position θ_{re} is considered the transformation matrix $\boldsymbol{K_{qd}}$ and its inverse matrix $[\boldsymbol{K_{qd}}]^{-1}$, are already defined in the paragraph 1.3, are given:

$$\boldsymbol{K_{qd}} = \frac{2}{3}\begin{bmatrix} cos(\theta_{re}) & cos(\theta_{re}-2\pi/3) & cos(\theta_{re}+2\pi/3) \\ sin(\theta_{re}) & sin(\theta_{re}-2\pi/3) & sin(\theta_{re}+2\pi/3) \end{bmatrix}$$

$$[\boldsymbol{K_{qd}}]^{-1} = \begin{bmatrix} cos(\theta_{re}) & sin(\theta_{re}) \\ cos(\theta_{re}-2\pi/3) & sin(\theta_{re}-2\pi/3) \\ cos(\theta_{re}+2\pi/3) & sin(\theta_{re}+2\pi/3) \end{bmatrix} \tag{2.3.3}$$

In fact, the IPMSM mathematical model in qd-axis reference frame is already defined in (2.2.6) and (2.2.7). By considering the above first hypothesis the currents flowing in the stator winding can be expressed as:

$$i_a = I_s\, cos(\theta_{re}-\gamma) \qquad i_b = I_s\, cos(\theta_{re}-\gamma-2\pi/3) \qquad i_c = I_s\, cos(\theta_{re}-\gamma+2\pi/3) \tag{2.3.4}$$

The expressions (2.3.4) can be rewritten in qd-axis reference frame, as:

$$\begin{bmatrix} i_{q1} \\ i_{d1} \end{bmatrix} = \boldsymbol{K_{qd}} \begin{bmatrix} i_a \\ i_b \\ i_c \end{bmatrix} = I_s \begin{bmatrix} cos(\gamma) \\ sin(\gamma) \end{bmatrix} \tag{2.3.5}$$

Geometrically, the current vector can be decomposed along the qd-axis by means the following Fig. 2.3.2:

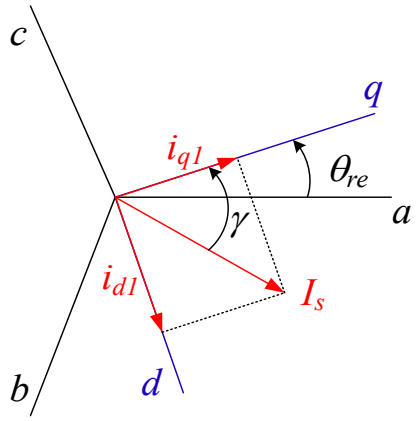

Figure 2.3.2 *Main Winding Stator Current Vector in qd Synchronous Reference Frame*

In these conditions and under the second hypothesis (γ = *constant*), the *qd-axes* currents and its derivatives can be computed in (2.3.6):

$$i_{q1} = I_s\, cos(\gamma) \qquad i_{d1} = I_s\, sin(\gamma) \qquad pi_{q1} = 0 \qquad pi_{d1} = 0 \tag{2.3.6}$$

By substituting the expressions (2.3.6) in the (2.2.6) and (2.2.7), the IPMSM mathematical model in *qd-axis* reference frame can be rewritten as:

$$\begin{cases} v_{q1} = R_s\, I_s\, cos(\gamma) + \omega_{re}\, L_d\, I_s\, sin(\gamma) + \omega_{re}\, \lambda_{pm} \\ v_{d1} = R_s\, I_s\, sin(\gamma) - \omega_{re}\, L_q\, I_s\, cos(\gamma) \end{cases} \tag{2.3.7}$$

$$\begin{cases} v_{q2} = \omega_{re}\, M_{md}\, I_s\, sin(\gamma) + \omega_{re}\, \lambda_{pmSC} \\ v_{d2} = -\, \omega_{re}\, M_{mq}\, I_s\, cos(\gamma) \end{cases} \tag{2.3.8}$$

From the equations systems (2.3.8), the induced voltages in the SCs, expressed in the synchronous reference frame with the real rotor flux position, are very simple but impractical for the angular rotor position estimation, because in a generic sensorless control algorithm the rotor flux position must be estimated and thus the analytical approach should be change as well as in the next sub-paragraph.

2.3.2 IPMSM Mathematical Model in $\widehat{qd}$-axis Reference Frame

For this reason, starting from the mathematical model (2.2.1) and (2.2.2) it is necessary to consider a model of the machine in a synchronous reference frame aligned to the estimated rotor flux position, i.e. $\hat{\boldsymbol{K}}_{\boldsymbol{qd}}$ and its inverse matrix $[\hat{\boldsymbol{K}}_{\boldsymbol{qd}}]^{-1}$; furthermore, since it is a sensorless algorithm, the rotor position must be estimated and therefore the transformation angle used in vector control is precisely the estimated angular rotor position $\hat{\theta}_{re}$.

$$\hat{\boldsymbol{K}}_{\boldsymbol{qd}} = \frac{2}{3}\begin{bmatrix} cos(\hat{\theta}_{re}) & cos(\hat{\theta}_{re}-2\pi/3) & cos(\hat{\theta}_{re}+2\pi/3) \\ sin(\hat{\theta}_{re}) & sin(\hat{\theta}_{re}-2\pi/3) & sin(\hat{\theta}_{re}+2\pi/3) \end{bmatrix}$$

$$[\hat{\boldsymbol{K}}_{\boldsymbol{qd}}]^{-1} = \begin{bmatrix} cos(\hat{\theta}_{re}) & sin(\hat{\theta}_{re}) \\ cos(\hat{\theta}_{re}-2\pi/3) & sin(\hat{\theta}_{re}-2\pi/3) \\ cos(\hat{\theta}_{re}+2\pi/3) & sin(\hat{\theta}_{re}+2\pi/3) \end{bmatrix} \tag{2.3.9}$$

The IPMSM mathematical model in $\widehat{qd}$-axis reference frame is obtained by applying the transformation matrices (2.3.9) in (2.2.1) and (2.2.2):

$$\begin{bmatrix} \hat{v}_{q1} \\ \hat{v}_{d1} \end{bmatrix} = \hat{\boldsymbol{K}}_{\boldsymbol{qd}} \begin{bmatrix} v_a \\ v_b \\ v_c \end{bmatrix} = \hat{\boldsymbol{K}}_{\boldsymbol{qd}}\, \boldsymbol{R_s}\, [\hat{\boldsymbol{K}}_{\boldsymbol{qd}}]^{-1} \begin{bmatrix} \hat{i}_{q1} \\ \hat{i}_{d1} \end{bmatrix} + \hat{\boldsymbol{K}}_{\boldsymbol{qd}} \frac{d}{dt}\left([\hat{\boldsymbol{K}}_{\boldsymbol{qd}}]^{-1} \begin{bmatrix} \hat{\lambda}_{q1} \\ \hat{\lambda}_{d1} \end{bmatrix} \right)$$

$$\begin{bmatrix} \hat{\lambda}_{q1} \\ \hat{\lambda}_{d1} \end{bmatrix} = \hat{\boldsymbol{K}}_{\boldsymbol{qd}} \begin{bmatrix} \lambda_a \\ \lambda_b \\ \lambda_c \end{bmatrix} = \hat{\boldsymbol{K}}_{\boldsymbol{qd}}\, \boldsymbol{L_s}(\theta_{re})\, [\hat{\boldsymbol{K}}_{\boldsymbol{qd}}]^{-1} \begin{bmatrix} \hat{i}_{q1} \\ \hat{i}_{d1} \end{bmatrix} \tag{2.3.10}$$

$$\begin{bmatrix} \hat{v}_{q2} \\ \hat{v}_{d2} \end{bmatrix} = \hat{\boldsymbol{K}}_{\boldsymbol{qd}} \begin{bmatrix} v_x \\ v_y \\ v_z \end{bmatrix} = \hat{\boldsymbol{K}}_{\boldsymbol{qd}} \frac{d}{dt}\left([\hat{\boldsymbol{K}}_{\boldsymbol{qd}}]^{-1} \begin{bmatrix} \hat{\lambda}_{q2} \\ \hat{\lambda}_{d2} \end{bmatrix} \right)$$

$$\begin{bmatrix} \hat{\lambda}_{q2} \\ \hat{\lambda}_{d2} \end{bmatrix} = \hat{\boldsymbol{K}}_{\boldsymbol{qd}} \begin{bmatrix} \lambda_x \\ \lambda_y \\ \lambda_z \end{bmatrix} = \hat{\boldsymbol{K}}_{\boldsymbol{qd}}\, \boldsymbol{M_s}(\theta_{re})\, [\hat{\boldsymbol{K}}_{\boldsymbol{qd}}]^{-1} \begin{bmatrix} \hat{i}_{q1} \\ \hat{i}_{d1} \end{bmatrix} \tag{2.3.11}$$

$$\begin{bmatrix} \hat{i}_{q1} \\ \hat{i}_{d1} \end{bmatrix} = \hat{\boldsymbol{K}}_{\boldsymbol{qd}} \begin{bmatrix} i_a \\ i_b \\ i_c \end{bmatrix} \tag{2.3.12}$$

where $\hat{v}_{qd1}$, $\hat{i}_{qd1}$ and $\hat{\lambda}_{qd1}$ are the main winding voltages, currents and fluxes in the estimated synchronous reference frame $\hat{qd}$, respectively; while $\hat{v}_{qd2}$ and $\hat{\lambda}_{qd2}$ are the SCs voltages and currents in the estimated synchronous reference frame $\hat{qd}$.

By manipulating the expressions (2.3.11) and (2.3.12), the following results are obtained:

$$\begin{bmatrix} \hat{v}_{q1} \\ \hat{v}_{d1} \end{bmatrix} = \begin{bmatrix} R_s & 0 \\ 0 & R_s \end{bmatrix} \begin{bmatrix} \hat{i}_{q1} \\ \hat{i}_{d1} \end{bmatrix} + \begin{bmatrix} p & \omega_{re} \\ -\omega_{re} & p \end{bmatrix} \begin{bmatrix} \hat{\lambda}_{q1} \\ \hat{\lambda}_{d1} \end{bmatrix}$$

$$\begin{bmatrix} \hat{\lambda}_{q1} \\ \hat{\lambda}_{d1} \end{bmatrix} = \begin{bmatrix} L_{ls} + \frac{3}{2}L_A - \frac{3}{2}L_B \cos(2\varepsilon_\theta) & \frac{3}{2}L_B \sin(2\varepsilon_\theta) \\ \frac{3}{2}L_B \sin(2\varepsilon_\theta) & L_{ls} + \frac{3}{2}L_A + \frac{3}{2}L_B \cos(2\varepsilon_\theta) \end{bmatrix} \begin{bmatrix} \hat{i}_{q1} \\ \hat{i}_{d1} \end{bmatrix} + \lambda_{pm} \begin{bmatrix} \sin(\varepsilon_\theta) \\ \cos(\varepsilon_\theta) \end{bmatrix} \tag{2.3.13}$$

$$\begin{bmatrix} \hat{v}_{q2} \\ \hat{v}_{d2} \end{bmatrix} = \begin{bmatrix} p & \omega_{re} \\ -\omega_{re} & p \end{bmatrix} \begin{bmatrix} \hat{\lambda}_{q2} \\ \hat{\lambda}_{d2} \end{bmatrix}$$

$$\begin{bmatrix} \hat{\lambda}_{q2} \\ \hat{\lambda}_{d2} \end{bmatrix} = \frac{3}{2} \begin{bmatrix} M_A - M_B \cos(2\varepsilon_\theta) & M_B \sin(2\varepsilon_\theta) \\ M_B \sin(2\varepsilon_\theta) & M_A + M_B \cos(2\varepsilon_\theta) \end{bmatrix} \begin{bmatrix} \hat{i}_{q1} \\ \hat{i}_{d1} \end{bmatrix} + \lambda_{pmSC} \begin{bmatrix} \sin(\varepsilon_\theta) \\ \cos(\varepsilon_\theta) \end{bmatrix} \tag{2.3.14}$$

By further mathematical manipulations, the final expressions of the main winding voltages and SCs voltages in the estimated synchronous reference frame $\hat{qd}$ are:

$$\begin{bmatrix} \hat{v}_{q1} \\ \hat{v}_{d1} \end{bmatrix} = \begin{bmatrix} R_s & 0 \\ 0 & R_s \end{bmatrix} \begin{bmatrix} \hat{i}_{q1} \\ \hat{i}_{d1} \end{bmatrix} + \begin{bmatrix} L_{ls} + \frac{3}{2}L_A - \frac{3}{2}L_B \cos(2\varepsilon_\theta) & \frac{3}{2}L_B \sin(2\varepsilon_\theta) \\ \frac{3}{2}L_B \sin(2\varepsilon_\theta) & L_{ls} + \frac{3}{2}L_A + \frac{3}{2}L_B \cos(2\varepsilon_\theta) \end{bmatrix} \begin{bmatrix} p\hat{i}_{q1} \\ p\hat{i}_{d1} \end{bmatrix} +$$
$$+ \omega_{re} \begin{bmatrix} \frac{3}{2}L_B \sin(2\varepsilon_\theta) & L_{ls} + \frac{3}{2}L_A + \frac{3}{2}L_B \cos(2\varepsilon_\theta) \\ -L_{ls} - \frac{3}{2}L_A + \frac{3}{2}L_B \cos(2\varepsilon_\theta) & -\frac{3}{2}L_B \sin(2\varepsilon_\theta) \end{bmatrix} \begin{bmatrix} \hat{i}_{q1} \\ \hat{i}_{d1} \end{bmatrix} + \omega_{re}\, \lambda_{pm} \begin{bmatrix} \cos(\varepsilon_\theta) \\ -\sin(\varepsilon_\theta) \end{bmatrix} \tag{2.3.15}$$

$$\begin{bmatrix} \hat{v}_{q2} \\ \hat{v}_{d2} \end{bmatrix} = \frac{3}{2} \begin{bmatrix} M_A - M_B \cos(2\varepsilon_\theta) & M_B \sin(2\varepsilon_\theta) \\ M_B \sin(2\varepsilon_\theta) & M_A + M_B \cos(2\varepsilon_\theta) \end{bmatrix} \begin{bmatrix} p\hat{i}_{q1} \\ p\hat{i}_{d1} \end{bmatrix} +$$
$$+ \frac{3}{2}\, \omega_{re} \begin{bmatrix} M_B \sin(2\varepsilon_\theta) & M_A + M_B \cos(2\varepsilon_\theta) \\ -M_A + M_B \cos(2\varepsilon_\theta) & -M_B \sin(2\varepsilon_\theta) \end{bmatrix} \begin{bmatrix} \hat{i}_{q1} \\ \hat{i}_{d1} \end{bmatrix} + \omega_{re}\, \lambda_{pmSC} \begin{bmatrix} \cos(\varepsilon_\theta) \\ -\sin(\varepsilon_\theta) \end{bmatrix} \tag{2.3.16}$$

where, the position error ε_θ is given:

$$\varepsilon_\theta = \theta_{re} - \hat{\theta}_{re} \tag{2.3.17}$$

From the expressions (2.3.15) e (2.3.16) it is evident that the resulting model is quite complex, and it is difficult to extract any information on the angular position.

However, even in the follow estimated synchronous reference frame $\hat{qd}$-*axes* it is possible to assume that the stator currents, in steady state conditions, are written as:

$$i_a = I_s \cos(\hat{\theta}_{re}-\gamma) \qquad i_b = I_s \cos(\hat{\theta}_{re}-\gamma-2\pi/3) \qquad i_c = I_s \cos(\hat{\theta}_{re}-\gamma+2\pi/3) \tag{2.3.18}$$

In this case, the expressions of the stator current (2.3.18) are depending by the estimate rotor position $\hat{\theta}_{re}$. Even in this case the follow results are given:

$$\begin{bmatrix} \hat{i}_{q1} \\ \hat{i}_{d1} \end{bmatrix} = \hat{\boldsymbol{K}}_{\boldsymbol{qd}} \begin{bmatrix} i_a \\ i_b \\ i_c \end{bmatrix} = I_s \begin{bmatrix} \cos(\gamma) \\ \sin(\gamma) \end{bmatrix} \tag{2.3.19}$$

Geometrically, the current vector can be decomposed along the $\hat{qd}$-*axes* by means the following Fig. 2.3.3:

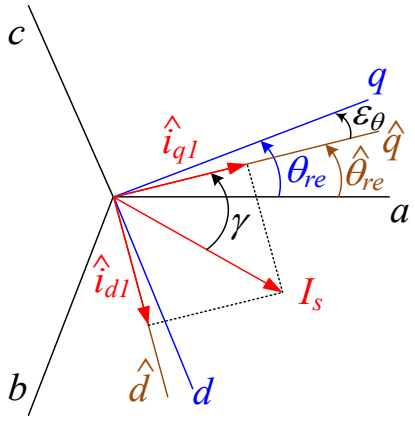

Figure 2.3.3 *Main winding current vector in estimated qd Synchronous Reference Frame*

By considering the second hypothesis, γ = *constant*, the $\hat{qd}$-*axes* currents and its derivatives can be computed in (2.3.20):

$$\hat{i}_{q1} = I_s \cos(\gamma) \qquad \hat{i}_{d1} = I_s \sin(\gamma) \qquad p\,\hat{i}_{q1} = 0 \qquad p\,\hat{i}_{d1} = 0 \tag{2.3.20}$$

By substituting the conditions (2.3.19) and (2.3.20) in the expressions (2.3.15) and (2.3.16), the equations became:

$$\begin{cases} \hat{v}_{q1} = R_s I_s \cos(\gamma) + \frac{3}{2} \omega_{re} I_s \left[(L_{ls}+L_A) \sin(\gamma) + L_B \sin(2\varepsilon_\theta + \gamma)\right] + \omega_{re} \lambda_{pm} \cos(\varepsilon_\theta) \\ \hat{v}_{d1} = R_s I_s \sin(\gamma) - \frac{3}{2} \omega_{re} I_s \left[(L_{ls}+L_A) \cos(\gamma) - L_B \cos(2\varepsilon_\theta + \gamma)\right] - \omega_{re} \lambda_{pm} \sin(\varepsilon_\theta) \end{cases} \tag{2.3.21}$$

$$\begin{cases} \hat{v}_{q2} = \frac{3}{2} \omega_{re} I_s \left[M_A \sin(\gamma) + M_B \sin(2\varepsilon_\theta + \gamma)\right] + \omega_{re} \lambda_{pmSC} \cos(\varepsilon_\theta) \\ \hat{v}_{d2} = -\frac{3}{2} \omega_{re} I_s \left[M_A \cos(\gamma) - M_B \cos(2\varepsilon_\theta + \gamma)\right] - \omega_{re} \lambda_{pmSC} \sin(\varepsilon_\theta) \end{cases} \tag{2.3.22}$$

Considering the expressions (2.3.22) related to the inducted voltages on the SCs, it is easy to observe that the magnitude of $\hat{v}_{qd2}$ depends on the mutual inductance coefficients M_A, M_B and by the permanent magnet flux linkage on the SCs, λ_{pmSC}.

Through this estimated synchronous reference frame it is not possible to directly detect the rotor flux position independently from the parameters M_A, M_B ed λ_{pmSC}, both for SPMSM and SynchRel motor drives.

2.3.3 ,IPMSM Mathematical Model in $q\hat{d}\gamma$-axis Reference Frame

In order to obtain a direct information on the estimated rotor flux position completely independent of the motor parameters, it is necessary to consider a further reference frame synchronous to $\hat{\theta}_{re}$ - γ which is denoted by $qd\hat{\gamma}$-*axes*.

Starting from the transformation matrices $\hat{\boldsymbol{K}}_{qd\gamma}$ and its inverse matric $[\hat{\boldsymbol{K}}_{qd\gamma}]^{-1}$ (2.3.23)

$$\hat{\boldsymbol{K}}_{qd\gamma} = \frac{2}{3}\begin{bmatrix} cos(\hat{\theta}_{re}\text{-}\gamma) & cos(\hat{\theta}_{re}\text{-}\gamma\text{-}2\pi/3) & cos(\hat{\theta}_{re}\text{-}\gamma\text{+}2\pi/3) \\ sin(\hat{\theta}_{re}\text{-}\gamma) & sin(\hat{\theta}_{re}\text{-}\gamma\text{-}2\pi/3) & sin(\hat{\theta}_{re}\text{-}\gamma\text{+}2\pi/3) \end{bmatrix}$$

$$[\hat{\boldsymbol{K}}_{qd\gamma}]^{-1} = \begin{bmatrix} cos(\hat{\theta}_{re}\text{-}\gamma) & sin(\hat{\theta}_{re}\text{-}\gamma) \\ cos(\hat{\theta}_{re}\text{-}\gamma\text{-}2\pi/3) & sin(\hat{\theta}_{re}\text{-}\gamma\text{-}2\pi/3) \\ cos(\hat{\theta}_{re}\text{-}\gamma\text{+}2\pi/3) & sin(\hat{\theta}_{re}\text{-}\gamma\text{+}2\pi/3) \end{bmatrix} \tag{2.3.23}$$

it is possible to obtain the following equations:

$$\begin{bmatrix} \hat{v}_{q1\gamma} \\ \hat{v}_{d1\gamma} \end{bmatrix} = \hat{\boldsymbol{K}}_{qd\gamma}\begin{bmatrix} v_a \\ v_b \\ v_c \end{bmatrix} = \hat{\boldsymbol{K}}_{qd\gamma}\boldsymbol{R_s}\,[\hat{\boldsymbol{K}}_{qd\gamma}]^{-1}\begin{bmatrix} \hat{i}_{q1\gamma} \\ \hat{i}_{d1\gamma} \end{bmatrix} + \hat{\boldsymbol{K}}_{qd\gamma}\frac{d}{dt}\left([\hat{\boldsymbol{K}}_{qd\gamma}]^{-1}\begin{bmatrix} \hat{\lambda}_{q1\gamma} \\ \hat{\lambda}_{d1\gamma} \end{bmatrix}\right)$$

$$\begin{bmatrix} \hat{\lambda}_{q1\gamma} \\ \hat{\lambda}_{d1\gamma} \end{bmatrix} = \hat{\boldsymbol{K}}_{qd\gamma}\begin{bmatrix} \lambda_a \\ \lambda_b \\ \lambda_c \end{bmatrix} = \hat{\boldsymbol{K}}_{qd\gamma}\boldsymbol{L_s}(\theta_{re})\,[\hat{\boldsymbol{K}}_{qd\gamma}]^{-1}\begin{bmatrix} \hat{i}_{q1\gamma} \\ \hat{i}_{d1\gamma} \end{bmatrix} \tag{2.3.24}$$

$$\begin{bmatrix} \hat{v}_{q2\gamma} \\ \hat{v}_{d2\gamma} \end{bmatrix} = \hat{\boldsymbol{K}}_{qd\gamma}\begin{bmatrix} v_x \\ v_y \\ v_z \end{bmatrix} = \hat{\boldsymbol{K}}_{qd\gamma}\frac{d}{dt}\left([\hat{\boldsymbol{K}}_{qd}]^{-1}\begin{bmatrix} \hat{\lambda}_{q2\gamma} \\ \hat{\lambda}_{d2\gamma} \end{bmatrix}\right)$$

$$\begin{bmatrix} \hat{\lambda}_{q2\gamma} \\ \hat{\lambda}_{d2\gamma} \end{bmatrix} = \hat{\boldsymbol{K}}_{qd\gamma}\begin{bmatrix} \lambda_x \\ \lambda_y \\ \lambda_z \end{bmatrix} = \hat{\boldsymbol{K}}_{qd\gamma}\boldsymbol{M_s}(\theta_{re})\,[\hat{\boldsymbol{K}}_{qd\gamma}]^{-1}\begin{bmatrix} \hat{i}_{q1\gamma} \\ \hat{i}_{d1\gamma} \end{bmatrix} \tag{2.3.25}$$

$$\begin{bmatrix} \hat{i}_{q1\gamma} \\ \hat{i}_{d1\gamma} \end{bmatrix} = \hat{\boldsymbol{K}}_{qd\gamma}\begin{bmatrix} i_a \\ i_b \\ i_c \end{bmatrix} \tag{2.3.26}$$

where $\hat{v}_{qd1\gamma}$, $\hat{i}_{qd1\gamma}$ and $\hat{\lambda}_{qd1\gamma}$ are the main winding voltages, currents and fluxes respectively, in the new estimated reference frame $qd\hat{\gamma}$, while $\hat{v}_{qd2\gamma}$ and $\hat{\lambda}_{qd2\gamma}$ are the voltages and fluxes of the SCs in the new estimated reference frame $qd\hat{\gamma}$.

$$\begin{bmatrix} \hat{v}_{q1\gamma} \\ \hat{v}_{d1\gamma} \end{bmatrix} = \begin{bmatrix} R_s & 0 \\ 0 & R_s \end{bmatrix}\begin{bmatrix} \hat{i}_{q1\gamma} \\ \hat{i}_{d1\gamma} \end{bmatrix} + \begin{bmatrix} p & \omega_{re} \\ -\omega_{re} & p \end{bmatrix}\begin{bmatrix} \hat{\lambda}_{q1\gamma} \\ \hat{\lambda}_{d1\gamma} \end{bmatrix} \tag{2.3.27}$$

$$\begin{bmatrix} \hat{\lambda}_{q1\gamma} \\ \hat{\lambda}_{d1\gamma} \end{bmatrix} = \begin{bmatrix} L_{ls}+\frac{3}{2}L_A-\frac{3}{2}L_B\cos(2\varepsilon+2\gamma) & \frac{3}{2}L_B\sin(2\varepsilon_\theta+2\gamma) \\ \frac{3}{2}L_B\sin(2\varepsilon_\theta+2\gamma) & L_{ls}+\frac{3}{2}L_A+\frac{3}{2}L_B\cos(2\varepsilon_\theta+2\gamma) \end{bmatrix} \begin{bmatrix} \hat{i}_{q1\gamma} \\ \hat{i}_{d1\gamma} \end{bmatrix} + \lambda_{pm} \begin{bmatrix} \sin(\varepsilon_\theta+\gamma) \\ \cos(\varepsilon_\theta+\gamma) \end{bmatrix}$$

$$\begin{bmatrix} \hat{v}_{q2\gamma} \\ \hat{v}_{d2\gamma} \end{bmatrix} = \begin{bmatrix} p & \omega_{re} \\ -\omega_{re} & p \end{bmatrix} \begin{bmatrix} \hat{\lambda}_{q2\gamma} \\ \hat{\lambda}_{d2\gamma} \end{bmatrix}$$

(2.3.28)

$$\begin{bmatrix} \hat{\lambda}_{q2\gamma} \\ \hat{\lambda}_{d2\gamma} \end{bmatrix} = \frac{3}{2} \begin{bmatrix} M_A-M_B\cos(2\varepsilon_\theta+2\gamma) & M_B\sin(2\varepsilon_\theta+2\gamma) \\ M_B\sin(2\varepsilon_\theta+2\gamma) & M_A+M_B\cos(2\varepsilon_\theta+2\gamma) \end{bmatrix} \begin{bmatrix} \hat{i}_{q1\gamma} \\ \hat{i}_{d1\gamma} \end{bmatrix} + \lambda_{pmSC} \begin{bmatrix} \sin(\varepsilon_\theta+\gamma) \\ \cos(\varepsilon_\theta+\gamma) \end{bmatrix}$$

By considering the appropriate substitutions, the final voltages expressions of the main winding and SCs, in the $qd\hat{\gamma}$ reference frame, are given respectively:

$$\begin{bmatrix} \hat{v}_{q1\gamma} \\ \hat{v}_{d1\gamma} \end{bmatrix} = \begin{bmatrix} R_s & 0 \\ 0 & R_s \end{bmatrix} \begin{bmatrix} \hat{i}_{q1\gamma} \\ \hat{i}_{d1\gamma} \end{bmatrix} + \begin{bmatrix} L_{ls}+\frac{3}{2}L_A-\frac{3}{2}L_B\cos(2\varepsilon_\theta+2\gamma) & \frac{3}{2}L_B\sin(2\varepsilon_\theta+2\gamma) \\ \frac{3}{2}L_B\sin(2\varepsilon_\theta+2\gamma) & L_{ls}+\frac{3}{2}L_A+\frac{3}{2}L_B\cos(2\varepsilon_\theta+2\gamma) \end{bmatrix} \begin{bmatrix} p\hat{i}_{q1\gamma} \\ p\hat{i}_{d1\gamma} \end{bmatrix} +$$
$$+ \omega_{re} \begin{bmatrix} \frac{3}{2}L_B\sin(2\varepsilon_\theta+2\gamma) & L_{ls}+\frac{3}{2}L_A+\frac{3}{2}L_B\cos(2\varepsilon_\theta+2\gamma) \\ -L_{ls}-\frac{3}{2}L_A+\frac{3}{2}L_B\cos(2\varepsilon_\theta+2\gamma) & -\frac{3}{2}L_B\sin(2\varepsilon_\theta+2\gamma) \end{bmatrix} \begin{bmatrix} \hat{i}_{q1\gamma} \\ \hat{i}_{d1\gamma} \end{bmatrix} + \omega_{re}\lambda_{pm} \begin{bmatrix} \cos(\varepsilon_\theta+\gamma) \\ -\sin(\varepsilon_\theta+\gamma) \end{bmatrix} \quad (2.3.29)$$

$$\begin{bmatrix} \hat{v}_{q2\gamma} \\ \hat{v}_{d2\gamma} \end{bmatrix} = \frac{3}{2} \begin{bmatrix} M_A-M_B\cos(2\varepsilon_\theta+2\gamma) & M_B\sin(2\varepsilon_\theta+2\gamma) \\ M_B\sin(2\varepsilon_\theta+2\gamma) & M_A+M_B\cos(2\varepsilon_\theta+2\gamma) \end{bmatrix} \begin{bmatrix} p\hat{i}_{q1\gamma} \\ p\hat{i}_{d1\gamma} \end{bmatrix} +$$
$$+\frac{3}{2}\omega_{re} \begin{bmatrix} M_B\sin(2\varepsilon_\theta+2\gamma) & M_A+M_B\cos(2\varepsilon_\theta+2\gamma) \\ -M_A+M_B\cos(2\varepsilon_\theta+2\gamma) & -M_B\sin(2\varepsilon_\theta+2\gamma) \end{bmatrix} \begin{bmatrix} \hat{i}_{q1\gamma} \\ \hat{i}_{d1\gamma} \end{bmatrix} + \omega_{re}\lambda_{pmSC} \begin{bmatrix} \cos(\varepsilon_\theta+\gamma) \\ -\sin(\varepsilon_\theta+\gamma) \end{bmatrix} \quad (2.3.30)$$

Also in this case, based on the expressions (2.3.29) and (2.3.30), the mathematical model obtained in the $qd\hat{\gamma}$ reference frame is quite complex and it is very difficult to see the possibility of being able to extract some information on the rotor flux position. Considering steady state conditions, the qd-axis currents in the new reference frame $qd\hat{\gamma}$, can be written:

$$\begin{bmatrix} \hat{i}_{q1\gamma} \\ \hat{i}_{d1\gamma} \end{bmatrix} = \hat{\boldsymbol{K}}_{\boldsymbol{qd}\gamma} \begin{bmatrix} i_a \\ i_b \\ i_c \end{bmatrix} = \begin{bmatrix} I_s \\ 0 \end{bmatrix} \quad (2.3.31)$$

In this case, from (2.3.31), the decomposition of the current vector along the new estimated synchronous reference frame $qd\hat{\gamma}$ with the angular position $\hat{\theta}_{re} - \gamma$, provides that the current vector I_s is aligned with the axis $q\hat{\gamma}$, therefore the q-axis current $\hat{i}_{q1\gamma}$ is equal to the current vector amplitude I_s. Geometrically can be represented by the following Fig. 2.3.4:

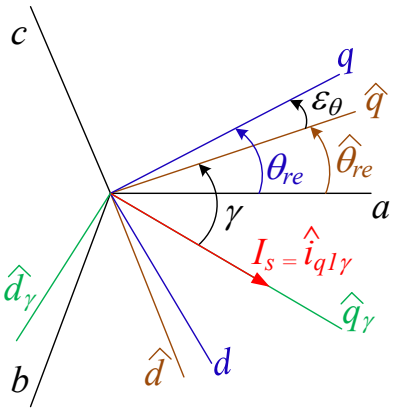

Figure 2.3.4 *Main Winding Stator Current Vector in qdγ-estimated Synchronous Reference Frame*

By considering the hypotheses on steady state conditions and γ = *constant*, the equations systems (2.3.30) and (2.3.31) can be rewritten as (2.3.32) and (2.3.33):

$$\begin{cases} \hat{v}_{q1\gamma} = R_s\, I_s + \frac{3}{2}\,\omega_{re}\, I_s\, L_B\, sin(2\varepsilon_\theta + 2\gamma) + \omega_{re}\, \lambda_{pm}\, cos(\varepsilon_\theta + \gamma) \\ \hat{v}_{d1\gamma} = -\frac{3}{2}\,\omega_{re}\, I_s \left[(L_{ls} + L_A) - L_B\, cos(2\varepsilon_\theta + 2\gamma)\right] - \omega_{re}\, \lambda_{pm}\, sin(\varepsilon_\theta + \gamma) \end{cases} \tag{2.3.32}$$

$$\begin{cases} \hat{v}_{q2\gamma} = \frac{3}{2}\,\omega_{re}\, I_s\, M_B\, sin(2\varepsilon_\theta + 2\gamma) + \omega_{re}\, \lambda_{pmSC}\, cos(\varepsilon_\theta + \gamma) \\ \hat{v}_{d2\gamma} = -\frac{3}{2}\,\omega_{re}\, I_s \left[M_A - M_B\, cos(2\varepsilon_\theta + 2\gamma)\right] - \omega_{re}\, \lambda_{pmSC}\, sin(\varepsilon_\theta + \gamma) \end{cases} \tag{2.3.33}$$

The final expressions obtained in (2.3.33) allow to derive the induced voltages on the SCs through the new reference frame $qd\hat{\gamma}$. In particular, (2.3.32) and (2.3.33) are valid in the generic case of an IPMSM; in this type of synchronous machine is more difficult to extract the information on the rotor flux position by using the induced voltages on the SCs. Similar expressions can be obtained for a SPMSM, where the saliency coefficients are null and the current vector angle is null ($\gamma = 0$) because the d-axis current is null ($i_{d1} = 0$):

$$\begin{cases} \hat{v}_{q1\gamma} = R_s\, I_s + \omega_{re}\, \lambda_{pm}\, cos(\varepsilon_\theta) \\ \hat{v}_{d1\gamma} = -\,\omega_{re}\, I_s\, L_s - \omega_{re}\, \lambda_{pm}\, sin(\varepsilon_\theta) \end{cases} \tag{2.3.34}$$

$$\begin{cases} \hat{v}_{q2\gamma} = \omega_{re}\, \lambda_{pmSC}\, cos(\varepsilon_\theta) \\ \hat{v}_{d2\gamma} = -\,\omega_{re}\, I_s\, M_{ms} - \omega_{re}\, \lambda_{pmSC}\, sin(\varepsilon_\theta) \end{cases} \tag{2.3.35}$$

From the expressions (2.3.35), as will be seen below, it is very easy to extract the information on the rotor flux position by using the induced voltages on the SCs. It should be noted that the self-inductive and mutual inductive coefficients have been grouped into two simple coefficients: $L_s = 3/2(L_{ls} + L_A)$ is the main winding self-inductive coefficient and $M_{ms} = 3/2 M_A$ is the SCs mutual inductive coefficient.

Similar simplification can be considered in case of SynchRel, where the permanent magnet is null:

$$\begin{cases} \hat{v}_{q1\gamma} = R_s\, I_s + \frac{3}{2}\,\omega_{re}\, I_s\, L_B\, sin(2\varepsilon_\theta + 2\gamma) \\ \hat{v}_{d1\gamma} = -\frac{3}{2}\,\omega_{re}\, I_s \left[(L_{ls} + L_A) - L_B\, cos(2\varepsilon_\theta + 2\gamma)\right] \end{cases} \tag{2.3.36}$$

$$\begin{cases} \hat{v}_{q2\gamma} = \dfrac{3}{2}\,\omega_{re}\,I_s\,M_B\,\sin(2\varepsilon_\theta + 2\gamma) \\ \hat{v}_{d2\gamma} = -\dfrac{3}{2}\,\omega_{re}\,I_s\,[M_A - M_B\cos(2\varepsilon_\theta + 2\gamma)] \end{cases} \tag{2.3.37}$$

In the following paragraphs the sensorless algorithms will be developed for the last two synchronous machine types: SPMSM and SynchRel, where the expressions (2.3.35) and (2.3.37) are suitably manipulated to extract the rotor flux position.

In particular, in this study, new sensorless algorithms implemented for SPMSM and SynchRel, are carried out on a classic filed-oriented control where the induced voltages on the SCs are first acquired by an appropriate conditioning circuit and subsequently processed by the microcontroller for the realization of the aforementioned algorithms.

2.4 Rotor Flux Position Estimation Through SCs for SPMSMs

According to the expression (2.3.35), in a SPMSM motor drive, the estimated rotor position can be computed by both *qd-axis* voltage components $\hat{v}_{qd2\gamma}$ proposed again in (2.4.1) and (2.4.2):

$$\hat{v}_{q2\gamma} = \omega_{re}\,\lambda_{pmSC}\cos(\varepsilon_\theta) \tag{2.4.1}$$

$$\hat{v}_{d2\gamma} = -\,\omega_{re}\,I_s\,M_{ms} - \omega_{re}\,\lambda_{pmSC}\sin(\varepsilon_\theta) \tag{2.4.2}$$

In general, for a SPMSM motor drive the control structure including the signals acquisition of the induced voltages on the SCs, is shown in Fig. 2.4.1:

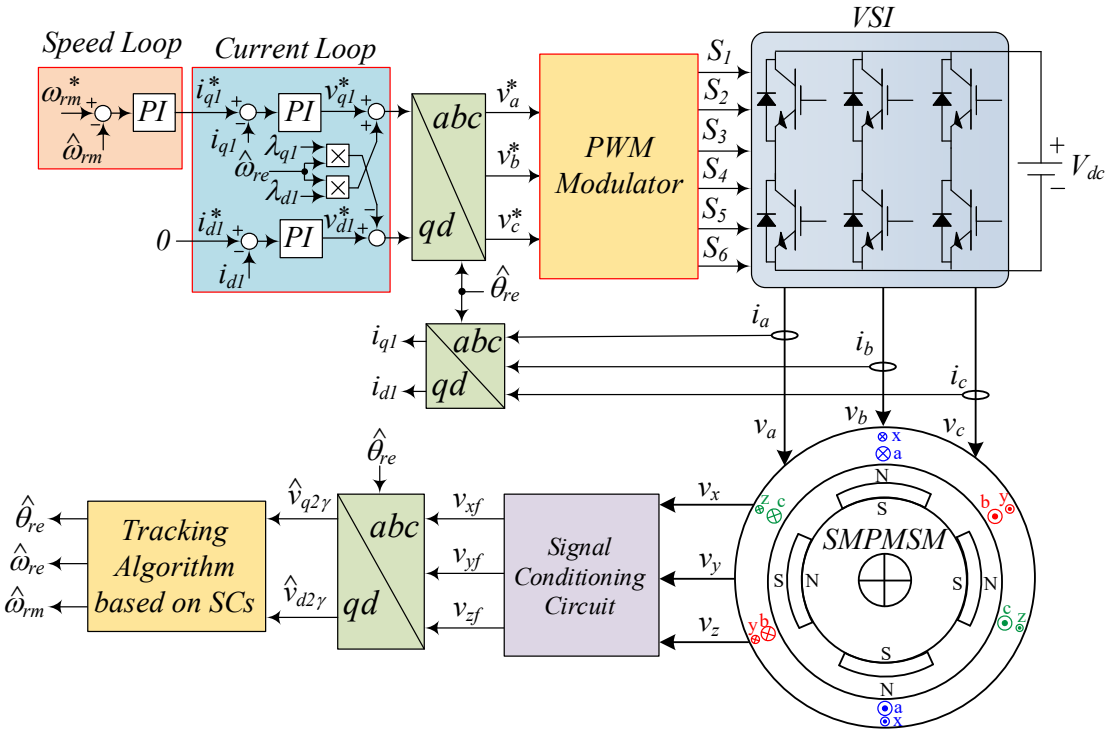

Figure 2.4.1 *Block diagram of the sensorless SPMSM motor drive including the SCs.*

In Fig. 2.4.1 the block named *"Tracking Algorithm based on SCs"* represents one of the generic rotor flux position estimation algorithm used for a SPMSM motor drive and

that they will be described in the following sub-paragraphs. In particular, the estimation algorithms exploit the two expressions (2.4.1) and (2.4.2) to estimate the rotor position.

The rotor position estimation algorithms have been validated by preliminary simulations as well. The results are referred to a SPMSM motor drive whose characteristics are shown in Tab. II. The control algorithm shown in Fig. 2.4.1 has been implemented in Simulink, where the SPMSM mathematical model and the power conversion has been executed with a sampling time $T_s = 1\mu s$.

The rotor position estimation algorithms have been validated experimentally by steady state and dynamic tests accomplished on a test rig, which, according to Fig. 2.4.2, consists of a SMPMSM, whose data are listed in Tab. II, mechanically coupled to a 2.6 kW IPM synchronous motor drive to emulate the mechanical load. The two IGBT-based three phase Voltage Source Inverters (VSIs) are operated with a standard space-vector pulse width modulation (SVPWM) method at *200V* DC bus voltage and *10 kHz* switching frequency. The control system schematized in Fig. 2.3.5 is implemented on a dSPACE DS1103 DSP board, where the execution times of the current loop and speed loop are $T_{si} = 100\mu s$ and $T_{s\omega} = 200\mu s$ respectively. Technical specifications of the search coils and embedded thermistors are listed in Tab. III. A torque transducer is placed in the mechanical coupling between the two electrical machines and two 2048 ppr encoders are exploited to measure the rotor positions of both motors.

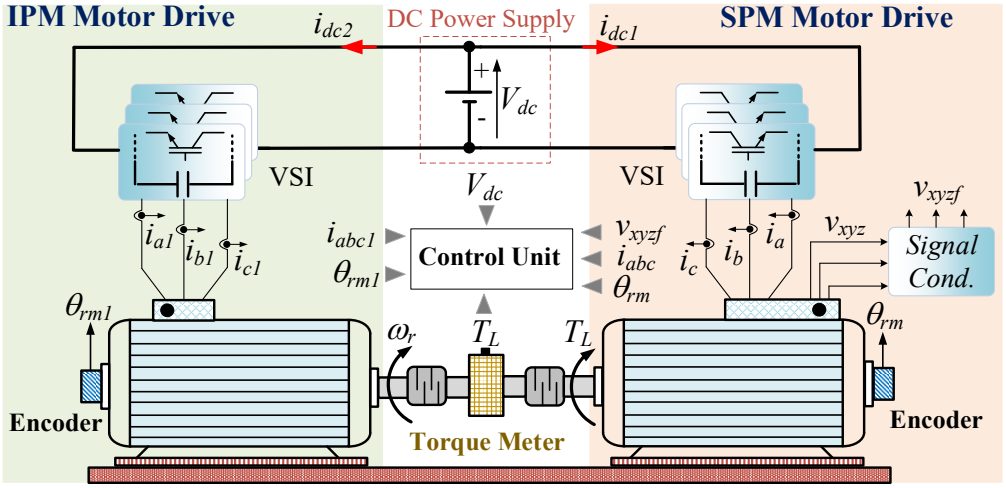

Figure 2.4.2 *Experimental Setup: SPM motor under test, IPM mechanical load.*

Table II *SPMSM Motor Data*

Parameter	***Value***
Rated torque	*5 Nm*
Rated speed	*6000 rpm*
Inertia	*0.0025 kg m²*
Pole pairs	*3*
Rated voltage	*565 V*
Rated current	*5 A*
Rs	*0.84 Ω*
Ls	*4.7 mH*

Table III *Technical specification of the Search Coils and Thermistors.*

Parameter	***Value***
Search Coils Mutual inductance M_{ms}	*0.2 mH*

Thermistor resistance value at 25 °C R_{25}	*210 kΩ*

A signal conditioning circuit is used to process the voltage induced on each SC, v_x, v_y and v_z, respectively, in order to remove the PWM high frequency components in each SC, by using a filtering stage cascaded connected to a buffer and a further filter for level adaption, v_{xf}, v_{yf} and v_{zf}, respectively. The electric scheme of the signal conditioning system is shown in Fig. 2.4.3, while an example of the signal waveforms sampled in different testing points are shown in Fig. 2.4.4. The deviation of the rotor position estimation from the measured one, due to the signal conditioning circuit, is mitigated by an off-line generated look-up table.

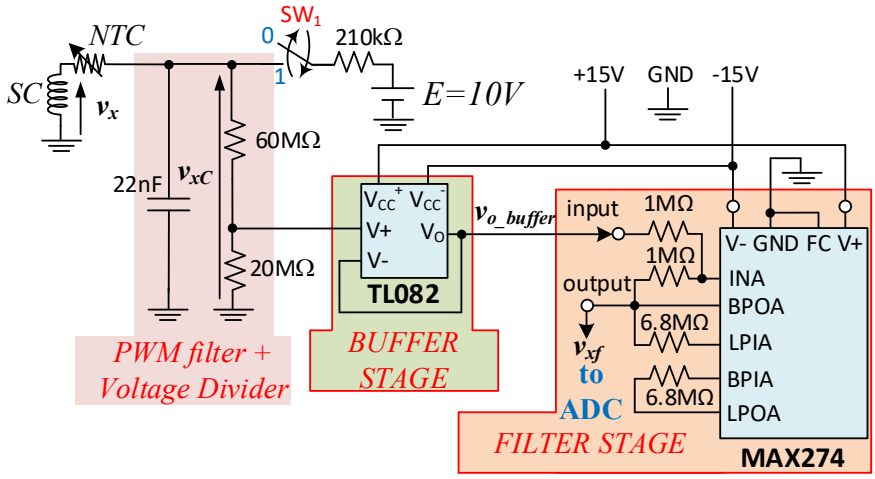

Figure 2.4.3 *Signal conditioning circuit used for SCs voltages acquisition and temperature monitoring. switch SW1: (0) SC is used for rotor position estimation, (1) SC is used for temperature monitoring.*

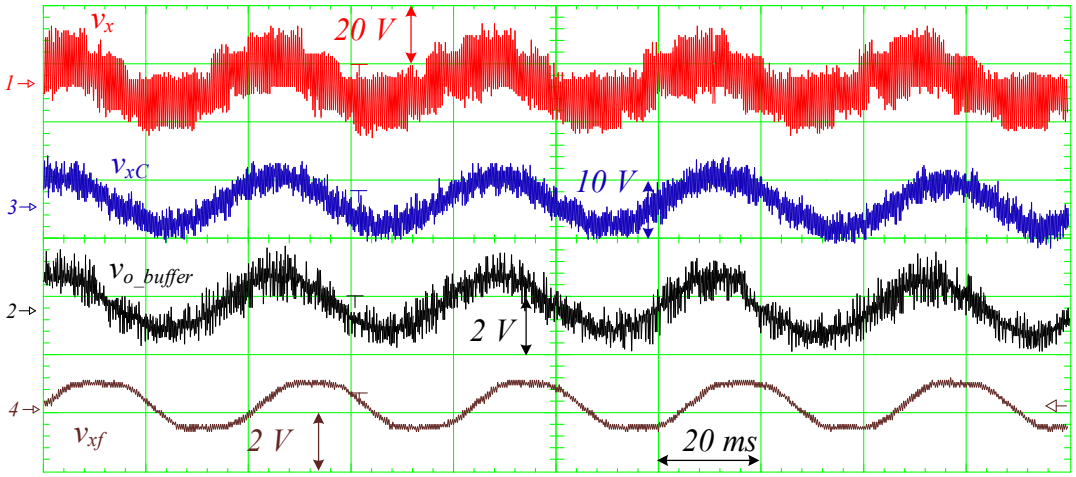

Figure 2.4.4 *Signal conditioning system waveforms for each SC stage. Test performed at 50 rad/s and 100% of rated torque.*

In order to assess the consistence of the proposed sensorless position estimation technique, some steady state tests have been performed at different rotational speeds and load conditions, as shown in Figs. 2.4.5 - 2.4.7.

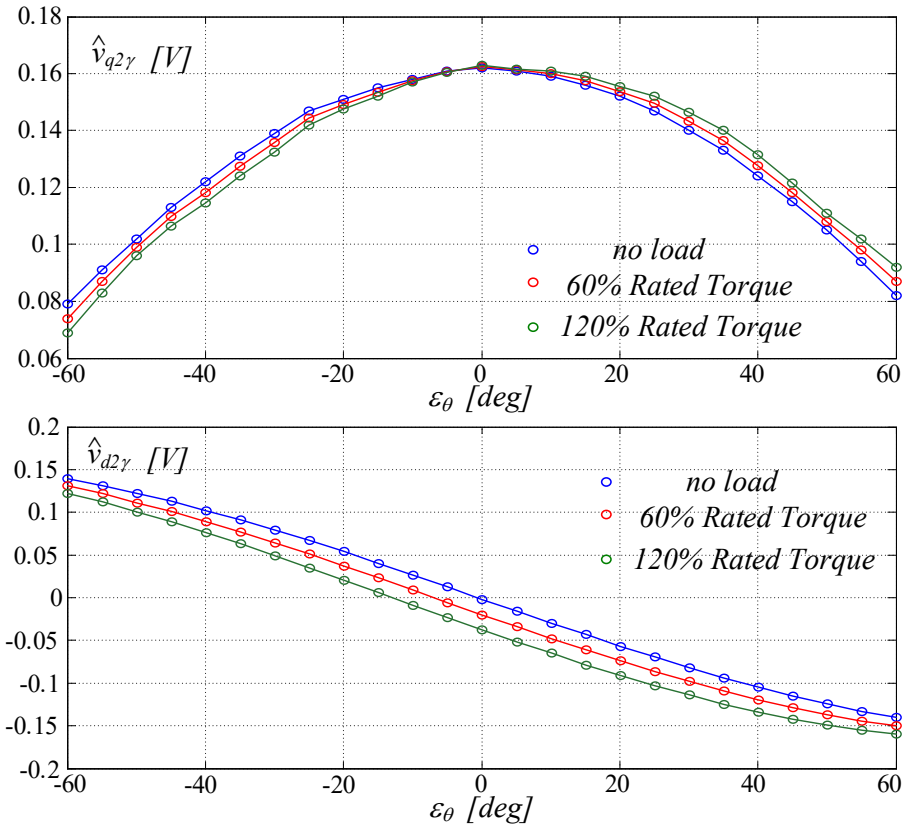

Figure 2.4.5 *Steady state tests: q and d axis SCs voltages in estimated synchronous reference frame measured at ω_{rm} = 10 rad/s and at different load conditions.*

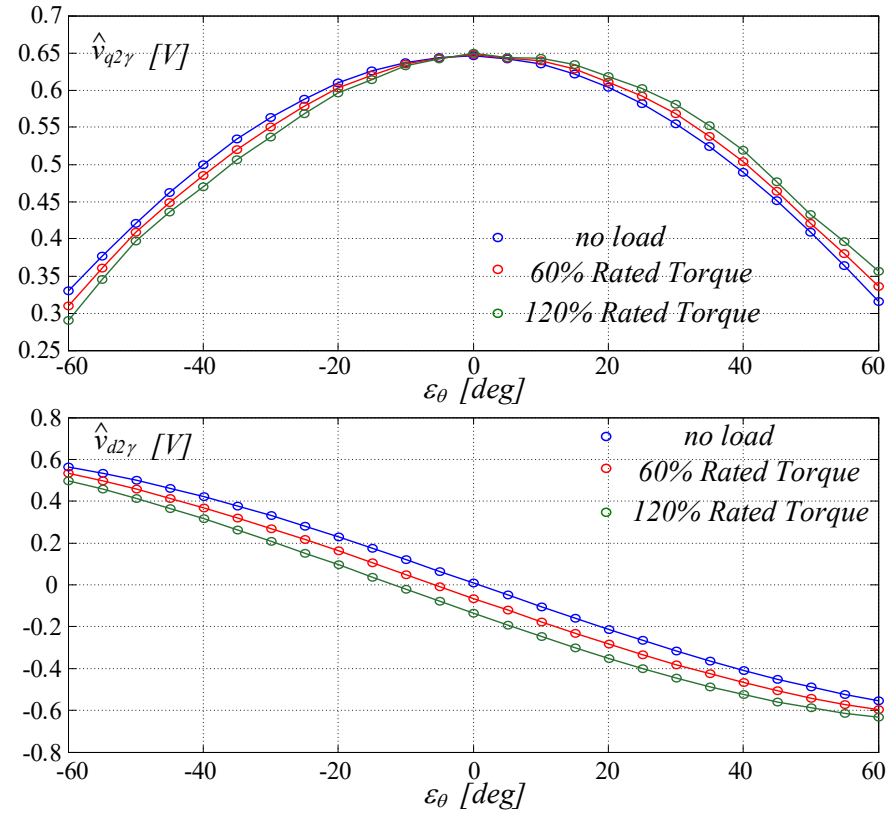

Figure 2.4.6 *Steady state tests: q and d axis SCs voltages in estimated synchronous reference frame measured at ω_{rm} = 40 rad/s and at different load conditions.*

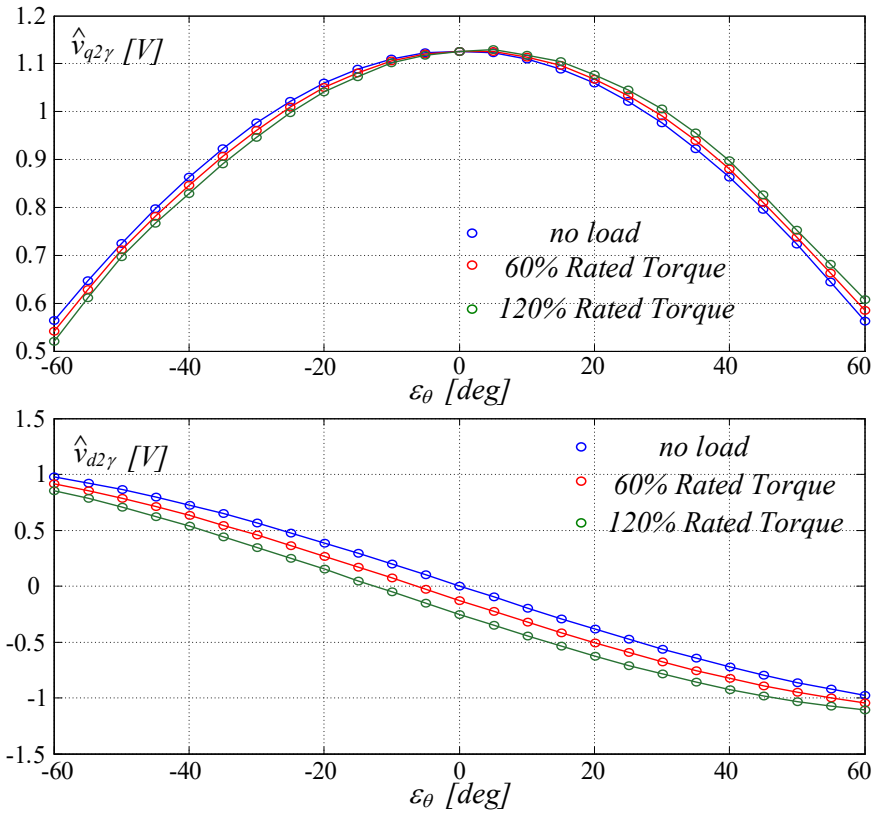

Figure 2.4.7 *Steady state tests: q and d axis SCs voltages in estimated synchronous reference frame measured at ω_{rm} = 70 rad/s and at different load conditions.*

Obtained results confirm that the rotor flux position error is null when by considering the equation (2.4.2) we obtain ($\hat{v}_{d2\gamma} + \hat{\omega}_{re} M_{ms} I_s$) is null, and when by considering the equation (2.4.1) $\hat{v}_{q2\gamma}$ is maximum. By tracking these two conditions it is possible to obtain an estimation of the rotor flux position theoretically independent from motor parameters.

Below are the simulations and experimental results regarding the various tracking algorithms.

2.4.1 Rotor Position and Speed Estimation via a Maximum Point Tracking Algorithm

A first possible implementation has been tested and shown in Fig. 2.4.8, in which a PI controller is used to process the error between the reference and measured induced voltage on the SCs $\hat{v}_{q2\gamma}$ along the estimated axis. Integration of the output of the PI controller provides the estimated rotor position.

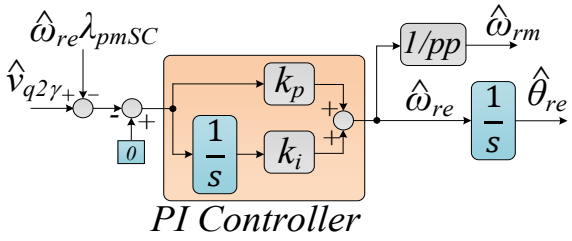

Figure 2.4.8 *Block Diagram of the SPMSM Rotor Position and Speed Estimation Algorithm exploiting a PI-based maximum point tracking.*

The proposed approach, Fig. 2.4.1, allows to estimate the rotor position and rotor speed by mathematical manipulation of the $\hat{v}_{q2\gamma}$ defined in (2.4.1):

$$\hat{v}_{q2\gamma} - \omega_{re}\,\lambda_{pmSC} = \omega_{re}\,\lambda_{pmSC}\,[cos(\varepsilon_\theta)-1] \qquad (2.4.3)$$

The induced voltage $\hat{v}_{q2\gamma}$ provides a straightforward information about the estimation error; in fact, ε_θ can be driven to zero by tracking the maximum value of $\hat{v}_{q2\gamma}$. The voltage $\hat{v}_{q2\gamma}$ has to be forced to zero, by using a PI controller, in order to drive the estimation error ε_θ to zero. In fact, if the estimation error ε_θ is force to zero by the PI controller, then the cosinusoidal term $cos(\varepsilon_\theta)$ would tend to one.

This first solution is quite easy implementation but is sensitive to the permanent magnet flux λ_{pmSC} variations; in fact, a slight variation of the permanent magnet flux could compromise the stability of the sensorless control system.

This sensorless control based on Maximum Point Tracking Algorithm has been validated by Matlab/Simulink environment, according to the schematic of the control algorithms shown in Fig. 2.4.8. Figs. 2.4.9-2.4.10 deal with the dynamic response of SPMSM drive to a sequence of torque and speed variations when the drive is current controlled.

In particular, Figs.2.4.9 and 2.4.10 display the rotational speed ω_{rm}, the electromagnetic torque T_e, the currents i_{q1}, i_{d1}, the rotor position error ε_θ and $\hat{v}_{q2\gamma}$ for the sensorless implementation in a SPMSM drive. Note that on the drive the tracking algorithm shown in Fig. 2.4.8 is able to keep quite low the estimation error, either at steady state and during transients.

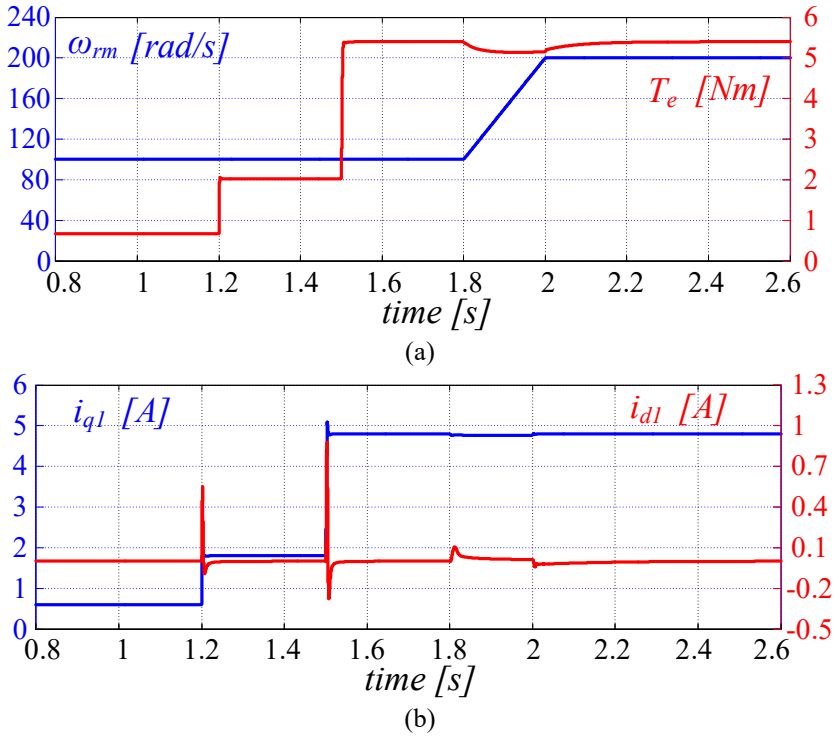

Figure 2.4.9 *Simulation Results: torque and speed transients for SPMSM drive, (a) mechanical speed ω_{rm} and electromagnetic torque T_e, (b) qd-axes currents i_{q1} and i_{d1}.*

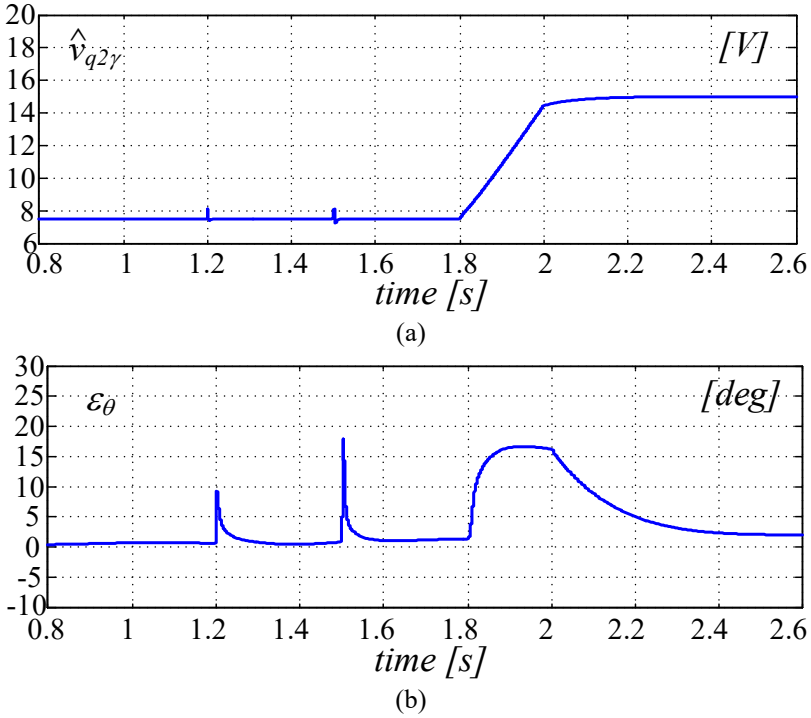

Figure 2.4.10 *Simulation Results: torque and speed transients for SPMSM drive, (a) q-axis voltage induced on SCs in estimated reference frame (b) position error.*

In Fig. 2.4.11 an experimental test is shown, where the SPMSM is driven according to the classical vector control shown in Fig. 2.4.1 while performing a speed transient. A quite satisfactory dynamic behavior is obtained in sensorless mode, with small estimation errors.

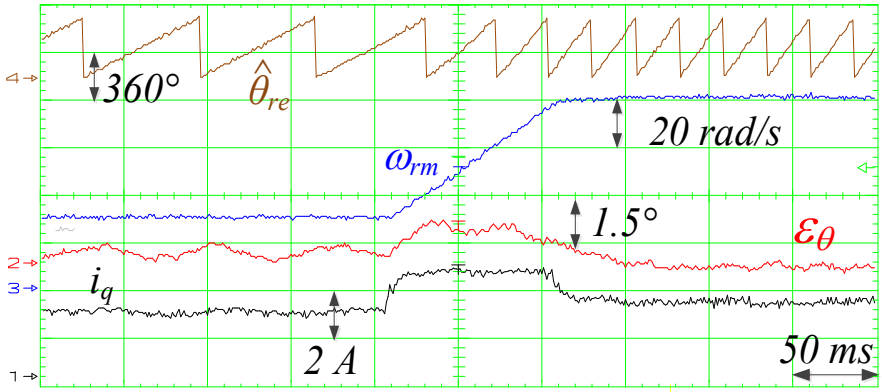

Figure 2.4.11 *SPMSM: speed transient from ω_{rm} = 30 rad/s to ω_{rm} = 80 rad/s.*

2.4.2 Rotor Position and Speed Estimation Based on Zero Crossing Tracking Algorithm

A second way to carry out the rotor position information relies on exploiting a zero crossing tracking algorithm, as the one shown in Fig. 2.4.12, to process the quantity ($\hat{v}_{d2\gamma} + \hat{\omega}_{re} M_{ms} I_s$) which according to (2.4.4), is directly related to the sine of the estimation error ε_θ. Speed estimation algorithm based on phase locked loop has been used to estimate the electrical rotor speed [45], [46].

$$\hat{v}_{d2\gamma} + \omega_{re} I_s M_{ms} = -\omega_{re} \lambda_{pmSC} \sin(\varepsilon_\theta) \tag{2.4.4}$$

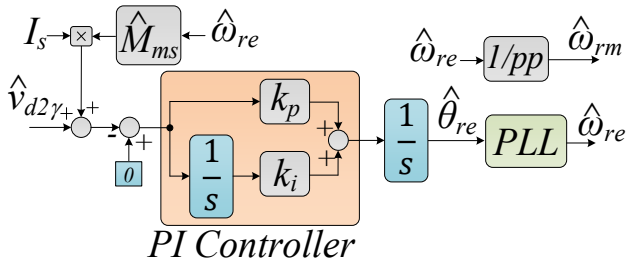

Figure 2.4.12 *Block Diagram of the SPMSM Rotor Position and Speed Estimation based on Zero Crossing Algorithm.*

This method is insensitive to stator resistance variations and thus giving a robust rotor position estimation at low speed and high loads. Moreover, satisfactory dynamic performance is achieved with small computational efforts.

Initially, in order to validate the rotor position estimation algorithm based on the zero-crossing tracking algorithm, has been implemented in Simulink by considering the control structure of Fig. 2.4.1.

Figs. 2.4.13a and 2.4.13b deal with the dynamic response of the sensorless SMPMSM algorithm in which the switch SW has been selected to 0.

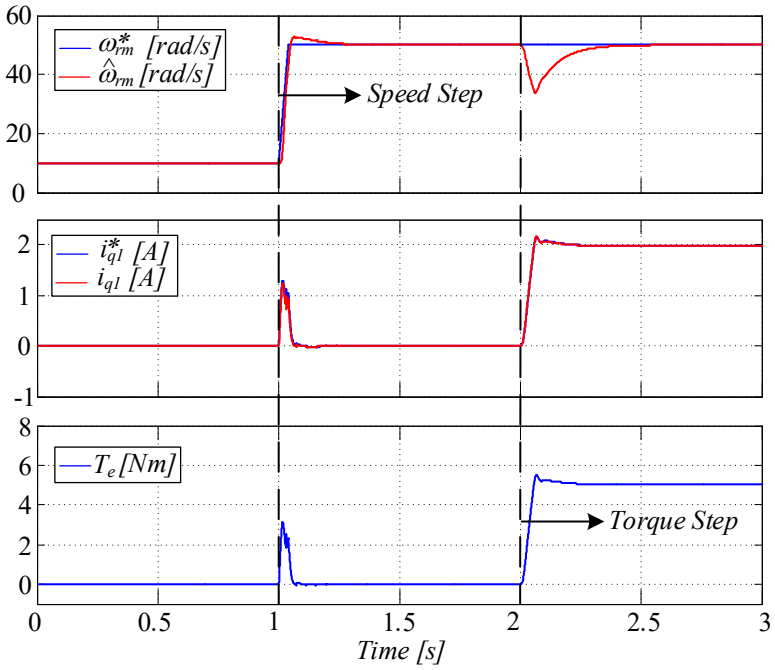

(a)

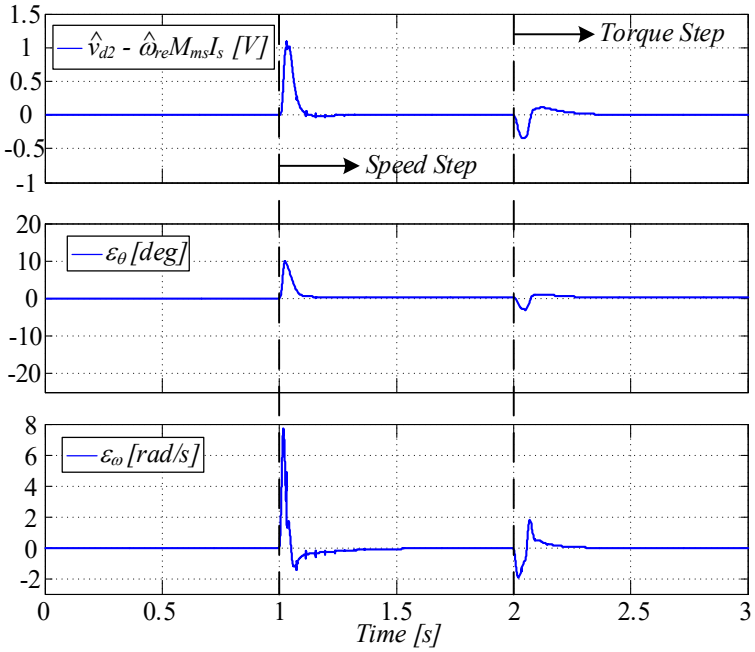

(b)

Figure 2.4.13 *SW = 0: speed step at 1s and torque step at 2s: (a) reference and estimated rotor speed, reference and measured torque component of the stator current vector, electromagnetic torque; (b) control variable, rotor position and speed errors.*

In particular, a sequence of torque and speed variations have been applied to the speed controlled drive. The machine is operated at $\omega_{rm} = 50rad/s$ and *100%* of the rated torque. You can note limited rotor position estimation error ε_θ and rotor speed estimation error ε_ω, during both transient conditions, whose entity is related to the dynamic of the tracking algorithm. In this test it has been assumed a perfect match between the estimated and motor parameters.

Fig. 2.4.14 highlights the effect of parameters variations on the rotor position estimation. In particular, a sequence of parameters variations has been imposed to the motor model and the estimation errors on the rotor position and speed have been computed. Note that a significant variation of the magnetizing inductance L_s (-50%) yield to a rotor position error of $\varepsilon_\theta = 10deg$, while the same percentage variation (+50%) on the stator resistance does not produce estimation errors [35] and [53].

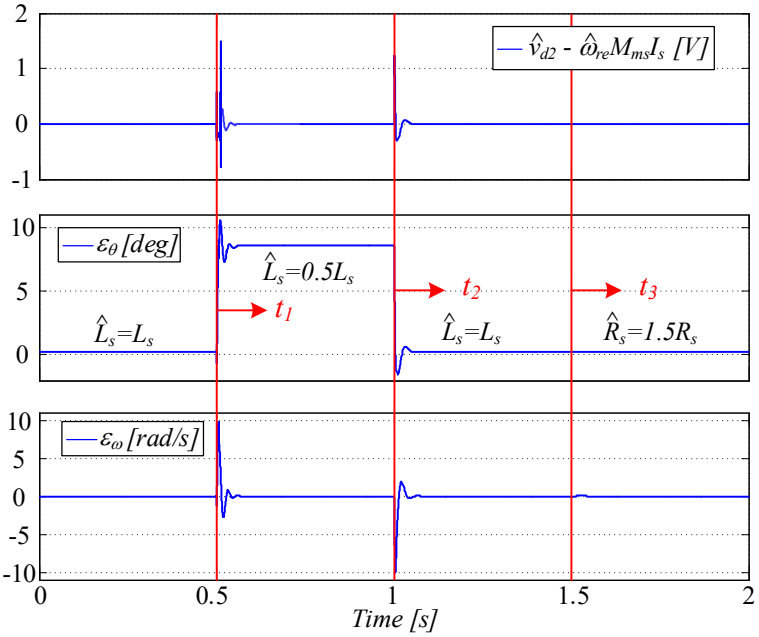

Figure 2.4.14 *Steady state test: at the instant t_1 a variation of L_s is imposed to the model (-50%), at the instant t_2 the initial value of L_s, is restored, and finally at instant t_3 R_s is changed of +50%.*

The effectivity of the proposed rotor position estimation method has been evaluated through experimental tests. In particular, the test shown in Fig. 2.4.15 deals with a step from no load to rated load. The tested motor drive was torque controlled, while the IPM motor drive held a constant rotational speed $\omega_{rm} = 50\ rad/s$. Only negligible estimation errors were recorded.

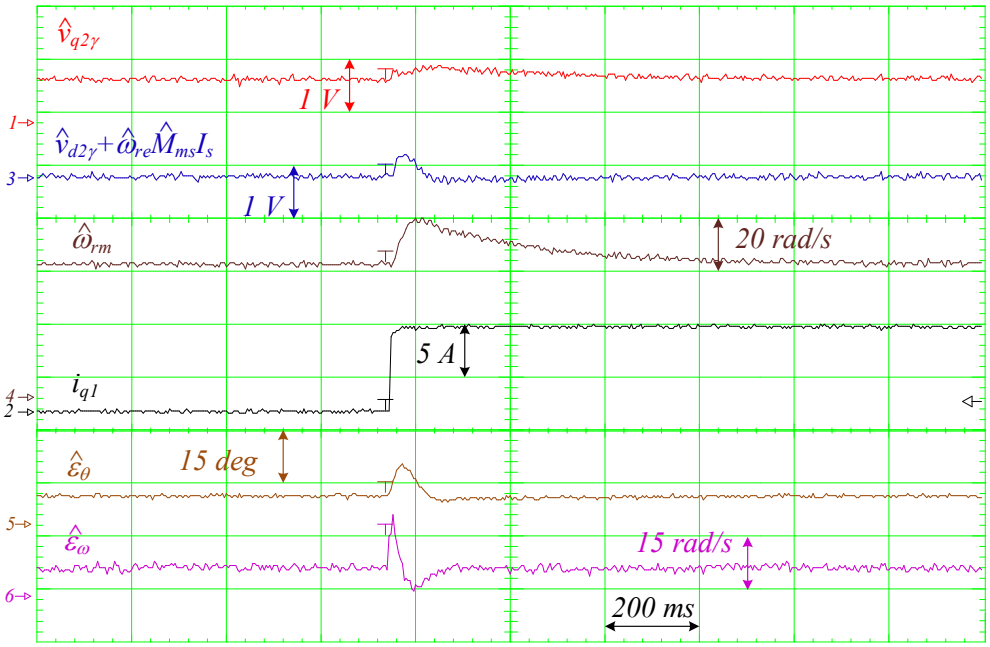

Figure 2.4.15 *Torque transient from no-load condition to rated torque at $\omega_{rm} = 50$ rad/s.*

The test of Fig. 2.4.15 highlights the dynamic behavior of the sensorless control during a speed variation from $\omega_{rm} = 10\ rad/s$ to $\omega_{rm} = 50\ rad/s$ at rated load. In this case the tested motor drive was speed controlled while the IPM motor drive set a step load variation. Also in this test a quite small estimation error was observed.

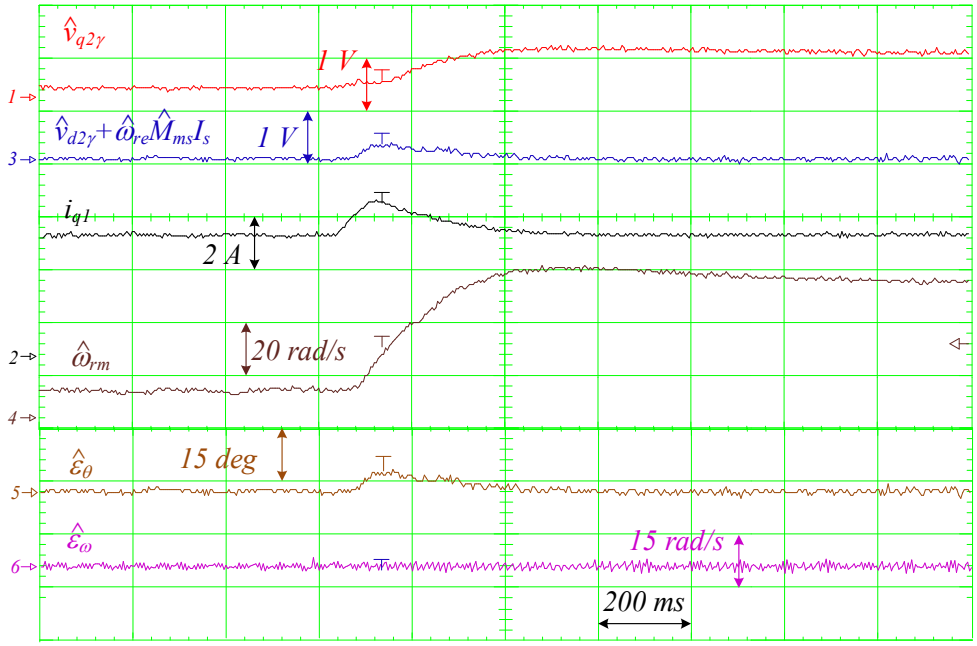

Figure 2.4.16 *Speed transient from ω_{rm} = 10 rad/s to ω_{rm} = 50 rad/s at rated torque.*

2.4.3 Combined Zero Crossing Tracking Sensorless Control Approach with MVPT Position Error Estimation Tracking Algorithm

However, the rotor position estimation is affected by the variation of the mutual inductance M_{ms}. This can be mitigated by tracking the maximum of the voltage $\hat{v}_{q2\gamma}$, (2.4.1), which coincides with a zero-estimation error $\varepsilon_\theta = 0$, independently from motor parameters variations. Hence, a maximum voltage point tracking (MVPT) based on the perturb and observe (P&O) algorithm has been integrated into the zero crossing tracking algorithm, [47], [48].

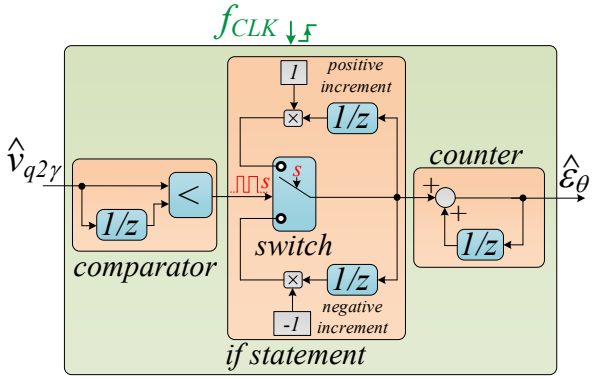

Figure 2.4.17 *MVPT based on P&O algorithm for position error estimation.*

In Fig. 2.4.17 is shown the MVPT for position error estimation $\hat{\varepsilon}_\theta$ used in this study. The classical two-point P&O block diagram is composed of three stages: the first stage is a comparator between the actual $\hat{v}_{q2\gamma}$ sample and its previous sample, the second stage is an if statement, and finally the third stage is a counter. Obviously, the estimated position error ε_θ depend on the clock frequency f_{CLK} used for triggered the P&O algorithm.

In this way the MVPT processes $\hat{v}_{q2\gamma}$ and provides the estimation of the position error $\hat{\varepsilon}_\theta$ between the estimated $\hat{\theta}_{re}$ and the its correction by updating the rotor position estimation $\tilde{\theta}_{re}$.

$$\tilde{\theta}_{re} = \hat{\theta}_{re} + \hat{\varepsilon}_\theta \tag{2.4.3}$$

Also in this case a similar control block diagram has been adopted in Fig.2.4.18 , where both rotor position estimation algorithms provided from the equations (2.4.1) and (2.4.2) are combined:

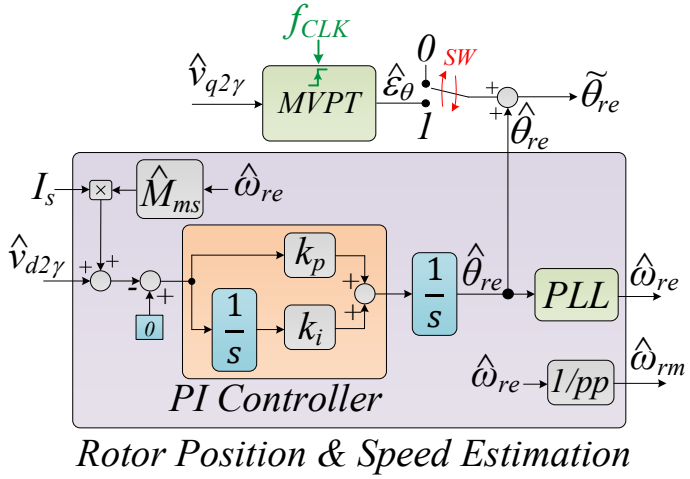

Figure 2.4.18 *Combined Zero-Crossing Tracking Sensorless Control Approach with MVPT position error estimation.*

The MVPT is of simple implementation, but is characterized by a low dynamic, thus it is used to compensate the parameters mismatching in the rotor position tracking algorithm of Fig. 2.4.18. Specifically, the MVPT can be exploited to build suitable compensation maps (2D – look up tables) with a small set of data, to provide a fast correction of the rotor position estimation. The MVPT may also continuously performed to update the compensation maps.

Fig. 2.4.19 shows the results achieved by selecting SW=1 in the estimation algorithm of Fig. 2.4.18, where the estimation error carried out by the MPVT algorithm is added to the estimated angle $\hat{\theta}_{re}$. The drive is initially working at $\omega_{rm} = 80rad/s$ and 100% of the rated, SW=0, and a perfect match between the estimated and motor parameters is assumed. At the instant t_1 a step variation of L_s is imposed to the motor model yielding to an error ε_θ. At the instant t_2 the P&O based MVPT sensorless algorithm is active nullifying the estimation error.

A sequence of torque and speed transients is applied at the instants t_3 and t_4, respectively. Finally, a further step variation of L_s is imposed in the motor model.

It is worth noting that when both tracking implementations are active the estimation error is always kept below a few degrees. Alternative technical solutions are under investigations in order to improve the dynamic of the tracking method.

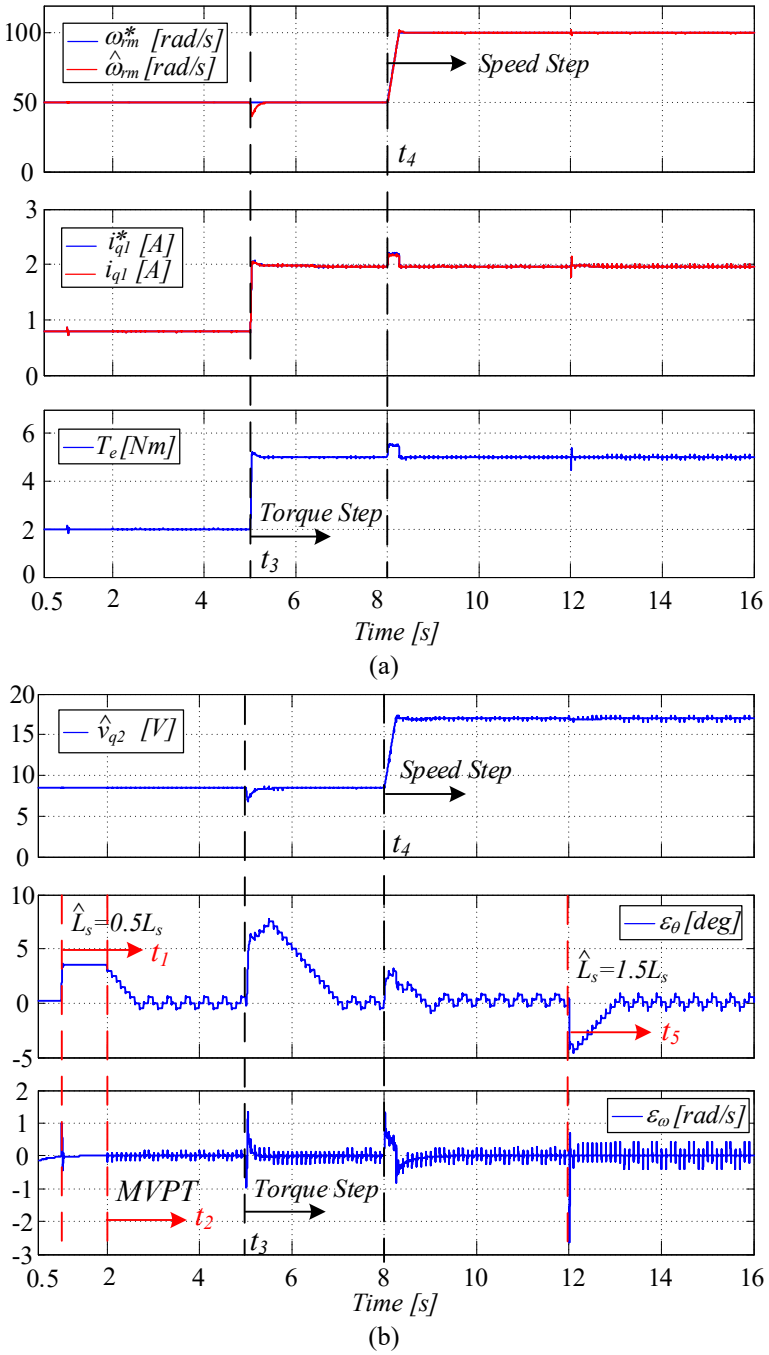

Figure 2.4.19 *SPMSM motor drive dynamic behaviours during combined zero tracking cross algorithm sensorless approach with MVTP position error correction at different torque load conditions, speed conditions and with L_s steps variation.*

A remarkably smaller estimation error is obtained with the proposed approach in sub-paragraph 2.4.2, even at high load. A quite large variation of the mutual inductance M_{ms} with the load has been purposely included in the algorithm of Fig. 2.4.18 to assess the operation of the additional MVPT tracking loop. In Fig. 2.4.20 a load step is first set with SW=0. At time t^* the switch SW is set to 1 and the error ε_θ is added to $\hat{\theta}_{re}$, driving the estimation error to zero.

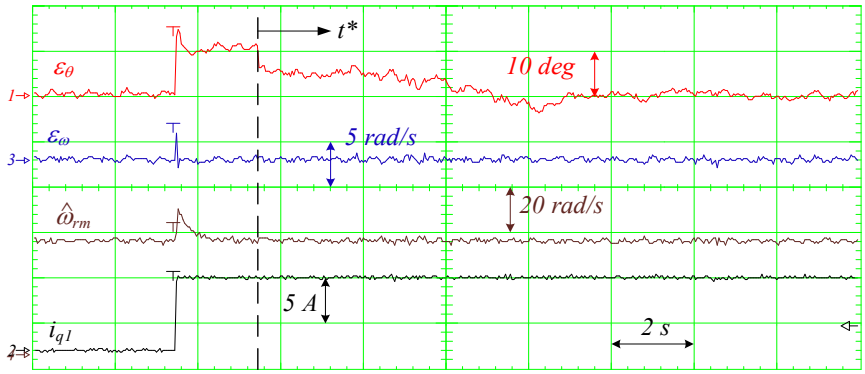

Figure 2.4.20 *Activation of the MVPT algorithm on the estimated rotor position at the instant t*.*

2.5 Rotor Flux Position Estimation Through SCs for SynchRel Drives

The detection of the Search Coils electromotive force related to the PM flux linkage has been implemented in case of Surface Permanent Magnet Synchronous Motors (SPMSM) as well explained in the previously paragraph 2.4.

Conversely, in this paragraph will be explained how it will be straightforward to extract the Search Coils electromotive force associated to the salient magnetic structure in Synchronous Reluctance motors (SynchRel).

In general, for a SynchRel motor drive the control structure including the signals acquisition of the induced voltages on the SCs, is shown in Fig. 2.5.1, where also in this case the block named *"Tracking Algorithm based on SCs"* represents the generic rotor flux position estimation algorithm used for SynchRel motor drive.

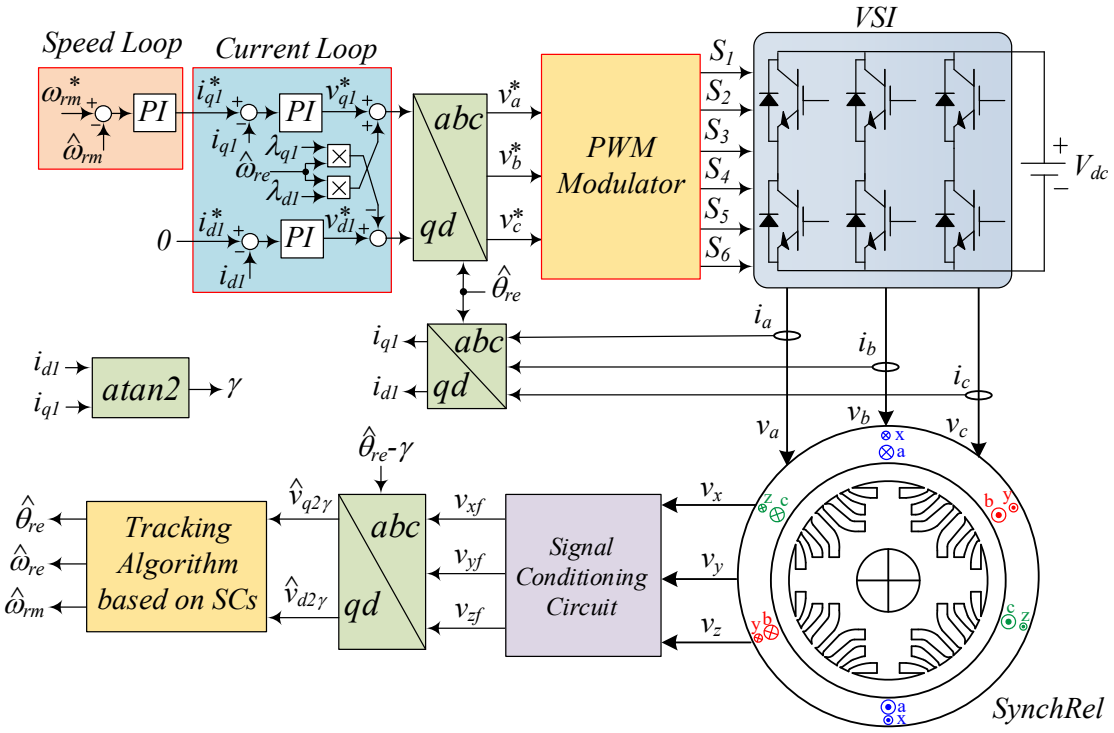

Figure 2.5.1 *Block diagram of the sensorless SynchRel motor drive with including the SCs.*

According to the theoretical studies developed in the sub-paragraph 2.3.3 the estimated rotor position in SynchRel motor drive with including SCs can be computed by exploit the *qd-axis* voltage components $\hat{v}_{qd2\gamma}$, equations (2.5.1) and (2.5.2).

$$\hat{v}_{q2\gamma} = \frac{3}{2}\,\omega_{re}\,I_s\,M_B\,sin(2\varepsilon_\theta + 2\gamma) \tag{2.5.1}$$

$$\hat{v}_{d2\gamma} = -\frac{3}{2}\,\omega_{re}\,I_s\,[M_A - M_B\,cos(2\varepsilon_\theta + 2\gamma)] \tag{2.5.2}$$

Compared to the rotor position estimation algorithm by using SCs for SPMSM in this case only the q-axis component (2.5.1) will be used to implement the rotor position estimation algorithm.

Initially, the rotor position estimation algorithms have been validated by preliminary simulations. The results are referred to a SynchRel motor drive whose characteristics are shown in Tab. IV. The control algorithm shown in Fig. 2.5.1 has been implemented in Simulink, where the SynchRel mathematical model and the power conversion has been executed with a sampling time $T_s = 1\mu s$.

A specific test bench, tailored around a SynchRel motor drive, has been realized to accomplish a practical evaluation of the proposed approach. The block diagram of the experimental setup is shown in Fig. 2.5.2.

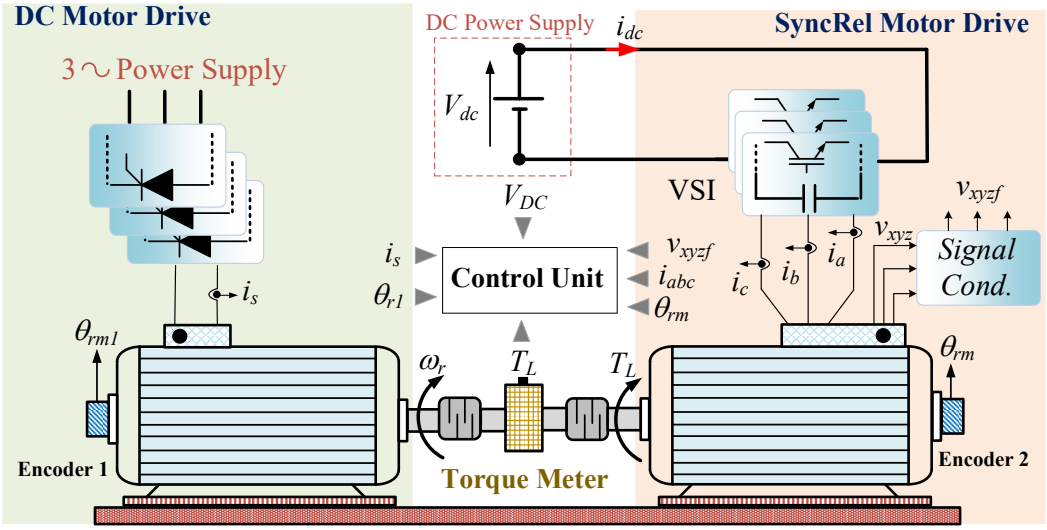

Figure 2.5.2 *Experimental Setup: SynchRel motor under test. DC motor mechanical load.*

The SynchRel machine is driven according to a quite conventional maximum torque per ampere (MTPA) strategy, based on setting the ratio of d and q axes components of the stator current in order to minimize the magnitude of the current required to generate a given motor torque value. Specifically, a constant $\gamma = 55\ deg$ current vector phase angle has been set for experimental tests. Technical specifications of the SyncRel machine, search coils and embedded thermistors are listed in Tab. IV, Tab. V and Tab. VI, respectively.

Table IV *SynchRel Motor Technical Specifications*

Parameter	***Value***
Rated torque	*5 Nm*
Rated speed	*1500 rpm*
Inertia	*0.0045 kg m²*
Pole pairs	*4*
Rated voltage	*400 V*

Rated current	*8 A*
Rs	*1. 4 Ω*
Lq	*11 mH*
L_d	*57 mH*

Table V *Search Coils Technical Specifications*

Parameter	***Value***
M_q	*2.3 mH*
M_d	*11.5 mH*
Coil Resistance	*0.2 Ω*
Cable diameter	*1 mm*
Number of turns	*5*

Table VI *Thermistors Technical Specifications*

Parameter	***Value***
Max. Power (at 25°C) P_{25}	*60 mW*
Temperature tolerance (0…70 °C) ΔT	*±0.2*
Rated Temperature T_R	*25 °C*
Heat Capacity C_{th}	*22.5 mJ/K*
Resistance value at 25 °C R_{25}	*30 kΩ*

The experimental rig includes a three-phase 0.*75 kW* SyncRel motor, which is supplied by a two-level PWM inverter connected on the DC side to a *500V/5A* power supply. The current vector control system features a f_{sw} *= 10 kHz* sampling frequency and is implemented on a dSPACE DS1104 DSP board. The AD converters used to acquire the SCs voltages feature a 12 bits resolution with input voltages between -10V and 10V. The SyncRel motor is mechanically coupled to a DC motor drive used as controllable mechanical load, whose inertia is 0.021 kg m^2.

A 1024 ppr encoder is used to compare the estimated and measured mechanical quantities. The thermistor wirings have been modified according to Fig. 2.5.3 in order to obtain a set of three SCs. The search coils have been located before placing the main winding, in the bottom stator winding. Original external cables were retained for connection to the control unit. Moreover, a further single SC not connected to any thermistor has been introduced in the machine for testing purposes, as well as a conventionally wired thermistor.

Each SC voltage is acquired by using the signal conditioning circuit shown in Fig. 2.5.3, identically to Fig. 2.4.3.

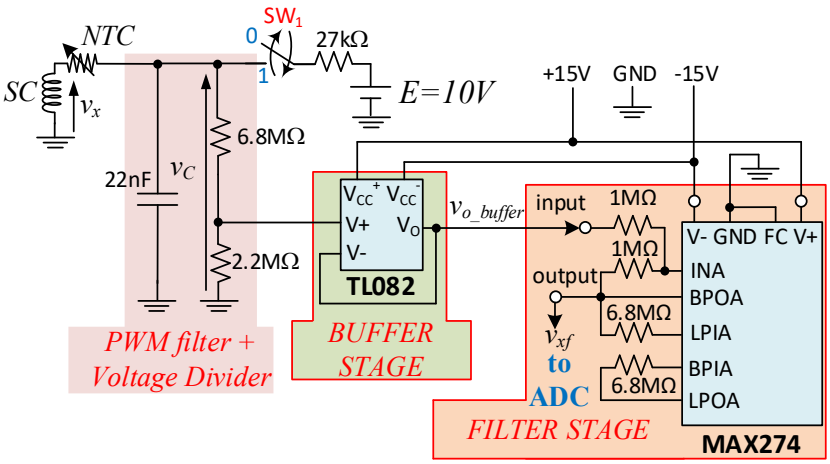

Figure 2.5.3 *Signal conditioning circuit used for SCs voltages acquisition and temperature monitoring. Switch SW1: (0) SC is used for rotor position estimation, (1) SC is used for temperature monitoring.*

It encompasses a front-end section including a PWM filter, a high impedance voltage divider and AD converters. The filter suppresses the high frequency components caused by PWM operation, while the voltage divider suitably reduces the voltages of the SCs. The output section is composed of a buffer stage and an analog Butterworth low-pass filter with a corner frequency of *300Hz* to improve the signal to noise ratio.

The rotor position estimation mode, or the temperature monitoring mode, can be selected by acting on the switch SW_1. Fig. 2.5.4 displays some signal waveforms acquired in different points of the conditioning circuit, while Fig. 2.5.5 shows the filtered SCs voltage signals v_{xyzf}.

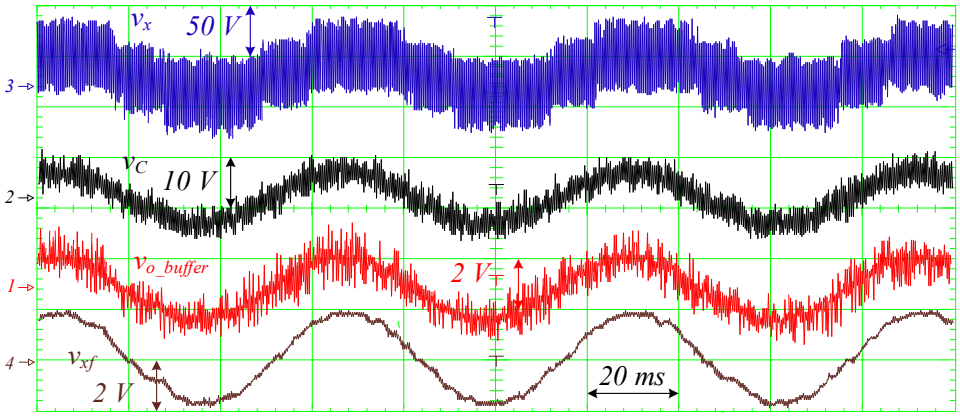

Figure 2.5.4 *Signal conditioning circuit waveforms with the drive running at ω_{rm} = 50 rad/s and T_L = 60% of the rated torque.*

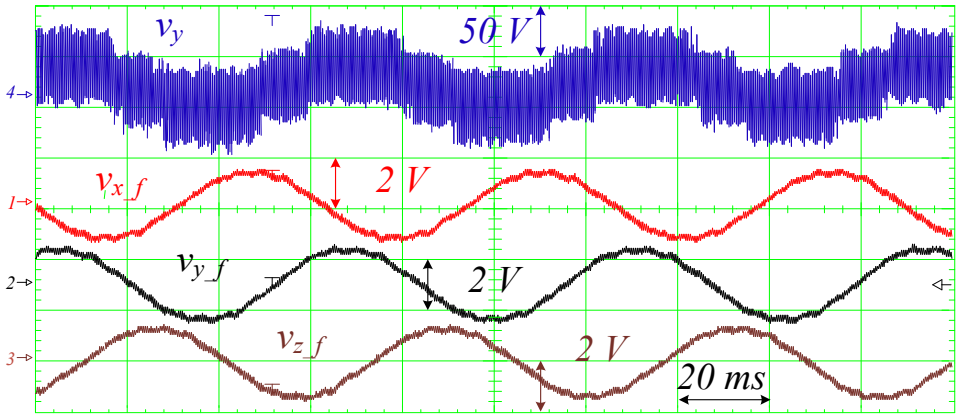

Figure 2.5.5 *Voltages induced in the SCs at the search coils terminals of the SynchRel and after the filtering process, with the drive running at ω_{rm} = 50 rad/s and T_L = 60% of the rated torque.*

The consistence of the sensorless position estimation approach has been then assessed through steady state tests, dealing with different values of the rotational speed and load. Some results are shown in Figs. 2.5.6, 2.5.7 and 2.5.8, which confirm that the rotor flux position error is null when $\hat{v}_{q2\gamma}$ is approaching to zero, independently from operating conditions.

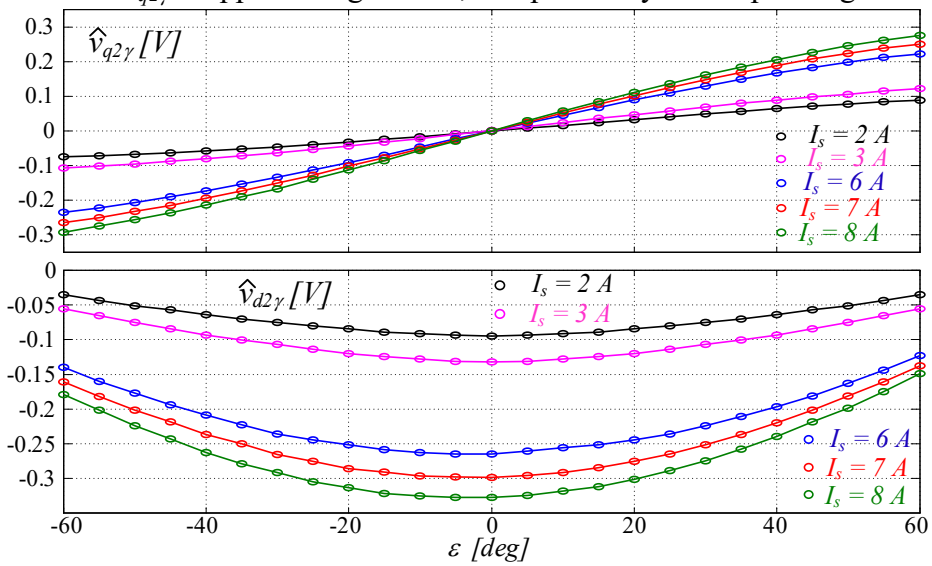

Figure 2.5.6 *Steady state qd axis SCs voltages in estimated reference frame at ω_{rm} = 10 rad/s and different load conditions.*

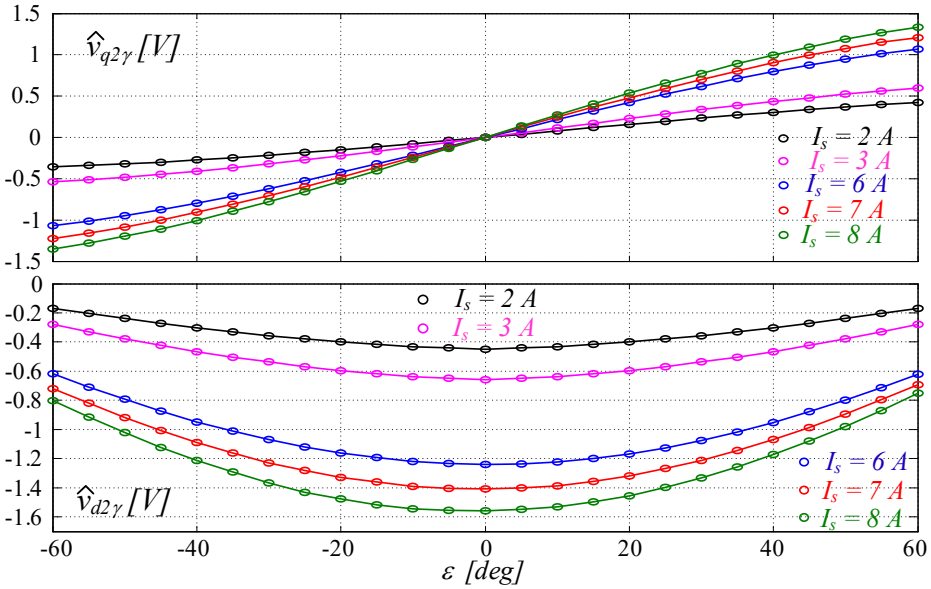

Figure 2.5.7 *Steady state qd axis SCs voltages in estimated reference frame at ω_{rm} = 50 rad/s and different load conditions.*

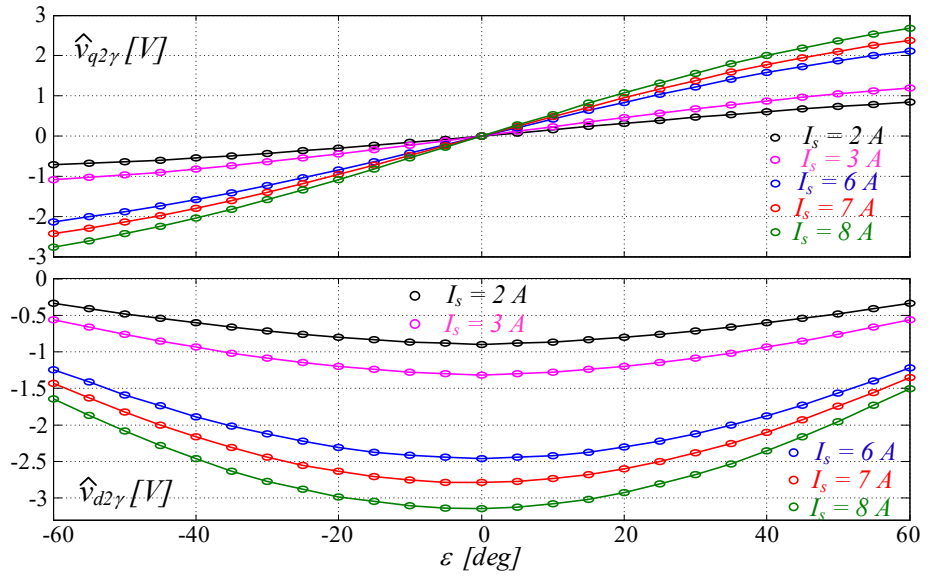

Figure 2.5.8 *Steady state qd axis SCs voltages in estimated reference frame at ω_{rm} = 100 rad/s and different load conditions.*

Previous experimental tests were accomplished according to the MTPA technique. In order to assess the effect of magnetic cross-coupling in suboptimal operation some tests were performed modifying the angle γ. According to results shown in Figs. 2.5.9-2.5.11 a constant rotor position estimation error is detected compared to the MTPA operations of Figs. 2.5.6-2.5.8. Since this error is only related to the current vector orientation, which is known, it can be easily compensated through a look-up table (LUT).

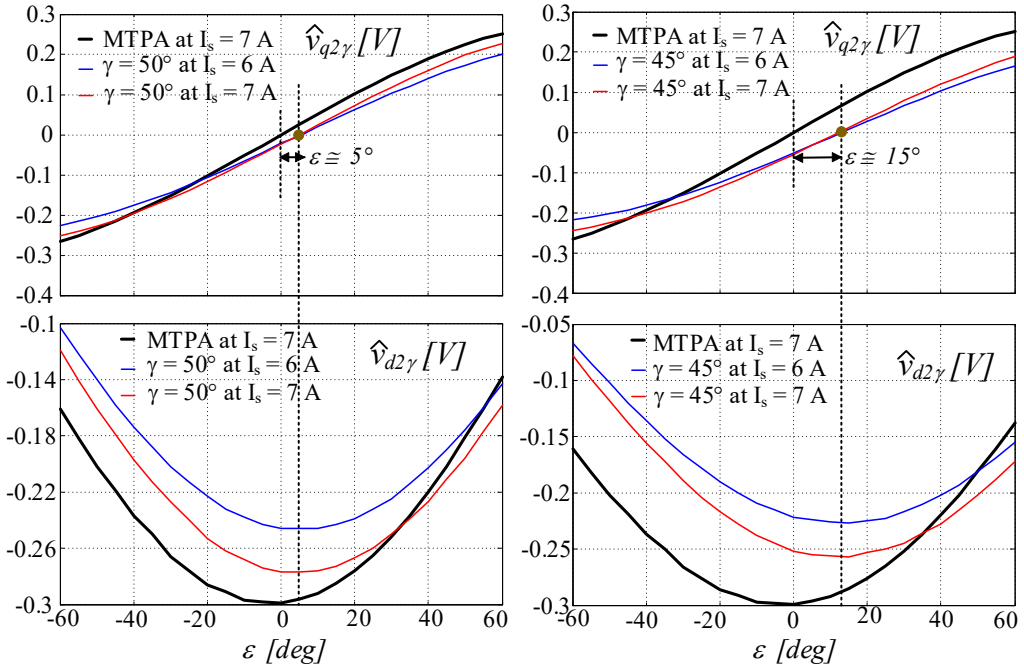

Figure 2.5.9 *Steady state qd axis SCs voltages in estimated reference frame at ω_{rm} = 10 rad/s and different load and current vector orientation conditions.*

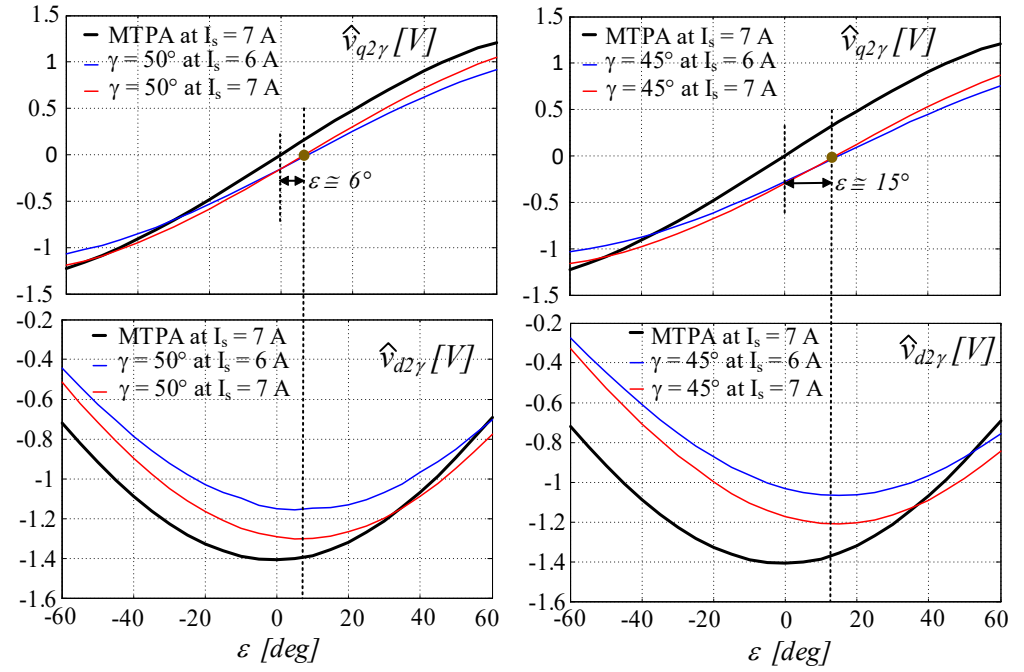

Figure 2.5.10 *Steady state qd axis SCs voltages in estimated reference frame at ω_{rm} = 50 rad/s and different load and current vector orientation conditions.*

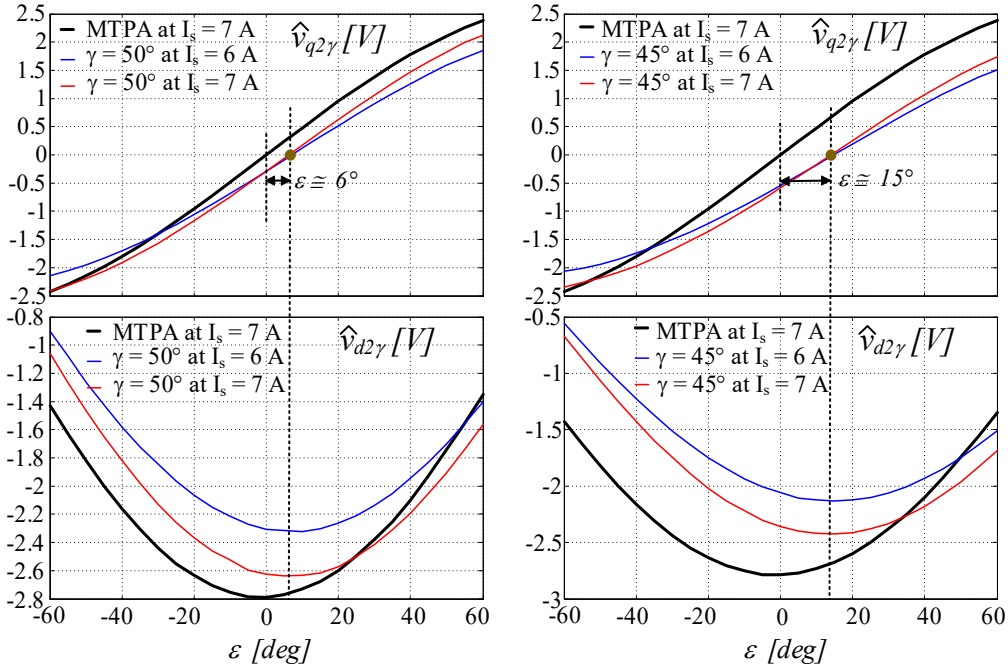

Figure 2.5.11 *Steady state qd axis SCs voltages in estimated reference frame at ω_{rm} = 100 rad/s and different load and current vector orientation conditions.*

2.5.1 Rotor Position and Speed Estimation exploiting a Zero Crossing Tracking Algorithm

According to (2.5.1) the q-axis induced voltage $\hat{v}_{q2\gamma}$ is proportional to $sin(2\varepsilon+2\gamma)$. This suggests a straightforward approach to track the actual rotor position, taking into account that the MTPA angle γ is known.

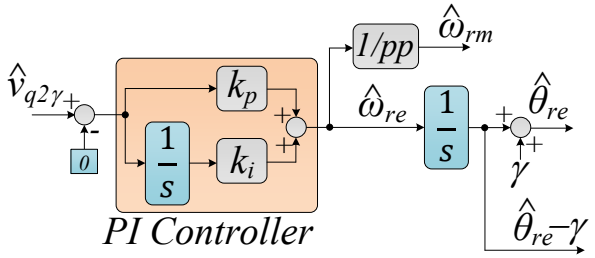

Figure 2.5.12 *Block Diagram of the rotor position and speed estimation for SynchRel Motor Drive.*

In fact, by assuming $I_s \neq 0$ and $\omega_{re} \neq 0$, when forcing $\hat{v}_{q2\gamma}$ to zero, the estimation error ε_θ becomes equal to the known quantity $-\gamma$. Such an approach can be easily integrated in a standard current control vector (CVC) algorithm, as illustrated in Fig. 2.5.1. In practice, γ is first computed from $\hat{\theta}_{re}$ and the angular position of the stator current vector in the *abc* stationary reference frame. The voltage induced in the search coils are then processed through the reference frame transformation $qd\hat{\gamma}$ to obtain $\hat{v}_{q2\gamma}$. A PI regulator finally forces $\hat{v}_{q2\gamma}$ to zero by adjusting the estimated rotor position $\hat{\theta}_{re}$. Such a regulator acts as a digital PLL system, as those used in some well-known sensorless control strategies [49], [50].

A low pass filter is applied to the estimated speed estimation in order to obtain an appropriate speed feedback signal for the sensorless drive [51], [52].

According to the proposed approach, the rotor position is tracked simply by driving $\hat{v}_{q2\gamma}$ to zero, thus no motor parameter estimation is required.

Experimental results shown in Fig. 2.5.13 deal with a test in which the drive operates in torque control, being the rotational speed held at *10rad/s* by the DC drive. The SyncRel motor is tasked to increase the torque from *60%* to *120%* of the rated value. A satisfactory dynamic behavior is observed with a quite small speed estimation error ε_ω.

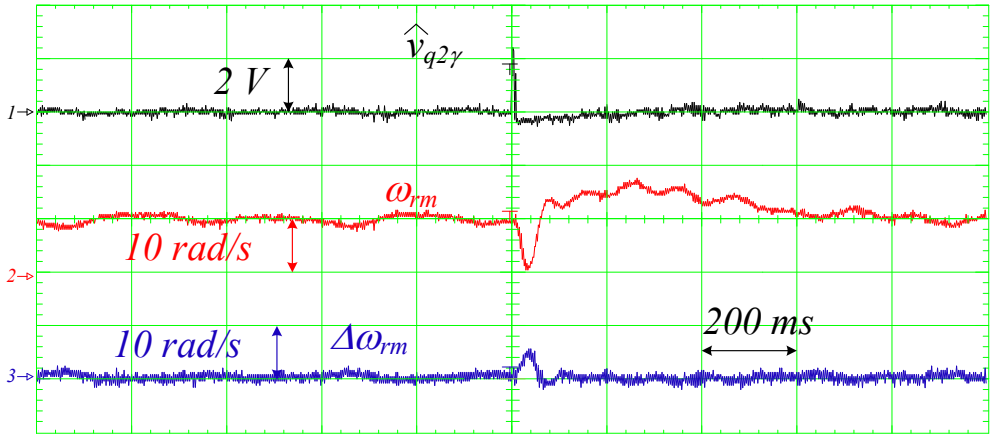

Figure 2.5.13 *Torque step from 60% to 120% of rated torque, at 10 rad/s.*

A direct comparison between the behavior of the proposed approach and that of a well known back-EMF based sensorless control technique [54], defined in chapter 1, is provided in Fig. 2.5.14. The drive in the two cases is tasked to perform a speed transient from ω_{rm}*=50 rad/s* to ω_{rm}*=10 rad/s* at no load. While the control is lost below *10 rad/s* using the back-EMF based solution, the proposed approach stably works even approaching the zero speed, featuring an almost negligible estimation error

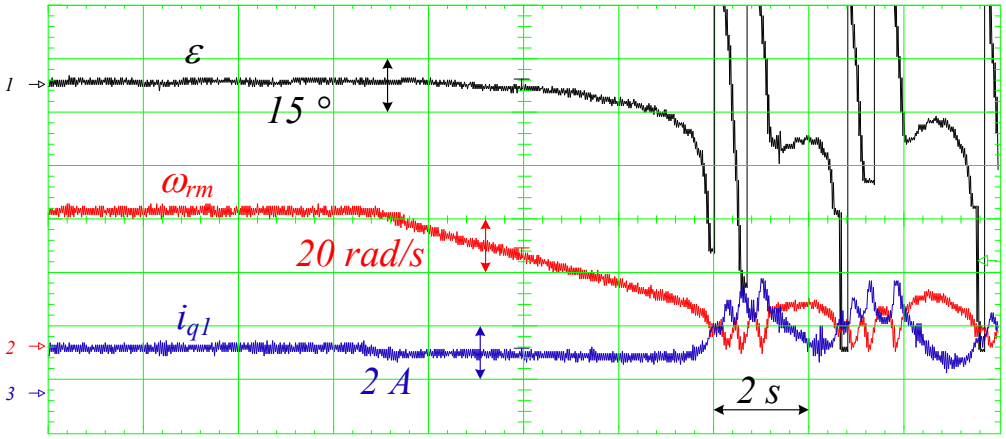

(a)

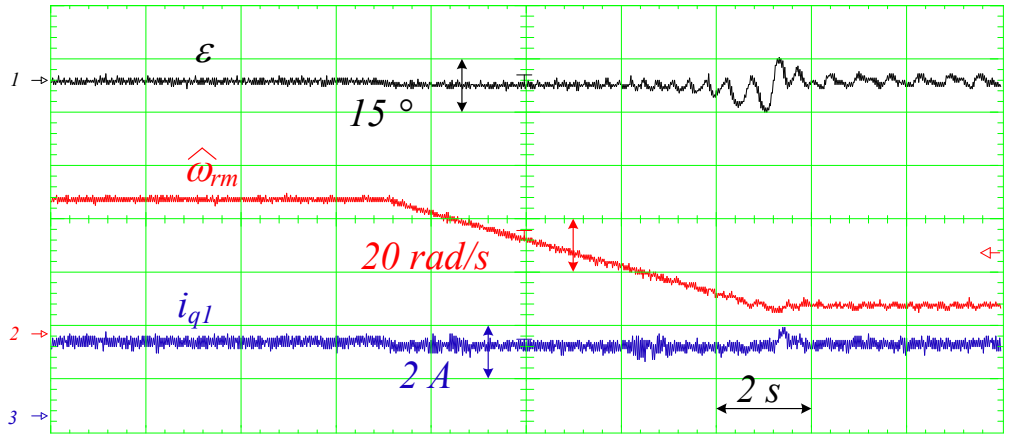

(b)

Figure 2.5.14 *Comparisons between back-EMF based (a) and SCs-based (b) sensorless techniques: Speed variation from 50 rad/s to 10 rad/s, at no load condition.*

A speed transient from *20* to *100 rad/s* is shown in Fig. 2.5.15, confirming the ability of the proposed approach to properly operate at high rotational speeds.

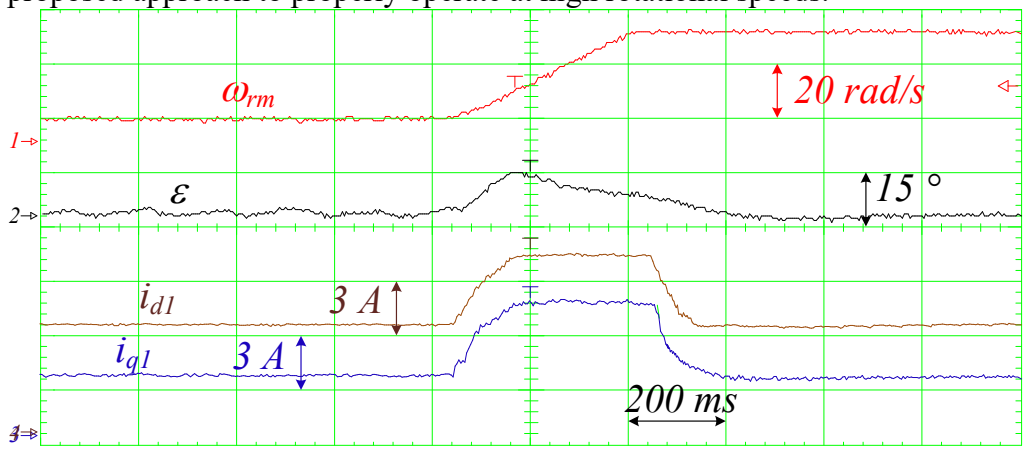

Figure 2.5.15 *Speed variation from 20 rad/s to 100 rad/s at 60% of the rated torque.*

2.5.2 Combined Back-EMF Sensorless Control Approach with Zero Crossing Tracking Error Estimation Algorithm

The proposed approach could be also integrated in model-based observers to correct the rotor position estimation, thus avoiding any kind of on-line motor parameters adjustment. A combination of the proposed approach and a back EMF based sensorless algorithm is shown in Fig. 2.5.16:

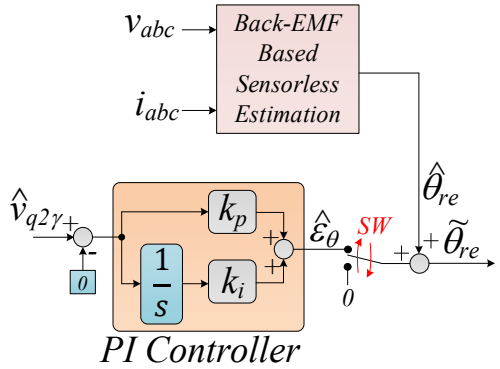

Figure 2.5.16 *Combined sensorless control approach.*

In this case, the estimation provided by the model-based estimator/observer is continuously corrected till $\hat{v}_{q2\gamma}$ is forced to zero.

The effectiveness of such a combined approach is confirmed in Fig. 2.5.17. In this low-speed test the rotor angular position provided by the back-EMF sensorless technique is first used. At $t=t_1$ the load is suddenly increased from 40% to 80% of the rated torque, resulting in an increment of the rotor position estimation error ε. At $t=t_2$ the proposed approach is successfully exploited to correct the rotor position estimation.

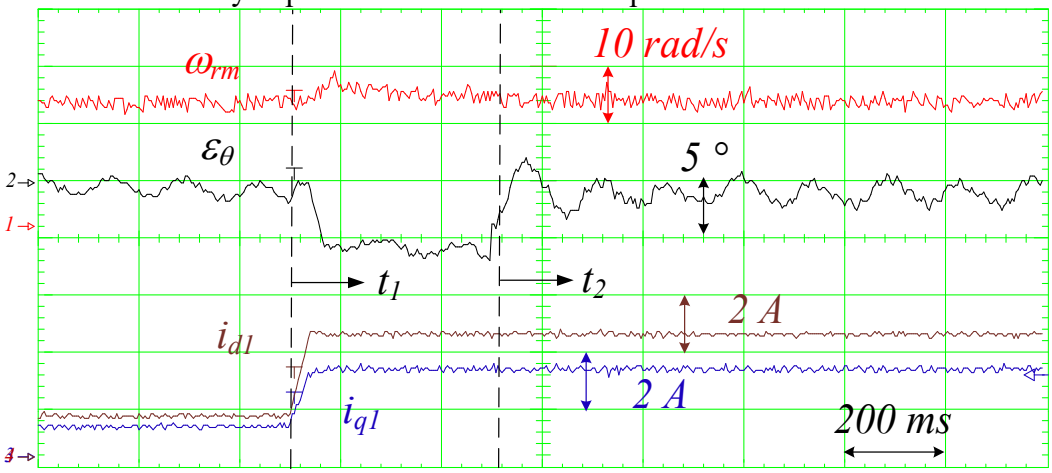

Figure 2.5.17 *Load transient from 40% to 80% of the rated torque, at* ω_{rm} *= 20 rad/s.*

2.6 Temperature Monitoring Experimental Results

Finally, the temperature monitoring by using the Search Coils has been experimentally developed both for SPMSM and for SynchRel. The signal conditioning circuit described in paragraphs 2.4 and 2.5 has been used to acquire each SC voltages in order to implement the rotor position estimation algorithms when the switch *SW1 = 0* and the temperature monitoring when the switch *SW1 = 1*.

The influence of thermistors on the induced voltages on the SCs has been initially addressed, by evaluating the induced voltage on an additional SCs which is not connected with the thermistors.

According to Figs. 2.8.1 and 2.8.2, no appreciable variation due to the presence of the additional resistor or with a thermistor is observed in the amplitude and phase of the voltage induced in the SCs.

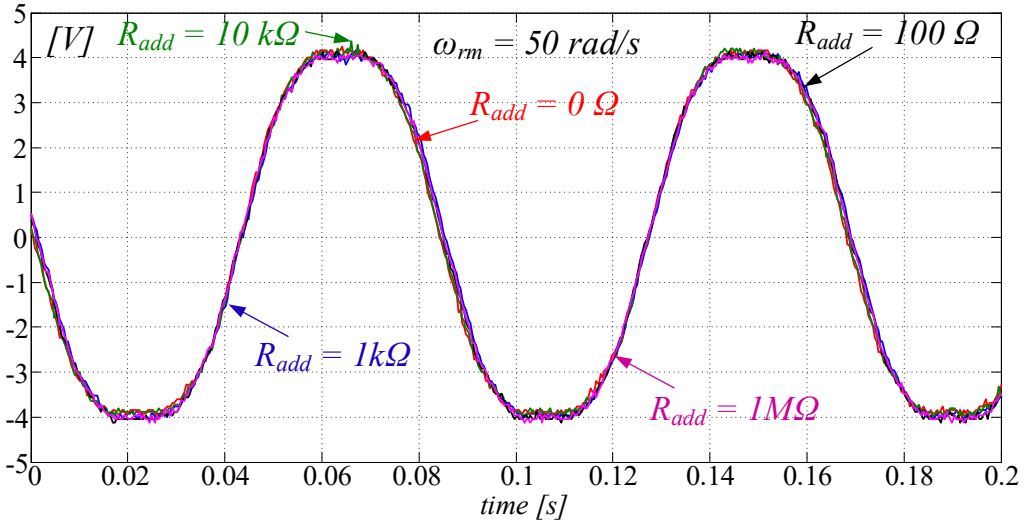

Figure 2.6.1 *Voltage at the terminals of the series of the SC and the additional resistor.*

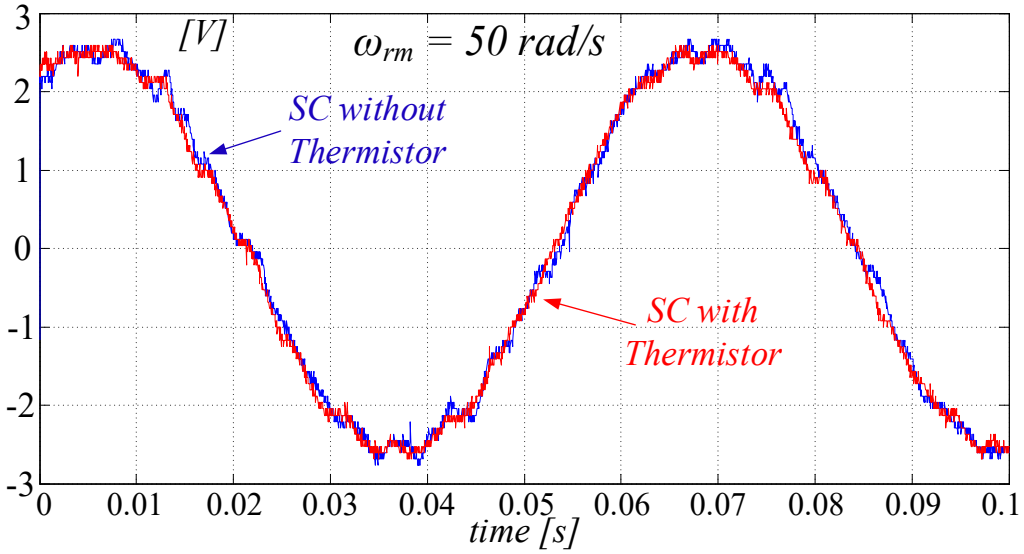

Figure 2.6.2 *Voltage at the terminals of a SCs with and without Thermistor.*

In particular, Fig. 2.8.1 shows the voltage measured at the terminals of the series connection of SCs an additional resistors R_{add}; Fig. 2.8.2 shows the voltage measured at the terminal of the SC without and when a thermistor is connected in series with the SC. No appreciable variation in the amplitude and phase of the voltage induced in the SCs is observed in the range of resistance of commercially available thermistors.

Finally, the temperature estimated according to Fig. 2.8.3a has been compared with that carried out by exploiting the classical Ohm's law, supplying the thermistor with a constant DC voltage and measuring both voltage and current, Fig. 2.8.3b.

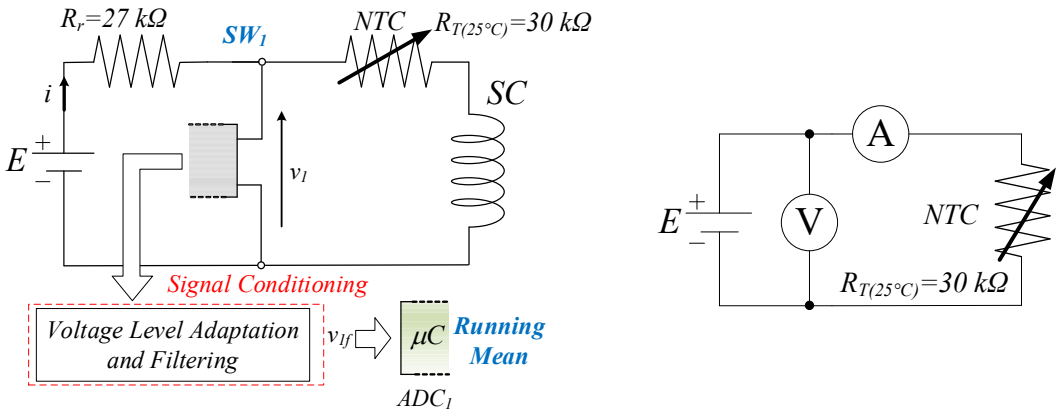

Figure 2.6.3 *Temperature monitoring in the synchronous motor drive (SPMSM and SynchRel) via: (a) DC supply of the series connection of the thermistor and SC; (b) typical temperature measurement by exploiting a DC supply voltage.*

In Figs. 2.8.4 - 2.8.5 the comparison has been executed in case of both synchronous motors (SPMSM or SynchRel) initially operated at no load and ω_{rm}=50 rad/s; soon after, a step torque is applied and the temperature periodically estimated with both methods shown in Fig. 2.8.3.

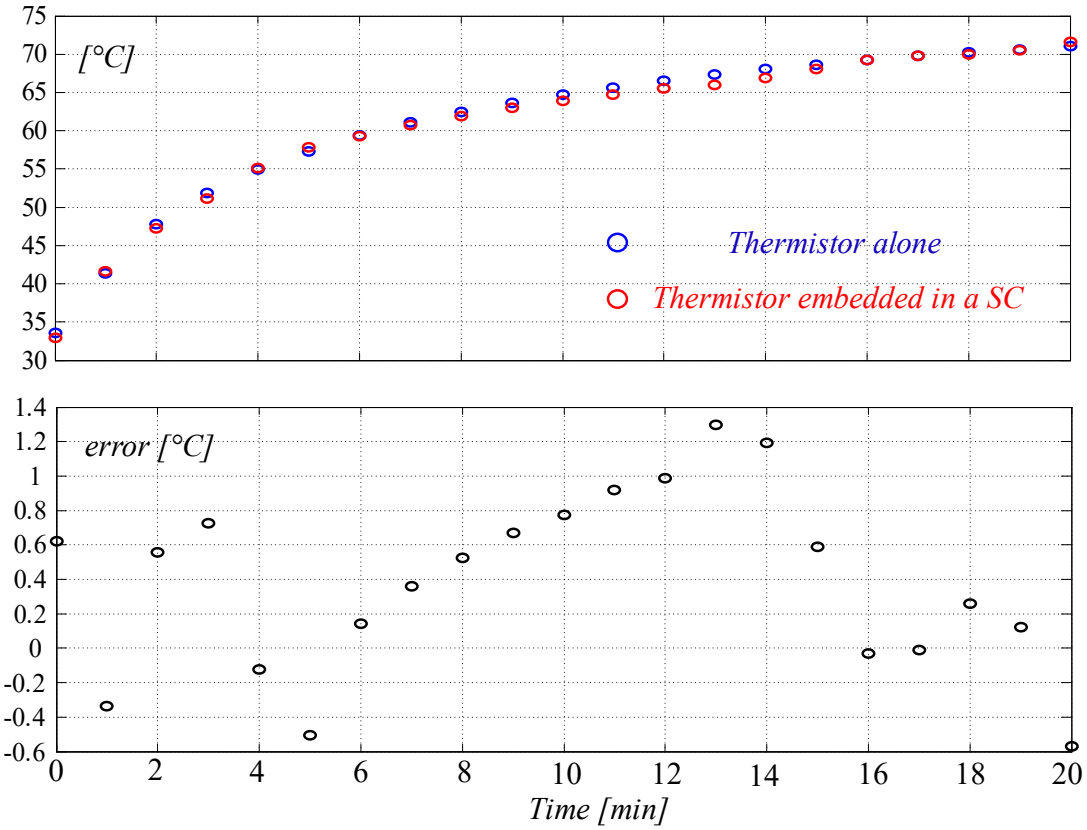

Figure 2.6.4 *Temperature measurement through a simple Thermistor and an SC embedded Thermistor in SPMSM motor drive, at ω_{rm} = 50 rad/s and 100% of the rated torque load.*

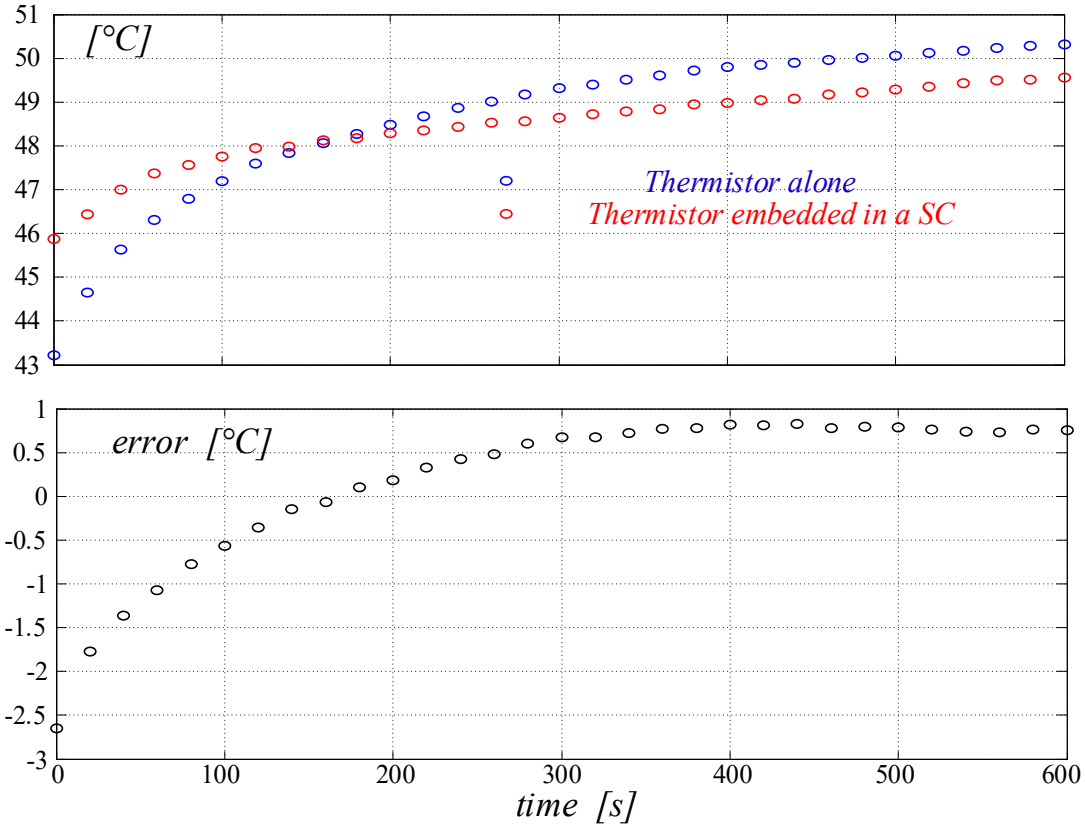

Figure 2.6.5 *Temperature measurement through a simple Thermistor and an SC embedded Thermistor in SynchRel motor drive, at ω_{rm} = 50 rad/s and 80% of the rated torque load.*

It is worth noting that the measurement error is quite small, lower than *1C°* at steady state.

After having evaluated the effectiveness of the rotor position estimation algorithm, some further tests have been performed to investigate possible influence of the voltages induced in the search coils to temperature monitoring. According to the conventional technique for temperature measurement through a thermistor, an additional DC voltage E is exploited to detect the resistance of the thermistor through measurement of the voltage v_1 at the terminals of a search coil, as shown in Fig. 2.8.3a. The actual thermistor resistance thus is given by:

$$R_T = \frac{R_r}{\frac{E}{g\, v_{1f}} - 1} \tag{2.8.1}$$

Where g is the gain of the signal conditioning circuit. Since only the DC component of the voltage should be taken into account, AC components due to the voltage induced in the SC must be wiped out. This can be accomplished by computing the mean value of v_1. The same signal condition circuit is used to carry out this measure, by selecting the switch SW_1=1. A low pass filter (LPF) is also required to cancel high frequency components of v_1 caused by PWM.

Fig. 2.8.6 shows the voltage v_{1f} acquired by the control unit during a step torque while the drive is operating under sensorless control. It is possible to note that the tracking algorithm is still working properly.

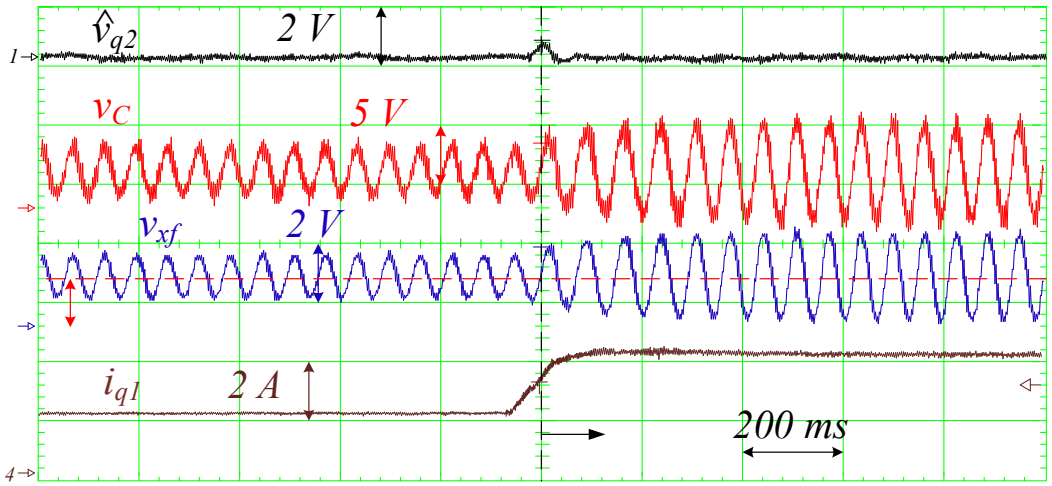

Figure 2.6.6 *q axis SCs voltage in estimated reference frame, v_c, v_{xf} and i_{q1} measured according to Figure 56(a), with the drive operating in sensorless mode.*

2.7 Conclusions

The contribution of my research in this topic regard an alternative way to sensorless estimate the rotor position in AC motors, exploiting the wiring of Thermistor embedded in the stator winding for temperature monitoring purposes.

Specifically, thermistor wirings embedded in the stator winding are suitably modified in order to turn them in a set of search coils. Since these coils can be connected to the drive control system exploiting existing thermistor cablings, only a minimal departure from a standard machine design is required.

A several suitable rotor position estimation techniques fully independent from motor parameters have been then developed using the obtained set of search coils. Such a techniques can be used alone or to improve the performance of conventional Back-EMF based sensorless techniques. The consistence of the proposed approaches, as well as the compatibility between rotor position estimation and temperature monitoring have been assessed by experimental tests.

The proposed techniques have been successfully applied on a Synchronous Reluctance motor drive and Surface Mounted Permanent Magnet Synchronous Machine motor drive however, it is of general use being exploitable on any kind of AC motor drive.

On the other hand, the proposed SCs based sensorless methods needs the placement of some additional coils in the stator winding, which could be an issue for small and very compact motors.

Moreover, even if the proposed methods requires only low-power and cheap circuitry to acquire the SCs voltages, in low cost applications the cost of these circuits could negatively affect the cost of the whole drive. Finally, the proposed approaches cannot be exploited on already assembled machines.

2.8 References

[1] Marko Hinkkanen, Seppo E. Saarakkala, Hafiz Asad Ali Awan, Eemeli Mölsä, Toni Tuovinen, “Observers for Sensorless Synchronous Motor Drives: Framework for Design and Analysis,” IEEE Transactions on Industry Applications, 2018, vol. 54, no.6 , pp. 6090-6100.

[2] A. M. El-Serafi and J.Wu, "Determination of the parameters representing the cross-magnetizing effect in saturated synchronous machines," IEEE Trans. Energy Convers., vol. 8, no. 3, pp. 333–342, Sep. 1993.
[3] Consoli A., Cavallaro C., Scarcella G., Testa, A., "Sensorless torque control of syncrel motor drives" IEEE Transactions on Power Electronics, Volume 15, Issue 1, January 2000, Pages 28-35.
[4] Consoli A., Scarcella G., Testa A., "Slip-Frequency Detection for Indirect Field-Oriented Control Drives" IEEE Transactions on Industry Applications Volume 40, Issue 1, January 2004, Pages 194-201.
[5] Z. Chen, M. Tomita, S. Ichikawa, S. Doki, S. Okuma, "Sensorless control of interior permanent magnet synchronous motor by estimation of an extended electromotive force", Conference Record of the 2000 IEEE Industry Applications Conference, vol. 3, paages 1814 – 1819, 2000.
[6] S. Morimoto, K. Kawamoto, M. Sanada and Y. Takeda, "Sensorless Control Stratedy for Salient-Pole PMSM Based on Extended EMF in Rotating Reference Frame", IEEE Transactions on Industry Applications, vol. 38, no. 4, july/august 2002.
[7] Y. Han, J. Choi, Y. Kim, "Sensorless PMSM drive with a sliding mode control based adaptive speed and stator resistance estimator'' IEEE Transactions on Magnetics, vol. 36, n. 5, pp. 3588 – 3591, 2000.
[8] Y. Liang, Y. Li, "Sensorless control of PM synchronous motors based on MRAS method and initial position estimation'' Sixth International Conference on Electrical Machines and Systems. ICEMS 20, pp. 3588 – 3591, 2003.
[9] S. Chi, Z. Zhang, L. Xu, "Sliding-Mode Sensorless Control of Direct-Drive PM Synchronous Motors for Washing Machine Applications'' IEEE Transactions on Industry Applications, vol. 45, n. 2, pp. 582 – 590, 2009.
[10] Z. Chen, M. Tomita, S. Doki, S. Okuma, "New adaptive sliding observers for position- and velocity-sensorless controls of brushless DC motors'' IEEE Transactions on Power Electronics, vol. 47, n. 3, pp. 582 – 591, 2000.
[11] A. Piippo, M. Hinkkanen, J. Luomi, "Adaptation of Motor Parameters in Sensorless PMSM Drives'' IEEE Transactions on Industry Applications, vol. 45, n. 1, pp. 203 – 212, 2009.
[12] R. Morales-Caporal, E. Bonilla-Huerta, M. A. Arjona, C. Hernández, "Sensorless Predictive DTC of a Surface-Mounted Permanent-Magnet Synchronous Machine Based on Its Magnetic Anisotropy'' IEEE Transactions on Industrial Electronics, vol. 60, n. 8, pp. 3016 – 3024, 2013.
[13] E. Levi, "Saturation modelling in d-q axis models of salient pole synchronous machines," IEEE Trans. Energy Convers., vol. 14, no. 1, pp. 44–50, Mar. 1999.
[14] B. Stumberger, G. Stumberger, D. Dolinar, A. Hamler, and M. Trlep, "Evaluation of saturation and cross-magnetization effects in interior permanent-magnet synchronous motor," IEEE Trans. Ind. Appl., vol. 39, no. 5, pp. 1264–1271, Sep./Oct. 2003.
[15] Silverio Bolognani, Ludovico Ortombina, Fabio Tinazzi, Mauro Zigliotto, "Model sensitivity of fundamental-frequency-based position estimators for sensorless pm and reluctance synchronous motor drives," IEEE Transactions on Industrial Electronics, vol. 65, no.1, pp. 77 – 85.
[16] P. Guglielmi, M. Pastorelli, A. Vagati, "Impact of cross-saturation in sensorless control of transverse-laminated synchronous reluctance motors," IEEE Trans. on Ind. Electronics, vol. 53, no. 2, pp. 429 – 439, April 2006.
[17] Youg – Cheol Kwon, Seung – Ki Sul, Noor Aamir Baloch, Sohji Mukarami, Shinya Morimoto, "Improved Design of IPMSM for Sensorless Drive With Absolute Rotor

Position Estimation Capability “, IEEE Transactions on Industry Applications, vol. 52, pages 1441 – 1451, 2016.
[18] T. Lipo, “Flux sensing and control of static AC drives by the use of flux coils,” IEEE Transactions on Magnetics, vol. 13, no. 5, pp. 1403 – 1408, 1977.
[19] Thomas A. Lipo, Kwong C. Chang, “A New Approach to Flux and Torque-Sensing in Induction Machines”, IEEE Transactions on Industry Applications, vol. IA-22, no. 4, pp. 731 – 737, 1986.
[20] D. S. Zinger, F. Profumo, T. A. Lipo, D. W. Novotny, “A direct field-oriented controller for induction motor drives using tapped stator windings,”, IEEE Transactions on Power Electronics, vol. 5, no. 4, pp. 446 – 453, 1990.
[21] Yao Da, Xiaodong Shi, Mahesh Krishnamurthy, “A Novel Universal Sensor Concept for Survivable PMSM Drives”, IEEE Transactions on Power Electronics, vol. 28, n. 12, pp. 5630 – 5638, 2013.
[22] J.M. Guerrero, M. Leetmaa, F. Briz, A. Zamarron, R.D. Lorenz, “Inverter nonlinearity effects in high-frequency signal-injection-based sensorless control methods,” IEEE Transactions on Industry Applications, 2005, vol. 41, no. 2, pp. 618-626.
[23] Toni Tuovinen, Marko Hinkkanen, Jorma Luomi, “Analysis and Design of a Position Observer With Resistance Adaptation for Synchronous Reluctance Motor Drives,” IEEE Transactions on Industry Applications, vol. 49, no1, pp. 66 – 73, Jan./Febr. 2013.
[24] Consoli A., Bottiglieri G., Letor R., Ruggeri R., Testa A., De Caro S., “Sensorless position control of DC actuators for automotive applications” Proc. of 2004 IEEE Industry Applications Conference; 39th IAS Annual Meeting; Seattle, USA, 2004, Volume 2, Pages 1217-1224.
[25] T. Matsuo, T. A: Lipo, “Current sensorless field oriented control of synchronous reluctance motor, “ Conference Record of the 1993 IEEE Industry Applications Conference Twenty-Eighth IAS Annual Meeting, vol. 1, pp. 672 – 678, 1993.
[26] T. Matsuo, T. A. Lipo, “Rotor position detection scheme for synchronous reluctance motor base on current measurements, “ IEEE Transactions on Industry Applications, vol. 31, pp. 860 – 868, 1995.
[27] R. Lagerquist, I. Boldea, T. J. E. Miller, “Sensorless-control of the synchronous reluctance motor,” IEEE Transactions on Industry Applications, vol. 30, no.3, pp. 673 – 682, May/June 1994.
[28] L. Kreindler, A. Testa, T.A. Lipo, “Position sensorless synchronous reluctance motor drive using the stator phase voltage third harmonic, “ Conference Record of the 1993 IEEE Industry Applications Conference Twenty Eighth IAS Annual Meeting, vol.1, pages 679-686, 1993.
[29] A. Consoli, F. Russo, G. Scarcella, A. Testa, “Low - and zero - speed sensorless control of synchronous reluctance motors “ IEEE Transactions on Industry Applications., vol. 35, pages 1050-1057, 1999.
[30] Francois J. W. Barnard, Wikus Theo Villet, Maarten J Kamper, “Hybrid Active Flux and Arbitrary Injection Position Sensorless Control of Reluctance Synchronous Machines “ IEEE Transactions on Industry Applications, vol. 51, pp. 3899 – 3906, 2015.
[31] Arzhang Yousefi-Talouki, Paolo Pescetto, Gianmario Pellegrino, “Sensorless Direct Flux Vector Control of Synchronous Reluctance Motors Including Standstill, MTPA, and Flux Weakening,” IEEE Transactions on Industry Applications, vol. 53, pages 3598-3608, 2017.
[32] Seung-Ki Sul, Yong-Cheol Kwon, Younggi Lee, “Sensorless control of IPMSM for last 10 years and next 5 years,” CES Transactions on Electrical Machines and Systems, vol. 1, no. 2, pp. 91 – 99, 2017.

[33] R. Bojoi, M. Pastorelli, J. Bottomley, P. Giangrande, C. Gerada, " Sensorless control of PM motor drives — A technology status review," 2013 IEEE Workshop on Electrical Machines Design, Control and Diagnosis (WEMDCD), 2013, pp. 168-182.
[34] Consoli A., Scarcella G., Testa A., "New zero frequency flux position detection approach for direct field oriented control drives" Proc. of the 1999 IEEE Industry Applications Conference - 34th IAS Annual Meeting; Phoenix, USA 1999, Pages 2290-2297.
[35] L. D. Tornello, G. Scelba, G. Scarcella, M. Cacciato, A. Testa, S. Foti, S. De Caro, M. Pulvirenti, Combined Rotor-Position Estimation and Temperature Monitoring in Sensorless, Synchronous Reluctance Motor Drives, IEEE Transactions on Industry Applications, 2019, vol. 55, no. 4, July-Aug. 2019, pp. 3851 – 3862.
[36] A.H. Bonnett, and G.C. Soukup, "Cause and analysis of stator and rotor failures in three-phase squirrel-cage induction motors," IEEE Trans. Ind. Appl., vol. 28, no. 4, pp. 921-937, 1992.
[37] S. F. Farag, R. G. Bartheld, and T. Habetler, "An integrated on-line motor protection system," IEEE Trans. Ind. Appl., vol. 2, no. 2, pp. 21–26, Mar./Apr. 1996.
[38] K.D. Hurst, and T.G. Habetler, "Thermal monitoring and parameter tuning scheme for induction machines," Conf. Rec. IEEE-IAS, vol. 1, pp. 136-142, 1997.
[39] A Boglietti,A Cavagnino,D. Staton,M. Shanel,M. MOller and C. Mejuto, "Evolution and Modern Approaches for Thermal Analysis of Electrical Machines," IEEE Transactions on Power Electronics, vol. 56,no. 3,pp. 871-882,2009.
[40] S. D. Wilson, P. Stewart, and B. P. Taylor, "Methods of Resistance Estimation in Permanent Magnet Synchronous Motors for Real-Time Thermal Management," IEEE Transactions on Energy Conversion, voL 25,no. 3,pp. 698-707,2012.
[41] F. Briz, M. W. Degner, J. M. Guerrero, and A. B. Diez, "Temperature estimation in inverter fed machines using high frequency carrier signal injection," IEEE Trans. Ind. Appl., vol. 44, no. 3, pp. 799–808, May/Jun. 2008.
[42] Nikola Z. Popov, Slobodan N. Vukosavic, Emil Levi, "Motor Temperature Monitoring Based on Impedance Estimation at PWM Frequencies," IEEE Transactions on Energy Conversion, vol. 29, no. 1, pp. 215 – 223.
[43] Anees Mohammed ; Siniša Djurović, "Stator Winding Internal Thermal Monitoring and Analysis UsingIn SituFBG Sensing Technology," IEEE Transactions on Energy Conversion, 2018, vol. 33, no. 3, pp. 1508-1518.
[44] Samuli Kallio, Mauro Andriollo, Andrea Tortella, Jussi Karttunen, "Decoupled d-q Model of Double-Star Interior-Permanent-Magnet Synchronous Machines", IEEE Transactions on Industrial Electronics, vol. 60, n.6, pp. 2486 – 2494, 2013.
[45] G. De Donato, G. Scelba, M. Pulvirenti, G. Scarcella, F. Giulii Capponi "Low-Cost, High-Resolution, Fault-Robust Position and Speed Estimation for PMSM Drives Operating in Safety-Critical Systems,", IEEE Transactions on Power Electronics, vol. 34, n. 1, pp. 550 – 564, 2019.
[46] G. R. Chen, S. C. Yang, Y. L. Hsu and K. Li, "Position and Speed Estimation of Permanent Magnet Machine Sensorless Drive at High Speed Using an Improved Phase-Locked Loop", Energies, october 2017.
[47] J. Ahmed, Z. Salam, "An Enhanced Adaptive P&O MPPT for Fast and Efficient Tracking Under Varying Environmental Conditions", IEEE Transactions on Sustainable Energy, vol. 9, no. 3, july 2013.
[48] S. K. Kollimalla and M. K. Mishra, "Variable Perturbation Size Adaptive P&O MPPT Algorithm for Sudden Changes in Irradiance", IEEE Transactions on Sustainable Energy, vol. 5, no. 3, july 2014.

[49] Alfio Consoli, Giuseppe Scarcella, Giacomo Scelba, Antonio Testa, Domenico Antonino Triolo, "Sensorless Rotor Position Estimation in Synchronous Reluctance Motors Exploiting a Flux Deviation Approach," IEEE Transactions on Industry Applications, 2007, vol. 43, no. 5, pp. 1266-1273.

[50] M. Linke, R. Kennel, J. Holtz, "Sensorless speed and position control of synchronous machines using alternating carrier injection," IEEE International Electric Machines and Drives Conference, 2003. IEMDC'03, vol. 2, pp. 1211-1217.

[51] X. Shen, Z. Q. Zhu, and D. Howe, "Improved speed estimation in sensorless PM brushless AC drives," IEEE Trans. Ind. Appl., vol. 38, no. 4, pp.1072–1080, Jul./Aug. 2002.

[52] Dong Wang, Kaiyuan Lu, Peter Omand Rasmussen, Zhenyu Yang, "Comparative Study of Low-Pass Filter and Phase-Locked Loop Type Speed Filters for Sensorless Control of AC Drives," IEEE Trans on Electrical.

[53] Yao Da, Xiaodong Shi, Mahesh Krishnamurthy, "A Novel Universal Sensor Concept for Survivable PMSM Drives", IEEE Transactions on Power Electronics, 2013, vol. 28, no. 12.

[54] H. Kim, M. C. Harke, R. D. Lorenz, "Sensorless Control of Interior Permanent-Magnet Machine Drives With Zero-Phase Lag Position Estimation", IEEE Transactions on Industry Applications, vol. 39, no. 6, nov/dec 2003.

[55] W. L. Soong, "Inductance Measurements for Synchronous Machines", Power Engineering Briefing Note Series, 8 May 2008.

Chapter 3. Speed Estimation Algorithms for AC Motor Drives

3.1 Introduction

AC servo drives require a rotor position feedback transducer to implement field orientation and thus produce a decoupled torque and flux control, in a manner analogous to DC machines [1], guaranteeing optimal dynamic performances.

In addition, velocity transducer is both costly and mechanically difficult, most drive developers prefer to estimate velocity from the position measurement. Hence, one feedback transducer is enough for both the field-oriented electromagnetic machine control and for the electro-mechanical velocity and position feedback control loops [1].

The usefulness of this approach is generally limited by the accuracy and quantization limits of the velocity estimation approach. This occurs because the velocity loop is the innermost state loop, and its performance must generally be better than outer state loops. Such performance implies that the state feedback gains for the velocity loop are higher than for the position and integrated position error loops and that the errors the velocity loop producers are not generally correctable by the lower performance position and integrated position error loops [1].

The higher gain requirement for the velocity loop will cause velocity quantization to appear directly as a larger (and unnecessary) variation (with significant RMS values) in the torque producing current component command. This is especially critical for ac drives because of the need for high current loop bandwidths to achieve proper instantaneous field orientation of the flux and current vectors [1].

This chapter will describe the different rotor position sensors technologies used in electrical motor drives. In addition, the main metrics of a position sensor are identified and finally the main techniques for estimating angular speed will be discussed.

3.2 Position Sensor Technologies

Different technologies exist for position measurement, Fig. 3.2.1, e. g. electromagnetic resolvers, optical encoders, Hall-effect sensors, magnetoresistive sensors, proximity switches [2].

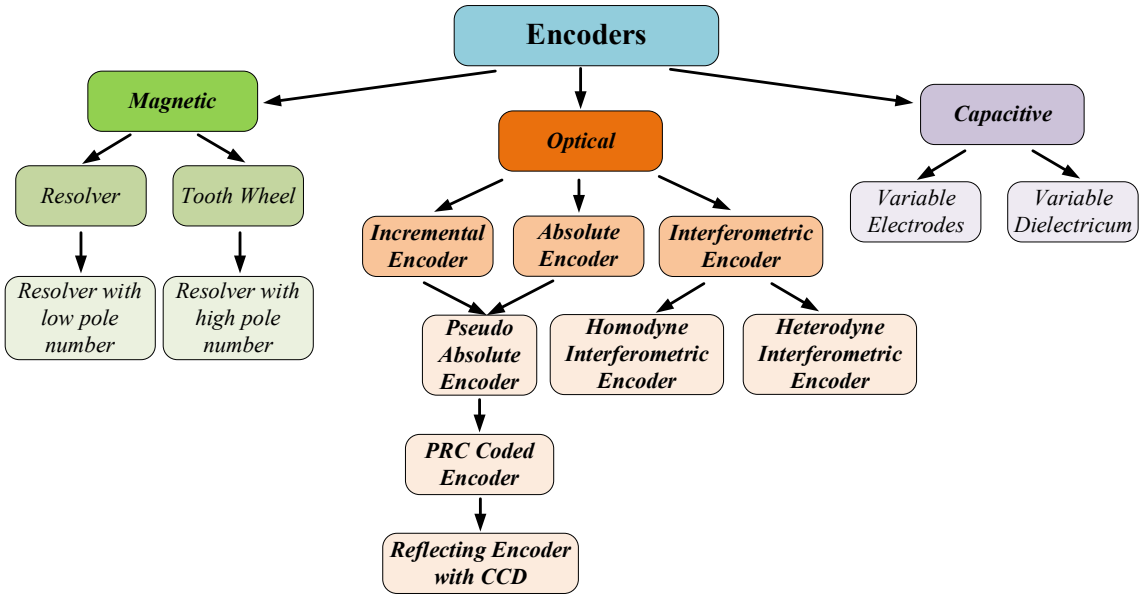

Figure 3.2.1 *Different Optical Encoder Technologies [3].*

Regardless of the specific technology, the quality of position measurement is fully assessed by three independent metrics: resolution, absolute accuracy and differential accuracy, [4]. Resolution is defined as the smallest sensed position increment. It can be indicated in angular units, in number of pulses per revolution, in number of bits or in the number of discrete states of the sensor's interface, N_{DS}.

$$r = \theta_{ideal(i)} - \theta_{ideal(i-1)} \tag{3.2.1}$$

Equivalently, it can be defined as the number of different angles the encoder can distinguish between each other. Fig. 3.2.2 shows an encoder that can distinguish 8 different positions within a complete revolution; the resolution is therefore 45° or 3 bits ($2^3 = 8$).

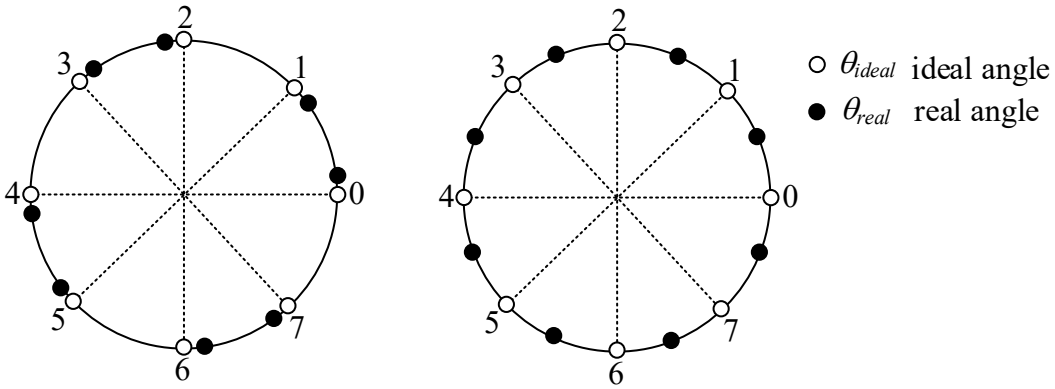

Figure 3.2.2 *Resolution, absolute accuracy and differential accuracy for encoders [3].*

Only the resolution is not sufficient to describe the performance of the position sensors because it gives no information regarding the correctness of the measured angle. For example, Fig. 3.2.2 shows two cases for the 3-bit encoder; in both cases the ideal rotor position shown by the encoder is different from the real rotor position, sensed on the shafted of the rotor. Absolute accuracy is defined as the ratio of the maximum error between the ideal and real position over the:

$$a = \frac{\max\left|\theta_{real(i)} - \theta_{ideal(i-1)}\right|}{r} \tag{3.2.2}$$

According to the above definition the encoder on the left of Fig. 3.2.2 has a good absolute accuracy compared to the encoder on the right; it is therefore better suited for commutation or for position feedback in a position loop.

However, this encoder is not useful in a speed control loop because the distance between the consecutive real angles is much variable in a whole revolution.

Average speed calculation would therefore produce evident errors even when the shaft is rotating at a constant speed, causing inevitable steady state speed ripple. On the contrary, the encoder on the right would produce a good average speed measurement because the variation in the distance between consecutive angles is smaller then as the left configuration shaft rotates. Differential accuracy is defined as the p.u. maximum deviation between an actual position increment and the resolution of the encoder:

$$a' = \frac{\max|\theta_{real(i)} - \theta_{real(i-1)}| - r}{r} \tag{3.2.3}$$

All three metrics have an impact on the quality of motion control, on the torque ripple produced by the motor and on the efficiency of the drive. As recognized in [3], [5], a high absolute accuracy is the key for precise position control, while a high differential accuracy is very important for precise speed control. Resolution affects both position and speed control in VSDs. In other words, the resolution not only does it have an impact on position controls, for example in terms of maximum position error at zero-speed, but also on speed control, since it affects the quality of speed estimation.

3.2.1 Optical Encoders

Optical rotary encoders use a glass disk with a pattern of lines deposited on it, a metal or plastic disk with slots Light from a LED shines through the disk or strip onto one or more photodetectors as shown in Fig. 3.2.3, which produce the encoder's output. This is one of the most common technologies used in electric drives.

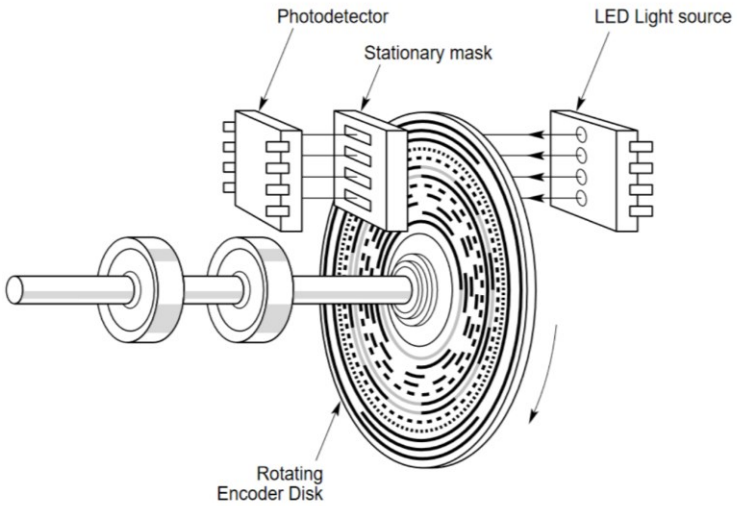

Figure 3.2.3 *Basic Operating Principle of "Geometrical" Angular Optical Encoders*

Rotary encoders can be absolute or incremental. The incremental encoder detects movement relative to a reference point. As a result a reference signal is usually supplied by the encoder at a fixed position in order to define a reference position. The current position is then incremented (or decremented) as appropriate. Unfortunately, a loss of count may not be detected until a reference point is reached. Furthermore, reading errors may accumulate. On the other hand, absolute encoders produce a set of binary signals

from which the absolute position can be deduced without the knowledge of the previous motion history. The current position is known right from powering-on. In the case of absolute rotary encoders, single and multiturn devices are available.

A fixed LED source is aimed at a rotating transparent disc coupled to the shaft, upon which opaque areas have been created around it's circumference. These areas may also be coded in some particular fashion. The number of variations in transmittance on a circumferential path is called "the number of lines". Behind the rotating disc there is a fixed grating which acts as an magnifier and creates magnified fringe patterns which move one fringe pitch for every "line" of angular motion. Arc segment planar photodiodes are placed behind the moiré grating in order to catch the fringe patterns and produce smooth, almost sinusoidal analog signals in response to the disc's rotation. Usually these signals are two and are in quadrature. The grating is important for encoders with a significant number of lines because without it the photodiodes wouldn't be able to resolve the line spacing.

The presence of coding on the rotating disc determines whether the encoder is incremental or absolute. In the first case the lines on the disc are not disposed in a coded fashion, but opaque areas are simply alternated with transparent areas, as shown in Fig. 3.2.4; the encoder detects incremental angular motion, but is not able to measure the absolute angular shaft position. A very common digital interface for the sinusoidal outputs in incremental encoders is the so-called A quad B interface: the signals are fed to zero crossing detectors which convert them to square wave type signals, as shown in Fig. 3.2.4. This interface is very cheap but the downside is a greatly reduced resolution. Fig. 3.2.4 shows that by using both A and B signals it is possible to obtain a maximum resolution equal to 4 times the number of lines of the encoder. Differential accuracy can often become an issue in average speed calculation due to phase errors between A and B; when this is the case the entire line period must be used as the angular increment, so the resolution then equals the number of lines. Direction of rotation is known by checking whether the A channel signal leads or lags the B channel signal.

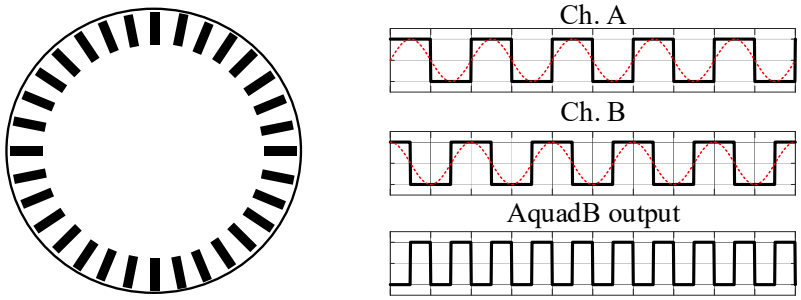

Figure 3.2.4 *Incremental Optical Encoder Disk Pattern and Output Signals.*

Absolute encoders overcome these problems since the coded lines on the disc, as shown in Fig. 3.2.5, allow absolute position measurement. The coding is sensed by the arc segment detectors and additional signal conditioning electronics transform the signal into a digital word which contains the absolute measurement of the particular angle that is being crossed by the shaft.

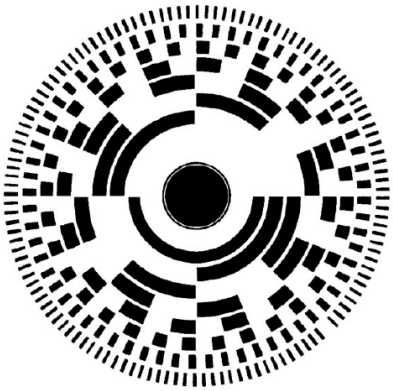

Figure 3.2.5 *Absolute Optical Encoder Disk with Gray Code Pattern.*

The Gray code is generally used on the disk: the Gray code notoriously provides the least uncertainty in case of wrong transmission because only 1 bit changes state for each line transition; however, it requires a special interface to be read by the microprocessor. To overcome this problem, most manufacturers include hardware interfaces within the encoder housing, which transform Gray code into pure binary or decimal binary code (BCD) signals; in this way the user can choose from a selection of three different types of encoding, the one that best suits their interface. Analog sine quadrature signals are sometimes also available as outputs. In this case, the resolution can be significantly increased.

Another aspect that must be taken into consideration is the relative lack of robustness of optical encoders. Temperature, humidity and electromagnetic interference can affect the signal conditioning electronics and mechanical shocks and vibrations can damage the discs. Many manufacturers offer extra-rugged encoders for operation in harsh environments.

3.2.2 Electromagnetics Resolver

The resolver is a rotating transformer consisting of a fixed part the stator and a rotating part the rotor, whose output voltages are related to the rotation angle of the shaft. Resolvers, in the past available with brushes and rotating collectors, are now of the brushless type. The stator houses three windings: a coil wound on a lamination, which is practically the primary winding of the rotating transformer and is used to excite the rotor, and two other windings fixed at right angles to each other. The rotor can have two or three windings: one is the secondary coil of the rotating transformer, also wound on a sheet, and the others are coupled to the two-phase windings on the stator. The basic resolvers have two poles, so the angular information is the mechanical angle of the rotor; these resolvers can reach an accuracy of up to 5 arc minutes. Multipole resolvers are also available that can provide better accuracy for mechanical angle measurement or be used for commutation purposes with multipolar brushless motors [5].

There are two main ways to obtain information on the position of the shafted rotor from resolvers. The first way, shown in Fig. 3.2.7, consists in energizing the two-phase stator windings (S1-S3 and S2-S4) with sinusoidal voltages in phase quadrature in order to obtain an induced voltage at the primary winding of the rotating transformer (R1 -R2) whose phase varies with the angle of the shaft. In this case, the following equations are valid where K is the transformation ratio of the rotating transformer:

$$V_{S1\text{-}S3} = V \sin(\omega_e t) \tag{3.2.4}$$

$$V_{S2\text{-}S4} = V \cos(\omega_e t) \tag{3.2.5}$$

$$V_{R1\text{-}R3} = K\, V_{S1\text{-}S3} \cos(\theta) - K\, V_{S2\text{-}S4} \sin(\theta) = K\, V \sin(\omega_e t - \theta) \tag{3.2.6}$$

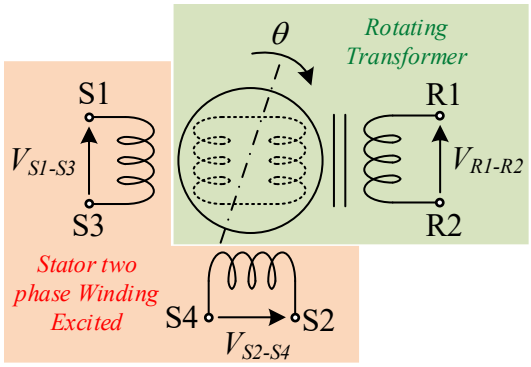

Figure 3.2.6 *Stator Winding Excited Resolver.*

A variant of resolver with excited stator winding is the one shown in Fig. 3.2.8 in which the secondary winding is not on the rotor but is also placed on the stator. The rotor is shaped in such a way that spatial information is conveyed to the secondary winding thanks to the variation of the reluctance of the magnetic circuit. The equations describing this variant are identical to those described in (3.2.4) - (3.2.6).

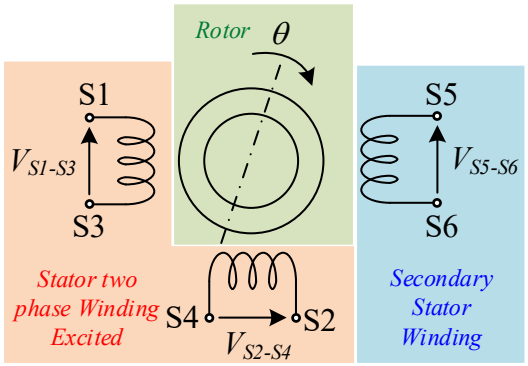

Figure 3.2.7 *Stator Windings Excited Resolver Variant.*

The second way, shown in Figure 3.2.9, consists in energizing the primary winding of the rotating transformer (R1-R2) with a sinusoidal voltage in order to obtain two voltages from the two-phase windings (S1-S3 and S2-S4) whose amplitudes vary with the angle of the tree. In this case, the following equations hold, with K previously defined:

$$V_{R1\text{-}R2} = V \sin(\omega_e t) \tag{3.2.7}$$

$$V_{S1\text{-}S3} = K\, V_{R1\text{-}R2} \cos(\theta) \tag{3.2.8}$$

$$V_{S2\text{-}S4} = K\, V_{R1\text{-}R2} \sin(\theta) \tag{3.2.9}$$

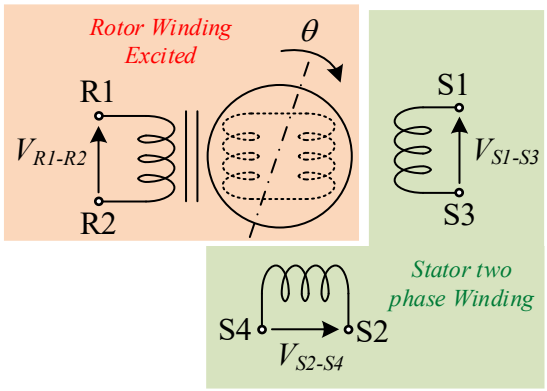

Figure 3.2.8 *Rotor Winding Excited Resolver.*

Having obtained voltages that contain position information in the phase or amplitude, it is necessary to extract this information and convert it from the analog domain to the digital one using ADC (Analog Digital Converter) converters which are now widespread in the market.

The main advantage of choosing resolvers as position sensors is that the position measurement is absolute and is readily available at start-up: this is the main reason for its widespread use in electric traction applications. Another reason is that the mechanical structure of the resolvers is relatively robust and immune to environmental contamination. Many ADCs offer high immunity to disturbances thanks to the double integration of the error signal; noise rejection is further enhanced by the detector rejection of any signal not at the excitation frequency such as wideband noise.

Important disadvantages are both technical and economic. The performance of the ADCs is limited by the sampling frequency of the demodulator which must be sampled at the excitation frequency of the rotor; this means that the dynamic content must be below half the excitation frequency. Also, the different excitation mode is not synchronized with the speed control sample rate. The resolver is a complex structure and therefore is destined to be more expensive than other technologies.

3.2.3 Hall Effect Sensors

Hall-effect sensors are among the most widely used kinds of sensors: they are cheap, rugged, practically maintenance free and easily integrated into virtually any kind of application design [6]. Typical examples of Hall-effect sensing applications can be found in crankshaft position or speed sensors, proximity sensors, office machine (copiers, fax machines, printers) sensors, anti-skid sensors, door interlock sensors, etc. Hall-effect plays an important role also in the electric drive industry: it is found as the sensing principle in high bandwidth linear current sensors and both in binary (digital) and linear position sensors.

It is known that when a current-carrying conductor is placed into a magnetic field, a voltage will be generated perpendicular to both the current and the field. This principle is known as the Hall effect. Fig. 3.2.9 illustrates the basic principle of the Hall effect. It shows a thin sheet of semiconducting material (Hall element) through which a current is passed.

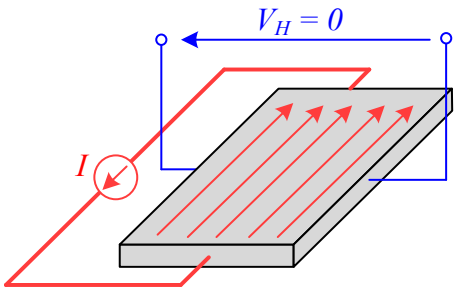

Figure 3.2.9 *Hall effect principle, no magnetic field.*

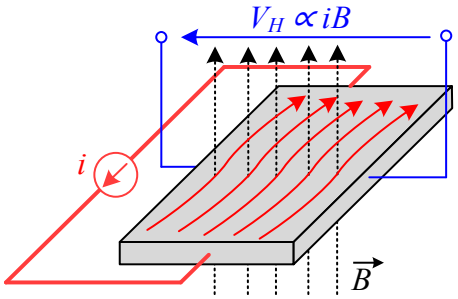

Figure 3.2.10 *Hall effect principle, magnetic field present.*

The output connections are perpendicular to the direction of current. When no magnetic field is present, Fig. 3.2.10, current distribution is uniform and the potential difference across the output is not observed. When a perpendicular magnetic field is present, as shown in Fig. 3.2.11, a Lorentz force is exerted on the current. This force disturbs the current distribution, resulting in a potential difference (voltage) across the output. This voltage is the Hall voltage V_H.

Hall effect sensors can be applied in many types of sensing devices. If the quantity (parameter) to be sensed incorporates or can incorporate a magnetic field, a Hall sensor will perform the task. The Hall voltage is proportional to the vector cross product of the current i and the flux density B.

The Hall voltage is a low-level signal on the order of $V_H = 30\ \mu V$ in the presence of a flux density $B = 100 \mu T$. This low-level output requires an amplifier with low noise, high input impedance and moderate gain. A differential amplifier is used to amplify the Hall voltage in order to make the output usable for most applications. In order to manage both positive and negative flux densities without requiring two power supplies, the amplifier is biased positively. The Hall voltage is also proportional to the input current, so a regulator is needed to maintain this current constant and maintain the output voltage only proportional to the external magnetic field. A basic analog sensor is shown in Fig. 3.2.12.

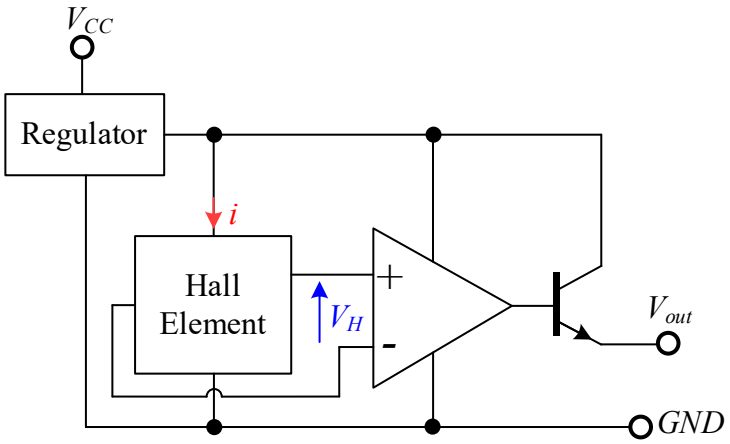

Figure 3.2.11 *Analog output Hall-effect sensor with internal regulator.*

Digital or binary output Hall-effect sensors have an output that is just one of two states: ON or OFF. An example of a binary Hall sensor configuration is shown in Fig. 3.2.13, where a Schmidt trigger compares the output of the differential amplifier to a set reference voltage in order to produce the binary output: when the amplifier output is greater than the reference, the trigger turns on, on the contrary it turns off. Furthermore, most general purpose digital Hall-effect ICs have an internal regulator. Hysteresis, of the Schmidt trigger, is used to avoid false triggering caused by noise in the input. As any digital circuit, the binary Hall-effect sensor has a large immunity to noise. The trade off is quite heavy and consists in having a 1 bit resolution, as the name “binary” implies.

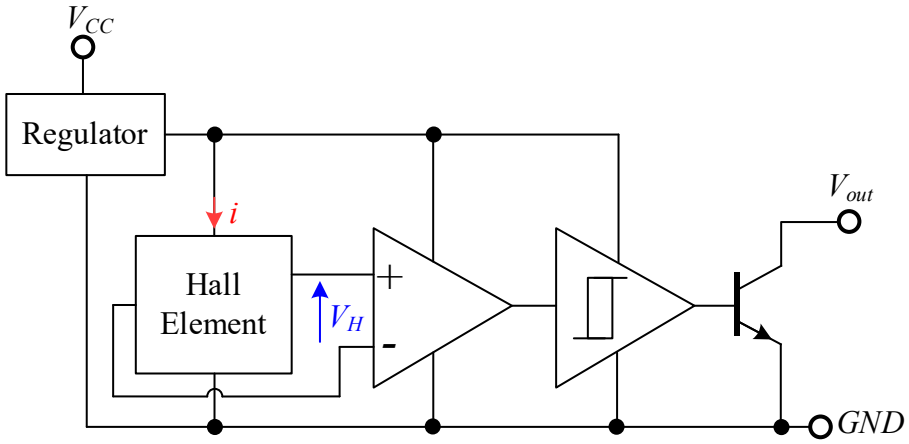

Figure 3.2.12 *Binary output Hall-effect sensor.*

Position encoders can be obtained by using Hall-effect sensors. A typical example of a binary sensor position encoder for a PM machine is shown in Fig. 3.2.14. This low resolution encoder is classically used to provide commutation for BLDC drives.

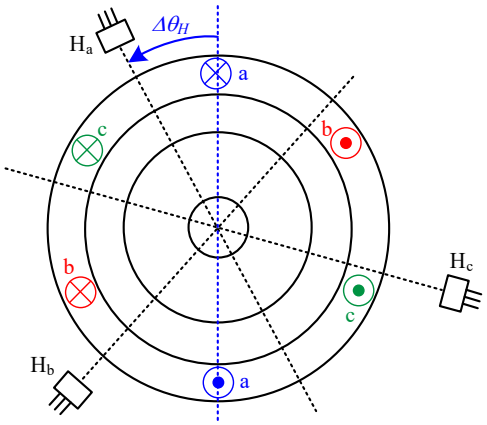

Figure 3.2.13 *Binary Hall-effect sensor shaft position encoder.*

Three sensors are placed around the periphery of the stator, 120° electrical degrees from each other, so that an encoder with a resolution equal to 6 is achieved. The sensors are typically glued onto the stator with epoxy resin or mounted on external supports. In general, the position encoder will be displaced by an angle $\Delta\theta_H$ with respect to the a-axis reference; this angle must be compensated for in the control software. The accuracy of this encoder is dependent on many factors: the way the sensors are mounted, the type of PM machine that is being used, the number of pole pairs, the type of magnets etc. For example, it is more difficult to space sensors correctly on slotless machines than it is on slotted machines because there are no teeth that can help as an angular reference. Another difficulty arises in high pole number machines because the mechanical angle at which the sensors must be spaced decreases proportionally to the number of pole pairs. Even if the sensors are correctly spaced there is no guarantee on the accuracy of the measurements: variations in magnet flux levels between adjacent magnets or due to temperature effects or variations in hysteresis levels between sensors will decrease the accuracy of the encoder. In addition, the armature reaction can be strong enough to cause an error in the measurement that is dependent on the current density that is circulating in the stator windings.

3.2.4 Capacitive Encoders

A capacitive encoder uses the change in capacitance value of a capacitor as a means to measure displacement [7]. Typically, the capacitive sensor's principal elements are arranged so that the capacitance changes as a moving elements displace relative to the stationary plates of the capacitor. Capacitive encoders is a relatively new introduction, there are only a handful of vendors for capacitive encoders, but their suitability for applications requiring high precision and durability make them a good choice.

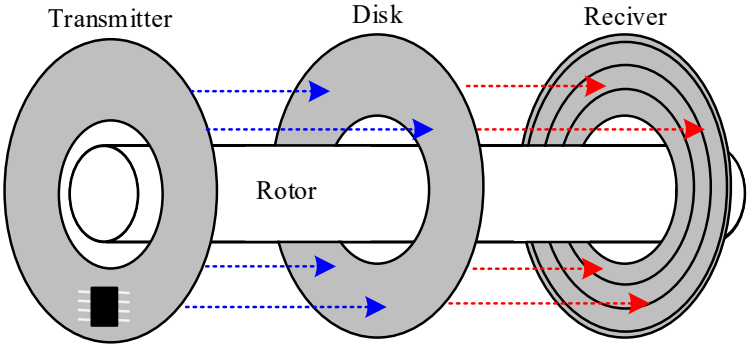

Figure 3.2.14 *Capacitive Encoder.*

Capacitive encoders work by transmitting a high-frequency signal through a rotor that is etched with a sinusoidal pattern [8]. As the rotor moves, this pattern modulates the signal in a predictable way. The receiver reads the modulations, and on-board electronics translate them into increments of rotary motion.

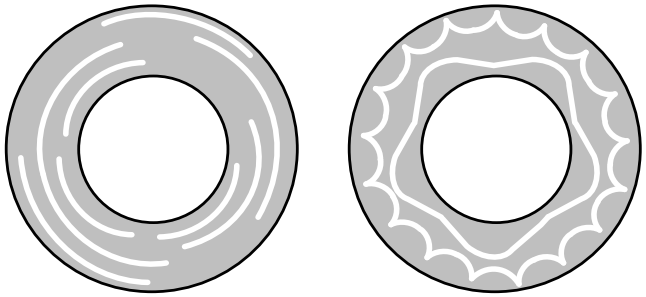

Figure 3.2.15 *Optical and Capacitive discs.*

Optical encoders cannot work in harsh environments like those with dust, moisture, frequent mechanical vibrations, and high temperature, because the optical disc inside the encoder is easily affected and damaged by ambient factors [9]. Furthermore, optical encoders have only a light beam focused at a certain point on optical disc, instead the whole area of a capacitive encoder board contributes to the output signal. This makes capacitive versions more robust, less susceptible to contamination and less influenced by temperature variations than optical encoders are. And with no LED to burn out, capacitive encoders can achieve a much longer life than optical versions. They are also more efficient, with current consumption typically less than *10 mA* as compared to the *20 mA* or higher consumption of an optical encoder.

3.2.5 Magnetic Encoders

Magnetic encoders are inherently rugged and operate reliably under shock and vibration and high temperature. Magnetic pollution can degrade rotary magnetic encoder performance, but other contaminants do not. Therefore, rotary magnetic encoders are often used instead of optical encoders [10]. Passive variable reluctance or magnetized strips on a rotating code rotor, wheel, or band are sensed by either a Hall-effect or magnetoresistive sensor. Motor speed and position accuracy dictate which of the two is better suited for an application.

Among magnetic encoders we can distinguish several technologies which are using this principle to convert magnetic field into a physical quantity useful in electronic devices (typically current or tension). The most common are inductive encoder, magneto-resistive encoder and Hall effect encoder [11].

Based on the geometrical aspect of the magnetic encoder, it is possible to distinguish two kinds of encoders:

1. On-axis encoders: an encoder that is located on the rotation axis of a generic rotor.
2. Off-axis encoder: an encoder that is located outside of the rotation axis of the rotor.

When the motor shaft rotates, the magnetic field created by the ring magnet rotates. A Hall element placed next to the ring magnet receives a magnetic field whose strength and direction change simultaneously [12]. The Hall element detects this change in magnetic field distribution and converts it into an electrical signal. The Hall element is a magnetic sensor that can only detect the strength of a magnetic field in a single direction. Therefore, in order to detect the rotational position, Hall elements are required to detect the magnetic

field strengths of the X-axis component (Bx) and the Y-axis component (By) of the rotating surface.

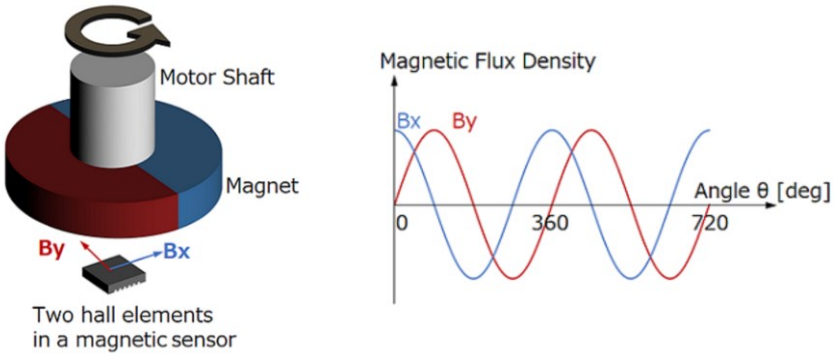

Figure 3.2.16 *On axis configuration magnetic encoder and magnetic flux density strength detected by Hall element [12].*

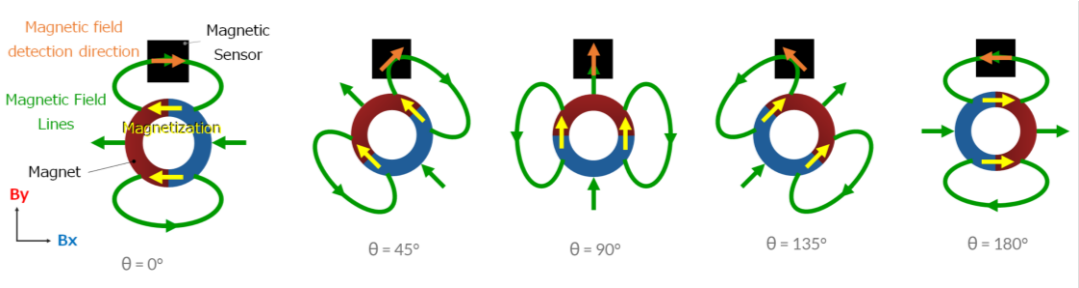

Figure 3.2.17 *Magnetic density field input to Hall element in Off-Axis configuration [12].*

3.3 Mathematical Formulations of the Quantized Rotor Position and Angular Speed

Recently, particular interest has arisen for low-cost position sensors. For example, magneto-resistive and linear Hall-effect sensors have been investigated in [13]-[16]. The main concern of these technologies is their limited accuracy and ways to improve it have been proposed in [15]. Other contributions have focused on low-resolution binary Hall-effect sensors, [17]-[22]. In these contributions the main concern is the quantization noise present in the measurement and ways to reduce it have been investigated.

Although it is known that as the sensor resolution decreases speed estimation deteriorates, [23]-[24], a complete understanding of the effects of position sensor resolution in VSDs has yet to be obtained. One fundamental, yet open issue is: how does a specific sensor resolution impact the performance of the drive under periodic torque disturbances? Such knowledge would be of great help to an engineer when selecting the resolution of the position sensor, in order to minimize the cost and achieve the required disturbance rejection at the same time. Some studies have analyzed the torque ripple induced by the resolution of the rotor position sensor, [25]-[28]. However, the main limitation in these papers is that the effect of finite resolution is modeled as an error in the rotor position measurement; this approach doesn't allow to distinguish accuracy from resolution and therefore gives limited insight into the effects of resolution alone. Conversely, a much more insightful way to model resolution is via spatial Fourier analysis of the rotor position space vector, [17] and [29]. Although it is known that these so-called spatial quantization harmonics generate ripple in the speed estimation, no direct theoretical connection has ever been derived.

These contribution intends to complete the spatial Fourier approach by deriving the missing link between the spatial quantization harmonics in the measured rotor position and the time harmonic ripple in the estimated speed. It is shown that this link resides in a new concept, i.e. the instantaneous quantized speed, which constitutes the effective input to any speed estimation algorithm. Time harmonic expressions for both quantized position and instantaneous quantized speed that are valid under periodic torque disturbances are also derived. Numerically verified analytic expressions are provided for a well-known observer structure to quantify its filtering action on the instantaneous quantized speed.

The measured, spatially quantized rotor electrical angle $\theta_{re}^{(q)}$ can be interpreted as a quasi-rotating space vector $\boldsymbol{\Theta}_{\alpha\beta}^{(q)}(\theta_{re})$ in the stationary reference plane, where θ_{re} is the instantaneous rotor electrical angle. Its locus corresponds to the vertices of a regular polygon with N_{DS} sides. As an example, Fig. 3.3.1 depicts the $\boldsymbol{\Theta}_{\alpha\beta}^{(q)}(\theta_{re})$ loci for two different resolutions.

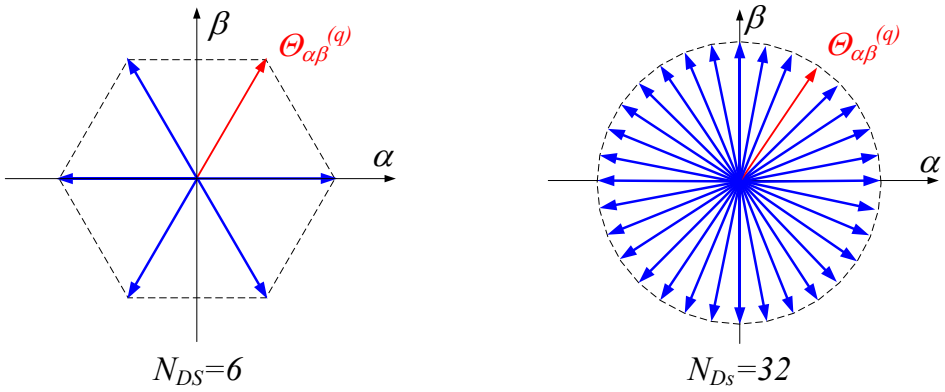

Figure 3.3.1 *$\boldsymbol{\Theta}_{\alpha\beta}^{(q)}(\theta_{re})$ loci for N_{DS} = 6 and N_{DS} = 32.*

Such a spatial representation is valid for any N_{DS} and its analytical formulation, in terms of a spatial Fourier series, was derived in [29] and is reported in (3.3.1), where θ_{re} is the instantaneous rotor position. In addition to the fundamental space vector, which would be the only vector present for an infinitely high resolution, there are positively and negatively rotating quantization harmonic vectors produced by the finite resolution of the position sensor interface. The harmonic order and amplitude of these vectors both depend on N_{DS}.

$$\boldsymbol{\Theta}_{\alpha\beta}^{(q)}(\theta_{re}) = e^{j\left(\theta_{re}-\frac{\pi}{N_{DS}}\right)} + \sum_{k=1}^{+\infty}\left[-\frac{1}{N_{DS}k-1}e^{-j\left((N_{DS}k-1)\theta_{re}+\frac{\pi}{N_{DS}}\right)} + \frac{1}{N_{DS}k+1}e^{j\left((N_{DS}k+1)\theta_{re}-\frac{\pi}{N_{DS}}\right)}\right] \quad (3.3.1)$$

3.3.1 Formulations Under Constant Speed

In general, any temporal formulation of (3.3.1) is obtained by specifying how θ_{re} depends on time. The simplest case is for a constant electrical angular frequency $\omega_{re0}=2\pi f_{re0}$, i.e. a constant speed of rotation. The mathematical formulation of $\boldsymbol{\Theta}_{\alpha\beta}^{(q)}(t)$ in this case is given by (3.3.2), by substituting $\theta_{re}=\omega_{re0}t$.

$$\boldsymbol{\Theta}_{\alpha\beta}^{(q)}(t) = e^{j\left(\omega_{re0}t-\frac{\pi}{N_{DS}}\right)} + \sum_{k=1}^{+\infty}\left[-\frac{1}{N_{DS}k-1}e^{-j\left((N_{DS}k-1)\omega_{re0}t+\frac{\pi}{N_{DS}}\right)} + \frac{1}{N_{DS}k+1}e^{j\left((N_{DS}k+1)\omega_{re0}t-\frac{\pi}{N_{DS}}\right)}\right] \quad (3.3.2)$$

Though straightforward, this models an ideal scenario since it implies the absence of any torque disturbance on the shaft.

Fig. 2 shows the harmonic spectrum of $\boldsymbol{\Theta_{\alpha\beta}}^{(q)}(t)$ for $N_{DS} = 6$ and $\omega_{re0} = 2\pi 10$ rad/s. The only physically meaningful harmonic containing the sought-after position information is the fundamental, shown in red. All the other harmonics are an undesired effect of the finite resolution of the position sensor interface. In Fig. 3.3.2 the first order quantization harmonic vectors ($k = 1$) are the negatively rotating fifth and positively rotating seventh. Each harmonic vector is separated by N_{DS} times the fundamental frequency, i.e. six times in this case.

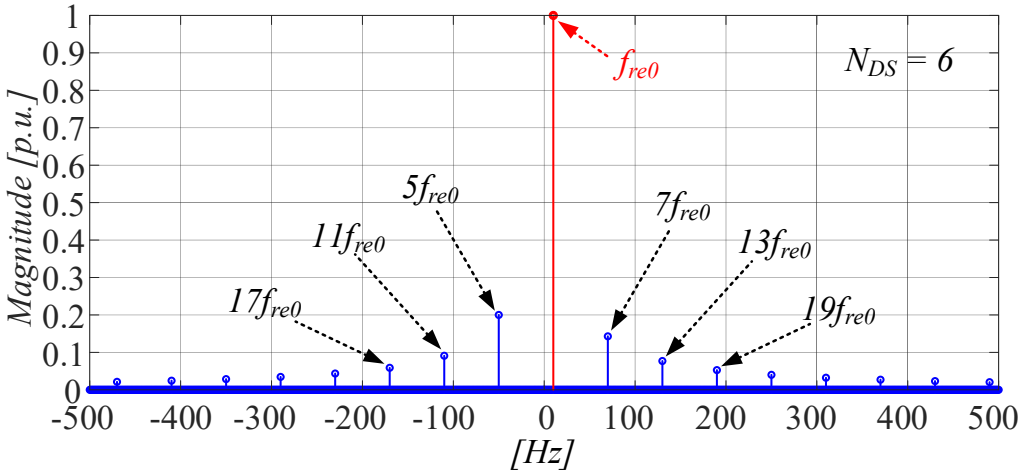

Figure 3.3.2 *Harmonic spectra of* $\boldsymbol{\Theta_{\alpha\beta}}^{(q)}$ *for* $\omega re0 = 2\pi 5$ *rad/s and* $N_{DS} = 6$.

As an alternative to the space vector formulation, the quantized electrical rotor angle $\theta_{re}{}^{(q)}(t)$, i.e. the phase angle of $\boldsymbol{\Theta_{\alpha\beta}}^{(q)}(t)$, is equal to:

$$\theta_{re}{}^{(q)}(t) = \omega_{re0}t + \sum_{k=1}^{+\infty} \frac{2}{N_{DS}\,k} \sin(N_{DS}k\omega_{re0}t) \tag{3.3.3}$$

It should be noted that (3.3.3) is not a Fourier series representation of $\theta_{re}{}^{(q)}$ since the term $\omega_{re0}t$ is not periodic, [30].

While the rotor rotates continuously at a constant speed, $\boldsymbol{\Theta_{\alpha\beta}}^{(q)}$ rotates discontinuously around its locus in the complex plane, like the ticking of a clock hand. Its speed, henceforth named instantaneous quantized speed $\omega_{re}{}^{(q)}(t)$, is defined as the time derivative of $\theta_{re}{}^{(q)}(t)$:

$$\omega_{re}{}^{(q)}(t) = \frac{d\theta_{re}{}^{(q)}(t)}{dt} \tag{3.3.4}$$

$\omega_{re}{}^{(q)}(t)$ is highly discontinuous and jumps between zero and infinity at each variation in the position measurement. For the case of constant speed of rotation, $\omega_{re}{}^{(q)}(t)$ is obtained by differentiating (3.3.3):

$$\omega_{re}{}^{(q)}(t) = \omega_{re0} + \sum_{k=1}^{+\infty} 2\omega_{re0} \cos(N_{DS}k\omega_{re0}t) \tag{3.3.5}$$

The above is a Fourier series, indicating that $\omega_{re}{}^{(q)}(t)$ is a periodic waveform in these operating conditions. An example, a reconstructed $\omega_{re}{}^{(q)}(t)$ waveform with $k_{max} = 100$ is shown in Fig. 3.3.3a, for the same resolution and operating conditions of Fig. 3.3.2; ω_{re0} is also shown as a dashed line. As expected, $\omega_{re}{}^{(q)}(t)$ features significant impulses every

time the position measurement changes. Fig. 3.3.3b shows its harmonic spectrum, which has an infinite number of equally spaced quantization harmonics at $kN_{DS}\omega_{re0}$, with amplitude $2\omega_{re0}$; the only physically meaningful harmonic, i.e. the dc component, is shown in red.

Due to the speed dependent nature of the harmonic frequencies, the quantization harmonics are spaced further apart from each other as speed increases.

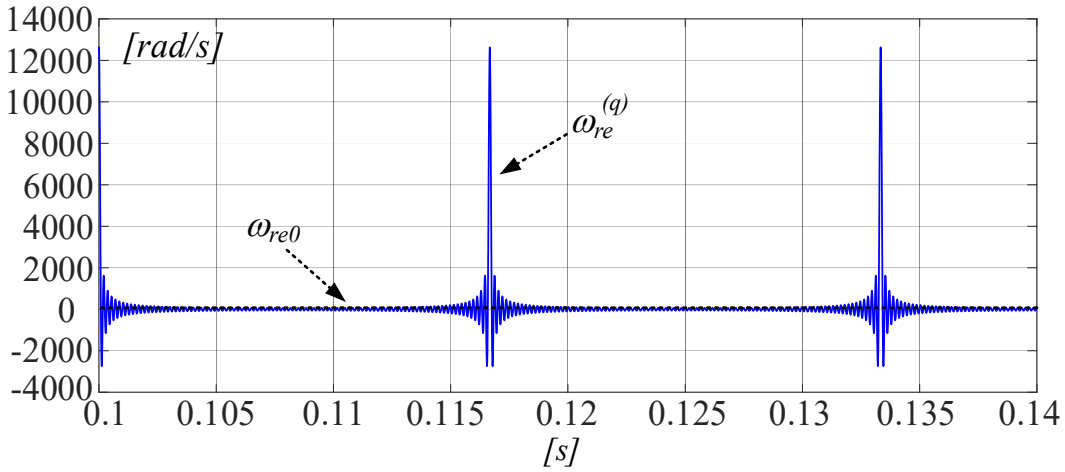

(a)

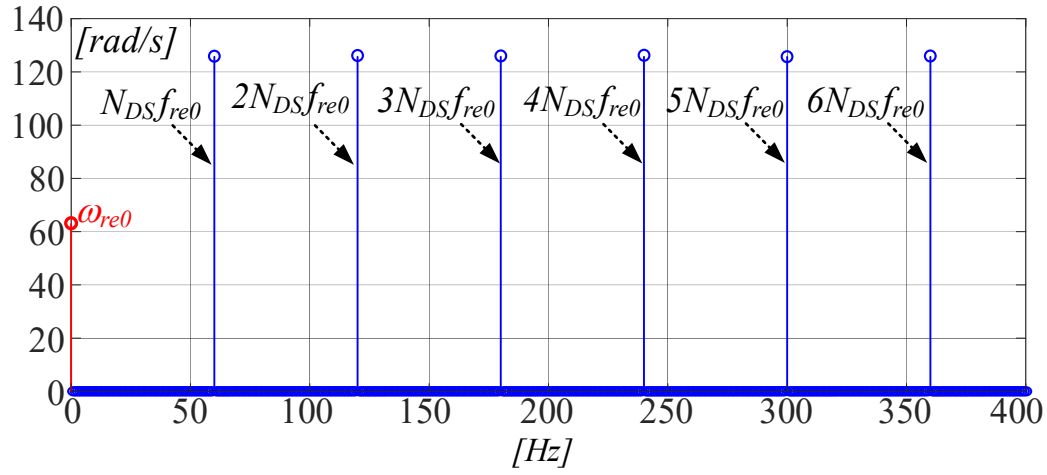

(b)

Figure 3.3.3 *Instantaneous quantized speed $\omega_{re}^{(q)}$ for $N_{DS} = 6$ and $\omega_{re0} = 2\pi 10$ rad/s. (a) reconstructed waveform for $k_{max} = 100$. (b) corresponding harmonic spectrum.*

3.3.2 Formulations Under Single Sinusoidal Disturbance

So as to model a more realistic condition, it is now assumed that a single sinusoidal torque disturbance T_d acts on the shaft, while it is spinning at an average speed corresponding to an electrical angular frequency ω_{re0}. In this case, the instantaneous electrical speed includes a co-sinusoidal oscillation with an amplitude $\Delta\omega_{re}$, a frequency $\omega_d=2\pi f_d$, and a phase φ_d:

$$\omega_{re}(t) = \omega_{re0} + \Delta\omega_{re}\cos(\omega_d t+\varphi_d) \tag{3.3.6}$$

Its integral provides the instantaneous rotor position:

$$\theta_{re}(t) = \int_0^t \omega_{re}(\lambda)d\lambda = \omega_{re0}t + \frac{\Delta\omega_{re}}{\omega_d}\sin(\omega_d t+\varphi_d) \tag{3.3.7}$$

By substituting (3.3.7) into (3.3.1), a novel expression for $\boldsymbol{\Theta_{\alpha\beta}}^{(q)}(t)$ is obtained, (3.3.8), in which a sinusoidal term is present in the phase angle of each harmonic space vector: $\boldsymbol{\Theta_{\alpha\beta}}^{(q)}$ undergoes a process of phase modulation for each harmonic space vector, just like in the renowned telecommunications technique, [31]. Applying the Jacobi-Anger expansion to each harmonic space vector in (3.3.8) leads to the Fourier series in (3.3.9), where J_n is the n-th order Bessel function of the first kind and its argument $(N_{DS}k\pm1)\Delta\omega_{re}/\omega_d$ is the k-th order modulation index.

$$\boldsymbol{\Theta_{\alpha\beta}}^{(q)}(t) = e^{j\left(\omega_{re0}t+\frac{\Delta\omega_{re}}{\omega_d}\sin(\omega_d t+\varphi_d)-\frac{\pi}{N_{DS}}\right)} + \sum_{k=1}^{+\infty}\left[-\frac{1}{N_{DS}k-1}e^{-j\left((N_{DS}k-1)\left(\omega_{re0}t+\frac{\Delta\omega_{re}}{\omega_d}\sin(\omega_d t+\varphi_d)\right)+\frac{\pi}{N_{DS}}\right)}\right. \tag{3.3.8}$$
$$\left. + \frac{1}{N_{DS}k+1}e^{j\left((N_{DS}k+1)\left(\omega_{re0}t+\frac{\Delta\omega_{re}}{\omega_d}\sin(\omega_d t+\varphi_d)\right)-\frac{\pi}{N_{DS}}\right)}\right]$$

$$\boldsymbol{\Theta_{\alpha\beta}}^{(q)}(t) = \sum_{n=-\infty}^{+\infty} J_n\left(\frac{\Delta\omega_{re}}{\omega_d}\right)e^{j\left[(\omega_{re0}+n\omega_d)t-\frac{\pi}{N_{DS}}+n\varphi_d\right]} + \sum_{k=1}^{+\infty}\left\{-\frac{1}{N_{DS}k-1}\sum_{n=-\infty}^{+\infty} J_n\left((N_{DS}k-1)\frac{\Delta\omega_{re}}{\omega_d}\right)\right. \tag{3.3.9}$$
$$\left. e^{-j\left\{[(N_{DS}k-1)\omega_{re0}+n\omega_d]t+\frac{\pi}{N_{DS}}+n\varphi_d\right\}} + \frac{1}{N_{DS}k+1}\sum_{n=-\infty}^{+\infty} J_n\left((N_{DS}k+1)\frac{\Delta\omega_{re}}{\omega_d}\right)e^{j\left\{[(N_{DS}k+1)\omega_{re0}+n\omega_d]t-\frac{\pi}{N_{DS}}+n\varphi_d\right\}}\right\}$$

To gain more insight into this phenomenon, Fig. 3.3.4 shows the harmonic spectrum of $\boldsymbol{\Theta_{\alpha\beta}}^{(q)}$ for N_{DS} = 6, assuming that the rotor is rotating at $\omega_{re0} = 2\pi 10$ rad/s and is subjected to a single sinusoidal torque disturbance at f_d = 11 Hz, which induces a speed oscillation with amplitude $\Delta\omega_{re} = 2\pi$ rad/s.

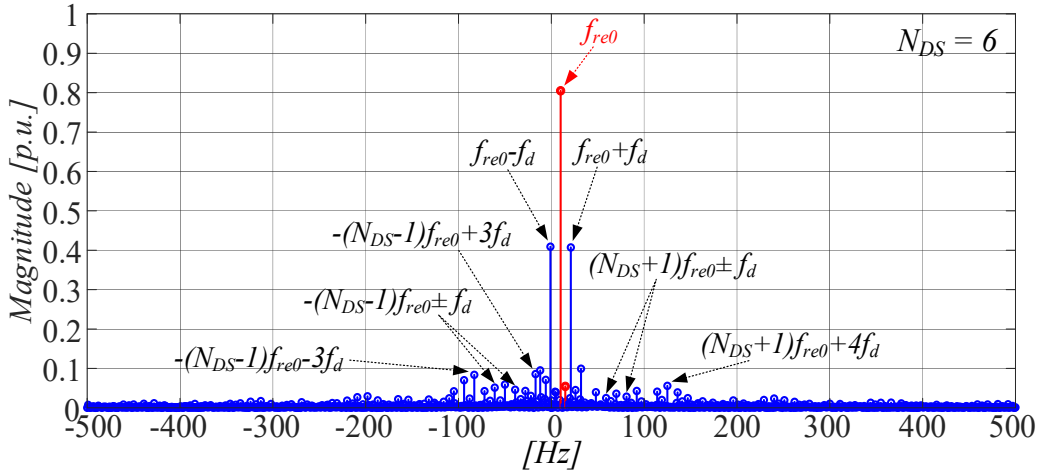

Figure 3.3.4 *Harmonic spectrum of $\boldsymbol{\Theta_{\alpha\beta}}^{(q)}$ for $\omega_{re0} = 2\pi 10$ rad/s, $\Delta\omega_{re} = 2\pi$ rad/s, $\varphi_d = 0$ rad and $\omega_d = 2\pi 11$ rad/s. (a) $N_{DS} = 6$.*

Compared to Fig. 3.3.1, additional harmonics are visible at $f_{re0} \pm f_d$, $-(N_{DS}\text{-}1)\, f_{re0} \pm f_d$, $(N_{DS}+1)\, f_{re0} \pm f_d$, etc. All of these can be explained by a term-by-term examination of (3.3.9), as done in the following.

The Jacobi-Anger expansion of the fundamental space vector produces an infinite number of harmonics at frequencies $f_{re0}+nf_d$, with n varying in the range $\{-\infty, +\infty\}$. Each harmonic has an amplitude J_n, which depends on the order n of the Bessel function and

on $\Delta\omega_{re}/\omega_d$, i.e. the modulation index for $k = 0$. In the event of a torque disturbance with a small amplitude and/or a high frequency, $\Delta\omega_{re}/\omega_d << 1$, the only significant harmonics produced by the modulation of the fundamental space vector are at f_{re0} and at $f_{re0} \pm f_d$, with amplitudes $J_0(\Delta\omega_{re}/\omega_d)$ and $J_1(\Delta\omega_{re}/\omega_d)$, respectively. This effect is known as narrow-band modulation. The modulation index for $k = 0$ is equal to 0.0833 for the spectrum in Fig. 3, confirming narrow-band modulation; this explains the presence of harmonics at f_{re0} and at $f_{re0} \pm f_d$ in both spectra. Conversely, whenever $\Delta\omega_{re}/\omega_d >> 1$, i.e. in the event of a torque disturbance with a large amplitude and/or a low frequency, upper and lower sidebands will appear around f_{re0}, giving rise to wide-band modulation. By extending this analysis to the higher order space vectors, narrow-band and wide-band modulation will occur depending on whether the respective modulation indices, $(kN_{DS}\pm1)\Delta\omega_{re}/\omega_d$, are much smaller or much greater than unity. In Fig. 3.3.4, the two modulation indices for $k = 1$ are still small, thereby explaining the presence of harmonics at $-(N_{DS}-1)\, f_{re0} \pm f_d$ and at $(N_{DS}+1)\, f_{re0} \pm f_d$. For higher order harmonic space vectors, the modulation becomes wide-band and the harmonics spread out.

For the same operating conditions, the scalar form of the quantized electrical rotor angle is given in (3.3.10) and its Bessel function equivalent representation is provided in (3.3.11). The resulting $\omega_{re}^{(q)}(t)$ is reported in (3.3.12) and is obtained by differentiating (3.3.11) with respect to time.

$$\theta_{re}^{(q)}(t) = \omega_{re0}t + \frac{\Delta\omega_{re}}{\omega_d}\sin(\omega_d t+\varphi_d) + \sum_{k=1}^{+\infty}\frac{2}{N_{DS}k}\sin\left(N_{DS}k\left(\omega_{re0}t + \frac{\Delta\omega_{re}}{\omega_d}\sin(\omega_d t+\varphi_d)\right)\right) \tag{3.3.10}$$

$$\theta_{re}^{(q)}(t) = \omega_{re0}t + \frac{\Delta\omega_{re}}{\omega_d}\sin(\omega_d t+\varphi_d) + \sum_{k=1}^{+\infty}\frac{2}{N_{DS}k}\sum_{n=-\infty}^{+\infty}J_n\left(\frac{N_{DS}k\Delta\omega_{re}}{\omega_d}\right)\sin((N_{DS}k\omega_{re0}+n\omega_d)t+n\varphi_d) \tag{3.3.11}$$

$$\omega_{re}^{(q)}(t) = \omega_{re0} + \Delta\omega_{re}\cos(\omega_d t+\varphi_d) + \sum_{k=1}^{+\infty}\frac{2}{N_{DS}k}\sum_{n=-\infty}^{+\infty}J_n\left(\frac{N_{DS}k\Delta\omega_{re}}{\omega_d}\right)(N_{DS}k\omega_{re0}+n\omega_d)\cos((N_{DS}k\omega_{re0}+n\omega_d)t+n\varphi_d) \tag{3.3.12}$$

Fig. 3.3.5 shows the spectrum of $\omega_{re}^{(q)}$. Compared to the case of constant speed, a significant number of additional harmonics appear, featuring amplitudes comparable to the average speed ω_{re0}. For instance, significant harmonics are now found at frequencies $N_{DS}f_{re0}-f_d$ and $N_{DS}f_{re0}+f_d$. In such a case it would be practically impossible to estimate the actual speed alone, i.e. the red harmonics, without introducing a non-negligible amount of quantization harmonics into the estimate.

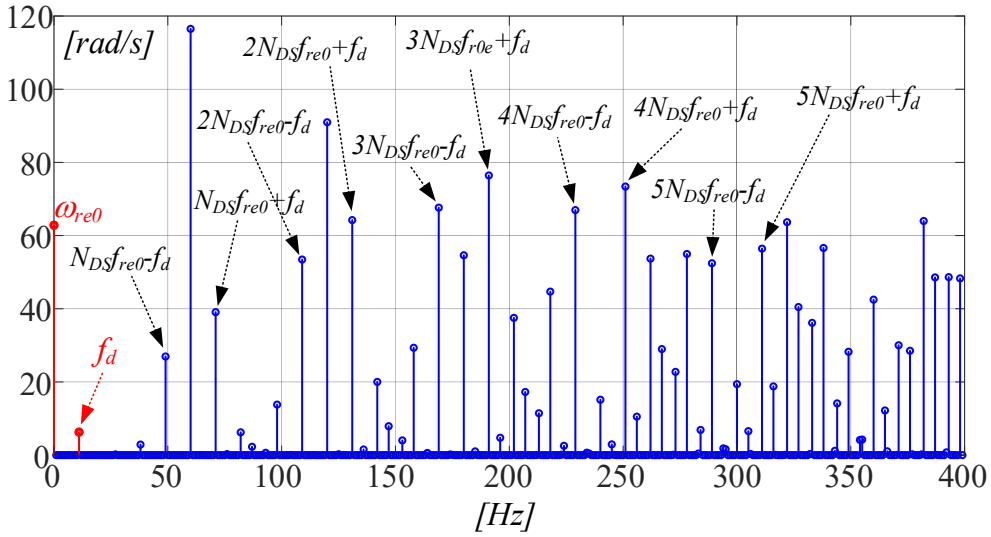

Figure 3.3.5 *Harmonic spectrum of $\omega_{re}^{(q)}$, using $k_{max} = 100$ and $n_{max} = 28$, for $\omega_{re0} = 2\pi 10$ rad/s, $\Delta\omega_{el} = 2\pi$ rad/s, $f_d = 11$ Hz, $\varphi_d = 0$ rad and $N_{DS} = 6$*

Resolution plays a key role in the spectral distribution of $\omega_{re}^{(q)}$: by increasing N_{DS}, all the quantization harmonics move to higher frequencies, facilitating their filtering by means of a speed estimation algorithm. This is confirmed in the harmonic spectra of $\omega_{re}^{(q)}$ shown in Fig. 3.3.6, which have been calculated for values of N_{DS} ranging from 32 to 1024, under the same torque disturbance as in Fig. 3.3.5. Carson's rule, [32], can be used to predict the approximate bandwidth occupied by each harmonic sideband, BW_k:

$$BW_k \approx 2f_d\left(\frac{N_{DS}k\Delta\omega_{el}}{\omega_d}+1\right) \tag{3.3.13}$$

Applying (3.3.13) for $k = 1$ gives $B_{W1} = 86$ Hz for the bandwidth of the sideband shown in Fig. 3.3.6a, $B_{W1} = 534$ Hz for Fig. 3.3.6b and $B_{W1} = 2070$ Hz for Fig. 3.3.6c. Good agreement between the predicted and actual bandwidths can be observed.

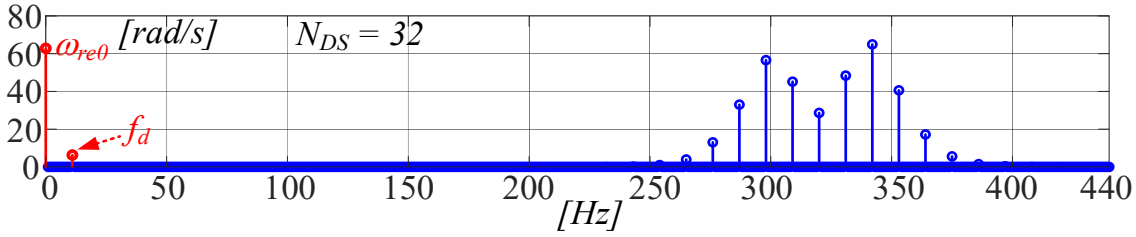

(a)

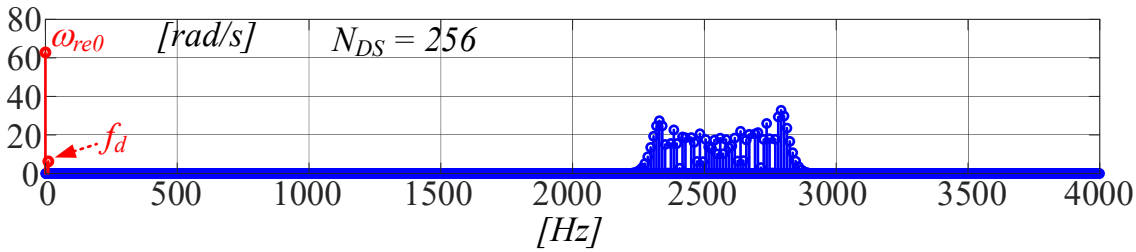

(b)

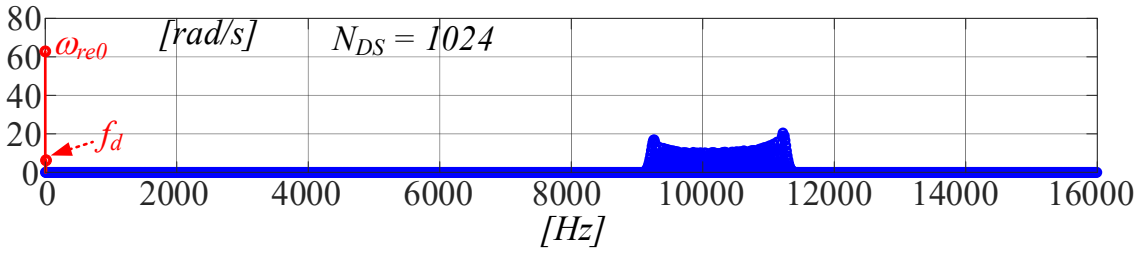

(c)

Figure 3.3.6 *Harmonic spectra of $\omega_{re}^{(q)}$, for $\omega_{re0} = 2\pi 10$ rad/s, $\Delta\omega_{re} = 2\pi$ rad/s, $f_d = 11$ Hz, $\varphi_d = 0$ rad. (a) $N_{DS} = 32$. (b) $N_{DS} = 256$. (c) $N_{DS} = 1024$.*

3.3.3 Formulations Under Periodic Disturbance

The previous case can be extended to the case of a generic periodic torque disturbance composed of h harmonic components. Analytical expressions for $\Theta_{\alpha\beta}^{(q)}(t)$ and $\omega_{re}^{(q)}(t)$ are obtained by following the same procedure as above, i.e. by integrating the instantaneous electrical frequency $\omega_{re}(t)$ to obtain $\theta_{re}(t)$. Substitution of the resulting $\theta_{re}(t)$ into (3.3.1) and application of Jacobi-Anger expansions leads to (3.3.14). Differentiating (3.3.14) with respect to time results in the expression for $\omega_{re}^{(q)}(t)$ shown in (3.3.15).

$$\Theta_{\alpha\beta}^{(q)} = \sum_{n_1=-\infty}^{+\infty} J_{n1}\left(\frac{\Delta\omega_{re1}}{\omega_{d1}}\right)\cdots\sum_{n_h=-\infty}^{+\infty} J_{nh}\left(\frac{\Delta\omega_{reh}}{\omega_{dh}}\right) e^{j\left[\left(\omega_{re0}+\sum_{i=1}^{h} n_i\omega_{di}\right)t+\sum_{i=1}^{h} n_i\varphi_{di}-\frac{\pi}{N_{DS}}\right]}+$$

$$+\sum_{k=1}^{+\infty}\left\{\frac{1}{N_{DS}k-1}\sum_{n_1=-\infty}^{+\infty} J_{n1}\left((N_{DS}k-1)\frac{\Delta\omega_{re1}}{\omega_{d1}}\right)\cdots\sum_{n_h=-\infty}^{+\infty} J_{nh}\left((N_{DS}k-1)\frac{\Delta\omega_{reh}}{\omega_{dh}}\right) e^{-j\left\{\left[(N_{DS}k-1)\omega_{re0}+\sum_{i=1}^{h} n_i\omega_{di}\right]t+\sum_{i=1}^{h} n_i\varphi_{di}+\frac{\pi}{N_{DS}}\right\}}\right.$$

$$\left.+\frac{1}{N_{DS}k+1}\sum_{n_1=-\infty}^{+\infty} J_{n1}\left((N_{DS}k+1)\frac{\Delta\omega_{re1}}{\omega_{d1}}\right)\cdots\sum_{n_h=-\infty}^{+\infty} J_{nh}\left((N_{DS}k+1)\frac{\Delta\omega_{reh}}{\omega_{dh}}\right) e^{j\left\{\left[(N_{DS}k+1)\omega_{re0}+\sum_{i=1}^{h} n_i\omega_{di}\right]t+\sum_{i=1}^{h} n_i\varphi_{di}-\frac{\pi}{N_{DS}}\right\}}\right\} \quad (3.3.14)$$

$$\omega_{re}^{(q)}(t) = \omega_{re0} + \sum_{i=1}^{h}\Delta\omega_{rei}\cos(\omega_{di}t+\varphi_{di}) + \sum_{k=1}^{+\infty}\frac{2}{N_{DS}k}\sum_{n_1=-\infty}^{+\infty} J_{n1}\left(\frac{N_{DS}k\Delta\omega_{re1}}{\omega_{d1}}\right)\cdots\sum_{n_h=-\infty}^{+\infty} J_{nh}\left(\frac{N_{DS}k\Delta\omega_{reh}}{\omega_{dh}}\right)$$
$$+\left(N_{DS}k\omega_{re0}+\sum_{i=1}^{h} n_i\omega_{di}\right)\cos\left(\left(N_{DS}k\omega_{re0}+\sum_{i=1}^{h} n_i\omega_{di}\right)t+\sum_{i=1}^{h} n_i\varphi_{di}\right) \quad (3.3.15)$$

As an example, Fig. 3.3.7 displays the harmonic spectrum of $\omega_{re}^{(q)}$ for $\omega_{re0} = 2\pi 10$ rad/s and $N_{DS} = 6$, with the shaft subjected to a periodic disturbance consisting of two harmonic components, leading to speed oscillations having $\Delta\omega_{re1} = 2\pi$ rad/s, $f_{d1} = 7$ Hz, $\varphi_{d1} = 0$ rad, and $\Delta\omega_{re2} = 2\pi$ rad/s, $f_{d2} = 12$ Hz, $\varphi_{d2} = 0$ rad. Compared to Fig.3.3.5, a significant increase in the number of harmonics is clearly visible, as result of the interaction between the two disturbance harmonics and the spatial quantization harmonics.

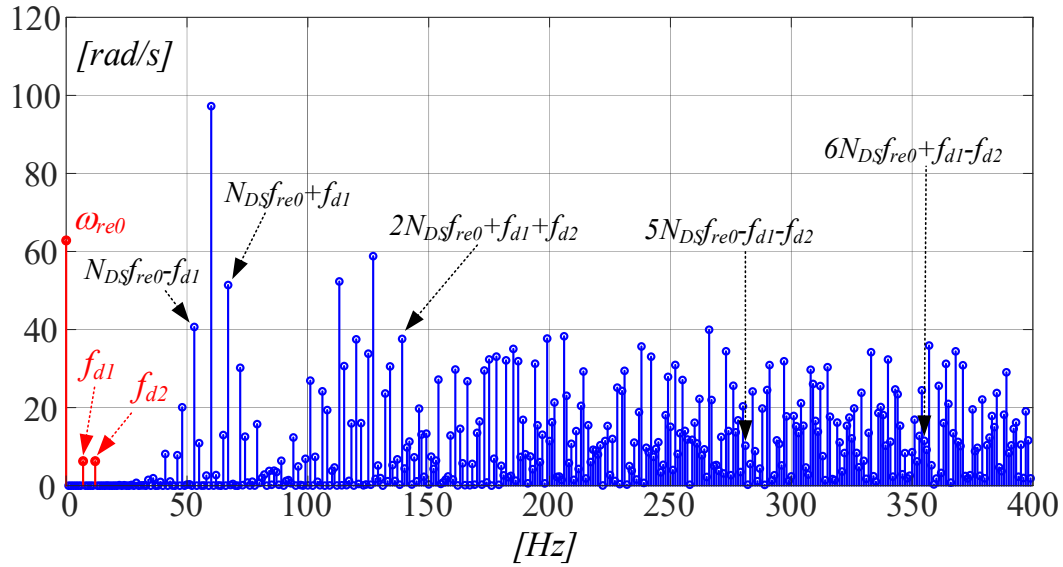

Figure 3.3.7 *Harmonic spectrum of $\omega_{re}^{(q)}$, for $\omega_{re0} = 2\pi 10$ rad/s, $\Delta\omega_{re1} = 2\pi$ rad/s, $f_{d1} = 7$ Hz, $\varphi_{d1} = 0$ rad, $\Delta\omega_{re2} = 2\pi$ rad/s, $f_{d2} = 12$ Hz, $\varphi_{d2} = 0$ rad and $N_{DS} = 6$.*

3.3.4 Extension to Non-Periodic Disturbance

As demonstrated above, analytical expressions of $\omega_{re}^{(q)}(t)$ can be obtained by differentiation of $\theta_{re}^{(q)}(t)$ with respect to time, provided that the quantized position can be expressed in closed form. When this is not possible, for example in the event of nonperiodic torque disturbances, $\omega_{re}^{(q)}(t)$ can still be calculated via numerical differentiation if $\theta_{re}^{(q)}(t)$ is available from measurement or from simulation. Fig.3.3.8 shows this for the case of two successive torque disturbance pulses which cause the rotor speed to increase and then decrease linearly. The instantaneous quantized speed is calculated using the forward Euler method:

$$\omega_{re}^{(q)}(t) \approx \frac{\theta_{re}^{(q)}[(k+1)T_s] - \theta_{re}^{(q)}[kT_s]}{T_s} \tag{3.3.16}$$

with T_s equal to the sampling period of $\theta_{re}^{(q)}(t)$.

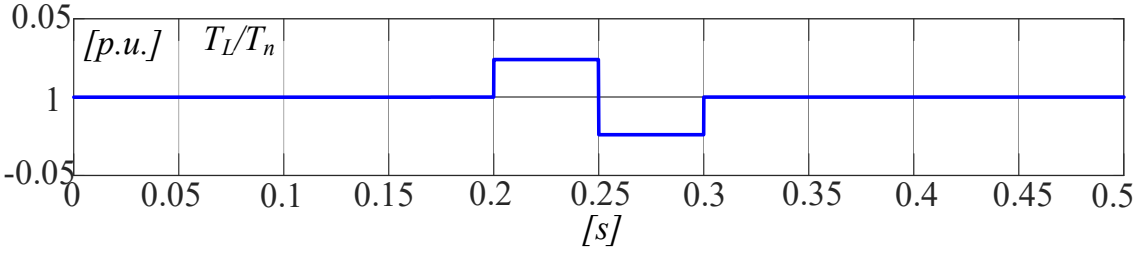

(a)

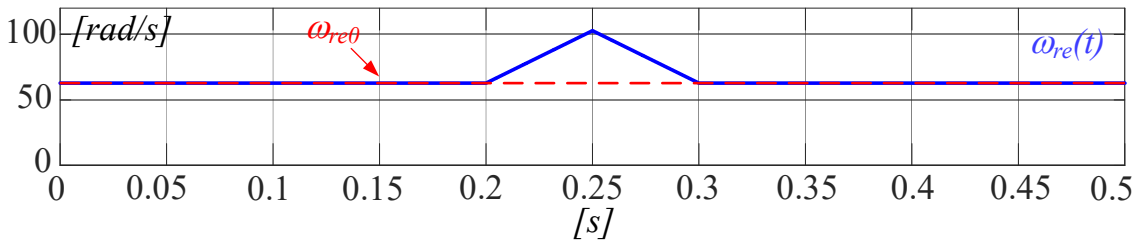

(b)

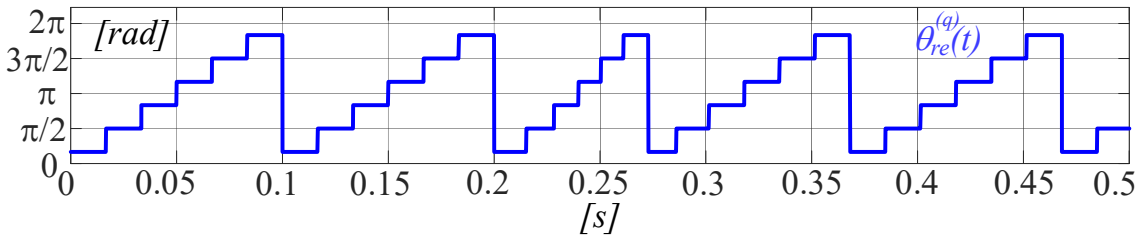

(c)

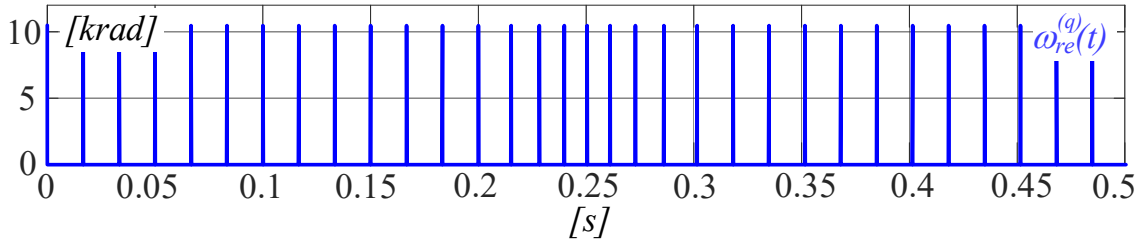

(d)

Figure 3.3.8 *$\omega_{re}(t)$, $\theta_{re}^{(q)}(t)$ and $\omega_{re}^{(q)}(t)$ for the case of a nonperiodic torque disturbance with $N_{DS} = 6$ and $T_s = 1\mu s$.*

3.4 Speed Estimation Techniques

In an electric drive, rotor position measurement is required to ensure high dynamic performances. In many applications, where the speed feedback is required, such as in VSDs (Variable Speed Drives) widespread in many industries: manufacturing industry, automotive, naval, aerospace, etc. wherever speed control is required for energy saving or for process control.

The position transducer is considered the best compromise in terms of preference and costs for speed controlled drives. The position transducer is sufficient both to realize the vector control of the electric machine and to realize the speed and position control loops.

Different techniques can be exploited to estimate the angular speed, starting from the measurement of the rotor position; the choice of one technique rather than another may depend on various factors, such as the position sensor technology, position sensor resolution, minimum and maximum speed, etc.

Regardless of the factors of choice the estimation techniques can be classified into model-based and non-model-based methods, [33].

3.5 Model Based Speed Estimation Techniques

Among the former group, which require knowledge of the mechanical model of the load, one can mention vector tracking observers and Kalman filters, [1], [34]-[35]. The main advantages of model-based methods are their performance and design flexibility. Disadvantages arise for particular applications in which the mechanical proprieties of the load are unknown. For these, it is quite common to use non-model-based methods, which don't require any additional information other than the position measurement.

3.5.1 Luenberger Observer

Knowledge of the system's state is necessary to solve several control systems problems; in the most feedback control systems is not possible to measure the system's state directly, for instance the rotor speed estimation in electric drives; or even when, although it is possible to measure the system's state the measurement errors is greater than the errors computed by system's state estimation, for instance when the rotor angular position measurement is carried out by low resolution sensors.

If the system's state estimation to be possible, it is necessary that the system must be observable. In this way it is possible to reconstruct the system's state from the system's output observation. The observer characterization depends on its convergence velocity.

In control theory, the so-called Luenberger observer, is a dynamic system that allows to estimate the state evolution of the observable system.

Typically, when the characterization depends on the convergence velocity a deterministic observer, such as Luenberger observer, is defined; when the characterization depends on the uncertainty of measurement, a non-deterministic observer, such as the Kalman filter, is defined.

Fig. 3.5.1 shows a typical control structure that uses a state observer:

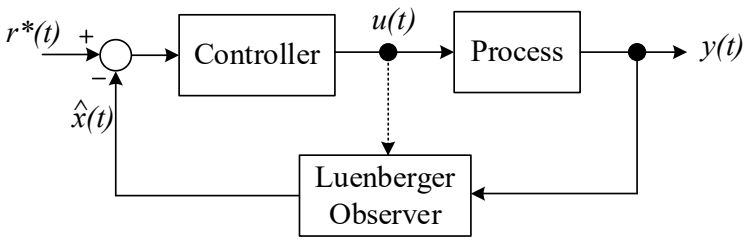

Figure 3.5.1 *Typical control system structure with an observer.*

Given a linear time invariant dynamic system (LTI), it is characterized by the following equations of state:

$$\begin{cases} \dot{x}(t) = A\,x(t) + B\,u(t) \\ y(t) = C\,x(t) + D\,u(t) \end{cases} \tag{3.5.1}$$

In Fig. 3.5.2 a general Luenberger observer structure is presented:

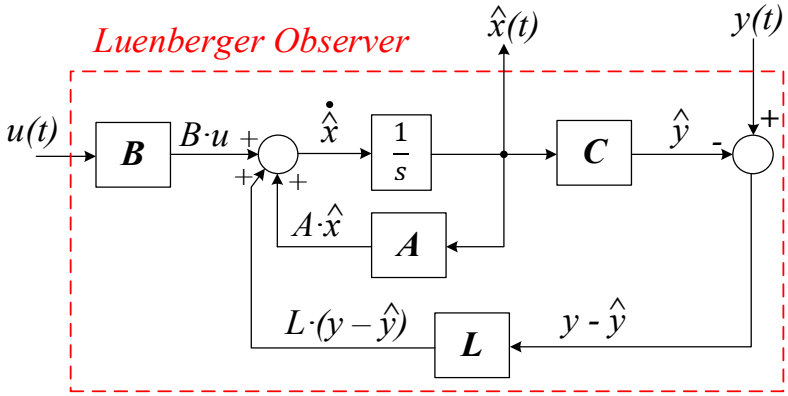

Figure 3.5.2 *Luenberger Observer: Typical Structure.*

From Fig. 3.5.2 it is possible to compute the derivative of the estimate state *x(t)*:

$$\dot{\hat{x}}(t) = A\,\hat{x}(t) + B\,u(t) + L\left(y(t) - \hat{y}(t)\right) \tag{3.5.2}$$

Starting from the definition (3.5.3) of the asymptotic observability of the system's state:

$$\lim_{t\to\infty} \|x(t) - \hat{x}(t)\| = 0 \tag{3.5.3}$$

This limit (3.5.3) is also valid for the derivative of the estimated state:

$$\lim_{t\to\infty} \|\dot{x}(t) - \dot{\hat{x}}(t)\| = 0 \tag{3.5.4}$$

Therefore:

$$\dot{\hat{x}}(t) - \dot{\hat{x}}(t) = (A - L\,C)\left(y(t) - \hat{y}(t)\right) \tag{3.5.5}$$

A necessary and sufficient condition for (3.5.3) is that all eigenvalues of the matrix $A_O = (A - L\,C)$ have a negative real part. This matrix is called the state matrix of the dynamic system of the (3.5.1) with included Luenberger observer. The Luenberger gains matrix L exits if and only if the system is completely observable. A necessary and sufficient condition for an LTI dynamic system to be completely observable is that the observability matrix O has maximum rank.

$$O = \begin{bmatrix} C \\ C\,A \\ . \\ . \\ C\,A^{n-1} \end{bmatrix} \tag{3.5.6}$$

Since it is necessary to estimate the rotor speed of an electric motor, the mechanical system to be considered is:

$$\begin{cases} T_e - T_L = J\dfrac{d\omega_{rm}}{dt} + F\,\omega_{rm} \\ \omega_{rm} = \dfrac{d\theta_{rm}}{dt} \end{cases} \tag{3.5.7}$$

By rewriting the (3.5.7) in matrix form:

$$\frac{d}{dt}\begin{bmatrix} \omega_{rm} \\ \theta_{rm} \end{bmatrix} = \begin{bmatrix} -\dfrac{F}{J} & 0 \\ 1 & 0 \end{bmatrix}\begin{bmatrix} \omega_{rm} \\ \theta_{rm} \end{bmatrix} + \begin{bmatrix} \dfrac{1}{J} \\ 0 \end{bmatrix}(T_e - T_L) \tag{3.5.8}$$

In (3.5.9) can be summarize the matrices related to the above model (3.5.8).

$$A = \begin{bmatrix} -\dfrac{F}{J} & 0 \\ 1 & 0 \end{bmatrix} \qquad B = \begin{bmatrix} \dfrac{1}{J} \\ 0 \end{bmatrix} \qquad C = \begin{bmatrix} 0 & 1 \end{bmatrix} \qquad D = 0 \tag{3.5.9}$$

The observability condition is computed and verified in (3.5.10):

$$O = \begin{bmatrix} C \\ C\,A \end{bmatrix} = \begin{bmatrix} 0 & 1 \\ 1 & 0 \end{bmatrix} \quad \det(O) \neq 0 \tag{3.5.10}$$

Starting from (3.5.10) the state matrix of the dynamic system with included the Luenberger observer is given:

$$A_O = A - L\,C = \begin{bmatrix} -\dfrac{F}{J} & -l_1 \\ 1 & -l_2 \end{bmatrix} \tag{3.5.11}$$

$$\lambda_{1,2} = \frac{-\left(l_2 + \dfrac{F}{J}\right) \pm \sqrt{\left(l_2 + \dfrac{F}{J}\right)^2 - 4\left(l_2\dfrac{F}{J} + l_1\right)}}{2} \tag{3.5.12}$$

From (3.5.12) it is possible to choosing appropriately the desired eigenvalues desired $\lambda_{1,2}$ from choosing the Luenberger matrix L gains l_1 e l_2.

Finally, the control speed structure with estimated speed by Luenberger observer is shown in Fig.3.5.3:

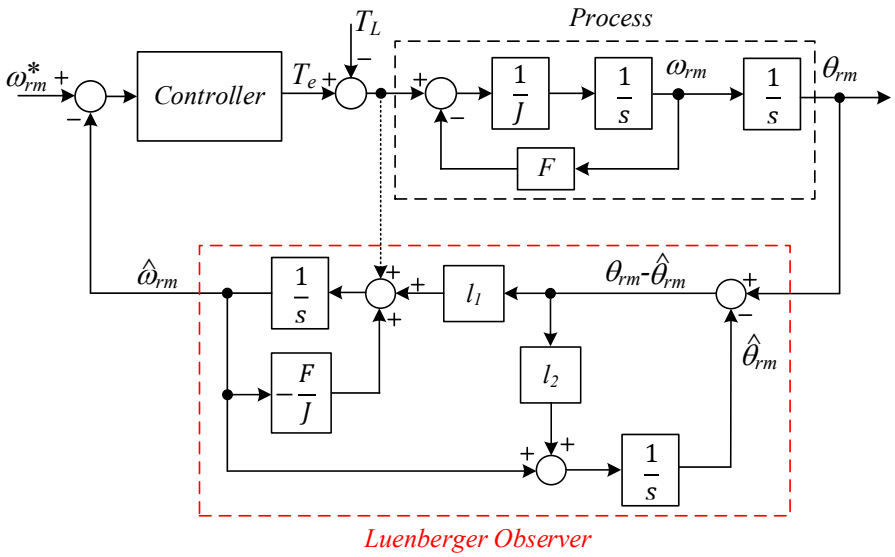

Figure 3.5.3 *Control System with the Luenberger Observer*

3.5.2 Vector Tracking Observer

The Vector Tracking Observer (VTO) is a non-linear adaptation of a Luenberger observer, in which vector cross-product phase detection is used, similar to that used in a PLL (phase locked loop). Typically, this observer is used in several areas concerning the position sensorless control of AC machines.

Fig. 3.5.4 shows the continuous-time block diagram of a VTO: the observer is estimating a generic rotating vector $\Theta_{\alpha\beta}$ and produces estimates of the angular position, or phase, and of the input speed. Four constructive parts of the VTO are highlighted: the phase detector of the vector cross product, a controller, a physical system model and a vector model.

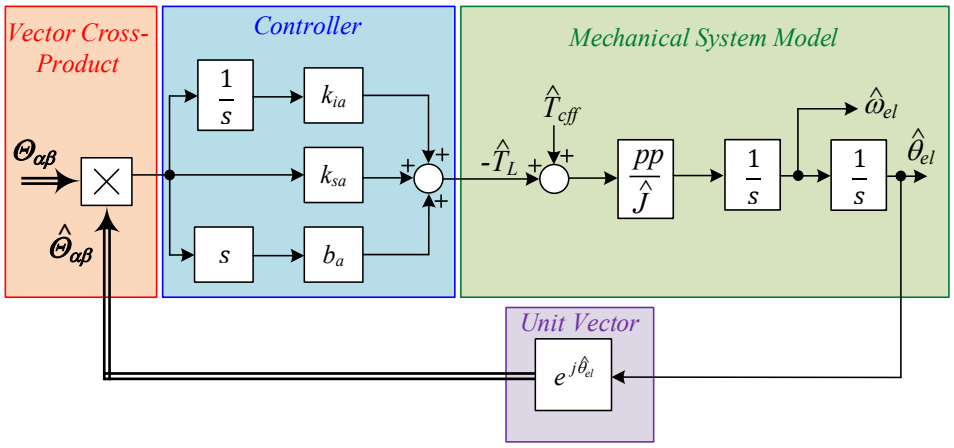

Figure 3.5.4 *Non-Linear Vector Tracking Observer (VTO) block diagram.*

The vector cross-product is responsible for the observer's non-linearity and its nature of vector tracking, which makes it extremely similar to a PLL. The controller is essentially a proportional, integral and derivative regulator (PID) and is present to force the convergence of the estimated vector towards the input vector; the estimated vector is formed using the estimate of the outermost state in combination with an appropriate vector model: in Fig. 3.5.4 the vector model was formed by assuming an input vector in continuous rotation. Finally, a physical system model must also be present because an

adequately trained observer should produce consistent estimates of the physical states: in Fig. 3.5.4 the physical system is assumed to be a rigidly coupled mechanical system, with zero damping, where *pp* is the number of polar pairs of the machine and $\hat{J}$ is the estimated total inertia of the system. A feedforward input can also be recognized in the physical system: a correct feedforward helps to maintain good tracking properties above the observer's bandwidth. In addition, the controller output can be used as a limited bandwidth noise estimate, as shown in Fig 3.5.4. The quality of the noise estimate depends on many factors, including the quality of the feedforward signal, the bandwidth of the observer and also the feedback vector model. If the feedforward input is not present, the structure becomes that of a state filter and will have reduced tracking properties above the filter bandwidth.

An alternative structure which avoids the unrealizable derivative present in Fig. 3.5.4 is shown for this particular physical system model in Fig. 3.5.5.

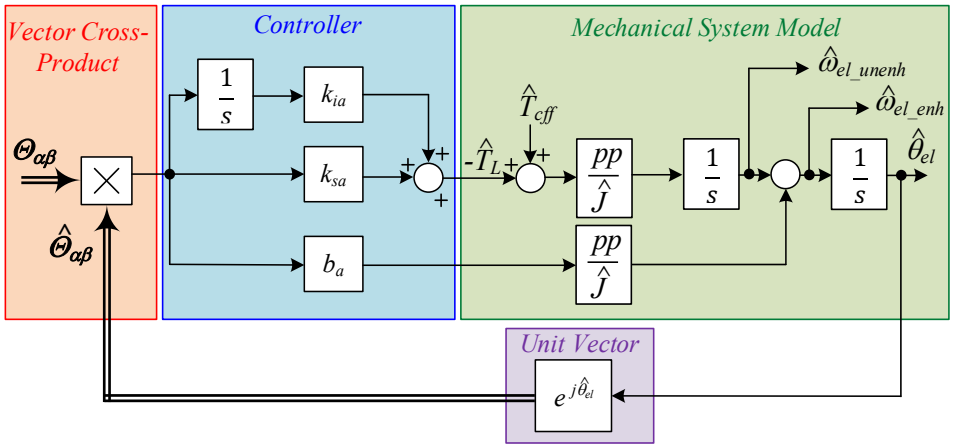

Figure 3.5.5 *Alternative Structure of a VTO.*

The general input/output characteristics remain unchanged, however there are two important internal changes. The first is that, since the derivative action is shifted to the speed state, the output of the PI controller cannot be considered a coherent disturbance estimate. Secondly, two speed estimates are now available, one that comes directly from the state integrator and is referred to as the "unenhanced" estimate, the other that also contains the term of the derivative action and is therefore an "enhanced" estimate ". Both estimates can be used, although the “unenhanced” version is not consistent with the estimated position and the two signals have different dynamic properties. In particular, since the enhanced signal is the same as the speed estimated in Fig 3.5.5, it has the same properties in terms of noise rejection; the “unenhanced” signal instead has reduced noise rejection properties because it is formed without the contribution of the derivative action of the controller.

The analysis of the operating point of the VTO was performed for the first time in [38]. The operating point model is obtained using a first order Taylor series approximation around a specific equilibrium point; this requires taking the partial derivative of each state with respect to all the states and inputs of the system.

Assuming the both input vector and the estimated vector have unit amplitude, and defining ε_θ as:

$$\varepsilon_\theta = \theta_{re} - \hat{\theta}_{re} \tag{3.5.13}$$

the result of the vector cross-product at the VTO input is:

$$|\Theta_{\alpha\beta} \times \hat{\Theta}_{\alpha\beta}| = \sin\left(\theta_{re} \times \hat{\theta}_{re}\right) = \sin(\varepsilon_\theta) \tag{3.5.14}$$

The open loop transfer function is:

$$C(s) = \frac{b_a\, pp}{\hat{J}} \frac{s^2 + \frac{k_{sa}}{b_a}s + \frac{k_{ia}}{b_a}}{s^3} \tag{3.5.15}$$

So the estimated position, i. e. phase of the estimated vector, $\hat{\theta}_{re}$ is obtained as:

$$\hat{\theta}_{re} = C(s)\, \sin(\varepsilon\theta) = \frac{b_a\, pp}{\hat{J}} \frac{s^2 + \frac{k_{sa}}{b_a}s + \frac{k_{ia}}{b_a}}{s^3} \sin(\varepsilon\theta) \tag{3.5.16}$$

By considering the position error defined in (3.5.13) the expression (3.5.16) can be rewritten as:

$$\frac{b_a\, pp}{\hat{J}} \frac{s^2 + \frac{k_{sa}}{b_a}s + \frac{k_{ia}}{b_a}}{s^3} \sin(\varepsilon\theta) = \theta_{re} - \varepsilon\theta \tag{3.5.17}$$

By applying the derivative in (3.5.17) and rearranging this equation obtain:

$$s^3\, \varepsilon\theta + \frac{b_a\, pp}{\hat{J}} \left(s^2 + \frac{k_{sa}}{b_a}s + \frac{k_{ia}}{b_a} \right) \sin(\varepsilon\theta) = s^3\, \theta_{re} \tag{3.5.18}$$

If the acceleration is assumed constant, the right part of (3.5.18) is zero and by transforming the equation (3.5.19) into the time domain yields:

$$\frac{d^3\varepsilon\theta}{dt^3} + \frac{b_a\, pp}{\hat{J}} \cos(\varepsilon\theta) \frac{d^2\varepsilon\theta}{dt^2} - \frac{b_a\, pp}{\hat{J}} \sin(\varepsilon\theta) \left(\frac{d\varepsilon\theta}{dt} \right)^2 + \frac{k_{sa}\, pp}{\hat{J}} \cos(\varepsilon\theta) \frac{d\varepsilon\theta}{dt} + \frac{k_{ia}\, pp}{\hat{J}} \sin(\varepsilon\theta) \tag{3.5.19}$$

This is the global non-linear differential equation for the VTO as a function of the position estimation error $\varepsilon\theta$.

The only partial derivatives that differ from the observer's actual gains are those relating to the result of the vector product (3.5.14). These partial derivatives are:

$$\frac{\partial^3 \sin(\varepsilon\theta)}{\partial t^3}\Big|_{\theta_{re0},\ \hat{\theta}_{re0}} = \cos\left(\theta_{re0} - \hat{\theta}_{re0} \right) \tag{3.5.20}$$

$$\frac{\partial^3 \sin(\varepsilon\theta)}{\partial t^3}\Big|_{\theta_{re0},\ \hat{\theta}_{re0}} = -\cos\left(\theta_{re0} - \hat{\theta}_{re0} \right) \tag{3.5.21}$$

where θ_{re0} and $\hat{\theta}_{re0}$ are the rotor position and estimated rotor position values in an operating point condition, respectively.

In Fig. 3.5.6 shows the resulting small signal model, formed using the equations (3.5.20) and (3.5.21):

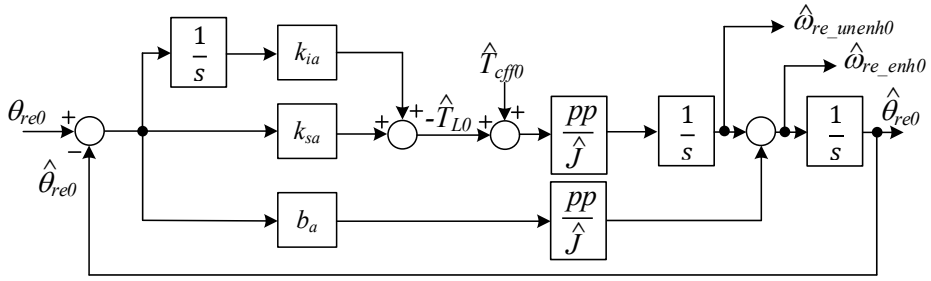

Figure 3.5.6 *Small Signal Model of VTO.*

Starting from the small signal model of VTO it is possible to define the closed loop transfer function, defined as a ratio between the estimated rotor position $\hat{\theta}_{re0}$ and input measured rotor position θ_{re0}:

$$W_{VTO}(s) = \frac{\hat{\theta}_{re0}(s)}{\theta_{re0}(s)} = \frac{k_1 s^2 + k_2 s + k_3}{s^3 + k_1 s^2 + k_2 s + k_3} \tag{3.5.21}$$

However, as the estimated speed, carried out of the VTO, is required in closed loop speed control it is possible to rewrite the VTO closed loop transfer function as:

$$W_{VTO}(s) = \frac{\hat{\theta}_{re0}(s)}{\theta_{re0}(s)} = \frac{\hat{\omega}_{re0}(s)}{\omega_{re0}(s)} = \frac{k_1 s^2 + k_2 s + k_3}{s^3 + k_1 s^2 + k_2 s + k_3} \tag{3.5.22}$$

Since the VTO provides two different estimated speed it is necessary to write two different closed loop transfer function. By considering the transfer function (3.5.22) it would be noted that the estimate speed $\hat{\omega}_{re0}$ coincides with the enhanced estimated speed $\hat{\omega}_{re\_enh0}$:

$$W_{VTOenh}(s) = \frac{\hat{\omega}_{re\_enh0}(s)}{\omega_{re0}(s)} = \frac{k_1 s^2 + k_2 s + k_3}{s^3 + k_1 s^2 + k_2 s + k_3} \tag{3.5.23}$$

while the transfer function related to the unenhanced estimated speed is given by:

$$W_{VTOunenh}(s) = \frac{\hat{\omega}_{re\_unenh0}(s)}{\omega_{re0}(s)} = \frac{k_2 s + k_3}{s^3 + k_1 s^2 + k_2 s + k_3} \tag{3.5.24}$$

In Fig. 3.5.7 the step time responses are shown of the both enhanced and un enhanced closed loop transfer functions of the VTO.

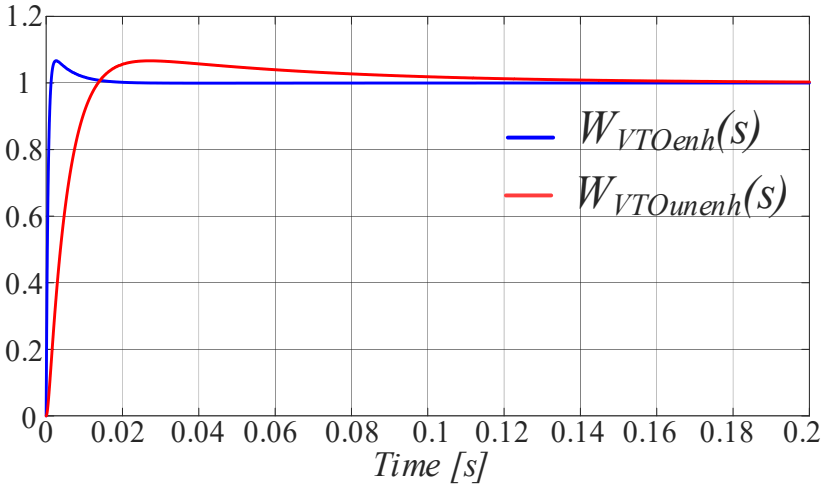

Figure 3.5.7 *Step Time Response of the VTO closed loop transfer functions.*

It can be noted that the enhanced estimated speed has a better dynamic transient then the unenhanced estimated speed considering the same VTO model parameters and controller gains.

By exploiting the small signal model of the VTO, it is possible to tune the observer and choose its dynamic performance and position estimation, speed enhanced and unenhanced. The tuning procedure of the VTO will be fully described in the next chapter.

3.6 Non-Model Based Speed Estimation Techniques

When the mechanical load is unknown, it is often convenient to use non-model based methods. In general, in these models, the signals coming from the position sensor are processed to estimate the speed.

Several algorithms have been presented in literature, based on the Taylor series expansion [24], [33], [37]-[41], the backward difference expansion [33], [42] and the least-squares fit [1], [33], [41].

Non-model-based algorithms can be classified into two broad types of velocity estimators, according to how time and position information is acquired.

An encoder typically produces two square waves in quadrature. Each transition of both waves is detected as an encoder line, so it is possible to count the number of encoder lines in a given period or the to measure the time between two lines of the encoder. In both cases, only one variable is measured and the other variable is assumed to be constant, which leads to a class definition of the speed estimator. Speed estimators implementing a "fixed time method" (FTM), those in which the time between successive samples is known (at least approximately) and the distance traveled in this fixed time interval is measured by counting the encoder lines. In case of "fixed position method" (FPM) speed estimators, the estimate is based on measuring the time required to travel two fixed lines of the encoder.

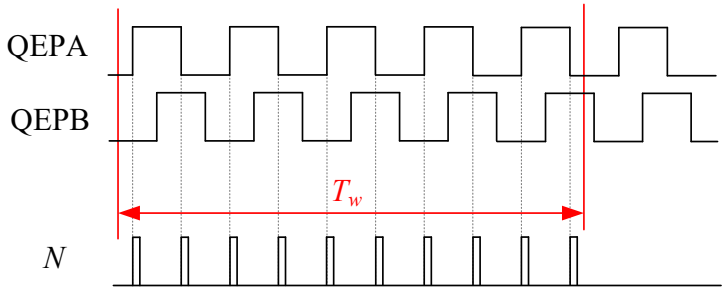

Figure 3.6.1 *Speed Estimation from Encoder Pulses and with FTM.*

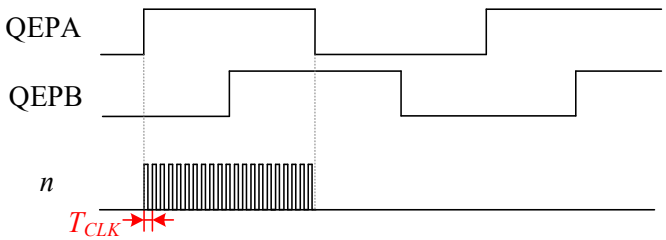

Figure 3.6.2 *Speed Estimation from Encoder Pulses and with FPM.*

Any numerical method that calculates a derivative from discrete position data as a function of time can be used for a velocity estimator.

The simplest speed estimator is based on the first order approximation, i.e., incremental ratio [33]; in fact, by considering with $\Delta\theta_{re} = \theta_{re}(k) - \theta_{re}(k-1)$ the different between two rotor position instant counted in time interval $\Delta t = t(k)-t(k-1)$, the speed estimate for the *k-th* interval is $\omega_{re}(k) = \Delta\theta_{re}/\Delta t$. The speed estimators with FTM and with FPM are mathematically equivalent, although (at first glance) these estimators appear to be different. The speed estimates are $\Delta\theta_{re}/\Delta t$ for both methods, with constant $\Delta\theta_{re}$ for the

FPM and constant Δt for the FTM. Assuming accurate data measurements, both of these methods provide an estimate of the rate for the current sample that corresponds to the average rate in the sampling interval. During a speed transient, the "true" speed at the sampling instant will be different from the average speed; this speed difference is equivalent to a time delay that can degrade the performance of a control system and can lead to instability. In general, the addition of higher-order terms should improve the transient response [33]. For velocity estimators, higher-order approximations than the derivative are obtained by combining the present and previous velocity estimates.

3.6.1 Taylor Series Expansion (TSE) Speed Estimator Method

Speed estimation methods introduced previously (FPM and FTM) are based on the first order approximation of an extensive formulation that will be described below. It is possible to estimate the velocity using Taylor series expansion of velocity [43]. The estimated speed $\hat{\omega}_{re}(k)$ at the instant time t_k can be estimated by the TSE from the estimated average speed $\hat{\omega}_{re0}$, during the most recently measured sampling interval, at the instant time t_0:

$$\hat{\omega}_{re}(k) = \hat{\omega}_{re0} + \sum_{j=0}^{+\infty} \frac{1}{j!} \frac{d^{(j)} \hat{\omega}_{re0}}{dt^{(k)}} (t_k - t_0)^j \qquad (3.6.1)$$

The estimated average speed $\hat{\omega}_{re0}$ is estimated to occur at the center of the sampling interval then:

$$\hat{\omega}_{re0} \approx \frac{\Delta\theta_{re}(k)}{\Delta t(k)} \qquad (t_k - t_0) \approx \frac{\Delta t(k)}{2} \qquad (3.6.2)$$

If the TSE is truncated after the first term, the estimated speed $\hat{\omega}_{re}(k)$ is given:

$$\hat{\omega}_{re}(k) \approx \frac{\Delta\theta_{re}(k)}{\Delta t(k)} \qquad (3.6.3)$$

Note that the estimated speed in (3.6.3) is the same as the reciprocal-time estimator for fixed position method data and is the same as the lines-per-period estimator for fixed time method data. A comparison between the rotor shaft measured speed and the estimated speed with first order approximation of the TSE is shown in Fig. 3.6.3:

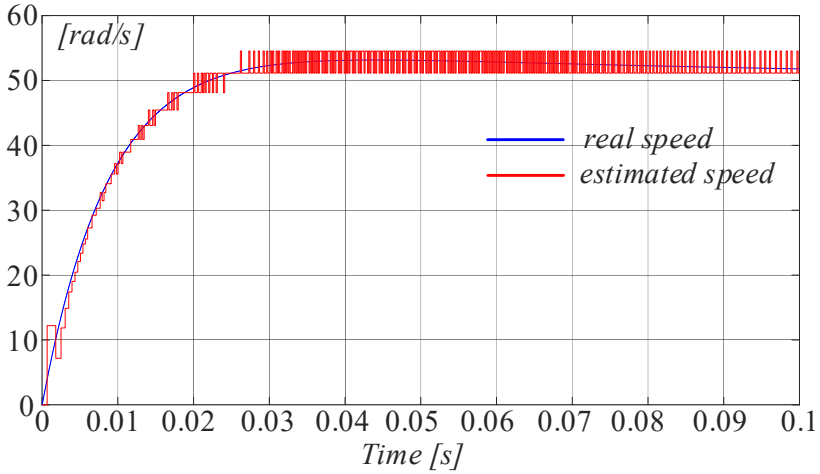

Figure 3.6.3 *First order approximation of the TSE speed estimation with N_{DS} = 32.*

When $\hat{\omega}_{re}(k)$ is estimated from the *k-th* period as (3.6.3) and $\hat{\omega}_{re}(k-1)$ is estimated from *(k-1)-th* period as $\Delta\theta_{re}(k-1)/\Delta t(k-1)$, the first derivative of the velocity at the middle of the *k-th* period can be approximated by:

$$\frac{d\hat{\omega}_{re0}(k)}{dt} \approx \frac{\Delta\hat{\omega}_{re}}{\Delta t} \approx \frac{\hat{\omega}_{re0}(k) - \hat{\omega}_{re0}(k-1)}{\Delta t(k)} \tag{3.6.4}$$

Higher order derivatives of $\hat{\omega}_{re0}(k)$ are also approximated in a similar expression of the (3.6.4) by:

$$\frac{d^{(j)}\hat{\omega}_{re0}(k)}{dt^{(j)}} \approx \frac{\Delta\hat{\omega}_{re}^{(j-1)}}{\Delta t} \approx \frac{\hat{\omega}_{re0}^{(j-1)}(k) - \hat{\omega}_{re0}^{(j-1)}(k-1)}{\Delta t(k)} \tag{3.6.5}$$

Some simple examples of the different TSE order approximation are presented below.

The first order approximation is already presented in (3.6.3), then the second order TSE approximation is computed in (3.6.6):

$$\hat{\omega}_{re}(k) = \hat{\omega}_{re0} + \frac{1}{1!}\frac{d\hat{\omega}_{re0}}{dt}(t_k - t_0) \tag{3.6.6}$$

Starting from the approximations defined in (3.6.2) it is possible to define the second order TSE approximation of the estimated speed at the instant *t(k)*:

$$\hat{\omega}_{re}(k) \approx \frac{\Delta\theta_{re}(k)}{\Delta t(k)} + \frac{\Delta t(k)}{2}\left(\frac{\Delta\theta_{re}(k)}{\Delta t(k)} - \frac{\Delta\theta_{re}(k-1)}{\Delta t(k-1)}\right) \tag{3.6.7}$$

The estimated speed in (3.6.7) when the fixed position method data are considered, i. e. the rotor position is constant during the position sensor signal acquisition $\Delta\theta_{re}(k) = \Delta\theta_{re} = constant$, is given:

$$\hat{\omega}_{re}(k) \approx \Delta\theta_{re}\left[\frac{1}{\Delta t(k)} + \frac{1}{2}\left(\frac{1}{\Delta t(k)} - \frac{1}{\Delta t(k-1)}\right)\right] \tag{3.6.8}$$

The estimated speed in (3.6.7) when the fixed time method data are considered, i.e., the time period is constant $\Delta t(k) = T_w = constant$, is given by:

$$\hat{\omega}_{re}(k) \approx \frac{1}{T_w}\left[\Delta\theta_{re}(k) + \frac{1}{2}\left(\Delta\theta_{re}(k) - \Delta\theta_{re}(k-1)\right)\right] \tag{3.6.9}$$

In Fig. 3.6.4 is shown the estimated speed with second order approximation of the TSE compared with rotor shaft measured speed:

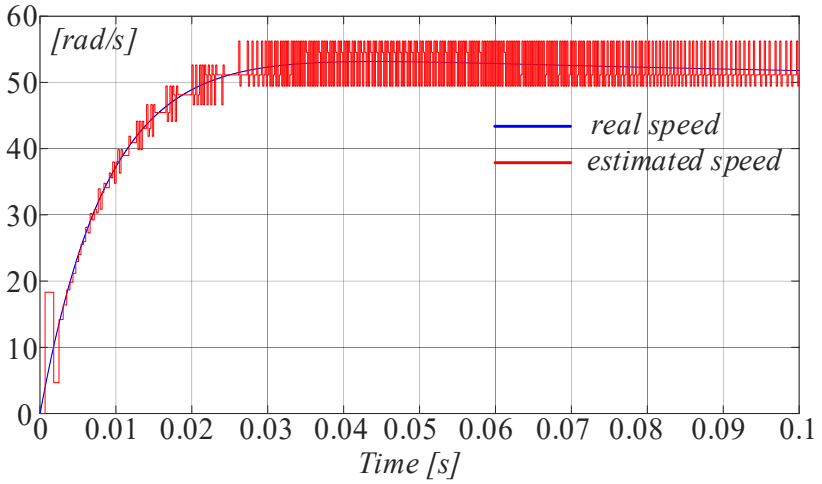

Figure 3.6.4 *Second order approximation of the TSE speed estimation* $N_{DS} = 32$.

The third order TSE approximation of the estimated speed is computed at the instant *t(k)*; in particular, the third order approximation with FPM is presented in (3.6.10) is

presented the third order approximation when FPM is considered, while the third order approximation with FTM is considered in (3.6.11):

$$\hat{\omega}_{re}(k) \approx \Delta\theta_{re}\left[\frac{1}{\Delta t(k)} + \frac{1}{2}\left(\frac{1}{\Delta t(k)} - \frac{1}{\Delta t(k-1)}\right) + \frac{\Delta t(k)}{8}\left(\frac{\frac{1}{\Delta t(k)} - \frac{1}{\Delta t(k-1)}}{\Delta t(k)} - \frac{\frac{1}{\Delta t(k-1)} - \frac{1}{\Delta t(k-2)}}{\Delta t(k-1)}\right)\right] \quad (3.6.10)$$

$$\hat{\omega}_{re}(k) \approx \frac{1}{T_w}\left[\Delta\theta_{re}(k) + \frac{1}{2}\left(\Delta\theta_{re}(k) - \Delta\theta_{re}(k-1)\right) + \frac{1}{8}\left(\Delta\theta_{re}(k) - 2\Delta\theta_{re}(k-1) + \Delta\theta_{re}(k-2)\right)\right] \quad (3.6.11)$$

In Fig. 3.6.5 is shown the comparisons between the rotor shaft measured speed and the third order TSE approximation speed estimation:

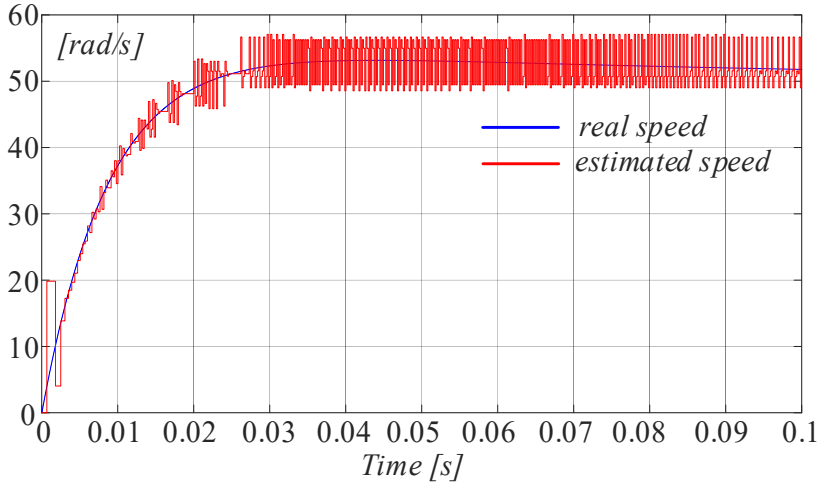

Figure 3.6.5 *Third order approximation of the TSE speed estimation N_{DS} = 32.*

Finally, a comparison between the average speed value and the estimated speeds with the three different TSE approximations defined above is shown in Fig. 3.6.6. Although the higher order of the TSE approximation slightly increases the dynamic performance of the estimated speed, such as shown in Figs. 3.6.3-3.6.5, the speed ripples increase with the TSE order approximation increasement.

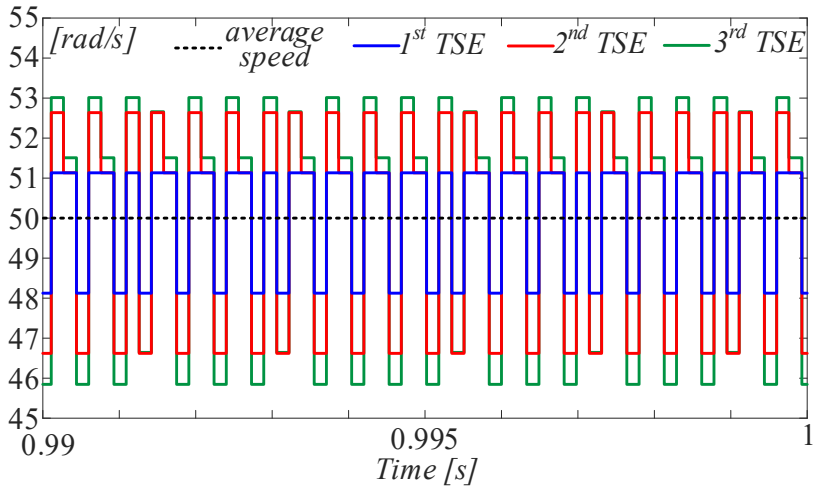

Figure 3.6.6 *TSE speed estimator comparisons*

3.6.2 Backward Difference Expansion (BSE) Speed Estimator Method [44]

The BDE method for obtaining the derivative of the function $t(\theta_{re}(k))$ or $\theta_{re}(t(k))$ is developed by assuming that the actual function can be replaced by an interpolating polynomial that exactly fits the data points. The first and higher order derivatives of the function are obtained in terms of the appropriate finite difference approximations for the derivatives of the approximating polynomial. For fixed position method data, the backward difference equation is obtained by expanding the function *t(k-1)* in Taylor series around *t(k)* and then solving for $dt(k)/d\theta_{re}$:

$$t(k\text{-}j) = t(k) + \sum_{j=1}^{+\infty} \frac{(-j)^j}{j!} \frac{d^{(j)}t(k)}{d\theta_{re}{}^{(k)}} \tag{3.6.12}$$

The first order BDE for is obtained by expanding t(k-1) using (3.6.12) and then truncating the expansion after the first term on the right-hand side, as shown in (3.6.13):

$$\frac{dt(k)}{d\theta_{re}} = \big(t(k) - t(k\text{-}1)\big) + \sum_{j=2}^{+\infty} \frac{(-j)^j}{j!} \frac{d^{(j)}t(k)}{d\theta_{re}{}^{(k)}} \tag{3.6.13}$$

Then the estimated speed can be computed by the following expression:

$$\hat{\omega}_{re}(k) = \frac{d\theta_{re}}{dt(k)} = \frac{1}{\big(t(k) - t(k\text{-}1)\big) + \sum_{j=2}^{+\infty} \frac{(-j)^j}{j!} \frac{d^{(j)}t(k)}{d\theta_{re}{}^{(k)}}} \tag{3.6.14}$$

The first order BDE is identical to the first order TSE, then the FPM and FTM approximation are the same:

$$\hat{\omega}_{re}(k) \approx \frac{\Delta\theta_{re}(k)}{\big(t(k) - t(k\text{-}1)\big)} = \frac{\Delta\theta_{re}(k)}{\Delta t(k)} \tag{3.6.15}$$

The second order BDE is obtained when both *t(k-1)* and *t(k-2)* are expanded in the Taylor series of (3.6.12), and the resulting two equations are solved for both $dt(k\text{-}1)/d\theta_{re}$ and $dt^2(k\text{-}1)/d\theta_{re}{}^2$ with third order derivative terms neglected. Then, the second order BDE approximation for FPM and FTM are presented in (3.6.16) and (3.6.17) respectively:

$$\hat{\omega}_{re}(k) \approx \frac{\Delta\theta_{re}}{\Delta t(k) + \frac{1}{2}\big(\Delta t(k) - \Delta t(k\text{-}1)\big)} \tag{3.6.16}$$

$$\hat{\omega}_{re}(k) \approx \frac{\Delta\theta_{re}(k) + \frac{1}{2}\big(\Delta\theta_{re}(k) - \Delta\theta_{re}(k)\big)}{T_w} \tag{3.6.17}$$

In Fig. 3.6.7 is shown the estimated speed with second order approximation of the BDE compared with rotor shaft measured speed:

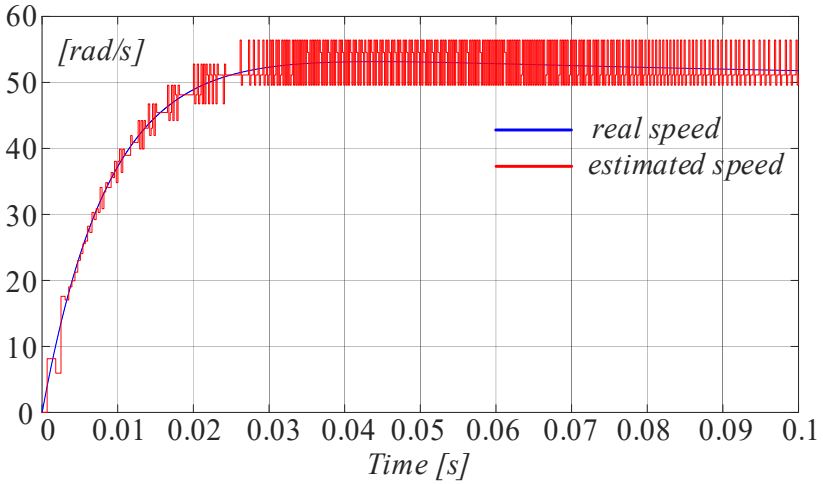

Figure 3.6.7 *Second order approximation of the BDE speed estimation* $N_{DS} = 32$.

This procedure is continued to include terms containing *t(k-3)*. Then the third order BDE approximation for FPM and FTM are (3.6.18) and (3.6.19) respectively:

$$\hat{\omega}_{re}(k) \approx \frac{\Delta\theta_{re}}{\Delta t(k) + \frac{1}{2}\left(\Delta t(k) - \Delta t(k\text{-}1)\right) + \frac{1}{3}\left(\Delta t(k) - 2\Delta t(k\text{-}1) + \Delta t(k\text{-}2)\right)} \tag{3.6.18}$$

$$\hat{\omega}_{re}(k) \approx \frac{\Delta\theta_{re}(k) + \frac{1}{2}\left(\Delta\theta_{re}(k) - \Delta\theta_{re}(k)\right) + \frac{1}{3}\left(\Delta\theta_{re}(k) - 2\Delta\theta_{re}(k\text{-}1) + \Delta\theta_{re}(k\text{-}2)\right)}{T_w} \tag{3.6.19}$$

In Fig. 3.6.8 is shown the comparisons between the rotor shaft measured speed and the third order BDE approximation speed estimation:

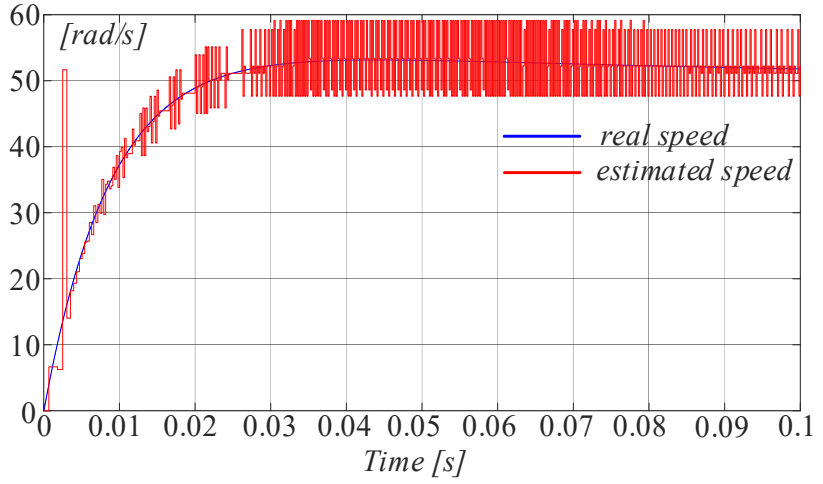

Figure 3.6.8 *Third order approximation of the BDE speed estimation* $N_{DS} = 32$.

Although when the BDE order approximation increase the dynamic performance slightly increases, as well as for TSE approximations. The speed ripples increase with the BDE order approximation increasement, but they are bigger then the respective speed ripples obtained with the TSE approximations.

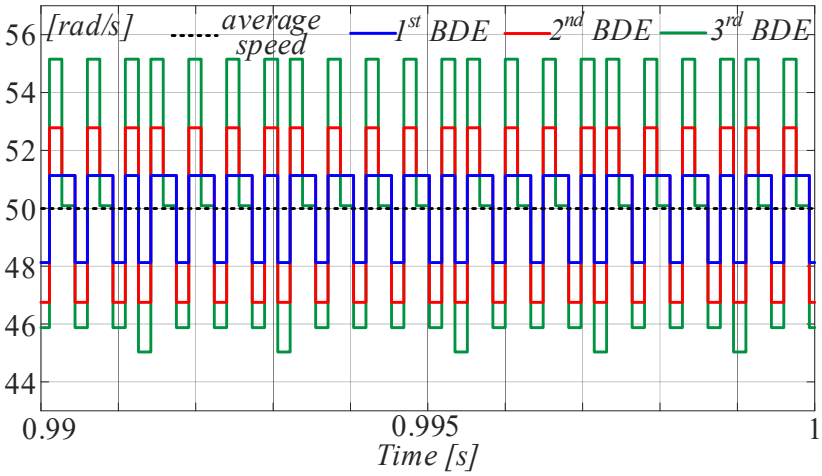

Figure 3.6.9 *BDE speed estimator comparisons*

3.7 Conclusions

In this chapter the contributions of my research regard the paragraph 3.3 relating on the Mathematical Formulations of the Quantized Rotor Position and Angular Speed. The theory developed in this paragraph completes the spatial Fourier approach to the modeling of position sensor resolution by connecting the spatial quantization harmonics to the time harmonic ripple in speed estimation. At the heart of the theory lies the concept of instantaneous quantized speed, defined as the time derivative of the quantized electrical rotor angle. This quantity plays a key role in the performance of any position-measurement-based speed estimation algorithm since it constitutes its effective speed input.

In particular, at a constant speed of rotation, the instantaneous quantized speed contains quantization time harmonics at multiples of NDSfre0; while, when the drive is subjected to periodic torque disturbances, the interaction between these and the quantization space harmonics produces additional time harmonics in both the measured position and in the instantaneous quantized speed, the amplitude of which can be obtained from phase modulation theory.

3.8 References

[1] R.D. Lorenz and K. Van Patten, “High-resolution velocity estimation for all-digital, ac servo drives,” IEEE Trans. Ind. Appl., vol. 27, no. 4, pp. 701 – 705, Jul./Aug. 1991.

[2] J. Fraden, Handbook of Modern Sensors: Physics, Designs and Applications, 5th ed., New York: Springer, 2015.

[3] P. Drabarek and R. M. Kennel Fiet, "Are interferometric encoders a reasonable alternative in servo drive applications?," 2008 4th IET Conference on Power Electronics, Machines and Drives, 2008, pp. 149-153.

[4] R.M. Kennel, “Encoders for simultaneous sensing of position and speed in electrical drives with digital control,” IEEE Trans. Ind. Appl., vol. 43, no. 6, pp. 1572 – 1577, Nov./Dec. 2007.

[5] J. Fraden, Handbook of Modern Sensors: Physics, Designs and Applications, 5th ed., New York: Springer, 2015.

[6] H. Inc, “Hall Effect Sensing and Application,” [Online]. Available: https://www.honeywell.com.
[7] C. Motion. [Online]. Available: https://www.celeramotion.com/zettlex/what-is-a-capacitive-encoder/.
[8] D. Collins, “What are capacitive encoders and where are they suitable?,” October 29, 2015. [Online]. Available: www.motioncontroltips.com.
[9] D. Zheng, S. Zhang, S. Wang, C. Hu and X. Zhao, “A Capacitive Rotary Encoder Based on Quadrature Modulation and Demodulation,” January 2015.
[10] Machinedesign, “Overview and update: Rotary encoders,” Oct 01, 2012. [Online]. Available: www.machinedesign.com.
[11] Exxelia, “Contactless Position Sensors - General Technical data,” Version 05/16.
[12] Asahi Kasei Microdevices (AKM), “Knowledge of Encoder - Magnetic encoder configuration,” [Online]. Available: www.akm.com.
[13] C.W. Secrest, J.S. Pointer, M.R. Buehner, and R.D. Lorenz, “Improving position sensor accuracy through spatial harmonic decoupling, and sensor scaling, offset, and orthogonality correction using self-commissioning MRAS methods,” IEEE Trans. Ind. Appl., vol. 51, no. 6, pp. 4492 – 4504, Nov./Dec. 2015.
[14] L. Masisi, and P. Pillay, “High-resolution low-cost position sensor for traction applications,” in Proc. of IEEE IECON, Oct. 2017, pp. 1971-1976.
[15] D. Reigosa, D. Fernandez, C. Gonzalez, S.-B. Lee, and F. Briz, “Permanent magnet synchronous machine drive control using analog Hall-effect sensors,” IEEE Trans. Ind. Appl., vol. 54, no. 3, pp. 2358 – 2369, May/Jun. 2018.
[16] R. Raja, T. Sebastian, M. Wang, A. Gebregergis, and M.S. Islam, “Effect of position sensor error on the performance of permanent magnet machine drives,” IEEE Trans. Ind. Appl., vol. 53, no. 6, pp. 5518 – 5526, Nov./Dec. 2017.
[17] M.C. Harke, G. De Donato, F. Giulii Capponi, T.R. Tesch, and R.D. Lorenz, “Implementation issues and performance evaluation of sinusoidal, surface-mounted PM machine drives with Hall-effect position sensors and a vector-tracking observer,” IEEE Trans. Ind. Appl., vol. 44, no. 1, pp. 161 – 173, Jan./Feb. 2008.
[18] A. Yoo, S.-K. Sul, D.-C. Lee, and C.-S. Jun, “Novel speed and rotor position estimation strategy using a dual observer for low-resolution position sensors,” IEEE Trans. Power Electron., vol. 24, no. 12, pp. 2897-2906, Dec. 2009.
[19] G. Scelba, G. De Donato, G. Scarcella, F. Giulii Capponi, and F. Bonaccorso, “Fault-tolerant rotor position and velocity estimation using binary Hall-effect sensors for low-cost vector control drives,” IEEE Trans. Ind. Appl., vol. 50, no. 5, pp. 3404-3413, Sep./Oct. 2014.
[20] G. Scelba, G. De Donato, G. Scarcella, M. Pulvirenti and F. Giulii Capponi, “Hall-effect sensor fault detection, identification and compensation in brushless DC drives,” IEEE Trans. Ind. Appl., vol. 52, no. 2, pp. 1542-1554, Mar./Apr. 2016.
[21] L. Dong, Y. Huang, J. Jatskevich, and L. Liu, “Improved fault-tolerant control for brushless permanet magnet motor drivs with defective Hall sensors,” IEEE Trans. Energy Convers., vol. 31, no. 2, pp. 789-799, Jun. 2016.
[22] G. De Donato, G. Scelba, M. Pulvirenti, G. Scarcella, and F. Giulii Capponi, “Low-cost, high-resolution, fault-robust position and speed estimation for PMSM drives operating in safety-critical systems,” IEEE Trans. Power Electron., vol. 34, no. 1, pp. 550-564, Jan. 2019.
[23] G. Liu, A. Kurnia, R. De Larminat, and S.J. Rotter, “Position sensor error analysis for EPS motor drive,” in Proc. of IEEE IEMDC, Jun. 2003, pp. 249-254.

[24] R. Petrella, M. Tursini, L. Peretti and M. Zigliotto, “Speed measurement algorithms for low-resolution incremental encoder equipped drives: a comparative analysis,” in Proc. of IEEE ACEMP, Sep. 2007, pp. 780-787.
[25] S. Chen, C. Namuduri, and S. Mir, “Controller-induced parasitic torque ripples in a PM synchronous motor, ” IEEE Trans. Ind. Appl., vol. 38, no. 5, pp. 1273 – 1281, Sep./Oct. 2002.
[26] K.-Y. Cho, Y.-K. Lee, H. Mok, H.-W. Kim, B.-H. Jun, and Y. Cho, “Torque Ripple Reduction of a PM Synchronous Motor for Electric Power Steering using a Low Resolution Position Sensor,” Journal of Power Electron., vol. 10, no. 6, pp. 709 – 716, Nov. 2010.
[27] T. Shi, Z. Wang, and C. Xia, “Speed Measurement Error Suppression for PMSM Control System Using Self-Adaption Kalman Observer,” IEEE Trans. Ind. Electr., vol. 62, no. 5, pp. 2753 – 2763, May 2015.
[28] J. Lara, J. Xu, and A. Chandra, “Effects of Rotor Position Error in the Performance of Field-Oriented-Controlled PMSM Drives for Electric Vehicle Traction Applications”, IEEE Trans. Ind. Electr., vol. 63, no. 8, pp. 4738 – 4751, Aug. 2016.
[29] T.R. Tesch and R.D. Lorenz, “Disturbance torque and motion state estimation with low resolution position interfaces using heterodyning observers,” IEEE Trans. Ind. Appl., vol. 44, no.1, pp. 124-134, Jan./Feb. 2008.
[30] N.M. Blachman, “The intermodulation and distortion due to quantization of sinusoids,” IEEE Trans. Acoust., Speech, Signal Process., vol. 33, no. 6, pp. 1417 – 1426, Dec. 1985.
[31] L.J. Giacoletto, “Generalized theory of multitone amplitude and frequency modulation,” Proc. IRE, vol. 35, no. 7, pp 680 – 693, Jul. 1947.
[32] J.R. Carson, “Notes on the theory of modulation,” Proc. IRE, vol. 10, no. 1, pp. 57-64, Feb. 1922.
[33] R. H. Brown, S. C. Schneider and M. G. Mulligan, "Analysis of algorithms for velocity estimation from discrete position versus time data," in IEEE Transactions on Industrial Electronics, vol. 39, no. 1, pp. 11-19, Feb. 1992
[34] Belanger, P. Dobrovolny, A. Helmy, and X. Zhang, “Estimation of angular velocity and acceleration from shaft-encoder measurements,” Int. J. Robot. Res., vol. 17, no. 11, pp. 1225–1230, 1998.
[35] Heui-Wook Kim and Seung-Ki Sul, "A new motor speed estimator using Kalman filter in low-speed range," in IEEE Transactions on Industrial Electronics, vol. 43, no. 4, pp. 498-504, Aug. 1996.
[36] M.W. Degner, “Flux, Velocity and Position Estimation in AC Machines Usin Carrier Signal Injection”, Ph.D. Dissertation, University of Wisconsin-Madison, Madison, WI, USA, 1998.
[37] L. Bascetta, G. Magnani and P. Rocco, "Velocity Estimation: Assessing the Performance of Non-Model-Based Techniques," in IEEE Transactions on Control Systems Technology, vol. 17, no. 2, pp. 424-433, March 2009.
[38] F. Briz, J. A. Cancelas and A. Diez, "Speed measurement using rotary encoders for high performance AC drives," Proceedings of IECON'94 - 20th Annual Conference of IEEE Industrial Electronics, 1994, pp. 538-542 vol.1.
[39] F. Brugnano, C. Concari, E. Imamovic, F. Savi, A. Toscani and R. Zanichelli, "A simple and accurate algorithm for speed measurement in electric drives using incremental encoder," IECON 2017 - 43rd Annual Conference of the IEEE Industrial Electronics Society, 2017, pp. 8551-8556.

[40] A. Anuchin, A. Dianov and F. Briz, "Synchronous Constant Elapsed Time Speed Estimation Using Incremental Encoders," in IEEE/ASME Transactions on Mechatronics, vol. 24, no. 4, pp. 1893-1901, Aug. 2019.
[41] S. M. Phillips and M. S. Branicky, "Velocity estimation using quantized measurements," 42nd IEEE International Conference on Decision and Control (IEEE Cat. No.03CH37475), 2003, pp. 4847-4852 Vol.5.
[42] M. Lemkin, P. H. Yang, A. C. Huang, J. Jones and D. M. Auslander, "Velocity estimation from widely spaced encoder pulses," Proceedings of 1995 American Control Conference - ACC'95, 1995, pp. 998-1002 vol.1.
[43] R. H. Brown and S. C. Schneider, “Velocity observations from discrete position encoders”, in Prod. IECON’ 87, Thirteenth Annu. IEEE Industrial Electronics Society Conf., Boston, MA, Nov., 1987, pp. 1111-1118.
[44] C. F. Gerald, Applied Numerical Analysis. New York: Addison-Wesley, 1970.

Chapter 4. Selection of Rotor Position Sensor Resolution in AC Motor Drives

Variable Speed Drives (VSDs) are popular in many industries applications, wherever speed control is required for energy saving or process control. Closed loop speed control requires speed feedback, although position feedback is also mandatory for field orientation in AC inverters and for switching in BLDC drives. Due to cost, reliability and space constraints, the only motion sensor used in VSDs is the position sensor, so the speed must be estimated from the position measurement, [1]-[2]. Although speed estimation is known to deteriorate as sensor resolution decreases, [3]-[4], there is a lack of methods in the literature for correct selection of position sensor resolution. These should allow the designer to choose the position sensor based on the drive performance specifications, with the aim of minimizing the cost. The following research intends to fill this gap. The idea is to approach allows to identify the minimum rotor position sensor resolution N_{DS} starting from the analysis of the filtering action provided by any speed estimation algorithm on the quantized instantaneous speed input. Appropriate system modeling is derived to link the minimum rotor position sensor resolution with the required performance of the drive which could be expressed in terms of maximum allowed speed ripple at minimum operating speed, speed control bandwidth and robustness of the drive expressed by means of the phase margin.

The procedure adopted to select the resolution of the rotor position sensor will be applied for two types of speed estimation algorithms: the first is a model-based algorithm, the VTO; the second concerns a non-model-based method, the FPM.

This chapter is composed as follows: a first paragraph defines the desired dynamic performances for a VSD; then the selection of the bandwidth and the robustness by means of phase margin; second, third and fourth paragraphs will introduces the tuning of the current loop (the innermost), the speed loop (the outermost) and the speed estimator, respectively; a fifth paragraph will introduce the impact of the resolution on the quantized position measurement and in the speed estimation algorithms, for a model-based speed estimation algorithm; finally sixth and seventh paragraphs will show the selection procedures of the minimum rotor position resolution that guarantees the desired designed performance.

4.1 Desired Performance in a Variable Speed Drive

In control system design it is necessary to define some desired specifications, these can be expressed in terms of time domain specifications or through frequency domain specifications, or by means the roots locus specifications [5]-[6]. Whatever is the type of specification they considered guarantee specific dynamic performances in terms of command tracking and robustness; for example, the rise time (time domain specific) is related to the bandwidth (frequency domain specific) which is also related to the natural pulsation (roots locus specific), while the overshoot (time domain specific) is related to the phase margin (frequency domain specific) which is also related to the damping (roots

locus specific). A summary the three ways to define the desired specifications for the control systems design.

4.1.1 Time-Domain Specifications

The closed loop control system design specifications for the design often involve certain requirements associated with the response time of the system. The requirements for a step response are expressed in terms of standard quantities shown in Fig. 4.1.1:

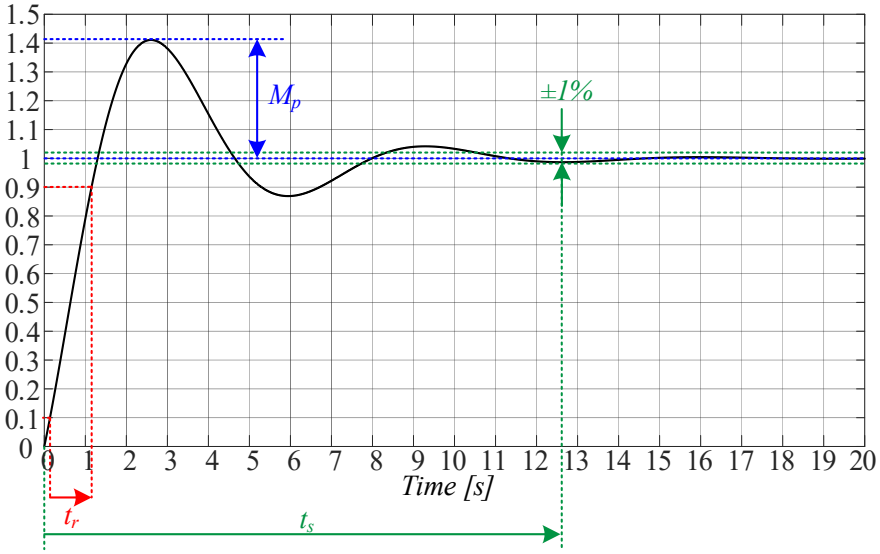

Figure 4.1.1 *Generic time response of a closed loop control system.*

where, the rise time t_r is the time required for the output to pass from 10% to 90% of the final value; the overshoot M_p is the maximum amount that the system overshoots its final value divided by its final value (and often expressed in percentage); the settling time t_s is the time required for the output to remain within ±1% of the final value.

4.1.2 Frequency-Domain Specifications

Generally, the time domain specifications defined in sub-paragraph 4.1.1 can be referred to frequency domain specifications and used for closed loop control systems design and for stability and robustness analysis.

A natural specification for system performance in terms of frequency response is the bandwidth f_{BW}, defined as the maximum frequency at which the output of a system will track an input sinusoid in a satisfactory manner [5]. By convention, for the system shown in Fig. 4.1.2 with sinusoidal input $r(t)$, the bandwidth is the frequency of $r(t)$ at which the output $y(t)$ is attenuated by a factor $1/\sqrt{2} \approx 0.707$ times the input (or $-3dB$). Fig. 4.1.3 graphically illustrates the idea for the frequency response of the closed-loop transfer function defined by equation (4.1.1):

$$W(s) = \frac{F(s)}{1+F(s)} \tag{4.1.1}$$

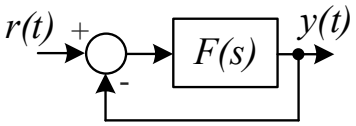

Figure 4.1.2 *A graphical representation of a Closed Loop System.*

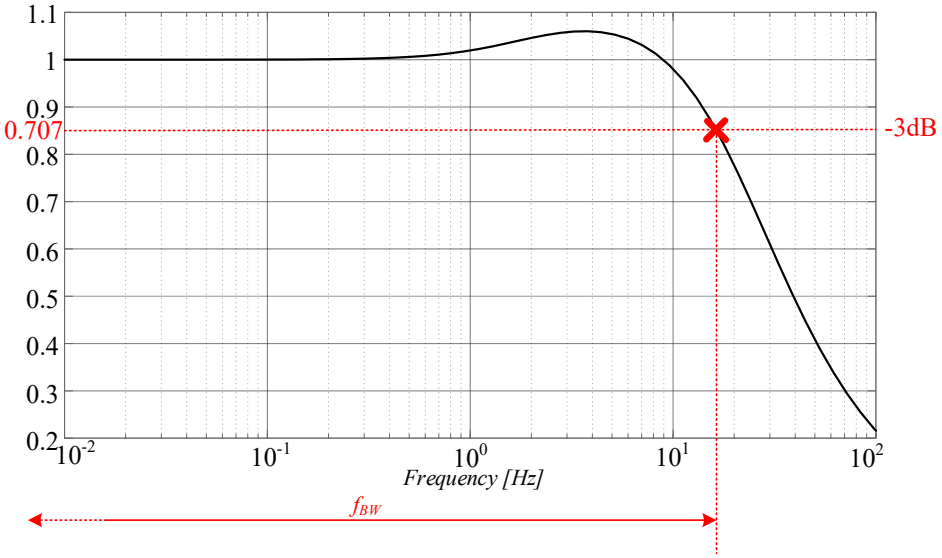

Figure 4.1.3 *Definitions of bandwidth* f_{BW}.

In addition to the bandwidth, another specification to be defined in the frequency domain concerns the concept of stability. In general, referring to Fig. 4.1.2, if the closed-loop transfer function *W(s)* is known, the stability of the system can be determined simply by inspecting the poles of the closed loop transfer function: if the closed loop poles values are all with negative real part the system *W(s)* is stable (Rooth- Hurwitz Criterion). However, a rigorous way to evaluate the stability condition of the closed loop function is the evaluation of the frequency response of the open loop transfer function based on the Nyquist Criterion which it is possible to measure the stability margins directly from two quantities defined as gain margin M_g and phase margin m_φ.

In general, the frequency domain specifications of a control system are the closed loop bandwidth and the gain and phase stability margins; in particular, these stability margins can be defined by means of a single vector stability margin.

4.1.3 Robustness

The robustness indicates the ability of a control system to guarantee stability and precision even in the presence of unknown variations of system model parameters []-[]. The unknow variations are usually divided into two groups:

- Structured uncertainties
- Unstructured uncertainties

The structured uncertainties are due to parameters well-defined within the model, an example, for an electric motor, are the stator resistance and the magnetizing inductance.

Unstructured uncertainties are perturbations due to non-modeled phenomena; in case of an electric motor, saturation, cross-saturation, non-linearity can be included among these types of phenomena that are often not modeled to simplify the dynamic analysis of the system.

Therefore, the robust stability of the closed-loop system provides both the stability of the system under normal conditions and the stability when perturbations are present in the open-loop function also.

There are several methods to provide an indication on the stability margins and robustness, but techniques of a graphic nature such as the Nyquist criterion or the roots locus provide some simple relationships.

4.1.4 Robustness by Nyquist Theory

A robustness metric is defined by the so-called vector stability margin (4.1.2) which represent the distance between the curve represented in Fig. 4.1.4, relative to the system of Fig. 4.1.2, and the critical point of coordinates *(-1, j0)*:

$$d = \min|1+F(j\omega)| \tag{4.1.2}$$

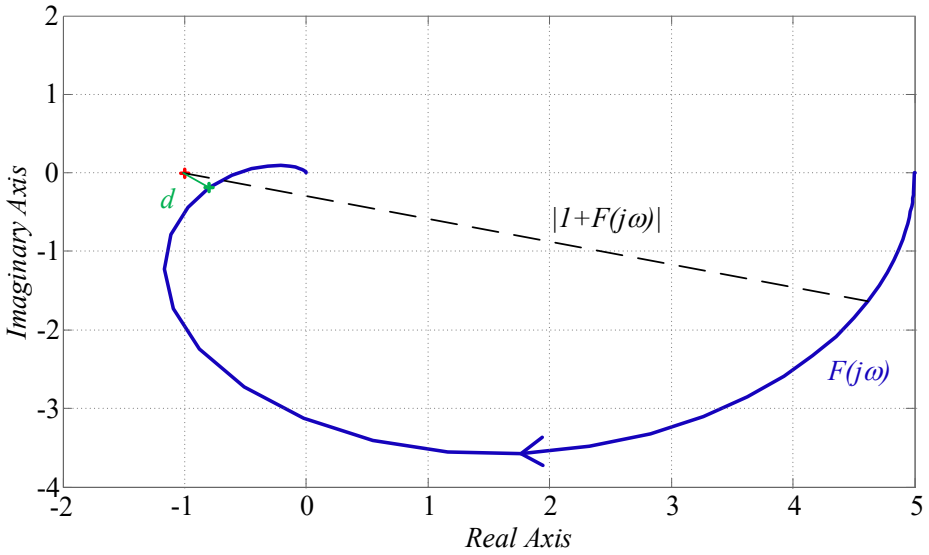

Figure 4.1.4 *Vector Margin Stability Condition.*

The vector stability margin gives a numerical value $0 < d < 1$, where 0 is an unstable system. Engineers familiar with the classic stability margin, gain margin and phase margin metrics can be easily derived from the Nyquist diagram, Fig. 4.1.5:

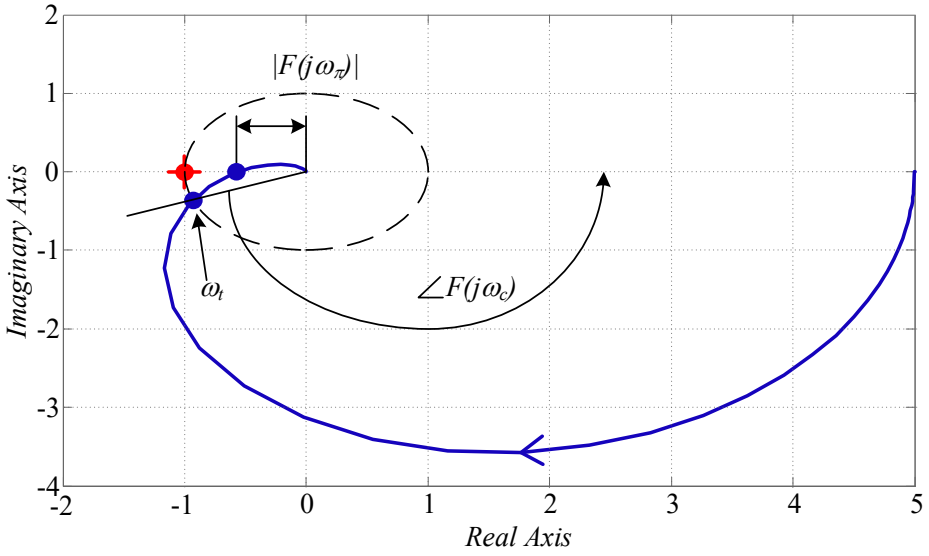

Figure 4.1.5 *Gain Margin and Phase Margin Definitions.*

- Gain Margin, M_g: is the maximum tolerable perturbation on the magnitude of the open loop transfer function before the closed loop system becomes unstable:

$$M_g = \frac{1}{|F(j\omega_\pi)|} \tag{4.1.3}$$

- Phase Margin, m_φ: is the maximum tolerable perturbation on the phase of the open-loop transfer function before the closed-loop system becomes unstable:

$$m_\varphi = \angle F(j\omega_c) + 180° \tag{4}$$

where ω_π is the angular frequency at the point $\angle F(j\omega_\pi) = 180°$; while ω_c is the angular crossover frequency, when the magnitude of the open loop function is unity $|F(j\omega_c)| = 1$.

Once these quantities have been defined, it is possible to write the stability margins in terms of gain margin and phase margin.

When the gain margin is considered:

- If $M_g > 1$ the closed loop system is stable.
- If $M_g < 1$ the closed loop system is unstable.

When the phase margin is considered:

- If $m_\varphi > 0$ the closed loop system is stable.
- If $m_\varphi < 0$ the closed loop system is unstable.

The same stability condition provided above can be evaluated by means of the Bode plot.

The conditions provided by the phase and gain margins are of a point nature, i.e. they concern the behavior of $F(j\omega)$ only in two points of its frequency response (ω_π e ω_c). The fulfillment of the requirements on the phase and gain margins does not generally guarantee that the Nyquist plot of $F(j\omega)$ remains between the frequencies ω_π and ω_c "sufficiently far" from the critical point $(-1, j0)$; for this reason is necessary to define the safety margins.

Considering the closed loop transfer function of the system model $F_m(s)$ and suppose that it is affected by uncertainty $\Delta F(s)$, such that the effective open loop function $F(s)$, defined in Fig. 4.1.2, is written:

$$F(s) = F_m(s) + \Delta F(s) \tag{4.1.5}$$

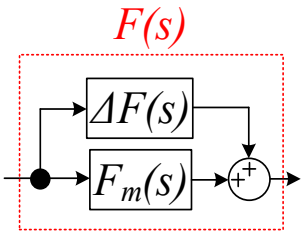

Figure 4.1.6 *Uncertainty on the open loop transfer function.*

Generally, the uncertainty function $\Delta F(s)$ is unknown but from some identification procedures it's possibly know its nature:

$$\Delta F(s): |F_m(j\omega)| \leq \gamma(j\omega) \leq \gamma \tag{4.1.6}$$

Since the information on the phase of the $\Delta F(s)$ is not generally available, the generic point in the Nyquist plot of $F(j\omega^*)$, at the frequency ω^*, is transformed into a circle centered in $F_m(j\omega^*)$ and with radius $\gamma(j\omega^*)$, Fig. 4.1.7:

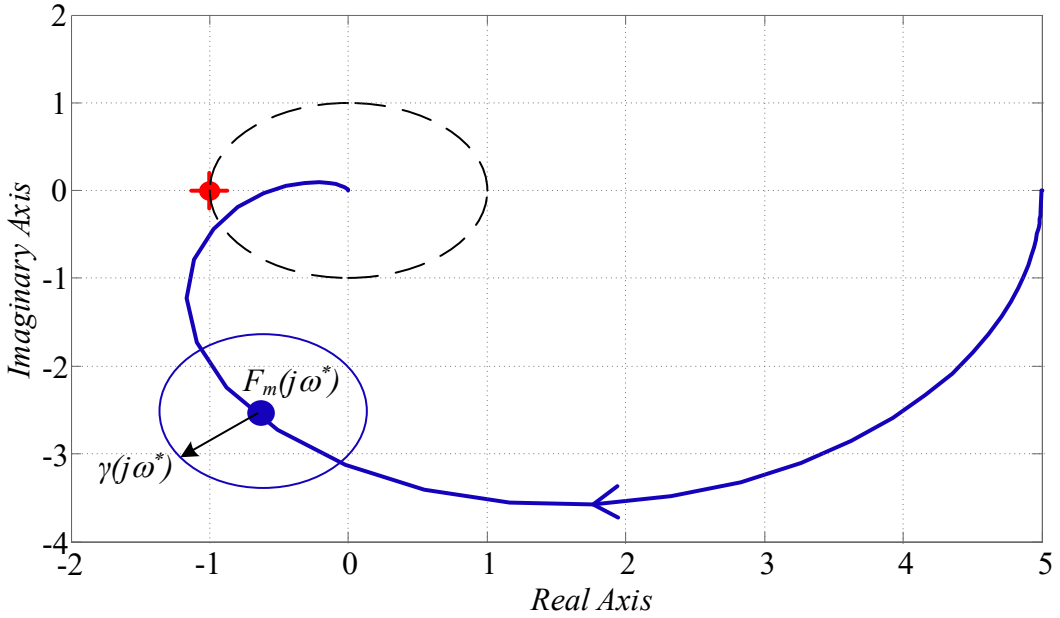

Figure 4.1.7 *Generic frequency point in Nyquist plot and uncertain circle.*

The corresponding point to $F(j\omega^*)$ can lie in any points inside on the circle with center $F_m(j\omega^*)$ and radius $\gamma(j\omega^*)$. In this way the Nyquist plot is transformed into an circles envelope:

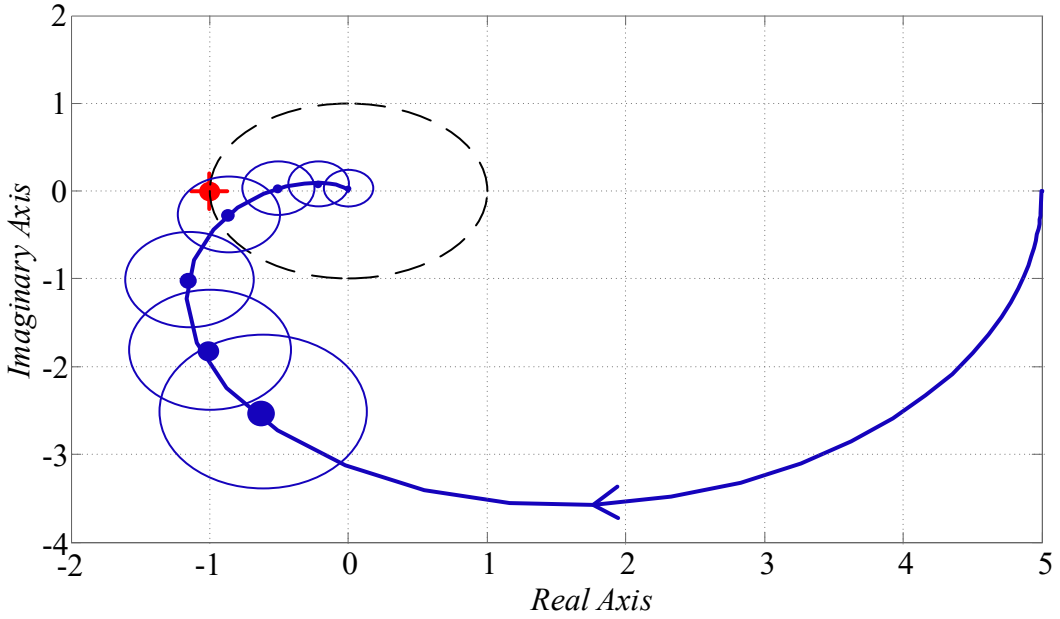

Figure 4.1.8 *Uncertain in Nyquist plot.*

The system is robust when the condition on the vector stability margin is:

$$|1 + F_m(j\omega^*)| > \gamma(j\omega^*) \tag{4.1.7}$$

Therefore, it's possible to define the so-called sensitivity function $S_m(s)$ whose magnitude is:

$$|S_m(j\omega^*)| = \frac{1}{|1 + F_m(j\omega^*)|} < \frac{1}{\gamma(j\omega^*)} \tag{4.1.8}$$

By defining with S_p the resonance peak of the sensitivity function $S_m(j\omega^*)$, then the resonance peak S_p represent a measure of the robust stability of the system. A low resonance peak S_p value, corresponding to a higher uncertainty rejection capability of the system:

$$S_p = < \frac{1}{\gamma} \tag{4.1.9}$$

However, the uncertainty is located in the transfer function of the plant system *P(s)*, Fig. 4.1.9, since the controller *C(s)* chosen and implemented by the designer is assumed to be free of uncertainties.

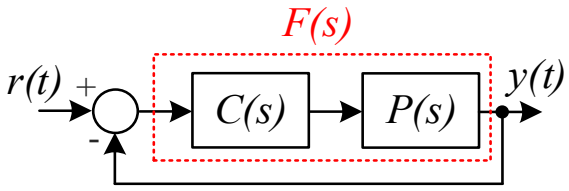

Figure 4.1.9 *Closed Loop Block Diagram: Controller and Plant.*

There are two rapresentation of uncertainty on plant *P(s)*: additive uncertainty and multiplicative uncertainty. In both cases, a transfer function of the plant model $P_m(s)$ is represented, while the uncertainty effects are represented by the function $\Delta P(s)$.

- ***Additive Uncertainty Model***

The additive uncertainty, Fig. 11, is represented by means the follow expression:

$$P(s) = P_m(s) + \Delta P(s) \qquad with \qquad |\Delta P(j\omega)| \leq \gamma_A(j\omega) \leq \gamma_A \tag{4.1.10}$$

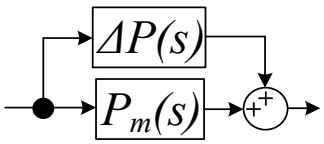

Figure 4.1.10 *Additive uncertainty model.*

In this way the open loop transfer function become:

$$F(s) = C(s)P(s) = C(s)[P_m(s) + \Delta P(s)] \tag{4.1.11}$$

The robust stability is given by the following expression:

$$|1 + F_m(j\omega^*)| > \gamma(j\omega^*) \tag{4.1.12}$$

$$|1 + F_m(j\omega^*)| > |C(j\omega^*)|\gamma_A(j\omega^*) \tag{4.1.13}$$

Where the sensitivity function is given:

$$|S_m(j\omega^*)| = \frac{1}{|1 + F_m(j\omega^*)|} < \frac{1}{|C(j\omega^*)|\gamma_A(j\omega^*)} \tag{4.1.14}$$

Also in this case, with a low resonance peak, of the sensitivity function magnitude, wider stability margins are obtained.

- ***Multiplicative Uncertainty Model***

The multiplicative uncertainty, Fig. 4.1.11, is represented by means the follow expression:

$$P(s) = P_m(s)[1+\Delta P(s)] \qquad with \qquad |\Delta P(j\omega)| \le \gamma_M(j\omega) \le \gamma_M \tag{4.1.15}$$

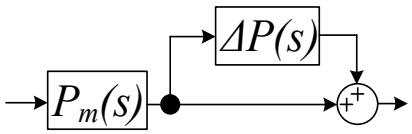

Figure 4.1.11 *Multiplicative Uncertainty Model.*

$$F(s) = C(s)P(s) = C(s)P_m(s)[1+\Delta P(s)] \tag{4.1.16}$$

The robust stability is given by the following expression:

$$|1 + F_m(j\omega^*)| > \gamma(j\omega^*) \tag{4.1.17}$$

$$|1 + F_m(j\omega^*)| > |C(j\omega^*)P_m(j\omega^*)|\gamma_M(j\omega^*) = |F_m(j\omega^*)|\gamma_M(j\omega^*) \tag{4.1.18}$$

From (4.1.18) the transfer function obtained is coincident with the closed loop function relating to the $F_m(j\omega^*)$:

$$|W_m(j\omega^*)| = \frac{|F_m(j\omega^*)|}{|1 + F_m(j\omega^*)|} < \frac{1}{\gamma_M(j\omega^*)} \tag{4.1.19}$$

Also in this case, the resonance peak W_p, of the closed loop transfer function $W_m(j\omega)$, is a measure of the robust stability of the system. A low resonance peak W_p value, corresponding to a higher rejection capability to multiplicative uncertainty from control system

- ***Safety Stability Margins***

Starting from the vector stability margin it is possible to define the relationships of the gain margin and phase margin, [7].

For additive uncertainty the stability margins (4.1.21) are linked to resonance peak of the sensitivity function $S_m(s)$:

$$S_m(s) = \frac{1}{1 + F_m(s)} \qquad \text{with} \qquad S_p \le \frac{1}{\gamma_A} = S_{max} \tag{4.1.20}$$

$$M_g \ge \frac{S_{max}}{S_{max} - 1} \qquad\qquad m_\varphi \ge 2arcsin\left(\frac{1}{2S_{max}}\right) \tag{4.1.21}$$

While, for multiplicative uncertainty the stability margins (4.1.23) are linked to resonance peak of the closed loop function $W_m(s)$:

$$W_m(s) = \frac{F_m(s)}{1 + F_m(s)} \qquad \text{with} \qquad W_p \le \frac{1}{\gamma_M} = W_{max} \tag{4.1.22}$$

$$M_g \geq 1 + \frac{1}{W_{max}} \qquad m_\varphi \geq 2arcsin\left(\frac{1}{2W_{max}}\right) \tag{4.1.23}$$

From these conditions, (4.1.22) and (4.1.23), it is possible to define a general condition on the robust stability margins in terms of gain margin and phase margin, in order to take into account simultaneously the additive and multiplicative uncertainty requirements:

$$M_g \geq \max\left(\frac{S_{max}}{S_{max} - 1}; 1 + \frac{1}{W_{max}}\right) \tag{4.1.24}$$

$$m_\varphi \geq \max\left(2arcsin\left(\frac{1}{2S_{max}}\right); 2arcsin\left(\frac{1}{2W_{max}}\right)\right) \tag{4.1.25}$$

4.1.5 Robustness by Root Locus

The roots locus is a particularly effective tool in the controller design when the specifications of the control system can be expressed directly by means the position of the closed-loop poles. The constraints of the poles position are:

- ***Damping Constraint*** $\xi = \overline{\xi}$

It allows to impose the closed loop poles in a particular region of the complex plane Fig. 4.1.12:

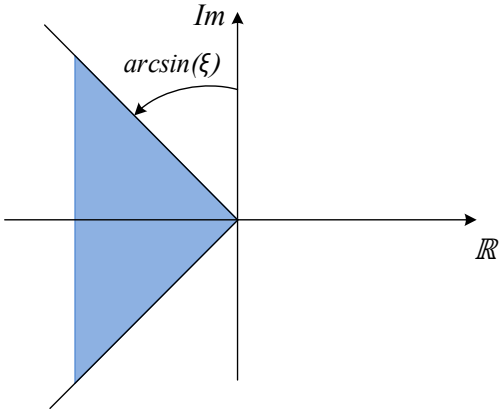

Figure 4.1.12 *Damping constraint in complex plane.*

The step time response of a stable continuous-time system can have oscillations depending on the damping value of the dominant poles. Furthermore, in a closed loop system, the damping value of the dominant poles is strongly related to the phase margin and therefore to the robust stability of the system. In fact, if the poles move along the negative real axis, i.e. $\xi = 1$ or $arcsin(\xi) = 0$, higher robustness of the system is achieved, i.e. higher phase margin and less oscillations are presented in the step response time [5]. By requiring that the damping value ξ be higher than a certain value $\overline{\xi}$, is equivalent to requiring that the transients of the system do not persist excessive oscillations before reaching the steady state condition.

Therefore, it is a constraint on the robustness and dynamic precision of the system. A typical damping value that guarantees robustness and dynamic precision is $\xi = 0.6$ which corresponds, for a second order system, at phase margin of about $m_\varphi = 60°$.

- ***Natural Angular Frequency Constraint*** $\omega_n = \bar{\omega}_n$

The constraint on the natural angular frequency corresponds to impose the closed loop poles outside of the circle of radius $\bar{\omega}_n$ and center of the origin, Fig. 4.1.13:

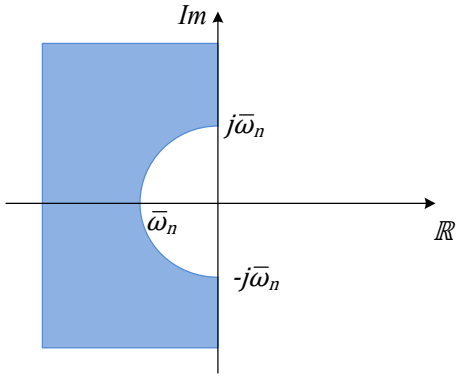

Figure 4.1.13 *Natural Angular Frequency Constraint in complex plane.*

In a closed loop system, the natural angular frequency of the dominant poles is approximately equal to the crossover angular frequency of the open loop system [5]-[6]. It is therefore strictly connected to the f_{BW} closed loop system bandwidth [5]-[6]. By requiring that the natural angular frequency value ω_n be higher than an assigned value $\bar{\omega}_n$, is equivalent to requiring that the bandwidth of the system has an upper limit.

Therefore, it is a constraint on the response speed of the system and is linked to the rise time and the bandwidth

- ***Maximum Settling Time Constraint*** $-\sigma \leq -\bar{\sigma}$

This constraint allow to imposing the real part of the absolute value of the closed loop poles is higher then an assigned value of the negative real axis $\bar{\sigma}$. This constraint corresponds to place the poles in the follow plane $s < -\bar{\sigma}$, Fig. 15.

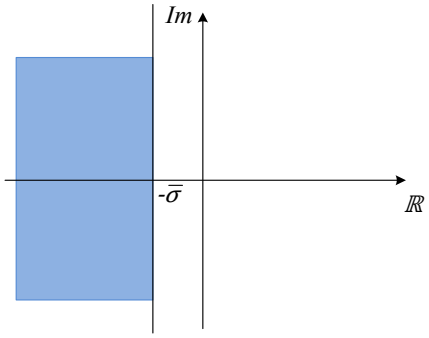

Figure 4.1.14 *Maximum Settling Time Constraint in complex plane.*

This condition is strictly linked to the settling time of the system and therefore to the steady-state error. Also, in this case it is a constraint on the speed of the system to reach the steady state condition.

4.1.6 Performances and Specifications of a Variable Speed Drive

Regarding an electric drive, in order to guarantees specific dynamic performances, by means of a vector control, the controllers used in the current, speed and position control loops must be properly designed [7].

Two of the main concerns when designing the controllers used in the various control loops of an electric drive are the dynamics and robustness of the closed loop systems which depend on the kind of application and operating point conditions. Generally, the controllers used in most motor drive applications are proportional-integral (PI) controllers, as their versatility and simplicity of design allows them to be used in the most motor drive applications.

In the speed controlled drives the only control loops to be designs are the current loop and the speed loop Fig. 4.1.15.

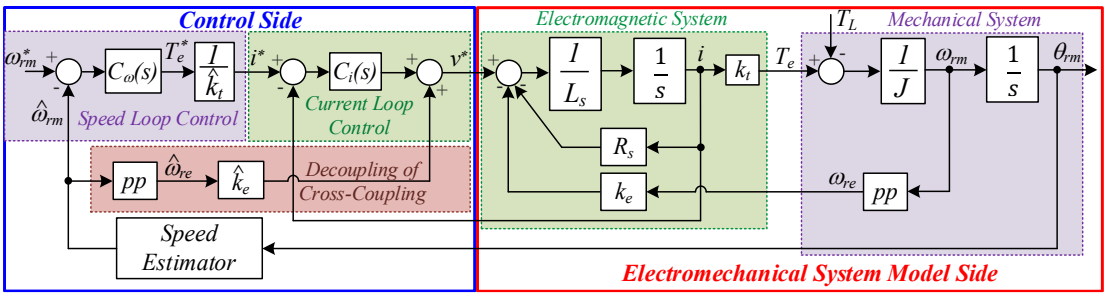

Figure 4.1.15 *Typical nested control structure: speed loop and current loop of a generic motor drive.*

As the current loop is intrinsically related to a faster dynamic due to the simplified ohmic-inductive equivalent circuit of a generic electric motor [8]-[9], Fig. 4.1.15, a higher current loop bandwidth is selected, generally ten times larger than the speed loop which is instead correlated to a slower dynamic related to the friction-inertial mechanical system, Fig. 4.1.15.

4.2 Current Control Loop Design

The torque control loop is the innermost loop of the electric drives. This control loop allows the motor to produce an electromagnetic torque that closely follows the torque reference that comes from the outermost motion control loops. In most drives, torque control is obtained indirectly from the current control. This paragraph will describe the calibration of the current loop using the zero-pole cancellation method and will be described in both continuous time domain and discrete time domain; in addition, it will be necessary to dedicate a sub-paragraph to the so-called decoupling of cross-coupling, which plays a key role in the calibration of the current loop using the zero-pole cancellation method.

Before introducing the current control loop design methodologies, it is necessary to define the mathematical model in *qd-axes* regarding the current loop for a generic IPM synchronous motor (4.2.1), from the block diagram of Fig.4.2.1.

$$\begin{bmatrix} v_q \\ v_d \end{bmatrix} = \begin{bmatrix} R_s & 0 \\ 0 & R_s \end{bmatrix} \begin{bmatrix} i_q \\ i_d \end{bmatrix} + \begin{bmatrix} pL_q & \omega_{re}L_d \\ -\omega_{re}L_q & pL_d \end{bmatrix} \begin{bmatrix} i_q \\ i_d \end{bmatrix} + \begin{bmatrix} \omega_{re}\lambda_{pm} \\ 0 \end{bmatrix} \tag{4.2.1}$$

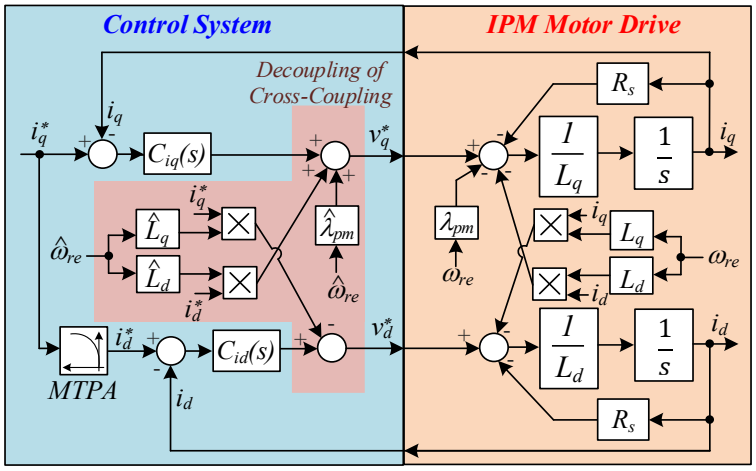

Figure 4.2.1 *Current Control Loop Block Diagram for an IPM Motor Drive.*

4.2.1 Decoupling of the Cross-Coupling

The so-called decoupling of cross-coupling is often performed in order to make the action of the current loop PI controllers more efficient in a synchronous reference frame, $C_{iq}(s)$ and $C_{id}(s)$ for the *qd-axes* currents respectively. The decoupling action of cross-coupling is carried out starting from the knowledge of the terms of cross-coupling related to the fluxes of *qd-axes*:

$$\begin{bmatrix} \lambda_q \\ \lambda_d \end{bmatrix} = \begin{bmatrix} L_q & 0 \\ 0 & L_d \end{bmatrix} \begin{bmatrix} i_q \\ i_d \end{bmatrix} + \begin{bmatrix} 0 \\ \lambda_{pm} \end{bmatrix} \tag{4.2.2}$$

As it is difficult and very expensive to carried out a direct measurement of the stator fluxes, often the voltage cross-coupling are computed as: $\hat{\omega}_{re}\left(\hat{L}_d\, i_d + \hat{\lambda}_{pm}\right)$ and $\hat{\omega}_{re}\hat{L}_q\, i_q$, for q-axis and d-axis respectively; therefore it is necessary to know the inductive coefficients and the permanent magnet flux, which in general must be estimated. Applying the decoupling of the cross-coupling, as shown in Fig. 4.2.1, at the equation system (4.2.1) and by assuming that the estimated speed is approximately equal to the real speed $\hat{\omega}_{re} \approx \omega_{re}$, the mathematical model of a IPM with the decoupling of the cross-coupling is given by:

$$\begin{bmatrix} v_q \\ v_d \end{bmatrix} = \begin{bmatrix} R_s & 0 \\ 0 & R_s \end{bmatrix} \begin{bmatrix} i_q \\ i_d \end{bmatrix} + \begin{bmatrix} pL_q & \omega_{re}\left(L_d - \hat{L}_d\right) \\ -\omega_{re}\left(L_q - \hat{L}_q\right) & pL_d \end{bmatrix} \begin{bmatrix} i_q \\ i_d \end{bmatrix} + \begin{bmatrix} \omega_{re}\left(\lambda_{pm} - \hat{\lambda}_{pm}\right) \\ 0 \end{bmatrix} \tag{4.2.3}$$

Based on the equation system (4.2.3), obtained by decoupling the cross-coupling, it shows that if the estimate of the parameters $\hat{L}_q$, $\hat{L}_d$, $\hat{\lambda}_{pm}$ are very similar to the actual values (4.2.4):

$$\hat{L}_q \approx L_q \qquad \hat{L}_d \approx L_d \qquad \hat{\lambda}_{pm} \approx \lambda_{pm} \tag{4.2.4}$$

Then it can be considered that the cross-coupling terms are canceled by the decoupling terms, and therefore the equations system (4.2.3) becomes:

$$\begin{bmatrix} v_q \\ v_d \end{bmatrix} = \begin{bmatrix} R_s & 0 \\ 0 & R_s \end{bmatrix} \begin{bmatrix} i_q \\ i_d \end{bmatrix} + \begin{bmatrix} pL_q & 0 \\ 0 & pL_d \end{bmatrix} \begin{bmatrix} i_q \\ i_d \end{bmatrix} \tag{4.2.5}$$

The equation system (4.2.5) shows that whenever the decoupling of the cross-coupling is carried out correctly, it is possible to consider a simple ohmic-inductive circuit for *qd-axes*, this allows to simplify the design of the current loop.

4.2.2 Continuous Time Current Control Loop Design

Starting from the equation system (4.2.5) referred to the block diagram of Fig. 4.2.1, it is possible to easily compute the Laplace transformation by replacing the derivative coefficient $p = d/dt$ with the Laplace coefficient s:

$$\begin{bmatrix} V_q(s) \\ V_d(s) \end{bmatrix} = \begin{bmatrix} R_s & 0 \\ 0 & R_s \end{bmatrix} \begin{bmatrix} I_q(s) \\ I_d(s) \end{bmatrix} + \begin{bmatrix} sL_q & 0 \\ 0 & sL_d \end{bmatrix} \begin{bmatrix} I_q(s) \\ I_d(s) \end{bmatrix} \tag{4.2.6}$$

From (4.2.6) it is possible to write the transfer functions of the current plant for each qd axes separately, as the effects of cross-coupling have been neglected as explained in sub-paragraph 4.2.1:

$$P_q(s) = \frac{I_q(s)}{V_d(s)} = \frac{1}{sL_q + R_s} \qquad P_d(s) = \frac{I_d(s)}{V_d(s)} = \frac{1}{sL_d + R_s} \tag{4.2.7}$$

Since the current plant transfer functions have the same shape for both axes, then in the subsequent analysis a generic ohmic-inductive circuit will be used as an example (4.2.8):

$$P_i(s) = \frac{I(s)}{V(s)} = \frac{1}{sL + R} \tag{4.2.8}$$

One of the most used methods for the PI controller design for the current loop control of an electric drive is the zero-pole cancellation method [8]-[9]. Although the zero-pole cancellation method simplify the closed-loop transfer function to a first order system, practically the position of the pole to be cancelled is not exactly known and furthermore, even assuming to know this pole precisely, it is not assured that the zero of the controller designs is exactly in the same position of the plant pole. In both cases, therefore, the zero-pole cancellation is not exactly perfect. If the zero-pole cancellation, as often happens, does not occur perfectly, ways are introduced in the time response of the closed-loop system that can worse the dynamic behavior of the system.

Fig. 4.2.2 shows the block diagram of a current control loop with a generic plant defined in (4.2.8)

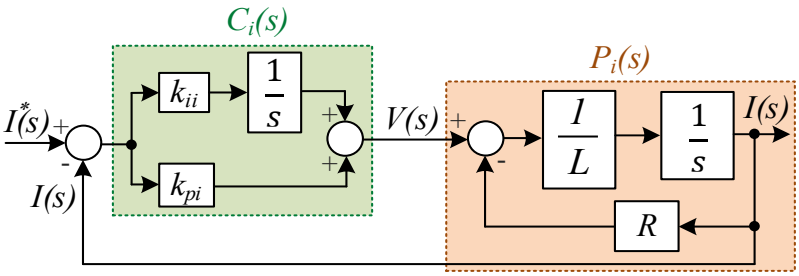

Figure 4.2.2 *Current Closed Loop Control.*

where $C_i(s)$ is the PI controller transfer function and k_{pi}, k_{ii} are the proportional and integral gains of the PI controller respectively:

$$C_i(s) = \frac{k_{pi}s + k_{ii}}{s} \tag{4.2.9}$$

$$F_i(s) = C_i(s)P_i(s) = \frac{k_{pi}s + k_{ii}}{s}\frac{1}{sL + R} = \frac{k_{ii}}{sR}\frac{\frac{k_{pi}}{k_{ii}}s + 1}{\frac{L}{R}s + 1} \tag{4.2.10}$$

Starting from the open loop transfer function $F_i(s)$ and rewritten in Bode forms (4.2.10) and (4.2.11) it is possible to cancel the pole of the plant $P_i(s)$ by means the controller zero $C_i(s)$:

$$\frac{k_{pi}}{k_{ii}} = \frac{L}{R} \tag{4.2.11}$$

In this way the open loop transfer function can be rewritten as:

$$F_i(s) = C_i(s)P_i(s) = \frac{k_{ii}}{sR} \tag{4.2.12}$$

By computing the closed loop transfer function (4.2.13) it is possible to note that the zero-pole cancellation method allow to simplify the closed loop transfer function $W_i(s)$ at a first order system, where the current loop bandwidth is selected in (4.2.14).

$$W_i(s) = \frac{F_i(s)}{1 + F_i(s)} = \frac{\frac{k_{ii}}{R}}{s + \frac{k_{ii}}{R}} \tag{4.2.13}$$

$$\frac{k_{ii}}{R} = 2\pi f_{BWi} \tag{4.2.14}$$

In conclusion, by imposing the current loop bandwidth in (4.2.14) and exploiting the zero-pole cancellation condition of (4.2.11), the PI controller gains are:

$$k_{ii} = 2\pi f_{BWi}R \qquad k_{pi} = 2\pi f_{BWi}L \tag{4.2.15}$$

The step response of the closed-loop transfer function $W_i(s)$ is shown in Fig. 4.2.3, where *500Hz* current loop bandwidth is selected with the corresponded ohmic-inductive circuit parameters $R = 0.84\Omega$ and $L = 4.7mH$. If during the current loop calibration, a correct decoupling of the cross-coupling phenomena is guaranteed and if the zero-pole cancellation method is performed correctly the closed loop step-time response coincides with a step-time response of a first order system, Fig. 4.2.3.

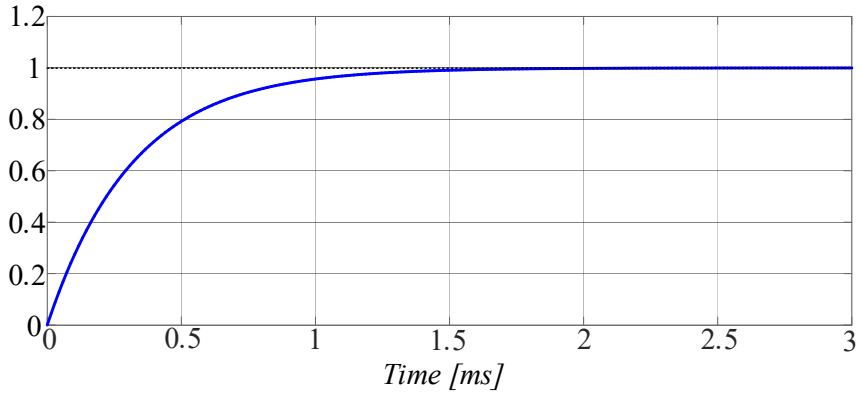

Figure 4.2.3 *Step Response of the current closed loop transfer function.*

The zero-pole map of the open and closed loop transfer functions is shown in Fig. 4.2.4, where it is possible to noted that the pole of the open loop function is well cancelled from the zero of the controller, i.e., the zero of the open loop function.

In fact, the closed loop function (4.2.13) is characterized by one pole associated to the desired closed loop bandwidth.

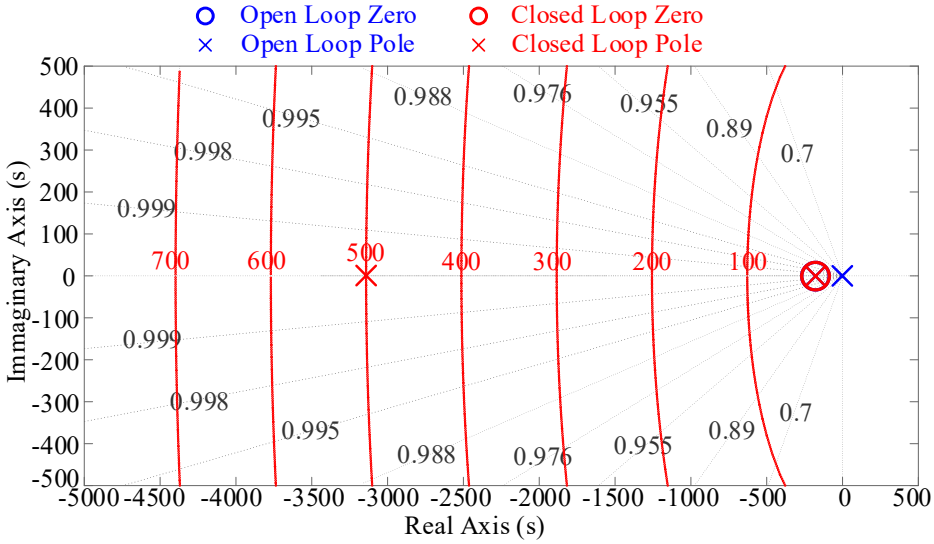

Figure 4.2.4 *Zero-Pole Map of the Current Loop.*

4.2.3 Discrete Time Current Control Loop Design

Fig. 4.2.5 shows the discrete time implementation of the current loop control. Inside the PI regulator, the continuous time integrator has been replaced by a simple accumulator. A latched voltage interface is present to model the effect of the digital control system on the motor voltage supply.

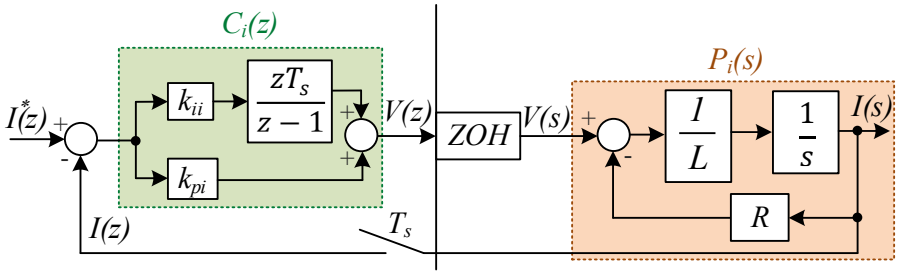

Figure 4.2.5 *Discrete Time Current Loop Control Block Diagram.*

As shown in Fig. 4.2.5 the plant $P_i(s)$ is a continuous time system but its information is acquired by the microcontroller, therefore it is necessary to transform the transfer function $P_i(s)$ in discrete time domain with a sampling time T_s by using the Z-transform. The unilateral Z-transform is the Laplace transform of an ideally sampled signal with the following substitution:

$$z = e^{sT_s} \tag{4.2.16}$$

where T_s is the acquisition time of the microcontroller.

There are several ways to approximate the Z-transform defined in (4.2.16): such as the Euler Forward, Euler Backward and the Tustin or Bilinear approximations [6], but when a physical signal is acquired by means of an ADC (analog digital converter), generally the continuous time information is sampled every T_s and is acquired by the microcontroller. Since the sample is acquired at each step, this type of acquisition is called Zero Order Hold (ZOH) and the impulse response transfer function is defined:

$$\mathcal{L}(ZOH) = \frac{1 - e^{-sT_s}}{s} = \frac{1 - z^{-1}}{s} \tag{4.2.17}$$

where $z^{-1} = e^{-sT_s}$ is defined as delay.

A generic transfer function $H(s)$ that include the ZOH is given:

$$H(z) = (1-z^{-1})\,\mathcal{Z}\left[\frac{H(s)}{s}\right] \tag{4.2.18}$$

Applying the (4.2.18) in (4.2.8) and placing $\tau = R/L$ obtain:

$$P_i(z) = \frac{(1 - e^{-T_s/\tau})\,z^{-1}}{R\,(1 - e^{-T_s/\tau}\,z^{-1})} = \frac{(1 - e^{-T_s/\tau})}{R\,(z - e^{-T_s/\tau})} \tag{4.2.19}$$

While the transfer function of the PI controller can be rewritten as:

$$C_i(z) = k_{pi} + \frac{k_{ii}\,T_s}{1 - z^{-1}} = (k_{pi} + k_{ii}\,T_s)\,\frac{z - \dfrac{k_{pi}}{k_{pi} + k_{ii}\,T_s}}{z - 1} = K_i\,\frac{z - \delta_i}{z - 1} \tag{4.2.20}$$

where the controller gains are defined as:

$$K_i = (k_{pi} + k_{ii}\,T_s) \qquad \delta_i = \frac{k_{pi}}{k_{pi} + k_{ii}\,T_s} \tag{4.2.21}$$

Now, it is possible to compute the open loop transfer function $F_i(z)$:

$$F_i(z) = C_i(z)\, P_i(z) = \frac{K_i\,(1 - e^{-T_s/\tau})}{R(z - 1)}\,\frac{z - \delta_i}{z - e^{-T_s/\tau}} \tag{4.2.22}$$

By cancelling the pole of the plant system $P_i(z)$ through the zero of the controller $C_i(z)$ this equation (4.2.23) is obtained:

$$\delta_i = e^{T_s/\tau} \tag{4.2.23}$$

Starting from the zero-pole cancellation condition (4.2.23) the open loop transfer function can be semplified in (4.2.24):

$$F_i(z) = C_i(z)\, P_i(z) = \frac{K_i\,(1 - e^{-T_s/\tau})}{R(1 - z)} \tag{4.2.24}$$

Then, the closed loop transfer function $W_i(z)$ is given:

$$W_i(z) = \frac{F_i(z)}{1 + F_i(z)} = \frac{K_i\,(1 - e^{-T_s/\tau})}{R(1 - z) + K_i\,(1 - e^{-T_s/\tau})} \tag{4.2.25}$$

Starting from the first order closed loop transfer function (4.2.25) it is possible to impose the bandwidth:

$$1 - \frac{K_i\,(1 - e^{-T_s/\tau})}{R} = e^{-2\pi f_{BWi} T_s} \tag{4.2.26}$$

Finally, in according to the zero-pole cancellation condition (4.2.23) and the bandwidth condition (4.2.26), the PI controller gains are obtained:

$$k_{pi} = R\,\frac{e^{-T_s/\tau}}{1 - e^{-T_s/\tau}}\left(1 - e^{-2\pi f_{BWi} T_s}\right) \qquad k_{ii} = \frac{R}{T_s}\left(1 - e^{-2\pi f_{BWi} T_s}\right) \tag{4.2.27}$$

Generally, both the continuous time and discrete time designing, a rule of thumb is to select the current loop bandwidth between 100 Hz e 1000 Hz [10]-[11].

In Figs. 4.2.6 and 4.2.7 the step time response of the current closed loop transfer function $W_i(z)$ and its discrete time zero-pole map.

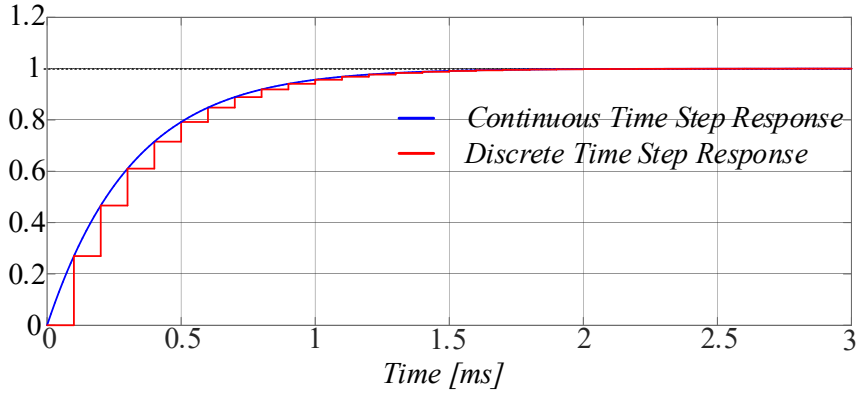

Figure 4.2.6 *Step Time Response Comparison between the Continuous Time and Discrete Time closed loop transfer function.*

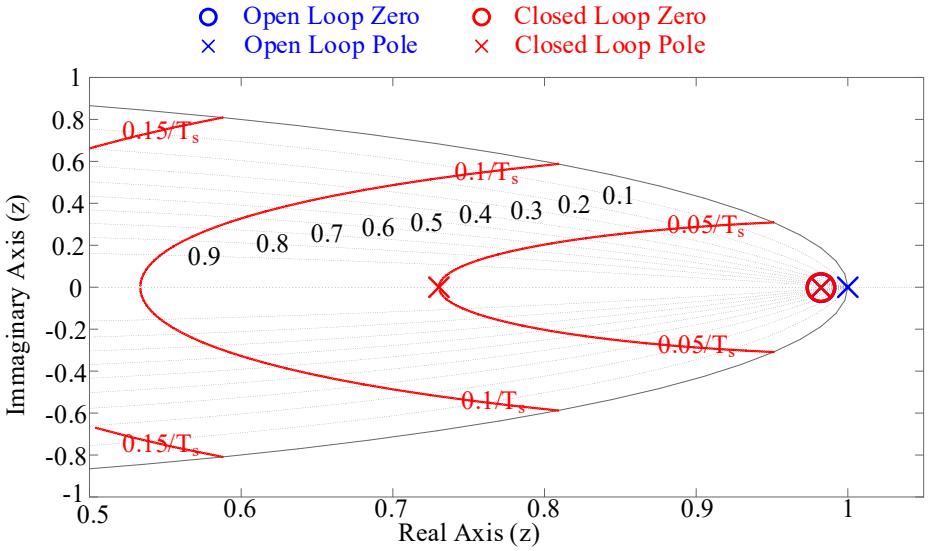

Figure 4.2.7 *Discrete Time Zero-Pole Map.*

4.3 Speed Control Loop Design

In those electric drives where speed control is required a speed control loop is present outermost than the current loop, that allow to maintain the reference speed value whatever the load torque. The electric drives that provide speed control are called Variable Speed Drives (VSD) or Variable Frequency Drives (VFD), where the Maximum-Torque-per-Ampere (MTPA) and Flux Weakening (FW) algorithms are typically implemented. However, both in MTPA (until rated speed) and in FW (until allowed maximum speed) a good dynamic performance and allowed torque load rejection must be provided by the speed control loop [12]-[13].

This paragraph will describe the speed control loop tuning using two methods: the pole-placement method and the Nyquist stability theory. In particular, the pole-placement method will be defined in both continuous and discrete time domain, while the tuning according to Nyquist theory will be done only in continuous time domain.

In Fig. 4.1.15 a generic speed control loop structure is shown, where the nested current control loop can be neglected by assuming the follow *"mechatronic assumption"*: the current loop bandwidth f_{BWi} is much larger with respect to the speed loop bandwidth $f_{BW\omega}$, generally $f_{BWi} = 10\, f_{BW\omega}$; therefore, it is possible to neglect the dynamics of the current loop as it is much faster than the dynamic of the speed loop, Fig. 4.3.1:

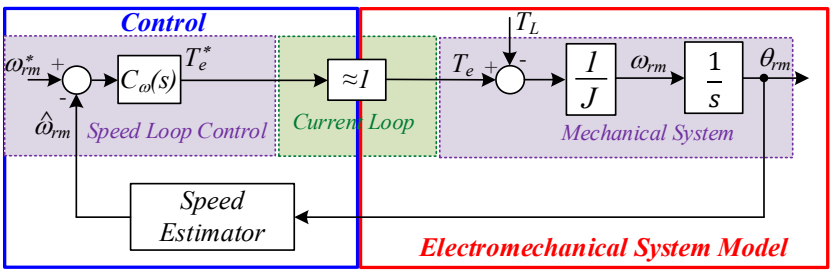

Figure 4.3.1 *Speed Closed Loop Control*

In this analysis it is assumed that the physical system is a rigidly coupled mechanical system, thus zero damping.

$$\begin{cases} T_e - T_L = J\dfrac{d\omega_{rm}}{dt} \\ \omega_{rm} = \dfrac{d\theta_{rm}}{dt} \end{cases} \tag{4.3.1}$$

Another aspect that cannot be neglected in Fig. 4.3.1 is that the control system includes the speed estimator. Generally, the presence of the estimator, as we will see in the following paragraphs, modified the speed closed loop control transfer function and introduces a delay on the estimated speed that leads to a worsen dynamic performance of the speed loop. The effects due to the presence of the speed estimator will be analyzed in the following paragraph.

4.3.1 Continuous Time Speed Control Loop Design with Pole Placement

Based on the above hypotheses, the speed control loop block diagram, with includes the speed controller $C_\omega(s)$ and the mechanical system $P_\omega(s)$, as shown in Fig. 4.3.2:

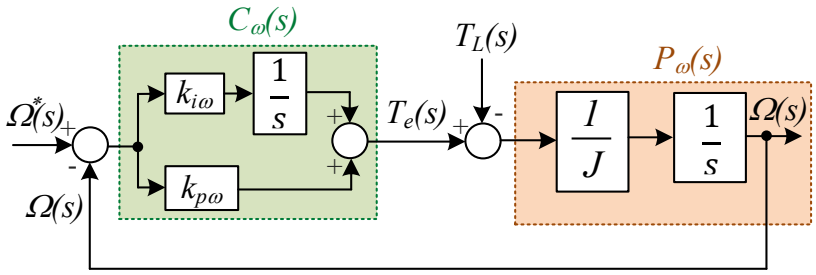

Figure 4.3.2 *Continuous Time Speed Control Loop*

$$P_\omega(s) = \frac{1}{sJ} \tag{4.3.2}$$

$$C_\omega(s) = \frac{k_{p\omega}\, s + k_{i\omega}}{s} \tag{4.3.3}$$

where $k_{p\omega}$ and $k_{i\omega}$ are the proportional and integral gains of the speed controller respectively. The open loop and closed loop transfer functions $F_\omega(s)$ are given:

$$F_\omega(s) = C_\omega(s)P_\omega(s) = \frac{k_{p\omega}\, s + k_{i\omega}}{s^2 J} \tag{4.3.4}$$

$$W_\omega(s) = \frac{F_\omega(s)}{1 + F_\omega(s)} = \frac{k_{p\omega}\, s + k_{i\omega}}{s^2 J + k_{p\omega}\, s + k_{i\omega}} \tag{4.3.5}$$

Starting from the denominator of (4.3.5), the poles can be placed in order to all have a real negative part. In particular, as it is a second-degree polynomial, two poles will be positioned. The poles placement must be done, as seen in sub-paragraph 4.1.5, trying to avoid unwanted oscillations during the step response, to avoid this it is good practice to position the poles directly on the real negative axis (therefore with unitary damping) in order to obtain a step response as overdamped as possible [5]-[6]; moreover, if the farthest pole $p_{1\omega}$, which is related to fast dynamics, is ten times larger than the closest pole $p_{2\omega}$,

which is related to slow dynamics, an excellent command tracking performance and stability margin, with a phase margin roughly equal to 85 ° [5]-[6].

As the frequency of the farthest pole is approximately equal to the closed loop bandwidth, then we can define:

$$p_{1\omega} = 2\pi f_{BW\omega} \qquad p_{2\omega} = \frac{p_{1\omega}}{10} \tag{4.3.6}$$

$$s^2 + \frac{k_{p\omega}}{J} s + \frac{k_{p\omega}}{J} = s^2 + (p_{1\omega} + p_{2\omega})\, s + p_{1\omega}\, p_{2\omega} \tag{4.3.7}$$

Starting from (3.4.7) is very easy to extract the speed controller gains.

$$k_{p\omega} = (p_{1\omega} + p_{2\omega})\, J \qquad k_{i\omega} = p_{1\omega}\, p_{2\omega}\, J \tag{4.3.8}$$

In Fig. 4.3.3 is shown the step time response of the closed speed loop transfer function $W_\omega(s)$, where $20Hz$ speed loop bandwidth is selected with the corresponded mechanical inertia $J = 0.0021 kgm^2$. It can be noted that from the conditions defined in (4.3.6), a step response equivalent to that of an overdamped second order system is obtained, characterized by a response time that depends on the chosen bandwidth and by a limited overshoot.

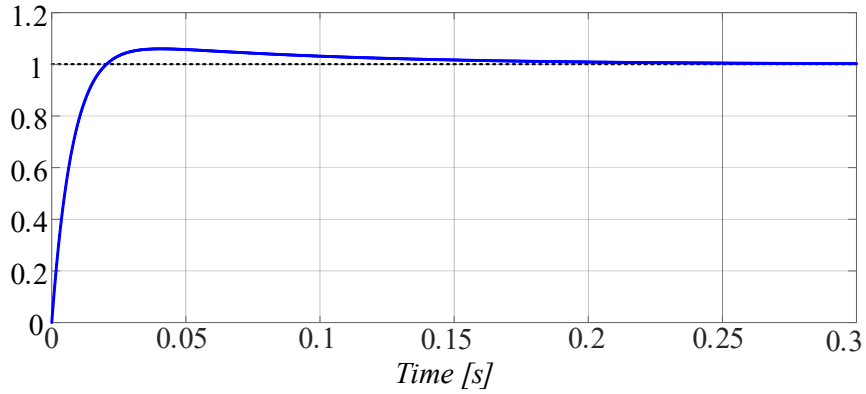

Figure 4.3.3 *Speed Loop Step Response.*

In Fig. 4.2.4 is shown the zero-pole map of the open and closed speed loop transfer functions, where the closed loop fastest pole is roughly near to the closed loop bandwidth while the closed loop slower pole is a quite near to the zero, in fact, the step-time response of the Fig. 4.3.3 it is similar to a first order step-time response.

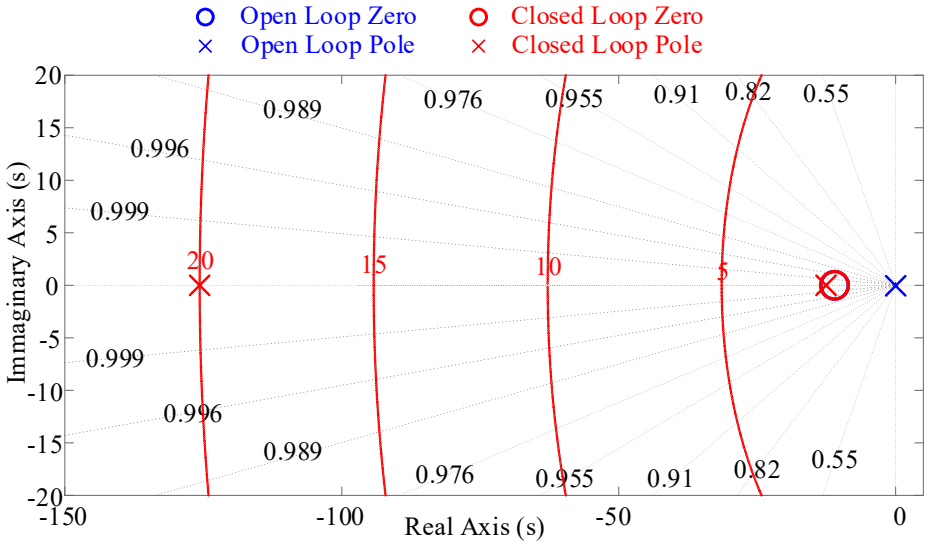

Figure 4.3.4 *Continuous Time Zero-Pole Map*

4.3.2 Continuous Time Speed Control Loop Design with Nyquist Theory

Another way to tune the control speed closed loop is based on the Nyquist stability theory, defined in the sub-paragraph 4.14.

Starting from the control speed closed loop system of Fig. 4.3.2 it is possible to define the specifications on the open loop transfer function $F_\omega(s)$ in order to guarantee stability and robustness on the closed loop transfer function $W_\omega(s)$.

As already defined in sub-paragraph 4.1.6, the dynamic performances of a closed loop system are provided by the follow specifications: the closed loop bandwidth, which is linked to the quick response of the closed loop system, and the phase margin, which represents one of the many robustness metrics of the system.

Generally, the bandwidth of the speed control loop $f_{BW\omega}$ can be selected from 10 to 100 Hz [10]-[11]; the phase margin will be chosen by means on the desired dynamic performance of the closed loop time step response, in terms of overshoot and transient oscillations [5]-[6]; typically, a good robustness performance is guaranteed by a phase margin $m_\varphi \geq 60°$; in order to obtain excellent robustness and to cancel the transient oscillations, it is good practice to place the closed loop poles of $W_\omega(s)$ on the negative real axis, that is equivalent to impose the phase margin $m_\varphi \geq 75°$ [5]-[6].

According to the Nyquist's theory, the stability conditions of the closed-loop function $W_\omega(s)$ with unitary feedback can be done by studying the open-loop function $F_\omega(s)$ [5]-[6]; therefore, after defining the desired speed loop specifications, it is possible to write the relationships (4.3.9) that allow to determine the PI speed controller gains [5]-[6], [14].

$$|F_\omega(j\omega_c)| = 1 \qquad \angle F_\omega(j\omega_c) = m_\varphi - 180° \tag{4.3.9}$$

where ω_c is the crossover frequency of the open loop function $F_\omega(s)$. It is shown that for a second order system the crossover frequency is approximately equivalent to the closed loop bandwidth frequency [5]-[6]:

$$f_{BW} \approx f_c \tag{4.3.10}$$

therefore, by setting the speed closed loop bandwidth $f_{BW\omega}$ and the phase margin m_φ:

$$|F_\omega(j\omega_c)| = \frac{\sqrt{\omega^2_{BW\omega}\, k^2_{p\omega} + k^2_{i\omega}}}{\omega^2_{BW\omega}\, J} = 1$$
$$\angle F_\omega(j\omega_c) = atan\left(\frac{\omega_{BW\omega}\, k_{p\omega}}{k_{i\omega}}\right) - 180° = m_\varphi - 180° \qquad (4.3.11)$$

Starting from the previously expressions (4.3.11), the PI speed controller gains are given:

$$k_{i\omega} = \frac{\omega^2_{BW\omega}\, J}{\sqrt{\omega^2_{BW\omega}\, \tau^2_{i\omega} + 1}} \qquad k_{p\omega} = k_{i\omega}\, \tau_{i\omega} \qquad \tau_{i\omega} = \frac{tan\,(m_\varphi)}{\omega_{BW\omega}} \qquad (4.3.12)$$

where $\tau_{i\omega}$ is the integral constant time of the PI speed controller.

In Fig. 28 the time step response of the closed-loop transfer function $W_\omega(s)$ is shown with the same closed loop bandwidth and mechanical inertia used in sub-paragraph 4.3.1. A comparison between the closed loop function obtained by pole-placement method and by choosing a phase margin of 85 ° is equivalent to choosing the two poles of $W_\omega(s)$ one decade distant from each other (4.3.6).

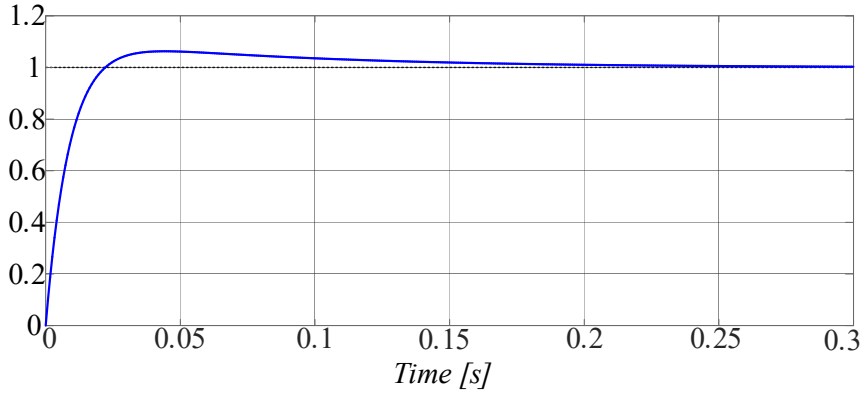

Figure 4.3.5 *Time Step Response of the Closed Speed Loop Transfer Function*

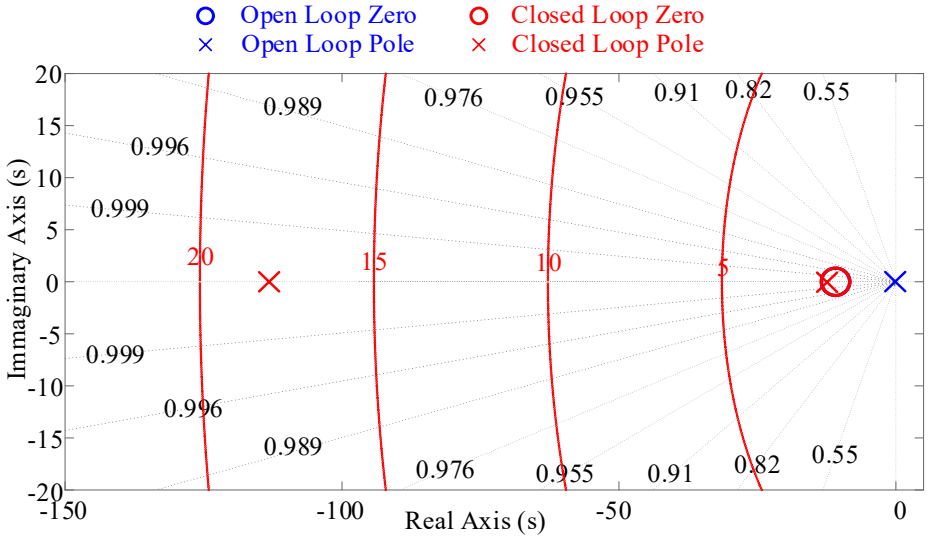

Figure 4.3.6 *Zero-Pole Maps of the Speed Loop Control System*

4.3.3 Discrete Time Speed Control Loop Design with Pole Placement

The block diagram of the speed control loop is shown in Fig. 4.3.7, where the speed controller is modeled in discrete time domain and the mechanical plant in continuous time domain. In order to model the effect of the digital control on the mechanical system, the speed controller will be connected to the mechanical system through a "latched" torque interface.

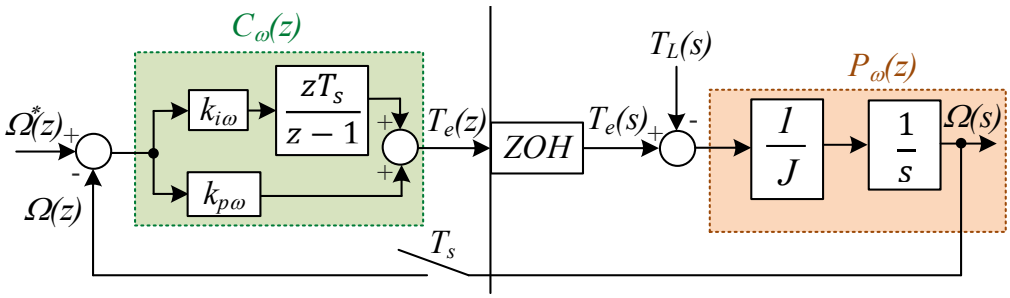

Figure 4.3.7 *Discrete Time Speed Loop Control Block Diagram.*

The discrete time domain transfer function of the mechanical system is given by (4.3.13):

$$P_\omega(z) = \frac{T_s}{J}\frac{1}{z-1} \tag{4.3.13}$$

while, the integral part of the PI controller is modeled as a discrete accumulator:

$$C_\omega(z) = k_{p\omega} + \frac{k_{i\omega}\,T_s\,z}{z-1} = K_\omega\frac{z-\delta_\omega}{z-1} \tag{4.3.14}$$

where:

$$K_\omega = (k_{p\omega} + k_{i\omega}\,T_s) \qquad \delta_\omega = \frac{k_{p\omega}}{k_{p\omega} + k_{i\omega}\,T_s} \tag{4.3.15}$$

The discrete time domain open loop $F_\omega(z)$ and closed loop $W_\omega(z)$ transfer functions are given by:

$$F_\omega(z) = C_\omega(z)\,P_\omega(z) = \frac{T_s}{J}\frac{K_\omega\,(z-\delta_\omega)}{(z-1)^2} = \frac{K'_\omega\,(z-\delta_\omega)}{(z-1)^2} \tag{4.3.16}$$

with $K'_\omega = \frac{T_s}{J}K_\omega$

$$W_\omega(z) = \frac{F_\omega(z)}{1+F_\omega(z)} = \frac{K'_\omega\,(z-\delta_\omega)}{z^2 + (K'_\omega - 2)\,z + (1 - K'_\omega\,\delta_\omega)} \tag{4.3.17}$$

According to the pole-placement method it is possible to place the closed loop poles by fixing the fastest pole $p_{1\omega}$ as the closest to the closed loop bandwidth and the slowest pole $p_{2\omega}$ with a frequency ten times smaller than the frequency of $p_{1\omega}$:

$$p_{1\omega} = e^{-2\,\pi f_{BW\omega}\,T_s} \qquad p_{2\omega} = e^{-(2\,\pi f_{BW\omega}\,T_s)/10} \tag{4.3.18}$$

In this way the $C_\omega(z)$ speed controller gains are obtained:

$$k_{p\omega} = \frac{J}{T_s}(1 - p_{1\omega}\, p_{2\omega}) \qquad k_{i\omega} = \frac{J}{T^2_s}(2 - p_{1\omega} - p_{2\omega}) - \frac{k_{p\omega}}{T_s} \tag{4.3.19}$$

In Figs. 4.3.8-4.3.9 the time step responses of the continuous time and discrete time closed loop transfer function and the zero-pole map are shown, respectively.

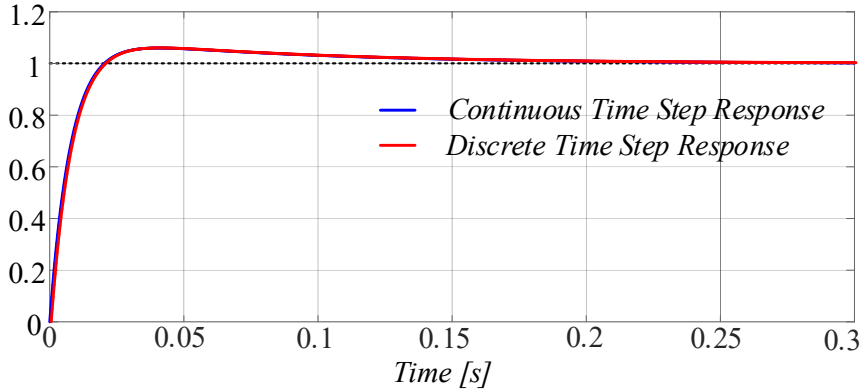

Figure 4.3.8 *Step Time Response Comparison between the Continuous Time and Discrete Time closed loop transfer function.*

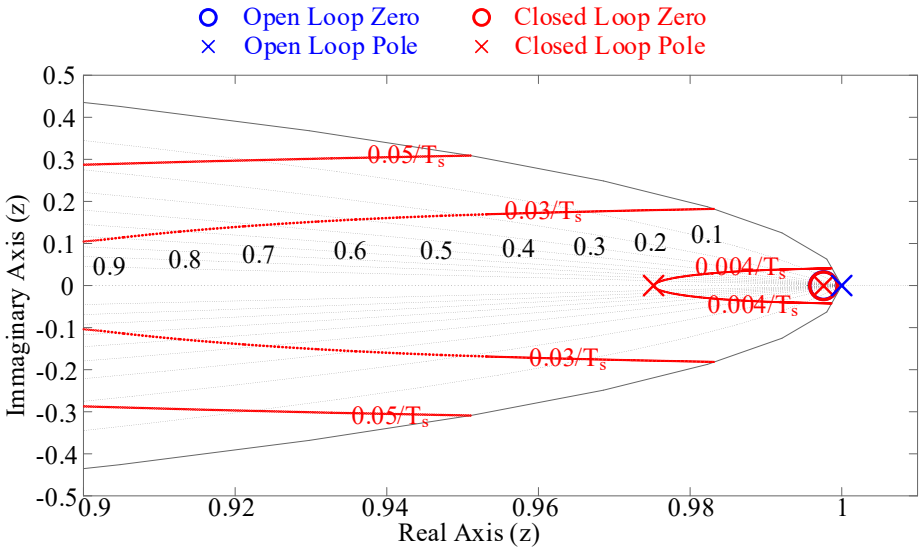

Figure 4.3.9 *Discrete Time Domain Zero-Pole Map.*

4.4 VTO Speed Estimator Tuning

In this sub-paragraph the tuning of the VTO will be introduces which is considered a model-based speed estimator and thus its calibration is easy and also useful in the following studies.

4.4.1 Continuous Time Design of Vector Tracking Observer

Fig. 4.4.1 displays the linearized model of the VTO:

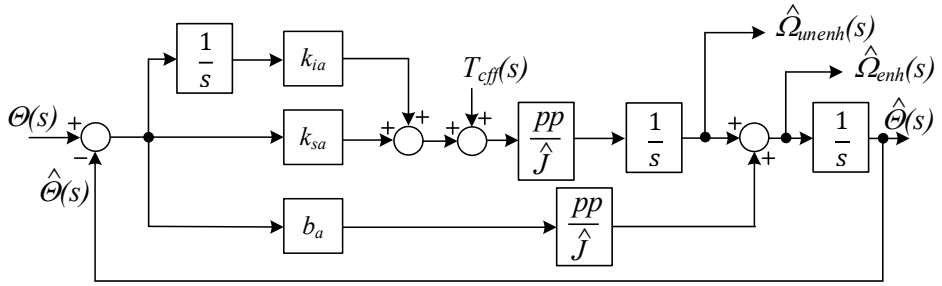

Figure 4.4.1 *Linearized VTO block diagram.*

In order to simplify the VTO tuning procedure, the term $pp/\hat{J}$ can be included into parameters k_{ia}, k_{sa}, b_a and in the feed-forward term:

$$k_1 = \frac{pp}{\hat{J}} b_a \qquad k_2 = \frac{pp}{\hat{J}} k_{sa} \qquad k_3 = \frac{pp}{\hat{J}} k_{ia} \qquad k_{cff} = \frac{pp}{\hat{J}} \tag{4.4.1}$$

To simplify the mathematical analysis, the feed-forward input of the command torque T_{cff} is set to zero, i.e. the observer VTO becomes a vector tracking state filter (VTSF).

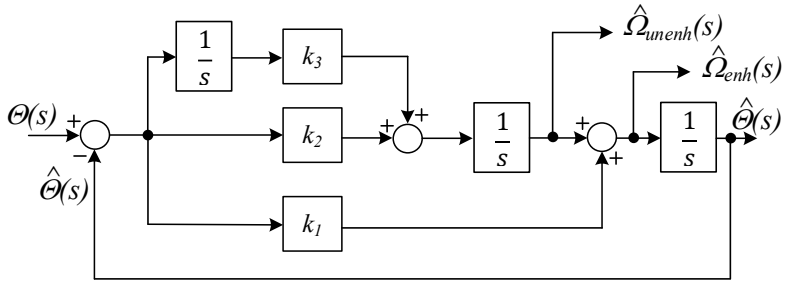

Figure 4.4.2 *Block diagram of the Vector Tracking State Filter.*

The open loop $F_{VTSF}(s)$ and closed loop $W_{VTSF}(s)$ transfer function of the linearized VTSF are respectively:

$$F_{VTSF}(s) = \frac{k_1 s^2 + k_2 s + k_3}{s^3} \tag{4.4.2}$$

$$W_{VTSF}(s) = \frac{k_1 s^2 + k_2 s + k_3}{s^3 + k_1 s^2 + k_2 s + k_3} \tag{4.4.3}$$

The tuning of the VTSF can be accomplished by exploiting the pole-placement method on the closed-loop transfer function. Since the characteristic polynomial is a third order

expression (4.4.5), three poles must be positioned (4.4.4): the faster pole p_1 has a frequency approximately equal to the close bandwidth of the VTSF, the pole p_2 which is ten time smaller then the pole p_1 and the pole p_3 chosen time smaller then the pole p_2:

$$p_1 = 2\pi f_{BWvto} \qquad p_2 = \frac{p_1}{10} \qquad p_3 = \frac{p_2}{10} \tag{4.4.4}$$

$$s^3 + k_1 s^2 + k_2 s + k_3 = (s + p_1)\,(s + p_2)\,(s + p_3) \tag{4.4.5}$$

The VTSF gains are:

$$k_1 = (p_1 + p_2 + p_3) \qquad k_1 = (p_1 p_2 + p_2 p_3 + p_3 p_1) \qquad k_1 = p_1 p_2 p_3 \tag{4.4.6}$$

In this way, by setting the closed loop bandwidth f_{BWvto} of the VTO it is possible to exploit the relationship (4.4.4) in order to compute the VTO gains (4.4.6).

The step-time response of the closed-loop transfer function $W_{VTSF}(s)$ is shown in Fig, 4.4.3 where $f_{BWvto} = 300Hz$ and $\hat{J} = 0.0021\ kgm^2$ are considered.

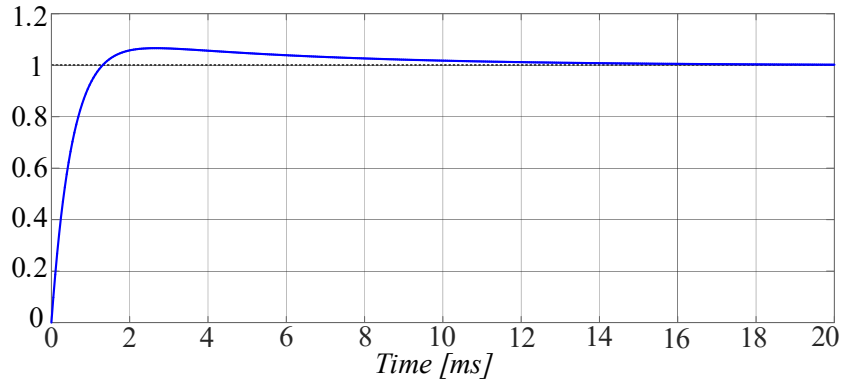

Figure 4.4.3 *Time Step Response of the VTSF Closed Loop Transfer Function.*

In Fig. 4.4.4, the zero-pole map of the VTO open and closed loop transfer functions highlights the one tenth distance between the closed loop poles; furthermore, it would be noted that the step-time response of the closed loop transfer function of the VTSF is a overdamped second order system, in fact each zeros of the closed loop function is respectively near with the closed loop pole while the fastest pole is alone.

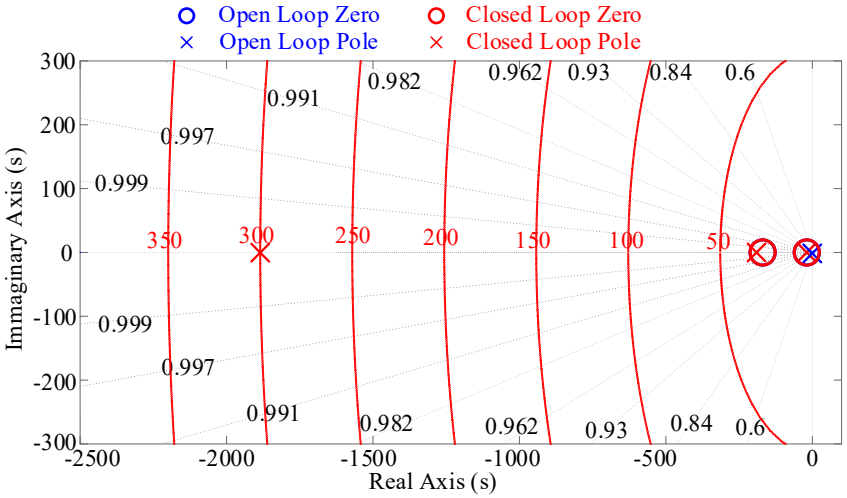

Figure 4.4.4 *Zero-Pole Map of the VTSF.*

4.4.2 Discrete Time Design of the Vector Tracking Observer

Fig. 4.4.5 shows the discrete time model of the operating point of the VTO, topologically equivalent to that shown in Fig. 4.4.1:

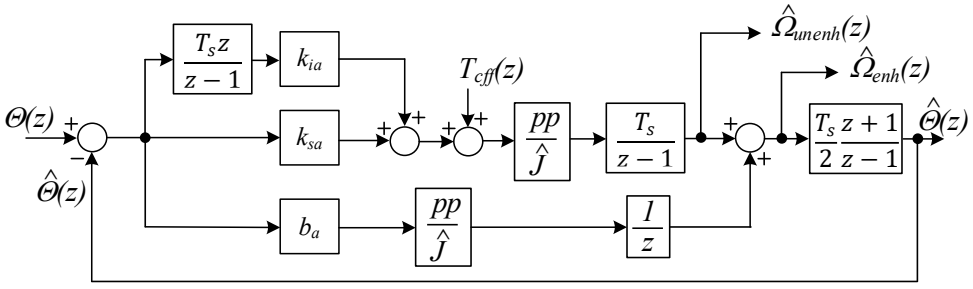

Figure 4.4.5 *Discrete Time Linearized VTO Block Diagram.*

In order to simplify the mathematical computation, it is possible to define, as done for the continuous time case, the following parameters which this time also depend on the sampling time:

$$k_1 = \frac{T_s}{2}\frac{pp}{\hat{J}}b_a \qquad k_2 = \frac{T_s^2}{2}\frac{pp}{\hat{J}}k_{sa} \qquad k_3 = \frac{T_s^3}{2}\frac{pp}{\hat{J}}k_{ia} \qquad k_{cff} = \frac{T_s^2}{2}\frac{pp}{\hat{J}} \tag{4.4.7}$$

However, since the feedforward term has no influence on the closed-loop observer pole-placement, it can be neglected in the small signal model used, Fig. 4.4.6:

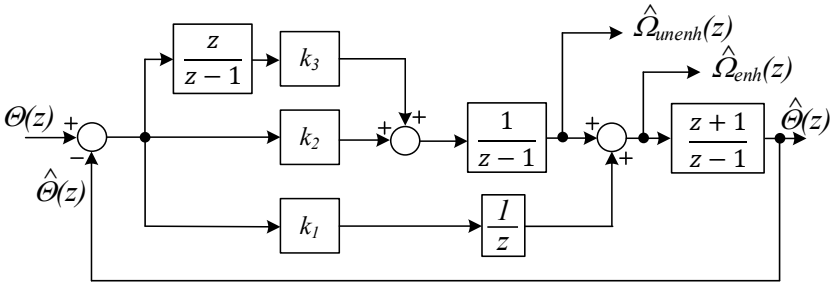

Figure 4.4.6 *Discrete Time VTSF without the Feed-Forward term.*

The open loop $F_{VTSF}(z)$ and closed loop $W_{VTSF}(z)$ transfer function of the discrete time VTSF are, respectively:

$$F_{VTSF}(z) = \frac{(k_1 + k_2 + k_3)\, z^3 + (k_3 - k_1)\, z^2 - (k_1 + k_2)\, z + k_1}{z^4 - 3\, z^3 + 3\, z^2 - z} \tag{4.4.8}$$

$$W_{VTSF}(z) = \frac{(k_1 + k_2 + k_3)\, z^3 + (k_3 - k_1)\, z^2 - (k_1 + k_2)\, z + k_1}{z^4 + (k_1 + k_2 + k_3 - 3)\, z^3 + (k_3 - k_1 + 3)\, z^2 - (k_1 + k_2 + 1) z + k_1} \tag{4.4.9}$$

It can be to note that the VTSF's gains are relative to three separate parallel paths in the VTSF; this topological feature helps to simplify the tuning, if the poles of the closed-loop transfer function are chosen sufficiently spaced, usually a tenth from each other. Fig. 4.4.7 helps to explain why: it shows an equivalent block diagram in which the parallel paths of Fig. 4.4.6 have been algebraically manipulated to explicitly show the nature of the three cascaded loops of the VTO.

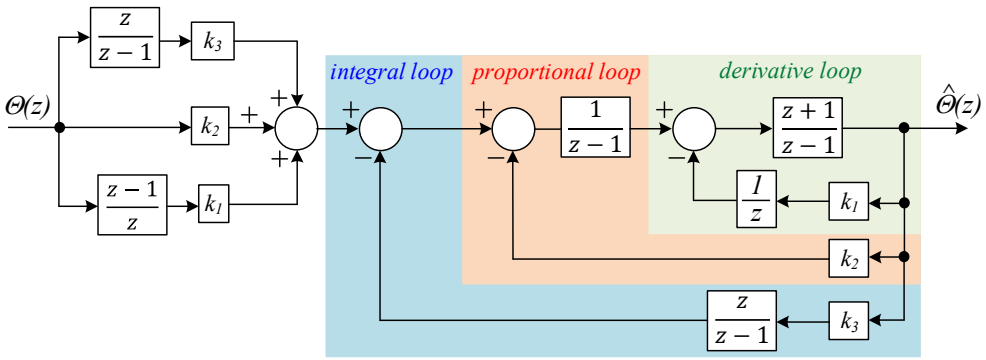

Figure 4.4.7 *Equivalent Operating Point Model with Derivative, Proportional and Integral Loops Explicitly Shown.*

A simple procedure for the VTO observer tuning will now be presented. If the derivative loop is calibrated to be the fastest of the three, it can be analyzed separately from the two outermost loops: proportional loop and integral loop respectively. The transfer function of the derivative loop is:

$$\frac{z^2 + z}{z^2 + (k_1 - 1)\, z + k_1} \tag{4.4.10}$$

Considering the characteristic polynomial of (4.4.10), to set the coefficient k_1, the smaller of the zeros of the characteristic polynomial (4.4.11) (i.e. the faster of the two closed-loop polynomials) is free to vary, while the other is set to z_1, as defined:

$$z^2 + (k_1 - 1)\, z + k_1 = 0 \tag{4.4.11}$$

By setting the desired passband of the VTO f_{BWvto}, as the frequency of the fastest pole, i.e. that of the derivative loop:

$$k_1 = z_1 \frac{1 - z_1}{1 + z_1} \qquad z_1 = e^{-2\pi f_{BWvto} T_s} \tag{4.4.12}$$

After the derivative loop tuning it is now possible to proceed with the tuning of the proportional loop. The transfer function which combines the two loops, derivative and proportional, holds:

$$\frac{z^2 + z}{z^3 + (k_1 + k_2 - 2)\, z^2 + (k_2 + 1)\, z - k_1} \tag{4.4.13}$$

Starting from the characteristic polynomial of the (4.4.13), defined in the following expression (4.4.14):

$$z^3 + (k_1 + k_2 - 2)\, z^2 + (k_2 + 1)\, z - k_1 = 0 \tag{4.4.14}$$

It is possible to set the proportional loop pole, z_2, with a frequency ten times lower than the frequency of the derivative loop pole. Thus, known the coefficient k_1 and set the pole z_2:

$$k_2 = \frac{-z_2^3 + (2 - k_1) z_2^2 - z_2 + k_1}{z_2 (z_2 + 1)} \qquad z_2 = e^{-2\pi \frac{fBWvto}{10} T_s} \tag{4.4.15}$$

Finally, the integral loop can be designed. In this case it is necessary to consider the entire transfer function (4.4.16) which incorporates the three loops: derivative, proportional and integral:

$$\frac{z^3 + z^2}{z^4 + (k_1 + k_2 + k_3 - 3) z^3 + (k_3 - k_1 + 3) z^2 - (k_1 + k_2 + 1) z + k_1} \tag{4.4.16}$$

It would be noted in (4.4.16) that the characteristic polynomial (4.4.17) is identical to the characteristic polynomial of the closed-loop transfer function $W_{VTSF}(z)$ defined in (4.4.9). Also in this case, from the VTSF gains k_1, k_2 and from the previous tuning and setting of the integral loop pole frequency, i.e., the slowest pole, as ten times smaller than the proportional loop pole, the gain k_3 can be determined.

$$z^4 + (k_1 + k_2 + k_3 - 3) z^3 + (k_3 - k_1 + 3) z^2 - (k_1 + k_2 + 1) z + k_1 = 0 \tag{4.4.17}$$

$$k_3 = \frac{-z_3^4 - (k_2 + k_1 - 3) z_3^3 + (k_1 - 3) z_3^2 + (k_1 + k_2 + 1) z_3 - k_1}{z_3^3 + z_3^2} \qquad z_3 = e^{-2\pi \frac{fBWvto}{100} T_s} \tag{4.4.18}$$

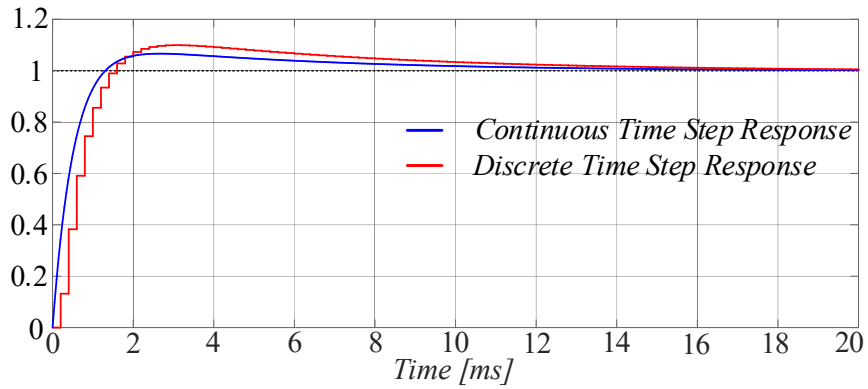

Figure 4.4.8 *Step Time Response Comparison between the Continuous Time and Discrete Time closed loop transfer function of the VTSF.*

4.5 Impact of the Rotor Position Sensor Resolution in AC drive using Speed Estimation Algorithm based on Vector Tracking Observer

Starting from the measurement of the rotor position sensor, the use of the speed estimators is used in those applications where knowledge of the rotor speed is required [15]-[16]. As already introduced in paragraph 3.2, the use of a position sensor involves the presence of some phenomena that affect the performance of an electric drive.

In particular, among the various properties that characterize a position sensor, the resolution is the one that among all the other properties has an important impact on the speed control since it affects the quality of the speed estimation. Furthermore, based on

the paragraph 3.3, the use of an intuitive and effective mathematical model of the resolution of a position sensor allows to analytically determine the effects that the resolution has in the estimation of the rotor speed and in its control.

In essence, $\omega_{re}^{(q)}$ is the instantaneous speed of the sensed position space vector; as such, it plays a key role in any position-measurement-based speed estimation algorithm. Ideally, speed estimated with an infinitely high estimation accuracy bandwidth would coincide with $\omega_{re}^{(q)}$, but such an estimate would contain unacceptably large harmonic content which would be detrimental to the operation of any speed controlled electrical drive. Filtering is therefore unavoidable, especially in low-speed operation, when a significant number of harmonics are concentrated in the low frequency range of $\omega_{re}^{(q)}$'s spectrum.

In this paragraph, the impact of the speed estimators on the filtering action and therefore reduction of quantization harmonics is dealt with in an analytical way. In particular, the whole analysis will be conducted using the VTO as a speed estimator; moreover, the study conducted here, for simplicity of analysis, will be done in continuous time.

4.5.1 Filtering Properties of the VTO

In order to keep the following mathematical analysis simple, the torque command feedforward input is set to zero, i.e. the VTO becomes a vector-tracking state filter (VTSF) Fig. 4.5.1. This is done to avoid quantization harmonics propagating into the observer from the current control loop via the feedforward term.

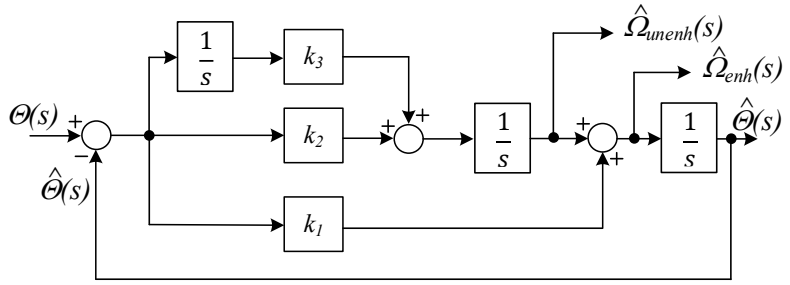

Figure 4.5.1 *Block Diagram of the Operating Point Model of the VTSF*

The closed loop transfer function of the VTSF, as already defined in paragraph 4.4, is given by:

$$W_{VTSF}(s) = \frac{k_1 s^2 + k_2 s + k_3}{s^3 + k_1 s^2 + k_2 s + k_3} \tag{4.5.1}$$

In order to simplify the mathematical computation, it is possible to decompose (4.5.1) into simple fractions; in fact the numerator of (4.5.1) is a second order equation and it is composed by two zeros, while the denominator is a third order equation, as already shown in paragraph 4.4, it is composed by three poles:

$$W_{VTSF}(s) = k_1 \frac{s^2 + \frac{k_2}{k_1}s + \frac{k_3}{k_1}}{s^3 + k_1 s^2 + k_2 s + k_3} = k_1 \frac{(s + z_1)(s + z_2)}{(s + p_1)(s + p_2)(s + p_3)} \tag{4.5.2}$$

The function (4.5.2) can be rewritten as:

$$W_{VTSF}(s) = k_1 \frac{(s + z_1)\,(s + z_2)}{(s + p_1)\,(s + p_2)\,(s + p_3)} = k_1 \left(\frac{A}{s + p_1} + \frac{B}{s + p_2} + \frac{C}{s + p_3} \right) \tag{4.5.3}$$

where A, B and C are the coefficients of the simple fractions:

$$W_{VTSF}(s) = k_1 \frac{(A + B + C)\,s^2 + [A\,(p_2 + p_3) + B\,(p_1 + p_3) + C\,(p_1 + p_2)] + s\,(A\,p_2\,p_3 + B\,p_1\,p_3 + C\,p_1\,p_2)}{(s + p_1)\,(s + p_2)\,(s + p_3)} \tag{4.5.4}$$

By comparing the (4.5.2) and (4.5.4), it is possible to obtain the following algebraic linear system:

$$\begin{bmatrix} 1 & 1 & 1 \\ (p_2 + p_3) & (p_1 + p_3) & (p_1 + p_2) \\ p_2\,p_3 & p_1\,p_3 & p_1\,p_2 \end{bmatrix} \begin{bmatrix} A \\ B \\ C \end{bmatrix} = \begin{bmatrix} 1 \\ z_1 + z_2 \\ z_1\,z_2 \end{bmatrix} \tag{4.5.5}$$

The solution of the algebraic linear system (4.5.5) provides the following coefficients:

$$\begin{cases} A = \dfrac{(p_1 - z_1)\,(p_1 - z_2)}{(p_1 - p_2)\,(p_1 - p_3)} \\ B = -\dfrac{(p_2 - z_1)\,(p_2 - z_2)}{(p_1 - p_2)\,(p_2 - p_3)} \\ C = \dfrac{(p_3 - z_1)\,(p_3 - z_2)}{(p_1 - p_3)\,(p_2 - p_3)} \end{cases} \tag{4.5.6}$$

According to the tuning of the VTO in continuous time domain, sub-paragraph 4.4.1, the VTO gains are selected in (4.4.4) and can be rewritten as:

$$\begin{cases} k_1 = (p_1 + p_2 + p_3) = \dfrac{111}{100}\,p_1 \\ k_2 = p_1\,p_2 + p_1\,p_3 + p_2\,p_3 = \dfrac{111}{1000}\,p_1^2 \\ k_3 = p_1\,p_2\,p_3 = \dfrac{p_1^3}{1000} \end{cases} \tag{4.5.7}$$

From the relationship defined in (4.5.2) it is possible to compute the zeros of the (4.5.1) as function of the poles:

$$\begin{cases} z_1 = \dfrac{k_2 + \sqrt{k_2^2 - 4\,k_1\,k_3}}{2\,k_1} = \dfrac{p_1}{20}\left(1 + \sqrt{\dfrac{71}{100}}\right) \approx \dfrac{9\,p_1}{100} \\ z_2 = \dfrac{k_2 - \sqrt{k_2^2 - 4\,k_1\,k_3}}{2\,k_1} = \dfrac{p_1}{20}\left(1 - \sqrt{\dfrac{71}{100}}\right) \approx \dfrac{p_1}{100} \end{cases} \tag{4.5.8}$$

From (4.5.7) and (4.5.8) the coefficients A, B and C can be approximately rewritten as:

$$\begin{cases} A \approx \dfrac{\left(p_1 - \dfrac{9p_1}{100}\right)\left(p_1 - \dfrac{p_1}{100}\right)}{\left(p_1 - \dfrac{p_1}{10}\right)\left(p_1 - \dfrac{p_1}{100}\right)} = \dfrac{91}{90} \\ B \approx \dfrac{\left(\dfrac{p_1}{10} - \dfrac{9p_1}{100}\right)\left(\dfrac{p_1}{10} - \dfrac{p_1}{100}\right)}{\left(p_1 - \dfrac{p_1}{10}\right)\left(\dfrac{p_1}{10} - \dfrac{p_1}{100}\right)} = -\dfrac{1}{90} \\ C \approx \dfrac{\left(\dfrac{p_1}{100} - \dfrac{9p_1}{100}\right)\left(\dfrac{p_1}{100} - \dfrac{p_1}{100}\right)}{\left(p_1 - \dfrac{p_1}{100}\right)\left(\dfrac{p_1}{10} - \dfrac{p_1}{100}\right)} = 0 \end{cases} \tag{4.5.9}$$

From (4.5.9) it can be noted that the main contribution of the VTSF closed loop transfer function (4.5.3) is given by the coefficient A; in fact, by computing the impulse response of (4.5.3) three impulse responses are obtaining, where each component is linked to coefficients A, B e C:

$$w_{VTSF}(t) = \mathcal{L}^{-1}\left[W_{VTSF}(s)\right] = k_1\left[A\, e^{-p_1 t} + B\, e^{-p_2 t} + C\, e^{-p_3 t}\right] \tag{4.5.10}$$

while the transfer functions of each impulsive response defined in (4.5.10) are given by:

$$W_{VTSF1}(s) = \frac{k_1 A}{s + p_1} \qquad W_{VTSF2}(s) = \frac{k_1 B}{s + p_2} \qquad W_{VTSF3}(s) = \frac{k_1 C}{s + p_3} \tag{4.5.11}$$

From the approximations obtained in (4.5.9) it is possible to neglect the terms related to the coefficients B and C.

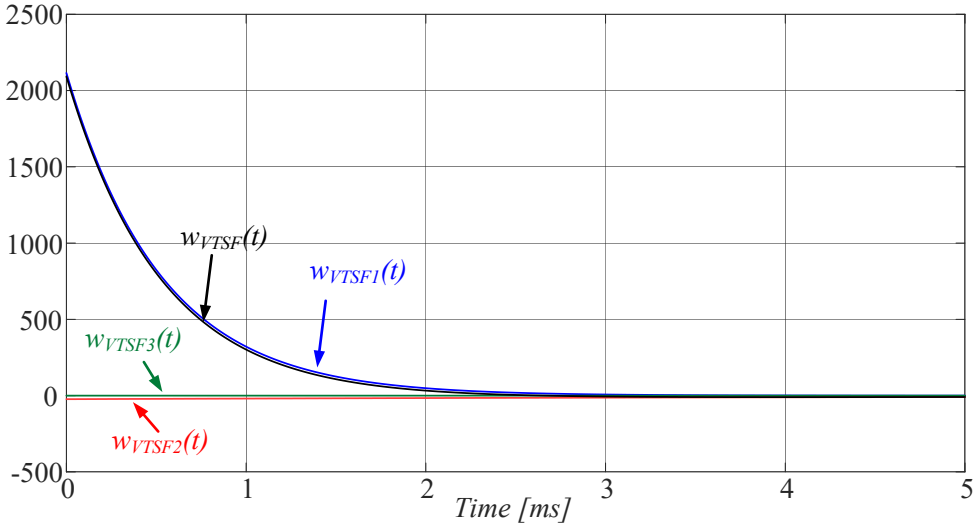

(a)

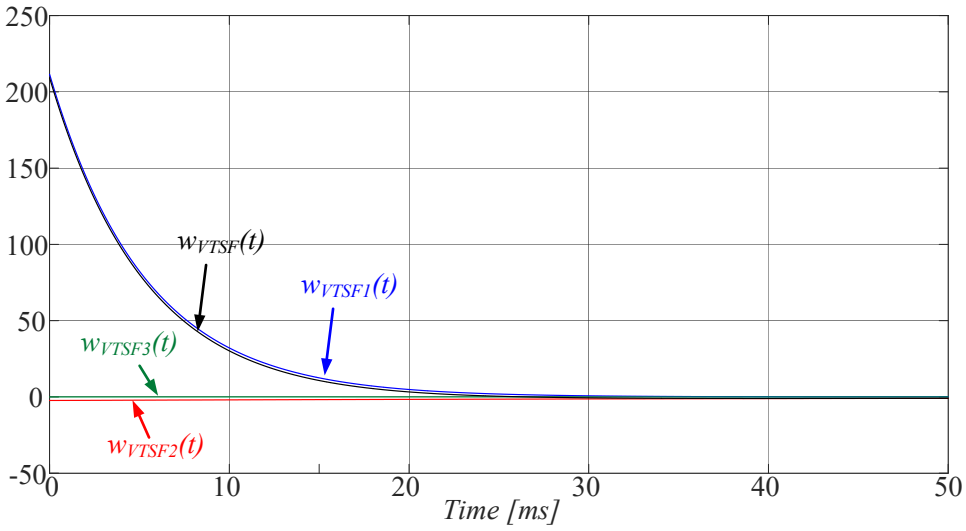

(b)

Figure 4.5.2 *Impulse Response of the VTSF and the decompose fractions components with two different VTO bandwidth values, respectively: (a) f_{BWvto}=300 Hz, (b) f_{BWvto}=30 Hz.*

It is possible to noted that both impulsive responses Fig. 4.5.2a and Fig. 4.5.2b have a similar behavior, also with different poles-placement selected values: p_1=300 Hz, p_2=30 Hz, p_3=3 Hz, and p_1=30 Hz, p_2=3 Hz, p_3=0.3 Hz, for Fig. 4.5.2a and Fig. 4.5.2b, respectively, and by considering the same estimated inertia of the mechanical system model.

According to the approximations in (4.5.9) and from the impulse responses of Fig. 4.5.2, it is possible to approximate the overall transfer function of the VTSF as that associated only with the pole p_1, i.e., the fastest pole and with the frequency closest to the bandwidth of the VTO.

$$W_{VTSF}(s) \approx \widetilde{W}_{VTSF}(s) = W_{VTSF1}(s) = \frac{k_1 A}{s + p_1} \tag{4.5.12}$$

The gain provided by the VTSF at a generic frequency ω is approximately given by:

$$|\widetilde{W}_{VTSF}(j\omega)| = \frac{k_1 A}{\sqrt{p_1^2+\omega^2}} \tag{4.5.13}$$

In the following sub-paragraphs, comparisons between analytical results obtained using (4.5.13) and numerical simulations using the actual VTSF are provided. Fig. 4.5.3a shows a block diagram detailing how the analytical results are achieved, while Fig. 4.5.3b shows how the simulations using the actual VTSF are implemented.

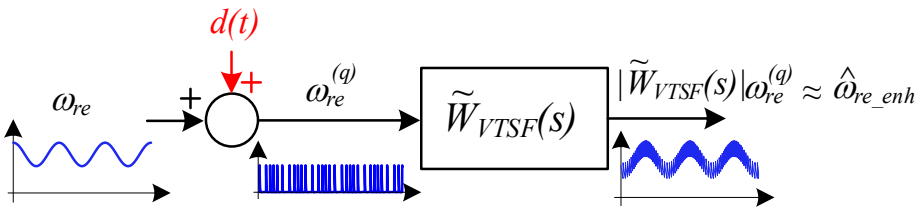

(a)

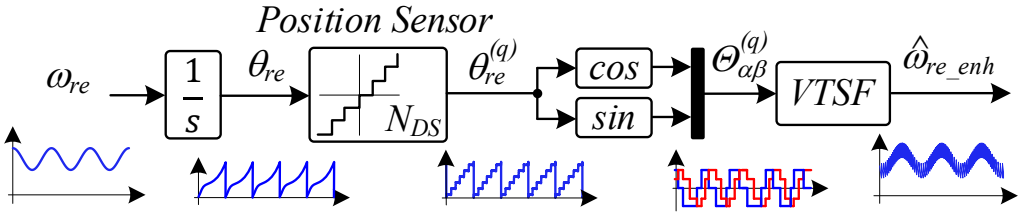

(b)

Figure 4.5.3 *Block Diagram of the VTSF based speed estimation.*

ω_{re} is the reference speed on which a sinusoidal disturbance is superimposed (4.5.14), while $d(t)$ is the disturbance related to the quantization phenomena (15):

$$\omega_{re}(t) = \omega_{re0} + \Delta\omega_{re}\cos(\omega_d t+\varphi_d) \tag{4.5.14}$$

$$d(t) = \sum_{k=1}^{+\infty} \frac{2}{N_{DS}\,k} \sum_{n=-\infty}^{+\infty} J_n\left(\frac{N_{DS}k\Delta\omega_{re}}{\omega_d}\right) (N_{DS}k\omega_{re0}+n\omega_d) \cos((N_{DS}k\omega_{re0}+n\omega_d)t+n\varphi_d) \tag{4.5.15}$$

In particular, will be shown the filtering capability of the VTSF based on the mathematical formulations of the quantized rotor position and angular speed described in paragraph 3.3; in fact, will be taken into consideration the several cases of the quantized rotor position and speed analyzed in paragraph 3.3: with constant case, with a single sinusoidal disturbance, with a periodic disturbance and finally with non-periodic disturbance.

The approximated expression of the VTSF magnitude (4.5.13) will be used in the next sub-paragraphs in order to simplify this mathematical analysis.

4.5.2 Case with Constant Speed

Starting from (4.3.13) the amplitude of the quantization harmonic at the angular frequency $\omega = kN_{ds}\omega_{re0}$ can be expressed as:

$$\hat{\omega}_{re\_enh}(kN_{DS}\omega_{re0}) \approx 2\omega_{re0}\,|\tilde{W}_{VTSF}(kN_{DS}\omega_{re0})| = 2\omega_{re0}\frac{k_1 A}{\sqrt{p_1^2+(kN_{DS}\omega_{re0})^2}} \tag{4.5.16}$$

The above equation provides a clear relationship between the fastest closed loop pole of the VTSF and the amplitude of any quantization harmonic in $\hat{\omega}_{re\_enh}$. Thus, it can be used to tune the VTSF to satisfy specifications on the allowable quantization harmonic amplitudes. Fig. 4.5.4a shows the waveform of $\hat{\omega}_{re\_enh}$ for $\omega_{re0} = 2\pi 10$ rad/s, p_1=300Hz, p_2=30Hz, p_3=3Hz and $N_{DS} = 6$. $\hat{\omega}_{re\_enh}$ features significant impulses at each position measurement update, making it practically unusable for speed feedback. Fig. 4.5.4b, shows the magnitude frequency response plots $|W_{VTSF}(j\omega)|$ and $|\tilde{W}_{VTSF}(j\omega)|$. The two responses differ in the low frequency range, with $|\tilde{W}_{VTSF}(j\omega)|$ overestimating the dc component by about 12%. Nonetheless, $|\tilde{W}_{VTSF}(j\omega)|$ is a good approximation of $|W_{VTSF}(j\omega)|$ starting from the first quantization harmonic frequency, i.e. 60 Hz. Fig. 4.5.4c shows the FFTs of $\omega_{re}^{(q)}$, $\hat{\omega}_{re\_enh}$ and $|\tilde{W}_{VTSF}(j\omega)|\omega_{re}^{(q)}$. It is verified that the harmonics of $\hat{\omega}_{re\_enh}$ are filtered versions of those of $\omega_{re}^{(q)}$, i.e. $\hat{\omega}_{re\_enh}(\omega) = |W_{VTSF}(j\omega)|\omega_{re}^{(q)}(\omega)$.

Furthermore, apart from the dc component, very good agreement can be seen between the harmonic amplitudes in $\hat{\omega}_{re\_enh}$ and $|\widetilde{W}_{VTSF}(j\omega)|\omega_{el}^{(q)}$, corroborating the validity and usefulness of (4.5.16). Fig. 4.5.4c also confirms that the amplitudes of the quantization harmonics contained in $\hat{\omega}_{re\_enh}$ are still quite significant compared to those of $\omega_{el}^{(q)}$.

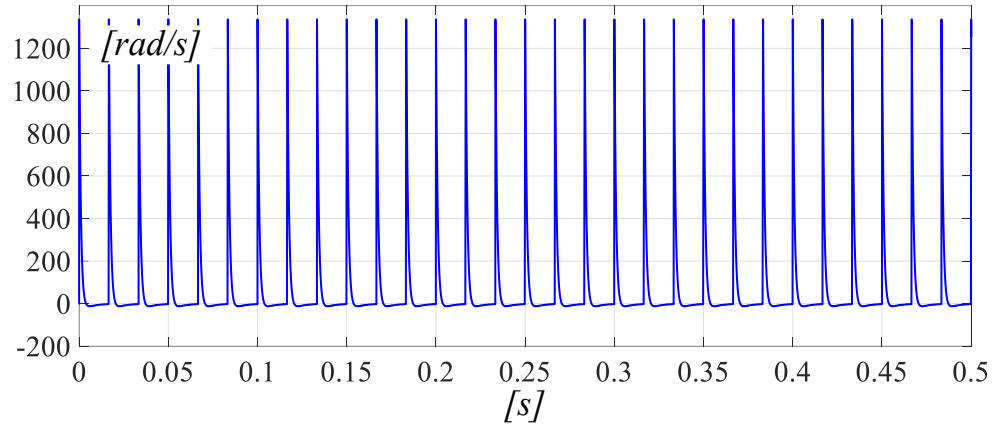

(a)

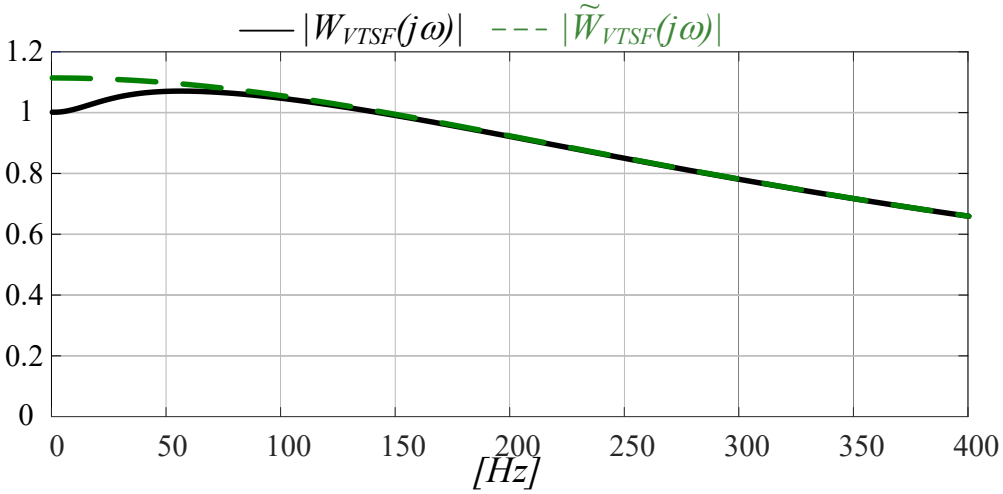

(b)

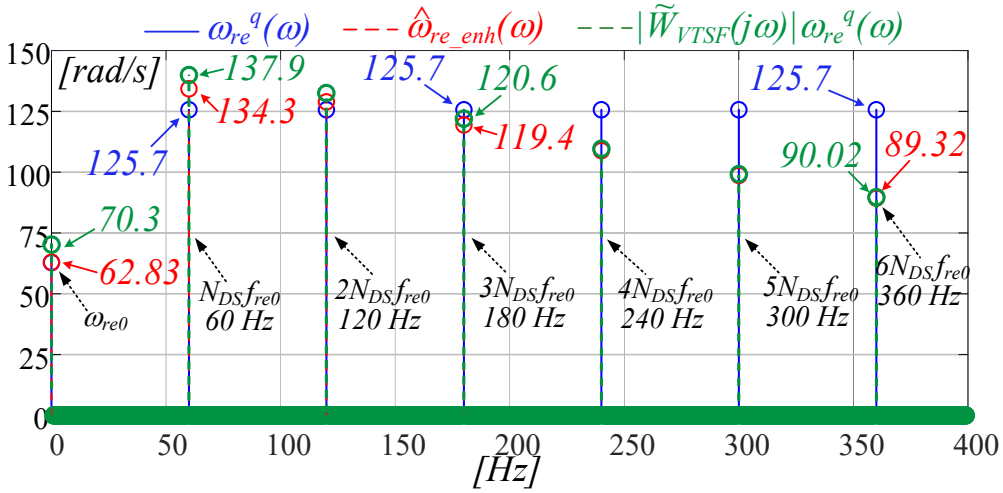

(c)

Figure 4.5.4 *Instantaneous quantized speed, estimated enhanced speed and estimated VTSF amplitude, for $\omega_{re0} = 2\pi 10$ rad/s, $N_{DS} = 6$ and p_1=300 Hz, p_2=30 Hz, p_3=3 Hz. (a) waveform of estimated enhanced speed (b) frequency responses of VTSF magnitude and estimated VTSF magnitude (c) FFTs.*

One well known way to reduce the impact of the quantization harmonics is to increase the filtering of the speed estimation algorithm, [17]. This is shown in Fig. 4.5.5, in which the closed loop poles of VTSF are lowered by a decade each to p_1=30 Hz, p_2=3 Hz, p_3=0.3 Hz. A significant increase in quantization harmonic attenuation is visible, at the expense of deteriorating the estimation accuracy bandwidth of the VTSF.

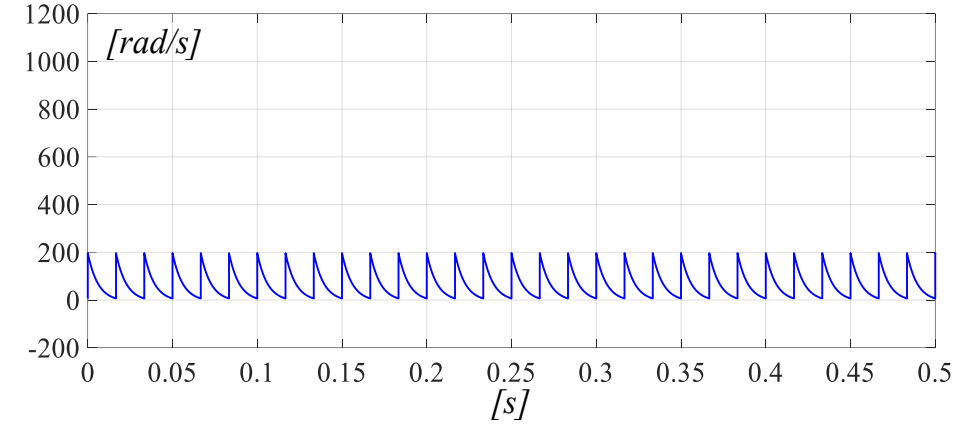

(a)

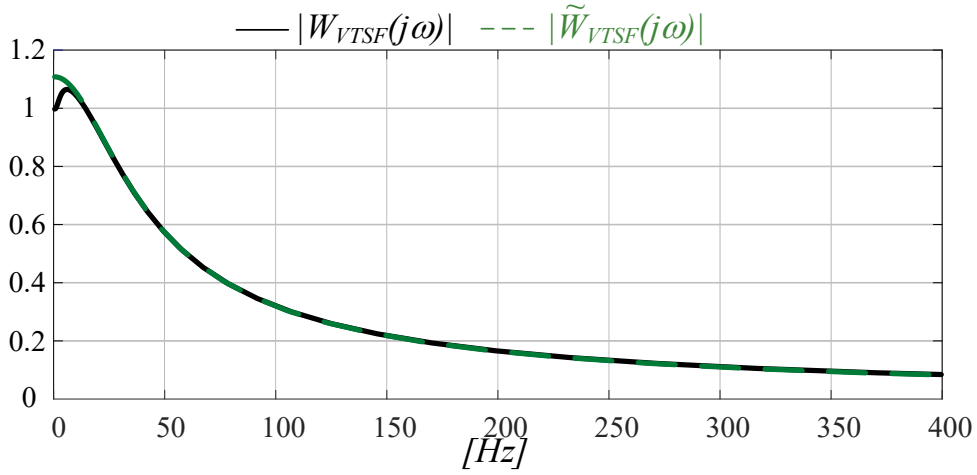

(b)

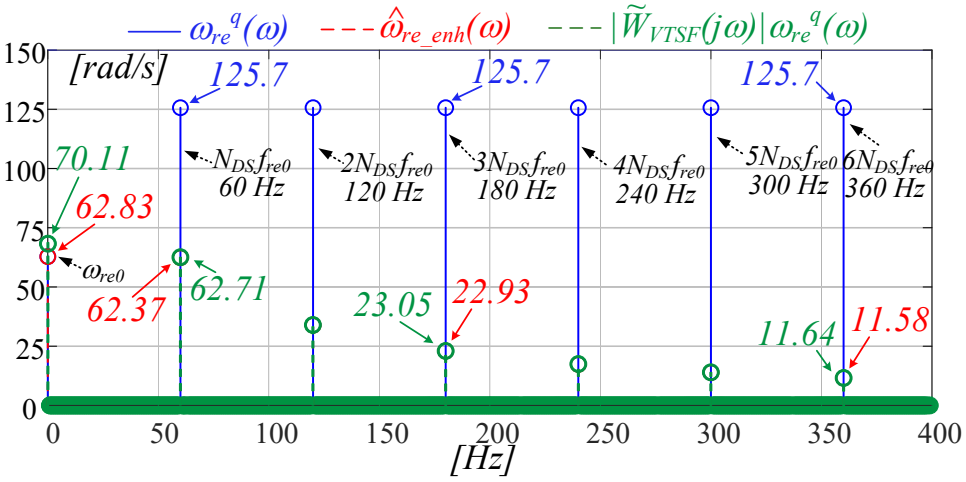

(c)

Figure 4.5.5 *instantaneous quantized speed, estimated enhanced speed and estimated VTSF amplitude for $\omega_{re0} = 2\pi 10$ rad/s, $N_{DS} = 6$ and p_1=30 Hz, p_2=3 Hz, p_3=0.3 Hz. (a) waveform of estimated enhanced speed (b) frequency responses of VTSF magnitude and estimated VTSF magnitude (c) FFTs.*

4.5.3 Case with a Single Sinusoidal Disturbance

The same analysis is now performed for a single sinusoidal disturbance. By virtue of (4.5.13), the amplitude of the quantization harmonics in $\hat{\omega}_{re\_enh}$ at $kN_{ds}\omega_{re0} \pm n\omega_d$ can be expressed as:

$$\hat{\omega}_{re\_enh}(kN_{DS}\omega_{re}\pm n\omega_d) \approx 2\omega_{re0}|\widetilde{W}_{VTSF}(kN_{DS}\omega_{re0}\pm n\omega_d)| = 2\omega_{re0}\frac{k_1 A}{\sqrt{p_1^2+(kN_{DS}\omega_{re0}\pm n\omega_d)^2}} \qquad (4.5.17)$$

Fig. 4.5.6 shows the related waveforms for $\omega_{re0} = 2\pi 10$ rad/s with a sinusoidal disturbance having $\Delta\omega_{re} = 2\pi$ rad/s, $\omega_d = 2\pi 11$ rad/s and $\varphi_d = 0$ rad. The VTSF is tuned with the follow bandwidth $f_{BWvto} = 30Hz$. Once again, it is confirmed that $\hat{\omega}_{re\_enh}(\omega) = |W_{VTSF}(j\omega)|\omega_{re}^{(q)}(\omega)$ and $\hat{\omega}_{re\_enh}(\omega) \approx |\widetilde{W}_{VTSF}(j\omega)|\omega_{re}^{(q)}(\omega)$, even under a single sinusoidal disturbance. As expected, an increased number of quantization harmonics appear in the spectrum of $\hat{\omega}_{re\_enh}$.

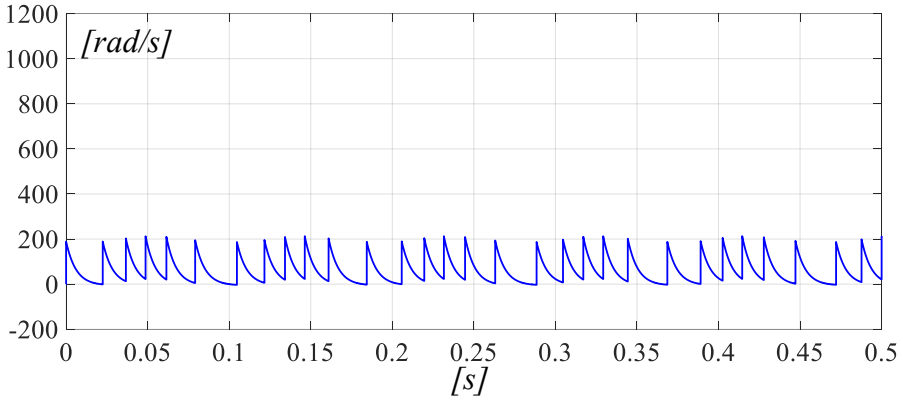

(a)

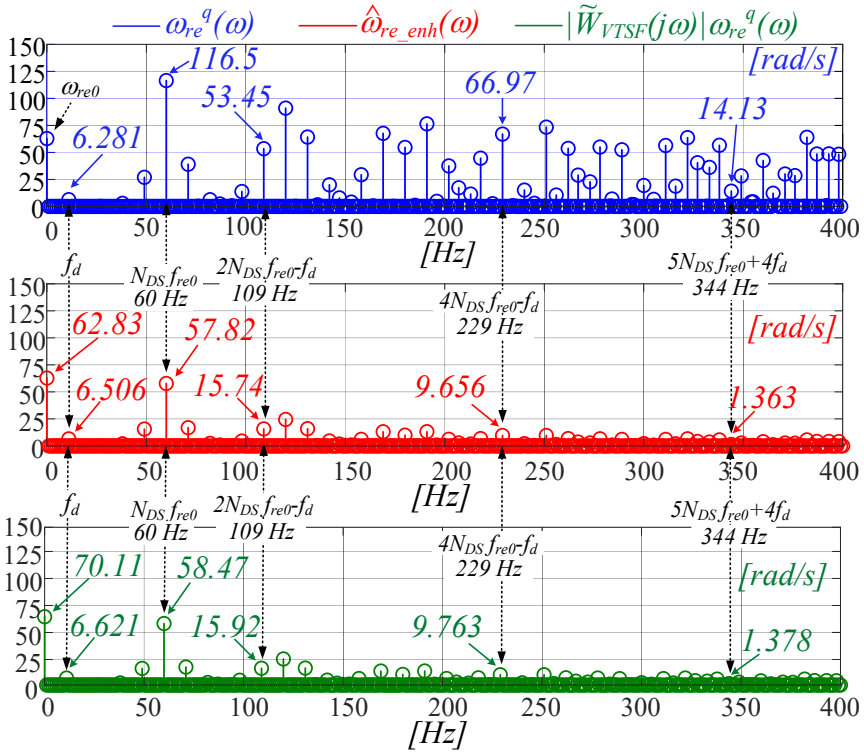

(b)

Figure 4.5.6 *instantaneous quantized speed, estimated enhanced speed and estimated VTSF amplitude for $\omega_{re0} = 2\pi 10$ rad/s, $\Delta\omega_{re} = 2\pi$ rad/s, $\omega_d = 2\pi 11$ rad/s, $\varphi_d = 0$ rad, $N_{DS} = 6$ and p_1=30 Hz, p_2=3 Hz, p_3=0.3 Hz. (a) waveform of estimated enhanced speed (b) FFTs.*

The VTSF has an impact on the estimation of the disturbance harmonic as well: compared to the actual value, its magnitude is amplified by 3.6 % and its phase is shifted by -18.8 deg. Consequently, a speed control loop wouldn't be able to fully compensate the disturbance. In addition, it can also be expected that the speed loop will try to counteract the quantization harmonics in $\hat{\omega}_{re\_enh}$, thereby inducing additional ripple on the shaft.

4.5.4 Case with a Periodic Disturbance

In case of a periodic disturbance the amplitude of the quantization harmonic should be defined with the follow generic angular frequency $\omega = kN_{ds}\omega_{re0} + \sum_{i=1}^{h} n_i\omega_{di}$; in fact, considering the expression (4.5.13) it is possible to write the following generic expression:

$$\hat{\omega}_{re\_enh}\left(kN_{ds}\omega_{re0} + \sum_{i=1}^{h} n_i\omega_{di}\right) \approx 2\omega_{re0}\left|\tilde{W}_{VTSF}\left(kN_{ds}\omega_{re0} + \sum_{i=1}^{h} n_i\omega_{di}\right)\right| = \tag{4.5.18}$$

$$= 2\omega_{re0}\frac{k_1 A}{\sqrt{p_1{}^2 + \left(kN_{ds}\omega_{re0} + \sum_{i=1}^{h} n_i\omega_{di}\right)^2}}$$

The mathematical formulation of the quantization harmonic amplitude with a periodic disturbance (4.5.18) is quite complex; in fact, in order to simplify this study two sinusoidal disturbances has been considered.

Fig. 4.5.7 shows the related waveforms for $\omega_{re0} = 2\pi 10$ rad/s with two sinusoidal disturbances having $\Delta\omega_{re1} = 2\pi$ rad/s, $\omega_{d1} = 2\pi 7$ rad/s, $\varphi_{d1} = 0$ rad and $\Delta\omega_{re2} = 2\pi$ rad/s, $\omega_{d1} = 2\pi 12$ rad/s, $\varphi_{d1} = 0$ rad. The VTSF is tuned with the follow closed loop bandwidth $f_{BWvto} = 30Hz$. Also with a periodic disturbance, it is confirmed that $\hat{\omega}_{re\_enh}(\omega) = |W_{VTSF}(j\omega)|\omega_{re}^{(q)}(\omega)$ and $\hat{\omega}_{re\_enh}(\omega) \approx |\widetilde{W}_{VTSF}(j\omega)|\omega_{re}^{(q)}(\omega)$, even under multiple sinusoidal disturbances. Once again, as expected, an increased number of quantization harmonics appear in the spectrum of $\hat{\omega}_{re\_enh}$.

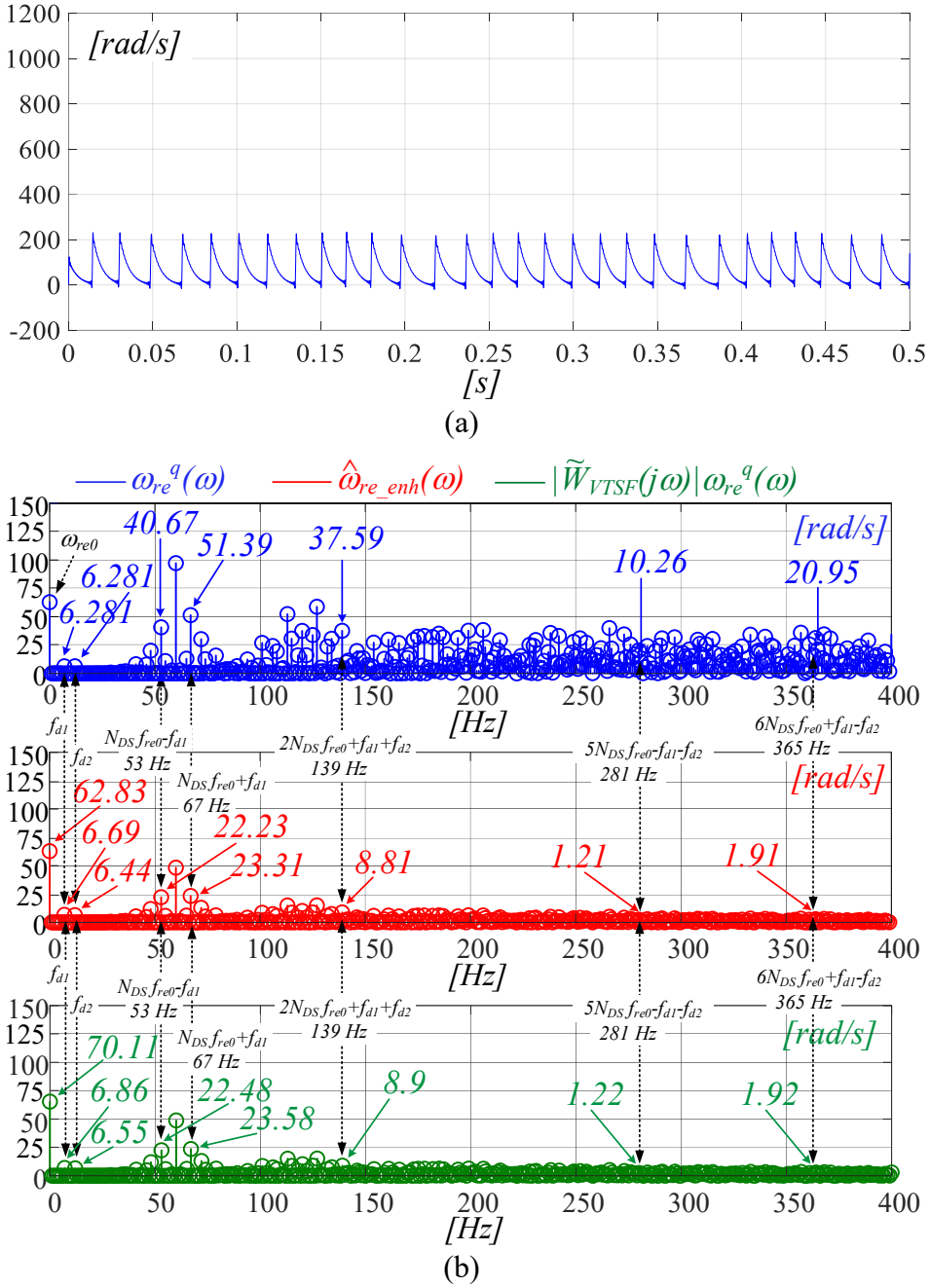

Figure 4.5.7 *Instantaneous quantized speed, estimated enhanced speed and estimated VTSF amplitude for $\omega_{re0} = 2\pi 10$ rad/s, $\Delta\omega_{re1} = 2\pi$ rad/s, $f_{d1} = 7$ Hz, $\varphi_{d1} = 0$ rad, $\Delta\omega_{re2} = 2\pi$ rad/s, $f_{d2} = 12$ Hz,*

φ_{d2} = 0 rad, N_{DS} = 6 and p_1=30 Hz, p_2=3 Hz, p_3=0.3 Hz. (a) waveform of estimated enhanced speed (b) FFTs.

Also in this case it is possible to note the VTSF impact on the estimation of the disturbances harmonics; in fact, compared to the actual values of the first sinusoidal disturbance, its magnitude is amplified by 6.5 % and its phase is shifted by -11 deg, while on the second sinusoidal disturbance, its magnitude is amplified by 2.5 % and its phase is shifted by -20.4 deg.

4.5.5 Case with a Nonperiodic Disturbance

Fig. 4.5.8 illustrates the waveforms for the example of nonperiodic torque disturbance pulses shown in Fig. 4.5.8. In this case, $\omega_{re}^{(q)}(t)$ is obtained numerically by using (3.3.16) defined in sub-section 3.3.4. The quantization harmonics are spread continuously throughout the spectrum, as can be expected for a nonperiodic waveform. The FFTs reported in Fig. 4.5.8b indicate that (4.5.1) - (4.5.13) are applicable to nonperiodic disturbances as well.

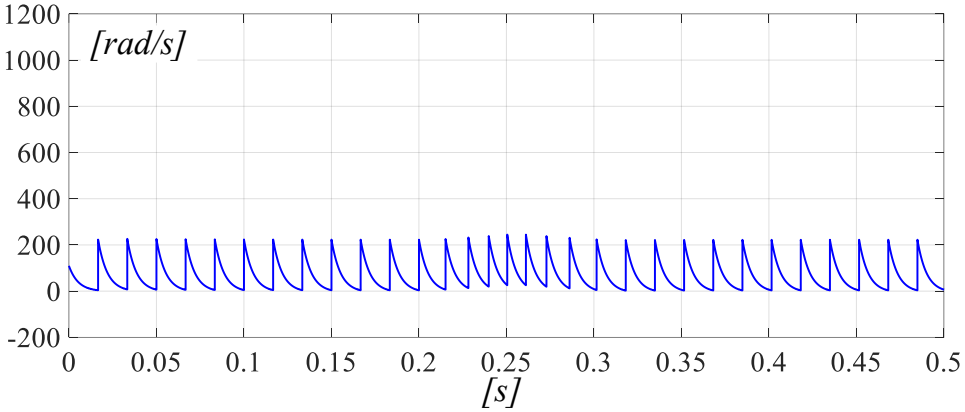

(a)

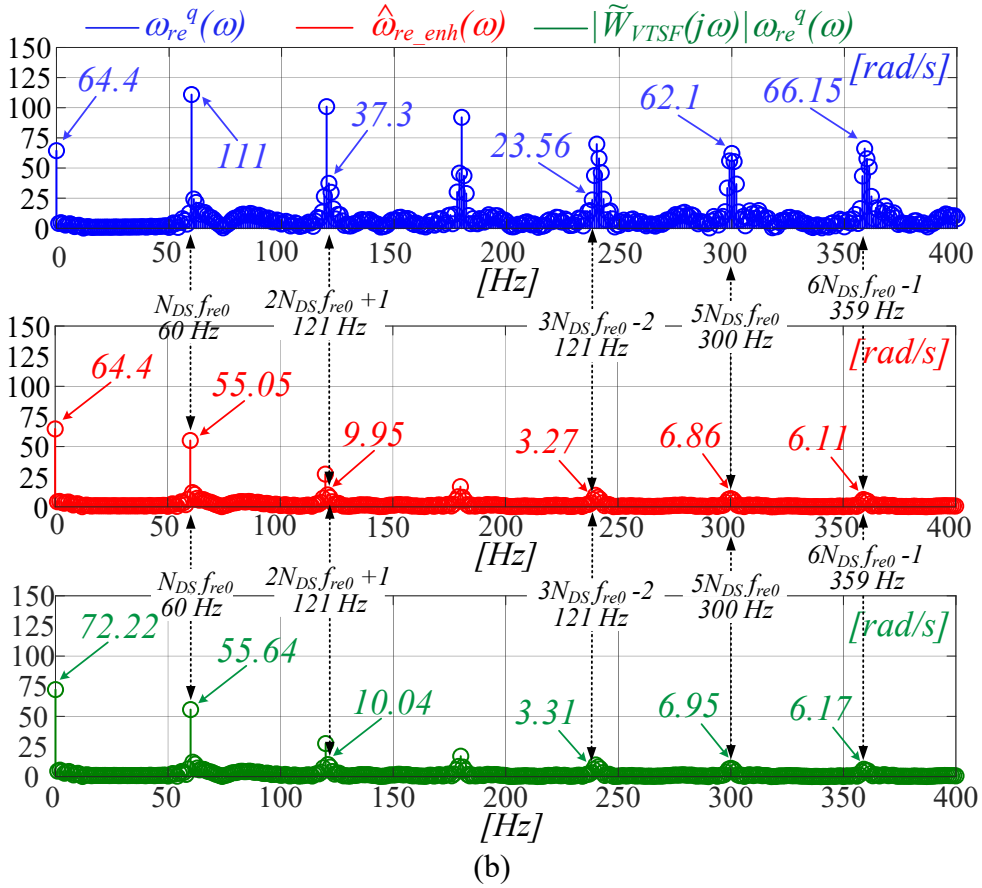

(b)

Figure 4.5.8 *instantaneous quantized speed, estimated enhanced speed and estimated VTSF amplitude for non-periodic disturbance and p_1=30 Hz, p_2=3 Hz, p_3=0.3 Hz. (a) waveform of estimated enhanced speed (b) FFTs*

The above results show that $\omega_{re}^{(q)}$ is the effective input to the VTSF in any operating condition, both periodic and nonperiodic. Since the VTSF has been represented with its operating point closed loop transfer function, the previous analyses also suggest that is possible to determine the speed estimate for any estimation algorithm by applying its own operating point closed loop transfer function to $\omega_{re}^{(q)}$.

4.5.6 Experimental Validation

To further validate the above modelling, this section is devoted to experimental tests on a 400 W servo-drive test bench. The setup shown in Fig. 4.5.9 comprises two permanent magnets synchronous motors (PMSM): an Estun EMJ-04APB22 surface PM servo-motor (SPM) and a Golden Age GK6025-8AF31 interior PM servo-motor (IPM); these are coupled together via bellow couplings to a HBM T22 torque-meter. The PMSM machines are supplied by two Texas Instruments High Voltage Motor Control Kits which use TI F28335 microcontrollers and Powerex IGBT three-phase inverters, operating from a common 310V dc bus at 10kHz switching frequency and 1µs dead time. Both machines can be operated as motor or generator interchangeably; in fact, both inverters share a common DC bus, ensuring regenerative power flow. Low-side resistive shunts are used to measure the three phase currents of both drives.

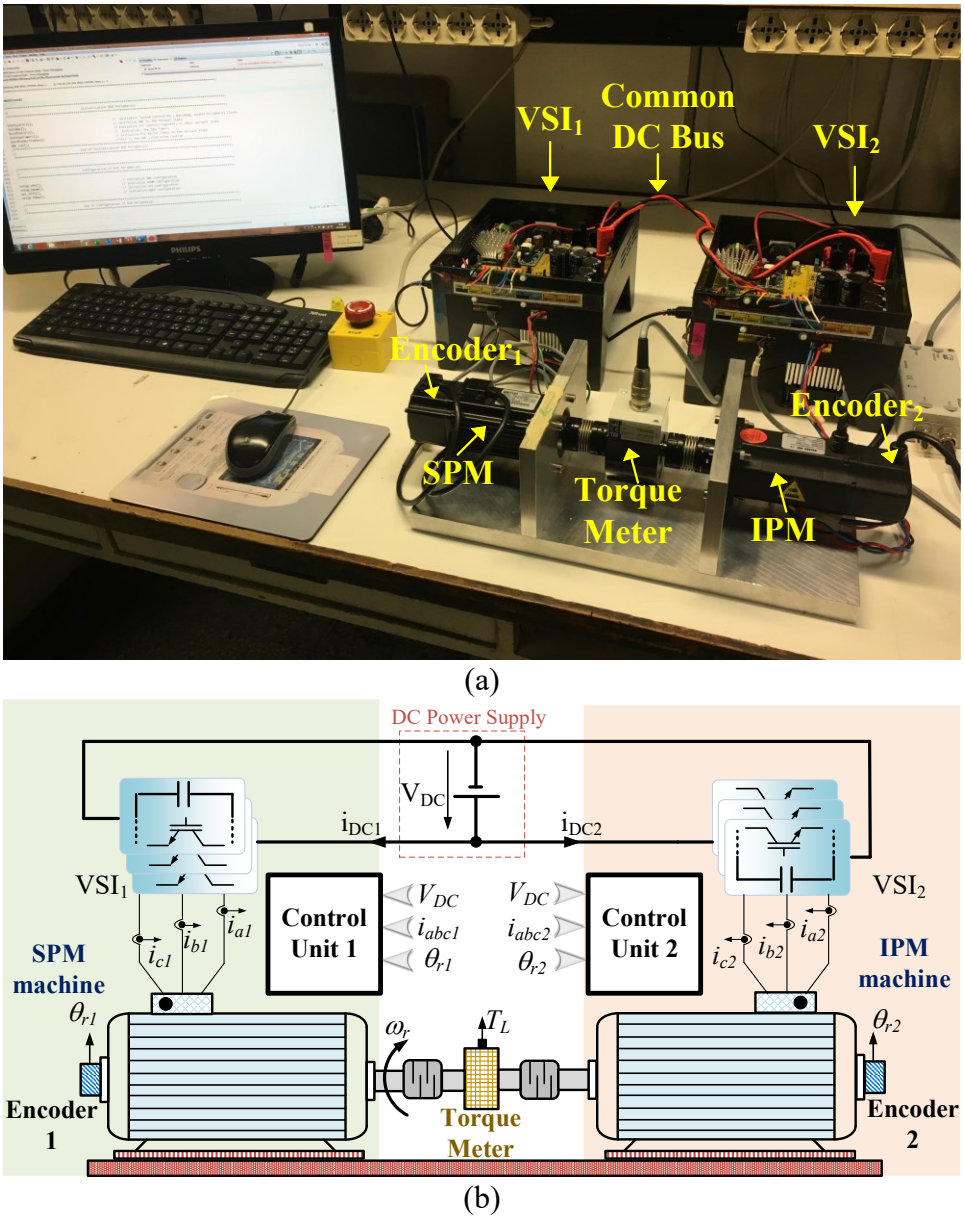

Figure 4.5.9 *Experimental servo-drive test bench. (a) photograph, (b) schematic.*

Standard field-oriented control with synchronous reference frame cross-coupling decoupling current regulators is implemented in the microcontrollers, as shown in Fig. 4.5.10. 10000 pulse per mechanical revolution optical encoders are mounted on each motor and tests are performed for different position sensor resolutions by down-sampling the encoder position measurement. The sampling frequency of the current control loop of both FOC algorithms is 10kHz, coinciding with the switching frequency. The sampling frequency of the speed control loop is 5 kHz. The bandwidth of the current control loop of both drives is 500 Hz, while two different bandwidths (50 Hz or 30 Hz) have been used for the speed control loop depending on the position sensor resolution, as indicated in the following. Two Analog Devices AD7568 digital to analog converters are used to visualize real time variables from both drives.

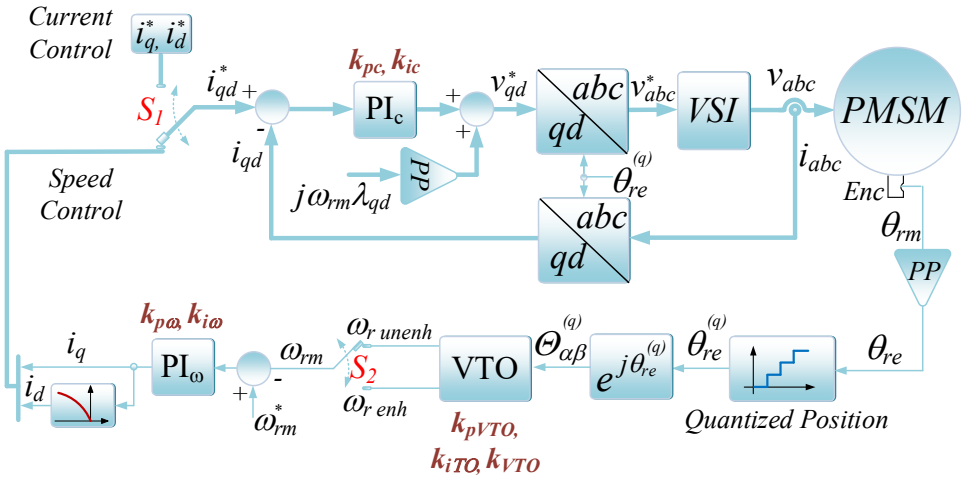

Figure 4.5.10 *Block diagram of the implemented field-oriented control.*

The main data of the two PM machines is reported in Tab. VII and Tab. VIII, while Tab. IX reports the moments of inertia of the various rotating elements of the test bench. Tab. X lists the settings of the motor control parameters.

Table VII *Data of SPM Servomotor ESTUN EMJ-04APB22*

Rated power	400 W	q/d inductances	14/14 mH
Rated speed	3000 rpm	Pole pairs	4
Rated current	2.7 A	*EMF* constant	0.0617 Vs/rad
Phase resistance	4.7 Ω	Torque constant	0.3702 Nm/A

Table VIII *Data of IPM Servomotor GOLDEN AGE GK6025-8AF31*

Rated power	400 W	q/d inductances	7.52/5.6 mH
Rated speed	3000 rpm	Pole pairs	4
Rated current	2.8 A	*EMF* constant	0.0598 Vs/rad
Phase resistance	2.44 Ω	Torque constant	0.45 Nm/A

Table IX *Moments of Inertia of the Test Bench Components*

SPM machine	$3.5\ 10^{-5}$ kg m^2
IPM machine	$4.5\ 10^{-5}$ kg m^2
Torque meter	$1.34\ 10^{-5}$ kg m^2
Bellows coupling (each)	$1.03\ 10^{-5}$ kg m^2

Table X *Main Control Parameters*

VTSF Controller Tuning	
Closed Loop Poles 300Hz, 30Hz, 3Hz	K_p= 6.198, K_i= 103.8, K_d=37.61e-3 T_s = 200 μs
Closed Loop Poles 30Hz, 3Hz, 0.3Hz	K_p= 90.44e-3, K_i= 151.7e-3, K_d= 5.342e-3 T_s = 200 μs
Speed Regulator	$K_{p\omega}$= 35.23e-3, $K_{i\omega}$= 443.2e-3 T_s = 200 μs
Current Regulator	K_{pc}= 37.11, K_{ic}= 12.67e3 T_s = 100 μs

For the experimental tests reported here, the torque command feedforward input is set to zero, to be consistent with the previous section. The VTSF is executed at the same sample rate as the speed loop. The three closed-loop poles of the VTSF are equal to 300 Hz, 30 Hz and 3 Hz. This choice results in an estimation accuracy bandwidth equal to 320 Hz, which is about an order of magnitude less than the 2.5 kHz Nyquist frequency.

4.5.7 Experimental Results: Effects on VTSF-Based Speed Estimation

An initial set of tests is performed to evaluate the effects of position measurement resolution on the VTSF speed estimates. The SPM machine is speed controlled using the full resolution of its encoder, i.e. N_{DS} = 2500, a closed loop speed control bandwidth equal to 50 Hz and $\hat{\omega}_{re\_enh}$ used as speed feedback; the IPM machine's winding is disconnected from its supply.

The first test consists in commanding a constant speed reference equal to 2.5 Hz mechanical, i.e. 10 Hz electrical, and analyzing the resulting speed estimates coming from the IPM drive's VTSF, when its encoder's resolution is varied. Fig. 4.5.11 shows the waveform and the FFT of $\hat{\omega}_{re\_enh}$ when N_{DS} = 2500. Aside from the average value of the electrical frequency which is consistent with the speed command, low order harmonics at 10 and 20 Hz are also present: these may be ascribed to a slightly dynamically unbalanced shaft. No other substantial harmonics are visible in the spectrum.

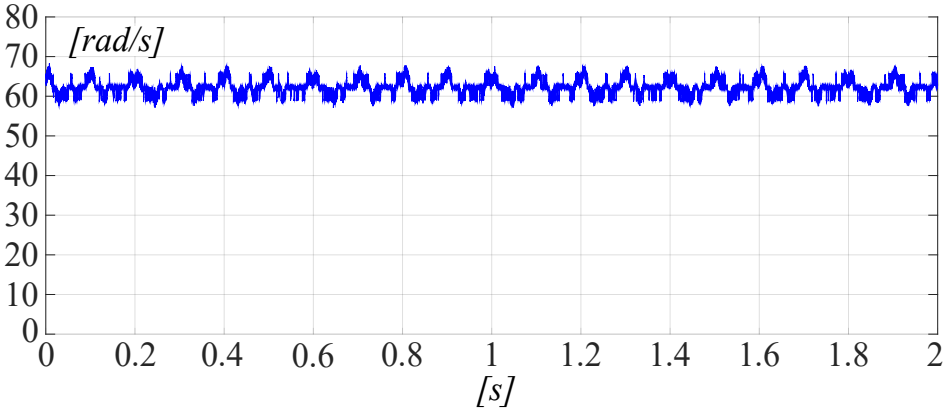

(a)

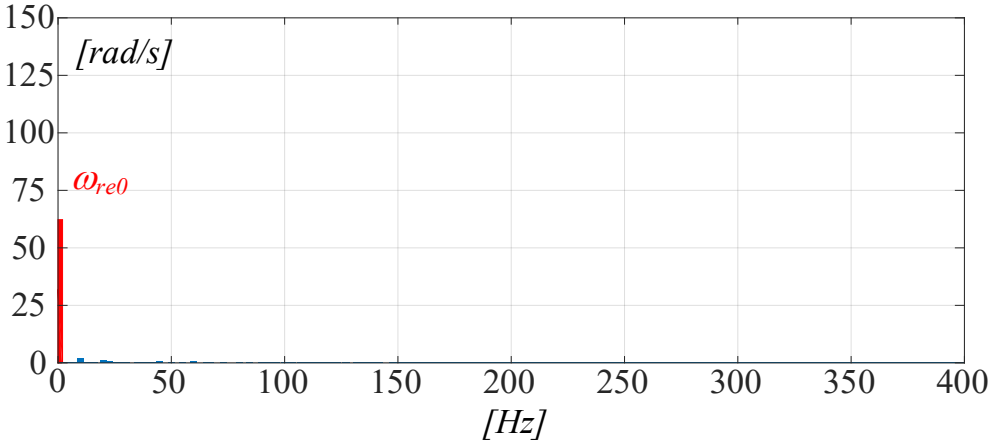

(b)

Figure 4.5.11 *VTSF-based speed estimate enhanced speed for $\omega_{re0} = 2\pi 10$ rad/s and $N_{DS} = 2500$. (a) waveform (b) FFT.*

Fig. 4.5.12 shows the waveform and FFT of $\hat{\omega}_{re\_enh}$ when $N_{DS} = 6$. The impulsive nature of $\omega_{re}^{(q)}(t)$, as shown in Fig. 4.5.12a, is also visible in this waveform. The FFT of $\hat{\omega}_{re\_enh}$ computed according to the approach described in sub-section 4.5.1 (including the disturbances at 10 Hz and 20 Hz) has been superimposed to the experimental FFT in Fig. 4.5.12b.

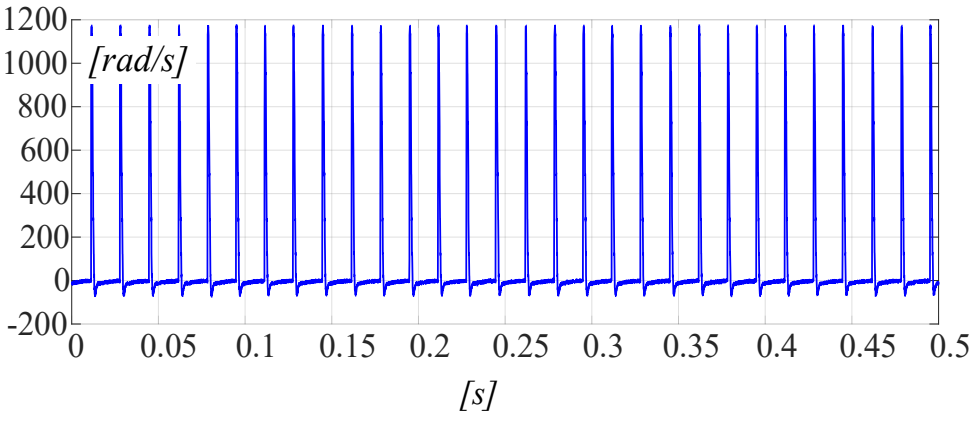

(a)

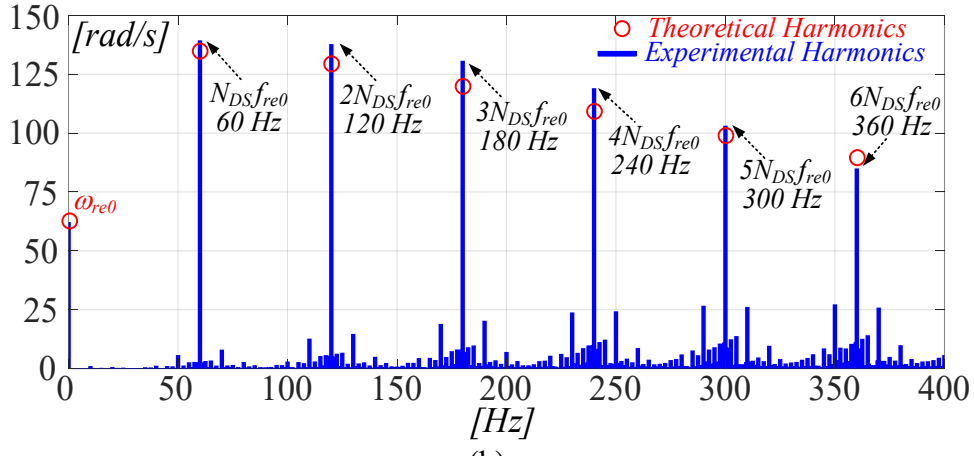

(b)

Figure 4.5.12 *VTSF-based speed estimate enhanced speed for $\omega_{re0} = 2\pi 10$ rad/s and $N_{DS} = 6$. (a) waveform (b) FFT.*

The expected harmonic amplitudes are in good agreement with the experimental data. Quantization harmonics appear at multiples of $6f_{re0}$ as predicted in section 3.3; their amplitudes fall off as the frequency increases due to the filtering properties of the VTSF. Furthermore, sideband harmonics appear at ±10 Hz from the main quantization harmonics due to modulation caused by the disturbances at 10 Hz and 20 Hz: this is an initial experimental proof of the results obtained in section 3.3.

The second test consists in superimposing a sinusoidal speed ripple with an amplitude of $\Delta\omega_{re} = 2\pi$ rad/s and an 11 Hz frequency f_d, thus emulating the effect of a sinusoidal torque disturbance acting on the shaft. Fig. 4.5.13 shows the resulting waveform and FFT for $N_{DS} = 2500$. 1 Hz beats are visible in the waveform due to the interaction between the 10 Hz disturbance and the 11 Hz commanded speed ripple. As expected, no quantization harmonics appear in the spectrum.

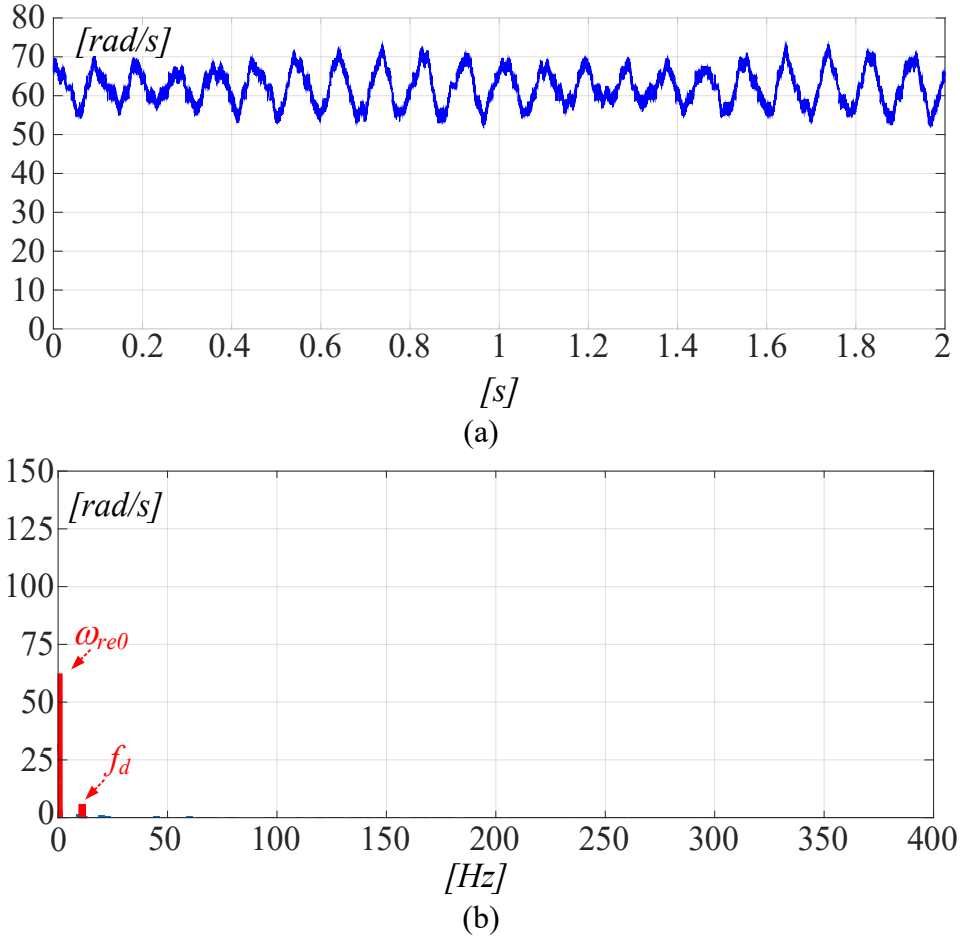

Figure 4.5.13 *VTSF-based speed estimate enhanced speed for $\omega_{re0} = 2\pi 10$ rad/s, $\Delta\omega_{re} = 2\pi$ rad/s, $\omega_d = 2\pi 11$ rad/s, $\varphi_d = 0$ rad and $N_{DS} = 2500$. (a) waveform (b) FFT.*

On the other hand, Fig. 4.5.14 shows the FFT when $N_{DS} = 6$. All the expected quantization harmonics are present in the spectrum. Narrow-band modulation is visible for the first and second harmonics orders N_{DS} and $2N_{DS}$ for both cases, while wide-band modulation is visible around the higher quantization harmonic orders.

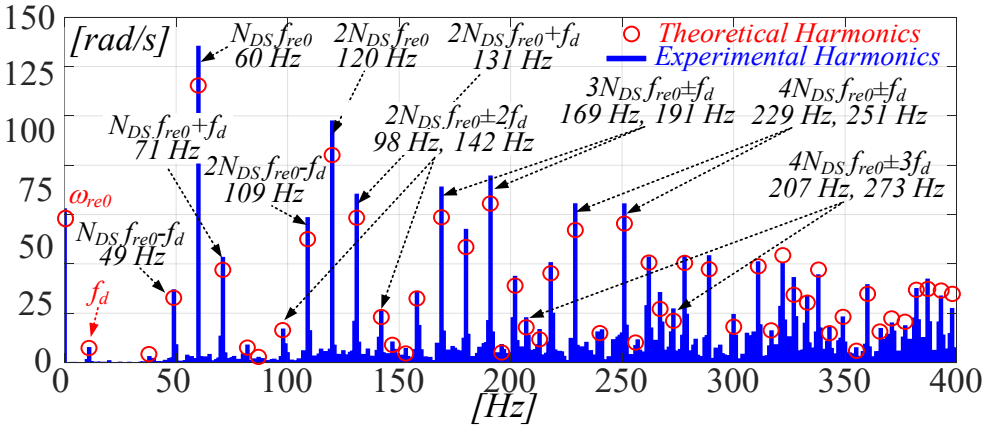

Figure 4.5.14 *Theoretical vs experimental VTSF-based speed estimate enhanced speed for ω_{re0} = $2\pi 10$ rad/s, $\Delta\omega_{re}$ = 2π rad/s, ω_d = $2\pi 11$ rad/s, φ_d = 0 rad. FFT for N_{DS} = 6.*

It was shown in Fig. 4.5.5 that the amplitudes of the quantization harmonics are lowered by reducing the estimation bandwidth of the VTSF. This is shown experimentally in Fig. 4.5.15 with the VTSF closed loop poles lowered to 30 Hz, 3 Hz and 0.3 Hz, i.e. an estimation bandwidth equal to 33 Hz. Even in this case a good agreement between the experimental data and theory can be seen.

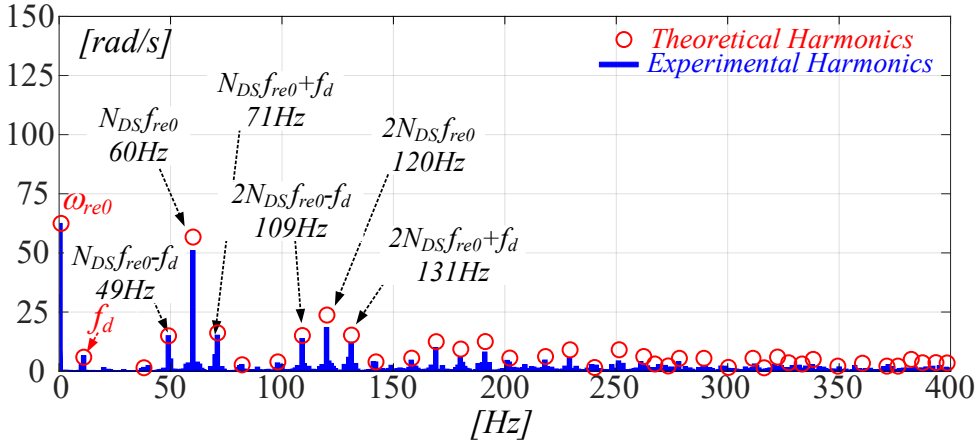

Figure 4.5.15 *Theoretical vs VTSF-based speed estimate enhanced speed (with the VTSF tuned for 30 Hz, 3 Hz and 0.3 Hz closed loop eigenvalues) for ω_{re0} = $2\pi 10$ rad/s, $\Delta\omega_{re}$ = 2π rad/s, ω_d = $2\pi 11$ rad/s, φ_d = 0 rad. (a) FFT for N_{DS} = 6.*

4.5.8 Experimental Results: Effects on Closed-Loop Speed Control

The last set of tests is performed to evaluate the impact of position sensor resolution on speed control. For this, the SPM machine is speed-controlled using N_{DS} = 6, while the IPM machine is torque-controlled using the full resolution of its encoder. From the above open-loop tests, it is evident that when using low resolution encoders, $\hat{\omega}_{re\_enh}$ is not suitable to be used for closed loop feedback, due to the significant presence of quantization harmonics throughout the entire spectrum. One way to reduce the harmonic content is to use $\hat{\omega}_{re\_unenh}$; another way is to reduce the estimation bandwidth of the VTSF, i.e. to increase the filtering. For these reasons and to guarantee stable operation during this test, the SPM drive's speed control bandwidth is reduced to 30 Hz and $\hat{\omega}_{re\_unenh}$ is used as speed feedback. The VTSF's closed loop eigenvalues are kept equal to 300 Hz, 30 Hz and 3 Hz. The test is performed by commanding the SPM machine with a constant speed of 2.5 Hz mechanical and by commanding the IPM machine to produce a sinusoidal

torque disturbance with ΔT_d = 45 mNm at f_d = 11 Hz. Fig. 4.5.16 shows the waveform and FFT of the electrical frequency measured by the IPM drive (i.e. $\hat{\omega}_{re\_enh}$ with maximum encoder resolution). Major oscillations are visible in the waveform, indicating a significant difficulty of the SPM drive in controlling the speed of rotation.

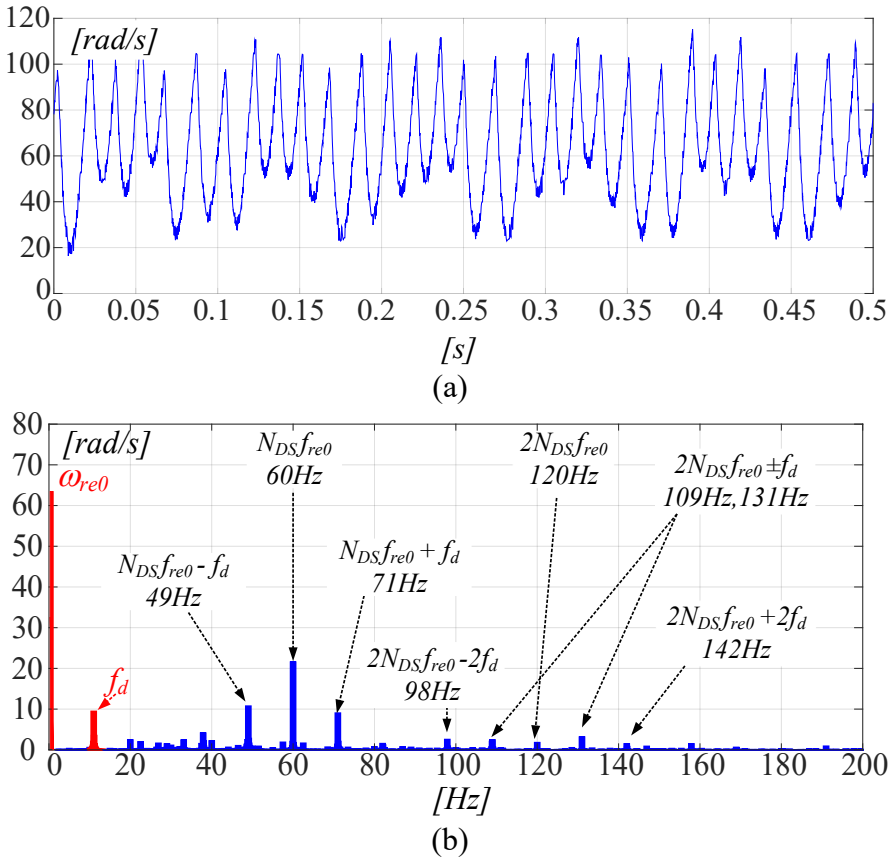

Figure 4.5.16 *Measured electrical frequency for $\omega_{re0} = 2\pi 10$ rad/s, ΔT_d = 45 mNm, $\omega_d = 2\pi 11$ rad/s, φ_d = 0 rad and N_{DS} = 6. (a) waveform (b) FFT.*

Moreover, the FFT shows that narrow band modulation of low order quantization harmonics is also present, as predicted in section 3.3. These effects are confirmed in the measured torque shown in Fig. 4.5.17. The time harmonics produced by the phase modulation of the quantization space harmonics that were present in the estimate in Fig. 4.5.16b, are now induced on the rotor shaft by the speed-controlled drive, in addition to the load torque disturbance. This formerly unreported phenomenon is now fully explained.

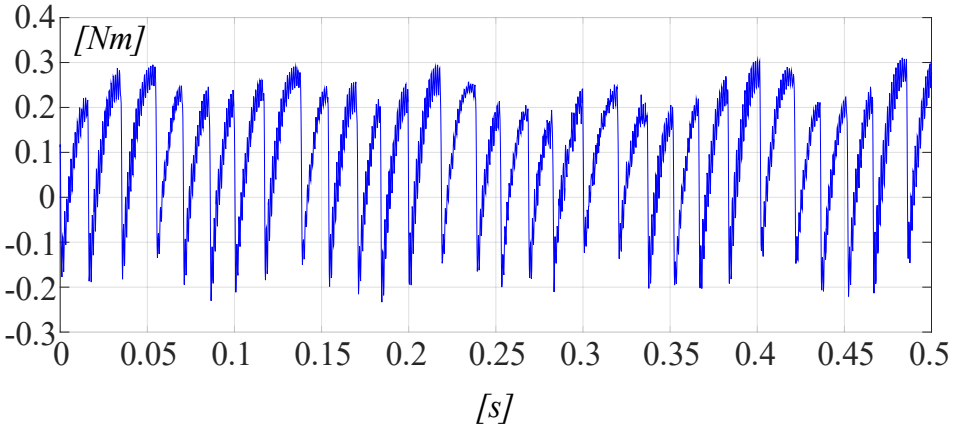

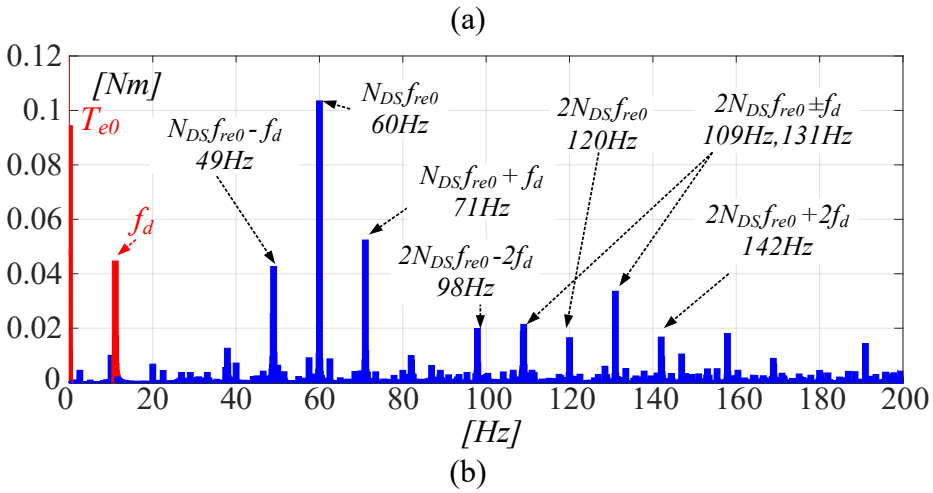

Figure 4.5.17 *Measured torque for $\omega_{re0} = 2\pi 10$ rad/s, $\Delta T_d = 45$ mNm, $\omega_d = 2\pi 11$ rad/s, $\varphi_d = 0$ rad and $N_{DS} = 6$. (a) waveform (b) FFT.*

4.6 Selection of the Rotor Position Sensor Resolution in Variable Speed Drives involving a Vector Tracking Observer in the Speed Loop

In this paragraph is presented a new approach, allowing to identify the minimum N_{DS} resolution of a position sensor starting from the analysis of the filtering action (section 4.5.1) of VTO, obtained by exploiting the theory of the spatial distribution of quantization harmonics, by means of Fourier series, of the rotor position measurement obtained by a finite resolution position sensor (paragraph 3.3).

A procedure has been developed to link the minimum sensor resolution N_{DS} with the required drive performance expressed in terms of speed control bandwidth and maximum speed ripple allowed at the minimum operating speed. Although the procedure adopted to select the rotor position sensor resolution has been applied to VFDs using a specific model-based estimation algorithm (i.e., VTO), it can be extended even to other estimation algorithms.

4.6.1 Estimated Speed Ripple Computation with Constant Speed of Rotation

The simplest scenario to consider in the estimation of the speed ripple is that for a constant electrical angular frequency $\omega_{re0}=2\pi f_{re0}$, i.e. a constant speed of rotation. By considering the expressions defined in section 3.3:

$$\theta_{re}^{(q)}(t) = \omega_{re0}t + \sum_{k=1}^{+\infty} \frac{2}{N_{DS}\,k} \sin(N_{DS}k\omega_{re0}t) \tag{4.6.1}$$

while, the instantaneous quantized speed $\omega_{re}^{(q)}(t)$, is defined as the time derivative of $\theta_{re}^{(q)}(t)$:

$$\omega_{re}^{(q)}(t) = \frac{d\theta_{re}^{(q)}(t)}{dt} = \omega_{re0} + \sum_{k=1}^{+\infty} 2\,\omega_{re0} \cos(N_{DS}k\omega_{re0}t) \tag{4.6.2}$$

By exploiting the decomposition of the VTSF transfer function done in sub-paragraph 4.5.1 it is possible to rewrite the function as:

$$W_{VTSF}(s) = \frac{k_1 A}{s + p_1} + \frac{k_1 B}{s + p_2} + \frac{k_1 C}{s + p_3} \tag{4.6.3}$$

By applying the inverse Laplace transform, the impulse response of (4.6.3) can be obtained:

$$w_{VTSF}(t) = \mathcal{L}^{-1}\left[W_{VTSF}(s)\right] = k_1\left[A\, e^{-p_1 t} + B\, e^{-p_2 t} + C\, e^{-p_3 t}\right] \tag{4.6.4}$$

In order to compute the estimated speed ripple in case of constant speed of rotation the block diagram shown in Fig. 4.6.1 has been considered.

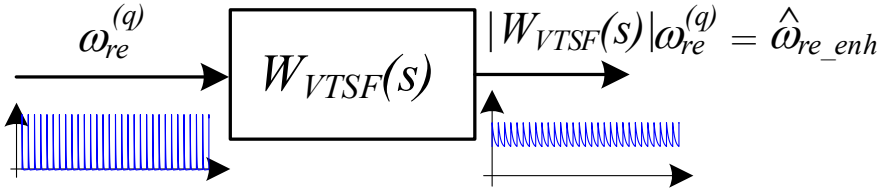

Figure 4.6.1 *VTSF Estimation from Instantaneous Quantized Speed.*

The analytical expression of the estimated speed $\hat{\omega}_{re\_enh}(t)$ is obtained by computing the convolution product between the instantaneous quantized speed $\omega_{re}^{(q)}(t)$ and the impulse response of the VTSF $w_{VTSF}(t)$.
Applying the convolution product allow to merge the temporal expression of the instantaneous quantized speed $\omega_{re}^{(q)}(t)$ with the VTSF transfer function $W_{VTSF}(s)$.
Generally, the convolution product between $\omega_{re}^{(q)}(t)$ and $w_{VTSF}(t)$ can be written as:

$$\hat{\omega}_{re\_enh}(t) = \omega_{re}^{(q)}(t) * w_{VTSF}(t) = \int_{-\infty}^{+\infty} \omega_{re}^{(q)}(\tau)\, w_{VTSF}(t - \tau)\, d\tau \tag{4.6.5}$$

By substituting the expressions (4.6.2) and (4.6.4) in (4.6.5) three components can be written, each of which is linked to each pole of the $W_{VTSF}(s)$, $\hat{\omega}_{re\_enh\_A}(t)$ to pole p_1, $\hat{\omega}_{re\_enh\_B}(t)$ to pole p_2 and $\hat{\omega}_{re\_enh\_C}(t)$ to polo p_3, respectively.

$$\hat{\omega}_{re\_enh\_A}(t) = \int_0^t \left[\omega_{re0} + 2\omega_{re0} \sum_{k=1}^{+\infty} \cos(N_{DS} k \omega_{re0} \tau)\right]\left[k_1 A\, e^{-p_1(t - \tau)}\right] d\tau \tag{4.6.6}$$

$$\hat{\omega}_{re\_enh\_B}(t) = \int_0^t \left[\omega_{re0} + 2\omega_{re0} \sum_{k=1}^{+\infty} \cos(N_{DS} k \omega_{re0} \tau)\right]\left[k_1 B\, e^{-p_2(t - \tau)}\right] d\tau \tag{4.6.7}$$

$$\hat{\omega}_{re\_enh\_C}(t) = \int_0^t \left[\omega_{re0} + 2\omega_{re0} \sum_{k=1}^{+\infty} \cos(N_{DS} k \omega_{re0} \tau)\right]\left[k_1 C\, e^{-p_2(t - \tau)}\right] d\tau \tag{4.6.8}$$

By exploiting the known properties of integration, the expressions (4.6.6) - (4.6.8) can be decomposed into two terms, the constant term linked to the reference speed ω_{re0}, which we will indicate for the three components with Ω_{0A}, Ω_{0B}, Ω_{0C} respectively, and the term linked to the quantization phenomena of the harmonics, which will be indicated for the three components with Ω_A, Ω_B, Ω_C respectively.

$$\Omega_{0A} = \omega_{re0}\, k_1\, A \int_0^t e^{-p_1(t-\tau)}\, d\tau = \omega_{re0}\, k_1\, A\, \frac{1 - e^{-p_1 t}}{p_1} \tag{4.6.9}$$

$$\Omega_{0B} = \omega_{re0}\, k_1\, B \int_0^t e^{-p_2(t-\tau)}\, d\tau = \omega_{re0}\, k_1\, B\, \frac{1 - e^{-p_2 t}}{p_2} \tag{4.6.10}$$

$$\Omega_{0C} = \omega_{re0}\, k_1\, C \int_0^t e^{-p_3(t-\tau)}\, d\tau = \omega_{re0}\, k_1\, C\, \frac{1 - e^{-p_3 t}}{p_3} \tag{4.6.11}$$

$$\Omega_A = 2\omega_{re0}\, k_1\, A \sum_{k=1}^{+\infty} \int_0^t \cos(N_{DS} k \omega_{re0} \tau)\, e^{-p_1(t-\tau)}\, d\tau \tag{4.6.12}$$

$$\Omega_B = 2\omega_{re0}\, k_1\, B \sum_{k=1}^{+\infty} \int_0^t \cos(N_{DS} k \omega_{re0} \tau)\, e^{-p_2(t-\tau)}\, d\tau \tag{4.6.13}$$

$$\Omega_C = 2\omega_{re0}\, k_1\, C \sum_{k=1}^{+\infty} \int_0^t \cos(N_{DS} k \omega_{re0} \tau)\, e^{-p_3(t-\tau)}\, d\tau \tag{4.6.14}$$

From the expressions (4.6.12) - (4.6.14) it is possible to define with $\Omega_A(k)$, $\Omega_B(k)$, $\Omega_C(k)$ the following integrations:

$$\Omega_A(k) = \int_0^t \cos(N_{DS} k \omega_{re0} \tau)\, e^{-p_1(t-\tau)}\, d\tau \tag{4.6.15}$$

$$\Omega_B(k) = \int_0^t \cos(N_{DS} k \omega_{re0} \tau)\, e^{-p_2(t-\tau)}\, d\tau \tag{4.6.16}$$

$$\Omega_C(k) = \int_0^t \cos(N_{DS} k \omega_{re0} \tau)\, e^{-p_3(t-\tau)}\, d\tau \tag{4.6.17}$$

where:

$$\Omega_A(k) = \frac{A\left[-p_1\, e^{-p_1 t} + p_1 \cos(N_{DS} k \omega_{re0} t) + N_{DS} k \omega_{re0} \sin(N_{DS} k \omega_{re0} t)\right]}{p_1^2 + (N_{DS} k \omega_{re0})^2} \tag{4.6.18}$$

$$\Omega_B(k) = \frac{B\left[-p_2\, e^{-p_2 t} + p_2 \cos(N_{DS} k \omega_{re0} t) + N_{DS} k \omega_{re0} \sin(N_{DS} k \omega_{re0} t)\right]}{p_2^2 + (N_{DS} k \omega_{re0})^2} \tag{4.6.19}$$

$$\Omega_C(k) = \frac{C\left[-p_3\, e^{-p_3 t} + p_3 \cos(N_{DS} k \omega_{re0} t) + N_{DS} k \omega_{re0} \sin(N_{DS} k \omega_{re0} t)\right]}{p_3^2 + (N_{DS} k \omega_{re0})^2} \tag{4.6.20}$$

Finally, by grouping the results obtained, the complete expression of the estimated speed by VTSF can be written, in case of constant input speed:

$$\hat{\omega}_{re\_enh}(t) = \Omega_0 + 2\,\omega_{re0}\, k_1 \sum_{k=1}^{+\infty} \left[\Omega_A(k) + \Omega_B(k) + \Omega_C(k)\right] \tag{4.6.21}$$

with $\Omega_0 = \Omega_{0A} + \Omega_{0B} + \Omega_{0C}$.

In Fig. 4.6.2 are shown each expression of the estimated speed components $\hat{\omega}_{re\_enh}(t)$ obtained by means of the convolution product:

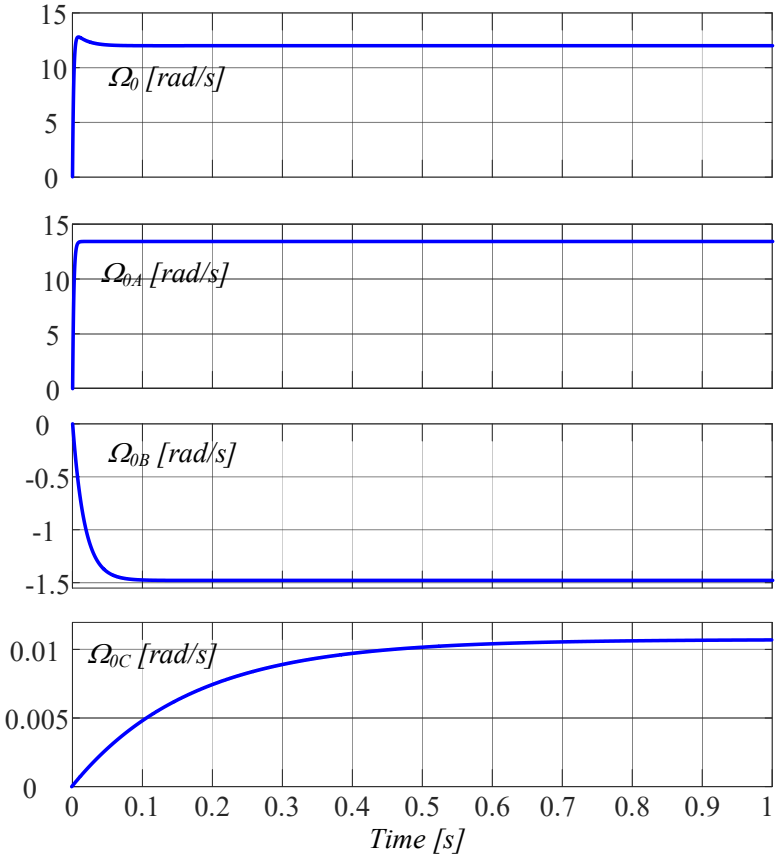

(a)

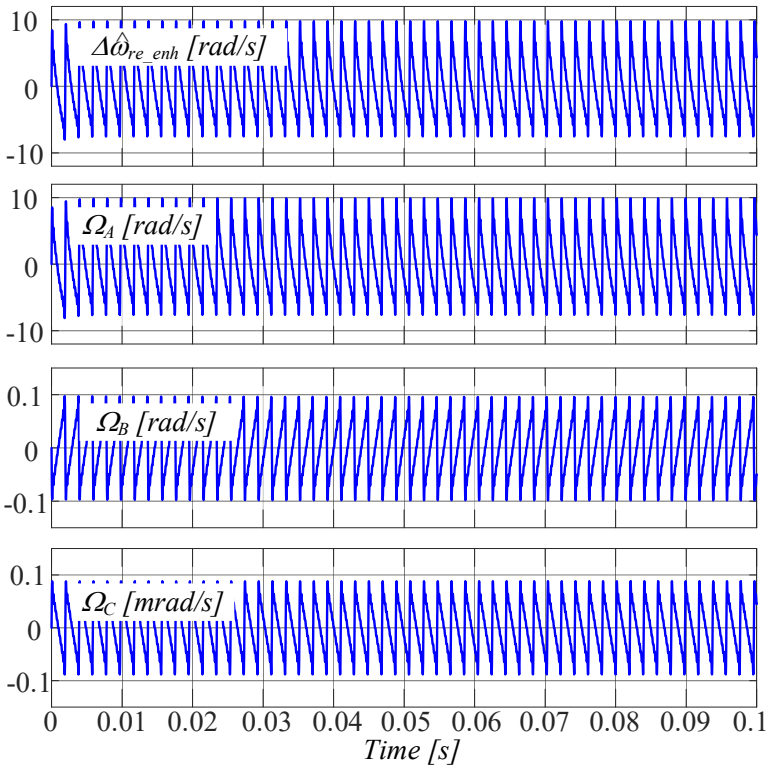

(b)

Figure 4.6.2 *Each Computed Components of the estimated speed enhanced speed: (a) related to constant reference speed ω_{re0}, (b) related to the quantization harmonics phenomena.*

The complete expression of the estimated speed ripple $\Delta\hat{\omega}_{re\_enh}(t)$ on the estimated speed $\hat{\omega}_{re\_enh}(t)$ can be written by considering the impact of the VTSF in the estimated speed. Since the VTSF transfer function has been decomposed in three parts (4.6.3) and from the convolution product computed in (4.6.5)-(4.6.20), the expression of the estimated speed ripple will be composed of three components defined above in (4.6.12)-(4.6.14):

$$\Delta\hat{\omega}_{re\_enh}(t) = 2\,\omega_{re0}\,k_1 \sum_{k=1}^{+\infty}\left[\Omega_A(k) + \Omega_B(k) + \Omega_C(k)\right] \tag{4.6.22}$$

As already described in sub-section 4.5.1 and as shown in Fig. 4.6.2, from this study it is possible to neglect the terms linked to the poles p_2 and p_3 and to consider only the fastest pole, i.e. p_1.

The block diagram considered in this study is shown in Fig. 4.6.3:

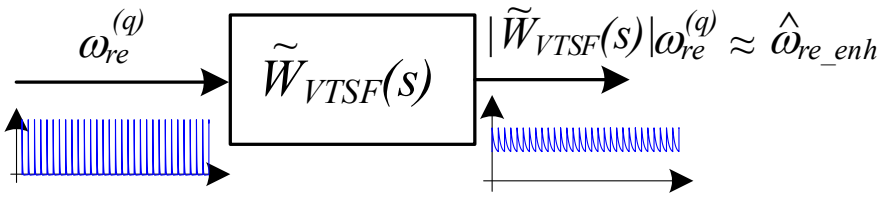

Figure 4.6.3 *Approximated VTSF Estimation from Instantaneous Quantized Speed.*

Therefore, the approximated speed ripple expression $\Delta\hat{\omega}_{re\_enh}(t)$ is given:

$$\Delta\hat{\omega}_{re\_enh}(t) \approx 2\omega_{re0}\, k_1 A \sum_{k=1}^{+\infty} \frac{-p_1\, e^{-p_1 t} + p_1 \cos(N_{DS} k \omega_{re0} t) + N_{DS} k \omega_{re0} \sin(N_{DS} k \omega_{re0} t)}{p_1^2 + (N_{DS} k \omega_{re0})^2} \tag{4.6.22}$$

By considering the approximation of the (4.6.22) in steady state condition, i.e. for $t \rightarrow +\infty$, the exponential part of (4.6.22) became to zero, thus:

$$\Delta\hat{\omega}_{re\_enh}(t) \approx 2\omega_{re0}\, k_1 A \sum_{k=1}^{+\infty} \frac{p_1 \cos(N_{DS} k \omega_{re0} t) + N_{DS} k \omega_{re0} \sin(N_{DS} k \omega_{re0} t)}{p_1^2 + (N_{DS} k \omega_{re0})^2} \tag{4.6.23}$$

Finally, the expression (4.6.23) can be rewritten as:

$$\Delta\hat{\omega}_{re\_enh}(t) \approx \sum_{k=1}^{+\infty} \frac{2\omega_{re0}\, k_1 A}{\sqrt{p_1^2 + (N_{DS} k \omega_{re0})^2}} \cos\left[N_{DS} k \omega_{re0} t - \operatorname{atan}\left(\frac{N_{DS} k \omega_{re0}}{p_1} \right) \right] \tag{4.6.24}$$

4.6.2 Estimated Speed Ripple Computation with Single Sinusoidal Disturbance

The computation of the estimated speed ripple can also be extended in case of a constant speed with superimposed a periodic disturbance. By referring the block diagram shown in Fig. 4.6.4 and considering the instantaneous quantized speed $\omega_{re}^{(q)}(t)$ with a periodic disturbance, already defined in section 3.3:

$$\omega_{re}^{(q)}(t) = \omega_{re0} + \Delta\omega_{re}\cos(\omega_d t + \varphi_d) + \sum_{k=1}^{+\infty} \frac{2}{N_{DS} k} \sum_{n=-\infty}^{+\infty} J_n\left(\frac{N_{DS} k \Delta\omega_{re}}{\omega_d} \right) (N_{DS} k \omega_{re0} + n\omega_d) \cos((N_{DS} k \omega_{re0} + n\omega_d)t + n\varphi_d) \tag{4.6.25}$$

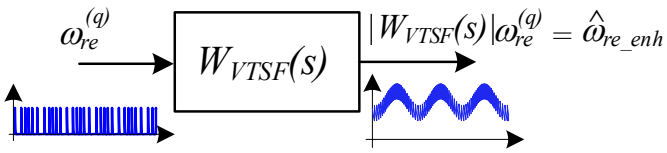

Figure 4.6.4 *VTSF Estimation from Instantaneous Quantized Speed with superimposed a periodic disturbance.*

By applying the convolution product of (4.6.5), the components of the final expression of the estimated speed are:

- The first components are exclusively linked to the constant speed value ω_{re0} and, as already defined in sub-section 4.6.1, are indicated with: Ω_{0A}, Ω_{0B} e Ω_{0C}

$$\Omega_0 = \Omega_{0A} + \Omega_{0B} + \Omega_{0C} = \omega_{re0}\, k_1 \left[A\, \frac{1 - e^{-p_1 t}}{p_1} + B\, \frac{1 - e^{-p_2 t}}{p_2} + C\, \frac{1 - e^{-p_3 t}}{p_3} \right] \tag{4.6.26}$$

- The second components are linked to a sinusoidal disturbance $\Delta\omega_{re}\cos(\omega_d t + \varphi_d)$ superimposed to ω_{re0} and are indicated with Ω_{dA}, Ω_{dB} e Ω_{dC}

$$\Omega_{dA} = \frac{\Delta\omega_d A\left[-p_1 e^{-p_1 t} + p_1 \cos(\omega_d t) + \omega_d \sin(\omega_d t)\right]}{p_1^2 + \omega_d^2} \tag{4.6.27}$$

$$\Omega_{dB} = \frac{\Delta\omega_d B\left[-p_2 e^{-p_2 t} + p_2 \cos(\omega_d t) + \omega_d \sin(\omega_d t)\right]}{p_2^2 + \omega_d^2} \tag{4.6.28}$$

$$\Omega_{dC} = \frac{\Delta\omega_d C\left[-p_3 e^{-p_3 t} + p_3 \cos(\omega_d t) + \omega_d \sin(\omega_d t)\right]}{p_3^2 + \omega_d^2} \tag{4.6.29}$$

where $\Omega_d = \Omega_{dA} + \Omega_{dB} + \Omega_{dC}$ is the sum of the three components (4.6.27) – (4.6.29) linked to a sinusoidal disturbance.

- Finally, the components related to the quantization harmonics phenomena of the $\omega_{re}^{(q)}$ can be considered for a generic pair of harmonics k e sub-harmonics n, are indicated with $\Omega_A(k,n)$, $\Omega_B(k,n)$ e $\Omega_C(k,n)$

$$\Omega_A(k,n) = \frac{k_1 A\left[-p_1 e^{-p_1 t} + p_1 \cos((N_{DS}k\omega_{re0} + n\omega_d)t + n\varphi_d) + (N_{DS}k\omega_{re0} + n\omega_d)\sin((N_{DS}k\omega_{re0} + n\omega_d)t + n\varphi_d)\right]}{p_1^2 + (N_{DS}k\omega_{re0} + n\omega_d)^2} \tag{4.6.30}$$

$$\Omega_B(k,n) = \frac{k_1 B\left[-p_2 e^{-p_2 t} + p_2 \cos((N_{DS}k\omega_{re0} + n\omega_d)t + n\varphi_d) + (N_{DS}k\omega_{re0} + n\omega_d)\sin((N_{DS}k\omega_{re0} + n\omega_d)t + n\varphi_d)\right]}{p_2^2 + (N_{DS}k\omega_{re0} + n\omega_d)^2} \tag{4.6.31}$$

$$\Omega_C(k,n) = \frac{k_1 C\left[-p_3 e^{-p_3 t} + p_3 \cos((N_{DS}k\omega_{re0} + n\omega_d)t + n\varphi_d) + (N_{DS}k\omega_{re0} + n\omega_d)\sin((N_{DS}k\omega_{re0} + n\omega_d)t + n\varphi_d)\right]}{p_3^2 + (N_{DS}k\omega_{re0} + n\omega_d)^2} \tag{4.6.32}$$

Therefore, the estimated speed ripple expression is given:

$$\Delta\hat{\omega}_{re\_enh} = \sum_{k=1}^{+\infty} \frac{2}{N_{DS}k} \sum_{n=-\infty}^{+\infty} J_n\left(\frac{N_{DS}k\Delta\omega_{el}}{\omega_d}\right)(N_{DS}k\omega_{el0}+n\omega_d)\left[\Omega_A(k,n)+\Omega_B(k,n)+\Omega_C(k,n)\right] \tag{4.6.33}$$

Fig. 4.6.5 shows the temporal waveforms of the various components of the estimated speed by the VTSF, when a single sinusoidal disturbance is considered. From Fig. 4.6.5 it can be observed how the components linked to ω_{re0} are identical to those obtained in the case with constant speed; the components Ω_{dA}, Ω_{dB} and Ω_{dC} are exclusively related to the sinusoidal disturbance; on the other hand, the components that composing the estimated speed ripple $\Omega_A(k,n)$, $\Omega_B(k,n)$ and $\Omega_C(k,n)$ have the same shape in the case with constant speed.

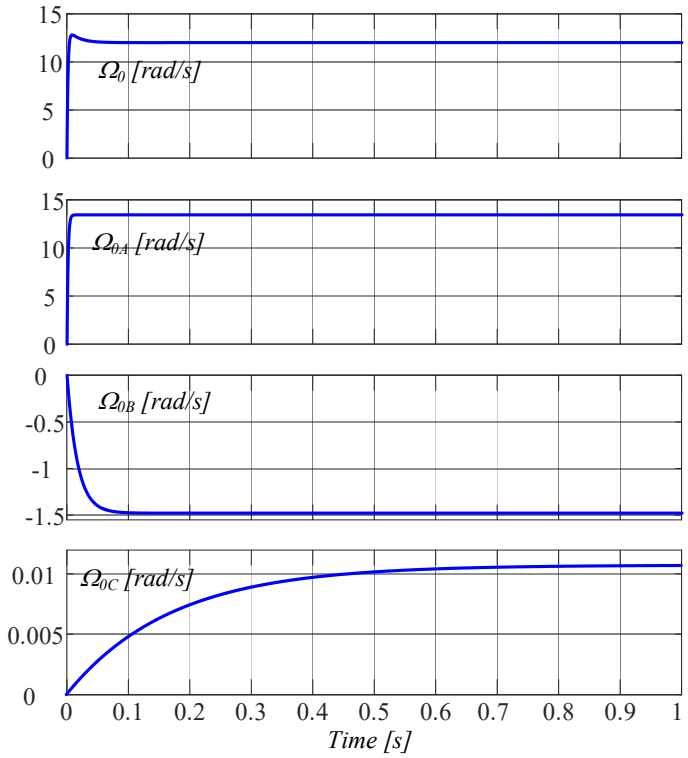
15
10
5
0
Ω0 [rad/s]
15
10
5
0
Ω0A [rad/s]
0
-0.5
-1
-1.5
Ω0B [rad/s]
0.01
0.005
0
Ω0C [rad/s]
0 0.1 0.2 0.3 0.4 0.5 0.6 0.7 0.8 0.9 1
Time [s]

(a)

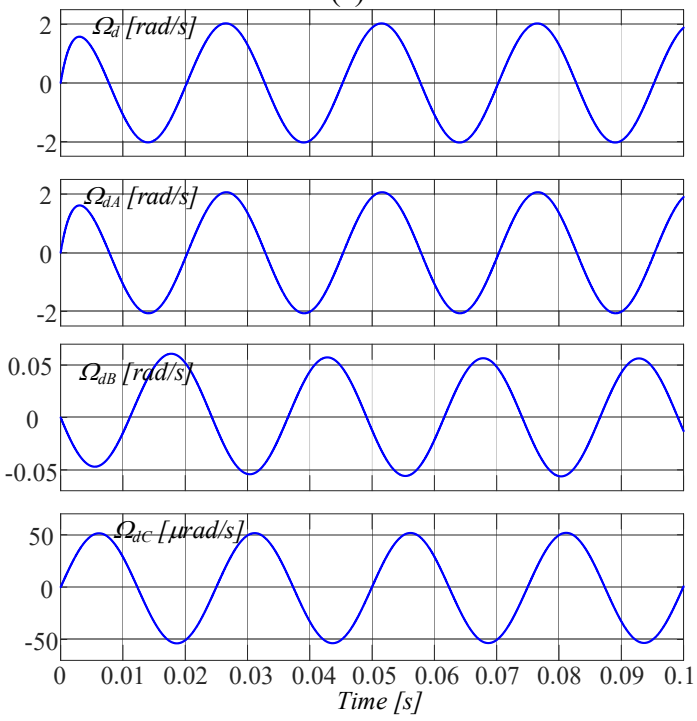
2
0
-2
Ωd [rad/s]
2
0
-2
ΩdA [rad/s]
0.05
0
-0.05
ΩdB [rad/s]
50
0
-50
ΩdC [μrad/s]
0 0.01 0.02 0.03 0.04 0.05 0.06 0.07 0.08 0.09 0.1
Time [s]

(b)

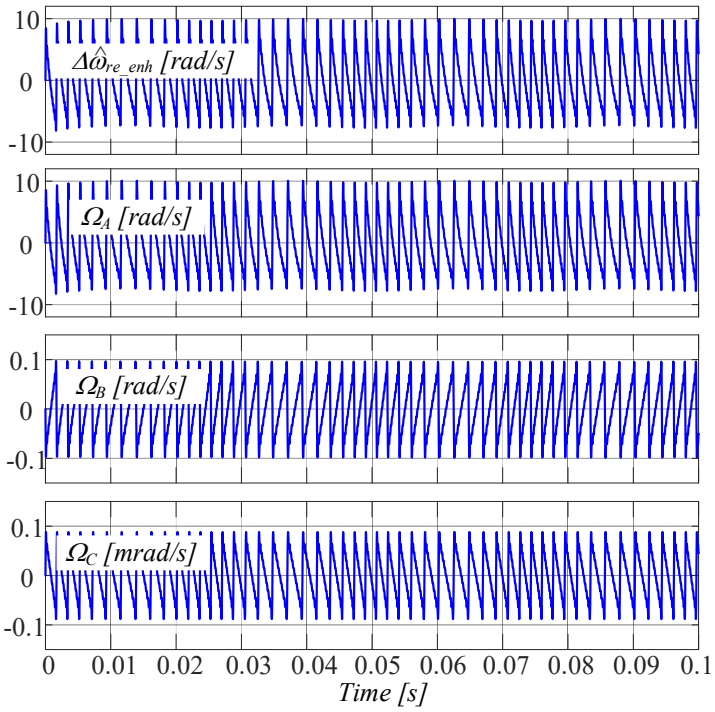

(c)

Figure 4.6.5 *Each Computed Components of the Estimated Speed enhanced speed: (a) related to constant reference speed ω_{re0}, (c) related to the a single sinusoidal disturbance and (c) related to the quantization harmonics phenomena.*

Finally, the estimated speed from the VTSF, when a single sinusoidal disturbance is considered, holds:

$$\hat{\omega}_{re\_enh}(t) = \Omega_0 + \Omega_d + \Delta\hat{\omega}_{re\_enh}(t) \tag{4.6.34}$$

Based on defined in sub-section 4.5.1 and deduced from the expressions (4.6.26) - (4.6.34) and even from Fig. 4.6.5, it is possible to exploit the same approximations that allow to simplify, also for this case with single sinusoidal disturbance, the final expression of the approximate estimated speed and therefore its ripple.

4.6.3 Computation of the peak to peak estimated speed ripple

Starting from the approximated expression of the speed ripple (4.6.35), defined in sub-paragraph 4.6.1, in order to numerically quantify the filtering action of the speed estimation algorithm, the speed ripple produced by the quantization harmonics in the speed estimate $\Delta\tilde{\omega}_{re}(t)$ is computed in the steady state and suitably manipulated, giving the expression (4.6.37). This latter expression is obtained by considering the approximations (4.6.36), which are satisfied whenever index $k \geq 10$, Fig. 4.6.6 and 4.6.7:

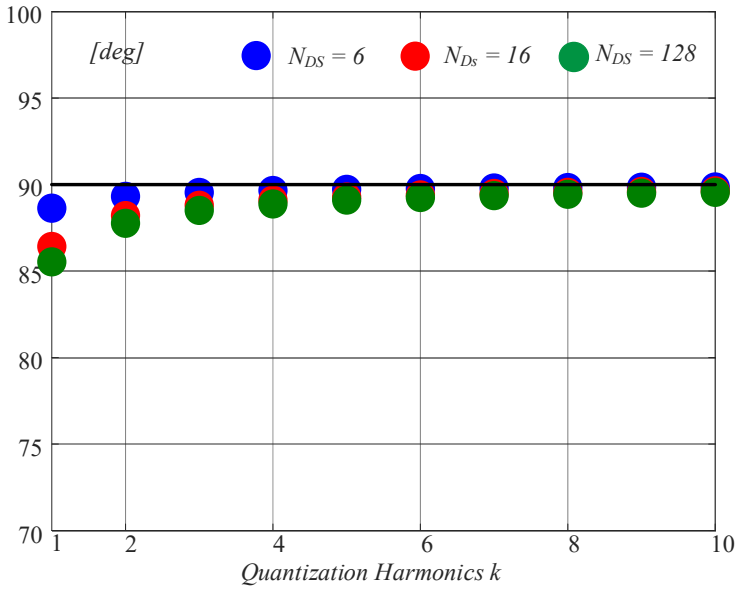

Figure 4.6.6 *Approximation of the arctangent in (4.6.36) relationships with different N_{DS} and considering the first 10^{th} harmonics of the quantized speed.*

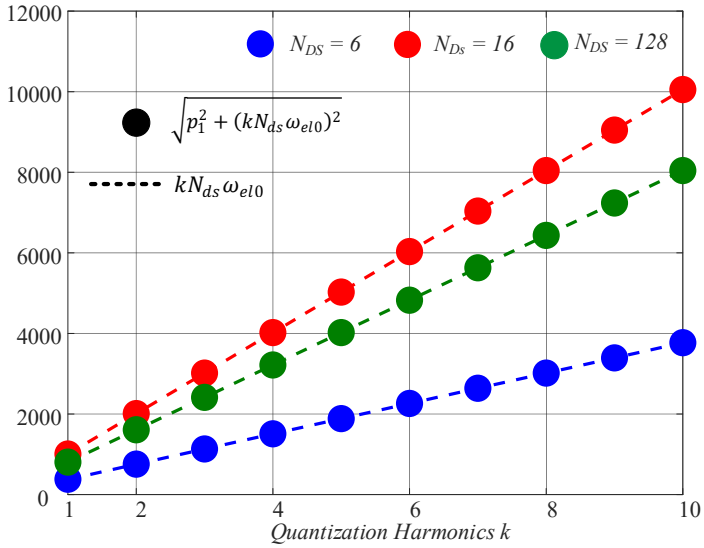

Figure 4.6.7 *Approximation of the square root in (4.6.36) relationships with different N_{DS} and considering the first 10^{th} harmonics of the quantized speed.*

$$\Delta\hat{\omega}_{re\_enh}(t) \approx \sum_{k=1}^{+\infty} \frac{2\omega_{re0}\, k_1 A}{\sqrt{p_1^2 + (N_{DS}k\omega_{re0})^2}} \cos\left[N_{DS}k\omega_{re0}t - \text{atan}\left(\frac{N_{DS}k\omega_{re0}}{p_1}\right)\right] \qquad (4.6.35)$$

$$atan\left(\frac{kN_{DS}\omega_{re0}}{p_1}\right) \approx \frac{\pi}{2} \qquad \sqrt{p_1^2+(kN_{DS}\omega_{el0})^2} \approx kN_{DS}\omega_{el0} \qquad (4.6.36)$$

$$\Delta\tilde{\omega}_{re}(t) = 2\omega_{re0}\, k_{1A} \sum_{k=1}^{+\infty} \frac{\sin(kN_{DS}\omega_{re0}t)}{kN_{DS}\omega_{re0}} \tag{4.6.37}$$

The effectiveness of the above modeling is confirmed by the results shown in Fig. 4.6.8, where the speed ripple carried out from the simulations of VTO implementation, and $\Delta\tilde{\omega}_{re}(t)$ have been compared at the same $f_{BWvto} = 10Hz$, at different f_{re0} and N_{DS}. In all cases good accuracy in the estimated speed ripple is achieved.

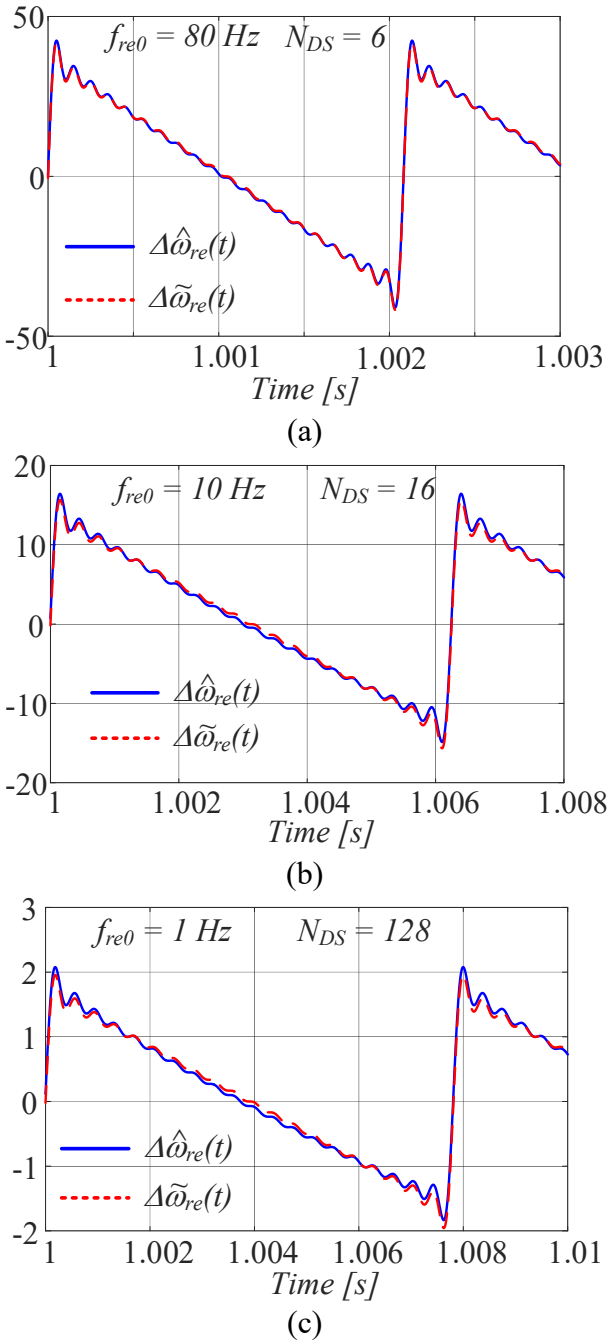

Figure 4.6.8 *Estimated rotor speed ripple with VTO implementation and approximated speed ripple at different operating points and sensor resolutions.*

The maximum value $\Delta\tilde{\omega}_{remax}$ of the estimated speed ripple can be calculated by truncating (4.6.37) to the first n quantization harmonics and computing its derivative, (4.6.38).

$$\frac{d\Delta\tilde{\omega}_{re}(t)|_n}{dt} = 2\omega_{re0}\, k_1 A \sum_{k=1}^{n} cos\left(kN_{DS}\omega_{re0}t\right) \tag{4.6.38}$$

To determine the zeros of the function (4.6.38) it is necessary to solve the following equation:

$$\sum_{k=1}^{n} cos\left(kN_{DS}\omega_{re0}t\right) = 0 \tag{4.6.39}$$

By exploiting the trigonometric operations it is possible to rework the equation (4.6.39) and rewrite it as follows:

$$2\sin\left(kN_{DS}\omega_{re0}t\right) \sum_{k=1}^{n} cos\left(kN_{DS}\omega_{re0}t\right) = 0 \tag{4.6.40}$$

It is shown that (40), through the sine addition formula, can be rewritten as follows:

$$\sum_{k=1}^{n} \left\{ sin\left[(k+1)N_{DS}\omega_{re0}t\right] - sin\left[(k-1)N_{DS}\omega_{re0}t\right] \right\} = 0 \tag{4.6.41}$$

The sum expressed in (4.6.41) is convergent, for any $n \in \mathbb{N}$, to the following result:

$$sin\left[(n+1)N_{DS}\omega_{re0}t\right] + sin\left(nN_{DS}\omega_{re0}t\right) - sin\left(N_{DS}\omega_{re0}t\right) = 0 \tag{4.6.42}$$

It is shown that the solutions of equation (4.6.42) are:

$$t_0 = \frac{\pi}{(n+1)N_{DS}\omega_{re0}} \tag{4.6.43}$$

By means the trigonometric operations performed in the equations (4.6.39) - (4.6.42), the result obtained in (4.6.43) is a zero of the equation (4.6.38), therefore the maximum point $\Delta\tilde{\omega}_{remax}$ occurs at the instant t_0, (4.6.43). Substituting (4.6.43) in (4.6.37) and by further algebraic manipulations we can obtain:

$$\Delta\tilde{\omega}_{remax} = \Delta\tilde{\omega}_{re}(t_0) = 2\omega_{re0}\, k_1 A \sum_{k=1}^{n} \frac{sin\left(\frac{k\pi}{n+1}\right)}{kN_{DS}\omega_{re0}} \tag{4.6.44}$$

The expression (4.6.44) can be rewritten as following:

$$\Delta\tilde{\omega}_{remax} = \Delta\tilde{\omega}_{re}(t_0) = \frac{2\omega_{re0}\, k_1 A}{N_{DS}\omega_{re0}} \frac{\pi}{n+1} \sum_{k=1}^{n} \frac{sin\left(\frac{k\pi}{n+1}\right)}{\frac{k\pi}{n+1}} \tag{4.6.45}$$

The expression defined in (4.6.46) $\Re$ is the result of the Riemann sum.

$$\Re = \frac{\pi}{n+1} \sum_{k=1}^{n} \frac{sin\left(\frac{k\pi}{n+1}\right)}{\frac{k\pi}{n+1}} \rightarrow \int_0^{\pi} \frac{\sin(x)}{x} dx = 1.851937 \tag{4.6.46}$$

the maximum value of (4.6.37) can be definitively expressed as:

$$\Delta\tilde{\omega}_{remax} = \Delta\tilde{\omega}_{re}(t_0) = \frac{2k_1 A\Re}{N_{DS}} \tag{4.6.47}$$

As it is necessary to calculate the peak-to-peak value $\Delta\tilde{\omega}_{reppk}$ of $\Delta\hat{\tilde{\omega}}_{re}$, it will be expressed as a percentage of the operating speed ω_{re0}, (4.6.48).

$$\Delta\tilde{\omega}_{reppk}\,\% = \frac{2\,\Delta\tilde{\omega}_{remax}}{\omega_{re0}} 100 = \frac{4k_1\, A\Re}{\omega_{re0} N_{DS}} 100 \tag{4.6.48}$$

4.6.4 Selection of Rotor Position Sensor Resolution

Starting from (4.6.48), it is possible to determine the minimum value of sensor resolution N_{DSmin} capable to satisfy the desired requirements of the speed observer, expressed in terms of with a desired speed loop bandwidth and maximum estimated speed ripple $\Delta\tilde{\omega}_{reppk}\%$ at the minimum operating speed ω_{re0min}:

$$N_{DSmin} = \frac{8.88\ \pi f_{BWvto}\, \Re}{\omega_{re0min}\Delta\hat{\tilde{\omega}}_{reppk}\%} 100 \tag{4.6.49}$$

In particular, the minimum rotor position sensor resolution expression (4.6.49), has been calculated from (4.6.48) by substituting the values of the coefficients, $A = 1.011$ and $k_1 = 2\pi f_{BWvto}$, calculated in sub-paragraph 4.5.1.

Fig. 4.6.9a displays $\Delta\tilde{\omega}_{reppk}\%$ vs N_{DS} at two different VTO bandwidths f_{BWvto} for a specific operating point f_{re0min}. It is worth noting that the filtering action of the speed observer on the quantization harmonics increases with N_{DS} increasing, and with f_{BWvto} decreasing. Moreover, (41) also confirms that for a specified N_{DS} at higher operating speeds, the filtering action in the speed estimation increases, Fig. 4.6.9b.

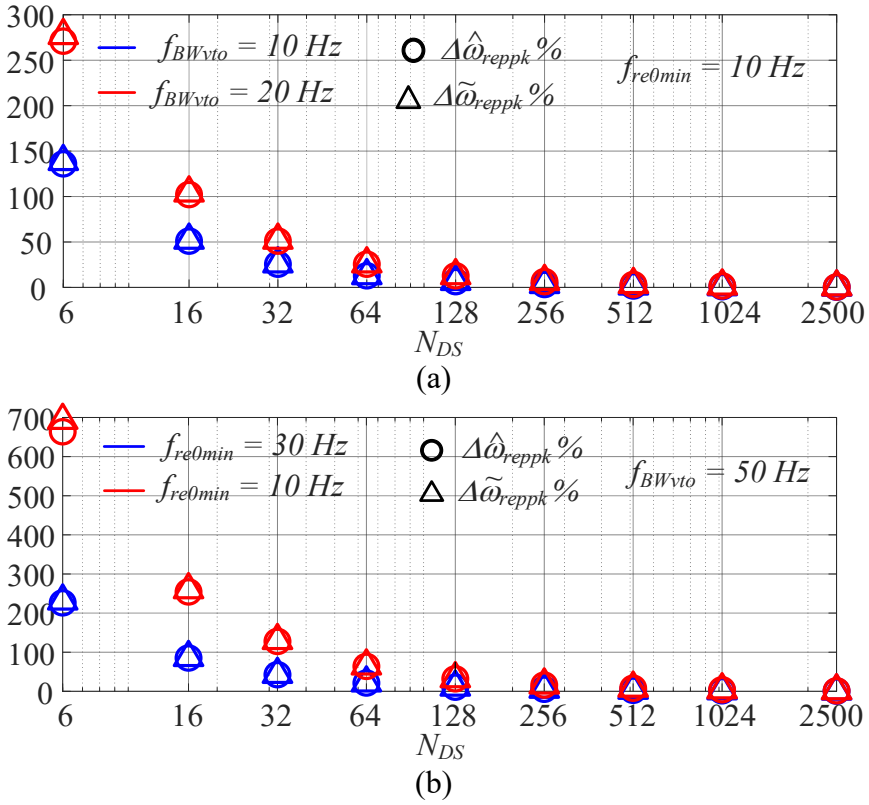

Figure 4.6.9 *approximated peak to peak speed ripple in p.u. vs* N_{DS}.

Although (4.6.49) provides a straightforward relationship between sensor resolution and speed estimation performances in the low speed operating region of the drive, the VTO bandwidth f_{BWvto} has to be properly selected in order to guarantee proper command tracking and disturbance rejection capabilities of the entire speed closed loop. The following section is addressed to establish a relationship between f_{BWvto} and the desired closed speed loop bandwidth $f_{BW\omega}$. Moreover, the effects of the speed closed loop on the quantization harmonic filtering process are investigated as well.

4.6.5 Speed Closed Loop Analysis

In the proposed approach the design of the speed loop is performed assuming an ideal measurement. The tuning of the PI speed controller $C_\omega(s)$ has been performed in paragraph 4.3. Hence, the poles placement method has been applied to impose the desired closed loop poles of the corresponding ideal closed loop transfer function $W_\omega(s)$. The ideal speed loop can be presented as in Fig. 4.6.10, with the plant transfer function $P_\omega(s)$ indicated in (4.6.50), where a purely inertial mechanical system is considered. As well already explained in paragraph 4.3, the mechatronic assumption is used here, i.e., the current control loop is assumed to be very fast, so its transfer function is approximated with a unity gain.

$$P_\omega(s) = \frac{1}{sJ} \qquad C_\omega(s) = \frac{k_p s + k_i}{s} \tag{4.6.50}$$

$$F_\omega(s) = C_\omega(s)\, P_\omega(s) = \frac{k_p s + k_i}{s^2 J} \qquad W_\omega(s) = \frac{F_\omega(s)}{1 + F_\omega(s)} = \frac{k_p s + k_i}{s^2 J + k_p s + k_i} \tag{4.6.51}$$

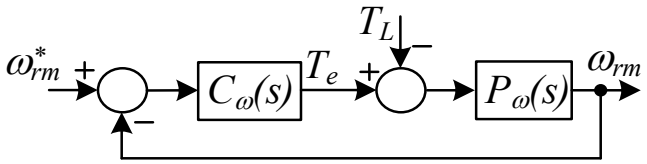

Figure 4.6.10 *Closed loop control structure with ideal speed sensor.*

Starting from the desired $f_{BW\omega}$, it is possible to assign the speed controller gains according to the pole placement method explained in sub-paragraph 4.3.1 and already defined in (4.6.52):

$$k_{p\omega} = (p_{1\omega} + p_{2\omega})\, J \qquad k_{i\omega} = p_{1\omega}\, p_{2\omega}\, J \tag{4.6.52}$$

the above specifications given in terms of poles ($p_{1\omega}$, $p_{2\omega}$) are equivalent to impose a desired ideal speed loop bandwidth $f_{BW\omega}$ and ideal phase margin $m_{\varphi i}$ to the controlled system. By assuming that the phenomena of quantization related to the finite sensor resolution can be modeled as a disturbance $d(t)$ superimposed to the electrical angular actual rotor speed ω_{re}, Fig. 4.6.11, it is possible to evaluate three transfer functions related to three different inputs: the reference speed ω^*_{rm}, the load torque T_L and the disturbance $d(t)$, and two different outputs: the actual rotor speed ω_{re} and the estimated rotor speed $\hat{\omega}_{rm}$.

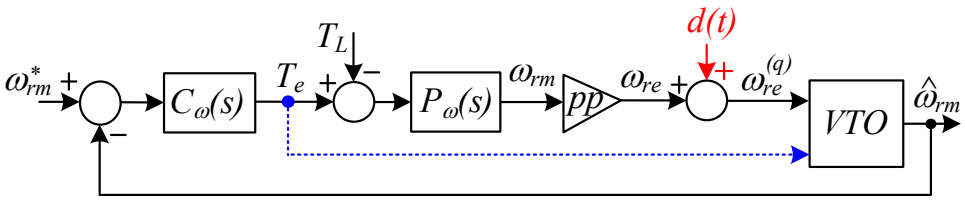

Figure 4.6.11 *Closed loop structure with the speed observer.*

where the disturbance $d(t)$ can be associated to the speed quantization harmonics when a single sinusoidal disturbance is superimposed to a constant speed:

$$d(t) = \sum_{k=1}^{+\infty} \frac{2}{N_{DS}\, k} \sum_{n=-\infty}^{+\infty} J_n\left(\frac{N_{DS} k \Delta\omega_{re}}{\omega_d}\right) (N_{DS} k \omega_{re0} + n\omega_d) \cos((N_{DS} k \omega_{re0} + n\omega_d)t + n\varphi_d) \tag{4.6.53}$$

When the reference speed ω^*_{rm} is considered as an input and the estimated rotor speed $\hat{\omega}_{rm}$ is considered as an output the transfer function obtained is the closed loop transfer function and is related to the command tracking performances:

$$W_{tot}(s) = \frac{\hat{\omega}_{rm}}{\omega^*_{rm}} = \frac{C_\omega(s)\left[W_{CFF}(s) + P_\omega(s) W_{VTSF}(s)\right]}{1 + C_\omega(s)\left[W_{CFF}(s) + P_\omega(s) W_{VTSF}(s)\right]} \tag{4.6.54}$$

$$F_{tot}(s) = C_\omega(s)\left[W_{CFF}(s) + P_\omega(s) W_{VTSF}(s)\right] \tag{4.6.55}$$

where $F_{tot}(s)$ is the control speed open loop transfer function.

When the load torque T_L is considered as an input and the actual rotor speed is considered as an output the transfer function obtained is the dynamic stiffness and is related to the disturbance rejection performances:

$$D_{tot}(s) = \frac{T_L}{\omega_{rm}} = \frac{1+C_\omega(s)\left[W_{CFF}(s) + P_\omega(s)W_{VTSF}(s)\right]}{P_\omega(s)\left[1 + C_\omega(s)W_{CFF}(s)\right]} \tag{4.6.56}$$

Finally, when the disturbance $d(t)$ is considered as an input and the actual rotor speed is considered as an output the transfer function obtained is the total filtering action on the quantization harmonics of the actual speed:

$$X(s) = \frac{\omega_{rm}}{d} = \frac{P_\omega(s)C_\omega(s)W_{VTSF}(s)}{1+C_\omega(s)\left[W_{CFF}(s)+W_{VTSF}(s)P_\omega(s)\right]} \tag{4.6.57}$$

In all transfer functions (4.6.54) - (4.6.57) have been consider two components of the VTO, the first one is the VTSF closed loop transfer function $W_{VTSF}(s)$, while the second one is the transfer function related to the feed forward input in the VTO, i.e., $W_{CFF}(s)$, defined as:

$$W_{CFF}(s) = \frac{\hat{\omega}_{rm}}{\hat{T}_e} = \frac{s^2}{\hat{J}\,(s^3 + k_1 s^2 + k_2 s + k_3)} \tag{4.6.58}$$

By considering that the estimation of the feed forward term is exactly $\hat{T}_e = T_e$ and also the estimated mechanical model is correct, i.e., $\hat{J} = J$, it is possible to consider the follow simplification:

$$P_\omega(s) = \left[W_{CFF}(s) + P_\omega(s)W_{VTSF}(s)\right] \tag{4.6.59}$$

Then, by considering the above simplifications the previously functions can be rewritten as:

$$W_{tot}(s) = \frac{\omega_{rm}}{\omega^*_{rm}} = \frac{C_\omega(s)P_\omega(s)}{1+C_\omega(s)P_\omega(s)} = W_\omega(s) = \frac{k_{p\omega}s+k_{i\omega}}{Js^2+k_{p\omega}s+k_{i\omega}} \tag{4.6.60}$$

$$D_{tot}(s) = \frac{T_L}{\omega_{rm}} = \frac{1+C_\omega(s)\left[W_{CFF}(s) + P_\omega(s)W_{VTSF}(s)\right]}{P_\omega(s)\left[1 + C_\omega(s)W_{CFF}(s)\right]} = \frac{1+C_\omega(s)P_\omega(s)}{P_\omega(s)\left[1 + C_\omega(s)W_{CFF}(s)\right]} \tag{4.6.61}$$

$$X(s) = W_\omega(s)\ W_{VTSF}(s) = \frac{k_{p\omega}s+k_{i\omega}}{Js^2+k_{p\omega}s+k_{i\omega}} \frac{k_1 s^2+k_2 s+k_3}{s^3+k_1 s^2+k_2 s+k_3} \tag{4.6.62}$$

It is possible to note that the closed loop transfer function $W_{tot}(s)$ coincides with the ideal closed loop transfer function; in particular, by considering the function $X(s)$ it is possible to note that the total filtering action on the quantization harmonics of the instantaneous speed is depending both on $f_{BW\omega}$ and f_{BWvto}. In fact, $k_{p\omega}$ and $k_{i\omega}$ are determined according to $f_{BW\omega}$, while the coefficients k_1, k_2 and k_3 are determined according to f_{BWvto}.

Furthermore, the expression of the dynamic stiffness $D_{tot}(s)$, considered when the VTO is included in closed speed loop, is a quite different then the dynamic stiffness $D(s)$ of the ideal speed loop:

$$D(s) = \frac{T_L}{\omega_{rm}} = \frac{1 + C_\omega(s)P_\omega(s)}{P_\omega(s)} = \frac{s}{Js^2 + k_p s + k_i} \tag{4.6.63}$$

In fact, $D_{tot}(t)$ can be rewritten as a function of the dynamic stiffness of the ideal speed loop:

$$D_{tot}(s) = \frac{T_L}{\omega_{rm}} = \frac{1+C_\omega(s)P_\omega(s)}{P_\omega(s)\left[1 + C_\omega(s)W_{CFF}(s)\right]} = \frac{D(s)}{1 + C_\omega(s)W_{CFF}(s)} \tag{4.6.64}$$

The main goal is to the combined selection of the ideal speed loop bandwidth and the VTO bandwidth allow to define the closed speed loop performance and also the mitigation of the quantization harmonics; in particular, the selection of the VTO bandwidth allow to mitigate the estimated speed quantization harmonics, while the combined selection of the ideal speed loop and VTO bandwidths allows to mitigate the quantization harmonics of the actual speed. Therefore, it is necessary to find a good compromise of the ratio between the speed loop and VTO bandwidths.

In order to find a good compromise on the ratio $f_{BW\omega}/f_{BWvto}$ it is necessary to evaluate the phase margin of the (4.6.55) and thus the robustness of the speed closed loop including the VTO. The phase margin of the (4.6.55) has been computed by using Matlab only to evaluate the robustness of the speed loop for some ratios of $f_{BW\omega}/f_{BWvto}$ selected. In Table XI four ratio has been selected and the associated phase margins have been computed:

Table XI $f_{BW\omega}/f_{BWvto}$ *vs* m_φ

$f_{BW\omega}/f_{BWvto}$	m_φ [deg]
1	42.7
3	66.1
5	74.5
10	81.8

From the results obtained in Table XI it possible to consider $f_{BW\omega}/f_{BWvto} \geq 1$ as a good compromise between the desired stability and robustness of the closed speed loop including the VTO and the mitigation of the quantization harmonics. In Fig. 4.6.12 shown the time-step responses of the (4.6.54) are shown with the considered ratios and phase margins of the Table XI:

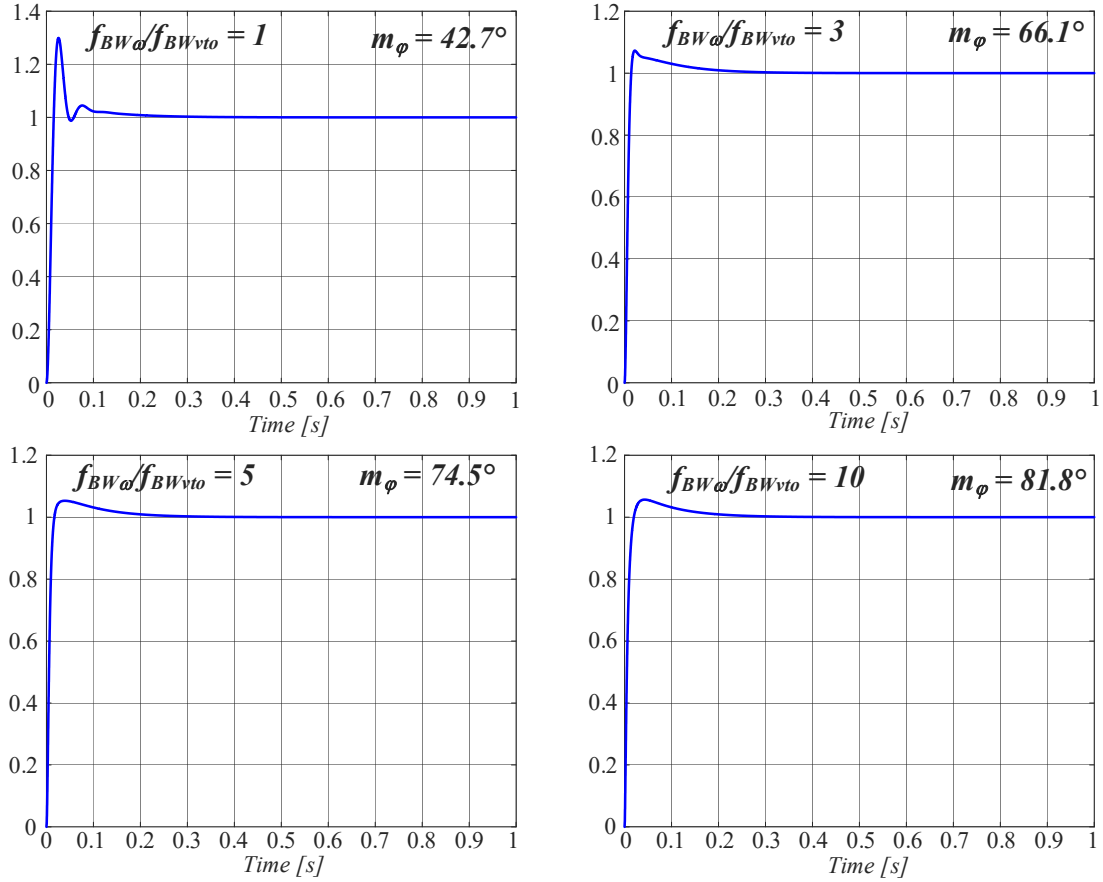

Figure 4.6.12 *Time-step responses of* $W_{tot}(s)$ *with different ratio* $f_{BW\omega}/f_{BWvto}$ *and by considering* $f_{BW\omega}$ = *20 Hz and* $J = 3.5\ 10^{-5}\ kgm^2$.

After having defined the ratio $f_{BW\omega}/f_{BWvto} \geq 1$ it is possible to include the finite resolution issues of the rotor position sensor in the speed closed loop. As explained in sub-paragraph 4.6.4 the minimum resolution can be selected by considering the expression (4.6.49) that depend on the minimum electrical angular rotor speed ω_{rm0min}, the desired ripple of the estimated electrical angular rotor speed $\Delta\hat{\omega}_{reppk}\%$ and the desired VTO bandwidth f_{BWvto}. In fact, the constraint on the desired ripple of the estimated electrical angular rotor speed allow to mitigate the quantization harmonics of the estimated rotor speed, however in the previously speed loop analysis the total filtering action on the actual speed has been computed in (4.6.62).

It is easy to show in Fig. 4.6.13 that the design constraint about the estimated speed ripple is more precautionary because the total filtering action mitigates more quantized harmonics then the VTO only and thus if the desired estimated speed ripple is fixed the actual speed ripple will be lower.

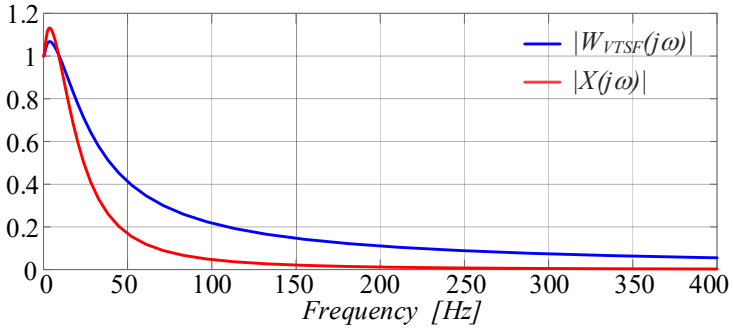

Figure 4.6.13 *Filtering action comparison between the $W_{VTSF}(s)$ and X(s) magnitudes.*

Finally, according to the above considerations it is possible to consider the effect of the finite resolution of the rotor position sensor in closed speed loop.

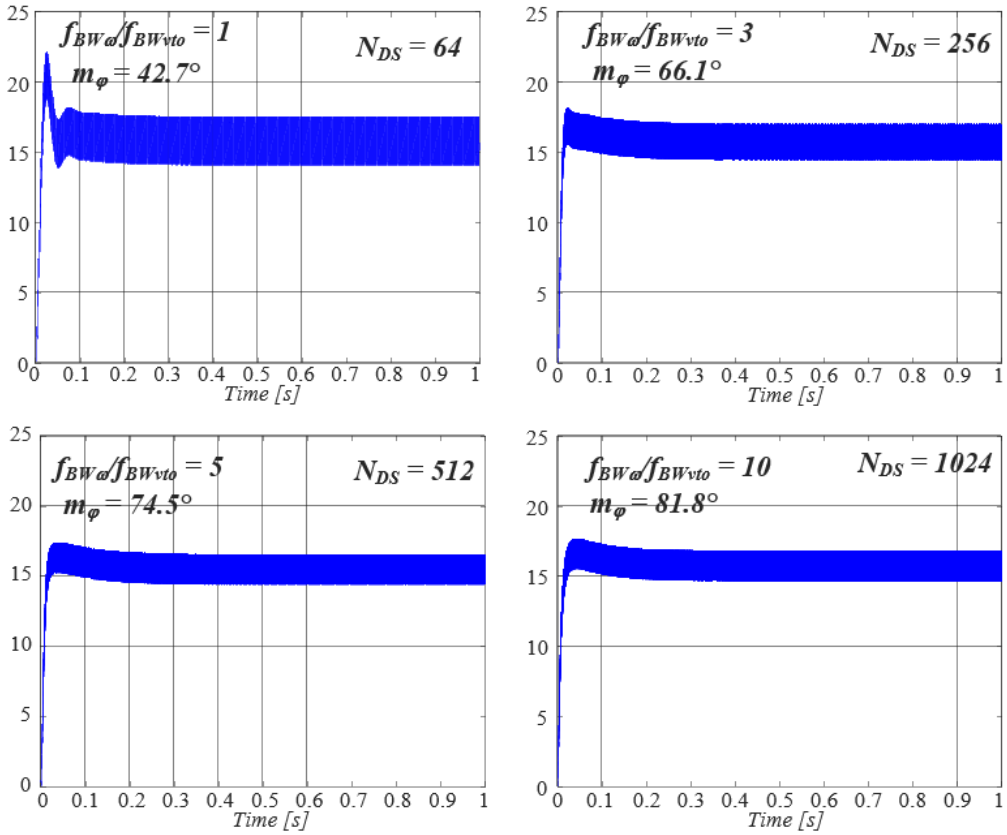

Figure 4.6.14 *Time-step responses of the estimated speed with different ratio $f_{BW\omega}/f_{BWvto}$ and different resolution, and by considering $f_{BW\omega}$ = 20 Hz, 20% of the estimated speed ripple and J = 3.5 10^{-5} kgm^2.*

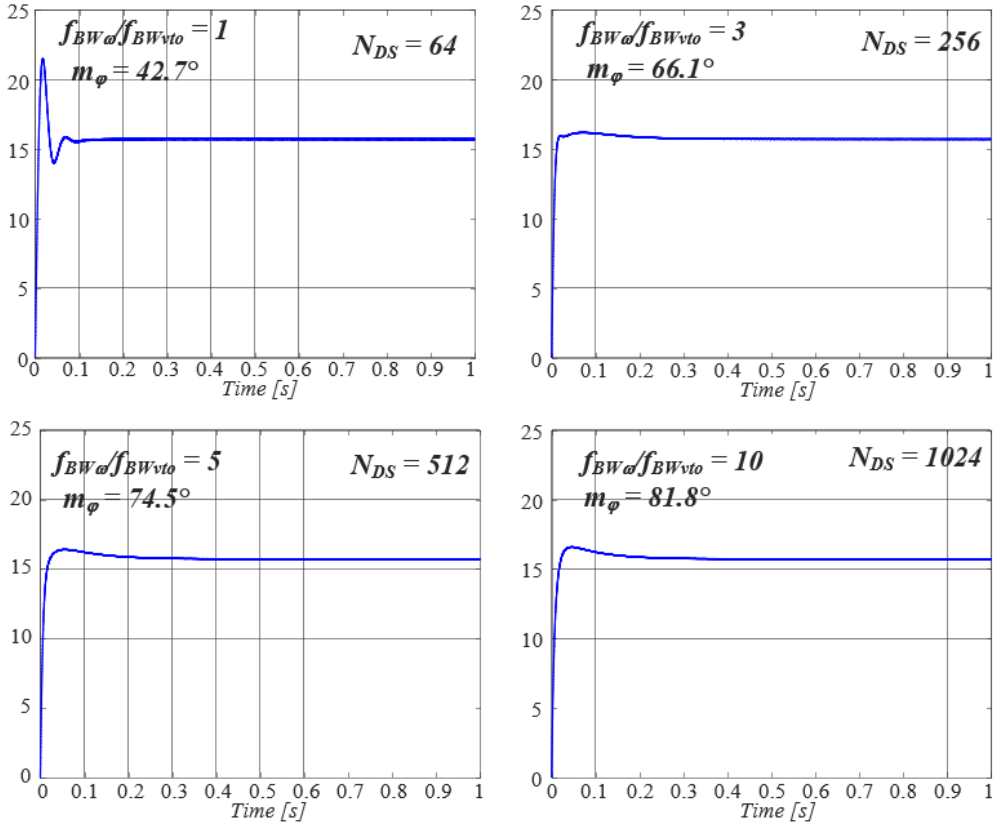

Figure 4.6.15 *Time-step responses of the actual speed with different ratio $f_{BW\omega}/f_{BWvto}$ and different resolution, and by considering $f_{BW\omega}$ = 20 Hz, 20% of the estimated speed ripple and J = 3.5 10^{-5} kgm^2.*

In Figs. 4.6.14 - 4.6.15 it would be noted that the finite resolution of the rotor position sensor has an impact on the estimated and actual speed ripple and thus on the stability and robustness of the closed speed loop.

A straightforward way to select the minimum value of rotor position resolution N_{DSmin} satisfying the design specifications of the drive in the low speed range can be achieved from the performance requirements of the drive expressed in terms of desired speed loop bandwidth $f_{BW\omega}$, the desired ratio between the speed loop and VTO bandwidth, typically $f_{BW\omega}/f_{BWvto} \geq 1$ and the estimated speed ripple in p.u. $\Delta\hat{\omega}_{reppk}\%$, all three referred to the minimum operating rotor speed ω_{rm_min}.

Therefore, starting from the above specifications, the selection of rotor position sensor resolution is achieved by the following steps:

1) Determination of the speed controller gains $k_{p\omega}$ and $k_{i\omega}$ according to the pole-placement method explained in sub-paragraph 4.3.1.

2) Determination of the VTO bandwidth according to:

$$f_{BW\omega}/f_{BWvto} \geq 1 \tag{4.6.65}$$

3) Computation of the minimum sensor's resolution N_{DSmin} allowed at the minimum rotating speed ω_{rm_min} according to the expression (4.6.49)

The above procedure can be exploited to identify the stability limits of the drive used for the experimental tests.

4.6.6 Experimental Test Bench

The experimental setup is shown in Fig. 4.6.16 and is consists of two mechanically coupled motors on the same shaft, Fig. 4.6.17, a common DC BUS supplied by a DC power supply 500V/5A, two SiC inverters operated at 20kHz. Both motor specifications are summarized in Tabs. XII and XIII. A dSpace DS1006 have been used to control the IPM drive under test and implementing the VTO algorithm.

Table XII *SPM Motor Drive Data*

Rated Power P_n	*2 kW*
Rated Speed ω_n	*6000 rpm*
Rated Torque T_n	*5 Nm*
Stator Resistance R_s	*0.84 Ω*
Synchronous Inductance L_s	*4.7 mH*
Pole pairs pp	*3*
Mechanical Inertia J	*3.4 kgcm²*

Table XIII *IPM Motor Drive Data*

Rated Power P_n	*3.6 kW*
Rated Speed ω_n	*2000 rpm*
Rated Torque T_n	*19.1 Nm*
Stator Resistance R_s	*2.4 Ω*
q-axis Inductance L_q	*12.189 mH*
d-axis Inductance L_d	*9.947 mH*
Pole pairs pp	*3*
Mechanical Inertia J	*21.7 kgcm²*

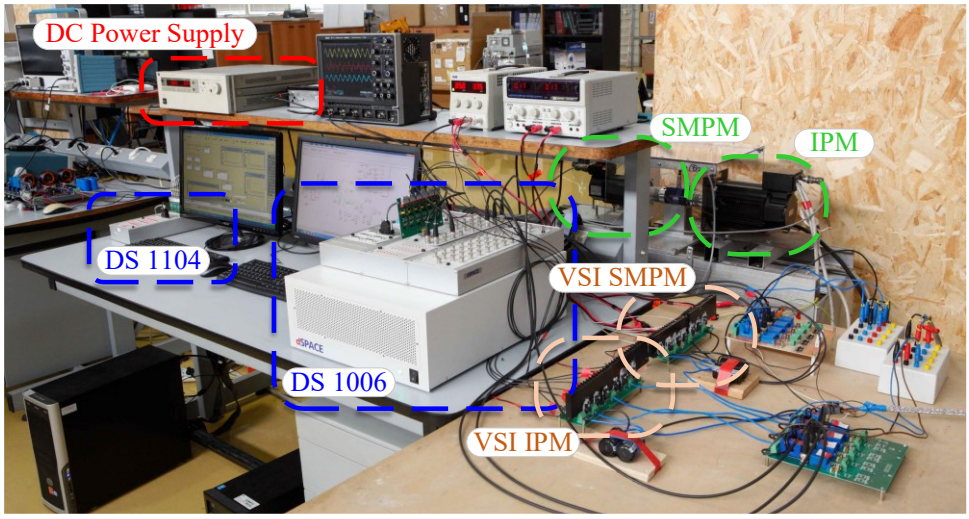

(a)

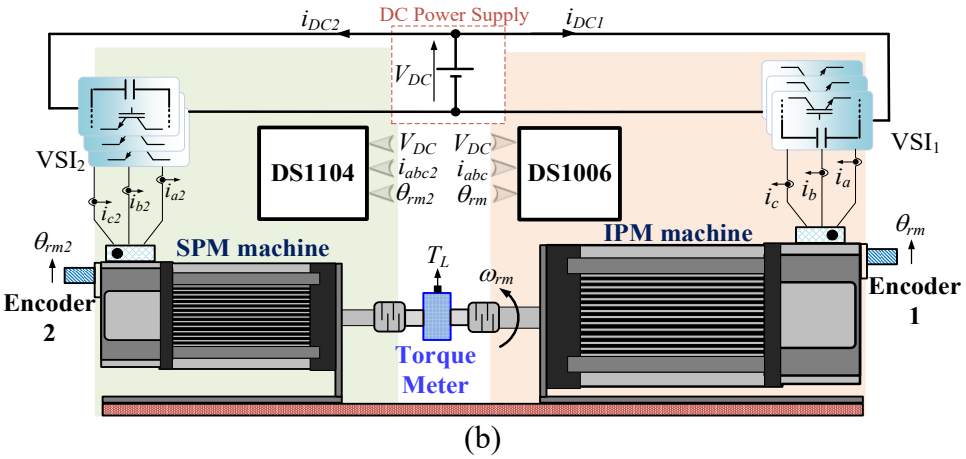

(b)

Figure 4.6.16 *Experimental servo-drive test bench: (a) photograph, (b) schematic.*

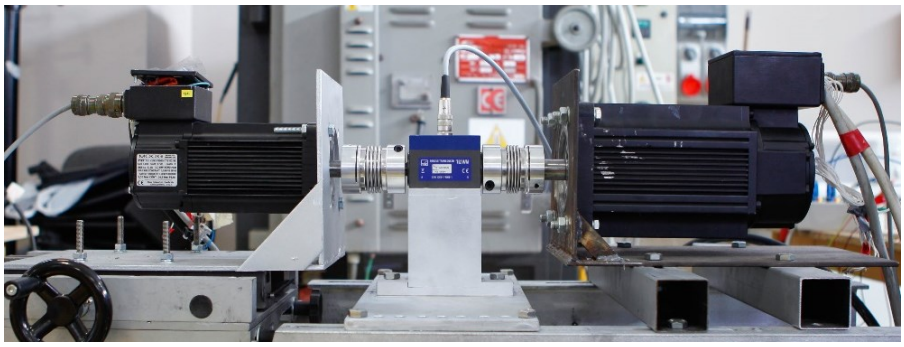

Figure 4.6.17 *IPMSM and SPMSM motors used in the experimental test bench.*

Both electric drives are equipped with incremental encoders with $N_{DS} = 2048$, and the different position sensor resolutions have been obtained by downsampling the encoder position measurement. Field oriented controls have been implemented in both drives, where the execution time of the current and speed loops are respectively $100\mu s$ and $200\mu s$. In all tests the current control loop bandwidth is fixed at 500Hz.

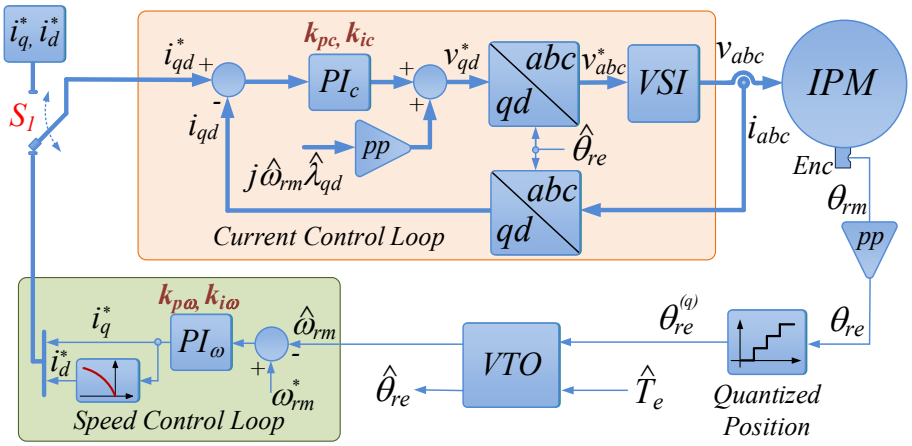

Figure 4.6.18 *Block diagram of the control implemented in the drive under test.*

4.6.7 Preliminary Experimental Tests

The consistence of the proposed approach of the rotor position resolution selection has been then assessed through steady state tests, dealing with three different values ratio of $f_{BW\omega}/f_{BWvto}$ = 1, 3 and 5, and fixing the speed loop bandwidth at $f_{BW\omega}$ = *20Hz* and the estimated speed ripple $\Delta\hat{\omega}_{reppk}\%$ = *20%*. Some results are shown in Figs. 4.6.19 - 4.6.23, which confirm the expression 4.6.49 and the theoretical approach explained in the previously sub-paragraphs 4.6.4 and 4.6.5.

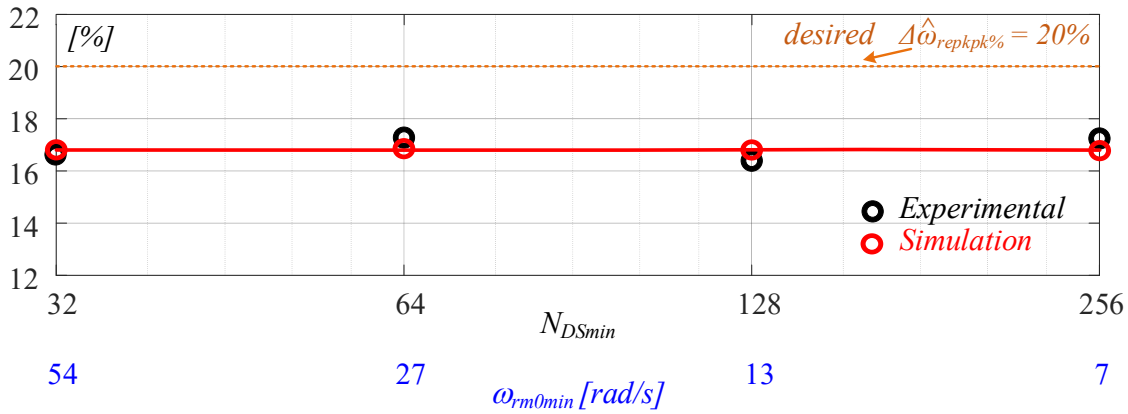

Figure 4.6.19 *Comparison between experimental and simulated estimated rotor speed ripple in p.u. at different sensor's resolution N_{DS} and with 20% desired speed ripple, 20Hz desired speed loop bandwidth and fixing the ratio $f_{BW\omega}/f_{BWvto}$ = 1.*

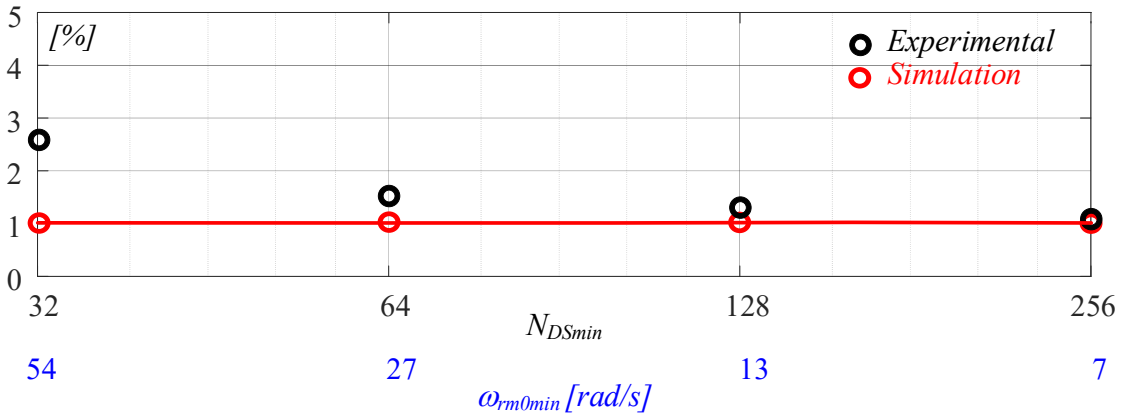

Figure 4.6.20 *Comparison between experimental and simulated actual rotor speed ripple in p.u. at different sensor's resolution N_{DS} and with 20% desired speed ripple, 20Hz desired speed loop bandwidth and fixing the ratio $f_{BW\omega}/f_{BWvto}$ = 1.*

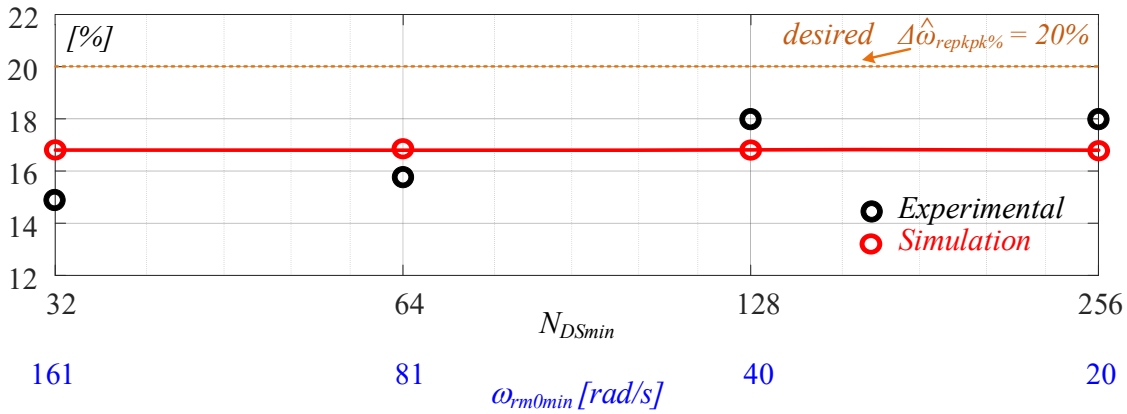

Figure 4.6.21 *Comparison between experimental and simulated estimated rotor speed ripple in p.u. at different sensor's resolution N_{DS} and with 20% desired speed ripple, 20Hz desired speed loop bandwidth and fixing the ratio $f_{BW\omega}/f_{BWvto} = 3$.*

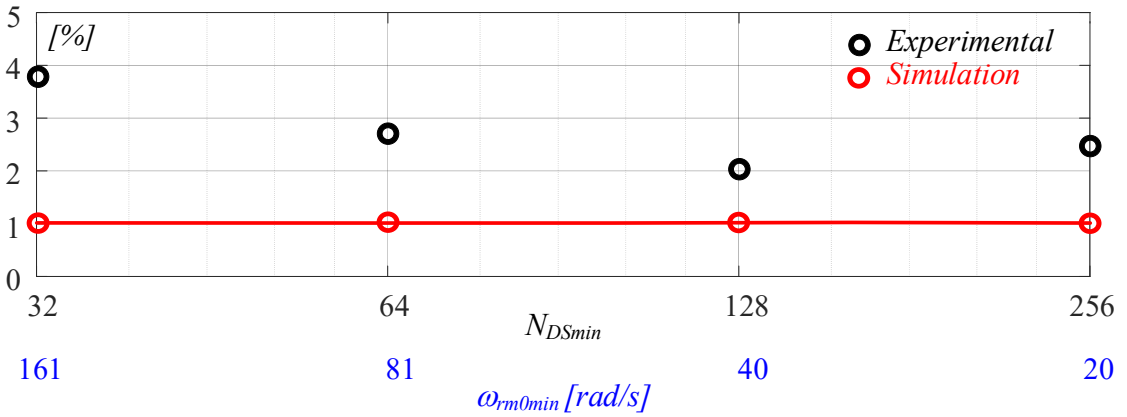

Figure 4.6.22 *Comparison between experimental and simulated actual rotor speed ripple in p.u. at different sensor's resolution N_{DS} and with 20% desired speed ripple, 20Hz desired speed loop bandwidth and fixing the ratio $f_{BW\omega}/f_{BWvto} = 3$.*

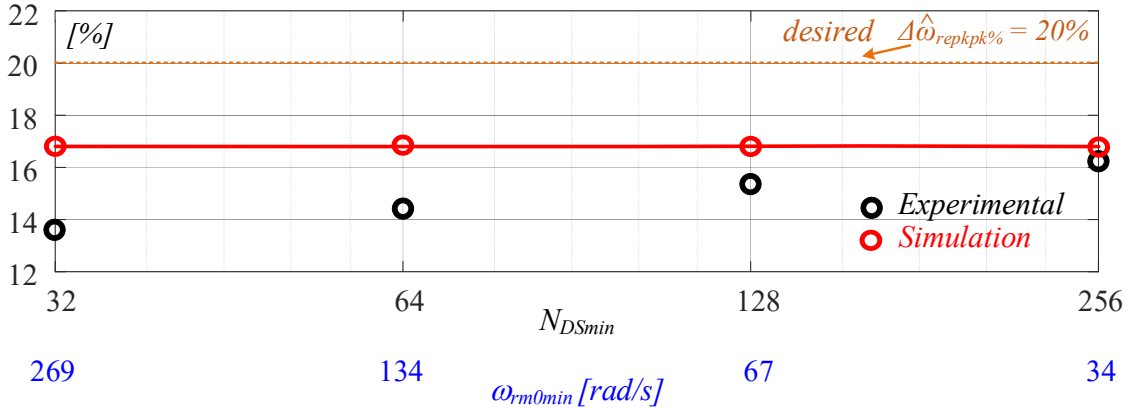

Figure 4.6.23 *Comparison between experimental and simulated estimated rotor speed ripple in p.u. at different sensor's resolution NDS and with 20% desired speed ripple, 20Hz desired speed loop bandwidth and fixing the ratio $f_{BW\omega}/f_{BWvto} = 5$.*

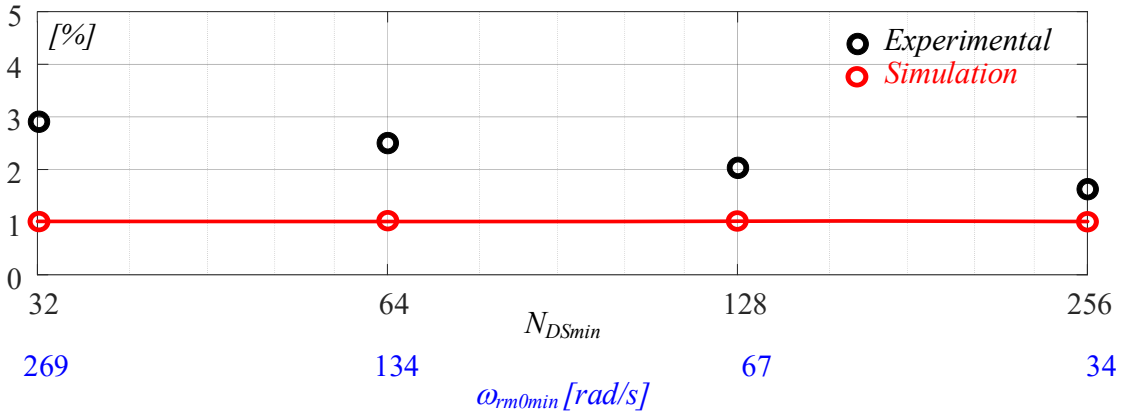

Figure 4.6.24 *Comparison between experimental and simulated actual rotor speed ripple in p.u. at different sensor's resolution N_{DS} and with 20% desired speed ripple, 20Hz desired speed loop bandwidth and fixing the ratio $f_{BW\omega}/f_{BWvto}$ = 5.*

These preliminary experimental tests shown the feasibility of the proposed approach and how the actual rotor speed measured through a full resolution position sensor has a very low percentage ripple respect then the estimated speed ripple. Obviously, the experimental values of the estimated and also actual rotor speed are affected to measurement uncertainty.

4.6.8 Experimental Disturbance Rejection Tests

In order to verify the disturbance rejection capability of the system under test the dynamic stiffness has been evaluated theoretically and experimentally.

In Figs. 4.6.25 - 4.6.27 show the dynamic stiffness at three different ratio $f_{BW\omega}/f_{BWvto}$ =1, 3 and 5 respectively, by considering 20Hz of the speed loop bandwidth and the sensor's resolution N_{DS} = *128*.

With the load motor (SPMSM) the load torque disturbance T_L is set, by means of a sinusoidal current iq with an amplitude equal to 3 A and a frequency range from 0.5 Hz up to 150Hz.

The following figures show the three different scenarios by comparing the data collected from the simulations of the model implemented on Simulink (in blue) and the data collected experimentally (in red).

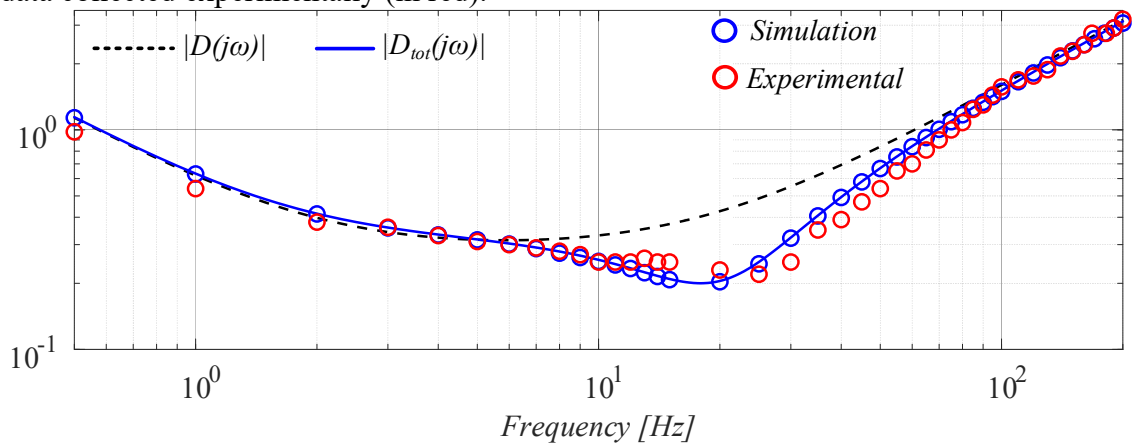

Figure 4.6.25 *Comparison between $|D(j\omega)|$, $|D_{tot}(j\omega)|$ and experimental and simulated dynamic stiffness with $f_{BW\omega}/f_{BWvto}$ = 1.*

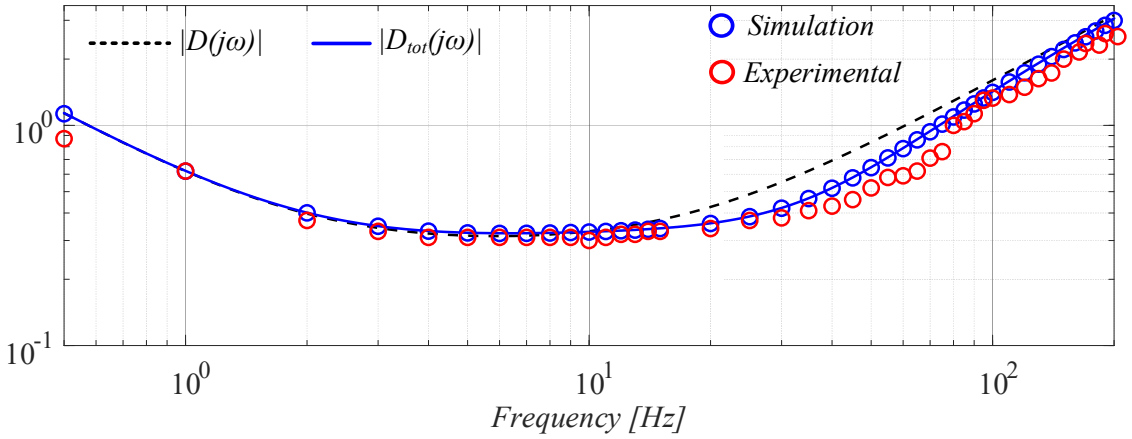

Figure 4.6.26 *Comparison between $|D(j\omega)|$, $|D_{tot}(j\omega)|$ and experimental and simulated dynamic stiffness with $f_{BW\omega}/f_{BWvto} = 3$.*

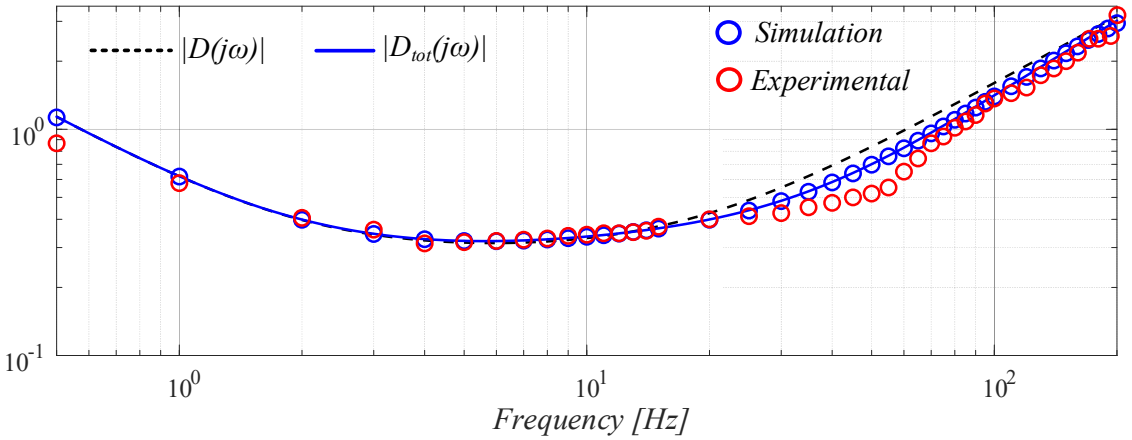

Figure 4.6.27 *Comparison between $|D(j\omega)|$, $|D_{tot}(j\omega)|$ and experimental and simulated dynamic stiffness with $f_{BW\omega}/f_{BWvto} = 5$.*

For high values of the ratio $f_{BW\omega}/f_{BWvto} = 3$ and $f_{BW\omega}/f_{BWvto} = 5$ in Fig. 4.6.26 and Fig 4.6.27 respectively, the dynamic stiffness $|D_{tot}(j\omega)|$ is very close to the ideal one $|D(j\omega)|$, which results in a high disturbance rejection capability. Only by choosing $f_{BW\omega}/f_{BWvto} = 1$, Fig. 4.6.25, the speed control loop worsens its disturbance rejection performance. These results, Figs. 4.6.25 – 4.6.27, confirm the correlation between the disturbance rejection capability and the robustness of the control speed loop, in fact it is consistent with the Table XI.

Finally, the disturbance rejection capability of the closed speed loop can be provided by considering a step torque load $T_L = 5Nm$ with a sensor's resolution $N_{DS} = 128$ and speed loop bandwidth $f_{BW\omega} = 20$Hz with three different ratio $f_{BW\omega}/f_{BWvto} = 1$, $f_{BW\omega}/f_{BWvto} = 3$ and $f_{BW\omega}/f_{BWvto} = 5$, Figs. 4.6.28 – 4.6.30 respectively.

The minimum rotor speed ω_{rm0min} has been evaluated from the expression (4.6.49).

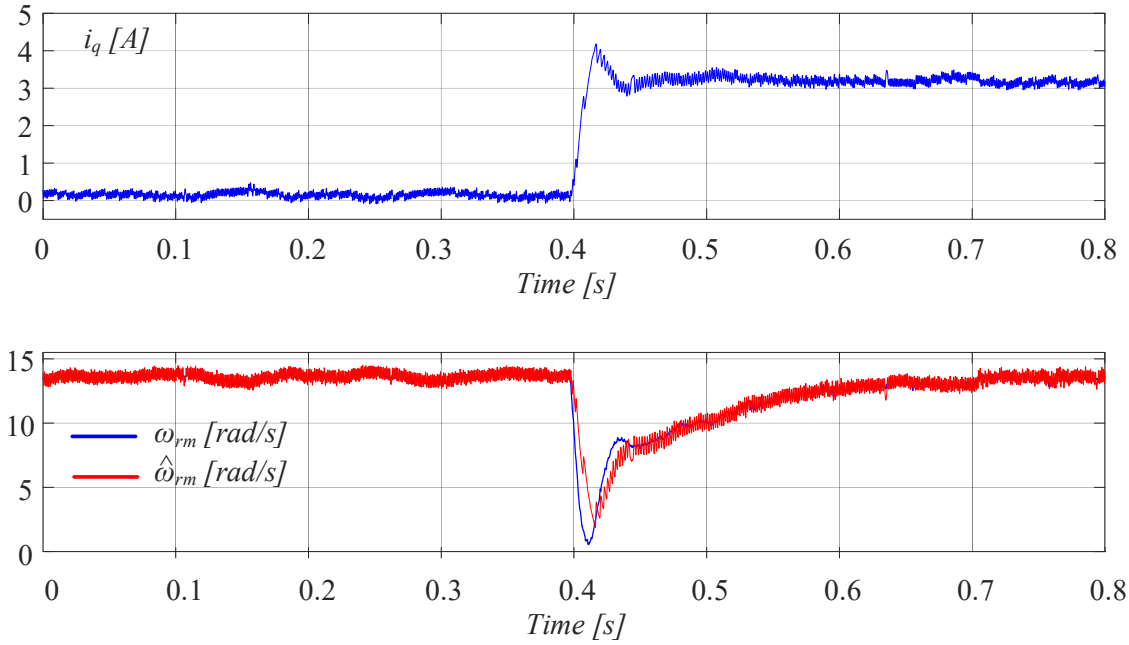

Figure 4.6.28 *Temporal disturbance rejection comparison between the actual rotor speed and estimated rotor speed with $f_{BW\omega}/f_{BWvto} = 1$.*

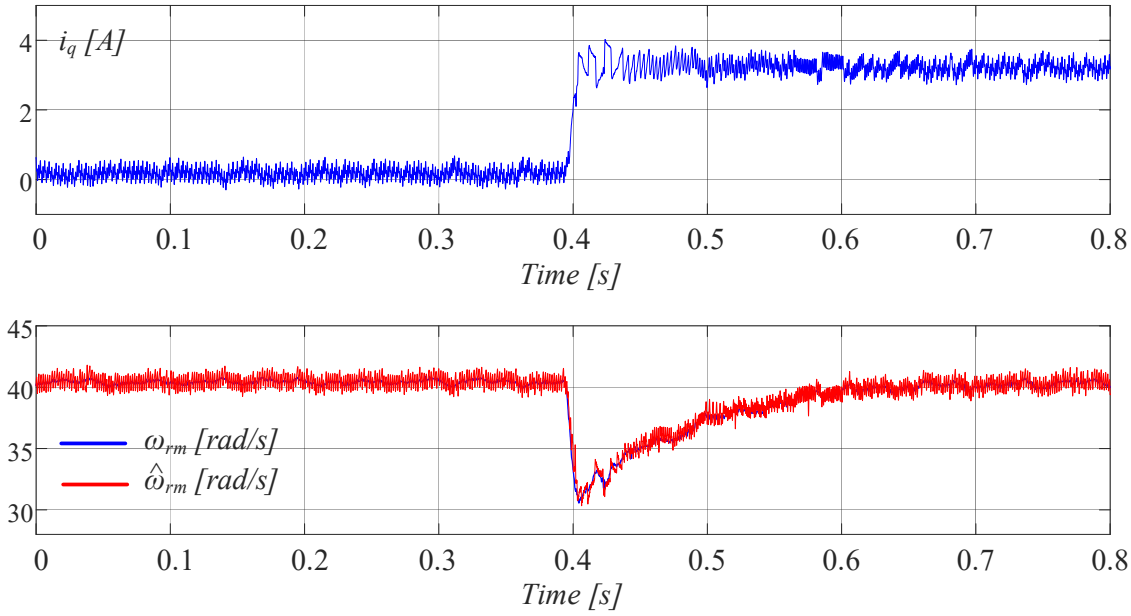

Figure 4.6.29 *Temporal disturbance rejection comparison between the actual rotor speed and estimated rotor speed with $f_{BW\omega}/f_{BWvto} = 2$.*

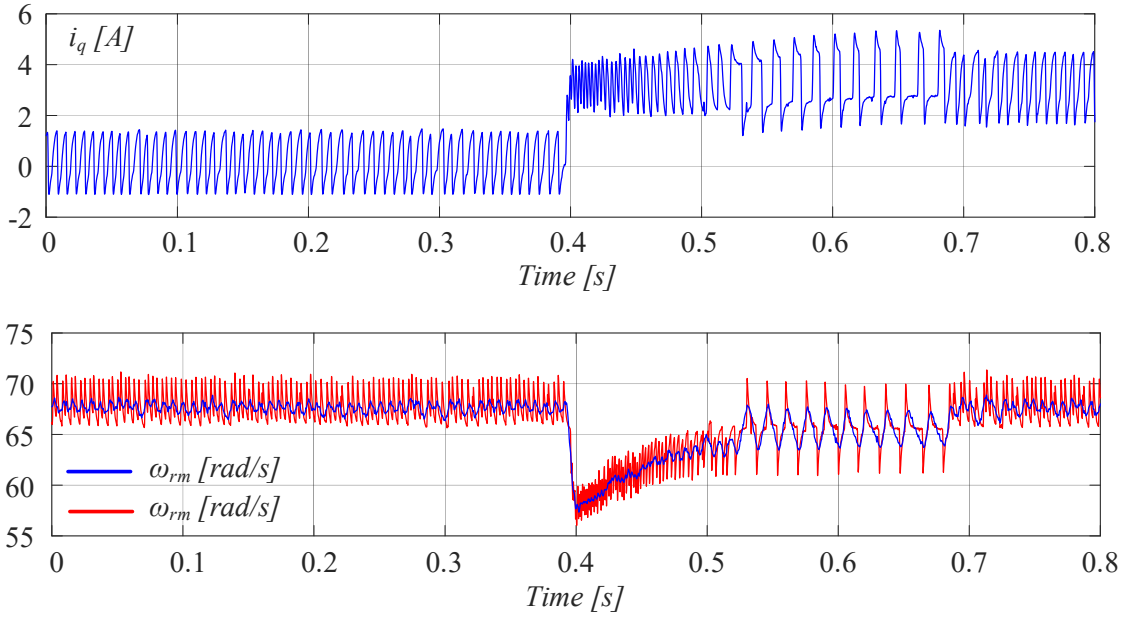

Figure 4.6.30 *Temporal disturbance rejection comparison between the actual rotor speed and estimated rotor speed with* $f_{BW\omega}/f_{BW\omega to} = 5$.

The temporal disturbance rejection analysis has been confirmed experimentally with three different ratio $f_{BW\omega}/f_{BW\omega to}$ as well the frequency responses evaluated in Figs. 4.6.25 - 4.6.27. Furthermore, according to the Table XI the desired performances have been consistent with the above disturbance rejection analysis, both in frequency and time domain.

However, in Figure 4.6.30, it is possible to note the effect of quantization that negatively impact on the current loop quantities as reference and feedback q-axis current which was not analyzed in this study.

4.7 Selection of the Rotor Position Sensor Resolution in Variable Speed Drives involving a Fixed-Position-Based Speed Estimation Algorithm in the Speed Loop

In this paragraph the selection of a rotor position sensor resolution based on a non-model based speed estimator is presented. As already introduced in paragraph 3.6 there are several non-model based speed estimation algorithms. Generally, most of these algorithms are based on the approximation of the derivative on the angular position measured by the position sensor. In fact, by definition, once the angular position is known, its angular speed is precisely defined by the derivation operation. Considering the angular position measurement coming from a finite resolution position sensor, as already widely seen in section 3.3, this is characterized by quantization harmonics and therefore we define with $\theta_{re}^{(q)}(t)$ the electrical angular position of the quantized rotor , while the time derivative of $\theta_{re}^{(q)}(t)$, is the instantaneous quantized speed $\omega_{re}^{(q)}(t)$.

Several such algorithms have been presented in literature, based on the Taylor series expansion [4], [18]-[23], the backward difference expansion [18], [24] and the least-squares fit [1], [18], [23].

The most commonly used non-model-based algorithms are based on the first order approximation as it is easy to implement with a very low calculation burden:

$$\omega_{re}(t) = \frac{d\theta_{re}(t)}{dt} \approx \hat{\omega}_{re} = \frac{\theta_{re}(t_1) - \theta_{re}(t_2)}{t_1 - t_2} = \frac{\Delta\theta_{re}}{\Delta t} \tag{4.7.1}$$

where θ_{re} is the electrical rotor angle, ω_{re} is the electrical frequency and $\hat{\omega}_{re}$ is the estimated speed. Two speed estimation algorithms belonging to non-model-based methods and implementing the first order approximation (4.7.1) are widely used electric drives: the first, widely known as the fixed time method (FTM) [4], [18]-[23], is based on counting the number of position measurement updates in a set time interval, while the second method measures the time elapsed between two consecutive position measurement updates, and is known as the fixed position method (FPM), or period-based speed estimation, [4], [18]-[23]. While FTM is very accurate at high speeds, FPM is suitable at low and medium speeds. Drives usually combine both methods to cover the full speed range, [4], [25].

Although it is known that speed estimation deteriorates as both position sensor resolution and minimum rotational speed decrease, [4], [19]-[24], methods for a proper selection of the resolution taking the low-speed performances of the drive into account are lacking in the literature. This is a critical issue in drive design, especially for low-cost applications.

It is expected that the designer will choose the position sensor based on drive performance specifications, including the minimum operating speed [26], with the aim of minimizing its cost, thus selecting the minimum required position sensor resolution satisfying the speed loop reference design specifications.

In this context, the main aim of this study is to provide a deterministic approach in the choice of sensor resolution according to some technical constraints imposed by the motor drive application and the speed estimation algorithm implementation. This target is reached by relating the phase margin of the drive at low rotational speeds with the minimum required sensor's resolution.

The proposed design methodology, although of general validity, has been developed in this paragraph for the FPM implementation, which is commonly used at low speeds by commercial, general purpose drives.

4.7.1 Fixed Position Based Speed Estimation Algorithm

The FPM implementation can be summarized as in Fig. 4.7.1, where the estimated speed is computed by measuring the time τ_d between two consecutive updates in the quantized angular position $\theta_{re}^{(q)}(t)$, Fig. 4.7.2; τ_d is determined as in (4.7.2), by counting the number of clocks n of a high-frequency counter with frequency $f_{CLK}=1/T_{CLK}$. This count can be expressed as the reciprocal value of the product between the sensor's resolution N_{DS} and the frequency f_{re0} associated to the rotor speed ω_{re0}. The average rotor speed is estimated according to (4.7.3).

$$\tau_d = nT_{CLK} = \frac{1}{N_{DS} f_{re0}} \tag{4.7.2}$$

$$\hat{\omega}_{re} = \frac{\Delta\theta_{re}}{\Delta t} = \frac{\Delta\theta_{re}}{\tau_d} = \frac{2\pi}{N_{DS} n T_{CLK}} \tag{4.7.3}$$

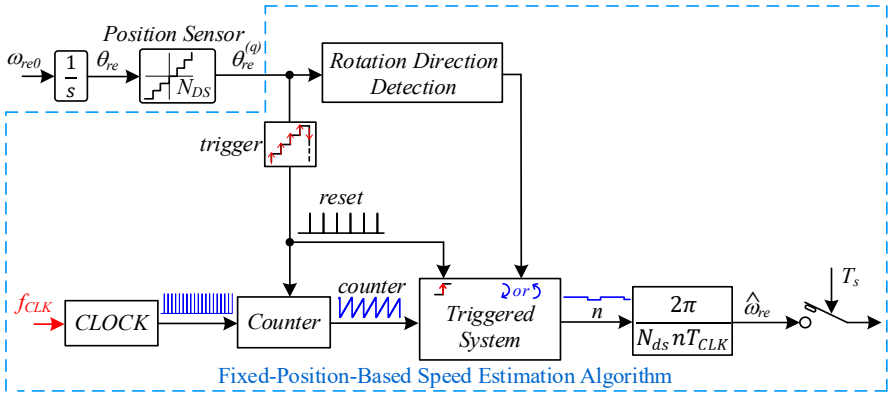

Figure 4.7.1 *Block Diagram of the speed estimation based on the fixed-position-based speed estimation algorithm.*

This speed estimation method inherently introduces a delay equal to τ_d. Moreover, the accuracy of the estimated speed is related to the ratio between f_{CLK} and $1/\tau_d = N_{DS}f_{re0}$, which depends on the motor speed, [19]-[27].

In the following paragraph a FPM operating point model reported is briefly described. The aim of this model is to approximate the nonlinear estimation process behavior around a specific operating point f_{re0}.

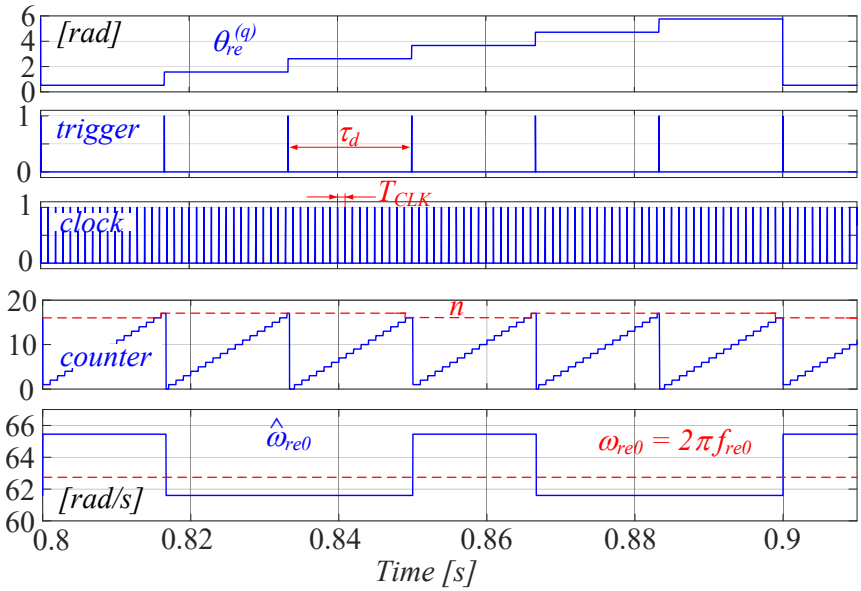

Figure 4.7.2 *Operating principle of the fixed-position-based speed estimation method.*

4.7.2 Operating Point Model of the FPM Algorithm

Several approaches have been presented in the literature to describe the small signal behavior of the FPM estimation algorithm [28]-[30]. Among them, the small signal model developed in [30] has been used in the following study. Assuming that the shaft rotates at a constant speed $\omega_{re0}=2\pi f_{re0}$, this model represents the dynamic behavior of the FPM algorithm by means of three cascaded transfer functions representing: a) the counter, with a moving average filter $H_{aveg}(s)$; b) the triggered system, with a sample and hold transfer function $H_{S\&H}(s)$; c) the control algorithm sampling period T_s with a further sample and hold transfer function $H_{Ts}(s)$. $H_{aveg}(s)$ is a moving average transfer function, determined by considering that the high frequency counter signal is asynchronous with respect to the position sensor pulses and the control algorithm sampling period:

$$H_{aveg}(s) = \frac{1}{n} \frac{1 - e^{-s\tau_d}}{1 - e^{-sT_{CLK}}} \tag{4.7.4}$$

With regards to the triggered system, the output of the counter is sampled by means of a trigger signal every τ_d, whose transfer function is given by the following expression:

$$H_{S\&H}(s) = \frac{1 - e^{-s\tau_d}}{s\tau_d} \tag{4.7.5}$$

However, the estimated speed $\hat{\omega}_{re}$ output by the FPM algorithm is not updated till the next sampling instant T_s of the control algorithm. This behavior is modeled by another sample and hold function:

$$H_{Ts}(s) = \frac{1 - e^{-sT_s}}{sT_s} \tag{4.7.6}$$

Hence, the overall transfer function of the FPM operating point model $H_{FPM}(s)$ is given by:

$$H_{FPM}(s) = H_{aveg}(s)\, H_{S\&H}(s)\, H_d(s) = \frac{1}{n} \frac{1 - e^{-s\tau_d}}{1 - e^{-sT_{CLK}}} \frac{1 - e^{-s\tau_d}}{s\tau_d} \frac{1 - e^{-sT_s}}{sT_s} \tag{4.7.7}$$

By considering that typical values of the T_s *(50-200μs)* and T_{CLK} *(1μs-10ns)* are much smaller than τ_d, in the following study we approximate the above transfer functions with the following (4.7.8) and (4.7.9):

$$H_{aveg}(s) \approx \lim_{T_{CLK} \to 0} \frac{1}{n} \frac{1 - e^{-s\tau_d}}{1 - e^{-sT_{CLK}}} = \frac{1 - e^{-s\tau_d}}{s\tau_d} \tag{4.7.8}$$

$$H_{Ts}(s) \approx \lim_{Ts \to 0} \frac{1 - e^{-sT_s}}{sT_s} = 1 \tag{4.7.9}$$

As a consequence, $H_{FPM}(s)$ can be represented as:

$$H_{FPM}(s) \approx \frac{1 - e^{-s\tau_d}}{s\tau_d} \frac{1 - e^{-s\tau_d}}{s\tau_d} = \frac{(1 - e^{-s\tau_d})^2}{s^2\tau_d^2} \tag{4.7.10}$$

Its magnitude, $|H_{FPM}(j\omega)|$, is a sinc-squared function, while its phase $\angle H_{FPM}(j\omega)$ is a linear function with the angular frequency ω:

$$|H_{FPM}(j\omega)| = \frac{\sin^2\left(\frac{\omega\tau_d}{2}\right)}{\frac{\omega^2\tau_d^2}{4}} \qquad \angle H_{FPM}(j\omega) = -\omega\tau_d \tag{4.7.11}$$

The filtering action can be explained by considering the modelling of the quantized rotor position and speed achieved by the measurement with a finite value of N_{DS}. In particular, the quantized electrical rotor angle $\theta_{re}^{(q)}(t)$ can be expressed as paragraph 3.3:

$$\theta_{re}^{(q)}(t) = \omega_{re0}t + \sum_{k=1}^{+\infty} \frac{2}{N_{DS}\,k} \sin(N_{DS}k\omega_{re0}t) \tag{4.7.12}$$

while the time derivative of $\theta_{re}^{(q)}(t)$, that is, the instantaneous quantized speed $\omega_{re}^{(q)}(t)$, is defined as:

$$\omega_{re}^{(q)}(t) = \frac{d\theta_{re}^{(q)}(t)}{dt} \tag{4.7.13}$$

This is highly discontinuous and jumps between zero and infinity at each position sensor transition. Assuming that the shaft rotates at ω_{re0}, $\omega_{re}^{(q)}(t)$ can be expressed as paragraph 3.3:

$$\omega_{re}^{(q)}(t) = \omega_{re0} + \sum_{k=1}^{+\infty} 2\omega_{re0} \cos(N_{DS}k\omega_{re0}t) \tag{4.7.14}$$

The speed waveform of an example of a reconstructed $\omega_{re}^{(q)}(t)$ is shown in Fig. 4.7.3a, where large impulses arise every time the position measurement is updated. The corresponding magnitude spectrum of $\omega_{re}^{(q)}(t)$ is displayed in Fig. 4.7.3b, featuring an infinite number of equally spaced quantization harmonics at $kN_{DS}\omega_{re0}$, each having an amplitude equal to $2\omega_{re0}$; the only physically meaningful harmonic, i.e. the dc component f_{re0}, is shown in red.

When the FPM is applied to $\omega_{re}^{(q)}$, the sinc-squared function filters the speed by cancelling all quantization harmonics, as shown in Fig. 4.7.4. In fact, $|H_{FPM}(j\omega)| = 0$ at frequencies $f = kf_{re0}N_{DS} = k/\tau_d$, with $k=1,2...,n$, which coincide with the quantization harmonic frequencies of $\omega_{re}^{(q)}$.

As regards the phase $\angle H_{FPM}(j\omega)$, it introduces a delay τ_d in the speed estimation loop, negatively impacting on the phase margin of the entire closed speed loop, thus worsening the stability of the speed-controlled drive.

This last issue is exploited in the following stability margin analysis of the drive at low rotational speeds in order to establish a relationship between the speed loop design specifications, given as the lowest operating speed ω_{rm_min} and corresponding bandwidth f_{BW}, and the minimum resolution of the position sensor guaranteeing such requirements.

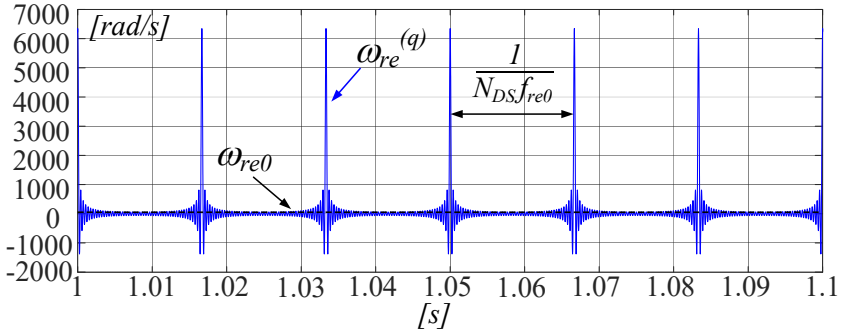

(a)

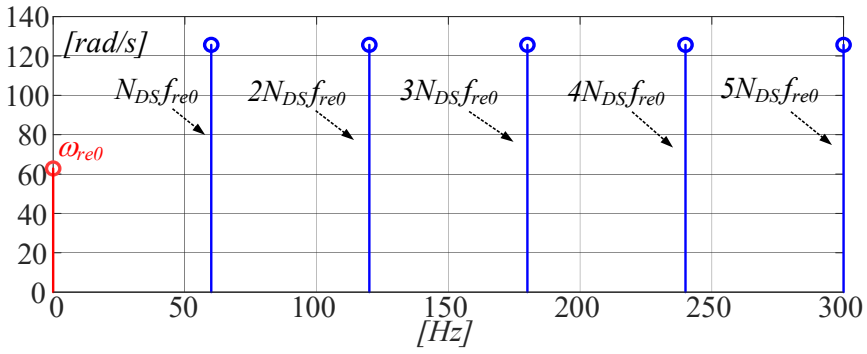

(b)

Figure 4.7.3 *$\omega_{re}^{(q)}$ for N_{DS} = 6 and ω_{re0} = 2π10 rad/s. (a) waveform using the first 100 harmonics. (b) corresponding amplitude spectrum.*

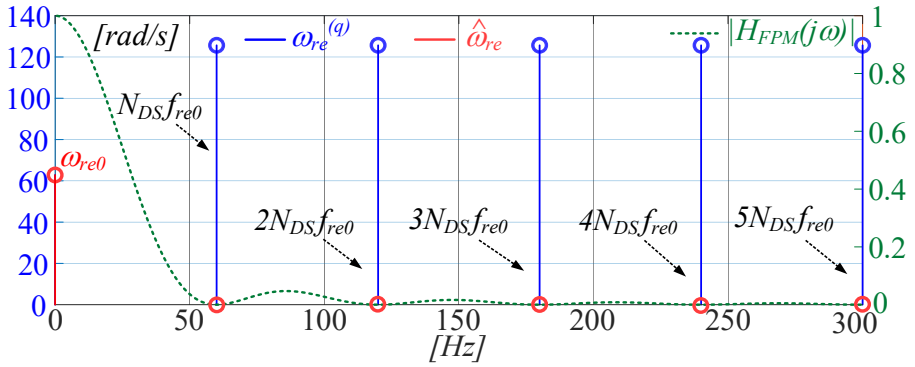

Figure 4.7.4 *Harmonic content of the instantaneous quantized speed $\omega_{re}^{(q)}$, estimated speed, and the magnitude of $H_{FPM}(s)$.*

4.7.3 Stability Analysis

The stability analysis of the closed speed loop is performed by linearizing the control system around the operating point, representing each quantity as a constant value X with a superimposed small perturbation $\delta x(t)$. Then, the design of speed loop controller is accomplished by assuming as feedback the shaft rotor speed, according to the bandwidth required by the drive performance specifications. Finally, the stability margin analysis of the drive is performed by including the speed estimator in the loop and investigating the impact of the FPM algorithm on the drive performance. In both cases the effect of the current loop is neglected as its bandwidth is significantly higher than speed control loop.

In the proposed approach the design of the speed loop is performed assuming an ideal speed measurement, as shown in Fig. 4.7.5, where the mechanical system is represented by the mechanical inertia J, while the mechanical losses due to frictions are neglected. The tuning of the PI speed controller $C(s)$ is performed to satisfy the desired dynamic performance of the speed closed loop, expressed as the speed loop bandwidth f_{BW} and phase margin $m_{\varphi i}$. This goal is obtained by applying the stability Nyquist theory to the ideal open loop transfer function $F(s)$, imposing the ideal crossover angular frequency $\omega_{ci} = 2\pi f_{ci}$ and the ideal phase margin $m_{\varphi i}$.

$$F(s) = \frac{k_p s + k_i}{s^2 J} \tag{4.7.15}$$

In particular, it is possible to obtain the speed controller gains from f_{ci} and $m_{\varphi i}$ with the following relationships, [5]-[6], [14]:

$$|F(j\omega_{ci})| = 1 \quad m_{\varphi i} = \angle F(j\omega_{ci}) + \pi = atan\left(\frac{\omega_{ci} k_p}{k_i}\right) \tag{4.7.16}$$

$$\tau_i = \frac{tan(m_{\varphi i})}{\omega_{ci}} \quad k_i = \frac{\omega^2_{ci} J}{\sqrt{\omega^2_{ci}\tau^2_i + 1}} \quad k_p = \tau_i k_i \tag{4.7.17}$$

where k_p and k_i are respectively the proportional and integral gains of $C(s)$, while τ_i is the integral constant time.

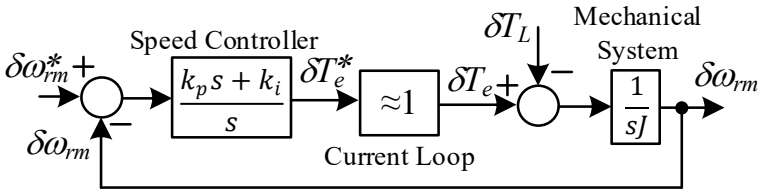

Figure 4.7.5 *Ideal closed loop small signal speed control structure.*

The corresponding closed loop dynamic performance, such as the bandwidth and the robustness, can be evaluated by means the ideal closed loop transfer function $W(s)$:

$$W(s) = \frac{k_p s + k_i}{s^2 J + k_p s + k_i} \tag{4.7.18}$$

In order to obtain a overdamped step response of $W(s)$ a rule of thumb is to select the k_p and k_i imposing one pole of $W(s)$ ten time bigger than the other one, and a phase margin $m_{\varphi i}$ roughly equal to 85° [5]-[6].

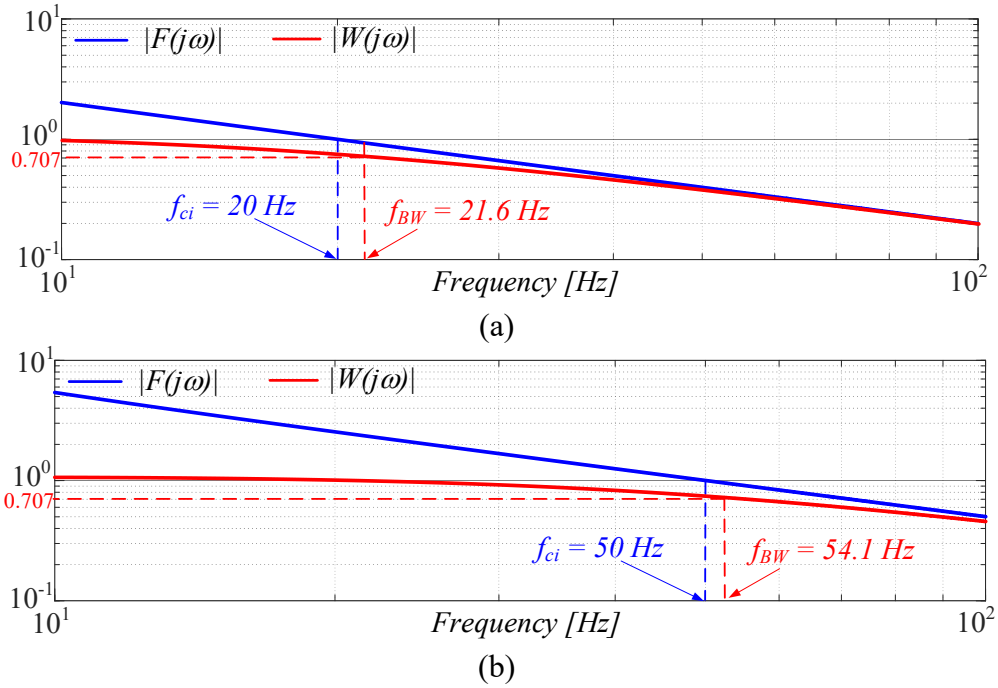

Figure 4.7.6 *Magnitude of F(s) and W(s): (a) f_{ci} = 20 Hz, (b) f_{ci} = 50 Hz.*

The analysis of $W(s)$ allows to achieve a key output useful in the next steps of the analysis. In fact, the differences between the crossover frequency f_{ci} and bandwidth f_{BW} can be considered quite small for this specific control loop structure and typical values of speed loop specifications, as clearly visible in Figs. 4.7.6a and 4.7.6b, where the transfer functions of the open $F(s)$ and closed $W(s)$ speed loops are displayed for two bandwidths. Hence, in the following study controller gains will be computed by assuming $f_{ci} \approx f_{BW}$, which is a slightly conservative result.

In order to evaluate the FPM speed estimator influence on the closed loop stability, it is necessary to include the model of the speed estimator $H_{FPM}(s)$ as shown in Fig. 4.7.7.

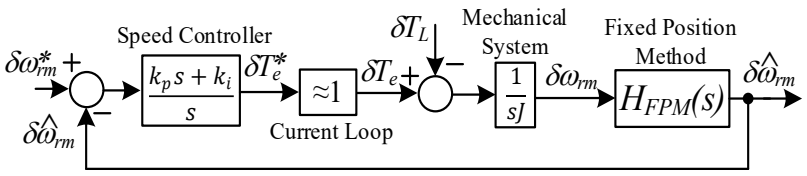

Figure 4.7.7 *Closed loop small signal speed control including the FPM algorithm.*

The open $F_{FPM}(s)$ and closed loop $W_{FPM}(s)$ transfer functions of the speed control of Fig. 4.7.7 become:

$$F_{FPM}(s) = \frac{k_p s + k_i}{s^2 J} \frac{(1 - e^{-s\tau_d})^2}{s^2 \tau^2_d} \tag{4.7.19}$$

$$W_{FPM}(s) = \frac{(k_p s + k_i)(1 - e^{-s\tau_d})^2}{s^4 \tau^2_d J + (k_p s + k_i)(1 - e^{-s\tau_d})^2} \tag{4.7.20}$$

Nyquist's stability theory applied to $F_{FPM}(s)$ results in a different phase margin m_φ and different crossover angular frequency ω_c compared to the previous case:

$$|F_{FPM}(j\omega_c)| = 1 \qquad m_\varphi = \angle F_{FPM}(j\omega_c) + \pi \tag{4.7.21}$$

Based on (4.7.19), the influence of τ_d in the magnitudes and phases of the open loop frequency response are shown in Figs. 4.7.8 and 4.7.9, with and without $H_{FPM}(s)$ in the loop. These curves have been determined for two different values of m_φ and thus τ_d, at two different f_{ci}. The same figures display the crossover angular frequency $\omega_c = 2\pi f_c$ and its variations when $H_{FPM}(s)$ is included in the open loop transfer function. The comparison between $F(s)$ and $F_{FPM}(s)$ shows limited differences between the ideal crossover frequencies f_{ci} and f_c, especially for higher phase margins m_φ. As a consequence, we can approximate $f_c \approx f_{ci} \approx f_{BW}$ and compute the phase of $F_{FPM}(s)$ at f_{BW} as:

$$\angle F_{FPM}(j2\pi f_{BW}) = atan\left(\frac{2\pi f_{BW} k_p}{k_i}\right) - 2\pi f_{BW}\tau_d - \pi \tag{4.7.22}$$

The corresponding phase margin is given by:

$$m_\varphi = \angle F_{FPM}(j2\pi f_{BW}) + \pi = m_{\varphi i} - \frac{2\pi f_{BW}}{N_{ds} f_{re0}} \tag{4.7.23}$$

The relationship (4.7.22) highlights the detrimental impact of τ_d on the phase lag required to reach the stability limit. In particular, one can note that m_φ can be significantly affected by the time delay τ_d and thus on the rotor position sensor resolution N_{ds}, (4.7.23).
At the operating point f_{re0}, m_φ increases with N_{ds} increasing, while it decreases with f_{BW} increasing; therefore, N_{ds} has to be selected in order to guarantee the desired phase margin of the speed closed loop at the minimum operating speed ω_{rm_min}, which represents the worst operating condition of the speed-controlled drive. In fact, according to (4.7.23), at higher rotational speeds the effects of delay time τ_d will have a lower impact on the phase margin and thus system stability.
The relationship (4.7.23) provides a straightforward relationship between the system robustness and the maximum delay time τ_{dmax} attributable to the FPM for a specific f_{re0}.

In the above relationships m_φ is a design variable that should be properly selected in order to guarantee a high disturbance-rejection capability of the drive including the FPM. Useful guidelines about the m_φ selection can be carried out from the analysis of the torque disturbance rejection capability of the closed loop control.

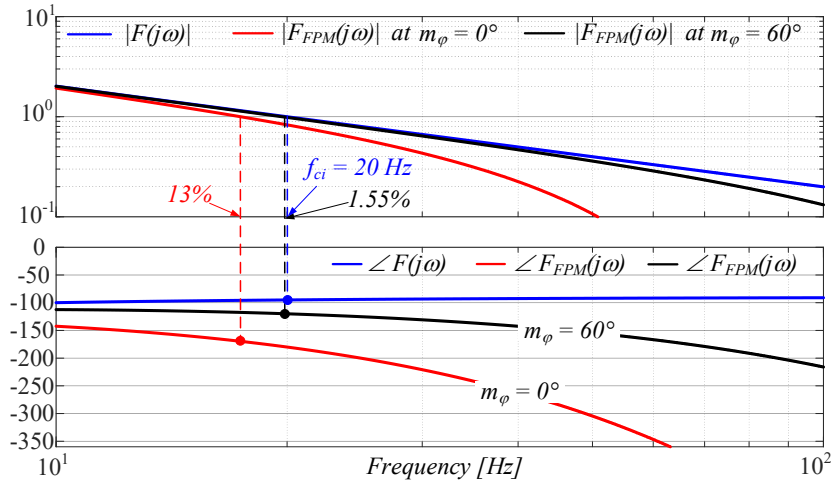

Figure 4.7.8 *Magnitude and Phase of F(s) and $F_{FPM}(s)$, at f_{ci} = 20 Hz and for different m_φ.*

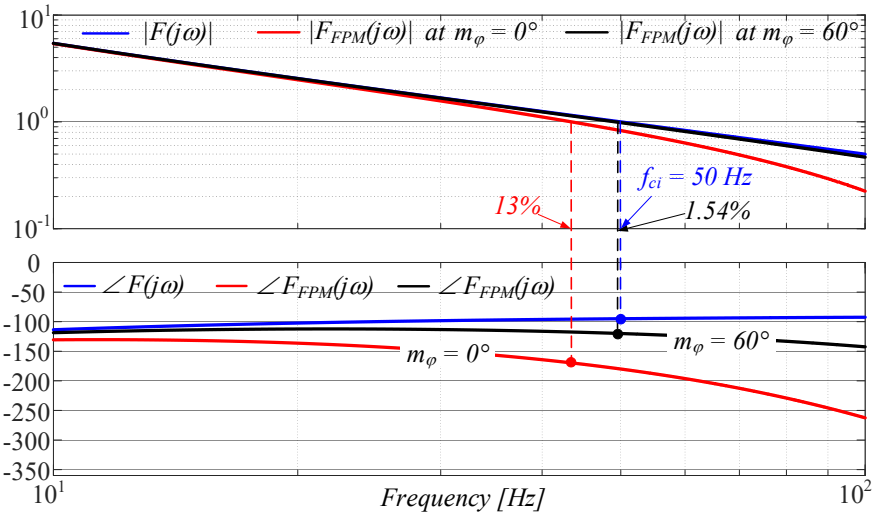

Figure 4.7.9 *Magnitude and phase comparisons between F(s) and $F_{FPM}(s)$, at f_{ci}=50Hz and for different m_φ.*

4.7.4 Disturbance Rejection Analysis

Generally, whatever feedback control loop is influenced by three external signals, the reference signal, the load disturbance, and the measurement noise. Any of the remaining signals can be of interest in controlled design, depending on the particular application [31]. In particular, the influence of the reference signal can be analyzed by the command tracking performance, i.e., the closed loop transfer function, while the influence of the load disturbance and the measurement noise can be analyzed with the load sensitivity and sensitivity functions respectively [31]. The robustness of the system should be evaluated by means the generic sensitivity function (sub-paragraph 4.1.4), since two sensitivity functions can be evaluated and the influence of the measurement noise is difficult to evaluate experimentally, in this study the load sensitivity has been considered as sensitivity function related to the robustness of the system [31].

In order to evaluate the frequency behavior of the load sensitivity function is often computed the inverse of the load sensitivity function, i.e., the dynamic stiffness [9], [17], [32]-[34].

In fact, in this study the robustness of the speed control loop system with included the speed estimator has been analyzed with the disturbance rejection analysis.

The dynamic stiffness transfer function can be computed as the ratio between the electromagnetic torque disturbance T_e applied to the drive and the corresponding rotor speed ω_{rm}. The relationship (4.7.24) shows the dynamic stiffness transfer function $D(s)$ of the ideal speed loop, while (4.7.25) show the dynamic stiffness $D_{FPM}(s)$ achieved by considering the presence in the loop of the FPM transfer function.

$$D(s) = \frac{s^2 J + k_p s + k_i}{s} \tag{4.7.24}$$

$$D_{FPM}(s) = \frac{s^4 \tau_d^2 J + (k_p s + k_i)(1 - e^{-s\tau_d})^2}{s^3 \tau_d^2} \tag{4.7.25}$$

A comparison between the frequency responses of these transfer functions highlights that a limited deviation of the $|D_{FPM}(j\omega)|$ curve from the ideal response $|D(j\omega)|$ is observed when m_φ is greater than 40°. To confirm this, Fig. 4.7.10 and 4.7.11 display the frequency responses of $|D(j\omega)|$ and $|D_{FPM}(j\omega)|$ for two different m_φ, at $f_{BW}=20Hz$ and $N_{ds} = 6$. It is worth noting that in case of $m_\varphi = 60°$ a limited deviation of the $|D_{FPM}(j\omega)|$ curve from the ideal response $|D(j\omega)|$ is observed, corresponding to a limited influence of τ_d on the disturbance rejection capability of the closed loop control. On the contrary, a low m_φ value, corresponding to a higher τ_d, can significantly compromise the drive performances. In the same figures the dynamic stiffness determined by simulating the electric drive with the speed closed loop including the FPM algorithm is displayed. In the last case the dynamic stiffness is computed by considering the ratio between the applied torque disturbance and the speed outgoing from the mechanical model of the system. A good agreement between the relationships (4.7.24) and (4.7.25) and simulations is achieved.

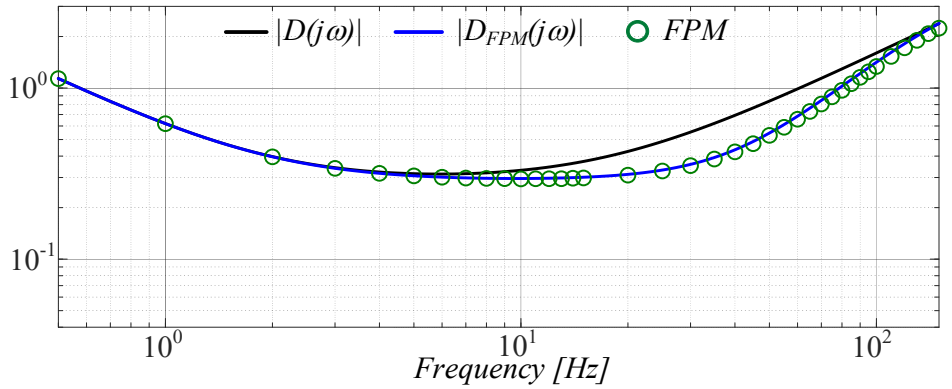

Figure 4.7.10 *Magnitude of D(s), $D_{FPM}(s)$ and FPM at 20Hz, with $m_\varphi = 60°$ and $N_{DS} = 6$.*

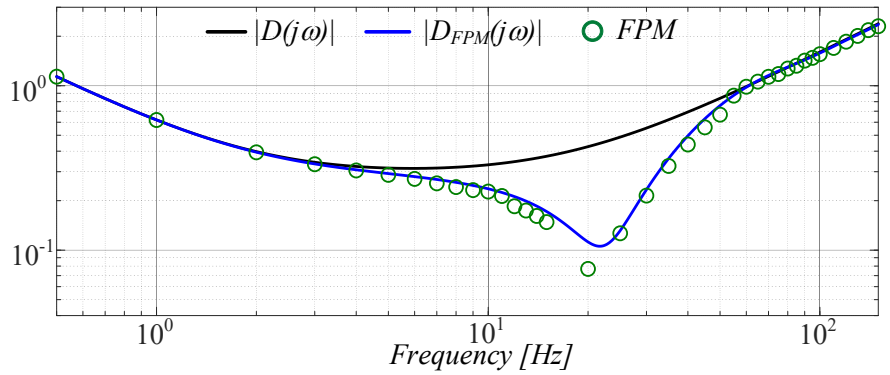

Figure 4.7.11 *Magnitude of D(s), $D_{FPM}(s)$ and FPM at 20Hz, with $m_\varphi = 20°$ and $N_{DS} = 6$.*

It has been verified that by selecting in (4.7.23) a m_φ comprises between 40° and 60° a good compromise in terms of dynamic response is obtained independently on N_{DS}.

4.7.5 Selection of Rotor Position Sensor Resolution

Starting from the previous consideration, a straightforward way to select the minimum value of rotor position resolution N_{DSmin} satisfying the design specifications of the drive in the low speed range can be achieved from the performance requirements of the drive expressed in terms of desired bandwidth f_{BW} of the speed closed loop and phase margin m_φ, both referred to the minimum operating rotor speed ω_{rm_min}. In particular, starting from the above information, the selection of rotor position sensor resolution is achieved by the following steps:

4) Determination of the controller gains k_p and k_i by (4.7.16) and (4.7.17), assuming $f_{ci} \approx f_{BW}$.

5) Computation of the max value of delay time τ_{dmax} allowed at the minimum rotating speed ω_{rm_min} according to:

$$\tau_{dmax} = \frac{atan\left(\frac{2\pi f_{BW} k_p}{k_i}\right) - m_\varphi}{2\pi f_{BW}} \tag{4.7.26}$$

6) Determination of minimum sensor's resolution:

$$N_{DSmin} = \frac{2\pi}{pp\ \omega_{rm\_min}\ \tau_{dmax}} \tag{4.7.27}$$

where pp is the number of pole pairs.

The above procedure can be exploited to identify the stability limits of the drive used for the experimental tests. For example, Fig. 4.7.12 displays ω_{rm_min} vs N_{DSmin} for two speed loop bandwidths f_{BW} and $m_\varphi = 0^\circ$. The values of ω_{rm_min} have been determined according to (4.7.26) and (4.7.27), and by simulating the FPM algorithm in Simulink. A very good agreement between the implementation and the proposed approach is achieved. By selecting the desired minimum operating condition of the drive ω_{rm_min} one can identify the minimum sensor resolution N_{dsmin}. Conversely, starting from N_{DS}, it is possible to find the minimum rotating speed ω_{rm_min} featuring a stable behavior of the drive, also meeting the control design requirements. Increasing f_{BW} requires an increased minimum sensor resolution N_{DSmin} for the same phase margin m_φ, (4.7.27).

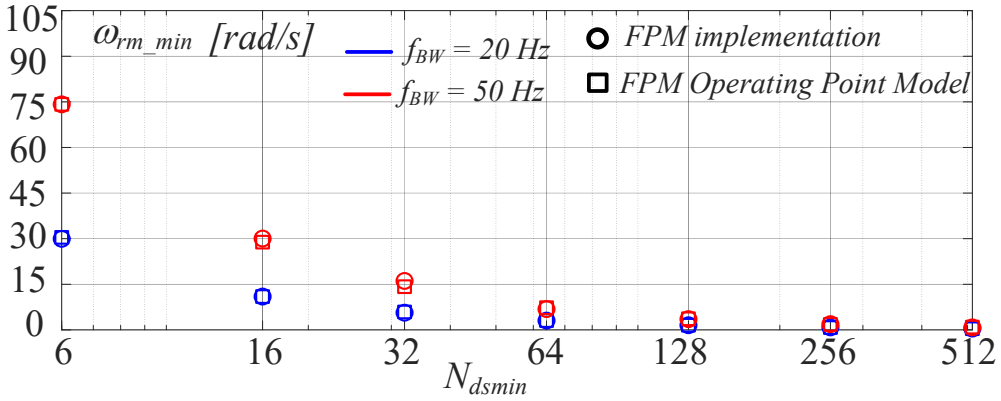

Figure 4.7.12 *Stability limits for different speed loop bandwidths and different N_{DS}, for $m_{\varphi}=0^{\circ}$.*

4.7.6 Experimental System Setup

An experimental test bench has been developed in order to validate the theoretical study, Fig. 4.7.13. A test rig has been arranged consisting of two PMSM drives whose shafts are mechanically coupled and sharing same DC bus. Motor specifications are summarized in Tabs. XIV and XV. Both motor drives are fed by SiC inverters operated at 20kHz. A dSpace DS1006 have been used to control the IPM drive under test and implementing the FPM algorithm, the last executed at 100 MHz.

Table XIV *SPM Motor Drive Data*

Rated Power P_n	*2 kW*
Rated Speed ω_n	*6000 rpm*
Rated Torque T_n	*5 Nm*
Stator Resistance R_s	*0.84 Ω*
Synchronous Inductance L_s	*4.7 mH*
Pole pairs pp	*3*
Mechanical Inertia J	*3.4 kgcm^2*

Table XV *IPM Motor Drive Data*

Rated Power P_n	*3.6 kW*
Rated Speed ω_n	*2000 rpm*
Rated Torque T_n	*19.1 Nm*
Stator Resistance R_s	*2.4 Ω*
q-axis Inductance L_q	*12.189 mH*
d-axis Inductance L_d	*9.947 mH*
Pole pairs pp	*3*
Mechanical Inertia J	*21.7 kgcm^2*

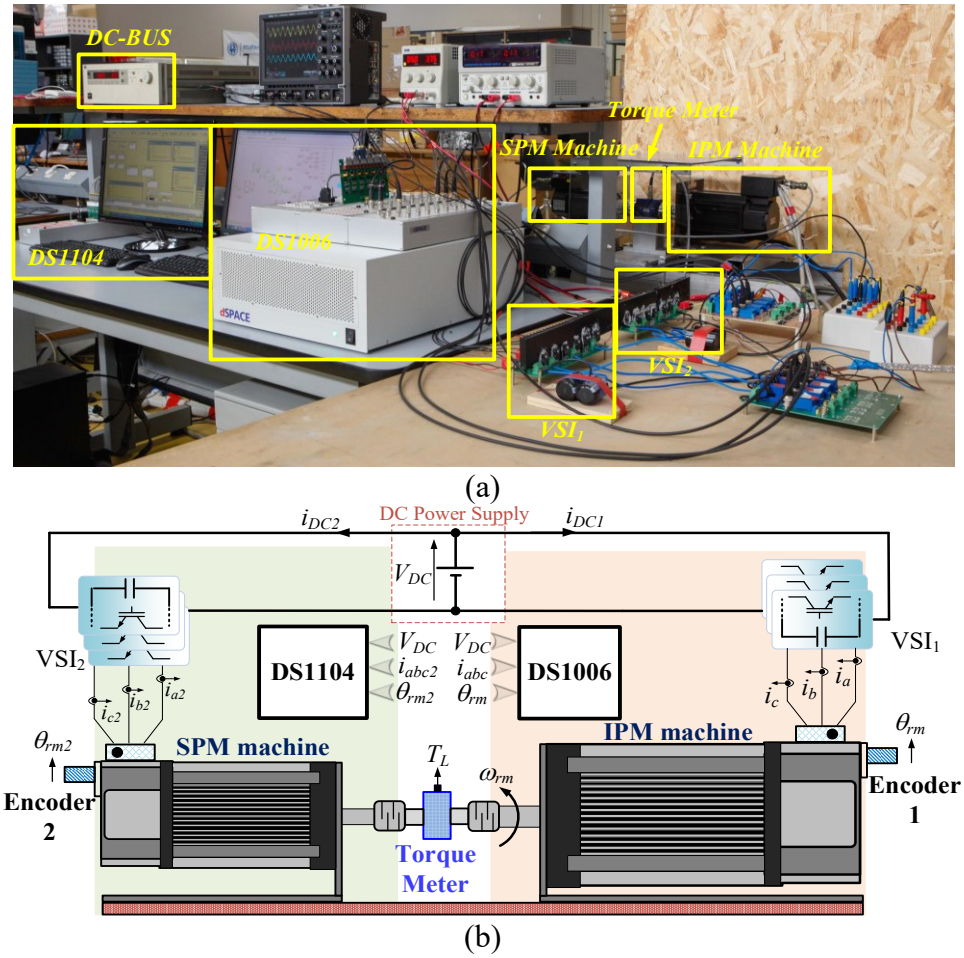

Figure 4.7.13 *Experimental servo-drive test bench: (a) photograph, (b) schematic.*

Both electric drives are equipped with incremental encoders with $N_{DS} = 2048$, and the different position sensor resolutions have been obtained by downsampling the encoder position measurement. Field oriented controls have been implemented in both drives, where the execution time of the current and speed loops are respectively $100\mu s$ and $200\mu s$. In all tests the current control loop bandwidth is fixed at 500Hz.

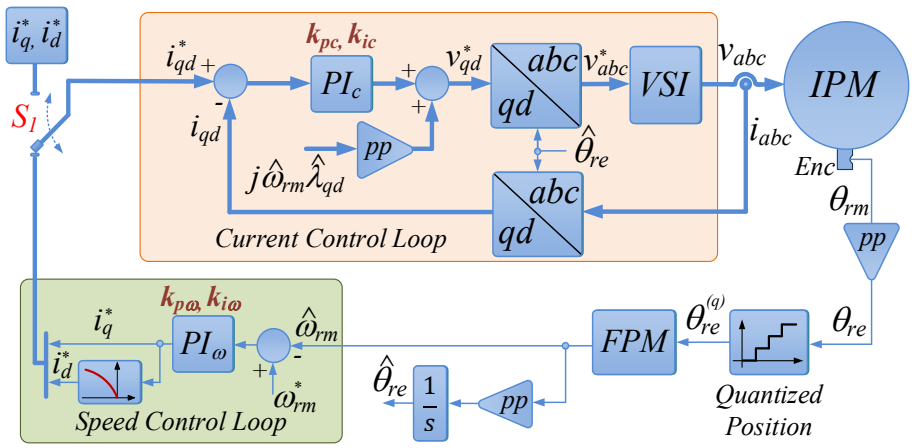

Figure 4.7.14 *Block diagram of the control implemented in the drive under test.*

4.7.7 Preliminary Experimental Results

The first tests were undertaken to verify the effectiveness of the theoretical study. In particular, Fig. 4.7.15 depicts the stability limits of the speed control loops implemented in the experimental setup and by using the proposed analytical approach for different rotor position sensor resolution N_{DS}. The speed loop bandwidth is set at f_{BW} = 20Hz for each N_{DS} configuration. It is noted that a good agreement between modelling and experimental tests is achieved.

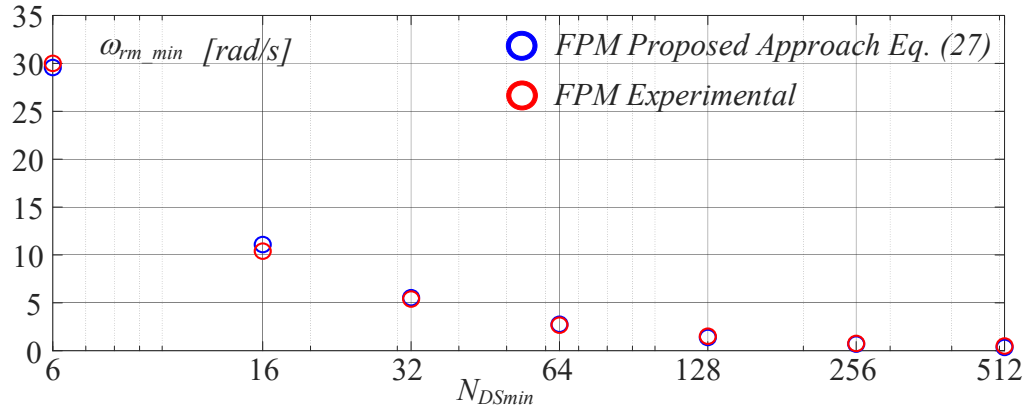

Figure 4.7.15 *Stability speed limits at m_φ=0˚and f_{BW}=20Hz.*

The main goal of the following tests was to experimentally validate the procedure of selection of rotor position sensor resolution described in section 4.7.5.

A first experimental test has been conducted on the current loops of both SPM and IPM motors with the aim of verifying the correct tuning of their current loops. These experimental tests allow to verify the mechatronic hypothesis, i.e. since the current loop bandwidth is selected at least ten times larger than speed loop bandwidth it is possible to neglect the dynamic effects of the current loop in the whole theoretical study and also during the experimental tests.

Furthermore, the robustness of the speed control loop system must be verifyed, indirectly, by means the disturbance rejection analysis by using the dynamic stiffness.

Since the SPM motor drive work as mechanical load (SPM), it imposes the electromagnetic torque disturbance on the rotor of the motor under test (IPM), a dynamic frequency limits of the current loop must be validated in order to impose the same torque disturbance amplitude for the whole range frequencies.

A first experimental result that verifies the current loops bandwidths are shown in Figs 4.7.16 – 4.7.17:

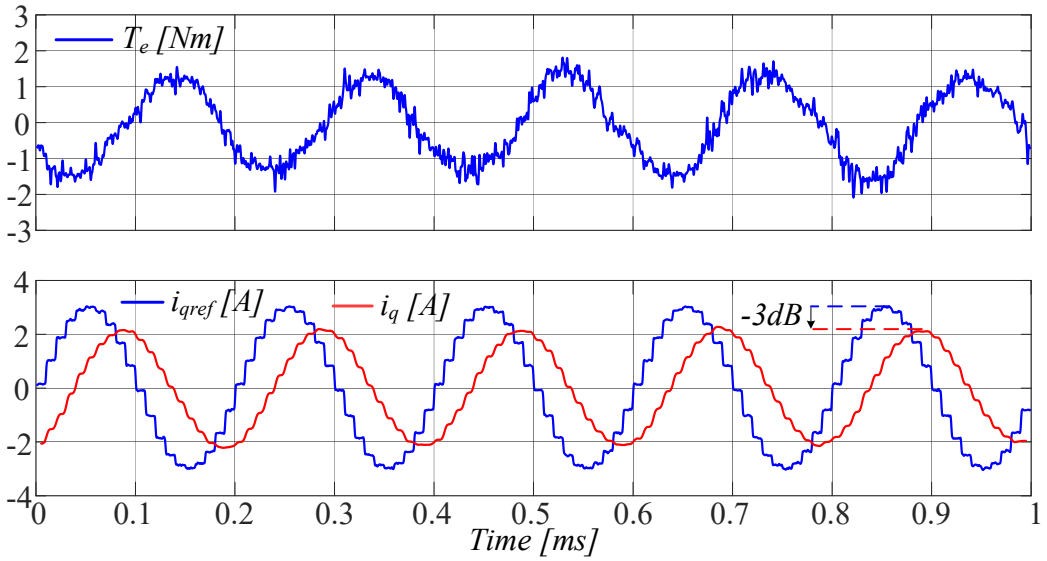

Figure 4.7.16 *SPM motor drive current loop performance at no load condition and with ΔT_e = 2Nm and f_d = 500 Hz.*

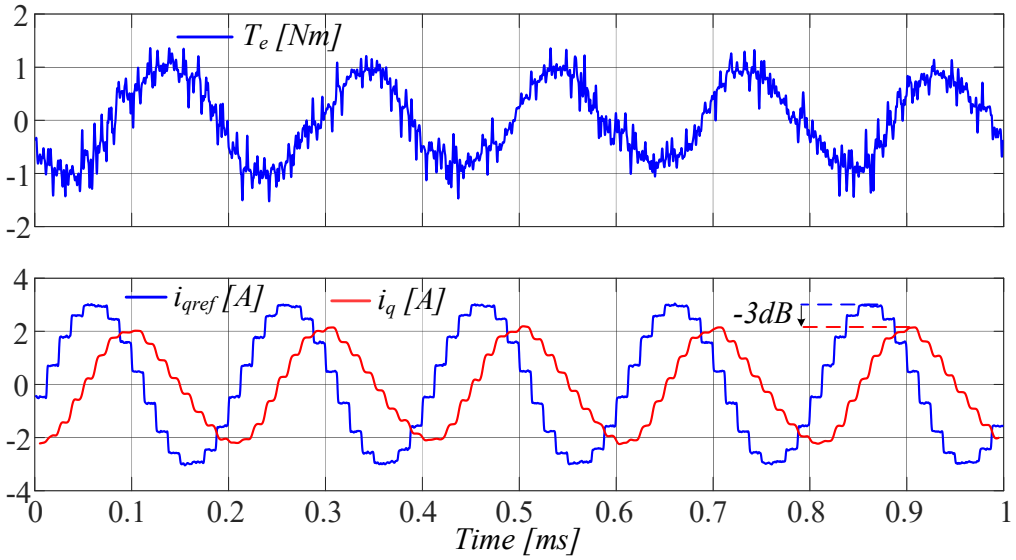

Figure 4.7.17 *IPM motor drive current loop performance at no load condition and with ΔT_e = 2Nm and f_d = 500 Hz.*

In Fig. 16 the SPM motor speed is setted at 50rad/s through the motor under test IPM, while the SPM motor drive imposes zero average value of current of axis q, and therefore no load condition, with superimposed a sinusoidal disturbance of amplitude 3A and frequency 500 Hz, in order to verify if the q axis current feedback reproduces a similar sinusoidal trend, but with phase-shift and with a reduced amplitude of -3dB.

The same test is repeated for the current loop of the IPM motor drive, Fig. 4.7.17. In fact, the SPM motor drive imposes the speed at 50rad / s, while the motor under test IPM provides zero average value of axis q current with superimposed a sinusoidal disturbance of 3A amplitude and 500Hz frequency.

Fig. 18 shows the same test but under load conditions, by imposing an average value of q axis current of 5A and superimposing a sinusoidal disturbance of amplitude 3A and frequency 500Hz.

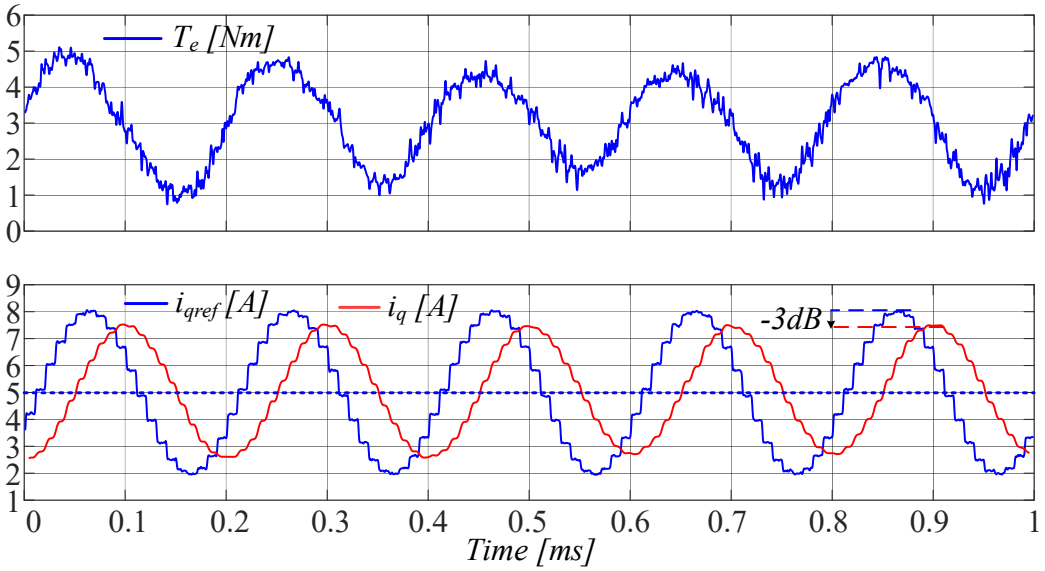

Figure 4.7.18 *IPM motor drive current loop performance at load condition and with ΔT_e = 2Nm and f_d = 500 Hz.*

After verifying the performance of the current loops, it is possible to validate the selection method of the rotor position sensor resolution N_{DS} by comparing the simulated and experimental minimum rotor speed limits, for a given speed loop bandwidth, Fig. 4.7.19. In particular, the theoretical and practical limits are shown for different resolution values N_{ds} and imposing, as a stability constraint $m_\varphi = 0$.

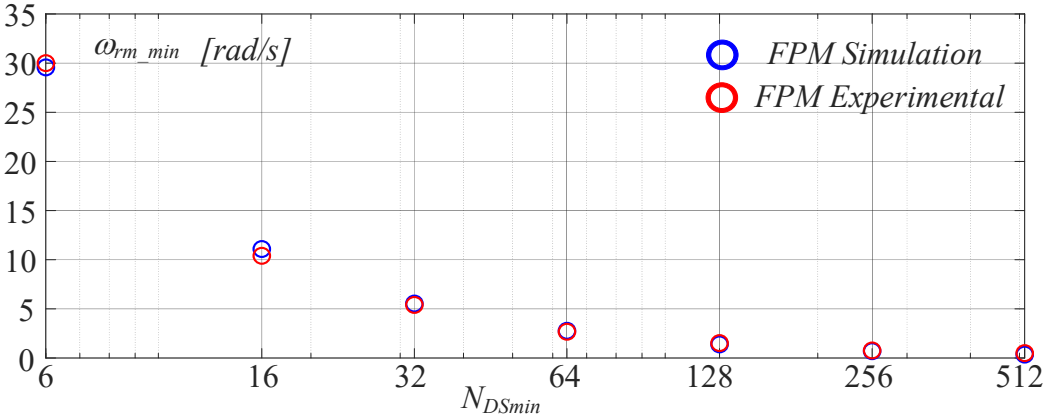

Figure 4.7.19 *Minimum Speed Limits at mf = 0 and fBW = 20 Hz.*

It would be notating, in Fig. 4.7.19, that the minimum rotor speed has been evaluated in steady state condition and an instant before the speed control loop was loser in no load condition. Starting from stability margins analysis performed in the section 4.7.3, a first experimental validation has been evaluated by choosing the control speed loop bandwidth $f_{BW} = 20$ Hz and two different phase margin conditions $m_\varphi = 60°$ and $m_\varphi = 20°$ by considering the same rotor position sensor resolution $N_{DS} = 6$. According to the expression (4.7.20) it is possible to evaluate the minimum rotor speed that to able guarantee the stability margins selected above.

Because in these first experimental tests has been selected 20Hz of the speed loop bandwidth, in Fig. 4.7.20 a comparison between the mechanical reference rotor speed ω^*_{rm} and estimated rotor speed ω_{rm} by using an incremental encoder with N_{DS} = 2048 has been shown, where the reference rotor speed ω^*_{rm} is a constant value 50 rad/s with an adding sinusoidal speed with 5 rad/s amplitude and 20 Hz frequency.

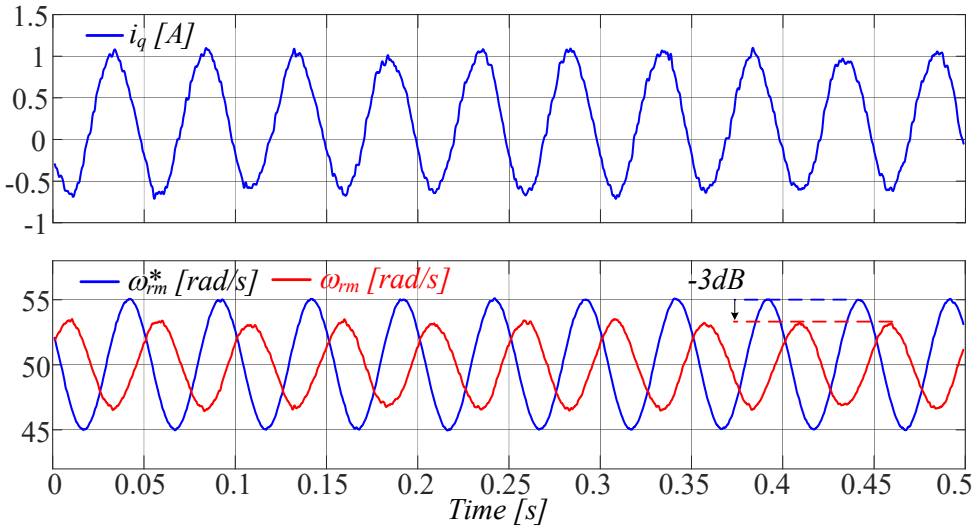

Figure 4.7.20 *IPM motor drive current loop performance with f_{BW} = 20Hz.*

In order to verify the robustness, i.e. the phase margin m_φ, indirectly, a dynamic stiffness has been performed in Figs. 4.7.21 and 4.7.22. In particular the experimental dynamic stiffness has been performed by control the SPM motor drive in torque control by providing a sinusoidal torque disturbance with peak to peak value ΔT_L = 2Nm and a variable range frequency from 0.5 ti 150 Hz. It would be notating that, since the current loops bandwidth of both motors drive in Figs. 16a and 16b have been verified at 500Hz with -3dB attenuation, in order to perform the dynamic stiffness, the same disturbance torque peak to peak ΔT_L has been provided and verified by torque-meter measurements for each frequency range values.

In the operating point conditions and for each frequency range values, a peak-to-peak mechanical speed $\Delta\omega_{rm}$ has been estimated by using the FPM and from a rotor position sensor with N_{DS} = *2048*.

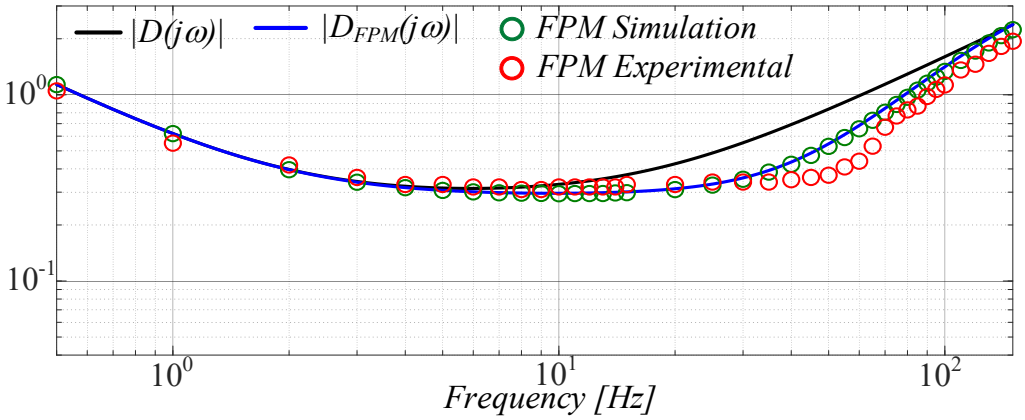

Figure 4.7.21 *$|D(s)|$, $|D_{FPM}(s)|$ carried out through the Simulink implementation of the speed controlled motor drive and experimental tests, with the following reference design specifications: f_{BW}=20Hz, m_φ=60°, ω_{rm_min}=100 rad/s and N_{DS}=6.*

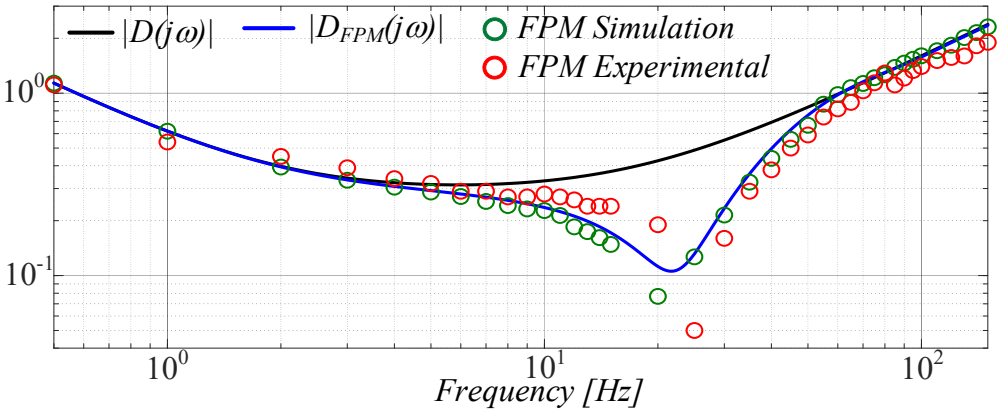

Figure 4.7.22 *$|D(s)|$, $|D_{FPM}(s)|$ carried out through the Simulink implementation of the speed controlled motor drive and experimental tests, with the following reference design specifications: f_{BW}=20Hz, m_φ=20°, ω_{rm_min}=38 rad/s and N_{DS}=6.*

The results obtained in Figs. 4.7.21 and 4.7.22 confirm the predicted phase margins defined during the desired procedure design. In fact, with the same closed control speed loop bandwidth $f_{BW} = 20\ Hz$ and with the same rotor position sensor resolution $N_{DS} = 6$, the comparisons between the theoretical, simulated, and experimental dynamic stiffness confirm indirectly the robustness achived.

4.7.8 Experimental Results: Case Study

Suppose that the speed loop design specifications are: desired closed loop speed bandwidth f_{BW}=30Hz and phase margin $m_\varphi = 60°$ at the minimum mechanical speed $\omega_{rm\_min} = 30\ rad/s$. By following the proposed approach we achieve the maximum time delay $\tau_{dmax} = 2.3ms$ allowing to approach at ω_{rm_min} (4.7.27) the desired m_φ. Then, the minimum resolution of the position sensor is determined by rounding the result of (4.7.28) to the available product on the market, (4.7.28):

$$N_{DSmin} = \frac{2\pi}{pp\ \omega_{rm\_min}\ \tau_{dmax}} = \frac{2\pi}{3\ 30\ 0.0023} = 30.35 \approx 32 \qquad (4.7.28)$$

In order to verify whether the above reference design specifications are satisfied by the drive, a first test has been performed to verify the bandwidth of the speed loop when the motor drive is set according to (4.7.16) and the speed feedback is carried out by the FPM algorithm configuring N_{DS}=32. Fig. 4.7.23 displays the reference ω^*_{rm} and feedback ω_{rm} rotor speed, the last estimated with the FPM algorithm applied to the full resolution rotor position measurement $N_{DS} = 2048$. In this test the reference rotor speed ω^*_{rm} is set to ω_{rm_min} plus an additional sinusoidal terms of magnitude equal to 5 rad/s and frequency equal to 30 Hz. The test clearly shows a 3dB decrease of the actual speed ω_{rm} at ω_{rm_min}, confirming the f_{BW} with N_{DS}=32.

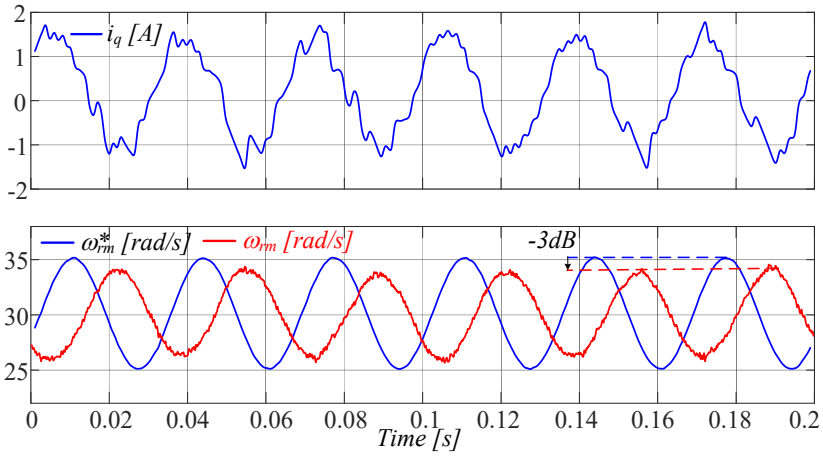

Figure 4.7.23 *Test performed by setting the IPM motor drive with f_{BW}=30Hz, phase margin m_φ=60° at ω_{rm_min} = 30 rad/s and N_{DS}=32.*

The robustness of the speed control loop has been evaluated through the dynamic stiffness analysis, which has been determined by controlling the drive under test at ω^*_{rm}=30 rad/s and generating with the other drive a sinusoidal torque disturbance of peak-to-peak amplitude ΔT_L = 2Nm and a variable frequency range from 0.5Hz to 150 Hz. The dynamic stiffness has been computed by considering the estimated speed with full resolution sensor. Note that experimental tests fit very well the curve $|D_{FPM}(j\omega)|$ carried out from the model (4.7.25) and from simulations of the tested motor drive, confirming the accuracy the modelling and validating the methodology used to select the rotor position sensor resolution.

The same analysis has been conducted by reducing the sensor resolution to N_{DS}=16 and keeping same ω_{rm_min} and f_{BW}. Consistent with the theory, the dynamic performances worsen as the delay time τ_d increased. According to (4.7.27), the corresponding m_φ is now decreased and equal to 40°. Fig. 4.7.25 confirms a worsening of the frequency response, and a good matching between modelling, numerical simulations and experimental tests.

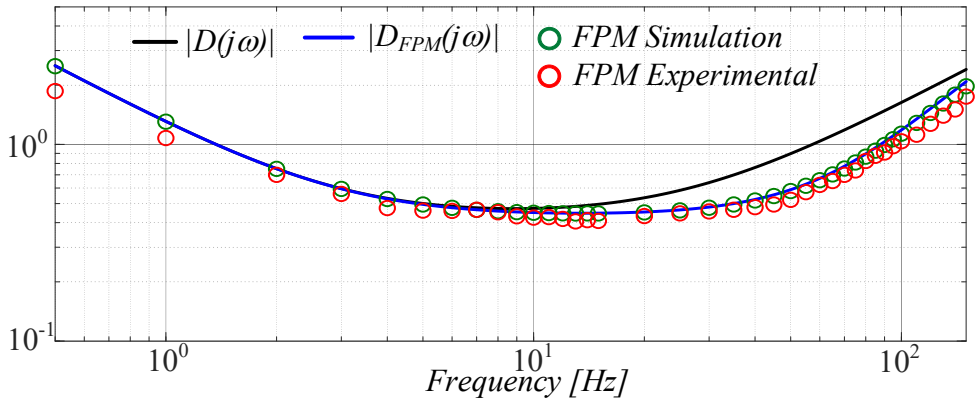

Figure 4.7.24 *$|D(s)|$, $|D_{FPM}(s)|$ carried out through the Simulink implementation of the speed controlled motor drive and experimental tests, with the following reference design specifications: f_{BW}=30Hz, m_φ=60°, ω_{rm_min}=30 rad/s and N_{DS}=32.*

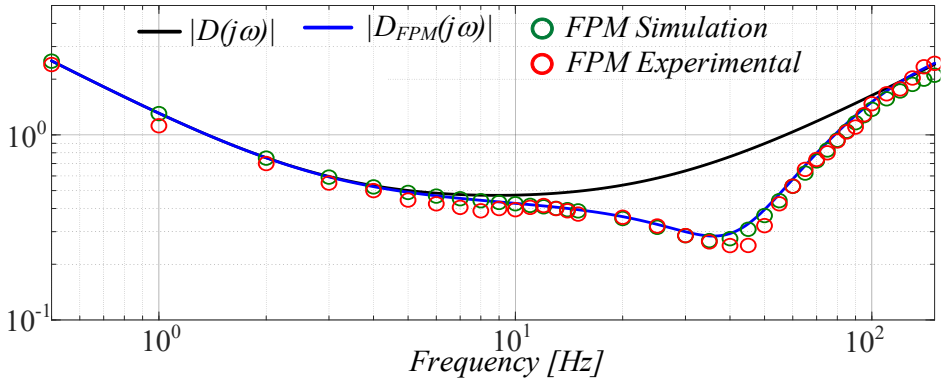

Figure 4.7.25 *$|D(s)|$, $|D_{FPM}(s)|$ carried out through the Simulink implementation of the speed controlled motor drive and experimental tests, with the following reference design specifications: f_{BW}=30Hz, m_{φ}=40°, ω_{rm_min}=30 rad/s and N_{DS}=16.*

Another way that allows to evaluate the dynamic performance of the closed speed loop control algorithm is the speed step response of the command tracking Fig. 4.7.26.

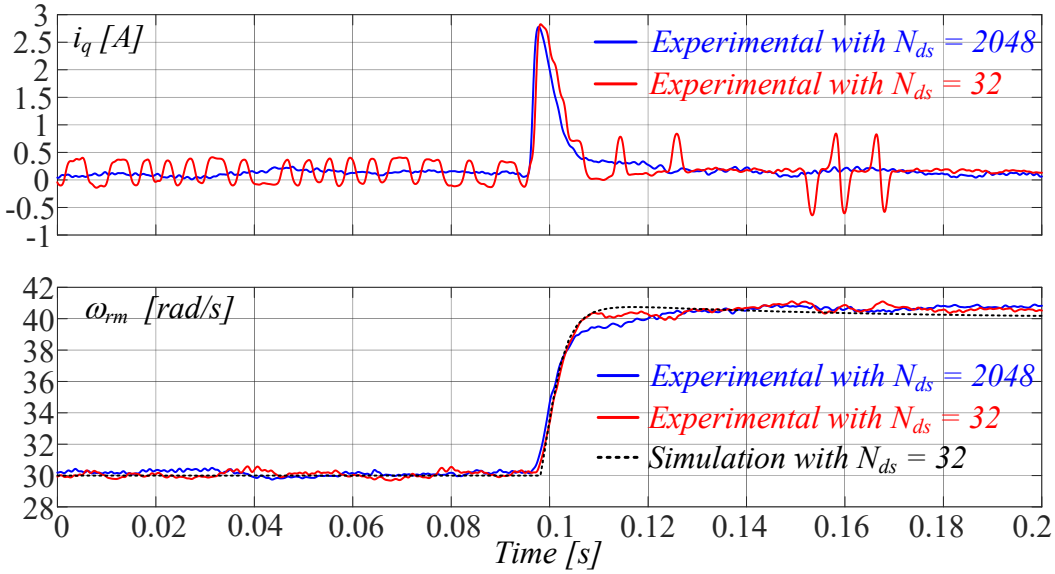

Figure 4.7.26 *Rotor speed step response comparisons between experimental results with N_{ds} = 2048 and N_{ds} = 32 and simulation result with N_{DS} = 32.*

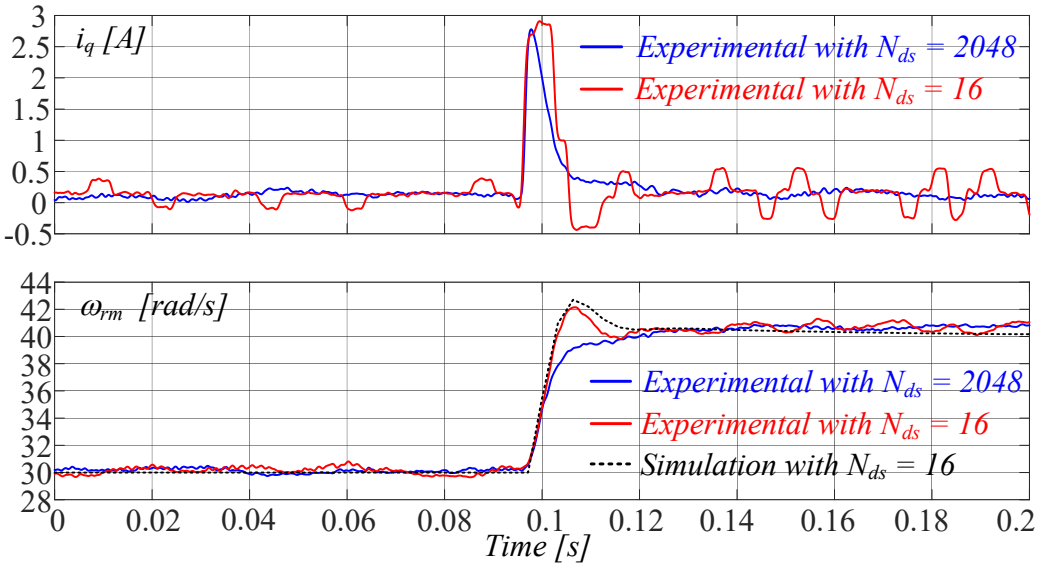

Figure 4.7.27 *Rotor speed step response comparisons between experimental results with $N_{DS} = 2048$ and $N_{DS} = 16$ and simulation result with $N_{DS} = 16$.*

The Figs. 4.7.26 and 4.7.27 show the speed step responses from 30 rad/s to 40 rad/s in order to compare the experimental results with different rotor position sensor resolutions.

In particular, it would be noted the different command tracking performance when a rotor position sensor is quantized with $N_{DS} = 32$ and with $N_{DS} = 16$; in fact, the command tracking performance observed in Figs. 4.7.26 - 4.7.27 have the same rise times, related to the same closed speed loop bandwidth $f_{BW} = 30Hz$, and different overshoots, related to the different phase margins $m_\varphi = 60°$ in the case $N_{DS} = 32$ and $m_\varphi = 40°$ for $N_{DS} = 16$ respectively.

A different way to verify the disturbance rejection of the closed speed loop is to provide a $T_L = 10Nm$ step torque load at minimum rotor speed $\omega_{rm\_min} = 30rad/s$ required in this case study, with different rotor position sensor resolutions $N_{DS} = 32$ and $N_{DS} = 16$ respectively. Therefore, in Figs. 4.7.28 - 4.7.29 the different temporals disturbance rejection have been performed in order to linked the different phase margins with the dynamic performance of the torque load disturbance rejection in the closed speed loop.

Furthermore, the comparisons between the experimental results and the simulation results of the FPM implementation model, in both cases $N_{DS} = 32$ ($m_\varphi = 60°$) and $N_{DS} = 16$ ($m_\varphi = 40°$), Figs. 4.7.28 and 4.7.29 respectively, are quite satisfactory.

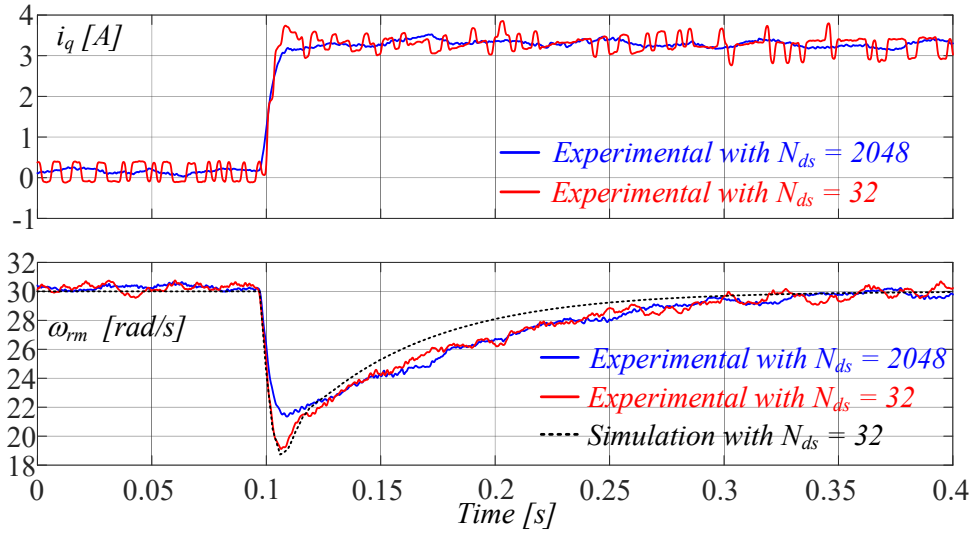

Figure 4.7.28 *Temporal disturbances rejection comparisons between experimental results with N_{DS} = 2048 and N_{DS} = 32 and simulation result with N_{DS} = 32.*

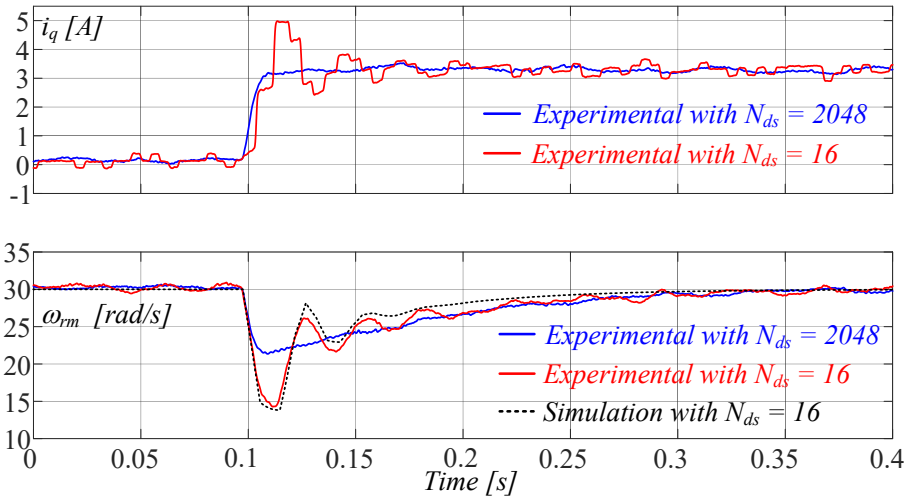

Figure 4.7.29 *Temporal disturbances rejection comparisons between experimental results with N_{DS} = 2048 and N_{DS} = 32 and simulation result with N_{DS} = 32.*

In conclusion, the experimental results conducted both in the preliminary tests (sub-paragraph 4.7.6) and in the case study (sub-paragraph 4.7.7) allow, not only to validate the proposed approach and therefore allowing to choose the minimum resolution of the position sensor starting from the desired specifications to be guaranteed for a VSD, but also to verify how closely the mathematical models proposed for this analysis are able to approach the real behavior of the system under test.

4.8 Conclusions

The contributions of my research regarding this chapter expect that will help engineers develop new and effective methodologies to determine the most appropriate position sensor resolution for the electric drives they are designing.

Starting from the theoretical contribution developed in paragraph 3.3 "Mathematical Formulations of the Quantized Rotor Position and Angular Speed" , in the paragraph 4.5 "Impact of the Rotor Position Sensor Resolution in AC drive using Speed Estimation Algorithm based on Vector Tracking Observer" has been verified theoretically and

experimentally that the quantization harmonics are inherently present in speed estimates obtained from the position measurement, albeit reduced by the filtering properties of the specific estimation algorithm. For the specific case of the VTSF, simple expressions for the amplitudes of the quantization harmonics in the estimated speed have been derived. It has also been verified experimentally that when the speed estimate is used for closed loop speed control, all of the lower order quantization harmonics may appear in the shaft torque and in the rotor speed, especially during low-speed operation, in addition to the oscillations produced by the torque disturbances.

A straightforward approach that allows to choose the position sensor for a speed controlled electrical drive according to the speed loop reference design specifications has been developed for both model-based and non-model based speed estimator algorithms.

In particular, in paragraph 4.6 "Selection of the Rotor Position Sensor Resolution in Variable Speed Drives involving a Vector Tracking Observer in the Speed Loop", by means of the VTO's small signal mathematical model a complete mathematical derivation has been initially derived; then, experimental tests performed on a PMSM drive have been executed to validate the theoretical study. The rotor position resolution selection has been developed by considering the relationship between the estimated speed ripple and the motor drive dynamic performance.

The same analysis has been developed by means of the FPM's small signal mathematical model, in paragraph 4.7 "Selection of the Rotor Position Sensor Resolution in Variable Speed Drives involving a Fixed-Position-Based Speed Estimation Algorithm in the Speed Loop", where the experimental results performed on a PMSM validate the theoretical study. The rotor position resolution selection has been developed by considering the stability and robustness conditions of the desired motor drive dynamic performance.

4.9 References

[1] R.D. Lorenz and K. Van Patten, “High-resolution velocity estimation for all-digital, ac servo drives,” *IEEE Trans. Ind. Appl.*, vol. 27, no. 4, pp. 701 – 705, Jul./Aug. 1991.

[2] R.M. Kennel, “Encoders for simultaneous sensing of position and speed in electrical drives with digital control,” *IEEE Trans. Ind. Appl.*, vol. 43, no. 6, pp. 1572 – 1577, Nov./Dec. 2007.

[3] G. Liu, A. Kurnia, R. De Larminat, and S.J. Rotter, “Position sensor error analysis for EPS motor drive,” in *Proc. of IEEE IEMDC,* Jun. 2003, pp. 249-254.

[4] R. Petrella, M. Tursini, L. Peretti and M. Zigliotto, “Speed measurement algorithms for low-resolution incremental encoder equipped drives: a comparative analysis,” in Proc. of IEEE ACEMP, Sep. 2007, pp. 780-787.

[5] Katsuhiko Ogata, University of Minnesota, “Discrete-Time Control Systems”, Second Edition 1995.

[6] Gene F. Franklin, J. David Powell, Michael Workman, “Digital Control of Dynamic Systems”, Third Edition, 1998.

[7] H. Kim, M. W. Degner, J. M. Guerrero, F. Briz and R. D. Lorenz, "Discrete-Time Current Regulator Design for AC Machine Drives," in IEEE Transactions on Industry Applications, vol. 46, no. 4, pp. 1425-1435, July-Aug. 2010.

[8] F. B. del Blanco, M. W. Degner and R. D. Lorenz, "Dynamic analysis of current regulators for AC motors using complex vectors," in IEEE Transactions on Industry Applications, vol. 35, no. 6, pp. 1424-1432, Nov.-Dec. 1999

[9] F. Briz, M. W. Degner and R. D. Lorenz, "Analysis and design of current regulators using complex vectors," in IEEE Transactions on Industry Applications, vol. 36, no. 3, pp. 817-825, May-June 2000.
[10] S. Lee, R. D. Lorenz and K. Lee, "Guidelines for Optimum Bandwidth Selection in the Observers and Performance Investigation of DB-DTFC Using Back-EMF Self-Sensing for SPM Machines," 2018 IEEE Energy Conversion Congress and Exposition (ECCE), 2018, pp. 3428-3435.
[11] ABB drives Technical guide No. 9, “Guide to motion control drives”, 2013, Aviable Online: https://library.e.abb.com/public/bbc682806eb5be78c125727c0043f50b/Technical_guide_No_9_3AFE68695201_EN_RevB_11_2.pdf.
[12] Jang-Mok Kim and Seung-Ki Sul, "Speed control of interior permanent magnet synchronous motor drive for the flux weakening operation," in IEEE Transactions on Industry Applications, vol. 33, no. 1, pp. 43-48, Jan.-Feb. 1997.
[13] S. Bolognani, S. Calligaro, R. Petrella and F. Pogni, "Flux-weakening in IPM motor drives: Comparison of state-of-art algorithms and a novel proposal for controller design," Proceedings of the 2011 14th European Conference on Power Electronics and Applications, 2011, pp. 1-11.
[14] D. G. Holmes, T. A. Lipo, B. P. McGrath and W. Y. Kong, "Optimized Design of Stationary Frame Three Phase AC Current Regulators," in IEEE Transactions on Power Electronics, vol. 24, no. 11, pp. 2417-2426, Nov. 2009.
[15] Olivier Brunel, Electricfil Automotive, “Rotor Position Sensor for Hybrid Drives and Eletric Drives”, AMAA, June 18th 2013.
[16] Nidec, “An Engineering Guide to Position and Speed Feedback Devices for variable speed drives and servos”, 2011.
[17] M.C. Harke, G. De Donato, F. Giulii Capponi, T.R. Tesch, and R.D. Lorenz, “Implementation issues and performance evaluation of sinusoidal, surface-mounted PM machine drives with Hall-effect position sensors and a vector-tracking observer,” IEEE Trans. Ind. Appl., vol. 44, no. 1, pp. 161 – 173, Jan./Feb. 2008.
[18] R. H. Brown, S. C. Schneider and M. G. Mulligan, "Analysis of algorithms for velocity estimation from discrete position versus time data," in IEEE Transactions on Industrial Electronics, vol. 39, no. 1, pp. 11-19, Feb. 1992
[19] L. Bascetta, G. Magnani and P. Rocco, "Velocity Estimation: Assessing the Performance of Non-Model-Based Techniques," in IEEE Transactions on Control Systems Technology, vol. 17, no. 2, pp. 424-433, March 2009.
[20] F. Briz, J. A. Cancelas and A. Diez, "Speed measurement using rotary encoders for high performance AC drives," Proceedings of IECON'94 - 20th Annual Conference of IEEE Industrial Electronics, 1994, pp. 538-542 vol.1.
[21] F. Brugnano, C. Concari, E. Imamovic, F. Savi, A. Toscani and R. Zanichelli, "A simple and accurate algorithm for speed measurement in electric drives using incremental encoder," IECON 2017 - 43rd Annual Conference of the IEEE Industrial Electronics Society, 2017, pp. 8551-8556.
[22] A. Anuchin, A. Dianov and F. Briz, "Synchronous Constant Elapsed Time Speed Estimation Using Incremental Encoders," in IEEE/ASME Transactions on Mechatronics, vol. 24, no. 4, pp. 1893-1901, Aug. 2019.
[23] S. M. Phillips and M. S. Branicky, "Velocity estimation using quantized measurements," 42nd IEEE International Conference on Decision and Control (IEEE Cat. No.03CH37475), 2003, pp. 4847-4852 Vol.5.

[24] M. Lemkin, P. H. Yang, A. C. Huang, J. Jones and D. M. Auslander, "Velocity estimation from widely spaced encoder pulses," Proceedings of 1995 American Control Conference - ACC'95, 1995, pp. 998-1002 vol.1.
[25] E. Galvan, A. Torralba and L. G. Franquelo, "ASIC implementation of a digital tachometer with high precision in a wide speed range," in IEEE Transactions on Industrial Electronics, vol. 43, no. 6, pp. 655-660, Dec. 1996.
[26] ABB drives Technical guide No. 7, “Dimensioning of a drive system”, 2011.
[27] G. Scelba, G. De Donato, A. M. Elsman, L. D. Tornello, G. Scarcella and F. G. Capponi, "Resolution of Rotor Position Measurement: Modelling and Impact on Speed Estimation," in IEEE Journal of Emerging and Selected Topics in Power Electronics.
[28] L. Bascetta, G. Magnani, P. Rocco and A. M. Zanchettin, "Performance Limitations in Field-Oriented Control for Asynchronous Machines With Low Resolution Position Sensing," in IEEE Transactions on Control Systems Technology, vol. 18, no. 3, pp. 559-573, May 2010.
[29] Y. Vázquez-Gutiérrez, D. L. O'Sullivan and R. C. Kavanagh, "Study of the impact of the incremental optical encoder sensor on the dynamic performance of velocity servosystems," The 9th International Conference on Power Electronics, Machines and Drives (PEMD 2018), Volume 2019, Issue 17, June 2019, p. 3807-3811.
[30] Y. Vázquez-Gutiérrez, D. L. O'Sullivan and R. C. Kavanagh, "Small-Signal Modeling of the Incremental Optical Encoder for Motor Control," in IEEE Transactions on Industrial Electronics, vol. 67, no. 5, pp. 3452-3461, May 2020.
[31] Karl Johan Astrom, Richard M. Murray, “Feedbcak Systems: An Introduction for Scientists and Engineers”, Second Edition, 2009.
[32] R. W. Hejny and R. D. Lorenz, "Evaluating the Practical Low-Speed Limits for Back-EMF Tracking-Based Sensorless Speed Control Using Drive Stiffness as a Key Metric," in IEEE Transactions on Industry Applications, vol. 47, no. 3, pp. 1337-1343, May-June 2011.
[33] B. Hafez, A. S. Abdel-Khalik, A. M. Massoud, S. Ahmed and R. D. Lorenz, "Single-Sensor-Based Three-Phase Permanent-Magnet Synchronous Motor Drive System With Luenberger Observers for Motor Line Current Reconstruction," in IEEE Transactions on Industry Applications, vol. 50, no. 4, pp. 2602-2613, July-Aug. 2014.
[34] G. Scelba, G. De Donato, G. Scarcella and F. Giulii Capponi, "On the Effects of Position Sensor Resolution in Variable Speed Drives," 2018 IEEE Energy Conversion Congress and Exposition (ECCE), 2018, pp. 3386-3393.

Chapter 5: Other Activities

This chapter summarizes some other research activities carried out during the PhD period; in particular, research activities developed to the improvement of electric drives in terms of energy efficiency, power quality and fault tolerant issues have been addressed. The electric drives improvements are achieved by studying the open-end winding solutions combined with different multilevel converters and also new converter control strategies

Typically, in the Open Winding (OW) configuration the windings of electric machine (motor or transformer) is supplied from two sides. Thanks to some advantages compared to conventional configurations, such as: higher efficiency and better exploitation of the DC bus voltage, OW is gaining increasing interest over a wide set of applications [1]-[3]. A key aspect of open-end winding configurations is the growing interest of the multilevel inverters (MLIs) topologies, which take advantage from a reduced distortion of AC-side quantities and lower voltage gradient, switching stresses, switching losses, devices voltage rating [4]-[7]. On the other hand, MLI require a higher amount of power switches than conventional two-level pulse width modulated (PWM) inverters.

By developing a new control strategies and reducing the number of power devices, a lower switching losses, a higher efficiency and an improved power quality can be achieved compared to existing Multilevel Inverter topologies.

Furthermore, since the safety critical systems are taking on increasing importance in many applications, such as automotive, aerospace, marine, nuclear power and chemical plants, and military applications [8], [9] two different main concerns regarding the fault tolerant solutions has been addressed; on the one hand, the possibility to hold the electric drive in service, even after a open phase fault occurs, keeping the output DC voltage at the value generated by the system in healthy conditions, on the other hand a performance analysis of the combined selection of the fuse and DC link capacitor has been performed in order to ensure that the fuse acts breaking the circuit loop quickly to prevent further damage on power source, inverter leg and other circuit components.

5.1 A Novel Three-Phase Multilevel Inverter Topology with Reduced Device Count for Open-end Winding Motor Drives [10]

A novel three-phase multilevel inverter topology for open-end winding motor drives is proposed, featuring a reduced number of power devices. According to such a topology, only two of the motor phase windings are fed by a single-phase neutral point clamped inverter from one side, and a single-phase full bridge inverter from the other, the third motor phase being connected between the midpoints of the two inverters. The proposed topology can generate five different voltage levels in each motor phase and compared to a conventional three-phase three-level neutral point clamped inverter features a reduced amount of power devices and a higher efficiency. Simulations dealing with steady-state and transient conditions have been performed on a 1kW permanent magnet synchronous motor drive to demonstrate the effectiveness of the proposed configuration in a wide operating range.

5.1.1 Introduction

Multi-Level Inverters (MLIs) have widely replaced in the last years conventional Two-Level Inverters (TLIs) in medium voltage, high power, industrial motor drives applications. In fact, if compared with TLIs, MLIs feature lower *dv/dt* levels across the semiconductor devices, reduced EMI/EMC issues and lower power devices voltage ratings. Moreover, the higher amount of output voltage levels lead to a substantial improvement of the voltage and current harmonic content, thus reducing the torque ripple [11]-[15]. This has powered the development of new MLI topologies exploiting low switching frequency multilevel modulation strategies [16]. Among them, those based on selective harmonic elimination, feature better efficiency and power factor levels if compared with conventional pulse width modulation (PWM) based TLI, as well as low bearing stresses in motor drive applications.

A key issue in order to ensure proper operations of multilevel power converters deals with balancing the voltages of the DC bus capacitors. Various PWM techniques can be found in literature specifically developed to balance the capacitor voltages [17]-[21] as well as additional voltage balancing circuits [19]. The drift of capacitor voltages mainly occurs due to the occurrence of a nonzero average current at the neutral point of the power converter, due to non-idealities of the real system. Although it is possible to mitigate the voltage drift by suitably modifying the modulation pattern, a low-frequency voltage oscillation at the DC bus midpoint may still appear at steady-state.

MLI systems using Open-end Winding (OW) configurations have been also investigated since nineties [22]- [30]. According to these configurations the AC machine (motor, generator or transformer) is fed by two power converters, placed on the two sides of an open-end winding. In [31]-[34] an Asymmetrical Hybrid Multilevel Inverter (AHMLI) has been proposed, where a main inverter manages the active power flow, while an auxiliary unit acts as an active filter, providing a null-average power to the machine. It acts differently from conventional OW systems, where the two inverters share between them both the active and reactive power provided to the machine. According to the AHMLI concept, the main inverter is of the multilevel type and exploits a step voltage modulation in order to minimize the switching power losses. The auxiliary inverter is instead a two level one, operated at lower DC bus voltage through a high frequency PWM technique to accurately control the phase voltage harmonic content. Hence, the main

inverter can be equipped with very low on-state voltage drop IGBT devices, while fast IGBT, or even Power MOS devices, can be used on the auxiliary TLI.

A modification of the AHMLI topology is presented in this paragraph in an effort to reduce circuital complexity and costs. A three-phase five-levels inverter is obtained by supplying two of the three motor phase windings by a single-phase Three-Level Neutral Point Clamped Inverter (3L-NPC) from one side, and a single-phase Two-Level Inverter (TLI) on the other, as shown in Fig. 5.1.1. The third phase winding is instead connected between the midpoints of the two inverters n' and n''. The obtained three-phase, Two-Poles, Open-end Winding Motor Drive (TPOWMD) encompasses a lower number of power devices compared to a traditional three-phase three level NPC inverter, but it is more efficient and feature a slightly higher Total Harmonic Distortion (THD) in the motor phase currents.

5.1.2 TPOWMD Configuration

According to the scheme of the TPOWMD shown in Fig. 5.1.1, motor phase voltages V_{jm} ($j = a,b,c$) can be obtained from the Kirchhoff laws:

$$\begin{cases} V_{am} = V_{aMn'} - V_{aTn''} + V_{n'n''} \\ V_{bm} = V_{bMn'} - V_{bTn''} + V_{n'n''} \\ V_{cm} = V_{am} - V_{aMn'} + V_{aTn'} = V_{bm} - V_{bMn'} + V_{bTn'} \\ V_{cm} = V_{n'n''} \end{cases} \tag{5.1.1}$$

where $V_{aMn'}$ and $V_{bMn'}$ are the 3L-NPC pole voltages, $V_{aTn''}$ and $V_{bTn''}$ are the TLI pole voltages, V_{jm} is the AC motor phase voltage ($j=a,b,c$) while $V_{n'n''}$ is the voltage between n' and n''.

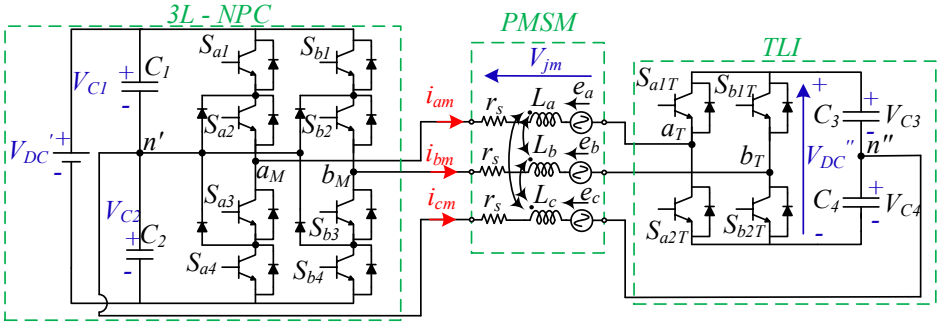

Figure 5.1.1 *Two-Poles, Open-end Winding Motor Drive (TPOWMD) Scheme.*

Moreover, the *c-phase* current i_{cm} is equal to $-(i_{bm}+i_{am})$, while the *c-phase* voltage V_{cm} is equal to $V_{n'n''}$. By considering a symmetrical and balanced system, the motor phase voltages can be expressed as a function of inverter pole voltages $V_{aMn'}$, $V_{bMn'}$, $V_{aTn''}$ and $V_{bTn''}$ as follows:

$$\begin{cases} V_{am} = \frac{2}{3}(V_{aMn'} - V_{aTn''}) + \frac{1}{3}(V_{bTn''} - V_{bMn'}) \\ V_{bm} = \frac{2}{3}(V_{bMn'} - V_{bTn''}) + \frac{1}{3}(V_{aTn''} - V_{aMn'}) \\ V_{cm} = \frac{V_{bTn''} - V_{bMn'} + V_{aTn''} - V_{aMn'}}{3} \end{cases} \tag{5.1.2}$$

$$\begin{cases} V_{aMn'} = (S_{a1} + S_{a2} - 0.5)V'_{DC} \\ V_{aTn''} = (S_{a1T} - 0.5)V''_{DC} \\ V_{bMn'} = (S_{b1} + S_{b2} - 0.5)V'_{DC} \\ V_{bTn''} = (S_{b1T} - 0.5)V''_{DC} \end{cases} \quad (5.1.3)$$

According to equations (5.1.2) and (5.1.3), the phase voltage V_{jm} is a function of the 3L-NPC switches states: S_{a1}, S_{a2}, S_{a3}, S_{a4}, S_{b1}, S_{b2}, S_{b3}, S_{b4}, and TLI switches states: S_{a1T}, S_{b1T}, as well as of the two DC bus voltages V_{DC}' and V_{DC}''. Space vector diagrams of a conventional three-phase three-level NPC inverter and of a TPOWMD working with $V_{DC}'=V_{DC}''$ are shown in Fig. 5.1.2. Under the last constraint, the TPOWI feature five voltage levels with the same amount of power switches.

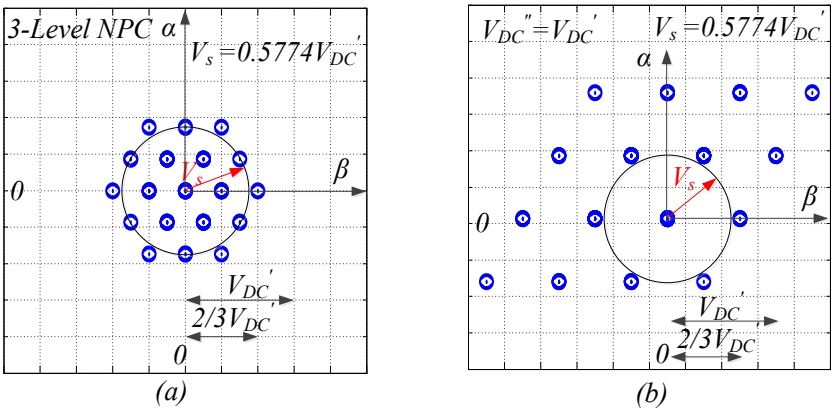

Figure 5.1.2 *Space vector diagrams: (a) 3L-NPC. (b) TPOWMD.*

5.1.3 Control Strategy

A control strategy different from that of a standard 3L-NPC, needs to be developed to manage the TPOWMD. It must able not only to control the output voltage, but also to handle the TLI DC bus voltage, to balance MLI capacitor voltages and to mitigate the low-order current harmonics generated by the 3L-NPC step modulation. The control strategy for a TPOWMD powering a permanent magnet synchronous motor (PMSM) is shown in Fig. 5.1.3. It consists of two main sections, dealing respectively with the 3L-NPC and the TLI. The 3L-NPC delivers the whole active power and is step operated to generate a voltage whose fundamental component V_s is equal to the sum of the estimated motor back-EMF, and the *qd-axes* control voltage components V_{qdcap} provided by the TLI DC Bus voltage control [20]. The *qd* axes motor back-EMF are given by:

$$\begin{cases} \hat{E}_q = \hat{L}_s\, \omega_{re}\, i_d + w_{re}\hat{\lambda}_{pm} \\ \hat{E}_d = -\,\hat{L}_s\, \omega_{re}\, i_q \end{cases} \quad (5.1.4)$$

where $\hat{L}_s$ is the synchronous inductance, $\hat{\lambda}_{pm}$ is the permanent magnet flux and $\omega_{re} = pp\ \omega_{rm}$, where pp is the number of pole pairs and ω_{rm} is the mechanical angular speed. The inverter phase voltage is regulated by acting on the switching angle γ, according to the following functions:

$$\gamma = \arccos(m) \qquad m = \frac{\pi |V^*_s|}{V'_{DC}} \qquad |V^*_s| = \sqrt{V^2_q + V^2_d} \qquad \phi = \operatorname{atan}\left(\frac{V_d}{V_q}\right) \quad (5.1.5)$$

where m is the modulation index.

The TLI is PWM modulated and tasked to control the phase currents, the TLI Bus voltage, and balancing the capacitor voltages on the two DC buses. Without a proper current shaping, in fact, the PMSM phase current would be highly non-sinusoidal, due to the stepwise waveform of the 3L-NPC phase voltage. This, in turn, would lead to low conversion efficiency and poor power factor. A phase current shaping is thus accomplished by the TLI, which is managed to operate as an active power filter. As shown in Fig. 5.1.3, a predictive input current filtering is exerted by including in the auxiliary inverter voltage reference V_{abTLI}^{*} a suitable compensation term V_{abh}, which is obtained as the difference between the staircase phase voltage V_{ab3L} and its fundamental harmonic component V_{1ab3L}:

$$\begin{cases} V_{1a3L} = 2\dfrac{V''_{DC}}{\pi}\cos(\alpha)\sin(\theta_{re}+\phi) \\ V_{1b3L} = 2\dfrac{V''_{DC}}{\pi}\cos(\alpha)\sin\left(\theta_{re}+\phi-\dfrac{2}{3}\pi\right) \end{cases} \tag{5.1.6}$$

In the above expressions $\theta_{re}=pp\ \theta_{rm}$, where θ_{rm} is the PMSM rotor position.

A TLI current vector control strategy is also implemented to control the torque i_{qs} and flux i_{ds} current components of the PMSM. Reference signal i_{qs}^{*} is provided by a traditional speed control loop, while i_{ds}^{*} is kept equal to zero. Phase currents i_{am} and i_{bm} are regulated through Proportional-Integral-Resonant (PIR) controllers in the *abc* reference frame. The reference signals being obtained from i_{qs} and i_{ds}. The third motor phase current, i_{cm} is instead forced according to the Kirchhoff law.

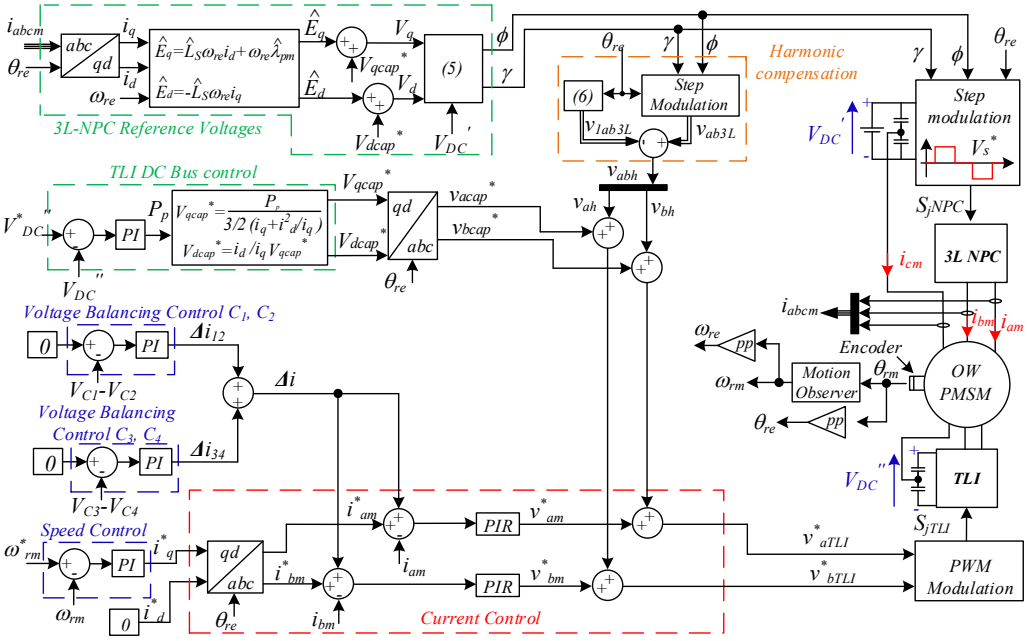

Figure 5.1.3 *Block diagram of the TPOWMD control system.*

The open winding configuration is exploited either to accomplish the control of the TLI DC Bus voltage either the balancing of 3L-NPC DC buses capacitors voltage. A progressive discharge of the TLI DC-bus flying capacitors is prevented by holding V''_{DC} constant by establishing a controlled active power stream P_p between the two inverters [21]. Such a power stream is managed by a V_{DC}'' closed loop controller relying on a standard PI controller, as described in Fig. 5.1.3. Possible unbalancing of 3L-NPC DC buses capacitors voltage may affect operations of the TPOWMD configuration. This is avoided by controlling the four capacitor voltages V_{c1}, V_{c2}, V_{c3} and V_{c4}. This is possible

because, as shown in Tabs. XVI and XVII, depending on the 3L-NPC and TLI switching states, a specific pair of capacitors is directly connected to the AC machine. Hence, according to Figs. 5.1.4 and 5.1.5, when the 3L-NPC takes the state 2 it is possible to charge C_1 and discharge C_2, independently on the switching state of the TLI. This is obtained by temporarily increasing by Δi the phase current reference, in order to estabilish a suitable energy transfer between the DC buses of the two inverters. Similarly, if the 3L-NPC takes the state 6, C_1 is discharged while C_2 is charged, hence, an energy transfer to C_1 can be managed if $V_{C1}>V_{C2}$. Moreover, also V_{C3} and V_{C4} can be regulated with the same approach, which does not require additional circuits, leading to a reduction of cost and power losses.

Table XVI *3LI Switching States*

State	***S_{a1}***	***S_{a2}***	***S_{b1}***	***S_{b2}***	***Capacitors***
1	*0*	*0*	*0*	*0*	*C1 charge C2 discharge*
2	*0*	*1*	*0*	*0*	*C1 charge C2 discharge*
3	*1*	*1*	*0*	*0*	*C1 discharge C2 charge*
4	*0*	*0*	*0*	*1*	*C1 discharge C2 charge*
5	*0*	*1*	*0*	*1*	*C1 charge C2 discharge*
6	*1*	*1*	*0*	*1*	*C1 discharge C2 charge*
7	*0*	*0*	*1*	*1*	*C1 charge C2 discharge*
8	*0*	*1*	*1*	*1*	*C1 charge C2 discharge*
9	*1*	*1*	*1*	*1*	*C1 discharge C2 charge*

Table XVII *TLI Switching States*

State	***S_{a1T} & S_{b2T}***	***S_{b1T} & S_{a2T}***	***Capacitors***
1T	*0*	*0*	*charging and discharging of C3 and C4 depends on the sign of the phase currents*
2T	*0*	*1*	
3T	*1*	*0*	
4T	*1*	*1*	

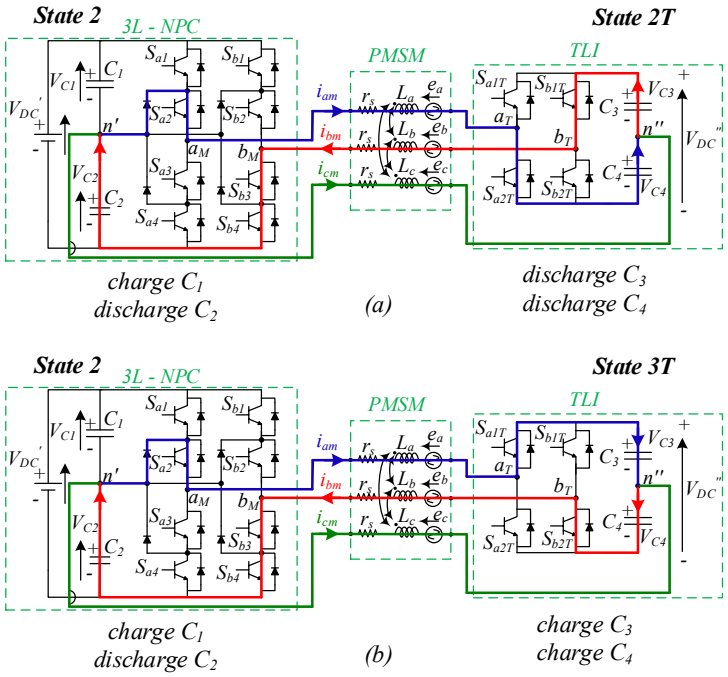

Figure 5.1.4 *Capacitor voltage balancing: (a) State 2 for 3LI and State 1T for TLI. (b) State 2 for 3LI and State 3T for TLI.*

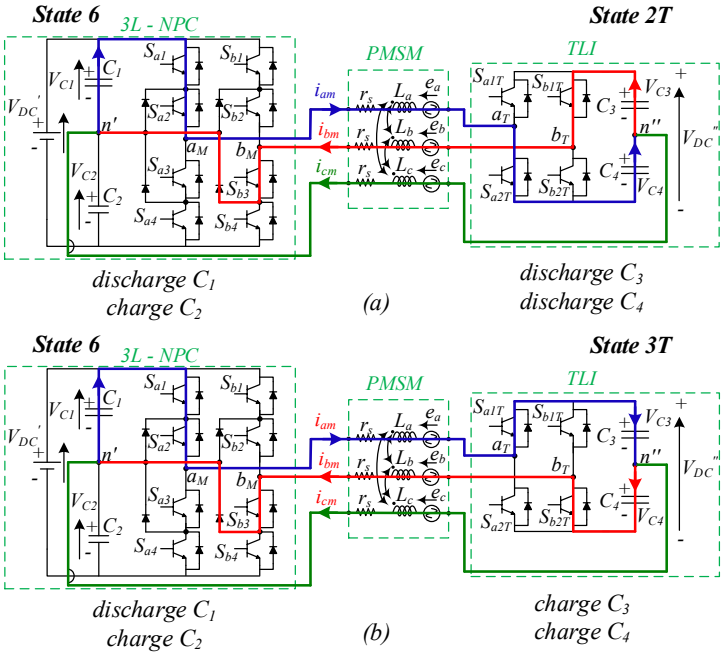

Figure 5.1.5 *Capacitor voltage balancing: (a) State 6 for 3LI and State 2T for TLI. (b) State 6 for 3LI and State 3T for TLI.*

Fig. 5.1.6 deals with active balancing of the 3L-NPC DC bus voltages capacitors.

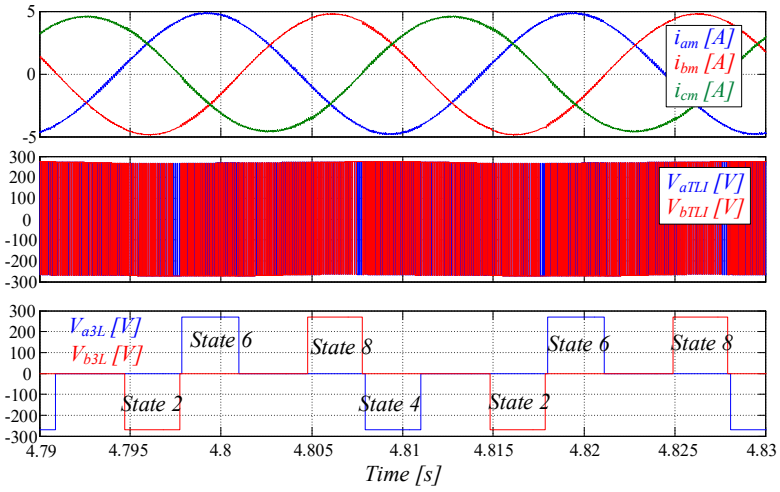

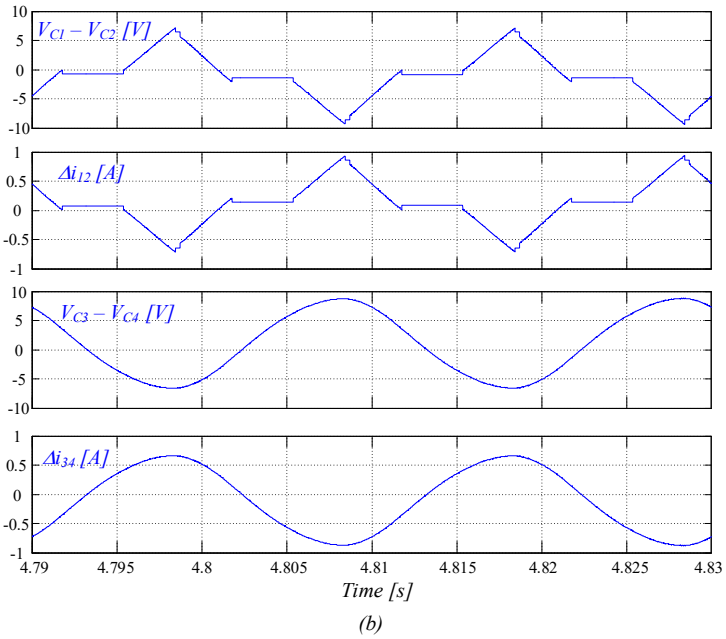

(b)

Figure 5.1.6 *Active balancing of 3L-NPC DC bus voltages capacitors: a). i_{abcm}, V_{abTLI}, V_{ab3L}. b) Capacitor voltage errors V_{C1}- V_{C2} and V_{C3}- V_{C4}, outputs of balancing controls C_1, C_2, C_3 and C_4.*

The number of devices required by TPOWMD, NPC, FC and CHB topologies is shown in Tab. XVIII. The proposed topology is fairly equivalent to a three level NPC inverter, however providing five voltage levels.

Table XVIII *Comparison among TPOWMD, NPC, FC and CHB topologies.*

Devices	TPOWMD	NPC		FC		CHB	
	5-lev.	3-lev.	5-lev.	3-lev.	5-lev.	3-lev.	5-lev.
Main Switches	12	12	24	12	24	12	24
Main Diodes	12	12	24	12	24	12	24
Clamping Diodes	4	6	36	0	0	0	0
DC Capacitors	2	2	4	2	4	1	2
Flying Capacitors	2	0	0	1	6	0	0

5.1.4 Power Losses Assessment

In a standard PWM NPC inverter all the power switches are driven at a high switching frequency, while only some of the TPOWMD switches do it. In the last, in fact, the 3L-NPC section is operated at a low switching frequency, according to a step modulation approach [21], while only the TLI section is PWM operated. A comparison between an PWM-NPC and the proposed TPOWMD configuration in terms of estimated total power losses is shown in Fig. 5.1.7. Total power losses are given by composition of switches, clamp diodes and capacitor power losses. Switches power losses, which consist of the

switching losses P_{sw} and conduction losses P_{on}, can be estimated as [23]:

$$P_{sw} = 0.5\ V_{ce}\ I_{RMS}\ f_{sw}\ (t_{rise} + t_{fall}) \qquad P_{on} = \delta\ V_{ceON}\ I_{RMS} \tag{5.1.7}$$

being δ the duty cycle, t_{rise} and t_{fall} the rise time and fall time of the power switches, respectively, I_{RMS} the rms value of the switch current, V_{ce} the collector-to-emitter voltage, V_{ceON} the collector-to-emitter saturation voltage. Clamping diodes power losses can be also estimated as [22]:

$$P_{drr} = V_{DR}\ f_{sw}\ (t_{rr}\ I_{RMS} + Q_{rr}) \qquad P_{don} = R_d\ I^2_d \tag{5.1.8}$$

where R_d diode resistance and I_d diode current in conduction mode, while V_{DR} is the diode reverse voltage, t_{rr} is the diode reverse recovery time and Q_r is the reverse recovery charge. Finally, DC bus capacitor losses are given by:

$$P_{cap} = R_{cap}\ I^2_{cap} \tag{9}$$

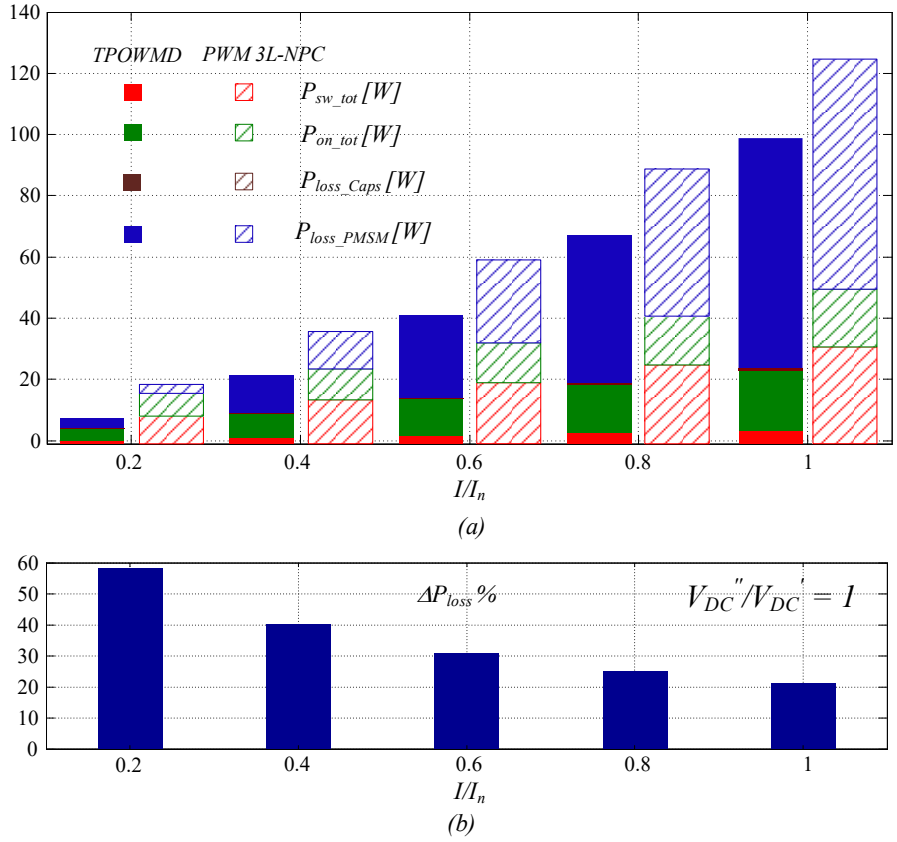

Figure 5.1.7 *Power losses comparison between a standard PWM 3L-NPC and the TPOWMD (ω_{rm} = 50 rad/s); (b) percentage loss reduction.*

The TPOWMD performs better than PWM-NPC all over the operating range, however, the best results in terms of percentage loss reduction are obtained at low loads, while a smaller improvement is observable at high loads.

Power losses on the TPOWMD can be reduced by lowering the DC bus voltage V_{DC}'', however, this leads to an increment of the Total Harmonic Distortion (THD) of the motor phase currents. In fact, as shown in Figs. 5.1.8 and 5.1.9, for V_{DC}''/V_{DC}' ratios lower than 0.8 a significant current distortion arises, worsening the performances of the power conversion and the torque ripple, as shown in Fig. 5.1.10, up to threatening the stability

of the system.

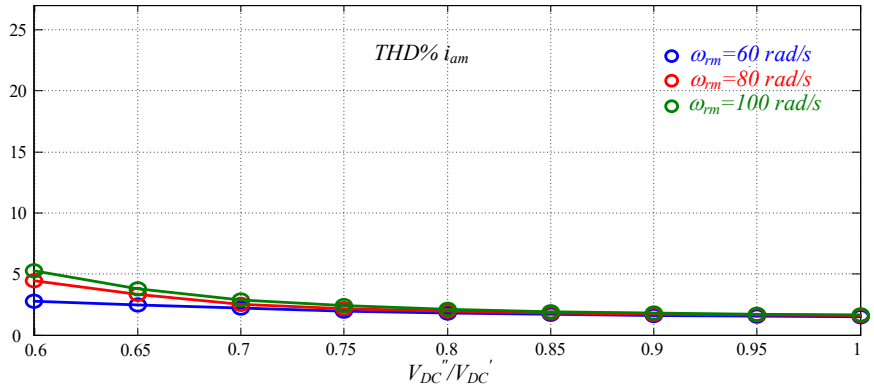

Figure 5.1.8 *THD% of i_{am} at rated torque vs the ratio V_{DC}''/V_{DC}'.*

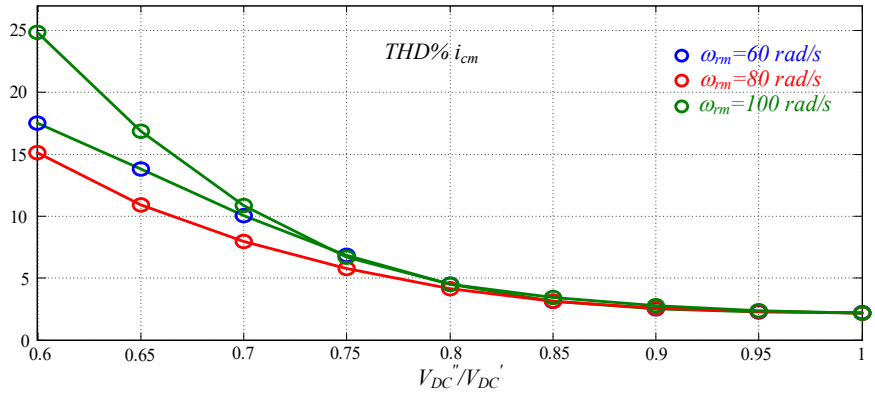

Figure 5.1.9 *THD% of i_{cm} at rated torque vs the ratio V_{DC}''/V_{DC}'.*

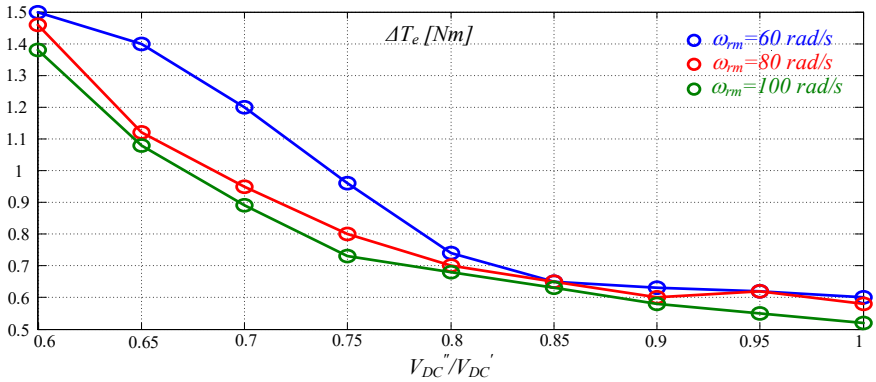

Figure 5.1.10 *Torque ripple at rated torque vs the ratio V_{DC}''/V_{DC}'.*

5.1.5 Simulation and Performance Analysis

An assessment of the consistence of the proposed TPOWMD topology and of its expected performance has been accomplished by simulation. An Open-end Permanent Magnet Synchronous Motor (PMSM) model is exploited neglecting non-linearities caused by the higher order airgap flux harmonics (greater than second) and the core saturation. Main technical specifications of the considered PMSM are listed in Table XIX. The 3L-NPC and the TLI are both equipped with IGBTs, whose technical data are summarized in Table XX. Four 870μF capacitors are used to realize the two DC buses. The drive is controlled according to the scheme of Fig. 5.1.3

Table XIX *OW PMSM Technical Specifications*

Paramenters	***Values***
Rated Power [kW]	*1*
PMSM resistance r_s [Ω]	*1*
PMSM inductance [mH]	*50*
Permanent Magnet Flux [Wb]	*0.45*
DC Voltage [V]	*540*
Torque/Current T_n/I_n [Nm/A]	*10/5*
Rated speed □$_{rm}$ [rpm]	*1000*
Pole Pairs pp	*3*

Table XX *IGBT Data IRG4PH30kPBF*

Paramenters	***Values***
Junction Temperature T_j [°C]	*125*
Collector-Emitter Voltage V_{ce} [V]	*1200*
Collector-Emitter Saturation Voltage V_{ceON} [V]	*3*
RMS Collector Current I_{RMS} [A]	*20*
Rise Time t_{rise} [ns]	*23*
Fall Time t_{fall} [ns]	*310*
Junction Temperature T_j [°C]	*125*
Collector-Emitter Voltage V_{ce} [V]	*1200*

Figure 5.1.11 and Fig. 5.1.12 show the result of simulations dealing with TPOWMD operations at two different rotating speeds ω_{rm}=30 rad/s and ω_{rm}=100 rad/s, at rated load conditions. In particular, Figs. 5.1.11(a) and 5.1.12(a) show the phase currents, the electromagnetic torque and rotor speed, highlighting a low current total harmonic distortion and quite low ripples in the mechanical quantities. Figs. 5.1.11(b) and 5.1.12(b) deal with the voltages of both DC buses and the capacitors voltages, only a low ripple being observable.

The dynamic behaviour of the drive is evaluated in Fig. 5.1.13, which deals with a speed variation from *50* to *100 rad/s* with the rated load. The drive shows satisfying dynamic performances, keeping quite limited the effects of the transient on the capacitor voltages and holding a stable behaviour. A sudden torque variation leads to similar considerations, as shown in Fig. 5.1.14.

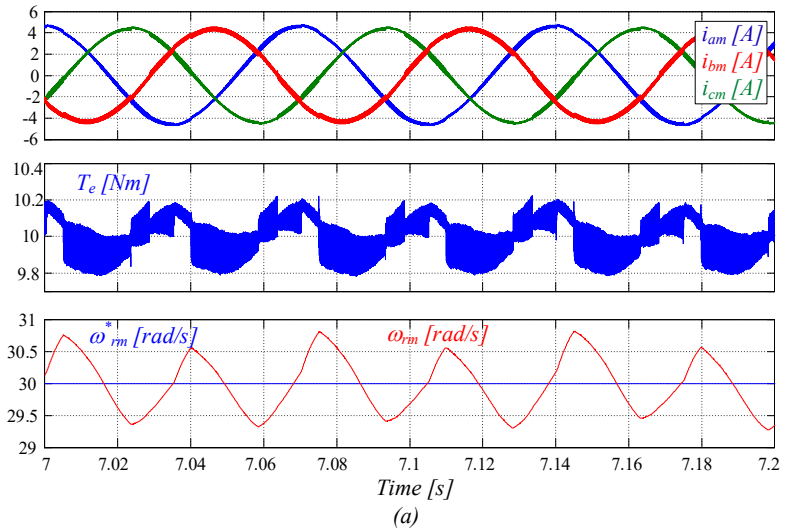

(a)

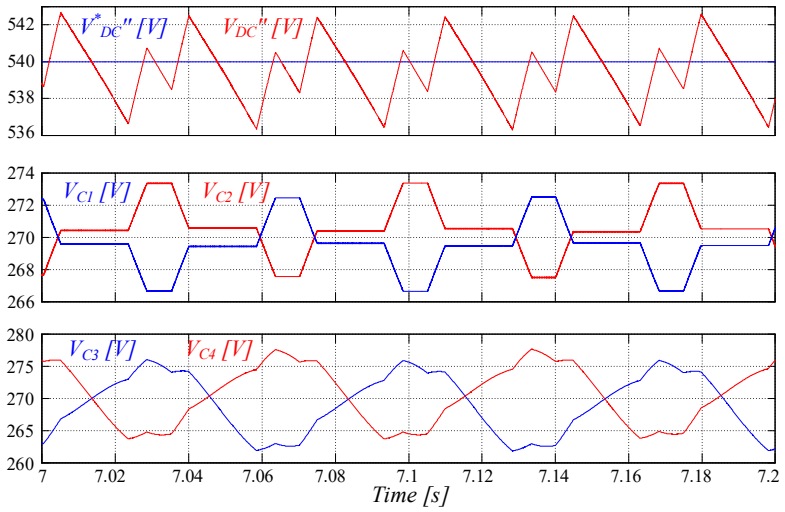

(b)

Figure 5.1.11 *Steady State, ω_{rm} = 30 rad/s, rated load, $V_{DC}'=V_{DC}''=540$ V.*

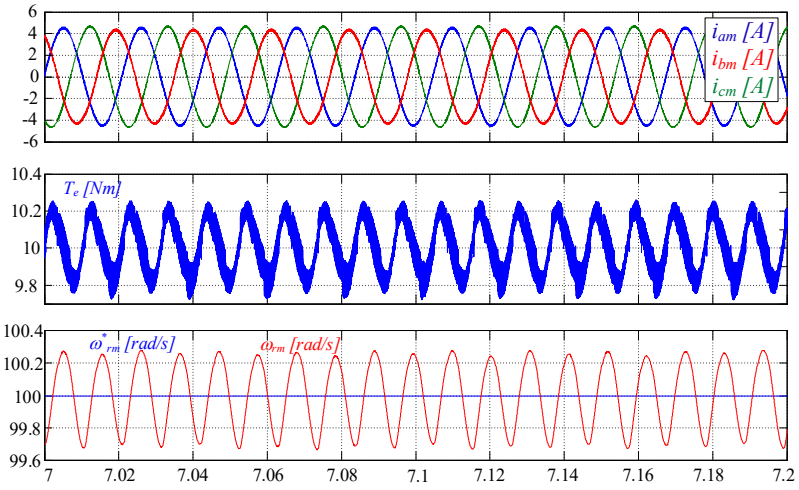

(a)

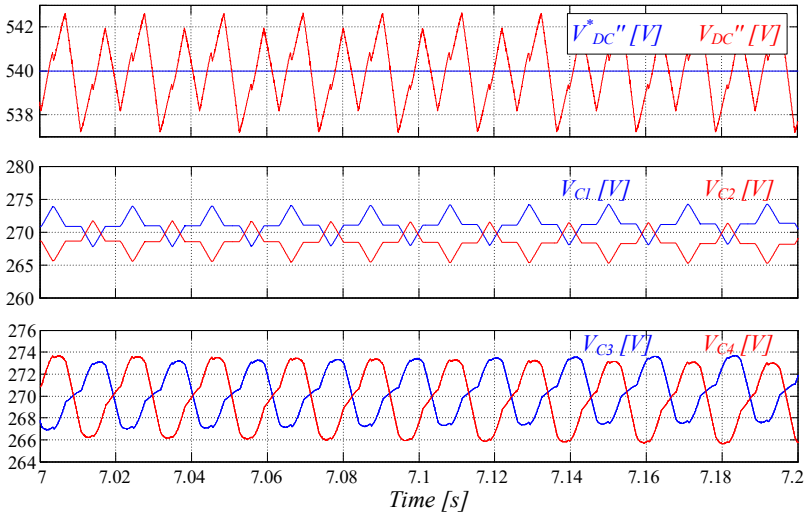

(b)

Figure 5.1.12 *Steady State, ω_{rm} = 100 rad/s, rated load, $V_{DC}'=V_{DC}''=540$ V.*

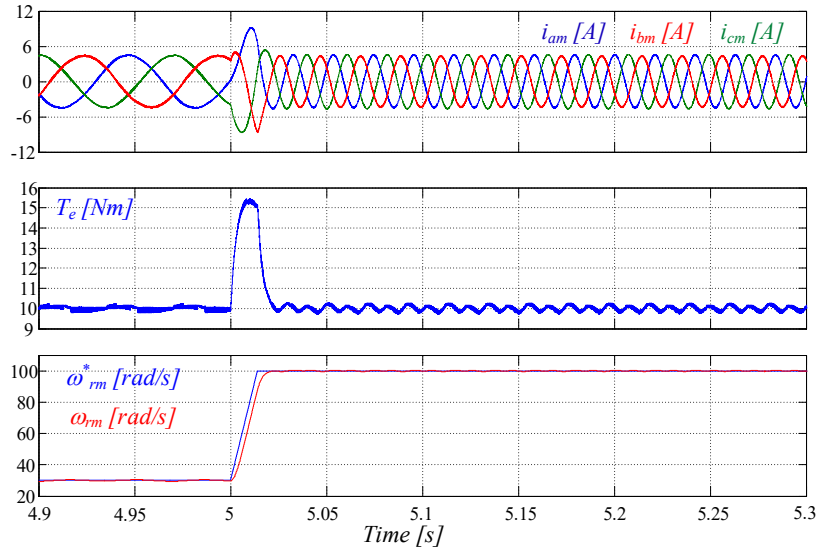

(a)

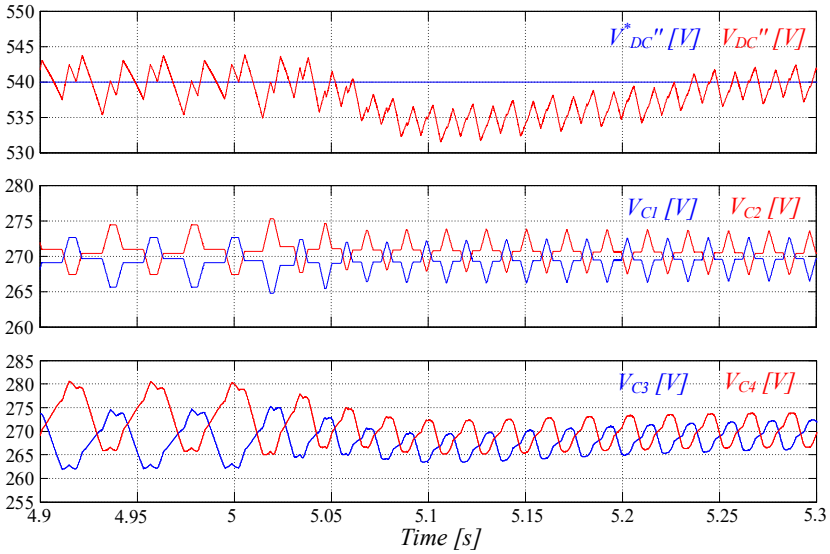

(b)

Figure 5.1.13 *Speed variation from 50 to 100 rad/s, rated load and* $V_{DC}'=V_{DC}''=540$ *V.*

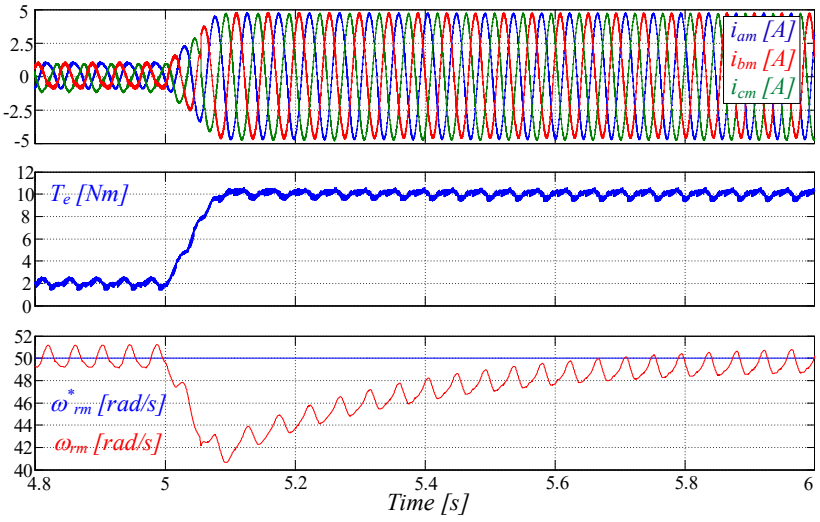

(a)

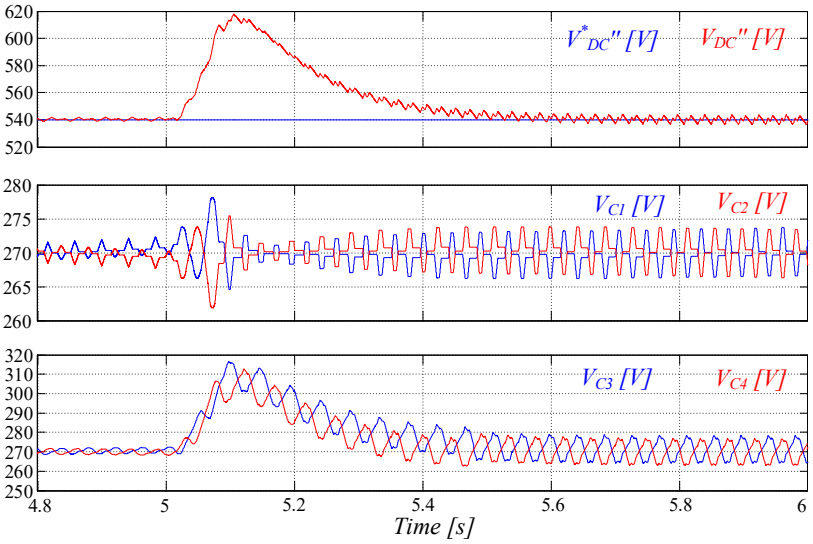

(b)

Figure 5.1.14 *Load torque variation from 10% to 100% , ω_{rm} = 50 rad/s and $V_{DC}'=V_{DC}''=540$ V.*

In Fig 5.1.15 a voltage unbalance is purposely generated on both DC buses by connecting some additional resistors of 100Ω in parallel to C_2 and C_4. The drive is spinning at $\omega_{rm}=1000$ *rpm* and at the rated torque $T_e = 10$ *Nm*.

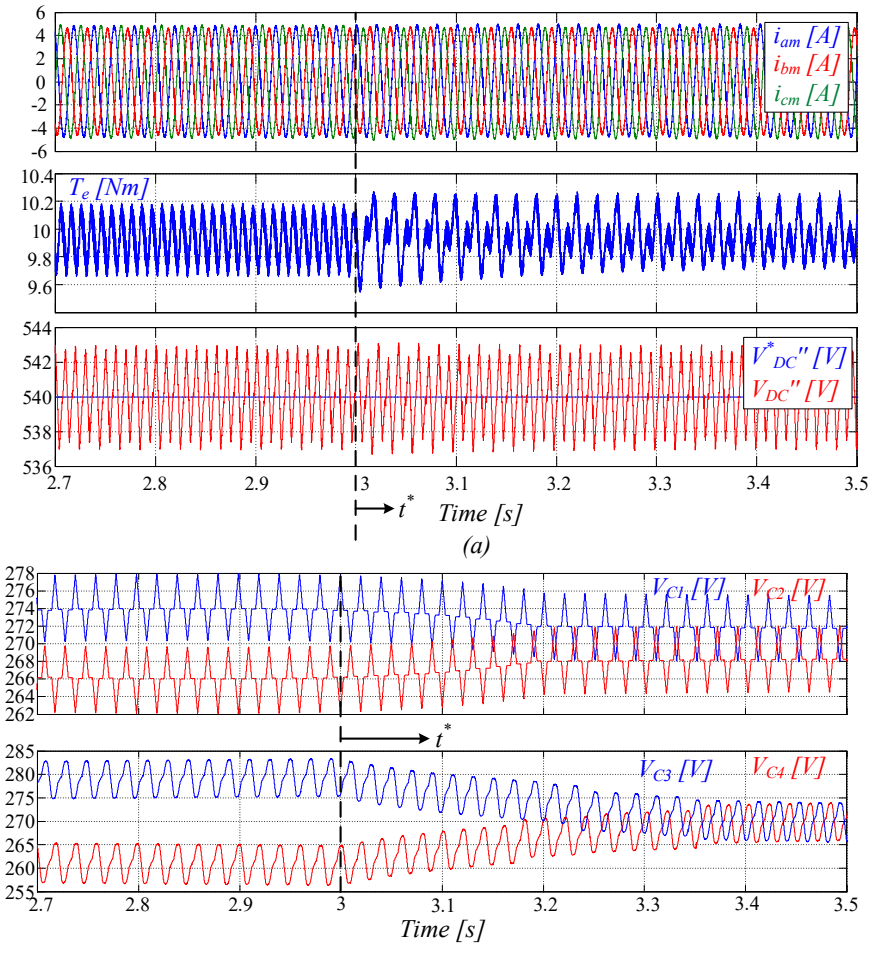

(a)

(b)

Figure 5.1.15 *Activation of the voltages balancing at t^*.*

Initially, the voltage balancing algorithm is not active and an unbalance is generated between the voltages of the two DC bus capacitors. At time t^* the active voltage balancing system is turned on, rapidly driving the system to the ideal condition given by $V_{c1}=V_{c2}$ and $V_{c3}=V_{c4}$.

5.1.6 Conclusions

A three phase multilevel inverter topology with a reduced number of power devices has been introduced exploiting an open-end winding topology. Only two of the motor phase windings are fed by an NPC single-phase inverter on one side and by a single-phase full bridge inverter from the other. The current of the third motor phase, which is instead connected between the midpoints of the two inverters, being determined according to the Kirchhoff law. The proposed topology encompasses a lower number of power devices compared to an equivalent traditional three-phase three level NPC inverter, but it is more efficient and feature a comparable Total Harmonic Distortion (THD), as proved by simulations dealing with steady-state, variable speed, variable load, and unbalanced DC bus voltages operations.

5.2 Optimal Selection of the Voltage Modulation Strategy for an Open Winding Multilevel Inverter [35]

An optimal design strategy for Open Winding Asymmetrical Three-Level Inverters is proposed in this paragraph, to improve the performance in a large set of applications. The Asymmetrical Multilevel Inverter is composed of an open-end winding AC machine connected on one side to a main three-level inverter and, on the other side, to an auxiliary two-level inverter. The main inverter efficiently controls the active power flow operating at a low switching frequency, exploiting a selective harmonic elimination technique, while the auxiliary inverter acts as an active power filter, driven by a conventional high frequency PWM technique. A key point to maximize the efficiency of the entire system is to properly share the task of eliminating the undesired low-frequency voltage harmonics between the two inverters. An optimal strategy is proposed in this paragraph according to specific figures of merit, which are function of the DC bus voltage and switching frequency of the two inverters.

5.2.1 Introduction

Multi-Level Inverters (MLIs) exploiting low switching frequency modulation strategies, such as the Selective Harmonic Elimination (SHE), are today used in variable speed AC motor drives for laminators, pumps, conveyors, compressors, fans, blowers, mills, as well as in railway and naval propulsion plants [36], [40]. MLI systems using Open-end Winding (OW) configurations have been also recently developed in [41]-[46], where the machine is fed by two separate power converters, in order to share the load and to improve the phase voltage harmonic content. A special two-level PWM technique has been proposed in dual two-level inverter-fed open-end winding motor drives, in order to eliminate the 5^{th}, 7^{th} and 9^{th} harmonic, while mitigating the 11^{th} and 13^{th}, [47]. A structure composed of an open-winding induction motor, a three-level step modulated inverter and a current-controlled two-level inverter switching at 1 kHz is proposed in [48], with the goal of eliminating the interphase reactors on high power AC drives.

An OW multilevel inverter structure named Asymmetrical Hybrid Multilevel Inverter (AHMLI) a main inverter is tasked to manage the active power flow, while an auxiliary unit acts as an active filter, ideally providing a null-average power to the machine. It acts differently from standard OW configurations, where the two inverters share between them both the active and reactive load power. According to the AHMLI concept, the main inverter is of the multilevel type and exploits a low switching frequency voltage modulation in order to minimize switching power losses. The auxiliary inverter is instead a two-level one, exploiting a high frequency PWM technique to cancel low-frequency phase voltage harmonics. The main inverter can be equipped with very low on-state voltage drop devices, such as IGBTs, while, fast power switches, as for instance the Power MOS devices can be used for the auxiliary TLI.

An AHMLI with the MLI driven by a simple step modulation has proved to be more efficient than conventional PWM operated multilevel inverters featuring the same amount of power devices, while also producing comparable voltage and current distortion.

Better results are expected to be obtained by driving the MLI through a SHE technique; however, when increasing the amount of voltage harmonics eliminated by the multilevel inverter, the minimum TLI DC bus voltage required to achieve a target total harmonic distortion THD_v and THD_i varies, affecting TLI switching power losses. Moreover, by increasing the order of the harmonics eliminated by the MLI, the switching frequency of the main converter must be increased, leading to a rise of the power losses. Hence, a proper selection of the switching frequencies of the MLI and TLI must be accomplished to obtain the target phase current THD_i with the maximum efficiency.

In this paper the problem of determining an optimal control strategy for the AHMLI is faced by defining specific figures of merit taking into consideration the total switching power losses, the THD_s ($s=i,v$) and the power conversion costs. These quantities are in turn estimated as function of some key parameters, such as the TLI DC bus voltage and the modulation strategies used in the two inverters as well. An AHMLI composed of a Three-Level Neutral Point Clamped Inverter (3NPC) and of a TLI, (3NPC-SHE + TLI-PWM) is taken into consideration in this paper, but the proposed design approach can be easily extended to other OW multi-level inverter configurations.

5.2.2 AHMLI Open-End Winding Topology

According to the AHMLI topology, an open-end winding electrical machine is supplied by an MLI providing the required active power and by an auxiliary TLI acting as an active power filter, as shown in Fig. 5.2.1, where p is the number of voltage levels, while indexes l' and l'' respectively determine the actual values of MLI and TLI output voltages.

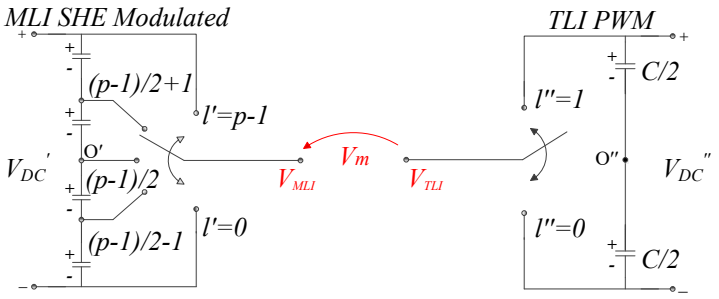

Figure 5.2.1 *Generic Open-end Winding AHMLI configuration.*

The DC buses of the two inverters are isolated between them in order to prevent the circulation of zero sequence currents. Moreover, the DC bus of the TLI consists of a floating capacitor to make use of a single power source. Assuming that the two inverters are supplied by two independent power sources, V'_{DC} and V''_{DC}, the voltage V_{jm} applied to the *j*-phase winding of the OW AC machine is given by:

$$V_{jm} = V_{jMLI} - V_{jTLI} - V_{o'o''} = \frac{l'-1}{2} V'_{DC} - \frac{2l''-1}{2} V''_{DC} - V_{o'o''} \tag{5.2.1}$$

where $l' = 0,1,2$ and $l'' = 0,1$, and being $V_{O'O''}$ the voltage between the mid points O' and O'' of the two inverter DC-buses, which can be computed as:

$$V_{o'o'} = \frac{1}{3}\left(V_{aMLI} + V_{bMLI} + V_{cMLI} - V_{aTLI} - V_{bTLI} - V_{cMLI}\right) \tag{5.2.2}$$

Power devices of the MLI may be selected in order to minimize the on-state power losses, while the devices of the TLI may be selected in order to operate at high switching frequency and lower voltage [48], [49].

As the MLI processes all the active power supplied to the load its efficiency is of major concern. MLI switching power losses can be minimized by adopting a staircase voltage modulation, tasking the TLI to eliminate all the phase voltage harmonics. Such an approach has found to be successful, as it has been proved that an AHMLI with the MLI driven by a simple step modulation is more efficient than conventional PWM multilevel inverters featuring the same amount of power devices, while achieving similar results in terms of output voltage THD_v. However, in order to further increase the efficiency of the system the modulation strategies used in the MLI and TLI should be accurately selected in order to minimize the total power losses, as well as, the stator current THD_i, which impacts on motor torque pulsations. Moreover, TLI switching power losses, the voltage rating and cost of TLI power switches can be reduced by lowering the TLI DC bus voltage, although at the cost of a current THD_i rise. These issues are coped in this paper by adopting a Selective Harmonic Elimination (SHE) technique for the MLI and determining the undesired low-order harmonics eliminated by the MLI and TLI through an accurate investigation of some design parameters according to specific figures of merit, which are function of the DC bus voltage of the two inverters, the switching frequency and the characteristics of power switches. The proposed approach has been validated through simulations.

5.2.3 Phase Voltage Modulation

Although of general validity, the proposed approach has been applied to an AHMLI topology encompassing a Three-Level Inverter (3LI) and a TLI. Among the different configuration that can be used to realize the three-level inverter, a Neutral Point Clamped inverter has been analyzed, as shown in Fig. 5.2.2.

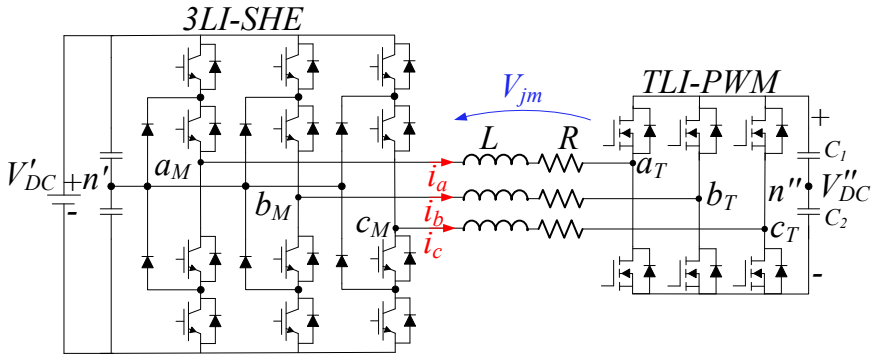

Figure 5.2.2 *The 3LI-SHE+TLI-PWM configuration.*

A SHE technique is exploited to drive the 3LI at low switching frequency, while a conventional high switching frequency PWM is used to drive the TLI. In particular, the 3LI *j-phase* output voltage V_{jMLI}, which is the voltage across nodes a_M and n' in Fig. 5.2.2, can be written as:

$$V_{jMLI} = \sum_{n=1}^{+\infty} V_{jn} \sin\left(n\left(\theta_e - \frac{2m\pi}{2}\right)\right) \qquad \begin{cases} j=a & m=0 \\ j=b & m=1 \\ j=c & m=-1 \end{cases} \tag{5.2.3}$$

where n is an odd number and the magnitude of the *n-th* harmonic is given by:

$$V_{jn} = \frac{4V'_{DC}}{n\pi} \sum_{k=1}^{N} (-1)^k \cos(n\alpha_k) \tag{5.2.4}$$

According to the SHE principle, it is possible to eliminate *N-1* harmonics from the 3LI output voltage waveform by suitably setting a set of N switching angles $\alpha_1 \ldots \alpha_N$ along each quarter of a period, as shown in Fig. 5.2.3, [38].

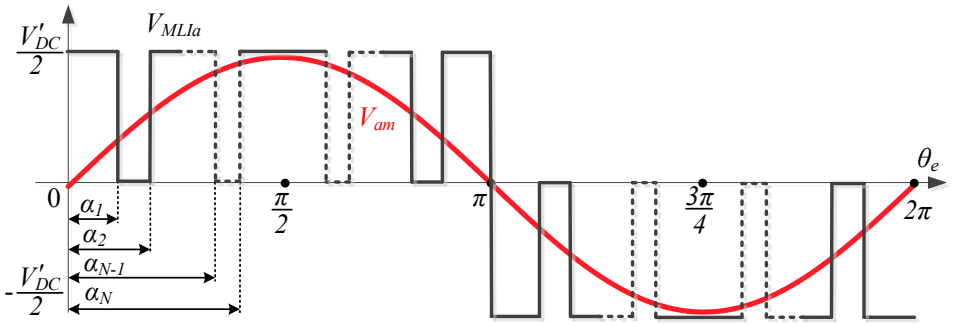

Figure 5.2.3 *3LI output voltage waveform according to the SHE approach.*

More precisely, the N switching angles are computed in order to eliminate a given set of *N-1* harmonics, while the remaining switching angle is set to obtain a given magnitude of the fundamental harmonic V_1. The last is related to the DC bus voltage through the amplitude modulation index M.

A set of N equations is obtained, whose solution provides the N switching angles $\alpha_1, \alpha_2, \ldots, \alpha_N$ with $0 \leq \alpha_1 \leq \alpha_2 \leq \ldots \leq \alpha_N < \pi/2$, [4]:

$$\begin{cases} \frac{4}{\pi}\sum_{k=1}^{N}(-1)^k\cos(\alpha_k) = \frac{V_1}{V'_{DC}} = M \\ \frac{4V'_{DC}}{5\pi}\sum_{k=1}^{N}(-1)^k\cos(5\alpha_k) = 0 \\ \frac{4V'_{DC}}{7\pi}\sum_{k=1}^{N}(-1)^k\cos(7\alpha_k) = 0 \\ \cdots \\ \frac{4V'_{DC}}{n\pi}\sum_{k=1}^{N}(-1)^k\cos(n\alpha_k) = 0 \end{cases} \tag{5.2.5}$$

Solutions of (5.2.5) have for different sets of switching angles are shown in Fig. 5.2.4, as described below:

- Fig. 5.2.4a: α_1 and α_2 are computed to eliminate the 5^{th} harmonic (*SHE* 5^{th});
- Fig. 5.2.4b: α_1, α_2 and α_3 are computed to eliminate the 5^{th} and 7^{th} harmonic (*SHE* $5^{th} \div 7^{th}$);
- Fig. 5.2.4c: α_1, α_2, α_3 and α_4 are computed to eliminate the 5^{th}, 7^{th} and 11^{th} harmonic (*SHE* $5^{th} \div 11^{th}$);
- Fig. 5.2.4d: α_1, α_2, α_3, α_4 and α_5 are computed to eliminate the 5^{th}, 7^{th}, 11^{th} and 13^{th} harmonic (*SHE* $5^{th} \div 13^{th}$);
- Fig. 5.2.4e: α_1, α_2, α_3, α_4, α_5 and α_6 are computed to eliminate the 5^{th}, 7^{th}, 11^{th}, 13^{th} and 17^{th} harmonic (*SHE* $5^{th} \div 17^{th}$);
- Fig. 5.2.4f: α_1, α_2, α_3, α_4, α_5, α_6 and α_7 are computed to eliminate the 5^{th}, 7^{th}, 11^{th}, 13^{th}, 17^{th} and 19^{th} harmonic (*SHE* $5^{th} \div 19^{th}$).

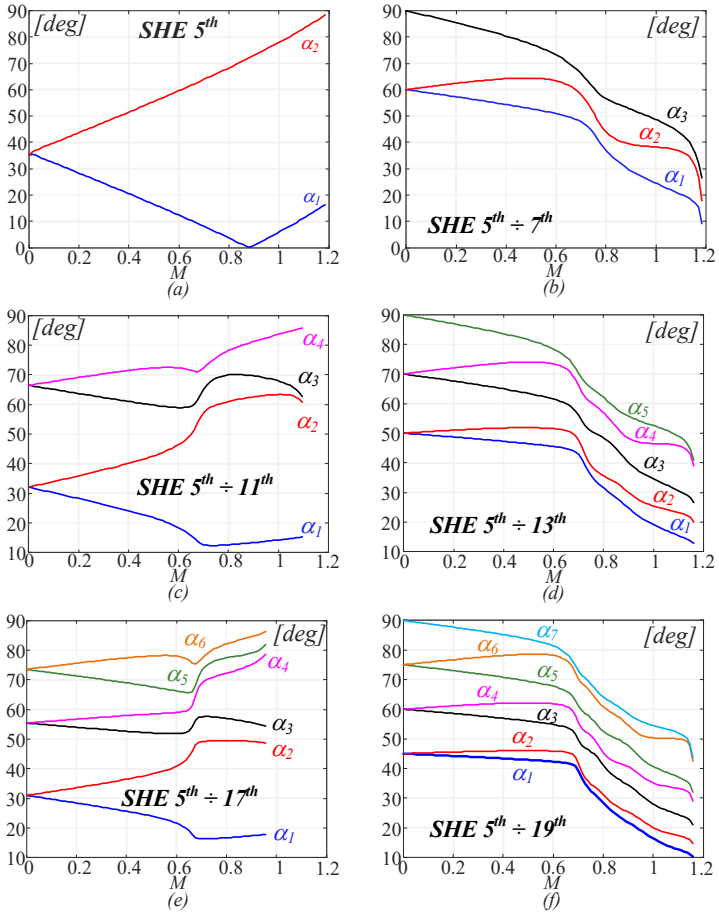

Figure 5.2.4 *3LI switching angles according to the SHE approach.*

Assuming a conventional wye connection with the considered SHE strategies, the V_{jm}^* output phase voltage features the harmonic content shown in Fig. 5.2.5.

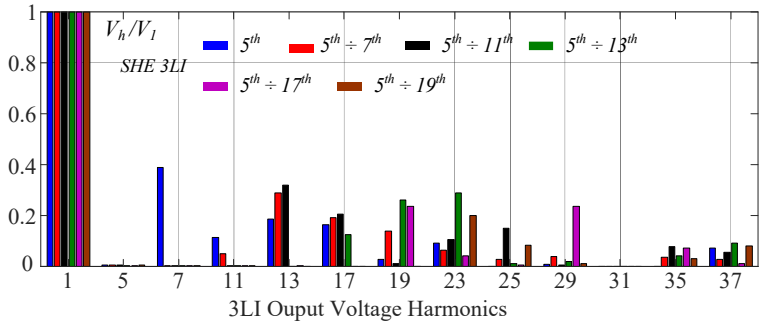

Figure 5.2.5 *Harmonic spectra of* V_{jm}^* *(wye connection).*

Although increasing the amount of switching angles the phase voltage the THD_v is improved, it anyway results quite unsatisfactory, due to residual low-order voltage harmonics caused by the low switching frequency. Such an issue is faced according to the OW configuration through the auxiliary TLI, which is tasked to suppress the residual low-order harmonics. In order to eliminate the residual low order harmonics, the TLI PWM reference phase voltage V_{jTLI}^* is computed as:

$$V_{jTLI}^* = V_{jm}^* - V_{jMLI}^* \tag{5.2.6}$$

where V_{jm}^* is the phase voltage reference. A schematic of the system accomplishing the modulation of the phase voltage is shown in Fig. 5.2.6.

Effects of voltage harmonics cancellation through the TLI are shown in Fig. 5.2.7, where each SHE technique is considered with different sets of harmonics cancelled through the TLI. As shown in Fig. 5.2.8, the phase voltage THD_v decreases when the amount of voltage harmonics cancelled through the TLI increases, while it can increase when the amount of voltage harmonics cancelled by the 3LI increases.

In order to cancel the selected set of harmonics, the TLI dc-bus voltage should be conveniently higher than the peak value of the TLI reference voltage computed according to (5.2.3), (5.2.4) and (5.2.6). Specifically, V''_{DC} should be greater than:

$$V''_{DCmin} = 2\left(\sum_{n > N_{maxMLI}}^{N_{maxTLI}} V_{jn} \sin(n\theta_e)\right) \tag{5.2.7}$$

being N_{maxMLI} and N_{maxTLI} the order of the highest harmonic respectively cancelled through the 3LI and TLI.

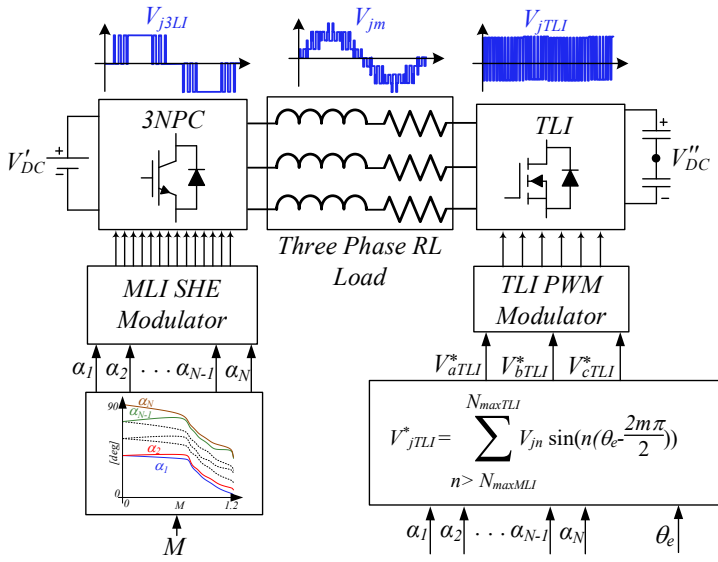

Figure 5.2.6 *Block diagram of the voltage modulator 3LI-SHE+TLI-PWM.*

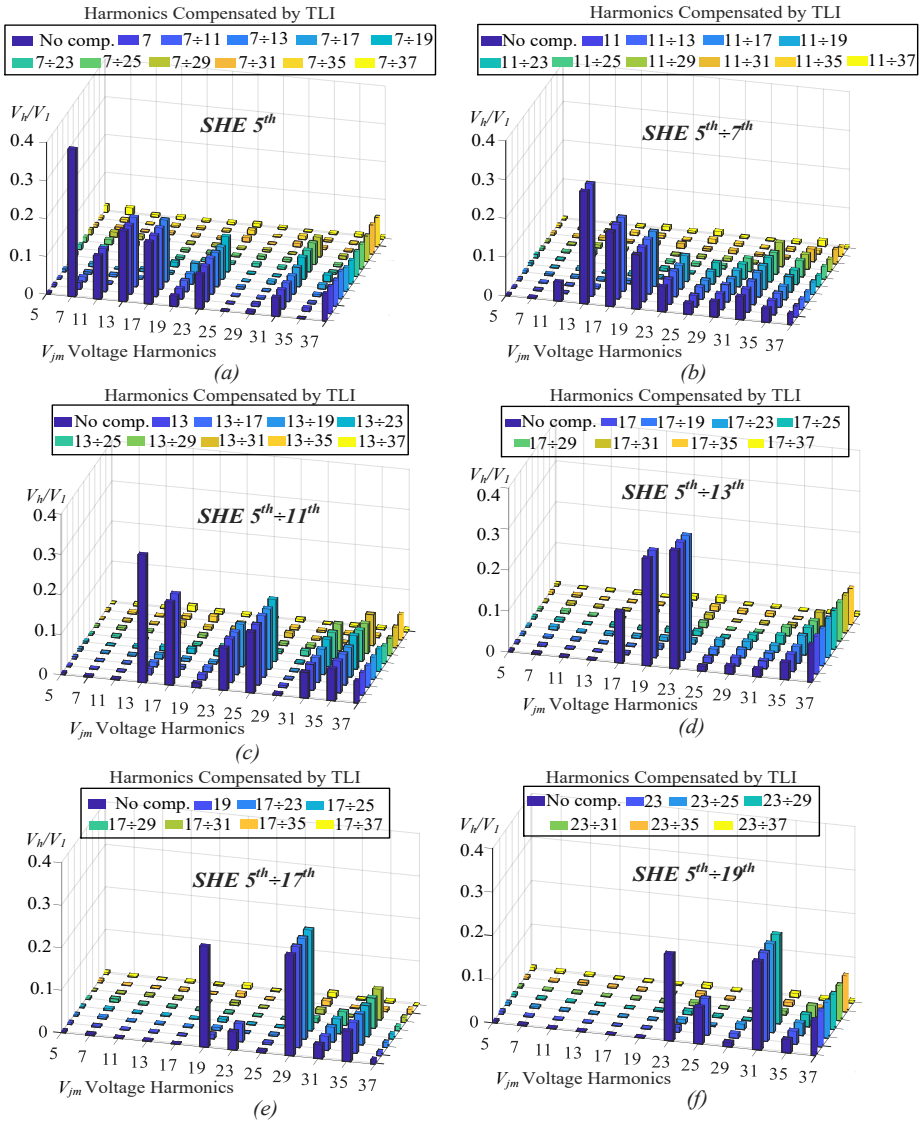

Figure 5.2.7 *Harmonic spectra of the phase voltage* V_{jm} *(*M=0.9).

According to Fig. 5.2.9, V''_{DCmin} decreases when the amount of voltage harmonics cancelled through the 3LI increases, while it increases when the amount of voltage harmonics cancelled by the TLI increases. Moreover, V''_{DCmin} affects the switching power losses of the TLI, as shown in Fig.5.2.10. By increasing N_{maxMLI}, the 3LI switching frequency f_{sMLI} increases, as shown in Fig. 5.2.11, while, as shown in Fig. 5.2.12 by increasing N_{maxTLI} increases the minimum TLI switching frequency required $f_{sTLImin}$, which is assumed to be five times the frequency of the highest harmonic to be cancelled.

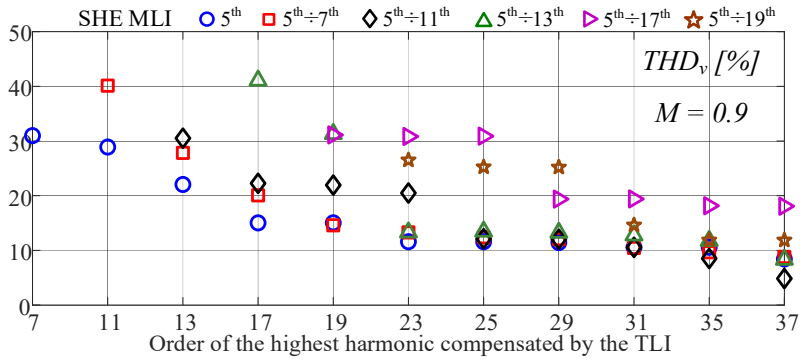

Figure 5.2.8 *Phase voltage* THD_v *(*M=0.9).

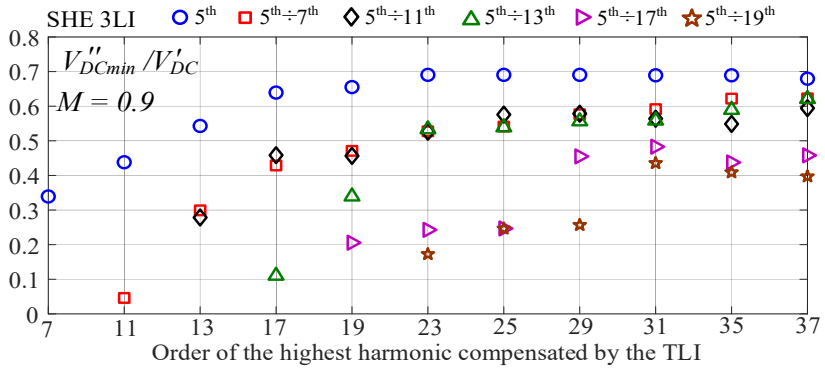

Figure 5.2.9 *Minimum TLI DC bus voltage required* V''_{DCmin} (M=0.9).

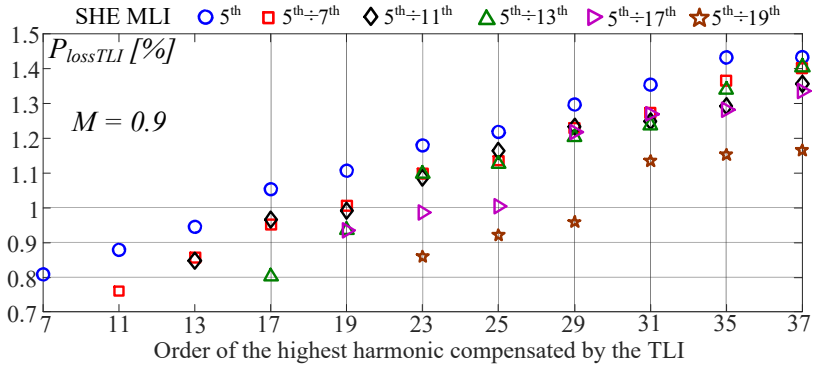

Figure 5.2.10 *TLI switching power losses. (*f_s*=10 kHz, M=0.9).*

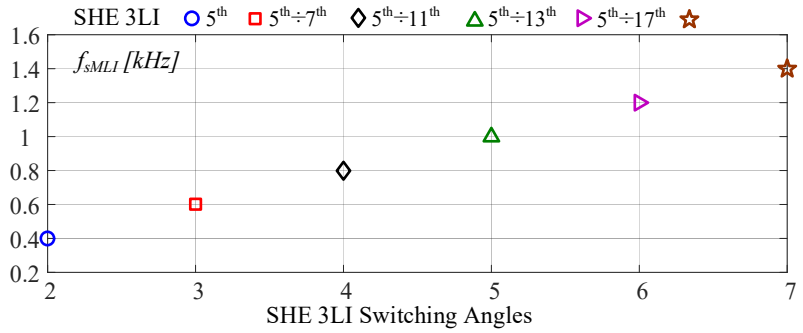

Figure 5.2.11 *MLI switching frequency for different SHE strategies (M=0.9, f=50 Hz).*

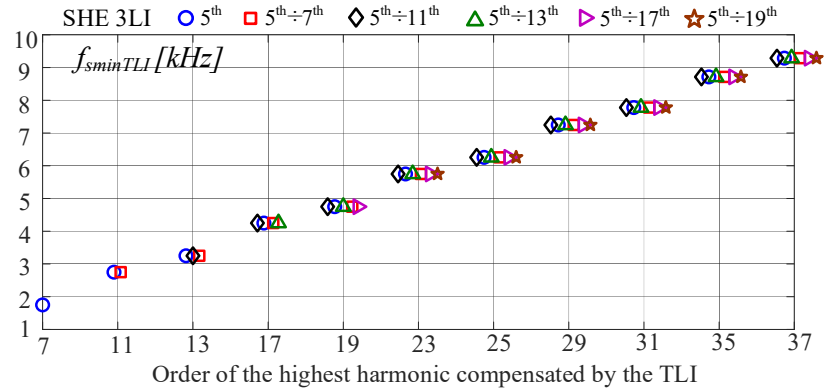

Figure 5.2.12 *Minimum TLI switching frequency (M=0.9, f=50Hz).*

5.2.4 AHMLI Performance Analysis

Three parameters should be properly selected when designing the AHMLI voltage modulation strategy, namely, the 3LI switching frequency, the TLI switching frequency and the TLI dc-bus voltage, all of them impacting on phase voltage and current THD_s, power losses and cost. In order to assess the effects of variation of these parameters on AHMLI performance, an AHMLI system has been simulated with an RL load ($R = 16\ \Omega$, $L = 130\ mH$) connected between the two power converters. The TLI floating capacitor is $470\mu F$, while $C_1=C_2=120\mu F$. The 3LI DC bus voltage V'_{DC} is $600V$. Both the 3LI and TLI are equipped with STGWA50M65DF2 IGBT devices, while the freewheeling and clamping diodes are of the STPSC10H12-Y type. Technical specifications of the power switches and diodes are given respectively in Tables XXI, and XXII. The fundamental voltage harmonic considered features $265V$ and 50Hz.

Table XXI *Specifications of IGBT devices*

V_{CE} [V]	$V_{CE(ON)}$ [V]	I_C [A]	t_{rise} [ns]	t_{fall} [ns]
650	2.1	50	21	104

Table XXII *Specifications of diodes*

V_{RRM} [V]	V_F [V]	$I_{F(RMS)}$ [A]	t_c [ns]
1200	1.35	25	21

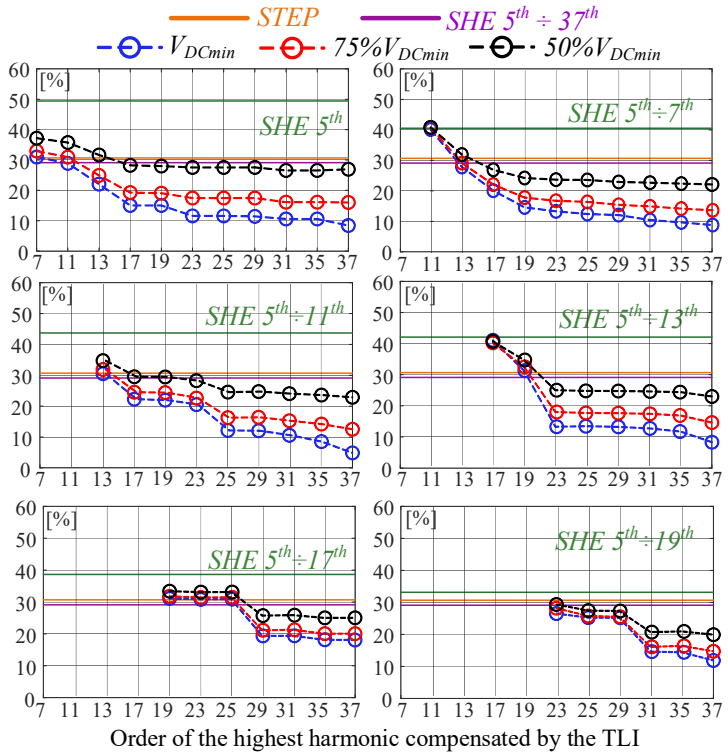

Figure 5.2.13 *THD_v Load Phase Voltage with $V''_{DC} \leq V''_{DCmin}$ and at $f_{sTLImin}$ (M=0.9).*

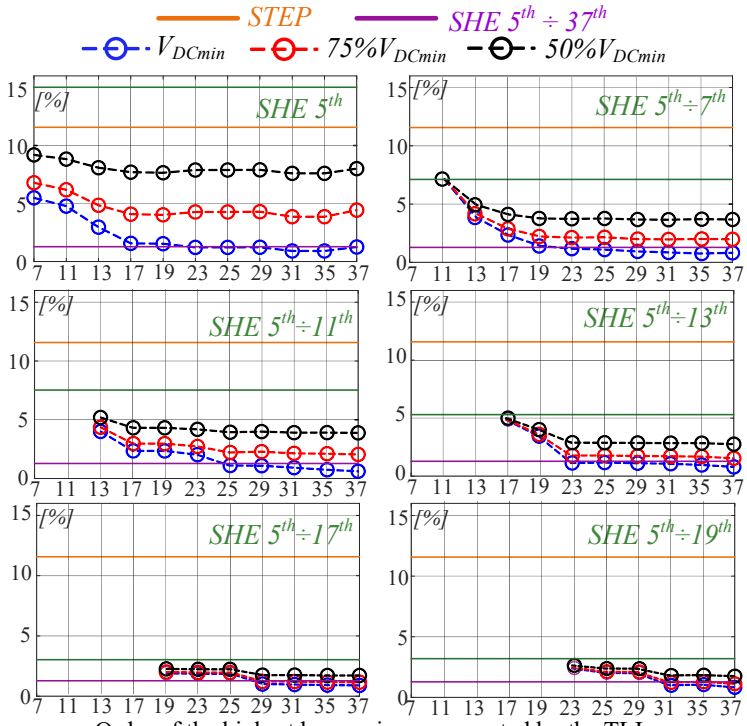

Figure 5.2.14 *THD$_i$ Load Phase Current with V"$_{DC}$ ≤ V"$_{DCmin}$ and at $f_{sTLImin}$ (M=0.9).*

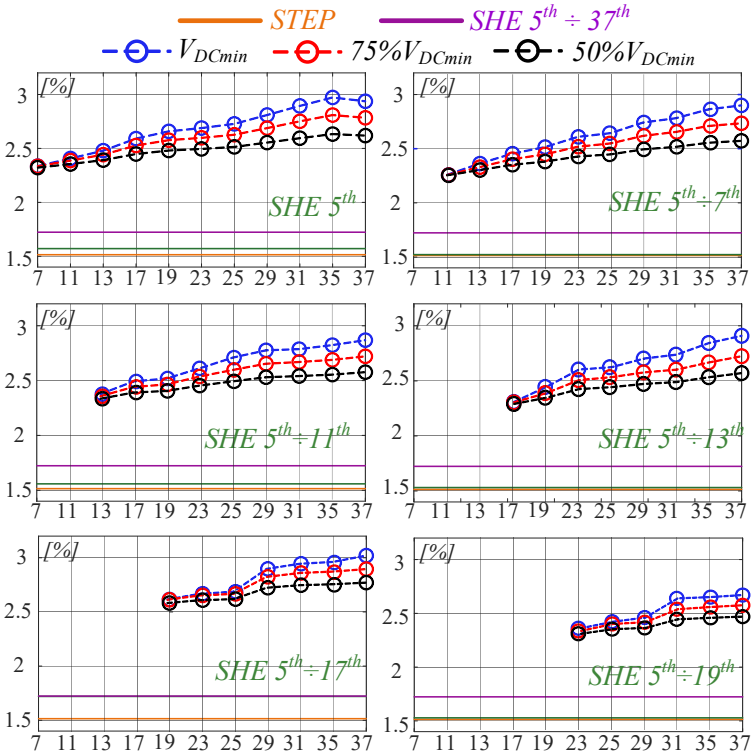

Figure 5.2.15 *Power losses with V"$_{DC}$≤V"$_{DCmin}$ and at $f_{sTLImin}$ (M=0.9).*

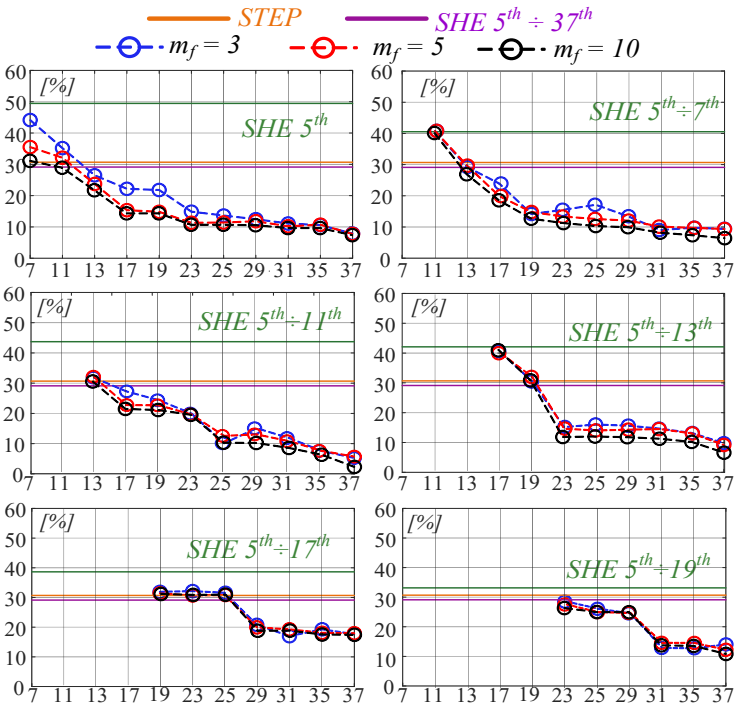

Figure 5.2.16 *THD_v Phase Voltage with $f_{sTLI} \leq f_{sTLImin}$ (M=0.9).*

The minimum dc-bus voltage level required for harmonic cancellation V''_{DCmin} is a function of either the 3LI switching frequency, either on the TLI switching frequency. The TLI dc-bus voltage impacts on the THD_v, power losses and cost.

By selecting a dc-bus voltage lower than V''_{DCmin} the voltage and current THD_s worsen, as shown in Figs. 5.2.13 and 5.2.14, where $V''_{DC} = V''_{DCmin}$, $V''_{DC} = 0.75\ V''_{DCmin}$ and $V''_{DC} = 0.5\ V''_{DCmin}$ are considered. Moreover, the THD_s achieved with a conventional wye connection operating the 3LI with a step modulation and with a SHE with a quite high number of switching angles *(SHE $5^{th} \div 37^{th}$)* is plotted for comparison.

By reducing the V''_{DCmin} the TLI switching power losses decrease, as shown in Fig. 5.2.15, as well as the voltage rating and the cost of power switches and dc-bus capacitor. Voltage and current THD_s, and power losses obtained by selecting $f_{sTLI} \leq f_{sTLImin}$ are shown in Figs. 5.2.16, 5.2.17, 5.2.18 respectively. In particular, the THD_s and power losses have been carried out at two different frequency modulation indexes m_f, defined as the ratio between the switching frequency of the TLI and f_e. By lowering the TLI switching frequency up to $0.5 f_{sTLImin}$ the THD_s remarkably worsens but going beyond, it remains almost constant.

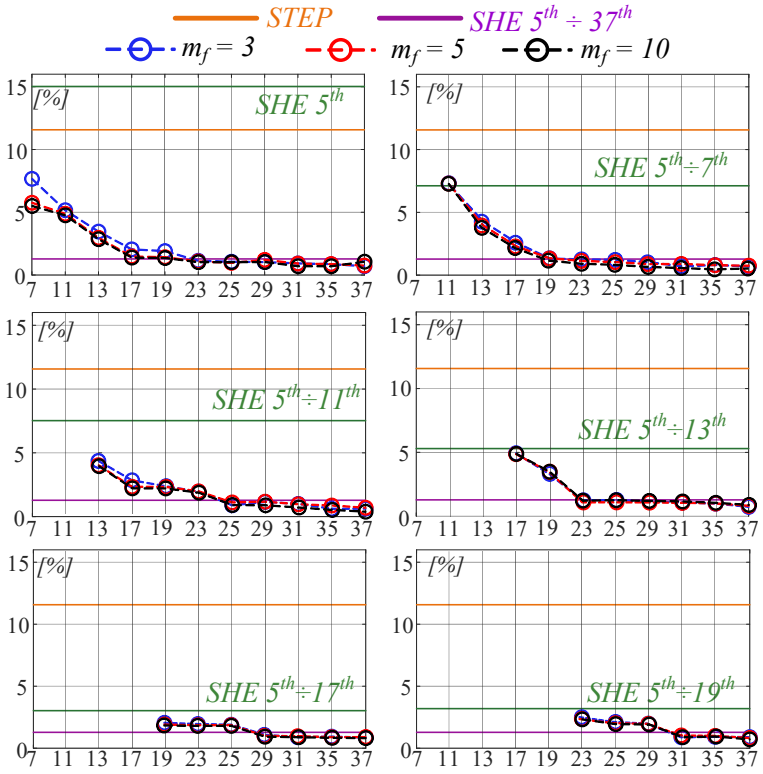

Figure 5.2.17 *THDi Phase Current with $f_{sTLI} \leq f_{sTLImin}$ (M=0.9).*

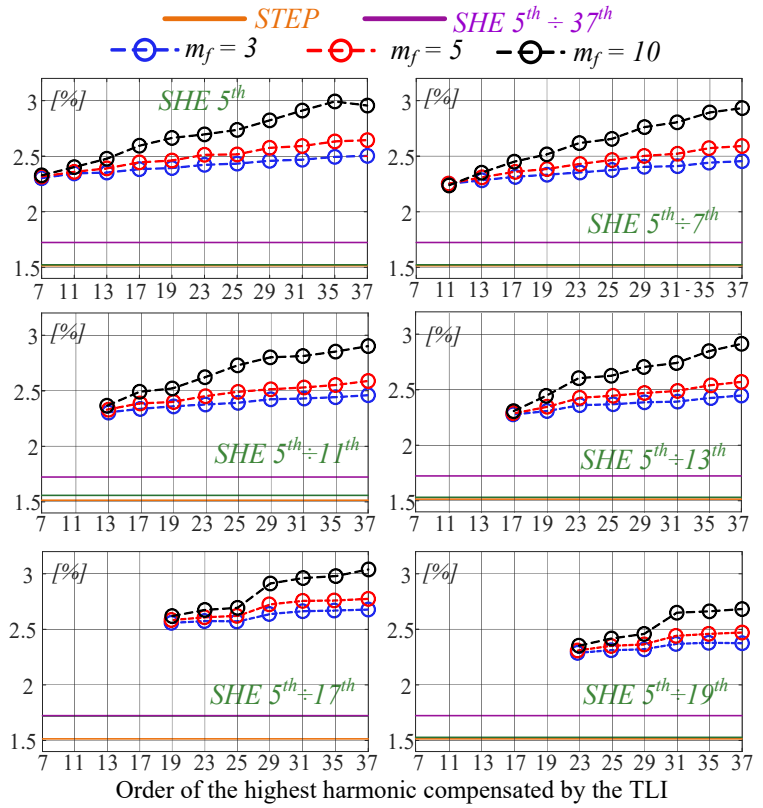

Figure 5.2.18 *Power losses for each SHE strategy with $f_{sTLI} \leq f_{sTLImin}$ (M=0.9).*

5.2.5 Optimal Voltage Modulation Strategy

The previous analysis highlights some critical issues that must be addressed to determine the most effective AHMLI voltage modulation strategy. A specific procedure has been developed. Firstly, the results shown in Figs. 5.2.8-5.2.18, are arranged in data sets F_1, F_2 and F_3 for each SHE, in order to detect the mathematical link among the power losses P_{loss}, the voltage or current THD_s and the cost of the power conversion system on one side and the SHE strategy, f_{sTLI} and the TLI dc-bus voltage on the other.

$$P_{loss} = F_1(f_{sTLI}, V''_{DC}) \qquad THD_s = F_2(f_{sTLI}, V''_{DC}) \qquad Cost = F_3(V''_{DC}) \tag{5.2.8}$$

The optimal combination of f_{sTLI} and V''_{DC} for each SHE strategy is found through a weighted sum, method combining all data coming from F_1, F_2 and F_3 into one scalar, objective function Γ using a weighted sum approach, [50], [51].

$$\Gamma = k_1 P_{loss} + k_2 THD_s + k_3 Cost \tag{9}$$

By suitably settings the three weighting coefficients k_1, k_2 and k_3, which range between 0 and 1, different forms of optimization can be accomplished, as shown in Tab. XXIII.

Table XXIII *Optimization problems.*

Weighting coefficients set	Target
(k_1,0,0)	Minimum Ploss
(0, k_2,0)	Minimum THDs
(0,0, k_3)	Minimum Cost
(k_1,k_1,0) $k_2 = k_1$	Best tradeoff among Ploss and THDs
(k_1,k_1,k_1) $k_3 = k_2 = k_1$	Best tradeoff among Ploss,, THDs and Cost
(k_1,k_2,k_3) $k_3 >> k_2$ & k_1	Best tradeoff emphasizing Ploss minimization
(k_1,k_2,k_3) $k_2 >> k_1$ & k_3	Best tradeoff emphasizing THDs minimization
(k_1,k_2,k_3) $k_3 >> k_1$ & k_2	Best tradeoff emphasizing Cost minimization.

Among several alternatives, three significant cases have been selected, namely, A=(k_1,0,0), B=(0, k_2,0) and C=(k_1,k_2,0). Starting from (5.2.8), the minimum of the objective function Γ is carried out for each SHE, for the three cases:

A. $\Gamma_1 = P_{loss}$ $\quad min\ [\Gamma_1]$

B. $\Gamma_2 = THD_i$ $\quad min\ [\Gamma_2]$

C. $\Gamma_3 = k_1 P_{loss} + k_2 THD_s$ $\quad min\ [\Gamma_3]$

An example of the minimum searching algorithm for *SHE* $5^{th} \div 19^{th}$ and M=0.9 is graphically shown in Fig. 5.2.19. In particular, the case C. is shown when k_1=1 and k_2 =1/5. The objective function Γ_3 reaches its lowest value at $f_{sTLImin}$ =5.75kHz and V''_{DCmin} =320V.

The minimum searching algorithm has been also applied to the data carried out at different V''_{DC} values, with the AHMLI operating as above. The results shown in Fig. 5.2.20 confirm that the optimal operating condition is achieved when the drive is working at V''_{DCmin}. In fact,

the DC bus voltage reduction leads to a reduction of the power loss, but at the same time to a significant increase of the THDs.

Minimum searching problem has to be applied to all SHE configurations, and the global minimum value of Γ among all identified minimum points represents the best configuration of the Voltage Modulation Strategy, according to the metric given by the specific set of weighting coefficients.

The optimal combination of SHE and TLI switching frequency is strongly related to the weighting coefficients values; some optimal configurations are shown in Table XXIV. Some of the optimal solutions may not be feasible because of some technical constraints, for instance the maximum switching frequency of the 3LI power devices, or the maximum voltage that can be sustained from the floating capacitor.

In Table XXIV the first two results of provide the optimal combination of SHE and TLI switching frequency when the target is that to minimize respectively the system losses (A.) and the harmonic distortion (B.) In the first case, V''_{DCmin} is significantly reduced in order to limit the TLI losses, yielding to an increase of the THD_i. On the contrary, in the second case the switching frequency of both 3LI and TLI is increased in order to reduce the harmonic content of the phase current. In the other three cases considered in Table IV, dealing with the best tradeoff between losses and THD_i, (C.), it is worthy to note that the optimal configuration changes according to the values assigned to the weighting coefficients k_1 and k_2. Increasing the k_1 value addresses the optimal AHMLI configuration towards losses minimization, while increasing k_2 the optimal solution moves towards that minimizing the THD_i.

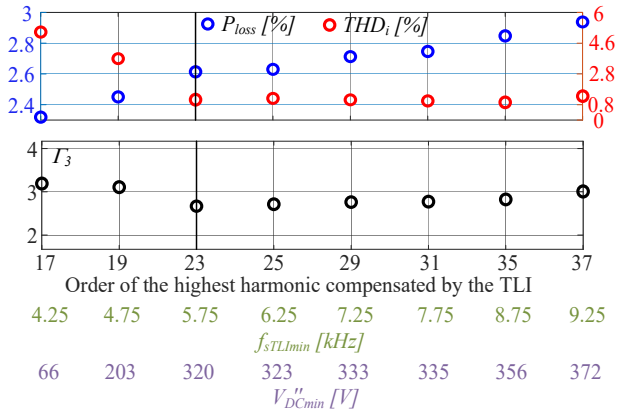

Figure 5.2.19 *Best tradeoff emphasizing P_{loss} minimization (k_1 = 1; k_2 = 1/5) when the 3LI is driven by the (SHE 5th ÷ 19th) technique. Optimal configuration for this SHE is given at $f_{sTLImin}$ =5.75kHz and V''_{DCmin} =320V.*

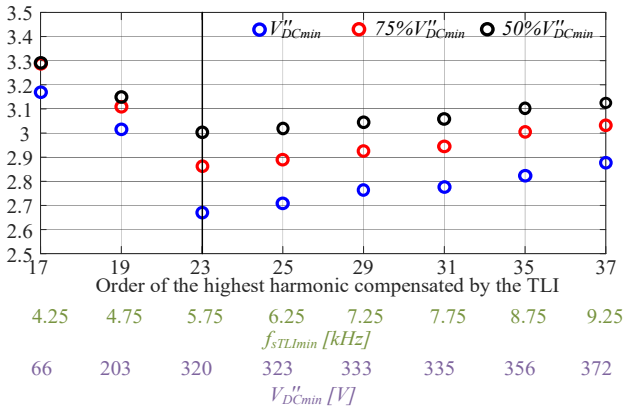

Figure 5.2.20 *Best tradeoff emphasizing P_{loss} minimization (k_1 = 1; k_2 = 1/5) when the 3LI is driven by the (SHE 5th ÷ 19th) technique, at different values of V''_{DC}.*

Table XXIV *Optimal Voltage Modulation Strategy*

A=(k_1,0,0) k_1=1						
SHE technique / f_{sMLI} (Hz)	Order of the highest harmonic compensated by the TLI	f_{sTLI} (Hz)	V''_{DC} (V)	THD_v (%)	THD_i (%)	P_{loss} (%)
SHE $5^{th} \div 7^{th}$ / 600	11^{th}	2750	27.6389	40.12	7.13	2.25
B=(0, k_2,0) k_2=1						
SHE technique / f_{sMLI} (Hz)	Order of the highest harmonic compensated by the TLI	f_{sTLI} (Hz)	V''_{DC} (V)	THD_v (%)	THD_i (%)	P_{loss} (%)
SHE $5^{th} \div 11^{th}$ / 800	37^{th}	9250	356.6222	4.845	0.61	2.87
C=(k_1, k_2,0) k_1=k_2=1						
SHE technique / f_{sMLI} (Hz)	Order of the highest harmonic compensated by the TLI	f_{sTLI} (Hz)	V''_{DC} (V)	THD_v (%)	THD_i (%)	P_{loss} (%)
SHE $5^{th} \div 11^{th}$ / 800	37^{th}	9250	356.6222	4.85	0.61	2.87
C=(k_1, k_2,0) k_1=1; k_2=1/5						
SHE technique / f_{sMLI} (Hz)	Order of the highest harmonic compensated by the TLI	f_{sTLI} (Hz)	V''_{DC} (V)	THD_v (%)	THD_i (%)	P_{loss} (%)
SHE $5^{th} \div 19^{th}$ / 1400	37^{th}	9250	238.3	11.86	0.83	2.67
C=(k_1, k_2,0) k_1=1; k_2=1/85						
SHE technique / f_{sMLI} (Hz)	Order of the highest harmonic compensated by the TLI	f_{sTLI} (Hz)	V''_{DC} (V)	THD_v (%)	THD_i (%)	P_{loss} (%)
SHE $5^{th} \div 13^{th}$ / 1000	17^{th}	4250	66.2423	41.0754	4.8750	2.3087

5.2.6 Conclusions

The optimization of the voltage modulation strategy for an Asymmetrical Hybrid Three-Level Inverter has been addressed. After a detailed analysis of effects of variation of some design parameters on the performance of the system, an optimization strategy has been developed which allows to achieve different combinations of optimization targets. Although the paper is focused on an asymmetrical Open-Wind configuration, the proposed optimal design technique can be extended to other OW configurations.

5.3 A Fault Tolerant AC/DC Converter for Electrical Gen-Set Applications [52]

A fault tolerant AC/DC Converter for Electrical Gen-Set applications is presented based on a multilevel, open-end winding, topology managed by a suitable control strategy. More precisely, the considered converter topology provides the mean to independently control the currents of two phases when the third one is open without the need to reconfigure the circuit through auxiliary switches. The electrical generator is thus forced to operate in a two-phase mode, while holding the output DC voltage at the value generated by the system in health conditions. According to the proposed approach, this is achieved only by modifying the reference frame transformation accomplished to control the current vector. The effectiveness of the proposed solution is evaluated by simulations performed on a 2kW PMSG system.

5.3.1 Introduction

Electrical GEN-SET are today widely used to provide electricity in remote locations, to supply critical loads, to improve the mobility of machinery and appliances in building industry, agricultural and military fields, to increase the range in hybrid vehicles, as well as to provide reliable auxiliary electrical power sources in ground, naval and air transport.

Reliability and fault-tolerance are key issues for electric generators when supplying critical loads requiring an uninterruptible power source. Several fault tolerant GEN-SET systems have been proposed in the past for different applications. They are able to identify and isolate single or multiple faults occurring in the power converter, or the electrical machine, and to reconfigure the system in order to hold it in service [53]-[55]. The easiest way to increase the reliability of the GEN-SET is through redundancy [56]-[61], however, this is definitely the most expensive and bulky approach. A good compromise between fault tolerance and costs can be achieved by multi three-phase machine systems, tailored around a special electric generator featuring multiple three-phase windings, each one connected to a standard converter. In case of fault occurring in one of the winding sets, the last is shut down while the other units can still guarantee the service continuity to the drive. Fault tolerant configurations allowing to overcome only some specific faulty conditions can also be realized by including extra devices in the power converter, e.g. additional legs, SCR, TRIACS. These devices are driven to suitably reconfigure the system whenever a fault occurs. In some case, for proper operation, the neutral point of the machine has to be connected to the midpoint of the dc voltage link during the faulty condition. Moreover, in any three-phase machine it is possible to obtain a rotating magnetomotive force (MMF) under an open-phase fault, by setting a 60° phase shift between the stator currents of the two working stator phase windings [62]-[63].

A fault tolerant AC/DC Converter for Electrical Gen-Set Applications is presented in this paragraph based on an open-end winding topology and a specific fault control strategy. As shown in Fig. 5.3.1, the converter is built around a three phase open-end winding Permanent Magnet Synchronous Generator (PMSG), which is connected on one side to the electrical load through a T-Type Rectifier (TTR), and, on the other side, to an auxiliary Two-Level Inverter (TLI), which acts as an active power filter. The main feature of such a converter topology is that a stable output DC voltage and almost sinusoidal input currents are obtained, although operating the TTR at the line frequency. As this converter processes the main power stream, very low switching power losses and a high efficiency are obtained. The TLI is tasked to control the TLI DC Bus Voltage and to suitably shape the input current. It is PWM operated and in normal operation mode works at a voltage remarkably lower than the rectifier DC output voltage. The voltages across the TTR DC bus capacitors are actively regulated by setting the switching angle of TTR devices.

Whenever an open phase fault occurs, the system quickly identifies and isolates the fault exploiting one of the approaches presented in [64]. When a phase winding is open, two-phase operations are allowed because the considered converter topology becomes a three-wires circuit, due to the connection of the mid points of the two DC buses. Hence, in order to hold the GEN-SET in service, the reference frame transformation accomplished in the current vector control is modified to force the electrical generator to operate in a two-phase mode, while holding the output DC voltage at the value generated by the system in health conditions. The electrical power produced by the machine is controlled as in healthy conditions, with no modifications of the control structure and switching strategy. Moreover, the control system is able to cope with global efficiency maximization and control of TLI floating DC bus voltage even under faulty operation.

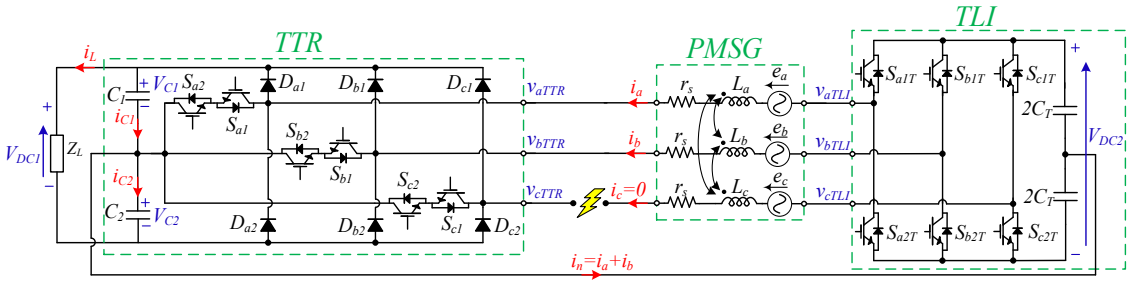

Figure 5.3.1 *Proposed fault tolerant Gen-Set topology.*

5.3.2 PMSG Model during open-phase fault

The voltage and flux equations of the mathematical model of a PMSG in the *abc* stationary reference frame, are given by:

$$\boldsymbol{v}_{abc} = \boldsymbol{R_s}\, \boldsymbol{i}_{abc} + \frac{d\boldsymbol{\Lambda}_{abc}}{dt} \qquad \boldsymbol{\Lambda}_{abc} = \boldsymbol{L_s}\, \boldsymbol{i}_{abc} + \lambda_{pm} \begin{bmatrix} \cos(2\theta_{re}) \\ \cos\left(2\theta_{re} - \frac{4}{3}\pi\right) \\ \cos\left(2\theta_{re} + \frac{4}{3}\pi\right) \end{bmatrix} \tag{5.3.1}$$

where $\boldsymbol{R_s}=diag(R_s)$, $\boldsymbol{v}_{abc}$, $\boldsymbol{i}_{abc}$ and $\boldsymbol{\Lambda}_{abc}$ are respectively the stator voltages, currents, and fluxes, θ_{re} is the rotor position and the terms of the matrix $\boldsymbol{L_s}$ are:

$$L_{hh} = L_{ls} + \frac{L_d + L_q - 2L_{ls}}{3} - \frac{L_d - L_q}{3}\cos[2(\theta_{re} + \alpha)] \tag{5.3.2}$$

$$L_{kh} = L_{hk} = -\frac{1L_d + L_q - 2L_{ls}}{2\quad 3} - \frac{L_d - L_q}{3}\cos[2(\theta_{re} + \gamma)] \tag{5.3.4}$$

$$\alpha = \begin{cases} 0 & \text{if } h = a \\ -\frac{2}{3}\pi & \text{if } h = b \\ \frac{2}{3}\pi & \text{if } h = c \end{cases} \qquad \gamma = \begin{cases} -\frac{\pi}{3} & \text{if } (h,k) = (a,b) \\ \pi & \text{if } (h,k) = (b,c) \\ \frac{\pi}{3} & \text{if } (h,k) = (a,c) \end{cases} \tag{5.3.5}$$

In (5.3.1) - (5.3.4) R_s is the stator resistance, L_{ls} is the leakage inductance and L_d and L_q are the d and q axis synchronous inductances. Parameters α and γ take into account the spatial phase displacement of the three stator windings.

Whenever an open-phase fault occurs, the analytical model of the PMSG must be modified due to the unbalanced working condition. The stator currents flowing into the two healthy phases are independent of each other, because of the connection between the mid points of the two DC buses, and the mathematical model can be rewritten as in (5.3.6). The inductance matrix $\boldsymbol{L}_{ij}$ has been divided into two components, namely: the matrix $\mathbf{L}_s$ including only constant coefficients, and the matrix $\boldsymbol{L}_{mij}$ including variable terms related to the magnetic saliency and rotor position. Moreover, the matrix $\boldsymbol{M}_{ij}$ provides the components of the permanent magnet flux linkage λ_{pm} in the *ij* stationary reference frame.

$$\boldsymbol{v}_{abc} = \boldsymbol{R_s}\, \boldsymbol{i}_{abc} + \frac{d\boldsymbol{\Lambda}_{abc}}{dt} \qquad \boldsymbol{\Lambda}^s_{ij} = (\boldsymbol{L_s} + \boldsymbol{L}_{mij})\, \boldsymbol{i}^s_{ij} + \boldsymbol{M}_{ij}\, \lambda_{pm} = \boldsymbol{L}_{ij}\, \boldsymbol{i}^s_{ij} + \boldsymbol{M}_{ij}\, \lambda_{pm} \tag{5.3.6}$$

where:

$$i,j=\begin{cases} b,c \rightarrow open\ \ phase\ 'a'\ \ fault \\ a,c \rightarrow open\ \ phase\ 'b'\ \ fault \\ a,b \rightarrow open\ \ phase\ 'c'\ \ fault \end{cases} \tag{5.3.7}$$

$$\boldsymbol{L_s}=\begin{bmatrix} L_{ls}+\dfrac{L_d+L_q-2L_{ls}}{3} & -\dfrac{1}{2}\dfrac{L_d+L_q-2L_{ls}}{3} \\ -\dfrac{1}{2}\dfrac{L_d+L_q-2L_{ls}}{3} & L_{ls}+\dfrac{L_d+L_q-2L_{ls}}{3} \end{bmatrix} \tag{5.3.8}$$

$$\boldsymbol{L}_{mij}=-\frac{L_d-L_q}{3}\begin{bmatrix} \cos\big(2(\theta_{re}+\beta_1)\big)\cos\big(2(\theta_{re}+\beta_2)\big) \\ \cos\big(2(\theta_{re}+\beta_2)\big)\cos\big(2(\theta_{re}+\beta_3)\big) \end{bmatrix} \tag{5.3.9}$$

$$\boldsymbol{M}_{ij}=\begin{bmatrix} \sin(\theta_{re}+\beta_1) \\ \sin(\theta_{re}+\beta_3) \end{bmatrix} \tag{5.3.10}$$

The expressions of β_1, β_2, β_3 are given in (5.3.11). Finally, neglecting the magnetic saturation the electromagnetic torque can be determined as the derivative of the magnetic co-energy W_f of model (5.3.6) with respect to rotor position:

$$(\beta_1,\beta_2,\beta_3)=\begin{cases} \left(-\dfrac{2}{3}\pi,0,\dfrac{2}{3}\pi\right)\ \ open\ \ phase\ 'a'\ \ fault \\ \left(0,\dfrac{\pi}{3},\dfrac{2}{3}\pi\right)\ \ \ open\ \ phase\ 'b'\ \ fault \\ \left(0,-\dfrac{\pi}{3},-\dfrac{2}{3}\pi\right)\ open\ \ phase\ 'c'\ \ fault \end{cases} \tag{5.3.11}$$

$$T_e=T_{er}+T_{em}=\frac{pp}{4}\,[\boldsymbol{i}^s_{ij}]^t\,\frac{\partial \boldsymbol{L}_{mij}}{\partial\theta_{re}}\,\boldsymbol{i}^s_{ij}+\frac{pp}{2}\,\lambda_{pm}\,[\boldsymbol{i}^s_{ij}]^t\,\frac{\partial \boldsymbol{M}_{ij}}{\partial\theta_{re}} \tag{5.3.12}$$

where T_{er} and T_{em} are due respectively to the reluctance and permanent magnet excitation, while pp is the poles number.

According to [65]-[67], by exploiting the reference frame transformations given in (5.3.13) and its inverse matrix in (5.3.14), the mathematical model of the machine can be rewritten as in (8) and (9).

$$\boldsymbol{K_F}=\begin{bmatrix} \dfrac{\sin\left(\theta_{re}+\dfrac{\beta_1-\beta_3}{2}+\beta_2\right)}{3\,\sin(\beta_1-\beta_3)} & \dfrac{\cos\left(\theta_{re}+\dfrac{\beta_1-\beta_3}{2}+\beta_2\right)}{\sin(\beta_1-\beta_3)} \\ \dfrac{\sin\left(\theta_{re}+\dfrac{\beta_3-\beta_1}{2}+\beta_2\right)}{3\,\sin(\beta_1-\beta_3)} & -\dfrac{\cos\left(\theta_{re}+\dfrac{\beta_3-\beta_1}{2}+\beta_2\right)}{\sin(\beta_1-\beta_3)} \end{bmatrix} \tag{5.3.13}$$

$$[\boldsymbol{K_F}]^{-1} = \begin{bmatrix} \cos\left(\theta_{re} + \frac{\beta_3 - \beta_1}{2} + \beta_2\right) & \cos\left(\theta_{re} + \frac{\beta_1 - \beta_3}{2} + \beta_2\right) \\ -\sin\left(\theta_{re} + \frac{\beta_3 - \beta_1}{2} + \beta_2\right) & -\sin\left(\theta_{re} + \frac{\beta_1 - \beta_3}{2} + \beta_2\right) \end{bmatrix} \tag{5.3.14}$$

$$\boldsymbol{v}_{qd} = \boldsymbol{R}^r_{\boldsymbol{s}}\, \boldsymbol{i}_{qd} + \omega_{re} \begin{bmatrix} 0 & 1 \\ -1 & 0 \end{bmatrix} \boldsymbol{\Lambda}_{qd} + \frac{d\boldsymbol{\Lambda}_{qd}}{dt} \qquad \boldsymbol{\Lambda}_{qd} = \boldsymbol{L}^r_{qd}\, \boldsymbol{i}_{qd} + \boldsymbol{M}^r_{qd}\, \lambda_{pm} \tag{5.3.15}$$

where:

$$\boldsymbol{R}^r_{\boldsymbol{s}} = 2\ \mathrm{diag}(R_s) + R_s\, R(\theta_{re}) \qquad \boldsymbol{L}^r_{qd} = \begin{bmatrix} L_q + L_{ls} & 0 \\ 0 & L_d + L_{ls} \end{bmatrix} + L_{ls}\, R(\theta_{re}) \tag{5.3.16}$$

$$\boldsymbol{M}^r_{qd} = \begin{bmatrix} 0 \\ 1 \end{bmatrix} \qquad R(\theta_{re}) = \begin{bmatrix} \cos(2(\theta_{re} + \beta_2)) & \sin(2(\theta_{re} + \beta_2)) \\ \sin(2(\theta_{re} + \beta_2)) & -\cos(2(\theta_{re} + \beta_2)) \end{bmatrix} \tag{5.3.17}$$

$$T_e = T_{er} + T_{em} = \frac{3}{2}\frac{pp}{2}\left[\lambda_{pm}\, i_q + (L_d - L_q)\, i_q\, i_d\right] \tag{5.3.18}$$

The main difference with the traditional model used in healthy conditions is related to the matrix structure of $\boldsymbol{R}^r_s$ and $\boldsymbol{L}^r_{qd}$. The matrix $\boldsymbol{L}^r_{qd}$ only features a dependence from the rotor flux position, that can be considered negligible as it is related to the leakage inductance. On the contrary, $\boldsymbol{R}^r_s$ is more heavily affected by unbalanced operation, implying that an amplitude modulation of the stator resistance occurs during the open-phase fault according to the rotor flux position. Finally, the torque equation maintains the same form of no-fault operation. This is a very important result in order to perform an effective current vector control during an open-phase fault.

5.3.3 Electrical Gen-Set Control Strategy

As aforementioned, the proposed converter is built around an open-end winding PMSG which is connected on one side to a unidirectional three-level T-Type Rectifier, and on the other side to an auxiliary Two-Level inverter. The load R_L is connected to the DC side of the TTR, being C_1 and C_2 the TTR DC Bus capacitors. A second DC bus is connected to the TLI, whose mid-point n'' is connected to the mid-point n' of the TTR DC bus. V_{DC1} and V_{DC2} are respectively the DC bus voltages of TTR and TLI.

The phase voltage V_{jg} of the PMSG ($j=a,b,c$) is given by (1), where: V_{jTLI} is the TTR input voltage and V_{jTLI} the TLI output voltage:

$$V_{jg} = V_{jTTR} - V_{jTLI} \tag{12}$$

The TTR input voltage V_{jTTR} may take three levels: $V_{DC1}/2$, 0 and $-V_{DC2}/2$.

The connection between n' and n'' leads to a Zero Sequence Current (ZSC) flowing through the connection of the mid points of the two DC buses, whose amplitude is strictly related to the load conditions. Due to the open-end winding connection of the electrical generator, the ZSC includes a third harmonic component, which is in practice canceled exploiting a suitable compensation algorithm [65], in order to avoid detrimental effects in terms of torque ripple,

A block diagram of the control system managing the fault tolerant GEN SET is shown in Fig. 5.3.2, consisting of two subsystems: the output DC voltage control, driving the

TTR, and the phase current control, which acts on the TLI. The last subsystem is in turn composed of three sections, respectively tasked to accomplish the PMSG phase current control, the compensation of voltage harmonics produced by the TTR, and the control of the TLI DC bus voltage.

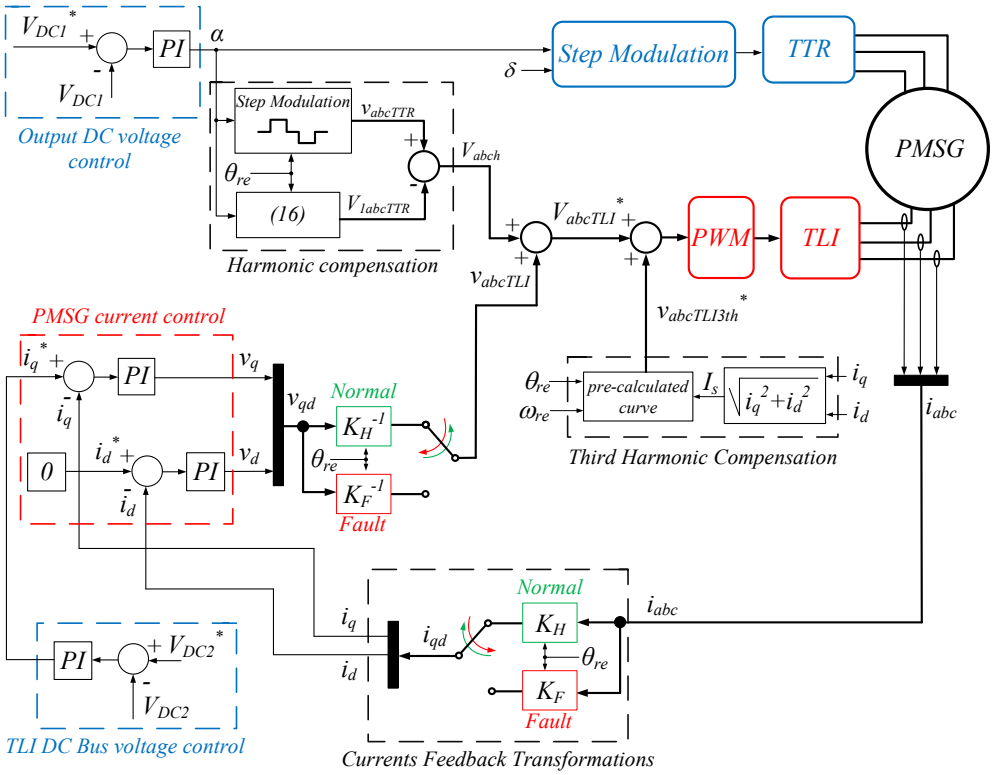

Figure 5.3.2 *Fault tolerant GEN-SET control system.*

The TTR operates at low frequency according to a three-step voltage modulation approach. Hence, the TTR input voltage V_{jTTR} is synchronized with the PMSG rotor position θ_{re}, featuring the stepwise waveform shown in Fig. 5.3.3. The state of a generic switch S_{jk} (j=a,b,c k=$1,2$) is a function of the voltage phase angle θ_{re}, the switching angle α and the sign of the phase current i_j, according to Table XXV. As given by (5.3.13), the modulation index m_{TTR} and the switching angle α are function of the DC output voltage V_{DC1} and of $\hat{V}_s$, the peak value of V_{jg}. For optimal TTR operations α must be greater than the input current phase delay φ, as described in detail in [34], where it is also demonstrated that, in order to avoid improper operations leading to extra power losses and voltage distortion, the phase delay δ between the voltage V_{js} and V_{jTTR} must be set according to (5.3.13).

$$\alpha = \arccos\left(\frac{\pi \hat{V}_s}{2 V_{DC1}}\right) \qquad m_{TTR} = \frac{\hat{V}_s}{V_{DC1}} \qquad \delta = \arctan\left(\frac{\omega L_s}{R_s}\right) \tag{5.3.13}$$

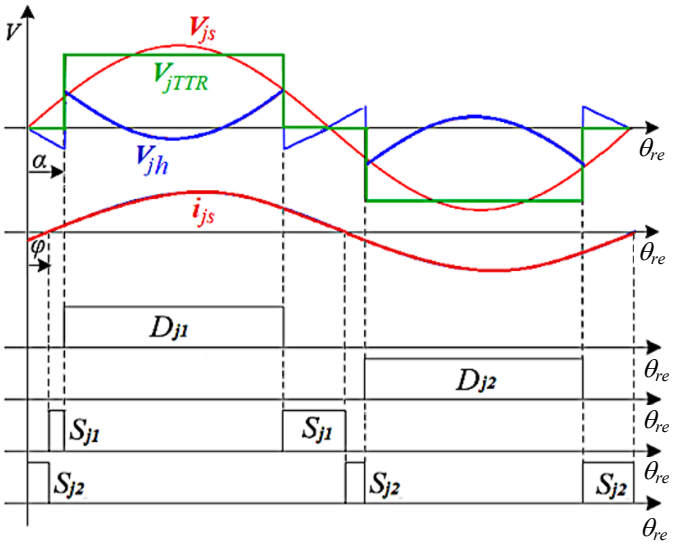

Figure 5.3.3 *Phase voltage waveforms and switching patterns.*

Table XXV *TTR Switching Rules*

Phase a	*if* $0<\theta_{re}<\alpha$ & $i_a>0 \rightarrow S_{a1}=ON,\ S_{a2}=OFF$ *if* $0<\theta_{re}<\alpha$ & $i_a<0 \rightarrow S_{a1}=OFF,\ S_{a2}=ON$
Phase b	*if* $0<(\theta_{re}-2/3\pi)<\alpha$ & $i_b>0 \rightarrow S_{b1}=ON,\ S_{b2}=OFF$ *if* $0<(\theta_{re}-2/3\pi)<\alpha$ & $i_b<0 \rightarrow S_{b1}=OFF,\ S_{b2}=ON$
Phase c	*if* $0<(\theta_{re}+2/3\pi)<\alpha$ & $i_c>0 \rightarrow S_{c1}=ON,\ S_{c2}=OFF$ *if* $0<(\theta_{re}+2/3\pi)<\alpha$ & $i_c<0 \rightarrow S_{c1}=OFF,\ S_{c2}=ON$

The DC output voltage regulator acts on α. Fundamental components V_{j1TTR} of V_{jTTR} are given by:

$$\begin{cases} V_{a1TTR} = 2\dfrac{V_{DC1}}{\pi}\cos(\alpha)\sin(\theta_{re}) \\ V_{b1TTR} = 2\dfrac{V_{DC1}}{\pi}\cos(\alpha)\sin\left(\theta_{re}-\dfrac{2}{3}\pi\right) \\ V_{c1TTR} = 2\dfrac{V_{DC1}}{\pi}\cos(\alpha)\sin\left(\theta_{re}+\dfrac{2}{3}\pi\right) \end{cases} \tag{5.3.14}$$

Assuming a constant DC output voltage V_{DC1}, the PMSG phase currents would be highly non-sinusoidal, due to the stepwise waveform of the TTR input phase voltages. This, in turn, would lead to low conversion efficiency and poor power factor. An input current shaping is thus accomplished by acting on the TLI, which is managed to operate as an active power filter. As shown in Fig. 5.3.2, a predictive input current filtering is exerted by including in the auxiliary inverter voltage reference V_{jTLI}^* a harmonic compensation term V_{jh}, which is obtained as the difference between the staircase phase voltage V_{jTTR} and its fundamental harmonic component V_{j1TTR}. A further term V_{jTLI3h} is also added to the TLI

voltage reference V_{jTLI}^{*} in order to mitigate the zero-sequence current circulating through the PMSG and the connection between n' and n''.

A closed loop PMSG phase current control system is added to the predictive filter in order to cope with unmodeled non-linearities and to improve the input current waveform and the system dynamic response.

$$\boldsymbol{K_H} = \frac{2}{3}\begin{bmatrix} cos(\theta_{re}) & cos(\theta_{re}-2\pi/3) & cos(\theta_{re}+2\pi/3) \\ sin(\theta_{re}) & sin(\theta_{re}-2\pi/3) & sin(\theta_{re}+2\pi/3) \\ \frac{1}{2} & \frac{1}{2} & \frac{1}{2} \end{bmatrix} \tag{5.3.15}$$

$$[\boldsymbol{K_H}]^{-1} = \begin{bmatrix} cos(\theta_{re}) & sin(\theta_{re}) & 1 \\ cos(\theta_{re}-2\pi/3) & sin(\theta_{re}-2\pi/3) & 1 \\ cos(\theta_{re}+2\pi/3) & sin(\theta_{re}+2\pi/3) & 1 \end{bmatrix} \tag{5.3.16}$$

A straightforward fault identification technique is exploited to trigger the switch between normal and fault mode of operation. It is based on the application at the terminals of the PMSG phase windings of an additional set of low amplitude, high frequency, symmetrical voltages and on an analysis of actual values of phase currents. When an open-phase fault occurs, the high-frequency current in the fault phase steadily decreases to zero in few milliseconds, allowing a very fast fault detection [68].

5.3.4 Simualtion Results

Simulations have been accomplished in order to assess the performance of the proposed converter in facing an open phase fault. The considered system is that of Fig. 5.3.1. The PMSG is rated at $P_n=3\ kW$, $V_n=300\ V$, $I_n=6.1\ A$, with *3* pole pairs. The stator inductance and resistance, are $L_s=20mH$ and $R_s=4.3\Omega$. The PMSG is running at the rated speed of *3000 rpm*, corresponding to a fundamental output voltage frequency of *50 Hz*. The TLI is PWM operated at 40kHz.

Fig. 5.3.4(a) and Fig. 5.3.5(a) deal with the main electrical and mechanical quantities of the healthy drive with $V_{DC1}=300V$, $V_{DC2}=75V$, $R_L=100\Omega$. Open phase fault operations are shown in Fig. 5.3.4 (b) and Fig. 5.3.5 (b). Compared to the healthy case, the voltage V_{DC2} has to be increased till V_{DC1}, in order to maintain similar performances in terms of THD and DC output voltage ripple. Moreover, the amplitude of phase currents has to be increased in order to produce same electromagnetic torque. A sixty degrees phase shift between the two healthy phase currents is obtained, confirming that a rotating MMF is generated into the PMSG.

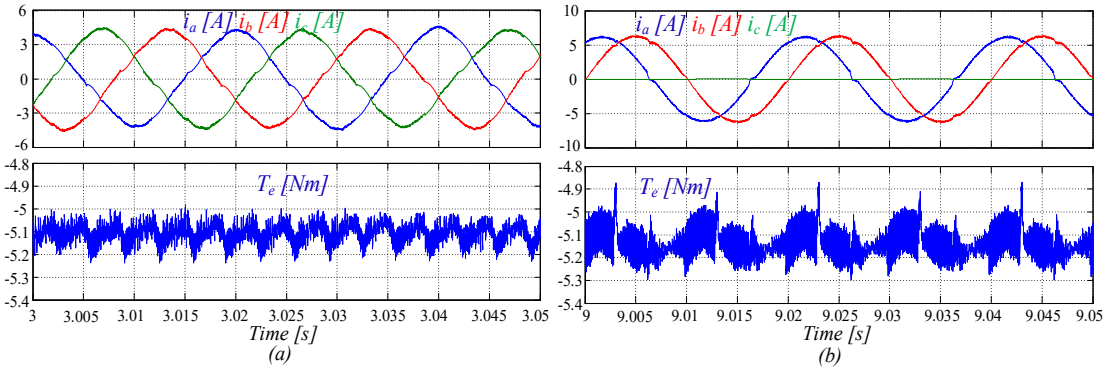

Figure 5.3.4 *PMSG phases current and electromagnetic torque in steady state condition with the system operating in: (a) normal mode and (b) open phase fault mode.*

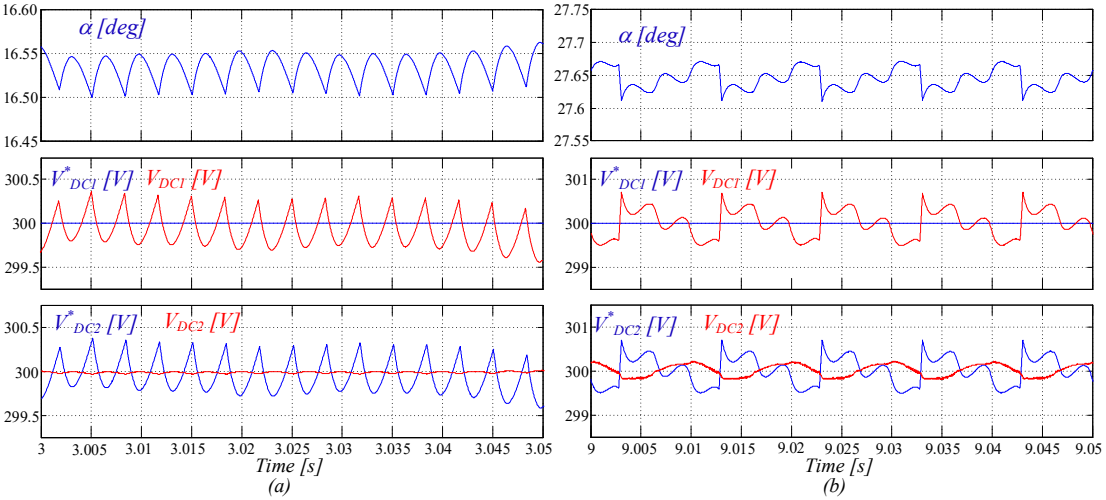

Figure 5.3.5 *System operating at steady state in: (a) normal mode and (b) open phase fault mode. Step modulation angle α, and DC bus Voltages V_{DC1} and V_{DC2}.*

The response of the faulty drive to a step load is shown in Figs 5.3.6 and 5.3.7. The system shows a quite stable behavior even under a remarkable load variation, producing only a low ripple on the Gen-Set output DC voltage and the PMSG electromagnetic torque.

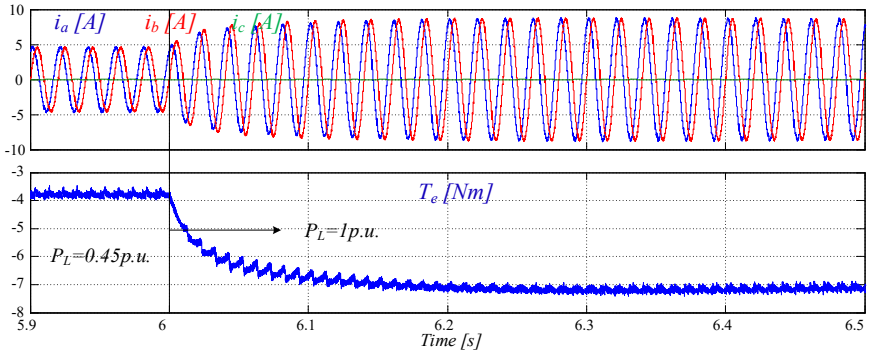

Figure 5.3.6 *Open phase fault operation: PMSG phases current and torque during a load step from 0.45 p.u. to 1 p.u.*

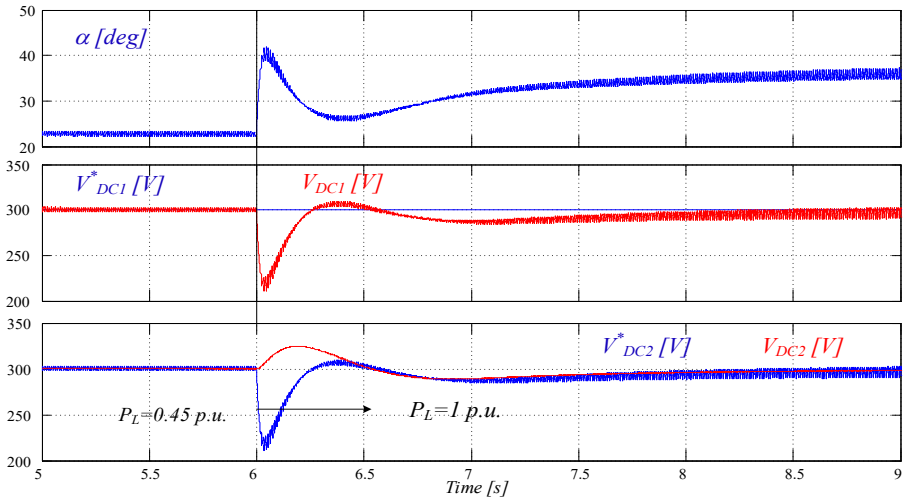

Figure 5.3.7 *Open phase fault operation: Switching angle α, V_{DC1} and V_{DC2} during a load step from 0.45 p.u. to 1 p.u.*

In the previous tests it is assumed that V_{DC2} is equal to V_{DC1}. This requires the voltage rating of TLI power devices to be the same of the devices equipping the TTR. A lower TLI power devices voltage rating can be adopted whenever a V_{DC2}/V_{DC1} ratio lower than unity is considered. However, this causes a derating of the Gen-Set performance as shown in Fig. 5.3.8. In particular, the THD of the phase currents increases as the V_{DC2}/V_{DC1} ratio decreases, yielding to an increment of the output DC voltage ripple and electromagnetic torque, although the stability of faulty operations in not threatened, as shown in Fig. 5.3.9, where a decreasing V_{DC2} is considered, while keeping constants the rotational speed and load.

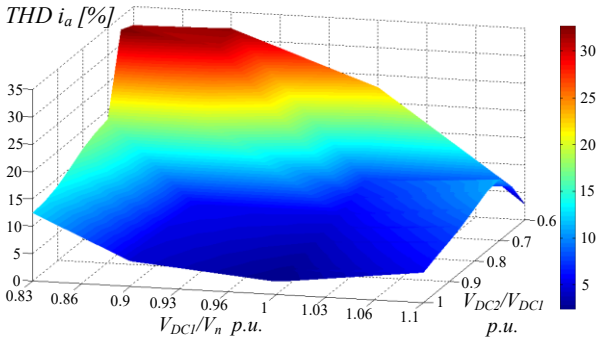

Figure 5.3.8 *THD% of the phase current i_a vs. V_{DC1}/V_n and V_{DC2}/V_{DC1}.*

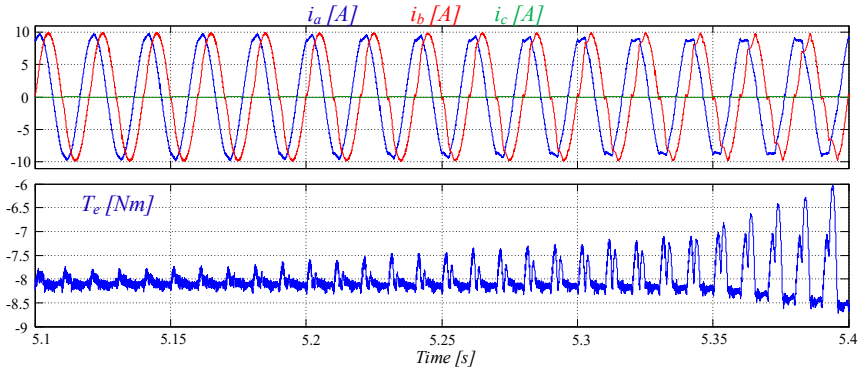

Figure 5.3.9 *PMSG phase currents and torque during a variation of V_{DC2}/V_{DC1} from 1 to 0.6.*

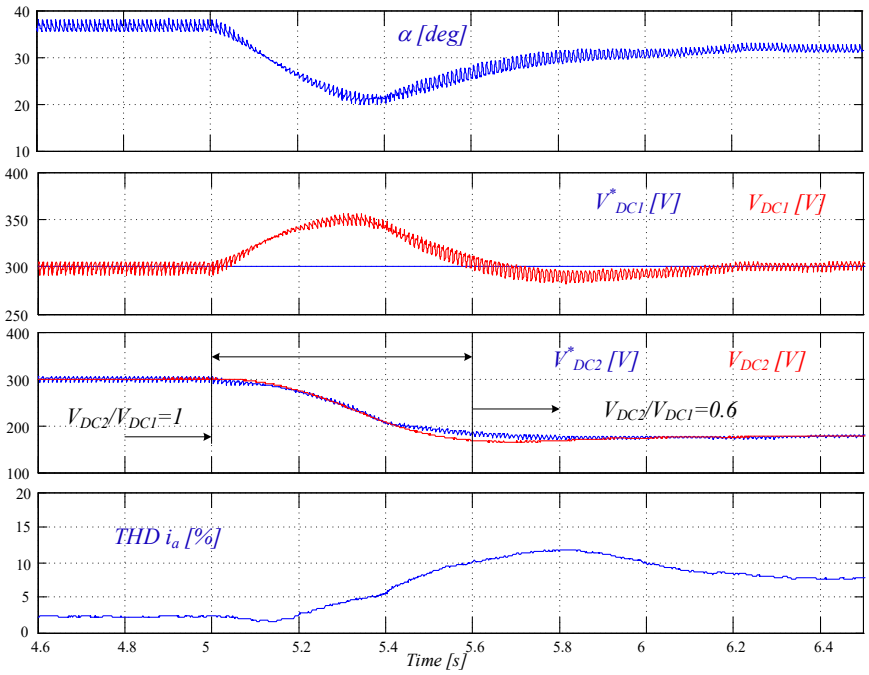

Figure 5.3.10 *Switching angle α, V_{DC1} and V_{DC2} during a variation of V_{DC2}/V_{DC1} from 1 to 0.6.*

5.3.5 Conclusions

A new approach to give fault tolerant capabilities to an Electrical Gen-Set system has been presented, relying on the exploitation of a three-phase open-end winding configuration. According such a configuration, a PMSG is connected on one side to the electrical load through a TTR, and, on the other side, to a TLI which acts as an active power filter, moreover, the mid-points of the DC buses of the TTR and TLI are connected between them. When an open phase fault occurs, the considered system becomes a tree-wires circuit, making possible an independent control of the two remaining phase currents only by modifying the reference frame transformation accomplished to control the current vector. Thus, no reconfiguration of the system through auxiliary switches is required, while a stable two-phase operation is obtained. The proposed approach, whose effectiveness has been assessed by simulations, could provide at no cost a valuable capacity to Open Winding GEN-SET systems supplying critical loads in industry, transportation and other application fields.

5.4 Performance Analysis of a Fault Isolation System for Fault-Tolerant Voltage-Fed PWM Motor Drives [69]

This paragraph presents the performance analysis of a DC short-circuit (SC) isolation system utilized in fault-tolerant voltage-fed PWM motor drives. The fault isolation is achieved by forcing a high-speed fuse to blow whenever a short-circuit condition occurs in one of the leg composing the inverter. The theoretical study allows to identify the influence of the electrical parameters composing the SC loop. Moreover, a detailed simulative and experimental investigation is provided to validate the theoretical study. The experimental results have been carried out by testing a single leg of a modular multiphase fault-tolerant inverter integrating high-speed fuse protections. The tests have

been performed by considering different high-speed fuses and DC-link capacitor bank configurations.

5.4.1 Introduction

Safety critical systems are taking on increasing importance in many applications, such as automotive, aerospace, marine, nuclear power and chemical plants, and military applications [70], [71]. Even civil, commercial, and industrial applications would benefit from the availability of cost-effective fault tolerant drives. In the last two decades numerous scientific contributions have been presented in literature, proposing several drive configurations able to cope single or multiple faults [72] occurring into the power converter and/or electrical machines [67], [68], [73]-[76]. In order to guarantee the service continuity of the drive, a fault identification and isolation system is necessary to isolate the faulty part of the system [65], [76]-[79]. Whatever is the fault isolation solution integrated in the drive, a high-speed fuse is mostly used. In fact, it is widely recognized the role of fuses in a wide range of power system and power electronics applications [67], [68]. They are simple and inexpensive current protection devices, used as a one-time sacrificial component for clearing an electrical fault [65]. In case of fault-tolerant motor drive, switching power inverters require a fast-acting fuse F for short-circuit (SC) protection [80], which are suitably designed to guarantee low energy let-through, low peak currents, low arc voltage and high heat dissipation, [81], [82]. When a SC occurs, it is expected that the fuse F acts breaking the circuit loop quickly to prevent further damage on power source, inverter leg and other circuit components. Moreover, a fast fault isolation must avoid the loss of drive control, which is relevant in safety critical applications, where the shut-down of the inverter yields to an unsafe system state.

An effective fault isolation system involves the DC-link capacitor bank C_{dc} during the faulty condition as well; it must be designed to be the principal energy source in the short-circuit loop, which is required to melt the fuse and thus clear the short-circuit. Furthermore, during the SC, C_{dc} must keep a limited voltage drop at its terminals in order to reduce power source overload.

In general, the DC-link bus capacitors in rectifier–inverter drives are usually selected to balance the instantaneous power difference between the input source and output load, and minimize voltage variation in the DC-link. Low-ripple currents in C_{dc} must be guaranteed as they significantly shorten its lifetime, [74], [83], [84]. Moreover, the DC-link design is aimed to reduce the size and price of the components while improving the inverter performance and reliability.

Many methods have been conducted for design the DC bus capacitor C_{dc} in motor drives, addressing different issues. In most cases, the dimensioning of the DC-link capacitor is based on the power loss tolerated by the capacitor, as in [74], [84], [85]. In that case, the power loss related to the equivalent series resistance (R_{ESR}) of the capacitor are computed starting from the RMS ripple current in the capacitor.

In [86], C_{dc} is determined by selecting the natural frequency of the LC filter composing the DC-link sufficiently higher than the sixfold mains frequency, and lower than the switching frequency. Recommendations for selection of the DC-link capacitor C_{dc} are also given in [83], by selecting C_{dc} in order to make the controlled inverter drive working for all normal operating conditions far from instability occurring in the form of oscillations in the DC-link voltage.

Generally, whenever a significant energy storage is not required, inverter drives with smaller DC-link capacitors are preferred as they provide a more compact solution [83]. This modus operandi could not be appropriated to guarantee the intervention of the high-

speed fuse during the DC short-circuit. An improper configuration of the fast-acting fuse F and DC-link capacitor bank C_{dc} may vanish the operation of the fault isolation system causing the inability to clear in an effective way a faulty current occurring in the DC-link.

While many studies dealt with fault tolerant configurations, to the best of the author's knowledge no papers have conduct an in-depth analysis concerning the transient behavior of the isolation system during the short-circuit conditions. Very generic information regarding the specifications required to the high-speed fuses and DC-link capacitors used to isolate the faulty condition in motor drives are given in [65], [77]-[78]. In [65], [80] the capacitor used to blow the fuse of the fault-tolerant drive is empirically determined on the base of a single experimental test, mentioning in a general way that an adequate value of C_{dc} is required in order to overcome the pre-arcing energy of the selected fuse. A generic fuse selection procedure for a fault-tolerant drive is also provided in [80], [87], starting from the computation of the current i_{fuse} flowing in the equivalent short-circuit loop, consisting of the DC-link LC filter and the equivalent resistance of the damaged power semiconductors. The Joule-integral of short-circuit current J_f is determined from the analytical expression of i_{fuse}, and then the melting integral of the fuse I^2t is computed as the ratio between J_f and a withstand factor achieved consulting a withstand factor curve for industrial fuses. In this computation a constant melting time is assumed, which is far from real system behavior, as it will be shown in this paper and no experimental analysis is presented. A single short circuit test is also shown in [88], [89] for a specific combination of DC bus voltage, IGBT power switch, DC-link capacitor and fuse. The short-circuit test confirms that the chosen fuse is capable to prevent a rupture of the IGBT switch under test and protecting the driver circuits as well.

Fuse manufacturers provides empirical approaches to select the high-speed fuse mostly for rectifier circuits [90]. In case of DC applications, only circuits including battery sources are taken into consideration; in the latter cases the fuse selection is obtained starting from the knowledge of the applied DC voltage, the circuit time constant of the short-circuit loop, the minimum prospective short-circuit current and pre-arcing integral of the selected fuse. In additions, a few curves related to a specific fuse are required to implement the empirical method [90].

From the above stated one deduces that little attention was paid to some key issues significantly impacting in the short-circuit transient. Firstly, all mentioned approaches neglect in the capacitor model the presence of the equivalent series resistance R_{ESR}, whose value can significantly compromise the effectiveness of the fault isolation system; it can be some order of magnitude higher than the resistances associated to the other elements composing the short-circuit loop (fuse and power switches).

This is especially true in low power applications, where electrolytic capacitors are often installed, which have a relatively high equivalent series resistance (ESR). Secondly, the impact of the short-circuit on the power grid side is even not addressed in the above studies, although it could yield to damage the rectifier or provoke the intervention of the AC side overload protections, vanishing the fault-tolerance capability of the drive. Thirdly, cost and size of the fault isolation system is not taken into consideration in previous studies, but represents a key aspect, especially for low-power and cost-effective drives.

The aim of this paragraph is to provide a detailed analysis of the dynamic behavior of the fault isolation system, involving most of the aspects mentioned above and providing useful indications to identify a good trade-off among technical specifications of the fast-acting fuses and DC-link bus capacitors, underlying the electrical stresses to which the components of the SC loop are subjected.

The analysis is supported by a suitable modeling of the system, allowing to underline the key parameters impacting on the fault isolation effectiveness.

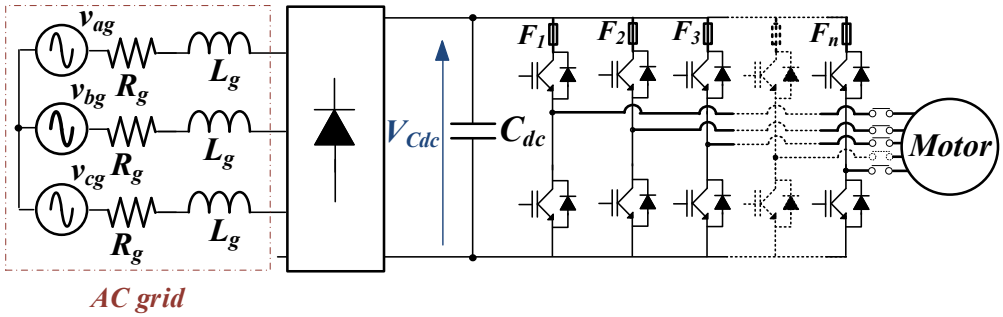

Figure 5.4.1 *Scheme of a fault-tolerant multiphase motor drive configuration.*

Simulations and experimental analysis are provided in case of an inverter composed of modular legs integrating fuse protections, as the one shown in Fig. 5.4.1, suitably designed for fault-tolerant multiphase motor drive configurations. Reconfiguration of the drive and control actions to restore the operation of the drive after having isolated the failure leg are not addressed in this study; however, numerous solutions are available in the technical literature [64], [71], [73], [75], [91].

5.4.2 Modeling of the Short Circuit Transient

The equivalent circuit of the DC-link bus capacitor bank, fuse and inverter leg during the short circuit can be represented as displayed in Fig. 5.4.1. In this model C_B is the value of the DC-link capacitor bank with an initial voltage across its terminal equal to the average rectified AC voltage V_{B0}, R_{ESR} is the equivalent series resistance of the capacitor; L includes the parasitic inductive elements of the capacitor, fuse and printed circuit board tracks involved in the short-circuit loop. The fuse F has been modeled according to its dynamic behavior under a heavy overload and short-circuit conditions, as shown in Fig. 5.4.2. In particular, the approximated model of F includes a constant resistance R_{fuse} during the melting phase also called the pre-arcing time, which is the interval from the initiation of the fault t_f to the fuse melting point t_M. At the end of this interval, the current flowing in the faulty loop reaches its maximum value $i_{fusemax}$. Moreover, an additional resistance R_{ARC} and capacitor C_{ARC} have been included in the fuse model to take into consideration the arc's heat vaporization of the element material after the melting phase, leading to the current interruption.

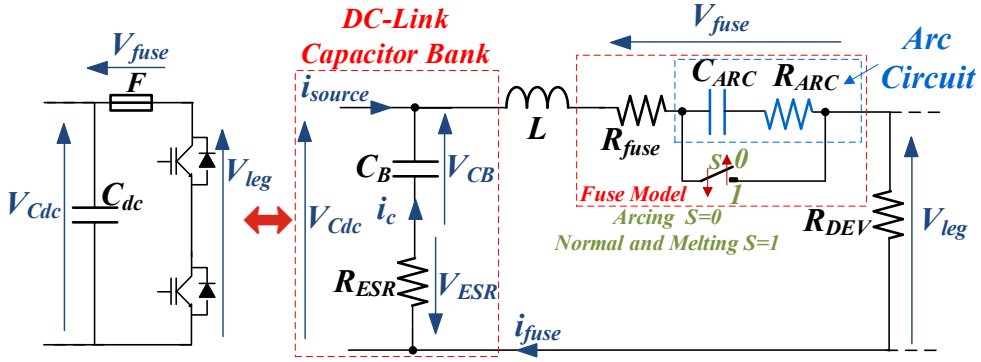

Figure 5.4.2 *Equivalent Circuit of the DC-link bus capacitor, fuse and inverter leg during the SC.*

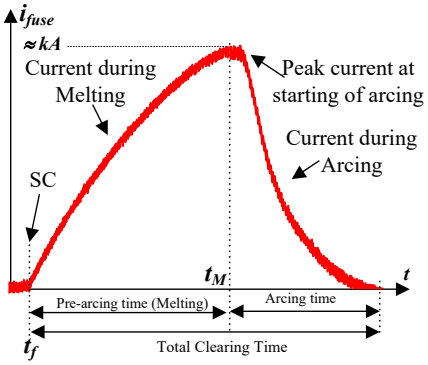

Figure 5.4.3 *Current waveform of the fuse blowing during the SC.*

The extinction of the arc occurs in a very short time achieving the final isolation of the circuit. The total time taken from initiation of fault to the final clearance of the circuit is very short, and in the experience of authors can be lower than a few milliseconds, and of these less than $50 \div 80 \mu s$ are attributable to the melting phase. The melting and arcing phases occurring in the fuse are related to the amount of energy released during the pre-arcing and the arcing times. Such energies are proportional to the integral of the square of the short-circuit current multiplied by the time the current flows, and often approximated as I^2t, where I is the RMS value of the current and t is the time in seconds for which the current flows. For high values of current, the melting time is very short and the pre-arcing or melting I^2t can be considered constant.

The DC-link bus capacitor C_B must be designed to let the fuse reaching the melting I^2t. In the equivalent circuit of Fig. 5.4.2 the damaged semiconductor power devices composing the faulty inverter leg are represented with a global equivalent resistance R_{DEV}.

For the purpose of this study, the dynamic behavior of this circuit under a SC has been analyzed by assuming that no current is delivered to the faulty inverter leg from the power source, i.e. $i_{source}=0$. Moreover, we assume that the current flowing through the inverter leg is initially zero $i_{fuse}(t_0)=0$; the last hypothesis is an approximation of real drive operation, as during normal drive operation i_{fuse} is several orders of magnitude lower than the SC current.

Under this hypothesis, the voltage at the C_B terminals during the fuse melting interval can be compute by solving the following system:

$$\begin{cases} \dfrac{d^2V_{CB}(t)}{dt^2} + 2\,\alpha \dfrac{dV_{CB}(t)}{dt} + \omega^2_0\, V_{CB}(t) = 0 \\ V_{CB}(0^+) = V_{B0} \\ \dfrac{dV_{CB}(0^+)}{dt} = -\dfrac{i_{fuse}(0^+)}{C_B} = 0 \end{cases} \tag{5.4.1}$$

where:

$$R_{eq} = R_{ESR} + R_{fuse} + R_{DEV} \qquad \alpha = \frac{R_{eq}}{2\,L} \qquad \omega_0 = \frac{1}{\sqrt{L\,C_B}} \tag{5.4.2}$$

The solution to the above system (5.4.1) is given by:

$$V_{CB}(t) = \frac{V_{B0}}{\alpha_1 - \alpha_2}\left(\alpha_1\, e^{-\alpha_2 t} - \alpha_2\, e^{-\alpha_1 t}\right) \tag{5.4.3}$$

where:

$$-\alpha_1 = -\alpha - \sqrt{\alpha^2 - \omega^2_0} \qquad -\alpha_2 = -\alpha + \sqrt{\alpha^2 - \omega^2_0} \tag{5.4.4}$$

The current flowing through the inverter leg i_{fuse} and the voltage V_{Cdc} are:

$$i_{fuse}(t) = -C_B \frac{dV_{CB}(t)}{dt} = V_{B0}\, C_B \frac{\alpha_1\, \alpha_2}{\alpha_1 - \alpha_2}\left(e^{-\alpha_1 t} - e^{-\alpha_2 t}\right) \tag{5.4.5}$$

$$V_{Cdc}(t) = V_{CB}(t) - R_{ESR}\, i_{fuse}(t) \tag{5.4.6}$$

Moreover, to guarantee the reaching of the fuse melting point, the capacitor must deliver enough energy to the fuse; the melting energy is proportional to the Joule-integral E_M of the short-circuit current i_{fuse}, defined as:

$$E_M = \int_{t_f}^{t_M} i^2_{fuse}\, dt \tag{5.4.7}$$

By performing a power balance in the SC loop of Fig. 5.4.2, it is possible to link the capacitor voltage drop occurring at the capacitor C_B terminals, the peak value of the SC current $i_{fusemax}$ and E_M. The minimum value of voltage V_{CBmin} at t_M can be estimated by:

$$V_{CBmin}(t_M) = \sqrt{V^2_{B0} - \frac{2}{C_B}\left(\frac{1}{2} L\, i^2_{fusemax} + R_{eq}\, E_M\right)} \tag{5.4.8}$$

The fault isolation system will be able to properly isolate the faulty inverter leg only if (5.4.9) is satisfied, that means ensuring an energy transfer from the capacitor to the fuse enough to let it reach the melting condition.

$$V^2_{B0} \geq \frac{2}{C_B}\left(\frac{1}{2} L\, i^2_{fusemax} + R_{eq}\, E_M\right) \tag{5.4.9}$$

During SC, the minimum value of the DC-link capacitor voltage V_{CBmin} is expected to be not far from the initial one V_{B0}; in fact, high values of i_{source} could potentially damage the upstream rectifier converter or yield to the automatic intervention of the over current protection devices placed in the AC main grid side, in both cases yielding to the shutdown of the electric drive.

V_{CBmin} can be kept close to V_{B0} at the fuse melting point by considering capacitors C_{dc} of large value C_B or fuses featuring low rated I^2t. Moreover, as the DC bus voltage is given by the algebraic sum of V_{CB} and the voltage drop at the R_{ESR} terminals, (5.4.10), capacitors C_B with low ESR should be selected to mitigate this detrimental effect as well.

$$V_{Cdcmin}(t_M) = V_{CBmin}(t_M) - R_{ESR}\, i_{fusemax} \tag{5.4.10}$$

Although it is not the purpose of this paper, from the above considerations it appears clear that an effective design of the fault isolation system can be achieved by suitably combining the specifications of the fuses and the DC-link capacitors. Among the numerous combinations, it is expected that the design procedure will select the one leading to the best compromise in terms of transient performance, cost, and size, which in most cases, it does not lead to select the bigger capacity and fastest fuse.

The influence of the main parameters composing the SC loop on the transient behaviour of the fault insulating system are investigated in the next sub-paragraph.

5.4.3 Simulation Results

Simulations of the SC loop of the single leg of a 2kVA fault tolerant inverter topology, as the one shown in Fig. 5.4.1, has been simulated with an electronic circuit simulation software. In the equivalent circuit of Fig. 5.4.2, the current i_{source} is provided by a rectified AC power supply, emulated as a DC source with a series inductance L_g representing the grid inductance.

A reference set of parameters has been utilized in the following simulations, whose values listed in Table XXVI have been measured from the prototype components or estimated through a curve fitting between the dynamic response achieved from simulations and experimental results.

It is worth noting that R_{ESR} is dominant in the computation of R_{eq}, thus plays a key role in the dynamic behaviour of the fault isolation system.

Fig. 5.4.4 displays the transient responses of the fault isolation unit when the DC-link capacitor value is changed from $500\mu F$ *to* $2500\mu F$, keeping constant the $R_{ESR}=150m\Omega$, and considering a fuse with $I^2t=80A^2s$.

The voltage at the DC-link capacitor terminals V_{Cdc}, the fuse voltage V_{fuse}, the current i_{fuse}, and the power source current i_{source} are displayed in this figure. Moreover, the time instant t_M corresponding to the fuse melting point is also shown in each subfigure.

This test highlights the key role played by the R_{ESR} during the short-circuit transient. In fact, capacitors featuring high value of R_{ESR} yield to a significant reduction of V_{Cdc}, even if high value of C_B are considered.

Moreover, high values of i_{source} are required from the power supply, independently on the C_B value, which could damage the rectifier or provoke the intervention of the overcurrent protections on the AC side, vanishing the fault-tolerance capability of the drive.

Table XXVI *Reference set of parameters utilized in the simulations.*

$V_{B0}=350V$	$R_{DEV}=20m\Omega$
$C_B=500\mu F$	$R_{FUSE}=5m\Omega$
$R_{ESR}=180m\Omega$	$C_{ARC}=200\mu F$
$L=0.2\mu H$	$R_{ARC}=100m\Omega$
$L_g=0.2\mu H$	

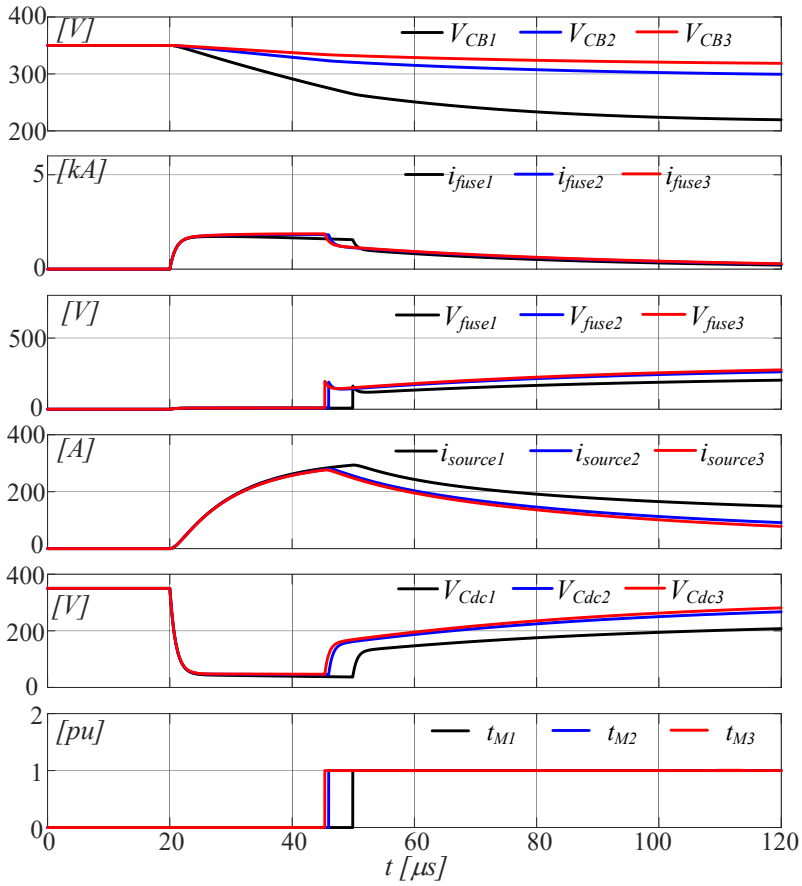

Figure 5.4.4 *Short circuit transients: different values of C_B: 500μF(1) - 1500μF(2) - 2500μF(3), at I^2t=80A^2s and ESR =180mΩ.*

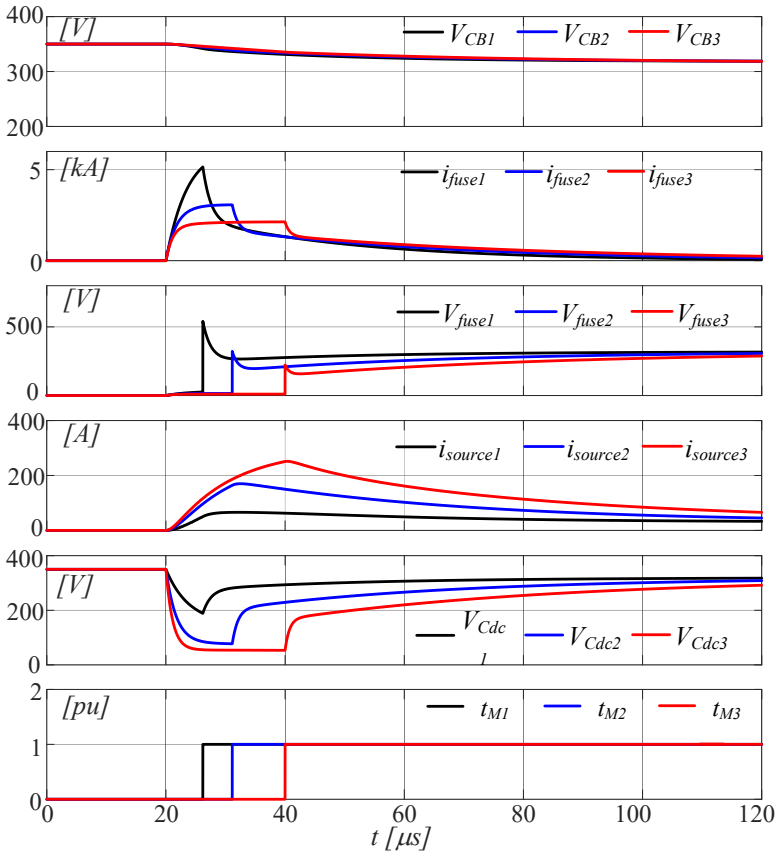

Figure 5.4.5 *Short circuit transients different values of R_{ESR}: 30mΩ(1) - 90mΩ(2) - 150mΩ(3), at I^2t=80A^2s and C_B=2500μF.*

The SC tests shown in Fig. 5.4.5 have been performed keeping constant the value of C_B=2500μF and I^2t=80A^2s, while changing R_{ESR} from 30mΩ to 150mΩ. It is possible to observe that V_{CBmin} is significantly increased when C_{dc} features a low R_{ESR}, reducing the voltage drop in the DC bus and, consequently, limiting the i_{source}. At lower R_{ESR} the fuse current i_{fuse} will reach higher peak values, reducing the melting time t_M; moreover, higher arc voltage V_{fuse} exceeding the system voltage are observed as well.

Finally, SC tests of Fig. 5.4.6 have been performed by selecting fuses featuring different melting energies I^2t and keeping constant C_B=2500μF and R_{ESR}=30mΩ. These tests confirm that by selecting fuses featuring lower rated E_{Ms} beneficial advantages will be observed in terms of lower t_M, higher V_{CBmin} and thus a significant reduction of the overload current i_{source} required from the grid.

The last quantity can be furtherly limited even by placing an AC or DC choke in the power supply line.

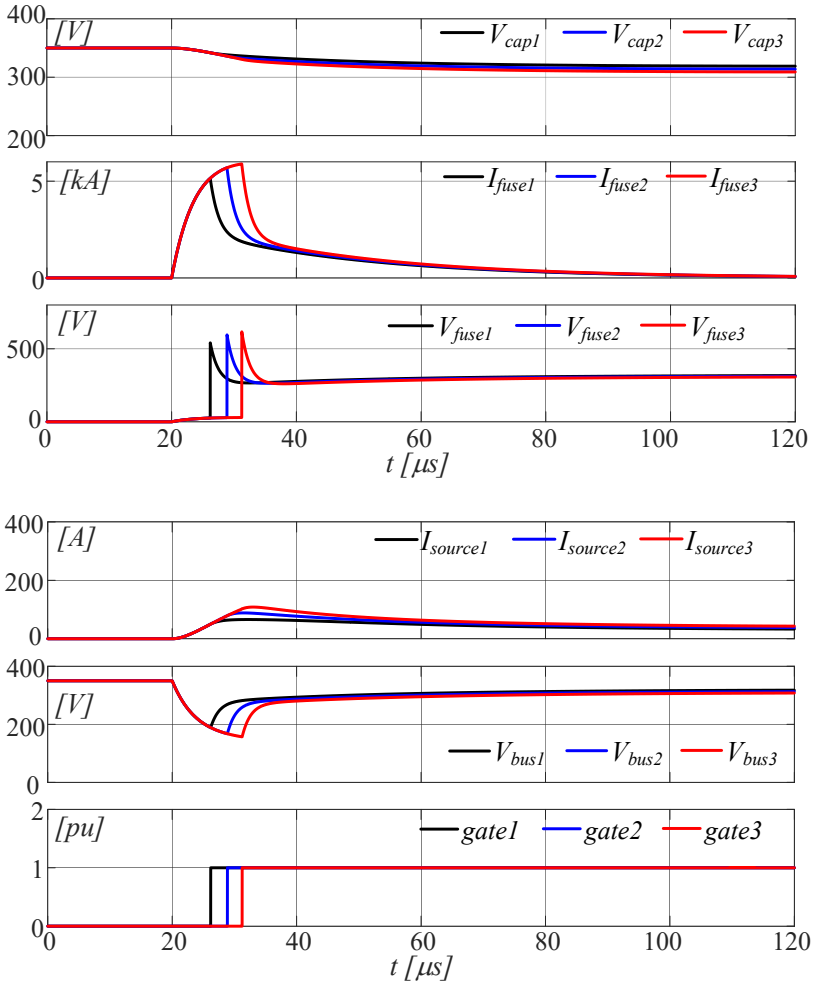

Figure 5.4.6 *Short circuit transients: different values of I^2t:80A^2s (1) - 160A^2s (2) - 240A^2s (3), at C_B=2500μF and ESR =30mΩ..*

5.4.4 Experimental Analysis

An experimental test rig has been arranged to validate the results carried out from the modeling and simulations.

A single inverter leg of a modular six-phase fault-tolerant voltage source inverter has been tested. In the following a description of the experimental setup and experimental results are provided.

The inverter leg is realized in a power board including gate driver circuits, power devices and heatsinks. Fig. 5.4.7 displays the experimental test bench, while the measurement setup is shown in Fig. 5.4.8.

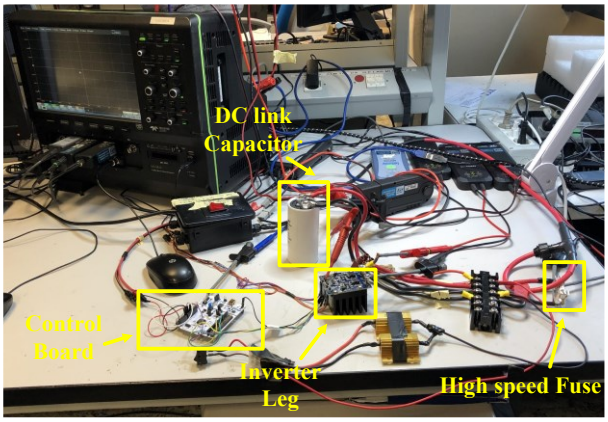

Figure 5.4.7 *Experimental test bench including the prototype of one of the inverter leg composing the fault-tolerant inverter.*

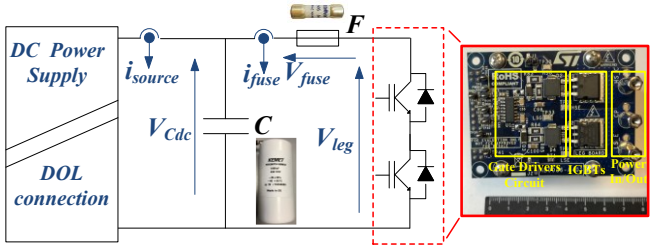

Figure 5.4.8 *Measurement setup.*

The specifications of the measurement system are listed in Tab. XXVII.

Table XXVII *List of measurement instruments*

N° 3 - LECROY HD3106 - High Voltage differential probe, 120 MHz, 1500 Vpk
N° 2 - LECROY CP500 500A – Hall effect current probe, 500A, DC/AC, 2 MHz
N° 1- PEM – CWT Mini HF60B - Rogowski current waveform transducer, 12kA, 0.5mV/A, 30MHz.
Oscilloscope, 1GHz, 12-bit, 10 GS/s, 8-channels
LCR Meter IM3536, DC, 4 Hz to 8 MHz.

The SC isolation system has been tested by considering three different high-speed fuses F_1, F_2, and F_3, and different sets of DC-link capacitors. Fuses feature different melting energies, and their specifications are listed in Tab. XXVIII, while electrical characteristics of the DC link capacitors are reported in Tab. XXIX.

Table XXVIII *Electrical Characteristic Specifications of High-Speed Fuses*

Fuse 1 (F_1) - Price: 20% of F_2			
Ampere Rating	30A	Nominal Cold Resistance	0.0038Ω
Voltage Rating	500V	Nominal Melting I^2t	280A^{2}s

Interrupting Rating	30kA@500VAC, 20kA@500VDC		
Fuse 2 (F_2)			
Ampere Rating	30A	Loss at 100%	10W
Voltage Rating	500VAC, 450VDC	Nominal Melting I^2t	77A^2s
Interrupting Rating	200kA@500VAC, 20kA@500VDC	Total Clearing I^2t (20kA@450VDC)	193 A^2s
Fuse 3 (F_3) - Price: 37% of F_2			
Ampere Rating	30A	Loss at 100%	4.8W
Voltage Rating	690VAC, 500VDC	Nominal Melting I^2t	107A^2s
Interrupting Rating	160kA	Total Clearing I^2t at rated voltage	675 A^2s

Table XXIX *Technical Specifications of DC Link Capacitors*

DC Link Capacitor 1 (C_1)			
Voltage Rating	400V	Capacitor Value	500μF
Equivalent Series Resistance (R_{ESR} @100Hz)	190mΩ	Case dimensions	25x30 mm
DC Link Capacitor 2 (C_2)			
Voltage Rating	500V	Capacitor Value	470μF
Equivalent Series Resistance (R_{ESR} @100Hz)	564mΩ	Case dimensions	35×60 mm
DC Link Capacitor 3 (C_3)			
Voltage Rating	450V	Capacitor Value	1mF
Equivalent Series Resistance (R_{ESR} @100Hz)	60mΩ	Case dimensions	50x105 mm

A DC power supply with current limitation is initially used to emulate the rectified single phase AC source with a DC link choke; the output voltage is set at 350V during all tests, while an 8-channel scope allows to measure the main electrical quantities, Fig. 5.4.8.

Main output characteristics of power devices composing the inverter leg are reported in Tab. XXX.

Table XXX *Specifications of the considered IGBTs*

IGBTs - STGB20M65DF2	
V_{CES} (V_{GE} = 0V)	650 V
$V_{CE(SAT)}$ @ (V_{GE} = 15V, I_C = 20A)	1.55 V (typ)@Ic=20A
I_C @ 100°C	20 A

The short circuit conditions in the leg are purposely realized through a control unit, including one short circuited power switch in the inverter leg, while the complementary switch is driven according to a single step signal.

A measurement campaign was conducted with a LCR meter on a number of faulty devices to determine their equivalent resistances, pointing out an average value of R_{DEV} lower than 10mΩ. A similar investigation has been carried out for the fuses F_1, F_2, and F_3, highlighting an ohmic behavior with average R_{fuse} equal to 5mΩ. Hence, the equivalent resistances R_{ESR} of C_{dc} are predominant in the SC loop.

The capacitor C_1 represents the DC-link capacitor C_{dc} whose capacitance value satisfies the design recommendations for this motor drive.

Experimental tests have been realized on the afore-described test rig with the main aim to evaluate the transient behavior of the fault isolation system during SCs, under different fuse and DC-link capacitor configurations.

The very early instants of the SC transient test are characterized by three typical time intervals, as shown in Fig. 5.4.9. Initially, the healthy power device of the inverter leg is purposely hold on in the interval from *0s* to t_f, causing the cross-conduction (DC short-circuit). In this interval the DC bus voltage is almost entirely applied to the healthy power device and limited current flows in the SC loop. At t_f both the power devices composing the inverter leg are damaged and the SC current significantly increases till reaching the melting point at t_M. Soon after, the arcing phenomena occurs till the SC clearance.

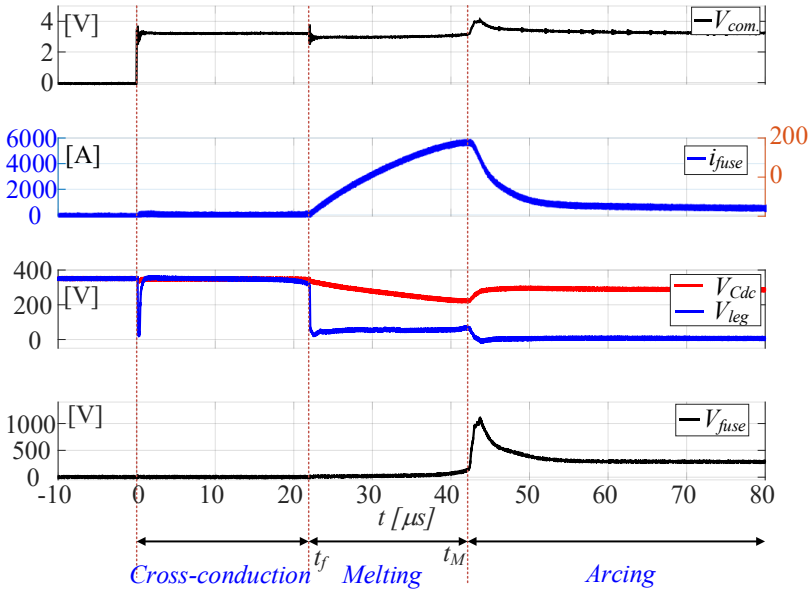

Figure 5.4.9 *Typical SC transient at very early stage of the phenomena.*

The first set of SC tests has been conducted by alternating the fuses installed in the SC loop, and keeping same C_{dc}=C_1. Fig. 5.4.10 shows the current i_{fuse}, the voltage at the DC-link capacitor terminals V_{Cdc}, the current delivered from the DC power supply i_{source} and the arc voltages V_{fuse} for each fuse. It has been experienced that when the high-speed fuse F_1 featuring highest I^2t is installed in the inverter leg board the fault isolation system is not capable to interrupt the SC loop; in fact, with this configuration the energy stored in C_1 is not enough to let the fuse to blow during SC, causing the activation of the over current protection of the DC power supply. The limited stored energy in C_1 is confirmed by the fact that V_{Cdc} goes to zero. Under a real rectified AC source power, this SC could damage the upstream rectifier converter or yield to the automatic intervention of the over current protection devices placed in the AC main grid side. SC tests with the same capacitor and the fuses F_2, and F_3 let to isolate the faulty circuit path, but still a significant voltage drop

at the DC-link capacitor is observed even due to the significant voltage drop $R_{ESR} \cdot i_{fuse}$. Furthermore, note that SC currents of the order of some kA flow through the faulty inverter leg.

These tests confirm that using high-speed fuses featuring very low I^2t is not enough to realize an effective fault isolation system. Hence, further tests have been carried out to investigate how to improve the fault isolation effectiveness.

A first action was to connect in parallel more capacitors to increase the capacitance and at the same time reduce R_{ESR}. With this aim, Fig. 5.4.11 displays SC tests performed with the DC-link capacitor bank composed by 5 capacitors C_1 connected in parallel, named hereafter as $5C_1$, making five times larger the capacitor value and reduce by one-fifth the R_{ESR}. According to (5.4.9), a limited variation of V_{Cdc} from its initial condition V_{B0}=350V is observed during the SC, thanks to the increased C_B value (2500μF) and reduced R_{ESR} (38mΩ), letting the fault isolation system to be effective in a very short time.

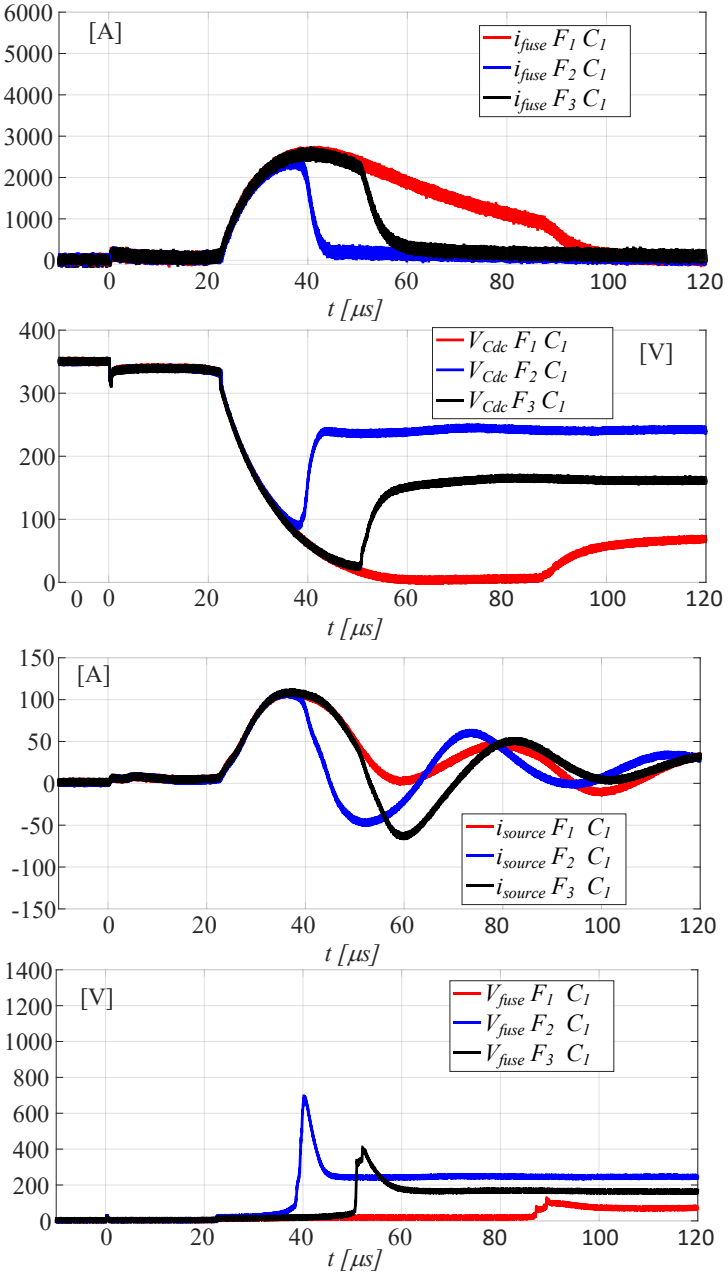

Figure 5.4.10 *SC tests by considering the fuses F_1, F_2, and F_3, and same C_{dc}=C_1.*

Fuses having lower I^2t lead to lower melting time intervals and SC peak currents. Moreover, these experimental tests confirm that a further benefit of considering a higher value of the capacitance C_B ($5C_1$) with reduced R_{ESR} is given by the lower peak value of i_{source} during the SC. Note that the fuse voltage V_{fuse} can exceed the system voltage during the arcing phase. This is another technical constraint that must be taken into consideration during the design of the SC isolation system.

The Figs. 5.4.12 and 5.4.13 have been performed to highlight the single influence of R_{ESR} and C_B on the SC transient.

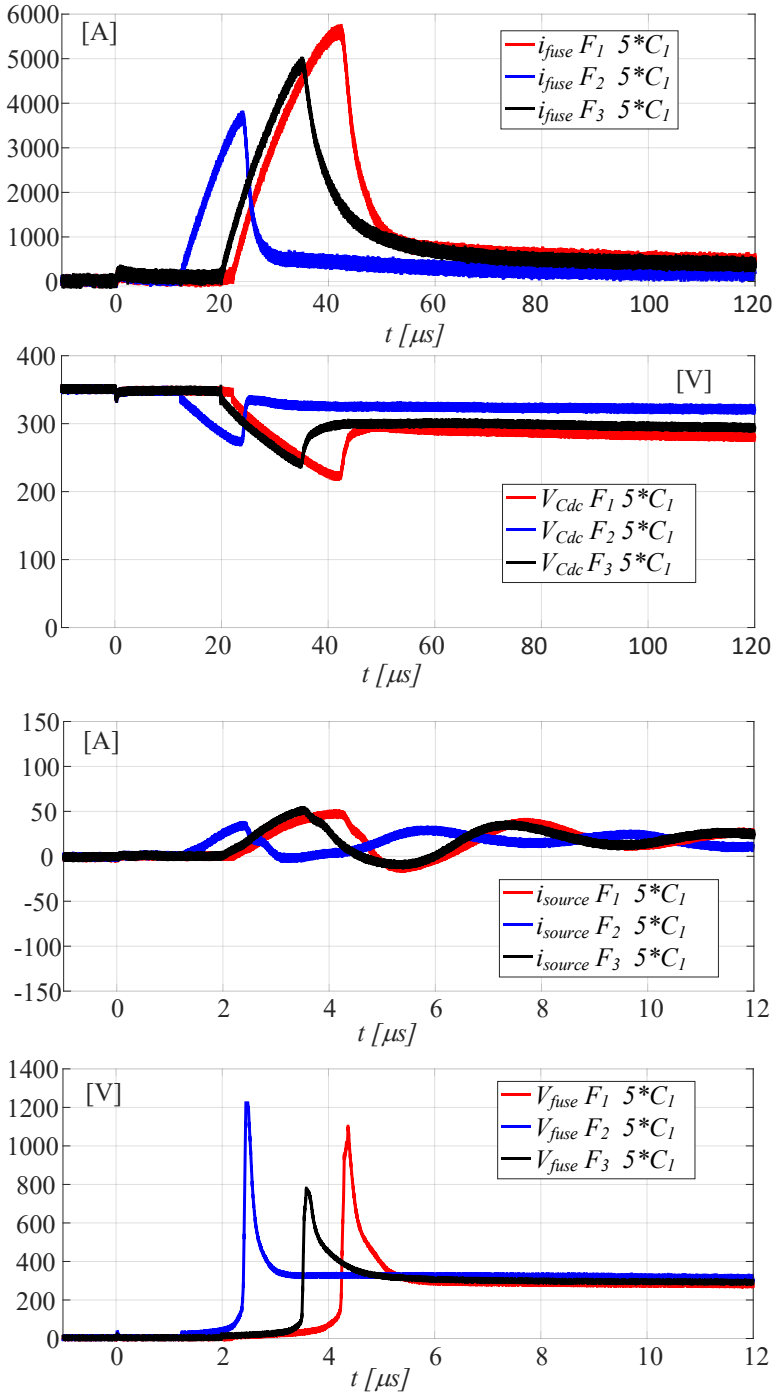

Figure 5.4.11 *SC tests by considering the fuses F_1, F_2, and F_3, and same C_{dc}=$5C_1$.*

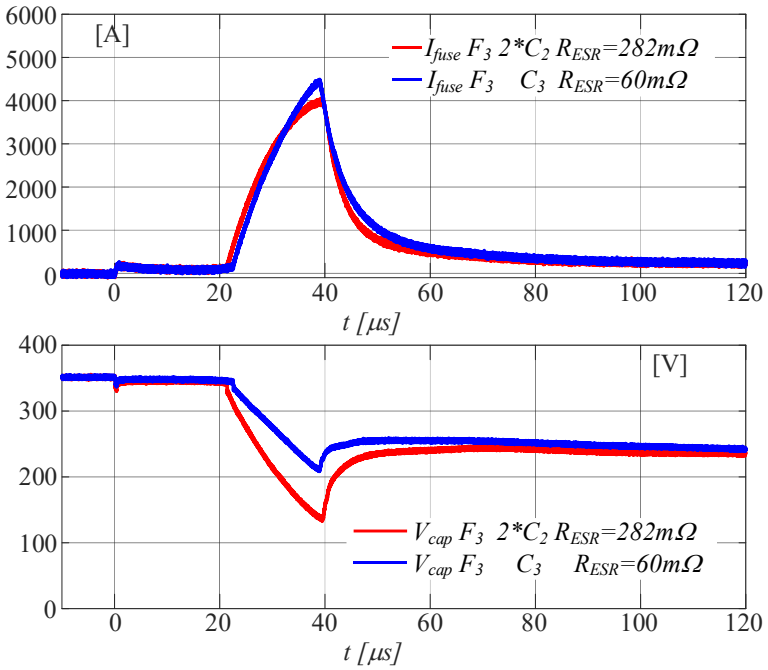

Figure 5.4.12 *SC tests by considering the fuse F_3 and C_{dc}≅1000μF, with different R_{ESR}.*

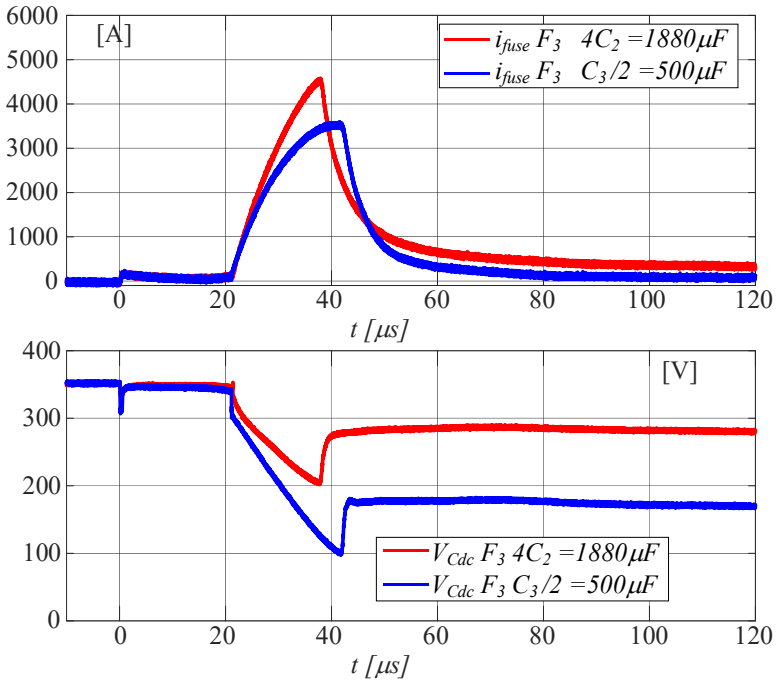

Figure 5.4.13 *SC tests by considering the fuse F_3 and R_{ESR}≅120mΩ, with different C_{dc}.*

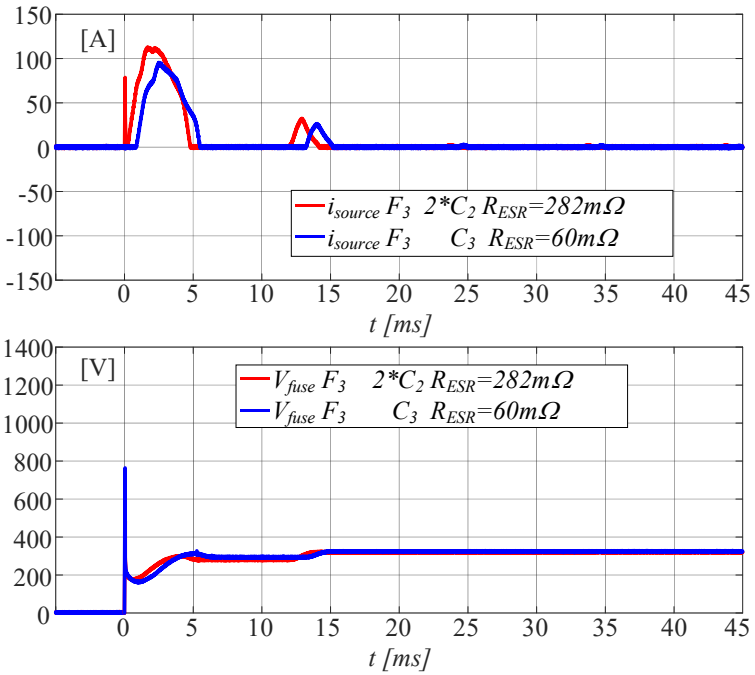

Figure 5.4.14 *SC tests with rectified AC source by considering the fuse F_3 and C_{dc}≅1000μF with different R_{ESR}.*

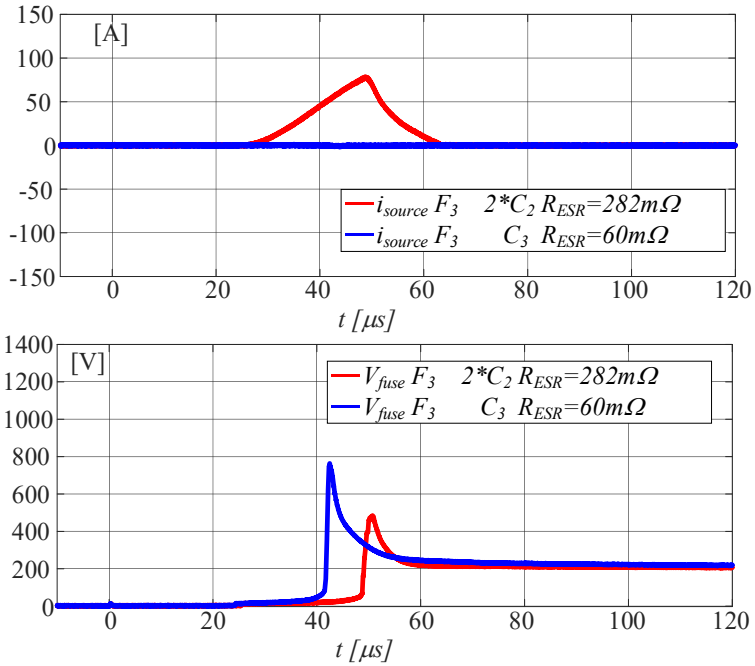

Figure 5.4.15 *Zoom-in view of SC tests shown in Fig. 14.*

Tests of Fig. 5.4.14 and 5.4.15 have been performed with the aim to measure the current delivered by the energy source during the SC and post-fault DC-link capacitor charging, when the inverter leg under test is supplied by a rectified single-phase AC grid. Two capacitors with very close capacitance C_{dc}=1000μF and different R_{ESR} have been tested. The specifications of the diodes composing the single phase full bridge rectifier are listed in Tab. XXXI.

Table XXXI *Main characteristics of diodes composing the single-phase full bridge rectifier – STTTH30L06.*

V_{RRM}	600 V	T_j	175 °C
V_F (typ.)	1.10 V	I_R @ ($V_R = V_{RRM}$, $T_j = 150°C$)	80 μA
$I_{F(AV)}$	30 A	t_{rr} (max.)	65 ns
$R_{th(JC)}$	1.1 °C/W	I_{FSM} t_p = 10ms sinusoidal	300 A

Note that during the SC (Fig. 5.4.15) the current absorbed by the grid is negligible when C_{dc} features a low value of R_{ESR}, while it becomes significant in case of C_{dc} with high R_{ESR}. Moreover, after the clearance of the faulty circuit, a further significant contribution i_{source} is required to charge the DC-link capacitors whose peak value (≅130A) could overcome the non-repetitive peak surge current of diodes if not properly chosen.

5.4.5 Conclusions

This paragraph dealt with the performance analysis of a DC SC isolation system utilized in fault-tolerant voltage-fed PWM motor drives. The theoretical study and experimental tests have underlined the transient behaviour of the fault isolation system, confirming that some freedom degrees in the design of the fault isolation system can be fruitfully combined and exploited to determine the best trade-off in terms of fast response, costs, and electrical stresses.

5.5 Reference

[1] S. Foti, A. Testa, , S. De Caro, T. Scimone, G. Scelba, G. Scarcella, “Multi-level open end windings multi-motor drives” Energies - Open Access, Volume 12, Issue 5, 5 March 2019, Art. n. 861.

[2] G. Scelba, G. Scarcella, S. Foti, A. Testa, S. De Caro, T. Scimone, “An open-end winding approach to the design of multi-level multi-motor drives”, 42nd Conference of the Industrial Electronics Society, IECON 2016, Florence, Italy, October 2016, pp. 5026-5032.

[3] S. Foti, G. Scelba, A. Testa, V. Sabatini, A. Lidozzi, L. Solero, “Asymmetrical hybrid unidirectional T-type rectifier for high-speed gen-set applications”, 9th Annual IEEE Energy Conversion Congress and Exposition, ECCE 2017, Cincinnati, USA, October 2017, pp. 4887-4893.

[4] A. Nabae, I. Takahasi, and H. Akagi, “A new neutral-point clamped PWM inverter,” IEEE Trans. Ind. Appl., vol. IA-17, no. 5, pp. 518–523, Sep. 1981.

[5] P. M. Bhagwat and V. R. Stefanovic, “Generalized structure of a multi-level PWM inverter,” IEEE Trans. Ind. Appl., vol. IA-19, no. 6, pp. 1057–1069, Nov. 1983.

[6] J.-S. Lai and F. Z. Peng, “Multi-level converters-A new breed of power converters,” IEEE Trans. Ind. Appl., vol. 32, no. 3, pp. 509–517, May/Jun. 1996.

[7] G. Carrara, S. Gardella, M. Marchesoni, and R. Salutari, “A new multilevel PWM method: A theoretical analysis,” IEEE Trans. Power Electron., vol. 7, no. 3, pp. 497–505, Jul. 1992.

[8] B. A. Welchko, T. A. Lipo, T. M. Jahns and S. E. Schulz, "Fault tolerant three-phase AC motor drive topologies: a comparison of features, cost, and limitations," in IEEE Trans. on Power Electr., vol. 19, no. 4, pp. 1108-1116, July 2004.

[9] I. Jlassi and A. J. M. Cardoso, "A Single Method for Multiple IGBT, Current, and Speed Sensor Faults Diagnosis in Regenerative PMSM Drives," in IEEE JESTPE, vol. 8, no. 3, pp. 2583-2599, Sept. 2020.
[10] S. Foti, A. Testa, S. De Caro, T. Scimone, L. D. Tornello, G. Scarcella, G. Scelba, "A Novel Three-Phase Multilevel Inverter Topology with Reduced Device Count for Open-end Winding Motor Drives," 2019 IEEE Energy Conversion Congress and Exposition (ECCE), 2019, pp. 3624-3630.
[11] T. Kawabata, E. C. Ejiogu, Y. Kawabata, and K. Nishiyama, "New open- winding configurations for high-power inverters," in Proc.IEEE Symp. Ind. Electron., vol. 2, Jul. 1997, pp. 457–462.
[12] Krishna Kumar Gupta, Shailendra Jain, "Comprehensive review of a recently proposed multilevel inverter", IET Power Electronics, vol. 7, Year 2014.
[13] Josep Pou, Jordi Zaragoza, Salvador Ceballos, Maryam Saeedifard, Dushan Boroyevich, "A Carrier-Based PWM Strategy With Zero-Sequence Voltage Injection for a Three-Level Neutral-Point-Clamped Converter", IEEE Transactions on Power Electronics, vol. 27, pp. 642-651, May 2010.
[14] S. De Caro, O. Giordano, T. Scimone, A. Testa, M. Cacciato, "A dual boost-NPC inverter working in time sharing mode", 2016 International Symposium on Power Electronics, Electrical Drives, Automation and Motion (SPEEDAM), pp. 962-967, May 2016.
[15] K. Sivakumar, A. Das, R. Ramchand, C. Patel, and K. Gopakumar, "A hybrid multilevel inverter topology for an open-end winding induction- motor drive using two-level inverters in series with a capacitor-fed H- bridge cell," IEEE Trans. Ind. Electron., vol. 57, no. 11, pp. 3707–3714, Nov. 2010.
[16] Bessem Omri, Kaiçar Ammous, Anis Ammous, "A New Method for Balancing Capacitors Voltages in NPC Inverter without DC-link Voltages Sensors", International Journal of Computer Applications (0975 – 8887) Volume 65– No.22, March 2013.
[17] Sarbani Mukherjee, Santu K. Giri, Subrata Banerjee, "A Flexible Discontinuous Modulation Scheme With Hybrid Capacitor Voltage Balancing Strategy for Three-Level NPC Traction Inverter", IEEE Transactions on Industrial Electronics, vol. 66, pp. 3333-3343, July 2018.
[18] Robert Stala, "Application of Balancing Circuit for DC-Link Voltages Balance in a Single-Phase Diode-Clamped Inverter With Two Three-Level Legs", IEEE Transactions on Industrial Electronics, vol. 58, pp. 4185-4195, Nov. 2010.
[19] Sergio Busquets Monge, Sergio Somavilla, Josep Bordonau, Dushan Boroyevich, "Capacitor Voltage Balance for the Neutral-Point- Clamped Converter using the Virtual Space Vector Concept With Optimized Spectral Performance", IEEE Transactions on Power Electronics, vol. 22, pp. 1128-1135, July 2007.
[20] H. du Toit Mouton, "Natural balancing of three-level neutral-point-clamped PWM inverters", IEEE Transactions on Industrial Electronics, vol. 49, pp. 1017-1025, Nov. 2002.
[21] E.Levi, I.N.W.Satiawan, N.Bodo, and M.Jones, "A space vector modulation scheme for multilevel open-end winding five-phase drives," IEEE Trans. Energy Convers., vol. 27, no. 1, pp. 1–10, Mar. 2012.
[22] K. A. Corzine, S. D. Sudhoff, and C. A. Whitcomb, "Performance charac- teristics of a cascaded two-level converter," IEEE Trans. Energy Convers., vol. 14, no. 3, pp. 433–439, Sep. 1999.

[23] Y. Wang, D. Panda, T.A. Lipo, D. Pan, “Open-Winding Power Conversion Systems Fed by Half-Controlled Converters”, IEEE Transactions on Power Electronics, vol. 28, pp. 2427-2436, Sep. 2012.
[24] B. K. Lee, B. Fahim and M. Ehsani, “Overview of Reduced Parts Converter Topologies for AC Motor Drives”, 2001 IEEE 32nd Annual Power Electronics Specialists Conference, vol.4, year 2001.
[25] Krishna Kumar Gupta, Alekh Ranjan, Pallavee Bhatnagar, Lalit Kumar Sahu, and Shailendra Jain, “Multilevel Inverter Topologies With Reduced Device Count: A Review”, IEEE Transactions on Power Electronics, vol. 31, pp. 135-151, Feb 2015.
[26] Pallavee Bhatnagar, Rekha Agrawal, Krishna Kumar Gupta, “Reduced device count version of single-stage switched-capacitor module for cascaded multilevel inverters”, IET Power Electronics, vol. 12, pp. 1079-1086, May 2019.
[27] Prabhat Ranjan Bana, Kaibalya Prasad Panda, R. T. Naayagi, Pierluigi Siano, Gayadhar Panda, “Recently Developed Reduced Switch Multilevel Inverter for Renewable Energy Integration and Drives Application: Topologies, Comprehensive Analysis and Comparative Evaluation”, IEEE Access, vol. 7, pp. 54888-54909, May 2019.
[28] Gopal Mondal, K. Gopakumar, P. N. Tekwani, Emil Levi, “A Reduced-Switch-Count Five-Level Inverter With Common-Mode Voltage Elimination for an Open-End Winding Induction Motor Drive”, IEEE Transactions on Industrial Electronics, vol. 54, pp. 2344-2351, July 2007.
[29] Abhijit Kshirsagar, R. Sudharshan Kaarthik, Arun Rahul, K. Gopakumar, Loganathan Umanand, Sujit K. Biswas, Carlo Cecati, “17-level inverter with low component count for open-end induction motor drives”, IET Power Electronics, vol. 11, pp. 922-929, April 2018.
[30] S. Foti, A. Testa, G. Scelba, S. De Caro, M. Cacciato, G. Scarcella, D. Bazzano, T. Scimone “A new approach to improve the current harmonic content on open-end winding AC motors supplied by multi-level inverters”. Proc. of 2015 IEEE Energy Conversion Congress and Exposition (ECCE): 20-24 Sept. 2015, Montreal, QC, Canada.
[31] G. Scelba, G. Scarcella, S. Foti, A. Testa, S. De Caro, T. Scimone “An Open-end Winding approach to the design of multi-level multi-motor drives” proc. of IECON 2016 - 42nd Annual Conference of the IEEE Industrial Electronics Society, 23-26 Oct. 2016, Florence, Italy.
[32] S. Foti, A. Testa, G. Scelba, S. De Caro, M. Cacciato, G. Scarcella, T. Scimone “An Open-End Winding Motor Approach to Mitigate the Phase Voltage Distortion on Multilevel Inverters” IEEE Transactions on Power Electronics, Vol. 33, Issue: 3, March 2018, pp: 2404 – 2416.
[33] S. Foti, S. De Caro, G. Scelba, T. Scimone, A. Testa, M. Cacciato, G. Scarcella, “An Optimal Current Control Strategy for Asymmetrical Hybrid Multilevel Inverters”, IEEE Transactions on Industry Applications, vol. 54, pp. 4425-4436, April 2018.
[34] S. Foti, G. Scelba, A. Testa, A. Sciacca “An averaged-value model of an asymmetrical hybrid multi-level rectifier”. Energies 2019, 12, no. 4: 589, Open access.
[35] A. Testa, S. Foti, S. De Caro, L. D. Tornello, G. Scelba and G. Scarcella, "Optimal Selection of the Voltage Modulation Strategy for an Open Winding Multilevel Inverter," 2020 IEEE Energy Conversion Congress and Exposition (ECCE), 2020, pp. 2231-223.

[36] S. Kouro, M. Malinowski, K. Gopakumar, J. Pou, L. G. Franquelo, Bin Wu, J. Rodriguez, M. A. Pérez, J. I. Leon, "Recent Advances and Industrial Applications of Multilevel Converters," in IEEE Transactions on Industrial Electronics, vol. 57, no. 8, pp. 2553-2580, Aug. 2010.
[37] H. Abu-Rub, J. Holtz, J. Rodriguez and G. Baoming, "Medium-Voltage Multilevel Converters—State of the Art, Challenges, and Requirements in Industrial Applications," in IEEE Transactions on Industrial Electronics, vol. 57, no. 8, pp. 2581-2596, Aug. 2010.
[38] M. S. A. Dahidah, G. Konstantinou, V. G. Agelidis, "A Review of Multilevel Selective Harmonic Elimination PWM: Formulations, Solving Algorithms, Implementation and Applications," in IEEE Transactions on Power Electronics, vol. 30, no. 8, pp. 4091-4106, Aug. 2015.
[39] K. Yang, Q. Zhang, J. Zhang, R. Yuan, Q. Guan, W. Yu, J. Wang, "Unified Selective Harmonic Elimination for Multilevel Converters," in IEEE Transactions on Power Electronics, vol. 32, no. 2, pp. 1579-1590, Feb. 2017.
[40] C. Buccella, C. Cecati, M. G. Cimoroni, G. Kulothungan, A. Edpuganti, A. K. Rathore, "A Selective Harmonic Elimination Method for Five-Level Converters for Distributed Generation," in IEEE Journal of Emerging and Selected Topics in Power Electronics, vol. 5, no. 2, pp. 775-783, June 2017.
[41] A. Edpuganti, A. K. Rathore, "New Optimal Pulsewidth Modulation for Single DC-Link Dual-Inverter Fed Open-End Stator Winding Induction Motor Drive," in IEEE Transactions on Power Electronics, vol. 30, no. 8, pp. 4386-4393, Aug. 2015.
[42] V. T. Somasekhar, K. Gopakumar, M. R. Baiju, K. K. Mohapatra, L. Umanand, "A multilevel inverter system for an induction motor with open-end windings," in IEEE Transactions on Industrial Electronics, vol. 52, no. 3, pp. 824-836, June 2005.
[43] Y. Kawabata, M. Nasu, T. Nomoto, E. C. Ejiogu, T. Kawabata, "High-efficiency and low acoustic noise drive system using open-winding AC motor and two space-vector-modulated inverters," in IEEE Transactions on Industrial Electronics, vol. 49, no. 4, pp. 783-789, Aug. 2002.
[44] K. Sivakumar, A. Das, R. Ramchand, C. Patel, K. Gopakumar, "A Hybrid Multilevel Inverter Topology for an Open-End Winding Induction-Motor Drive Using Two-Level Inverters in Series With a Capacitor-Fed H-Bridge Cell," in IEEE Transactions on Industrial Electronics, vol. 57, no. 11, pp. 3707-3714, Nov. 2010.
[45] S. De Caro, S. Foti, T. Scimone, A. Testa, G. Scelba, M. Pulvirenti, S. Russo, "Motor Overvoltage Mitigation on SiC MOSFET Drives Exploiting an Open-End Winding Configuration," in IEEE Transactions on Power Electronics, vol. 34, no. 11, pp. 11128-11138, Nov. 2019.
[46] T. Boller, J. Holtz, A. K. Rathore, "Optimal pulsewidth modulation of a dual three-level inverter system operated from a single dc link," 2011 IEEE Energy Conversion Congress and Exposition, Phoenix, AZ, 2011, pp. 3406-3410.
[47] K. K. Mohapatra, K. Gopakumar, V. T. Somasekhar and L. Umanand, "A harmonic elimination and suppression scheme for an open-end winding induction motor drive," in IEEE Transactions on Industrial Electronics, vol. 50, no. 6, pp. 1187-1198, Dec. 2003.
[48] H. Stemmler, P. Guggenbach, "Configurations of high-power voltage source inverter drives," in Proc. 1993 Power Electronics and Applications, vol.5, pp.7-14.
[49] A. Payam, L. Dong-Choon, " A Generalized Loss Analysis Algorithm of Power Semiconductor Devices in Multilevel NPC Inverters". Journal of Electrical Engineering and Technology. vol. 9. pp. 2168-2180, 2014.

[50] Salomaki J., Hinkkanen M., Luomi J., "Cost-Effective Design of Inverter Output Filters for AC Drives", IEEE 33rd Annual Conference of the Industrial Electronics Society, IECON 2007, pp.: 1220 -1226.
[51] M. Alsayed, M. Cacciato, G. Scarcella and G. Scelba, "Multicriteria Optimal Sizing of Photovoltaic-Wind Turbine Grid Connected Systems," in IEEE Transactions on Energy Conversion, vol. 28, no. 2, pp. 370-379, June 2013.
[52] S. Foti, A. Testa, S. de Caro, T. Scimone, G. Scelba and L. D. Tornello, "A Fault Tolerant AC/DC Converter for Electrical Gen-Set Applications," 2019 21st European Conference on Power Electronics and Applications (EPE '19 ECCE Europe), 2019, pp. P.1-P.10
[53] Y. Le, Y. Shuying, X. Zhen, Z. Xing, " Eliminating Scheme of Zero-Sequence Currents in Open-end Winding Induction Motor Drive With a Single DC Power Supply, " in Conf. 2017 Chinese Automation Congress (CAC), pp. 3538-3543.
[54] J. Kalaiselvi, S. Srinivas, " Bearing Currents and Shaft Voltage Reduction in Dual-Inverter-Fed Open-End Winding Induction Motor With Reduced CMV PWM Methods," IEEE Trans. Ind. Electronics, vol. 62, no. 1, pp. 144-152, Jan. 2015.
[55] H. Kubo, Y. Yamamoto, T. Kondo, K. Rajashekara, B. Zhu, "Zero-sequence current suppression for open-end winding induction motor drive with resonant controller ," IEEE Applied Power Electronics Conference and Exposition (APEC), pp. 2788-2793, 2016.
[56] A. M. S. Mendes and A. J. Marques Cardoso, "Fault-tolerant operating strategie13s applied to three-phase induction-motor drives," IEEE Trans. Ind. Electron., vol. 53, no. 6, pp. 1807–1817, Dec. 2006.
[57] W. N. W. A. Munim, M. J. Duran, H. S. Che, M. Bermudez, I. Gonzalez- Prieto, and N. A. Rahim, "A unified analysis of the fault tolerance capability in six-phase induction motor drive," IEEE Trans. Power Electron., vol. 32, no. 10, pp. 7824–7836, Oct. 2017.
[58] Marcelo Lobo Heldwein, Samir Ahmad Mussa, Ivo Barbi, "Three-Phase Multilevel PWM Rectifiers Based on Conventional Bidirectional Converters", IEEE Transactions on Power Electronics, 2010, vol. 25, no. 3, pp. 545 – 549.
[59] Márcio Silveira Ortmann ; Samir Ahmad Mussa ; Marcelo Lobo Heldwein "Three-Phase Multilevel PFC Rectifier Based on Multistate Switching Cells", IEEE Transactions on Power Electronics, 2015, vol. 30, no. 4, pp. 1843 – 1854.
[60] João Paulo Ramos Agra Méllo, Cursino Brandão Jacobina, Maurício Beltrão de Rossiter Corrêa, "Three-Phase Unidirectional Rectifiers With Open-End Source and Cascaded Floating Capacitor H-Bridges", IEEE Transactions on Industry Applications, 2018, vol. 54, no.3, pp. 2534 – 2549.
[61] O. Wallmark, L. Harnefors, and O. Carlson, "Control algorithms for a fault-tolerant PMSM drive," IEEE Trans. Ind. Electron., vol. 54, no. 4, pp. 1973–1980, Aug. 2007.
[62] T. H. Liu, J. R. Fu, and T. A. Lipo, "A strategy for improving reliability of field-oriented controlled induction motor drives," IEEE Trans. Ind. Appl., vol. 29, no. 5, pp. 910–918, Sep./Oct. 1993.
[63] B.A. Welchko, T.A. Lipo, T.M. Jahns, S.E. Schulz, "Fault Tolerant Three-Phase AC Motor Drive Topologies: A Comparison of Features, Cost, and Limitations", IEEE Transactions on Power Electronics, 2004, vol. 19, no. 4, pp. 1108 – 1116.
[64] N. Bianchi, S. Bolognani, M. Zigliotto, and M. Zordan,"Innovative remedial strategies for inverter faults in IPM synchronous motor drives," IEEE Trans. Energy Convers., vol. 18, no. 2, pp. 306–314, Jun. 2003.

[65] A. Gaeta, G. Scelba, A. Consoli, “Modeling and Control of Three-Phase PMSMs Under Open-Phase Fault,” IEEE Transactions on Ind. Applic., vol. 49, no. 1, pp. 74-83, Jan. 2013.
[66] G. Scarcella; G. Scelba ; M. Pulvirenti ; A. Gaeta, “A fault-tolerant power conversion topology for PMSG based Wind Power Systems”, proc. of IEEE 2014 International Conference on Electrical Machines (ICEM), 2014, 1688 – 1696.
[67] M. Pulvirenti, G. Scarcella, G. Scelba, M. Cacciato, A. Testa, “Fault-Tolerant AC Multidrive System”, IEEE Journal of Emerging and Selected Topics in Power Electronics, vol. 2, no. 2, pp. 224 – 235.
[68] G. Scarcella, G. Scelba, M. Pulvirenti, R. D. Lorenz, “Fault-Tolerant Capability of Deadbeat-Direct Torque and Flux Control for Three-Phase PMSM Drives”, IEEE Transactions on Industry Applications, 2017, vol. 53, no. 6, pp. 5496 – 5508, Nov.-Dec. 2017.
[69] L. D. Tornello, G. Scelba, A. Spampinato, G. Forte, "Performance Analysis of a Fault Isolation System for Fault-Tolerant Voltage-Fed PWM Motor Drives", accepted and under publication in 2021 IEEE Energy Conversion Congress and Exposition (ECCE 2021).
[70] B. A. Welchko, T. A. Lipo, T. M. Jahns and S. E. Schulz, "Fault tolerant three-phase AC motor drive topologies: a comparison of features, cost, and limitations," in IEEE Trans. on Power Electr., vol. 19, no. 4, pp. 1108-1116, July 2004.
[71] I. Jlassi and A. J. M. Cardoso, "A Single Method for Multiple IGBT, Current, and Speed Sensor Faults Diagnosis in Regenerative PMSM Drives," in IEEE JESTPE, vol. 8, no. 3, pp. 2583-2599, Sept. 2020.
[72] D. Kastha and B. K. Bose, "Investigation of fault modes of voltage-fed inverter system for induction motor drive," in IEEE Trans. on Ind. Appl., vol. 30, no. 4, pp. 1028-1038, July-Aug. 1994.
[73] Tian-Hua Liu, Jen-Ren Fu and T. A. Lipo, "A strategy for improving reliability of field-oriented controlled induction motor drives," in IEEE Trans. on Ind. Appl., vol. 29, no. 5, pp. 910-918, Sept.-Oct. 1993.
[74] F. D. Kieferndorf, M. Forster and T. A. Lipo, "Reduction of DC-bus capacitor ripple current with PAM/PWM converter," in IEEE Transactions on Industry Applications, vol. 40, no. 2, pp. 607-614, March-April 2004.
[75] R. L. de Araujo Ribeiro, C. B. Jacobina, E. R. C. da Silva and A. M. N. Lima, "Fault-tolerant voltage-fed PWM inverter AC motor drive systems," in IEEE Transactions on Industrial Electronics, vol. 51, no. 2, pp. 439-446, April 2004.
[76] S. Khwan-on, L. de Lillo, L. Empringham and P. Wheeler, "Fault-Tolerant Matrix Converter Motor Drives With Fault Detection of Open Switch Faults," in IEEE Transactions on Industrial Electronics, vol. 59, no. 1, pp. 257-268, Jan. 2012.
[77] S. Bolognani, M. Zordan and M. Zigliotto, "Experimental fault-tolerant control of a PMSM drive," in IEEE Transactions on Industrial Electronics, vol. 47, no. 5, pp. 1134-1141, Oct. 2000.
[78] M. Farhadi, M. T. Fard, M. Abapour and M. T. Hagh, "DC–AC Converter-Fed Induction Motor Drive With Fault-Tolerant Capability Under Open- and Short-Circuit Switch Failures," in IEEE Transactions on Power Electronics, vol. 33, no. 2, pp. 1609-1621, Feb. 2018.
[79] Yu-seok Jeong, Seung-Ki Sul, S. E. Schulz and N. R. Patel, "Fault detection and fault-tolerant control of interior permanent-magnet motor drive system for electric vehicle," in IEEE Transactions on Industry Applications, vol. 41, no. 1, pp. 46-51, Jan.-Feb. 2005.

[80] Mersen Reference Guide, “Semiconductor Fuse Applications Guide” https://www.mersen.de/sites/germany/files/publications-media/2-spm-semiconductor-fuse-applications-guide-mersen.pdf
[81] Bussmann Applications Guide, “High Speed Fuses”, https://www.cablejoints.co.uk/upload/Cooper_Bussman_High_Speed_Fuses___Applications.pdf
[82] K. Pietilainen, L. Harnefors, A. Petersson and H. -. Nee, "DC-Link Stabilization and Voltage Sag Ride-Through of Inverter Drives," in IEEE Transactions on Industrial Electronics, vol. 53, no. 4, pp. 1261-1268, June 2006.
[83] J. W. Kolar, T. M. Wolbank and M. Schrodl, "Analytical calculation of the RMS current stress on the DC link capacitor of voltage DC link PWM converter systems," 1999. Ninth International Conference on Electrical Machines and Drives, 1999, pp. 81-89.
[84] A. M. Hava, U. Ayhan and V. V. Aban, "A DC bus capacitor design method for various inverter applications," 2012 IEEE Energy Conversion Congress and Exposition (ECCE), 2012, pp. 4592-4599.
[85] M. Hinkkanen and J. Luomi, "Induction Motor Drives Equipped With Diode Rectifier and Small DC-Link Capacitance," in IEEE Trans. on Ind. Electr., vol. 55, no. 1, pp. 312-320, Jan. 2008.
[86] J. L. Soon and D. D. Lu, "Design of Fuse–MOSFET Pair for Fault-Tolerant DC/DC Converters," in IEEE Transactions on Power Electronics, vol. 31, no. 9, pp. 6069-6074, Sept. 2016.
[87] F. Blaabjerg, F. Iov, K. Ries, “Fuse Protection of IGBT Modules against Explosions”, Jour. of P. Electr., vol. 2, no. 2, pp. 88-94, 2002.
[88] F. Iov, F. Abrahamsen, F. Blaabjerg, K. Ries, H. Rasmussen, P. Bjornaa, “Fusing IGBT-based Inverters”, 2001 PCIM Conf., pp. 1-9.
[89] Cooper Bussmann, “High Speed Fuse Application Guide”, http://docplayer.net/24520978-High-speed-fuse-application-guide.html
[90] W. Wang, J. Zhang, M. Cheng and S. Li, "Fault-Tolerant Control of Dual Three-Phase Permanent-Magnet Synchronous Machine Drives Under Open-Phase Faults," in IEEE Transactions on Power Electronics, vol. 32, no. 3, pp. 2052-2063, March 2017.
[91] A. Tani, M. Mengoni, L. Zarri, G. Serra and D. Casadei, "Control of Multiphase Induction Motors With an Odd Number of Phases Under Open-Circuit Phase Faults," in IEEE Transactions on Power Electronics, vol. 27, no. 2, pp. 565-577, Feb. 2012.